Summer 2014

Measurement of Single and Double Spin Asymmetries in Semi-Inclusive Deep-Inelastic Scattering on Proton and Deuteron

Suman Bandhu Koirala
Old Dominion University

MEASUREMENT OF SINGLE AND DOUBLE SPIN ASYMMETRIES IN SEMI-INCLUSIVE DEEP-INELASTIC SCATTERING ON PROTON AND DEUTERON

by

Suman Bandhu Koirala
B.Sc. 1998, Tri Chandra College, Nepal
M.Sc. 2001, Tribhuvan University, Nepal
M.S. May 2010, Old Dominion University

A Dissertation Submitted to the Faculty of
Old Dominion University in Partial Fulfillment of the
Requirements for the Degree of

DOCTOR OF PHILOSOPHY

PHYSICS

OLD DOMINION UNIVERSITY
August 2014

Approved by:

S. E. Kuhn (Director)

A. Radyushkin (Member)

S. Boeltmann (Member)

A. Godunov (Member)

N. Diawara (Member)

ABSTRACT

MEASUREMENT OF SINGLE AND DOUBLE SPIN ASYMMETRIES IN SEMI-INCLUSIVE DEEP-INELASTIC SCATTERING ON PROTON AND DEUTERON

Suman Bandhu Koirala
Old Dominion University, 2014
Director: Dr. S. E. Kuhn

The EG1-DVCS experiment with CLAS at Jefferson Lab collected semi-inclusive pion electro-production data on longitudinally polarized solid state NH_3 and ND_3 targets with longitudinally polarized electrons of approximately 6 GeV energy. Data on all three pion channels, π^+, π^- and π^0, were collected simultaneously. The charged pions were identified by their time-of-flight information whereas the neutral pions were reconstructed from the invariant mass of two photons. The experiment covered a wide kinematic range: $1\,\mathrm{GeV}^2 \leq Q^2 \leq 3.2\,\mathrm{GeV}^2$, $0.12 \leq x_B \leq 0.48$, $0.0\,\mathrm{GeV} \leq P_{h\perp} \leq 1.0\,\mathrm{GeV}$ and $0.3 \leq z \leq 0.7$. The beam single (A_{LU}), target single (A_{UL}) and beam-target double (A_{LL}) spin azimuthal asymmetries in semi-inclusive deep-inelastic scattering (SIDIS) off the proton and the deuteron extracted from the data are presented. The results of the azimuthal asymmetries for the proton are presented as a function of two variables: (x_B, $P_{h\perp}$), (z, $P_{h\perp}$) and (x_B, z). Due to limited statistics, the azimuthal asymmetries for the deuteron are presented as a function of a single variable for the variables x_B, z and $P_{h\perp}$. Some theoretical and phenomenological predictions as well as earlier published results are compared with the results from this analysis. All the results are plotted and suitably tabulated for further analysis.

The SIDIS azimuthal asymmetries are convolutions of fragmentation functions and transverse momentum dependent parton distribution functions (TMDs). The TMDs describe transverse momenta and spins of quarks and gluons inside nucleons. They open a window on the contribution of the orbital angular momentum of the quarks and gluons to the total spin of the nucleons. The results presented in this work are sensitive to these leading twist TMDs: f_1, g_1, $h_{1L}^{\perp}$ and $h_1^{\perp}$. The significant precision of the results from this analysis will highly constrain the extractions of the associated TMDs which will substantially contribute towards further investigation into the partonic structure of nucleon intrinsic angular momentum.

ACKNOWLEDGMENTS

I would not have been able to reach this stage without the support, guidance and inspirations of many people in my life whom I would like to thank here. I am grateful to my parents who valued education above all else and worked hard their entire life, to my wife for the constant support and peaceful companionship and to my daughter for the parental pride.

I am grateful to Prof. Sebastian Kuhn for his perseverant guidance and empathetic encouragement, to Dr. Volker Burkhart, Prof. Keith Griffoen, Dr. Peter Bosted, Dr. Harut Avakian and Dr. FX Giroud for their suggestions and constructive criticisms. I am also grateful to Professors Anatoly Radyushkin, Rocco Schiavilla, Jozef Dudek, Ian Balitsky, Geoff Krafft, Alex Godunov, Moskov Amaryan, Stephen Bueltmann, Gail Dodge, Charles Hyde, Yelena Prok, Larry Weinstein, Charles Sukenik, Lepsha Vuskovic and Prof. Norou Diawara for their help in many ways, to Lisa Okun, Annette Guzman-Smith and Malin Delicia for the excellent administrative support, to Tom Hartlove for the opportunity to work on the Drift Chambers and to my Eg1-Dvcs colleagues Gary Smith, Sergio Pereria and Silvia Pisano for their support.

I am very thankful to my childhood friends Chandre Lama, Dinesh Kadel, Ravi Shrestha, Kavi Shrestha, Dipen Kunwar, Ranjan Kunwar, Shiva Raj and Hardhik Gurung for the soothing nostalgia. I am also thankful to Sanjaya Regmi, Daniel Tuladhar, Dipan Gurung, Ram Gurung, Dil Gurung, Ash Kumar Gurung, Rajan Joshi, Ekraj Sharma, Janak Malla, Prakash Shrestha, Gambhir Ranjit, Sudeep Poudel, Niraj Tiwari, Kesh Pun, Krishna Adhikari, Sanjaya Prabhakar, Bipin Choudhary, Palden Sherpa, Mike Mayer, Mladen Dordevic and Christian Schultz for their friendship.

I would like to thank Michael Hoschele, Georg Widhalm, Netra Bantawa, Clarence Rioux, Phurba Sherpa, Aidan Warlow, Shira Daryn, Yedu Sharma, Shanker Chimuria, Ujjwal Amatya, Naresh Pradhan, Neelam Gurung, Rishiram Poudel, Nabin Koirala, Binood Neupane, Rajan Neupane, Kamala Baral and Deepak Joshi for their help.

I would also like to thank Christoph Adolph, Nevzat Guler, Robert Fersh, Wesley Gohn, Alessandro Bacchetta, Hidekazu Tanaka, Carmine Elia and Federica Sozzi for their excellent PhD theses. Their work offered me an excellent guideline.

TABLE OF CONTENTS

LIST OF TABLES

LIST OF FIGURES

CHAPTER 1

MOTIVATION

This chapter starts with a short introduction on the historical background and the motivation of this analysis. The theoretical descriptions relevant to this analysis follow the introduction. For completeness, the theoretical descriptions of other related basic scattering processes precede the theoretical descriptions of the main focus of the analysis, semi-inclusive deep-inelastic scattering. Relations between the experimental observables and various functions describing the underlying nucleon structure are also established with the goal of giving the reader a broad overview of the field with a minimum of technical details. An overview of the experimental results are presented towards the end. Finally, some of the theoretical predictions relevant for this analysis are presented. Most of the theoretical developments in this chapter follow the works by M. Anselmino *et al.* [1] and A. Bacchetta [2], among others.

1.1 INTRODUCTION

In 1911 Rutherford discovered the atomic nucleus; he found out that almost all the mass of an atom is concentrated in the nucleus. A few years later, experiments found that the nucleus itself consists of protons and neutrons, collectively known as nucleons. About thirty years after the discovery of nucleons, it was found that the nucleons themselves are composed of fundamental particles called quarks which are bound together by gluons. The quarks are fermions whereas the gluons are bosons; they are collectively referred to as partons. Fermions have half-integer spin whereas bosons have integer spin. Exploration of the underlying principles of the structure of nucleons in terms of the partons and their interactions is currently a very active research area in particle physics.

Quantum chromodynamics (QCD) is a theory of the fundamental force known as strong interaction which explains the interactions between quarks and gluons. The theory is an integral part of the Standard Model of particle physics and there exists numerous experimental evidence for QCD. The Standard Model is a theoretical

framework that encapsulates the information about how the fundamental particles and the different forces are related to each other. However, nucleon properties like spin, quark content, charge, magnetic moment and charge radius cannot be explained from its first principles. We are still far from fully understanding QCD because we have not been able to rigorously derive quark confinement and bound state properties. As it stands, experiment is the most precise way to extract information on confinement and binding in nucleons and hadrons. One of the possible ways towards a full understanding of QCD is to investigate the properties of nucleons in more detail. One of the most important areas of investigation is their multi-dimensional structures in position and momentum space. Reconstructing the multi-dimensional picture of the nucleons allows us to access their properties at the fundamental level. One of such properties this analysis aims to address is the partonic structure of the nucleons' intrinsic angular momentum also known as "spin".

Results from several experiments carried out in the last three decades show that the contribution from quark spins ($\frac{1}{2}\Delta\Sigma$) accounts for only about 30% of the spin of a nucleon [3]. This staggering discovery was termed the "nucleon spin crisis". This discovery lead to a prediction that the remaining nucleon spin must be accounted for by quark orbital angular momentum (L_q), gluon orbital angular momentum (L_g) and by gluon spin (ΔG). The Jaffe and Manohar spin sum rule [3] equates nucleon spin and its various contributions as

$$\frac{1}{2} = \frac{1}{2}\Delta\Sigma + L_q + L_g + \Delta G. \tag{1}$$

The contribution from the gluon spin, ΔG, as measured so far has an upper limit of about 50% [4]. So it appears that the orbital angular momenta of the quarks and gluons could be significant contributions to the spin of a nucleon. So far L_q and L_g have not been measured. L_q and L_g can be inferred in principle from measurements of the partons multi-dimensional distribution in position and momentum space. For three dimensional structure in momentum space, one of the dimensions is the longitudinal momentum fraction of the partons; the other two dimensions are the orthogonal momentum components of the partons in the transverse plane, $\boldsymbol{p}_T$. The longitudinal direction is defined as the direction opposite to that of the probe, a virtual photon in the case of electron and nucleon scattering. It is assumed that the momentum components in the transverse plane are responsible for L_q, however, the quantitative correlation between the orbital angular momentum and the parton's multidimensional structure is an ongoing theoretical investigation.

Information on the three dimensional structure of the nucleon in terms of its guarks and gluons are encoded in the so-called Parton Distribution Functions (PDF). In particular, Transverse Momentum Dependent (TMD) PDFs describe the three dimensional structure in momentum space, while Generalized Parton Distributions (GPDs) describe the joint distribution in longitudinal momentum and transverse, two-dimensional, position space. These new types of PDFs open a window on the contribution of the orbital angular momentum of the quarks and gluons to the total spin of a nucleon. The TMDs can be accessed through the semi-inclusive deep-inelastic scattering (SIDIS) process. In SIDIS, a lepton scatters off an individual quark in a nucleon and the scattered electron and a hadron carrying the struck quark are detected in the final state. The GPDs can be accessed from exclusive processes such as deeply virtual Compton scattering (DVCS) and deeply virtual meson production (DVMP). This analysis is concerned with the measurement of SIDIS asymmetries for longitudinally polarized proton and deuteron targets with a longitudinally polarized electron beam.

Most of the currently known detailed informations about nucleon structure have been obtained from various types of lepton-nucleon scattering experiments. Different types of scattering processes access different aspects of the nucleon structure. Before the discussions of semi-inclusive deep-inelastic scattering, elastic and inclusive deep-inelastic scattering and the nucleon structure functions accessible from those processes are discussed in the following sections. The next section gives a brief description of the most general type of nucleon structure, Wigner distributions.

1.2 WIGNER DISTRIBUTIONS

In addition to color, charge, spin and flavor, partons within nucleons have six degrees of freedom, three in momentum and three in position space with respect to nucleon center of mass. Wigner distributions are the quantum mechanical constructions analogous to the classical probability density function in six dimensional phase-space [6]. They are the most general description of the nucleon structure in terms of position and momentum distributions of partons in a nucleon. However, due to quantum mechanical uncertainty, they cannot be strictly considered as probability densities, so they are referred to as the quasi-probability distributions. The expectation value of any physical observable can be extracted from the Wigner distributions. Due to this predictive property of Wigner distributions, it can be inferred that they

encode the maximum information on the partonic structure of a nucleon.

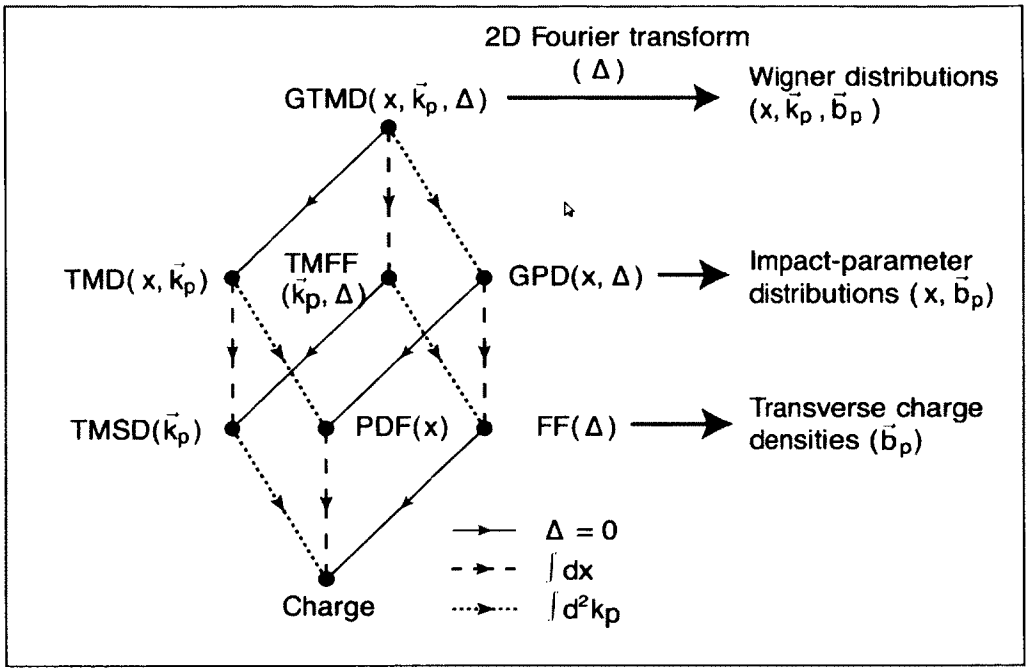

FIG. 1: Representation of the parton distributions and form factors as a projection of the GTMD. This figure is taken from [5], where it was adapted from [6]. The variable x is the longitudinal momentum fraction, $\vec{k_p}$ is the parton transverse momentum, Δ is the transverse momentum transfered to the nucleon and $\vec{b_p}$ is the impact parameter.

Due to Heisenberg uncertainty principle, the position and momentum distributions of partons cannot be measured simultaneously to an arbitrary precision. Hence position and momentum distribution measurements must be made separately. Parton position distributions in the two-dimensional transverse plane are accessed from generalized parton distributions (GPDs) which are Wigner distributions integrated over $\vec{k_p}$ and are measured from deeply virtual exclusive processes such as deeply virtual Compton scattering (DVCS) and deeply virtual meson production (DVMP). The nucleon electromagnetic form factors (FFs), which are integrals of GDPs over all x_B and which describe the spatial distributions of electric charge and current inside the nucleon, can be accessed from elastic electron-proton scattering. Parton momentum distributions in three dimensions are described by transverse momentum dependent parton distribution functions (TMDs) which are integrals over $\vec{b_p}$ of Wigner distributions and can be extracted from the studies of semi-inclusive deep-inelastic scattering (SIDIS) process. Parton longitudinal momentum fraction distributions (PDFs) are

integrals of TMDs over $\vec{k}_p$ and can be measured in various deep-inelastic scattering (DIS) processes.

Figs. 1 shows how form factors, parton distribution functions, generalized parton distribution functions and transverse momentum dependent parton distribution functions stem from the same generalized transverse momentum distribution (GTMD) which is related to the Wigner distribution by a Fourier transform. In the figure, x is the longitudinal momentum fraction, $\vec{k}_p$ is the parton transverse momentum, Δ is the transverse momentum transfered to the nucleon and $\vec{b}_p$ is the impact parameter or the position in the transverse plane defined with respect to the center of mass of the nucleon.

1.3 ELASTIC LEPTON SCATTERING

In an elastic scattering process, the particles before and after the scattering are the same. In the four momentum representation, a lepton-nucleon elastic scattering process in the target rest frame can be written as

$$l(E,\vec{k}) + N(M,\vec{0}) \rightarrow l(E',\vec{k'}) + N(E_N,\vec{p_N}), \tag{2}$$

where the quantities within parentheses are the respective four-momenta of lepton (l) and nucleon (N). For elastic scattering of relativistic electrons from point-like charged particle of charge q, the theoretical cross-section is given by the Mott cross-section relation [7]

$$\frac{d\sigma}{d\Omega} = \frac{\alpha^2}{4E^2 \sin^4 \theta/2} \frac{E'}{E} \cos^2 \theta/2, \tag{3}$$

where $d\Omega$ is the differential solid angle of the scattered electron, $\alpha = e^2/4\pi$ is the fine structure constant, θ is the scattering angle of the electron, E and E' are the energies of the electron before and after scattering. The comparison between the Mott cross-section and the experimental results for electron-proton scattering, taken from one of the ground-breaking papers in particle physics [8], are shown in Fig. 2. Later studies of the disagreement between the experimental curve and the theoretical curve showed that the protons are not point-like but have internal structure [9]. The internal structure of a proton probed by elastic scattering is described by two structure functions: the electric (G_E) and magnetic (G_M) form factors. The Rosenbluth cross-section [7] gives the relation between the Mott cross-section and

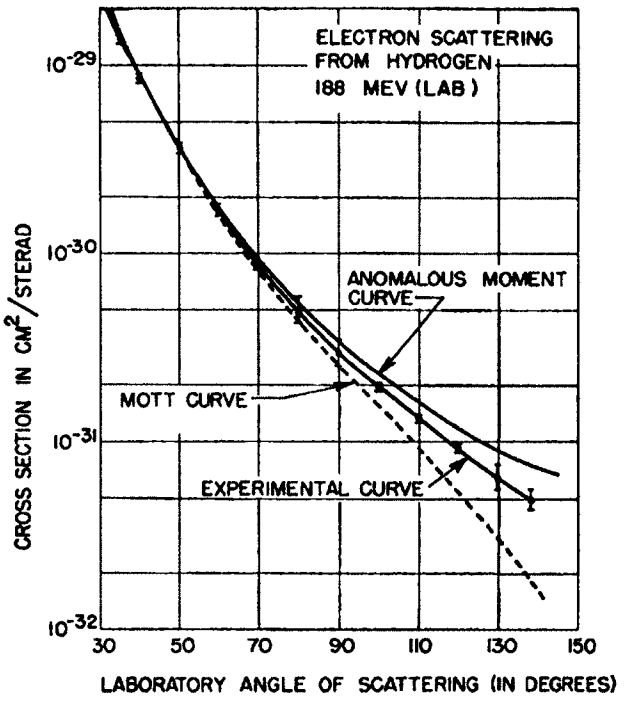

FIG. 2: The experimental curve, Mott curve and the curve taking into account the anomalous magnetic moment for electron scattering from the proton [8].

the experimental results as:

$$\frac{d\sigma}{d\Omega} = \left(\frac{d\sigma}{d\Omega}\right)_{\text{Mott}} \left[\frac{G_E^2(Q^2) + G_M^2(Q^2)\frac{Q^2}{4M^2}}{1+\frac{Q^2}{4M^2}} + \frac{Q^2}{2M^2} G_M^2(Q^2)\tan^2\frac{\theta}{2}\right], \qquad (4)$$

where Q^2 is the negative of the square of the four momentum transfer from the electron to the proton. The two form factors describe the electric and magnetic charge or the electrical current distributions inside the proton. The form factors are extracted from experimentally measured cross-sections and the Mott cross-sections at fixed values of Q^2 for various electron scattering angles. At low Q^2, the Fourier transform of the form factors gives the spatial distributions of electric charges and currents in the same way as the Fourier transform of the diffraction pattern of light gives the spatial distributions of its source.

1.4 INCLUSIVE DEEP-INELASTIC SCATTERING

Inclusive deep-inelastic scattering is a very common tool to study nucleon structure; the scattering process can be represented as

$$l(l) + N(P) \rightarrow l(l') + X, \tag{5}$$

where l and N respectively denote lepton beam and nucleon target; their four-momenta are given in the parentheses. In the experiment described here, the lepton is the electron. In an inclusive process, only the scattered lepton is detected; the hadronic final states are not detected. The lowest order Feynman diagram of an electron-nucleon deep-inelastic scattering process is shown in Fig. 3. In the process, in the same way as in case of the elastic scattering mentioned in the earlier section, Q^2 is defined as the negative of the squared four momentum transfer of the electron, i.e. $Q^2 = -q^2$, where $q = l - l'$. In a deep-inelastic process one typically requires $Q^2 > 1\,\mathrm{GeV}^2$ and the invariant mass of the hadronic final-state $W > 2\,\mathrm{GeV}$. Two new variables x_B and y are defined as:

$$x_B = \frac{Q^2}{2Pq} \tag{6}$$

and

$$y = \frac{Pq}{Pl}. \tag{7}$$

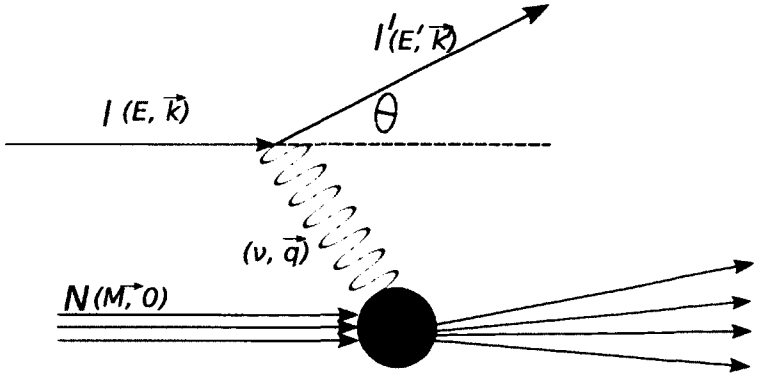

FIG. 3: Feynman diagram of an electron-nucleon inclusive deep-inelastic scattering process. The four-momenta of the incident and scattered electron are represented by l and l'. θ is the scattering angle of the electron in the Lab frame.

Let us denote the lepton helicity by λ_e, target spin vector by $\vec{S}$, the transverse component of $\vec{S}$ with respect to the photon momentum by $S_\perp$ and the component

of $\vec{S}$ along the virtual photon, equivalently the negative z direction, by $S_{\parallel}$. These quantities are shown in Fig. 7. The polarized electron-nucleon inclusive cross-section in a single photon exchange approximation can be written in the most general way as the contraction between leptonic and hadronic tensor as [2]:

$$\frac{d^3\sigma}{dx_B dy d\phi_s} = \frac{\alpha^2}{2sx_B Q^2} L_{\mu\nu}(l, l', \lambda_e) 2MW^{\mu\nu}(q, P, S), \tag{8}$$

where M is the mass of the nucleon. For a longitudinally polarized lepton in the massless limit, $m_e << E$, the leptonic tensor can be written as:

$$L_{\mu\nu} = \sum_{\lambda'_e} \Big(\bar{u}(l', \lambda'_e)\gamma_\mu u(l, \lambda_e)\Big)^* \Big(\bar{u}(l', \lambda'_e)\gamma_\mu u(l, \lambda_e)\Big) \tag{9}$$

where $u(p)$ are the Dirac spinors. The leptonic tensor can be further expressed as a sum of symmetric and antisymmetric parts as:

$$L_{\mu\nu} = -Q^2 g_{\mu\nu} + 2(l_\mu l'_\nu + l'_\mu l_\nu) + 2i\lambda_e \epsilon_{\mu\nu\rho\sigma} l^\rho l'^\sigma, \tag{10}$$

where $\epsilon_{\mu\nu\rho\sigma}$ is the Levi-Civita tensor. The first two terms in the above equation are symmetric with respect to the interchange of μ and ν. In the case of an unpolarized lepton beam, the antisymmetric part vanishes. All the components of the leptonic tensor can be calculated by means of perturbative quantum electrodynamics; these components contain all the information on the leptonic probe. The hadronic tensor contains all the information on the hadronic target; its components cannot be calculated from first principles but they can be suitably parameterized and can be extracted from experimental data. In this case, all the possible transition amplitudes from the target ground state to all its excited states should be considered. The hadronic tensor in Equation 8 can be parameterized in terms of four structure functions, $F_T(x_B, Q^2)$, $F_L(x_B, Q^2)$, $g_1(x_B, Q^2)$ and $g_2(x_B, Q^2)$ as [2]:

$$\begin{aligned}
&2MW^{\mu\nu}(q, P, S) = \\
&\frac{1}{x_B}\Big[- g_\perp^{\mu\nu} F_T(x_B, Q^2) + \hat{t}^\mu \hat{t}^\nu F_L(x_B, Q^2) \\
&+ iS_L \epsilon_\perp^{\mu\nu} 2x_B \left(g_1(x_B, Q^2) - \gamma^2 g_2(x_B, Q^2)\right) \\
&+ i\hat{t}^\mu \epsilon_\perp^\nu S_\rho 2x_B \gamma \left(g_1(x_B, Q^2) - g_2(x_B, Q^2)\right) \Big],
\end{aligned} \tag{11}$$

where $\gamma = 2Mx_B/Q$ and $\hat{t}^\mu = T^\mu/Q\sqrt{\kappa}$. The quantities used in the expression for $\hat{t}^\mu$ are defines as:

$$\kappa = 1 + \frac{4M^2 x_B^2}{Q^2}, \tag{12}$$

$$T^{\mu} = q^{\mu} + 2x_B P^{\mu}. \tag{13}$$

The cross-section for the inclusive deep-inelastic scattering from the contraction of leptonic and hadronic tensors is given by [2]:

$$\frac{d\sigma}{dx_B dy d\phi_s} = \frac{2\alpha^2}{x_B y Q^2} \frac{y^2}{2(1-\varepsilon)} \Big[F_T + \varepsilon F_L + S_{\parallel} \lambda_e \sqrt{1-\varepsilon^2} 2x_B (g_1 - \gamma^2 g_2) - |\mathbf{S}_{\perp}| \lambda_e \sqrt{2\varepsilon(1-\varepsilon)} \cos\phi_S 2x_B \gamma (g_1 + g_2) \Big], \tag{14}$$

where the ratio of longitudinal and transverse photon flux, ε, is calculated by: $\varepsilon = (1-y)/(1-y+\frac{1}{2}y^2)$.

In the quark parton model of the nucleons, nucleons consist of point-like spin $\frac{1}{2}$ particles called partons. In the infinite momentum frame, the partons move along the nucleon direction with negligible transverse momentum. In a scattering process at high Q^2, the partons can be resolved, and the process can be considered as the absorption of the virtual photon on the individual partons. In this case, the Bjorken scaling variable, x_B, represents the longitudinal momentum fraction of the nucleon carried by the struck quark. The probability of finding a parton with a longitudinal momentum fraction of the nucleon in the interval dx_B is given by $f_1^q(x_B)dx_B$, where $f_1^q(x_B)$ is the parton distribution function which is shown in Fig. 4. For the scattering off a longitudinally polarized nucleon, the parton distribution function $g_{1L}^q(x_B)$ is the difference in probability of finding a parton with spin parallel or anti-parallel with the polarization of the nucleon; $g_1(x_B)$ is shown in Fig. 5. The structure functions in Equation 14 can be expressed in terms of the parton distribution functions and the charge of the partons, e_q, as:

$$F_T = x_B \sum_q e_q^2 f_1^q(x_B), \tag{15}$$

$$F_L = 0, \tag{16}$$

$$g_1 = \frac{1}{2} \sum_q e_q^2 g_{1L}^q(x_B), \tag{17}$$

and

$$g_2 = 0. \tag{18}$$

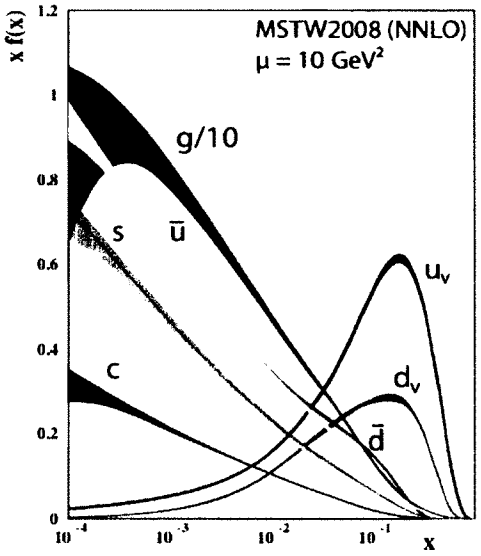

FIG. 4: Parton distribution functions, $f_1^q(x_B)$, for proton. Figs. from [10].

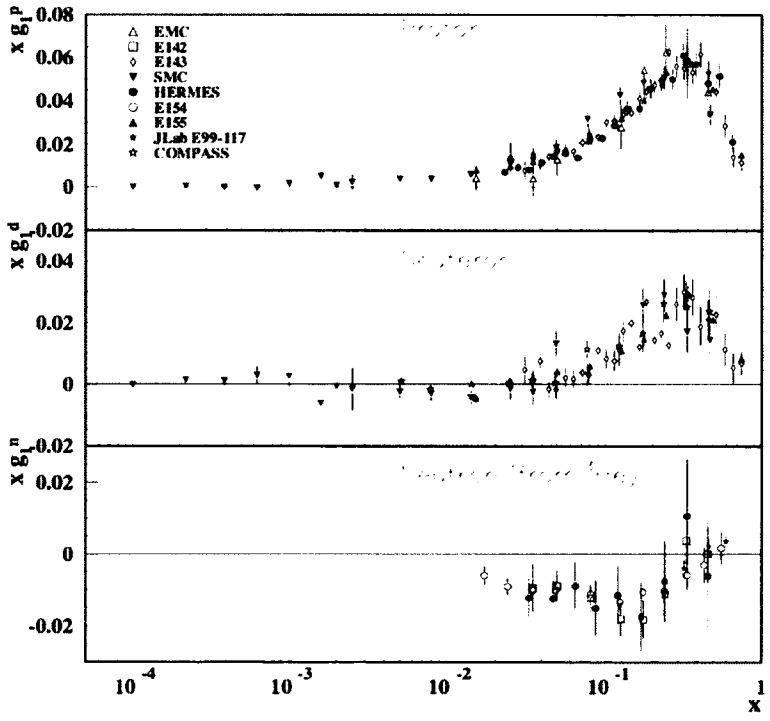

FIG. 5: Spin dependent structure function $g_1(x_B)$. Figs. from [10].

1.5 SEMI-INCLUSIVE DEEP-INELASTIC SCATTERING

In semi-inclusive deep inelastic scattering, a lepton scatters from an individual quark of a nucleon and the lepton and a hadron are detected in the final state. The kinematics of the process are selected such that the hadron has a relatively high probability of carrying the struck quark. Since the detected hadron carries the struck quark, the transverse momentum of the struck quark inside the nucleon is transferred to the hadron. So SIDIS is an ideal process to access the transverse momentum of the partons in the nucleons. In this analysis, the lepton is an electron and the hadrons are the three charged states of the π mesons, π^+, π^- and π^0. In symbols the process is written as $\vec{N}(\vec{e}, e'\pi^{+/-/0})X$. To define the relevant kinematic variables of the reaction, specific for the SIDIS process, we write:

$$l(E, \vec{k}) + N(M, \vec{0}) \rightarrow l(E', \vec{k'}) + h(E_h, \vec{P}_h) + X \tag{19}$$

where l denotes the lepton beam, N the nucleon target, h the detected hadron and X denotes the remainder of the hadronic final state. Their four-momenta are represented by the various symbols in the respective parentheses. The nucleon and hadron masses are represented by M and M_h. The Feynman diagram for the semi-inclusive deep inelastic scattering is shown in Fig. 6. The geometry of the process is shown in Fig. 7; the angle between the lepton and the hadron planes, ϕ_h, in the figure is consistent with the Trento conventions [11].

The following equations define some of the relevant kinematic variables of a semi-inclusive deep-inelastic scattering process in the lab-frame.

$$\nu = E - E', \tag{20}$$

$$z = \frac{E_h}{\nu}, \tag{21}$$

$$\vec{P}_{h\perp} = \vec{P}_h - \left(\vec{P}_h \cdot \hat{q}\right) \hat{q}, \tag{22}$$

In addition to the above variables and the variables defined in Section 1.4, a variable, M_x, is defined as the invariant mass of the undetected final state particles.

$$M_x^2 = \left[(\nu, \vec{q}) + (M, \vec{0}) - (E_h, \vec{P}_h)\right]^2 \tag{23}$$

As in the case of inclusive deep-inelastic scattering described in section 1.4, the polarized electron-nucleon semi-inclusive cross-section in a single photon exchange

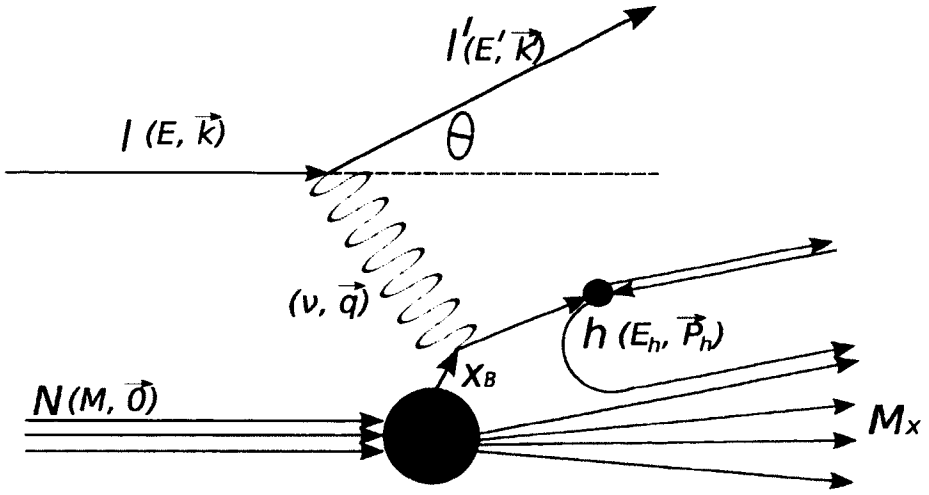

FIG. 6: Feynman diagram of the semi-inclusive deep inelastic scattering process. The symbols in parentheses are the four-momenta of the respective particles.

approximation can be written in the most general way as the contraction between leptonic and hadronic tensors as [2]

$$\frac{d^6\sigma}{dx_B dy dz d\phi_s d^2P_{h\perp}} = \frac{\alpha^2}{4zsx_BQ^2} L_{\mu\nu}(l, l', \lambda_e) 2MW^{\mu\nu}(q, P, S, P_h). \tag{24}$$

The variables are as same as described in the section 1.4. In that section, the expression for the leptonic tensor is also described. The hadronic tensor for semi-inclusive scattering is give by

$$2MW^{\mu\nu}(q, P, S, P_h) = \frac{1}{(2\pi)^4} \sum_{\chi'} \int \frac{d^3\boldsymbol{P}_{\chi'}}{2P^0_{\chi'}} 2\pi\delta^{(4)}(q + P - P_{\chi'} - P_h) H^{\mu\nu}(P, S, P_{\chi'}, P_h), \tag{25}$$

$$H^{\mu\nu}(P, S, P_{\chi'}, P_h) = \langle P, S \mid J^\mu(0) \mid P_h, \chi' \rangle \langle P_h, \chi' \mid J^\nu(0) \mid P, S \rangle. \tag{26}$$

In a semi-inclusive deep-inelastic process, the hadronic tensor is parameterized by 18 structure functions [12]. The resulting differential cross-section from the contraction of the leptonic and hadronic tensors in terms of the 18 structure functions is given

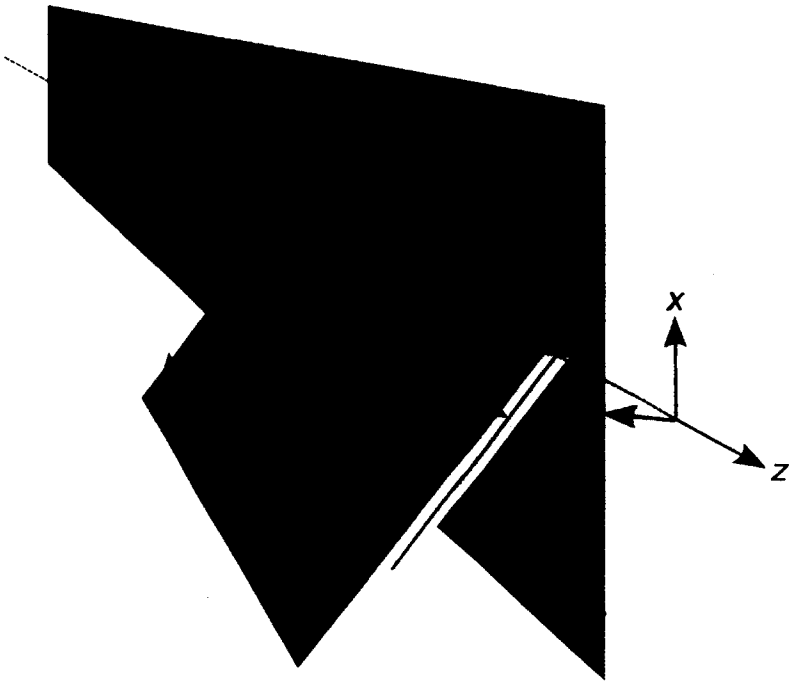

FIG. 7: Scattering planes of the semi-inclusive deep inelastic scattering reaction. The angle between the leptonic and hadronic planes are represented by ϕ_h.

by

$$
\begin{aligned}
&\frac{d\sigma}{dx_B dy d\phi_s dz d\phi_h dP_{h\perp}^2} = \\
&\frac{\alpha^2}{x_B y Q^2}\frac{y^2}{2(1-\varepsilon)}\Big[F_{UU,T} + \varepsilon F_{UU,L} + \sqrt{2\varepsilon(1+\varepsilon)}\cos\phi_h F_{UU}^{\cos\phi_h} \\
&+ \varepsilon\cos(2\phi_h)F_{UU}^{\cos 2\phi_h} + \lambda_e\sqrt{2\varepsilon(1-\varepsilon)}\sin\phi_h F_{LU}^{\sin\phi_h} \\
&+ S_\parallel\Big\{\sqrt{2\varepsilon(1+\varepsilon)}\sin\phi_h F_{UL}^{\sin\phi_h} + \varepsilon\sin(2\phi_h)F_{UL}^{\sin 2\phi_h}\Big\} \\
&+ S_\parallel\lambda_e\Big\{\sqrt{1-\varepsilon^2}F_{LL} + \sqrt{2\varepsilon(1-\varepsilon)}\cos\phi_h F_{LL}^{\cos\phi_h}\Big\} \\
&+ |\boldsymbol{S}_\perp|\Big\{\sin(\phi_h-\phi_s)\left(F_{UT,T}^{\sin(\phi_h-\phi_s)} + \varepsilon F_{UT,L}^{\sin(\phi_h-\phi_s)}\right) \\
&+ \varepsilon\sin(\phi_h+\phi_S)F_{UT}^{\sin(\phi_h+\phi_S)} + \varepsilon\sin(3\phi_h-\phi_S)F_{UT}^{\sin(3\phi_h-\phi_S)} \\
&+ \sqrt{2\varepsilon(1+\varepsilon)}\sin\phi_S F_{UT}^{\sin\phi_S} + \sqrt{2\varepsilon(1+\varepsilon)}\sin(2\phi_h-\phi_S)F_{UT}^{\sin(2\phi_h-\phi_S)}\Big\} \\
&+ |\boldsymbol{S}_\perp|\lambda_e\Big\{\sqrt{1-\varepsilon^2}\cos(\phi_h-\phi_s)F_{LT}^{\cos(\phi_h-\phi_S)} + \sqrt{2\varepsilon(1-\varepsilon)}\cos\phi_S F_{LT}^{\cos\phi_S} \\
&+ \sqrt{2\varepsilon(1-\varepsilon)}\cos(2\phi_h-\phi_s)F_{LT}^{\cos(2\phi_h-\phi_S)}\Big\}\Big]. \qquad (27)
\end{aligned}
$$

In Equation 27, the structure functions are represented by the letter F. The first and the second subscripts in the structure functions are the beam and target polarizations; the third subscript is the virtual photon polarization. The trigonometric functions in the superscripts represent the azimuthal moments of the structure functions.

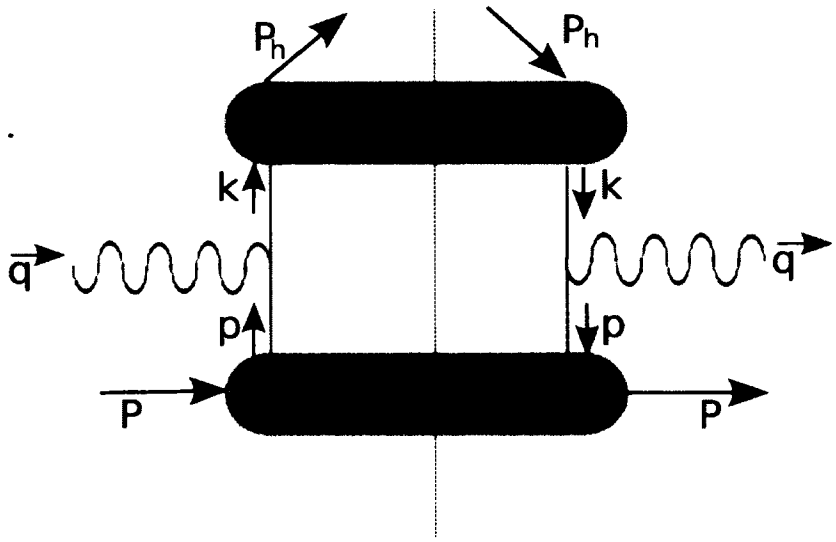

FIG. 8: SIDIS bull diagram. Φ is the quark-quark correlator and Δ is the fragmentation correlator.

In the partonic model, the virtual photon scatters from a single quark inside the nucleon. In current fragmentation, the struck quark is tagged in the final state hadron. The scattering process can be factorized into two soft hadronic parts connected by a hard scattering part as shown by the bull diagram in Fig. 8. Taking into account only the Born-level contribution to the hard scattering, the hadronic tensor can be written as [2]

$$2MW^{\mu\nu}(q,P,S,P_h) = \sum_q e_q^2 \int d^4p d^4k \delta^{(4)}(p+q-k) \times \mathrm{Tr}\left(\Phi(p,P,S)\gamma^\mu \Delta(p,P,S)\right), \tag{28}$$

where Φ and Δ are the quark-quark correlation function and fragmentation function respectively, p is the momentum of the parton in the distribution function and k is the momentum of the fragmenting parton. The quark-quark correlation function and

fragmentation function are defined as

$$\Phi_{ij}(p,P,S) = \frac{1}{(2\pi)^4}\int d^4\xi e^{ip\cdot\xi}\langle P,S \mid \bar{\psi}_i(0)\psi_j(\xi) \mid P,S\rangle$$
$$= \sum_X \int \frac{d^3\boldsymbol{P}_X}{(2\pi)^3 2P_X^0}\langle P,S \mid \bar{\psi}_i(0) \mid X\rangle\langle X \mid \bar{\psi}_j(0) \mid P,S\rangle\delta^{(4)}(P-p-P_X), \qquad (29)$$

$$\Delta_{kl}(k,P_h) = \frac{1}{(2\pi)^4}\int d^4\xi e^{ik\cdot\xi}\langle 0 \mid \psi_k(\xi) \mid P_h\rangle\langle P_h \mid \bar{\psi}_l(0) \mid 0\rangle$$
$$= \sum_Y \int \frac{d^3\boldsymbol{P}_Y}{(2\pi)^3 2P_Y^0}\langle 0 \mid \bar{\psi}_k(0) \mid P_h,Y\rangle\langle P_h,Y \mid \bar{\psi}_l(0) \mid 0\rangle\delta^{(4)}(k-P_h-P_Y). \qquad (30)$$

In a nucleon, multi-parton correlations are proportional to $1/Q^2$. In the power series expansion of the structure functions in terms of $1/Q^2$, the contributions from the leading terms are called the leading twist and the contributions from the non-leading terms are called the higher twist. At higher Q^2, the non-leading terms can be neglected. In the leading twist the expression for the hadronic tensor reduces to a compact expression as

$$2MW^{\mu\nu}(q,P,S,P_h) = 2z\int [\mathrm{Tr}(\Phi(x_B,\boldsymbol{p}_T,S)\gamma^\mu\Delta(z,\boldsymbol{k}_T)\gamma^\nu)]\, d^2\boldsymbol{p}_T d^2\boldsymbol{k}_T\delta^{(2)}(\boldsymbol{p}_T+\boldsymbol{q}_T-\boldsymbol{k}_T) \qquad (31)$$

The functions $\Phi(x_B,\boldsymbol{p}_T,S)$ and $\Delta(z,\boldsymbol{k}_T)$ are the transverse momentum dependent correlation functions, where the symbol $\boldsymbol{p}_T$ is used to denote the parton's transverse momentum in the distribution function and the symbol $\boldsymbol{k}_T$ is used to denote the transverse momentum of the fragmenting parton with respect to the final hadron. The function $\Phi(x_B,\boldsymbol{p}_T,S)$ describes the parton confinement inside the hadrons. The function $\Delta(z,\boldsymbol{k}_T)$, which is also called fragmentation correlation function, describes the way a struck quanta fragments into a hadron, a process known as hadronization. The fragmentation correlation function can be further expressed as

$$\Delta(z,\boldsymbol{k}_T) = \left\{D_1(z,\boldsymbol{k}_T^2) + iH_1^\perp(z,\boldsymbol{k}_T^2)\frac{\not{k}_T}{M_h}\right\}\frac{\not{n}_-}{2}. \qquad (32)$$

In the above equation, Feynman slash is introduced. It is defined as $\not{A} = \gamma^\mu A_\mu$, where A is a covariant vector and γs are the Dirac matrices. The unit vectors along the light cone components p^+ and p^- are represented by n^+ and n^- respectively. The function $D_1(z,\boldsymbol{k}_T^2)$ is the unpolarized transverse momentum dependent fragmentation function; the function $H_1^\perp(z,\boldsymbol{k}_T^2)$ is known as the Collins function [13]. The function

$D_1(z, \boldsymbol{k}_T^2)$ is the probability that the struck quark will hadronize into a final state hadron with energy z and transverse momentum $\boldsymbol{k}_T$ relative to the struck quark direction. It depends both on the quark flavor and the hadron type. Similarly $H_1^\perp(z, \boldsymbol{k}_T^2)$ describe the same process for a transversely polarized quark. Including the target polarization, the transverse momentum dependent correlation function becomes

$$\Phi(x_B, p_T^2) = \frac{1}{2}\Big[f_1 \not{n}_+ + f_{1T}^\perp \frac{\epsilon_T^{\rho\sigma} S_{T\rho} p_{T\sigma}}{M} \not{n}_+ + g_1 \gamma_5 \not{n}_+ + h_{1T}^\perp \frac{[\not{S}_T, \not{n}_+]\gamma_5}{2} + h_1^\perp \frac{[\not{p}_T, \not{n}_+]\gamma_5}{2M} + i h_1^\perp \frac{[\not{p}_T, \not{n}_+]}{2M}\Big], \tag{33}$$

where $\epsilon_T^{\alpha\beta} = \epsilon^{\alpha\beta\rho\sigma} n_{+\rho} n_{-\rho}$. The distribution functions on the right hand side of Equation 33 depend on x_B and p_T^2; they are referred to as the transverse momentum dependent parton distribution functions (TMDs). The probablistic interpretation of those TMDs are shown in Fig. 9. Some of the TMDs will be discussed very briefly in the next section.

1.6 TRANSVERSE MOMENTUM DEPENDENT PARTON DISTRIBUTION FUNCTIONS

There are numerous TMDs, each describing parton momentum distributions for a particular combination of parton and nucleon spin states. They are represented by letters e, f, g and h with some additional symbols in the subscripts and superscripts. They are suitably tabulated in Table 1. In the leading twist, the different TMDs describe different polarization states of the quarks in different polarization states of the nucleons. In higher twist, since the scattering is from a quark correlated with a gluon, quark polarization is undefined.

TABLE 1: The descriptions of various leading and higher twist TMDs. The U, L and T in the first row and first column denote the polarization of the quark and nucleons. U, L and T stand for unpolarized, longitudinal and transverse polarization.

N↓ q→	**U**	**L**	**T**	**Higher Twist**
U	f_1		$h_1^\perp$	$f^\perp$, $g^\perp$, h, e
L		g_1	$h_{1L}^\perp$	$f_L^\perp$, $g_L^\perp$, h_L, e_L
T	$f_{1T}^\perp$	g_{1T}	$h_{1T}^\perp$, h_1	f_T, $f_T^\perp$, g_T, $g_T^\perp$, $h^\perp$, e_T, $h_T^\perp$, $e_T^\perp$

The interpretation of the leading-twist transverse momentum dependent parton distribution functions are briefly described below. At leading order, they can be

interpreted as the number densities analogous with the number density interpretation of the ordinary parton distribution functions. The following names for these TMDs are commonly used in the literature [2].

Sivers Function $f_{1T}^{\perp}$

$f_{1T}^{\perp}$ describes the distribution of unpolarized quarks in a transversely polarized nucleon. $f_{1T}^{\perp} > 0$ means that the quark has a preference to move to the left if the nucleon is moving towards the observer with its spin pointing upwards. This is diagrammatically described in Fig. 9.

Boer-Mulders Function $h_1^{\perp}$

$h_1^{\perp}$ describes the distribution of transversely polarized quarks inside an unpolarized nucleon as shown in Fig. 9. $h_1^{\perp} > 0$ means that the quark whose spin is pointing upward has preference to move to the left in a nucleon moving towards the observer.

Worm-Gear Function g_{1T}

g_{1T} describes the distribution of longitudinally polarized quarks in a transversely polarized nucleon as shown in Fig. 9. $g_{1T} > 0$ means that the quark tends to have a positive helicity if its transverse momentum is in the direction of the nucleon spin. has preference to move towards right in a transversely polarized nucleon.

Kotzinian-Mulders Function $h_{1L}^{\perp}$

$h_{1L}^{\perp}$ describes the distribution of transversely polarized quarks in a longitudinally polarized nucleon as shown in Fig. 9. $h_{1L}^{\perp} > 0$ means that the transversely polarized quark has preference to move along its spin direction in a longitudinally polarized nucleon. This is one of the TMDs this analysis is sensitive to.

Pretzelosity Function $h_{1T}^{\perp}$

It describes the distribution of transversely polarized quark in a transversely polarized nucleon as shown in Fig. 9. The polarization of the quark in this case is along their intrinsic momentum. $h_{1T}^{\perp} > 0$ means that the projection of transverse quark spin on transverse quark momentum is anti-correlated with the projection of the transverse quark momentum on the nucleon spin.

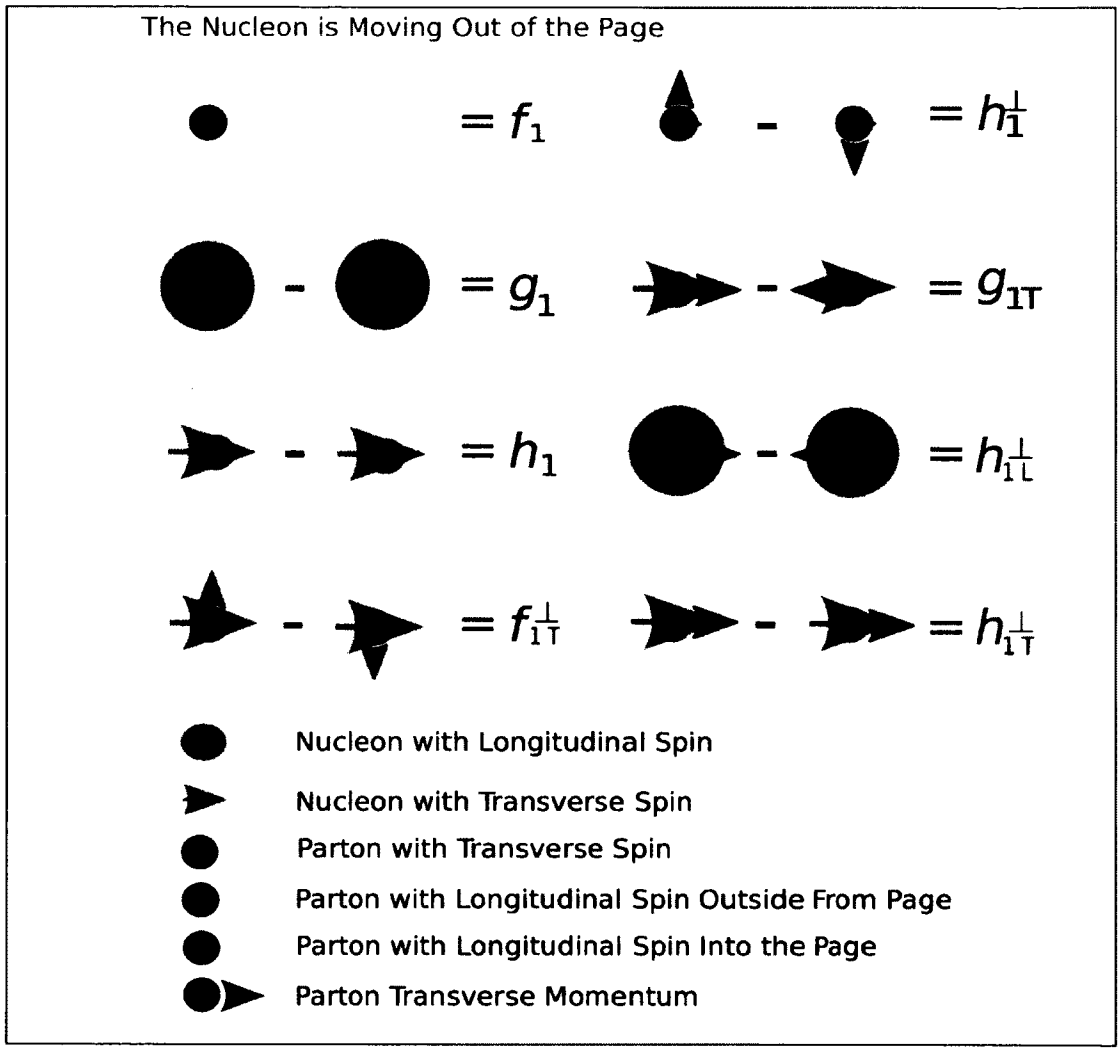

FIG. 9: The probabilistic interpretations of various leading twist TMDs.

1.7 RELATION BETWEEN THE STRUCTURE FUNCTIONS AND THE TMDS

The parameterizations of the hadronic tensor and its contraction with the leptonic tensor gives the lepto-production cross-section for semi-inclusive deep-inelastic scattering and project out the different structure functions. The following equations give the relations between the structure functions, the transverse momentum dependent parton distribution functions and the fragmentation functions [2]. For convenience, the symbol $\mathcal{C}$ is used to indicate convolution of a transverse momentum dependent parton distribution function with a fragmentation function. The symbol $\mathcal{C}$ is defined as

$$\mathcal{C}[wfD] = x_B \sum_q e_q^2 \int d^2\boldsymbol{p}_T d^2\boldsymbol{k}_T \delta^{(2)}(\boldsymbol{p}_T - \boldsymbol{k}_T - \boldsymbol{P}_{h\perp}/z) \times w(\boldsymbol{p}_T, \boldsymbol{k}_T) f^q(x_B, p_T^2) D^q(z, k_T^2), \tag{34}$$

where $\hat{\boldsymbol{h}} = \boldsymbol{P}_{h\perp}/|\boldsymbol{P}_{h\perp}|$ and $w(\boldsymbol{p}_T, \boldsymbol{k}_T)$ is an arbitrary function. Up to leading order, the following are the expressions for the structure functions relevent to this analysis [12].

$$F_{UU,T} = \mathcal{C}[f_1 D_1] \tag{35}$$

$$F_{UU,L} = 0 \tag{36}$$

$$F_{UU}^{\cos\phi_h} = \frac{2M}{Q}\mathcal{C}\left[-\frac{\hat{\boldsymbol{h}}\cdot\boldsymbol{k}_T}{M_h}\left(x_B h H_1^\perp + \frac{M_h}{M} f_1 \frac{\tilde{D}^\perp}{z}\right) - \frac{\hat{\boldsymbol{h}}\cdot\boldsymbol{p}_T}{M}\left(x_B f^\perp D_1 + \frac{M_h}{M} h_1^\perp \frac{\tilde{H}^\perp}{z}\right)\right] \tag{37}$$

$$F_{UU}^{\cos 2\phi_h} = \mathcal{C}\left[-\frac{2(\hat{\boldsymbol{h}}\cdot\boldsymbol{k}_T)(\hat{\boldsymbol{h}}\cdot\boldsymbol{p}_T) - \boldsymbol{k}_T\cdot\boldsymbol{p}_T}{M M_h} h_1^\perp H_1^\perp\right] \tag{38}$$

$$F_{LU}^{\sin\phi_h} = \frac{2M}{Q}\mathcal{C}\left[-\frac{\hat{\boldsymbol{h}}\cdot\boldsymbol{k}_T}{M_h}\left(x_B e H_1^\perp + \frac{M_h}{M} f_1 \frac{\tilde{G}^\perp}{z}\right) + \frac{\hat{\boldsymbol{h}}\cdot\boldsymbol{p}_T}{M}\left(x_B g^\perp D_1 + \frac{M_h}{M} h_1^\perp \frac{\tilde{E}^\perp}{z}\right)\right] \tag{39}$$

$$F_{UL}^{\sin\phi_h} = \frac{2M}{Q}\mathcal{C}\left[-\frac{\hat{\boldsymbol{h}}\cdot\boldsymbol{k}_T}{M_h}\left(x_B h_L H_1^\perp + \frac{M_h}{M} g_{1L} \frac{\tilde{G}^\perp}{z}\right) + \frac{\hat{\boldsymbol{h}}\cdot\boldsymbol{p}_T}{M}\left(x_B f_L^\perp D_1 - \frac{M_h}{M} h_{1L}^\perp \frac{\tilde{H}^\perp}{z}\right)\right] \tag{40}$$

$$F_{UL}^{\sin 2\phi_h} = \mathcal{C}\left[-\frac{2(\hat{\boldsymbol{h}}\cdot\boldsymbol{k}_T)(\hat{\boldsymbol{h}}\cdot\boldsymbol{p}_T) - \boldsymbol{k}_T\cdot\boldsymbol{p}_T}{M M_h} h_{1L}^\perp H_1^\perp\right] \tag{41}$$

$$F_{LL} = \mathcal{C}[g_{1L} D_1] \tag{42}$$

$$F_{LL}^{\cos\phi_h} = \frac{2M}{Q}\mathcal{C}\left[\frac{\hat{\boldsymbol{h}}\cdot\boldsymbol{k}_T}{M_h}\left(x_B e_L H_1^{\perp} - \frac{M_h}{M} g_{1L}\frac{\tilde{D}^{\perp}}{z}\right) - \frac{\hat{\boldsymbol{h}}\cdot\boldsymbol{p}_T}{M}\left(x_B g_L^{\perp} D_1 + \frac{M_h}{M} h_{1L}^{\perp}\frac{\tilde{E}^{\perp}}{z}\right)\right] \tag{43}$$

where e, f, g and h with various symbols in the subscripts and superscripts are the TMDs as described in Section 1.6; and D, E, G and H with various symbols in the subscripts and superscripts are the fragmentation functions.

1.8 THE EXPERIMENTAL OBSERVABLES

In the previous section, the relationship between the different structure functions and the TMDs were shown. However, the direct measurement of these structure functions is not straight forward. Instead, for experimental convenience, the primary observables are the various moments of beam single (A_{LU}), target single (A_{UL}) and beam-target double (A_{LL}) spin azimuthal asymmeties: $A_{LU}^{sin\phi_h}$, $A_{UL}^{sin\phi_h}$, $A_{UL}^{sin2\phi_h}$, A_{LL}^{Const} and $A_{LL}^{cos\phi_h}$, where the superscripts represent the different types of ϕ_h modulation of the asymmetry. Once the asymmetry moments are measured, the information on the structure functions can be extracted.

An asymmetry is the ratio of the cross-section difference between two beam helicities or between two target polarizations or their product to the total cross-section. It is more convenient to define various asymmetries directly from their measurement prescriptions. In the context of the EG1-DVCS experiment, where the beam and the target were simultaneously polarized, the beam single (A_{LU}), target single (A_{UL}) and beam-target double (A_{LL}) spin asymmetries are defined as,

$$A_{LU} = \frac{(d\sigma^{\uparrow\Uparrow} - d\sigma^{\downarrow\Uparrow}) + (d\sigma^{\uparrow\Downarrow} - d\sigma^{\downarrow\Downarrow})}{(d\sigma^{\uparrow\Uparrow} + d\sigma^{\downarrow\Uparrow}) + (d\sigma^{\uparrow\Downarrow} + d\sigma^{\downarrow\Downarrow})}, \tag{44}$$

$$A_{UL} = \frac{d\sigma^{\uparrow\Uparrow} + d\sigma^{\downarrow\Uparrow} - d\sigma^{\uparrow\Downarrow} - d\sigma^{\downarrow\Downarrow}}{(d\sigma^{\uparrow\Uparrow} + d\sigma^{\downarrow\Uparrow}) + (d\sigma^{\uparrow\Downarrow} + d\sigma^{\downarrow\Downarrow})}, \tag{45}$$

$$A_{LL} = \frac{-d\sigma^{\uparrow\Uparrow} + d\sigma^{\downarrow\Uparrow} + d\sigma^{\uparrow\Downarrow} - d\sigma^{\downarrow\Downarrow}}{(d\sigma^{\uparrow\Uparrow} + d\sigma^{\downarrow\Uparrow}) + (d\sigma^{\uparrow\Downarrow} + d\sigma^{\downarrow\Downarrow})}, \tag{46}$$

where $\Uparrow$ and $\Downarrow$ represent target polarizations; $\uparrow$ and $\downarrow$ represent beam polarizations both along the beam directions. The symbol $d\sigma$ is the differential cross-section integrated over some kinematic bin. It follows directly from the expression for the SIDIS differential cross-section that,

$$A_{LU} = \frac{\sqrt{2\,\varepsilon(1-\varepsilon)}\,\sin\phi_h\, F_{LU}^{\sin\phi_h}}{F_{UU,T} + \varepsilon\, F_{UU,L} + \sqrt{2\,\varepsilon(1+\varepsilon)}\,\cos\phi_h\, F_{UU}^{\cos\phi_h} + \varepsilon\cos(2\phi_h)\, F_{UU}^{\cos 2\phi_h}}, \tag{47}$$

$$A_{UL} = \frac{\sqrt{2\,\varepsilon(1+\varepsilon)}\,\sin\phi_h\,F_{UL}^{\sin\phi_h} + \varepsilon\sin(2\phi_h)\,F_{UL}^{\sin 2\phi_h}}{F_{UU,T} + \varepsilon\,F_{UU,L} + \sqrt{2\,\varepsilon(1+\varepsilon)}\,\cos\phi_h\,F_{UU}^{\cos\phi_h} + \varepsilon\cos(2\phi_h)\,F_{UU}^{\cos 2\phi_h}} \tag{48}$$

and

$$A_{LL} = \frac{\sqrt{1-\varepsilon^2}\,F_{LL} + \sqrt{2\,\varepsilon(1-\varepsilon)}\,\cos\phi_h\,F_{LL}^{\cos\phi_h}}{F_{UU,T} + \varepsilon\,F_{UU,L} + \sqrt{2\,\varepsilon(1+\varepsilon)}\,\cos\phi_h\,F_{UU}^{\cos\phi_h} + \varepsilon\cos(2\phi_h)\,F_{UU}^{\cos 2\phi_h}}. \tag{49}$$

If both the numerator and denominator are divided by $F_{UU,T} + \varepsilon\,F_{UU,L}$, we can write

$$A_{LU} = \frac{A_{LU}^{\sin\phi_h}\sin\phi_h}{1 + A_{UU}^{\cos\phi_h}\cos\phi_h + A_{UU}^{\cos 2\phi_h}\cos 2\phi_h}, \tag{50}$$

$$A_{UL} = \frac{A_{UL}^{\sin\phi_h}\sin\phi_h + A_{UL}^{\sin 2\phi_h}\sin 2\phi_h}{1 + A_{UU}^{\cos\phi_h}\cos\phi_h + A_{UU}^{\cos 2\phi_h}\cos 2\phi_h} \tag{51}$$

and

$$A_{LL} = \frac{A_{LL}^{Const} + A_{LL}^{\cos\phi_h}\cos\phi_h}{1 + A_{UU}^{\cos\phi_h}\cos\phi_h + A_{UU}^{\cos 2\phi_h}\cos 2\phi_h}, \tag{52}$$

where A with different subscripts and superscripts are the asymmetry moments. From the previous six equations, one to one relationship between the azimuthal moments of the asymmetries and the structure functions can be directly established.

1.9 SIDIS ON DEUTERON

In the previous sections, the structure functions, polarizations and their relation to the TMDs are defined for bare nucleons. However, in a simple approximation, those definitions and relations remain valid for the deuteron as well. There are two motivations to study SIDIS on the deuteron: first, understanding the deuteron is the first step towards understanding the nucleus, and second, knowledge of both the proton and the deuteron structure functions is very useful towards extracting information on the neutron. The deuteron in its ground state is in an isospin singlet state which is antisymmetric under the exchange of the proton and the neutron. So we can extract information on the u and d quarks separately from comparisons of the proton and the neutron. The complications due to Fermi motion and nuclear binding make the extraction of information on the u and d quark more difficult and put it beyond the scope of the present analysis.

1.10 PREVIOUS MEASUREMENTS

Over the last decade, a growing number of experiments have measured quantities related to TMDs, including some of the observables measured in this analysis. Most of the earlier measurements from HERMES, COMPASS and Hall B of the Jefferson Lab suffered from low statistics and the measurements were mostly limited to charged pions and to proton targets. Only a few of the quantities were measured on a deuteron target. In this section, some of the important previously published results related to this analysis are presented.

Measurement of $A_{UL}^{\sin 2\phi_h}$

The SIDIS asymmetry $A_{UL}^{\sin 2\phi_h}$ on proton was measured by the HERMES and the CLAS collaboration [14]; their results are shown in Fig. 10. HERMES measurements were only for charged pions whereas CLAS measurements were for all three pion flavors. In the figure, existing theoretical predictions [15] using the measured Collins function are shown. The significantly negative value of $A_{UL}^{\sin 2\phi_h}$ for charged pions measured by CLAS was the first observation of its kind. The CLAS and the HERMES measurements have different kinematics but still the difference is surprisingly large.

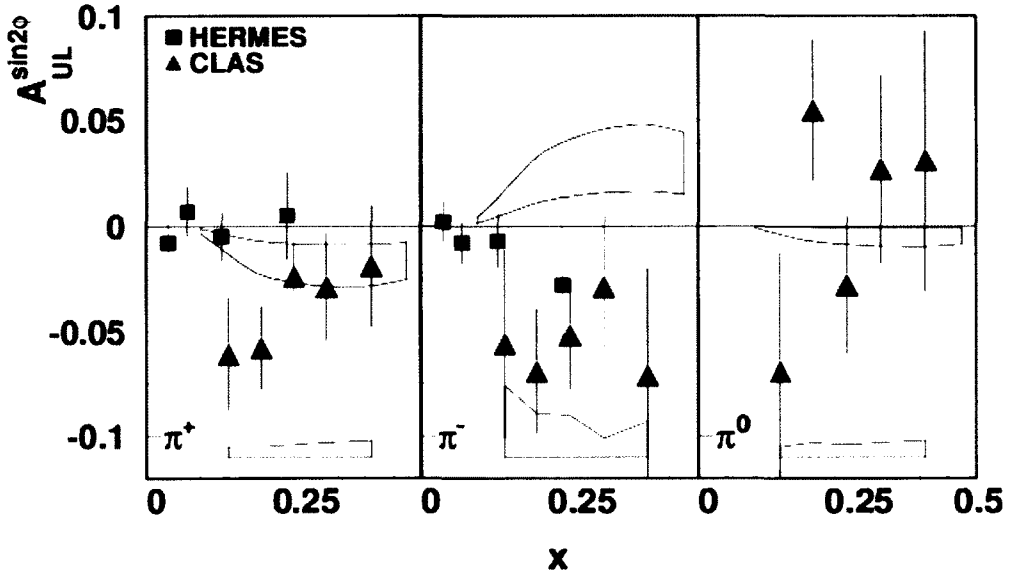

FIG. 10: The x_B dependence of the $A_{UL}^{\sin 2\phi}$ measured by the HERMES and the CLAS collaborations. The yellow band shows the existing theoretical prediction from Collins function [15].

Measurement of A_1

The quantity A_1 is extracted from the beam-target double spin asymmetry. It has been measured for all three types of pions as well as for kaons by various collaborations. Figs. 13 and 14 show the results from the CLAS and the HERMES collaborations [14]. Figs. 11 and 12 show A_1 results measured by the COMPASS collaboration on the proton and the deuteron targets for charged pions and kaons.

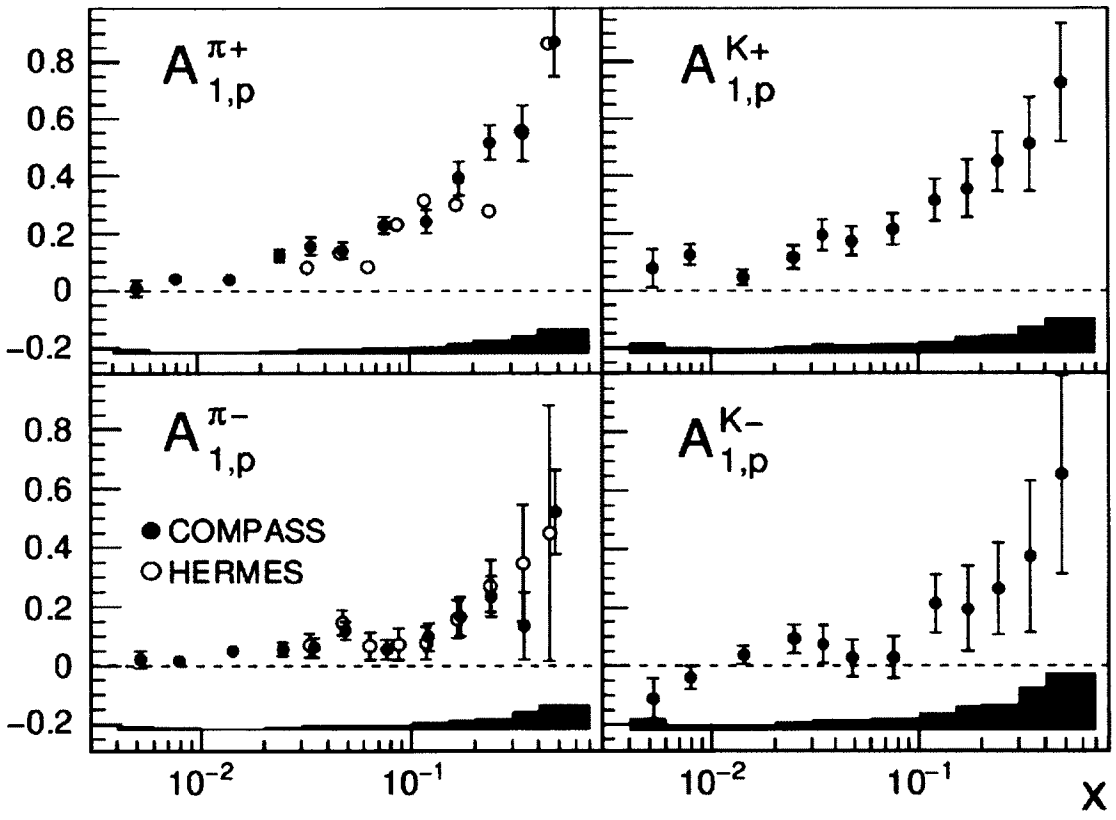

FIG. 11: The x_B dependence of the semi-inclusive longitudinal double-spin asymmetries for pions and kaons from COMPASS [18] and HERMES [19] for the proton.

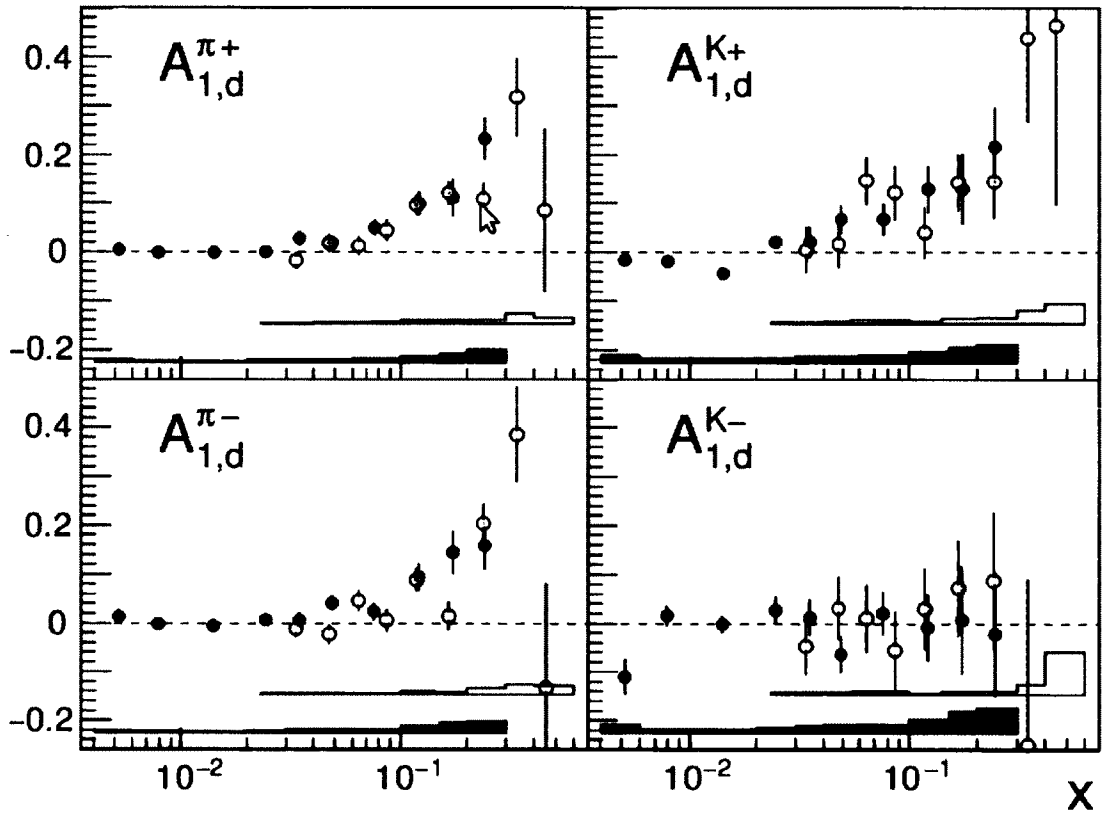

FIG. 12: The x_B dependence of the semi-inclusive longitudinal double-spin asymmetries for pions and kaons from COMPASS [18] and HERMES [19] for the deuteron.

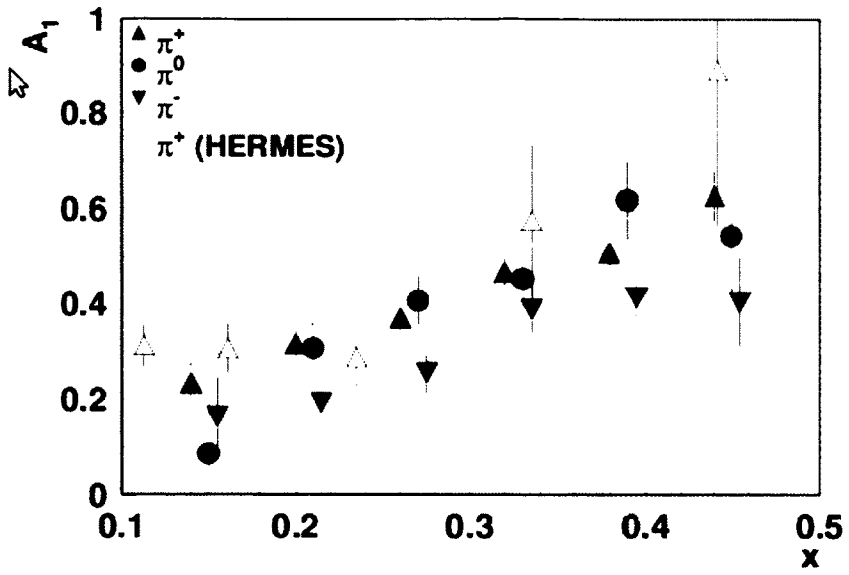

FIG. 13: The x_B dependence of A_1. The solid, dashed and dotted curves are calculated using the leading order GRSV PDF [16].

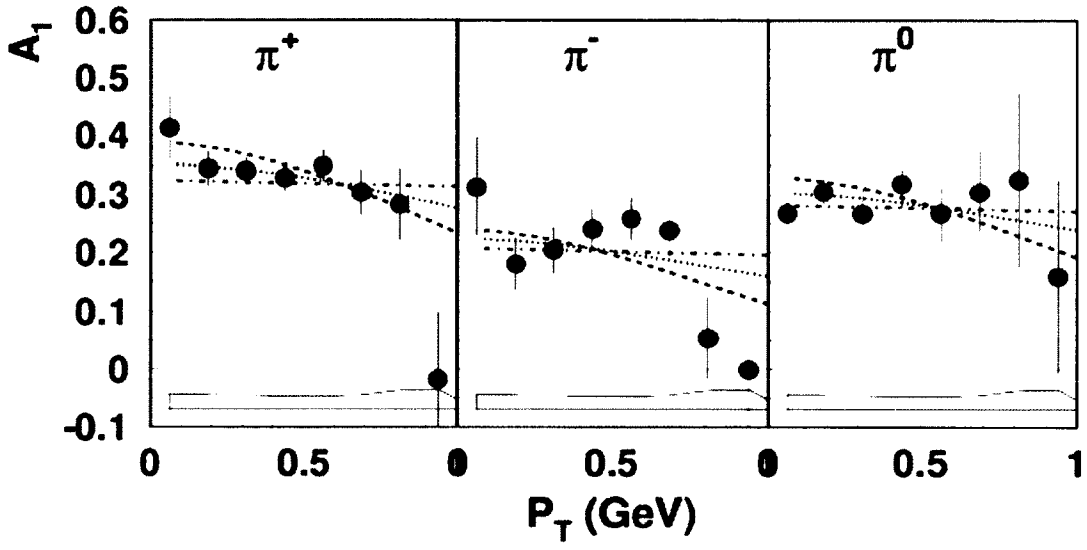

FIG. 14: The double spin asymmetry A_1 as a function of $P_{h\perp}$ [14]. The dashed, dotted and dash-dotted curves are calculations for different values for the ratio of Gaussian transverse momentum widths for g_1 and f_1 (0.40, 0.68, 1.0) for a fixed width for f_1 (0.25 GeV^2) [17].

1.11 THEORETICAL PREDICTIONS

Some of the quantities measured in this analysis have been theoretically predicted based on different phenomenological models. The predictions are predominantly for protons rather than for deuterons. Moreover, the predictions are calculated predominantly for leading twist observables. As can be seen from the relations between the structure functions in Section 1.7, A_{LL}^{Const} and $A_{UL}^{\sin 2\phi}$ have only leading twist components. Fig. 15 shows the predictions for A_{UL} moments from Ref. [20]. These predictions were based on the extraction of twist-3 distribution $e^a(x)$ by using the $H_1^\perp(z)$ information published in Ref. [21]. The prediction is also based on the assumption that the ratio between Collins fragmentation function, $H_1^\perp$, to unpolarized fragmentation function, D_1, to be 20%. The predictions shown in the figure are for CLAS kinematics. The $\sin 2\phi$ moment of A_{UL} are predicted to be negative for neutral and positive pions and positive for negative pion.

Fig. 16 shows the predictions for $A_{UL}^{\sin 2\phi}$ based on the calculations of g_{1T} and $h_{1L}^\perp$ in the light cone quark-diquark model [23]. Again, the $\sin 2\phi$ moments of A_{UL} are predicted to be negative for positive pion and positive for negative pion. The two curves in each plot correspond to two methods of parameterizations leading to the calculation of g_{1T} and $h_{1L}^\perp$ within the light cone quark-diquark model. The predicted curves in the figure correspond to CLAS kinematics.

Fig. 17 shows the predictions for A_{LL} within the CLAS kinematics based on the leading order QCD parton model with unintegrated quark distribution and fragmentation functions from Ref. [17]. The different curves in the figure correspond to different values of μ_2^2. The symbol μ_2 correspond to the the width of the parton transverse momentum distribution which is assumed to be Gaussian. The assumptions are: $f_1 \sim e^{-p_T^2/\mu_1^2}$ and $g_1 \sim e^{-p_T^2/\mu_2^2}$, $\mu_1^2 = 0.25$ is kept fixed and different values of A_{LL}^{Const} for different values of μ_2^2 are calculated.

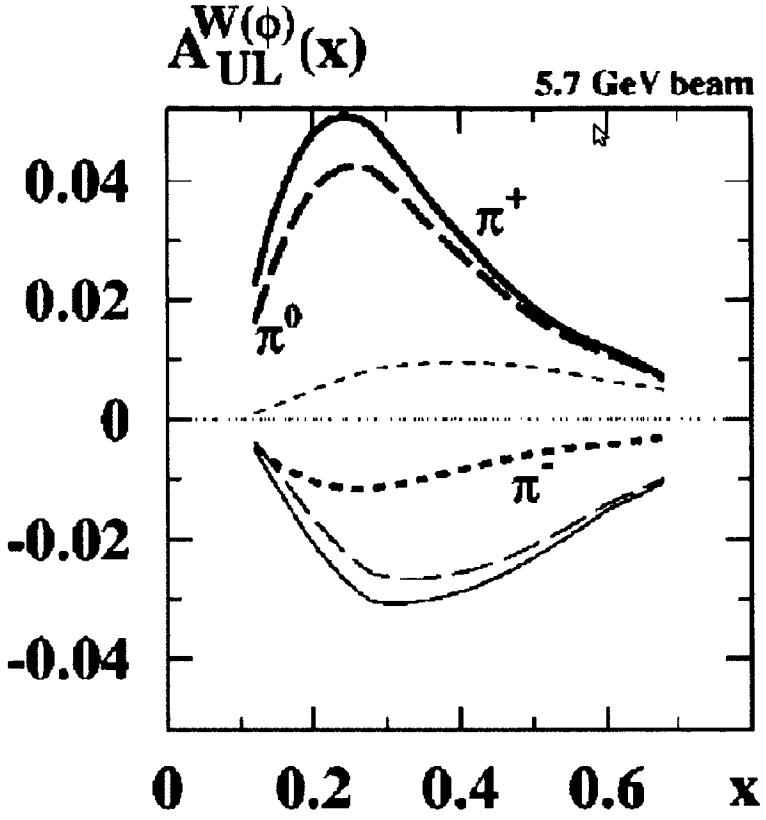

FIG. 15: Predictions for the A_{UL} azimuthal asymmetry moments from scattering of an unpolarized beam on a polarized proton target for CLAS kinematics [20]. The thick lines correspond to $\sin\phi$ moment. The thin lines correspond to $\sin 2\phi$ moment.

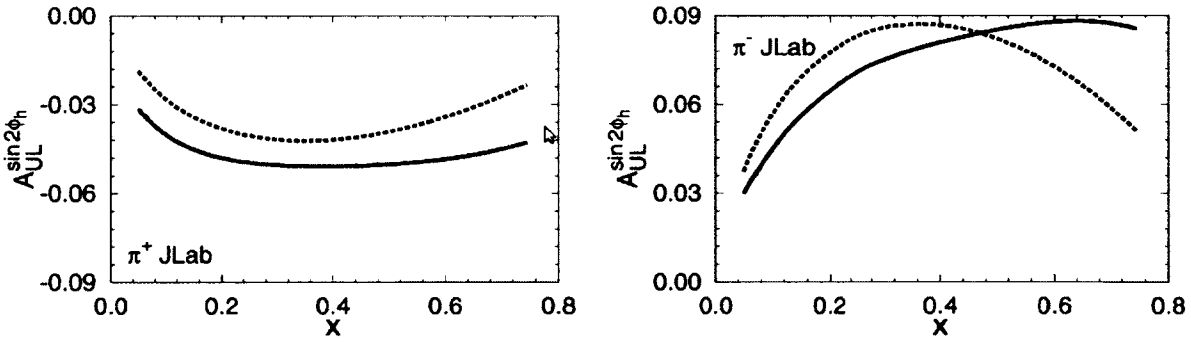

FIG. 16: Predictions for $\sin 2\phi$ moment for charged pions within the CLAS kinematics [23]. The solid and the dotted lines correspond to two different parameterizations of g_{1T} and $h_{1L}^{\perp}$.

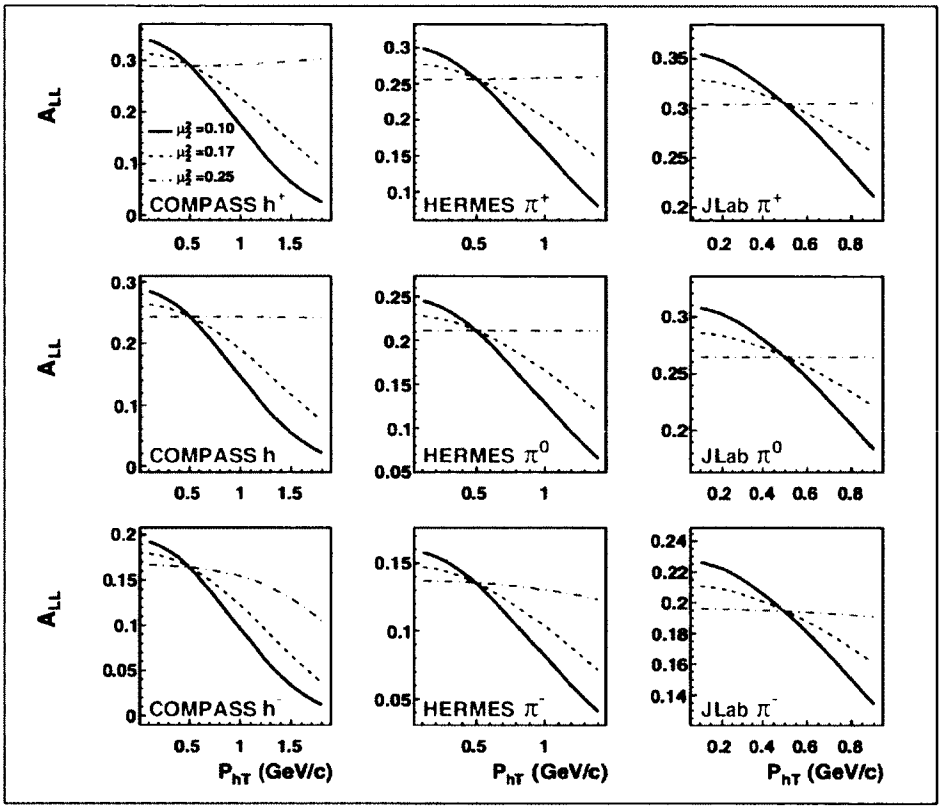

FIG. 17: Predictions for A_{LL} within the CLAS kinematics (third column) based on the leading order QCD parton model from Ref. [17]. The notation P_{hT} used in the plot is equivalent to $P_{h\perp}$ used in the main text of this analysis.

CHAPTER 2

EG1-DVCS EXPERIMENTAL OVERVIEW

Data from experiment EG1-DVCS were used in this analysis. Studies of inclusive deep-inelastic scattering (DIS), semi-inclusive deep-inelastic scattering (SIDIS) and deeply virtual Compton scattering (DVCS) were the primary objectives of the experiment. Hence, the experiment was configured to optimize the collection of data in the deep-inelastic region. In the experiment, a longitudinally polarized electron beam of about 6 GeV was scattered from longitudinally polarized stationary NH_3 and ND_3 targets. The scattered products were detected by a multi-layered large acceptance spectrometer. A brief overview of the experimental setup and how the data from the experiment were initially processed are presented in this chapter.

2.1 EG1-DVCS EXPERIMENT

The EG1-DVCS experiment was conducted at the Thomas Jefferson National Accelerator Facility from February to September 2009. In the experiment, a longitudinally polarized electron beam with an energy of approximately 6 GeV from the Continuous Electron Beam Accelerator Facility (CEBAF) was scattered from longitudinally polarized stationary solid state NH_3 and ND_3 targets. The NH_3 and ND_3 targets, which were dynamically polarized, were used as sources of longitudinally polarized proton and deuteron. The dynamic polarization technique is presented in Section 2.4. The scattered products were detected by the CEBAF Large Acceptance Spectrometer (CLAS). In addition to the usual CLAS set-up, an Inner Calorimeter (IC) was used at about 75 cm from the target to detect low polar angle photons.

Depending upon the type of target and the beam energy, the EG1-DVCS experiment was divided into three parts: Part-A, Part-B and Part-C. The different parts were divided into different runs; within each run, the experimental configurations remained unchanged. The basic configurations of the three parts are given in Table [2]. In addition to the primary targets NH_3 and ND_3, about 10% of the runs were dedicated to ^{12}C and ^{4}He targets to study nuclear backgrounds.

TABLE 2: Various experimental configurations of the different parts of the EG1-DVCS experiment. Vertex is defined as the position of the target relative to the nominal CLAS center.

Expt. Part	Runs	Target	Vertex	Beam Energy	Torus Current
Part-A	58799 - 59155	NH_3	-58 cm	5.88 GeV	+2250 A
Part-B	59456 - 60184	NH_3	-68 cm	5.95 GeV	+2250 A
Part-C (a)	60304 - 60565	ND_3	-68 cm	5.75 GeV	+2250 A
Part-C (b)	60566 - 60648	ND_3	-68 cm	5.75 GeV	-2250 A

2.2 CONTINUOUS ELECTRON BEAM ACCELERATOR FACILITY (CEBAF)

The Continuous Electron Beam Accelerator Facility (CEBAF) provides up to 6 GeV continuous-wave (cw) longitudinally polarized electron beams for experiments at the nuclear and particle physics interface to the detector facilities in three different halls where various electron scattering experiments are carried out. A schematic diagram of the facility is shown in Fig. 18. The two cylindrical shaped structures shown in the figure are the two linear accelerators; each of them have 20 cryomodules. The structures marked by letters A, B and C on the figure are the three experimental halls. Since the EG1-DVCS experiment was carried out at Hall-B with the CEBAF Large Acceptance Spectrometer (CLAS), CEBAF and various components of CLAS will be discussed very briefly in this section [24].

2.2.1 AN OVERVIEW OF CEBAF

Basically, CEBAF has two linear accelerators which are commonly referred to as linacs. The two linacs are linked by nine recirculation beam lines for up to five passes. Unlike most other accelerators, CEBAF provides high luminosity, up to 200 μA, longitudinally polarized and continuous electron beam. It uses superconducting radio frequency (srf) cavities operating in a continuous wave mode to accelerate electrons up to 6 GeV [24].

Illuminated with circularly polarized laser light, a GaAs photo-cathode provides a longitudinally polarized beam with polarization of approximately 80%. A half wave plate (HWP) is used to change the polarization phase of the laser beam by π to

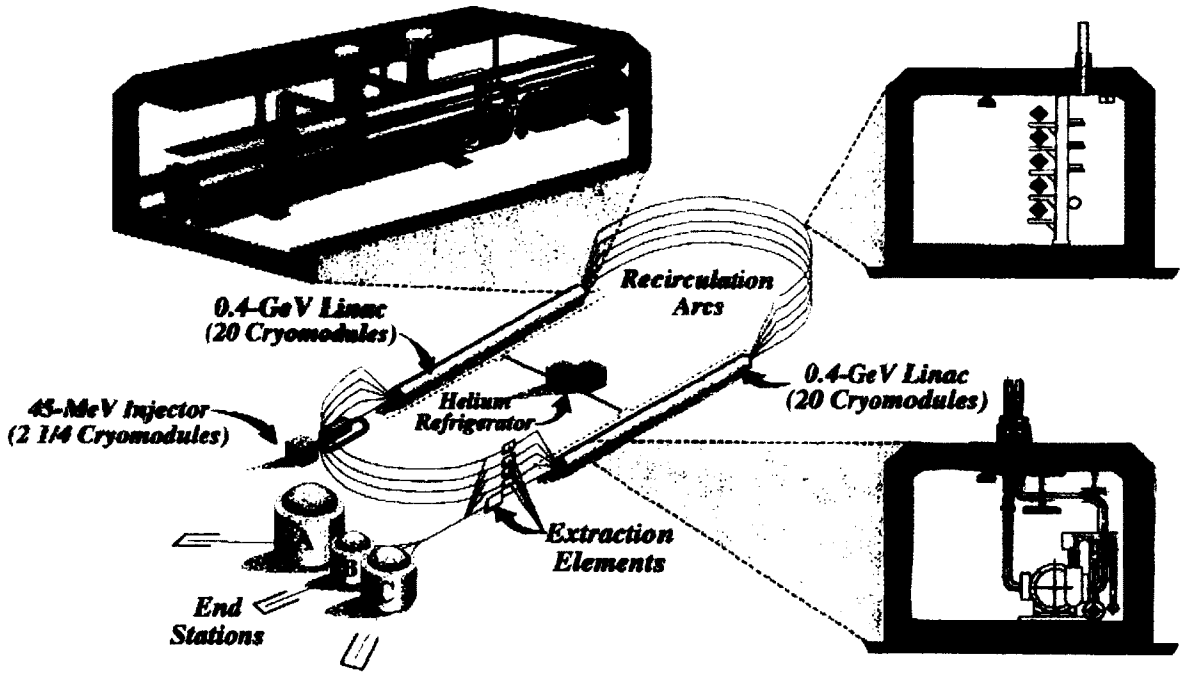

FIG. 18: A general view of the CEBAF and the three experimental halls.

minimize the systematic effects associated with beam polarization. The change in the phase of the laser beam by π changes the polarization phase of the produced electrons by π, so the status of the HWP is changed periodically during an experiment to make sure that there is no polarity dependent bias on the measured quantities. In the EG1-DVCS experiment, the half wave plate was altered after about each 20 runs. Longitudinally polarized electrons from the source are injected into the first linac at an energy of about 70 MeV. In every pass through each linac the beam gains about 600 MeV. The beam polarization in the experimental Hall B is measured by a Moller polarimeter, which uses the well-known asymmetry for elastic electron-electron scattering from a magnetized iron target. Since this is an invasive measurement, separate Moller recordings were periodically run during the experiment. For EG1-DVCS experiment, the beam polarization was about 80% with an uncertainty of approximately 2%.

The beam profile is measured by a "Harp" located upstream from the center of the CLAS detector. The Harp consists of a system of thin wires. The beam position and profile in the plane perpendicular to the beam axis is measured by moving the wires through the beam. In the process, Cherenkov light produced by the scattered

electrons from the wires is measured by a set of photomultiplier tubes. The spatial distribution of the scattered electron intensity gives the profile of the beam. Harp scans are an invasive technique so they are done only before and after Moller runs to note any changes in the beam profile.

The final beam-line element of the detector is the Faraday cup which is a 4 ton lead cylinder located 29 m downstream from the center of the detector. The beam passing through the target ends up in the Faraday cup. The Faraday cup is connected to a capacitor which measures the integrated current of the beam by collecting the total charge from the lead. The charge collection in the Faraday cup is synchronized with the beam helicity so that the luminosities for different beam helicities can be recorded.

2.2.2 CEBAF LARGE ACCEPTANCE SPECTROMETER (CLAS)

The spectrometer in Hall-B of the Thomas Jefferson National Accelerator Facility (TJNAF) is commonly referred to as the CLAS detector, which is the acronym for CEBAF Large Acceptance Spectrometer. Fig. 19 shows the different sections of the spectrometer. As a convention, the direction of the beam line, downstream, is defined as the positive z axis; commonly, spherical coordinates are used to refer to different geometrical configurations of the detector. As its name suggests, it has a large acceptance particularly in the azimuthal angle around the beam axis; along the polar axis it covers practically up to 45° for electrons. It is a multi-layered and multi-particle detector. Electrons from the CEBAF are scattered from a target located near the geometrical center of the detector. Most of the scattered particles from a scattering event are simultaneously detected. CLAS is based on 6 superconducting coils that separate the detector into six equivalent sectors; each of the sector is a complete spectrometer in itself. The superconducting coils, also called the Torus Magnet, are structured to produce a magnetic field circling around the beam axis. Three layers of Drift Chambers detect the momentum of the charged particles by measuring their curvature in the magnetic field produced by the Torus Magnet. Cherenkov Counters are used to distinguish electrons and positrons from charged pions by detecting Cherenkov light in a set of photo-multipliers. Scintillation Counters, due to their better time resolution, measure the time-of-flight of different particles; together with the information on the momentum of the particle, they can provide a good selection

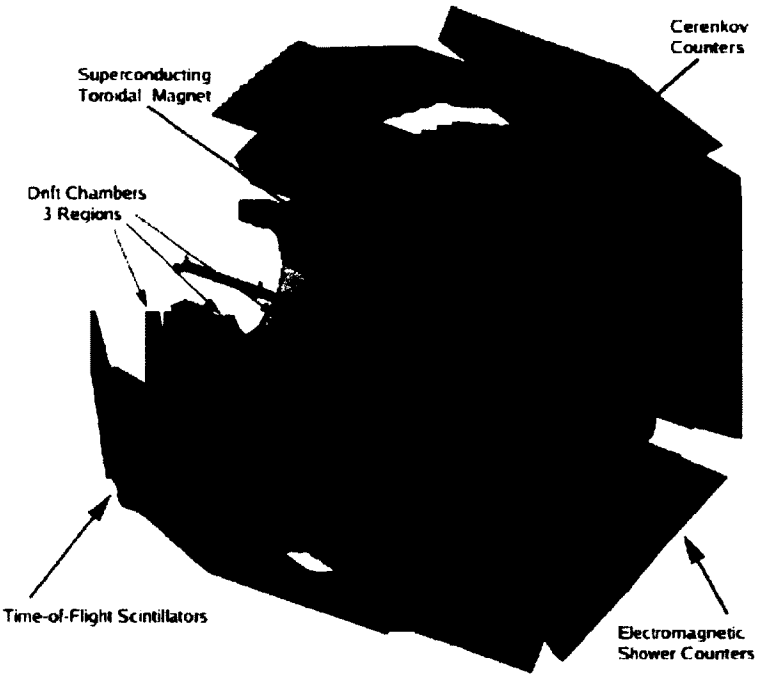

FIG. 19: The CEBAF Large Acceptance Spectrometer (CLAS). The different sections of the spectrometer are shown by different colours.

criterion for charged hadrons. The Electromagnetic Calorimeters are used to identify electrons as well as to measure the energy of photons. All of the detectors are described in more detail below.

Torus Magnet

The structure of the Torus Magnet used in the CLAS detector is shown in Fig. 20. It has six superconducting coils which produce a magnetic field up to 2 T inside the detector system, circling the beam line in azimuthal direction. The curvature of charged particles in this magnetic field is used to reconstruct their momenta. The charged particles deflect inward or outward depending upon their charge and the direction of the magnetic field. The orientation of the magnetic field can be reversed by reversing the direction of the current in the superconducting coils. A positive current bends negatively charged particles inward; this configuration is called in-bending configuration, the reverse is called the out-bending configuration. Because of the coil coverage arrangement, the magnetic field is mostly confined within the second region of the Drift Chambers making the target region field free which is

absolutely necessary for polarizing the target.

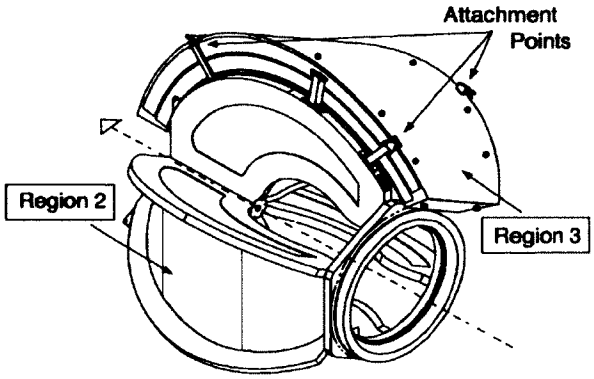

FIG. 20: Diagram of the superconducting torus coil.

Drift Chambers (DC)

There are three layers of Drift Chambers (DC): Region 1, Region 2 and Region 3 as shown in Figs. 21 and 22. All the regions contain six sectors. Region 1 and Region 3 are in a very low magnetic field of the Torus Magnet. Since Region 2 is at the center of the Torus Magnet coils, it is in a very high magnetic field region.

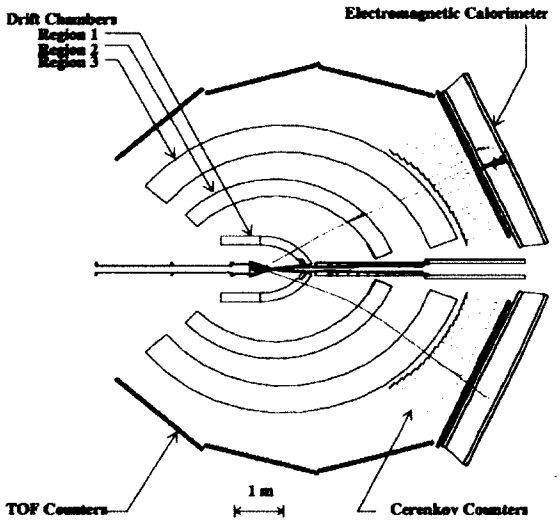

FIG. 21: The cross section of CLAS along the beam axis.

The Drift Chambers are used to measure the momentum and direction of the charged particles by determining their track and their curvature in the magnetic

field of the Torus Magnet, from their positions at three different locations. A drift chamber basically consists of a chamber filled with 80% argon and 20% carbon dioxide. When a charged particle passes through the chamber, it produces a trail of charged ions and electrons. A suitable arrangement of a large number of very fine anode and cathode wires within the chamber is used to reconstruct the trajectory of each particle by collecting the information on the location of the trail of charged electron-ion pairs in the chamber. Typical momentum resolution of the tracking system is about 0.5% – 1.0%.

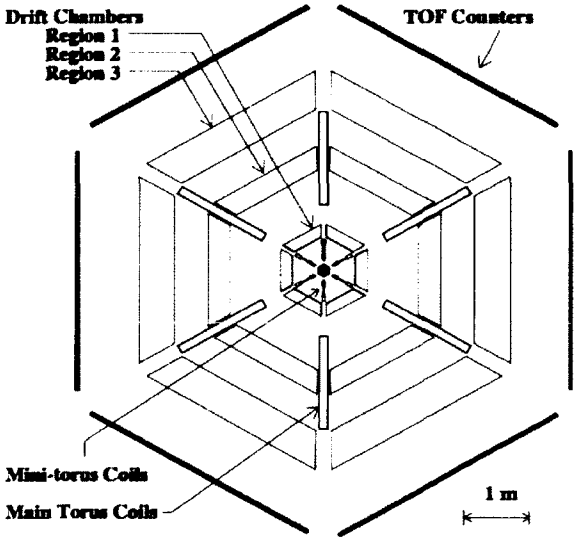

FIG. 22: The CLAS detector projected on a plane perpendicular to the beam axis

Cherenkov Counters (CC)

Cherenkov radiation is emitted by charged particles passing through a medium with a speed greater than that of light, c/n, in that medium, where c is the speed of light in vacuum and n is the refractive index of the medium. This phenomena is due to the disturbance of the electromagnetic field of the medium induced by the fast moving charged particles. The observed radiation is similar to a sonic boom caused by a supersonic aircraft. The radiation forms a cone whose angle is a function of the refractive index of the medium and the velocity of the charged particle. Hence, the cone angle of the Cherenkov radiation can be used as a particle identification parameter to identify different charged particles of known momentum. But the CC

used at CLAS does not measure the cone angle of the Cherenkov radiation; it only measures the number of photo-electrons emitted by the whole light cone collected in a photo multiplier tube (PMT). In the CC at CLAS, C_4H_{10} gas is used because of its higher refractive index ($n = 1.00153$) which increases photon count with a pion momentum threshold to about 2.6 GeV. So, for a charged particle of momentum below 2.6 GeV, if the number of photo-electrons is greater than zero then the particle is a good candidate for an electron or a positron. The schematic diagram of the path of a charged particle through the CC and the light collecting system is shown in Fig. 23. Different components of a single Cherenkov Counter sector are shown in Fig. 24. Photo-multipliers on the sides count the number of radiated photons as shown in the Figs. 23 and 24 .

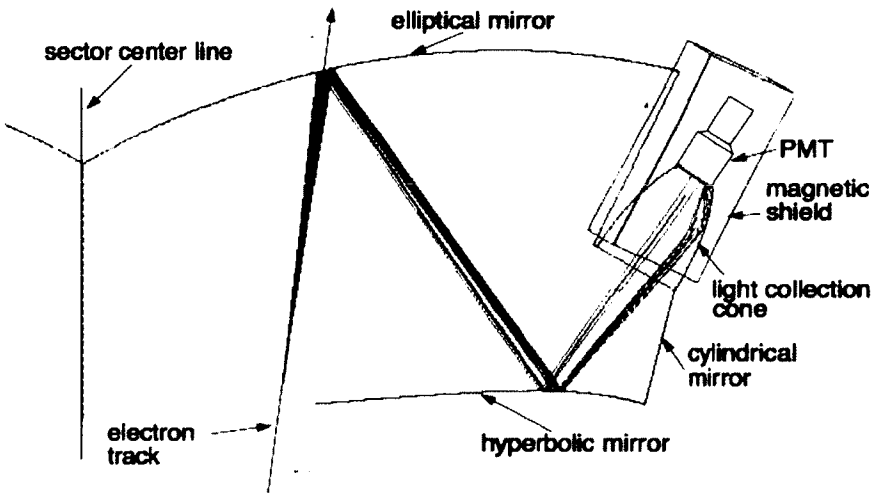

FIG. 23: A section of the CC showing the path of a charged particle through it and the light collecting system

Scintillation Counters (SC)

Due to their high time resolution ($\sim$ 0.15 ns), the Scintillation Counters (SC) are used to precisely measure the travel time of particles traversing through CLAS. Hence, the Scintillation Counters are often called time-of-flight detectors. The time interval between the time recorded in the SC and the event start time can be used to calculate the velocity of the particles. The velocity obtained from the SC and the momentum obtained from the DC can then be used to calculate the mass of the

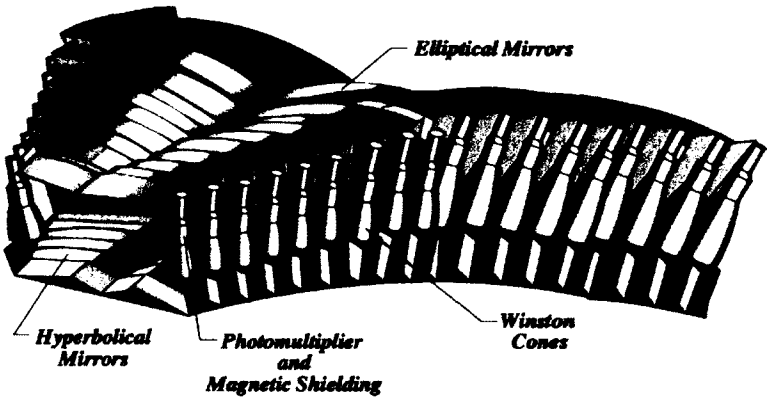

FIG. 24: Different components of a single CC sector

particles. This method is employed to identify charged hadrons.

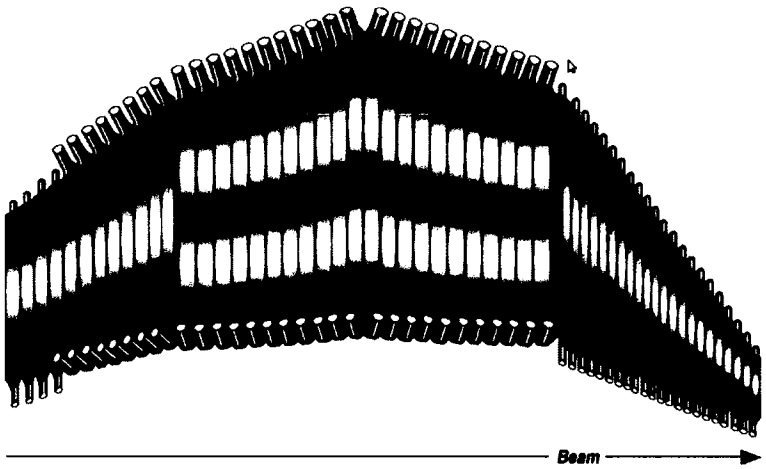

FIG. 25: A diagram of a Scintillation Counter sector. The scintillation counters are arranged in four panels perpendicular to the beam line. The light guide and the PMTs are at both ends [25].

The SC is basically a side-by-side arrangement of numerous plastic scintillation panels where each plastic scintillator panel is perpendicular to the beam axis. Each panel is either 15 cm or 22 cm wide and is optically connected to two PMTs at the end. The PMTs read the scintillation light produced by the panels. A diagram of a Scintillation Counter sector is shown in Fig. 25. As shown in the figure, the lengths of the panels are different at different values of polar angle. At lower polar angle, the length of each panel is around 30 cm and at higher angles the lengths are around 4.5

m. For shorter scintillator panels, the time resolution is 60 ps and 120 ps for longer pedals. The SC is capable of separating charged pions and charged kaons up to 2 GeV [25].

Electromagnetic Calorimeters (EC)

The Electromagnetic Calorimeters are made up of alternating layers of lead and plastic scintillators. The lead layers present a high-Z material which produces electromagnetic showers. The lead leads to conversions of photons to electron and positron pairs, $\gamma \rightarrow e^+e^-$, and bremsstrahlung $e \rightarrow e\gamma$. Both e^- and e^+ lose energy through ionization in both lead and plastic scintillators. The scintillators respond to the fraction of energy loss in it by emitting light. Since the shower process continues until all energy has been lost to ionization, the total light output is proportional to the energy for showering particles. The scintillation produced in the alternating layers of plastic is used to reconstruct the location, timing and energy of the particles that produced the electromagnetic showers.

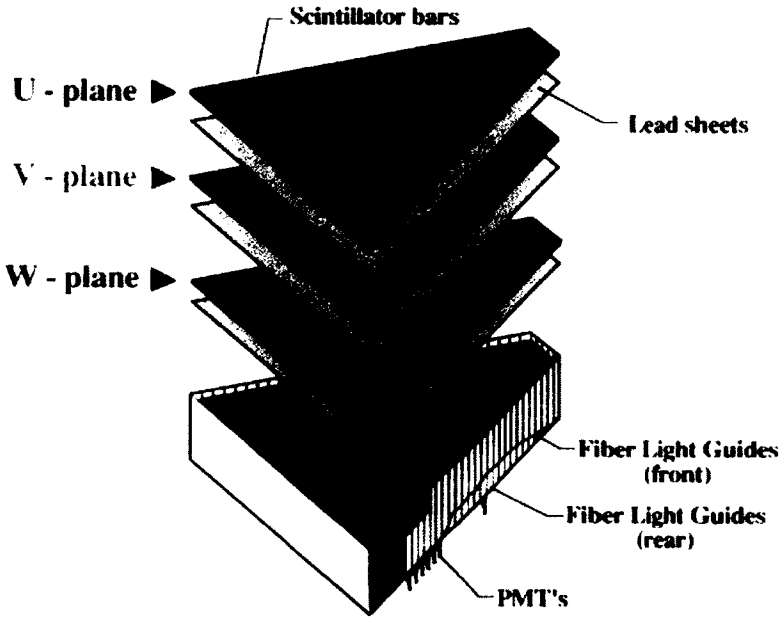

FIG. 26: Multi-layered structure of a sector of the Electromagnetic Calorimeter. The layers in different planes are differently colored [26].

The EC consists of six modules, one for each sector, and covers from 8° to 45°

along the polar direction. The different layers of the Electromagnetic Calorimeters are shown in Fig. 26. Each module consists of 39 layers of lead-scintillator pairs. Each lead layer is 2.2 mm thick and the scintillator plastic layers are 1 cm thick; the combination of all layers equals to about 16 radiation lengths. 36 scintillator plastic strips each of width about 10 cm, arranged side by side, make a scintillator layer. For good spatial resolution of the electromagnetic showers, the different layers are rotated by 120° successively. Each module is split into an inner stack and an outer stack; the inner stack has 15 layers of lead-scintillator pairs whereas the outer stack has 24 layers of them. The scintillators are connected via fiber-optic light guides to the PMTs. The information gathered by the PMTs are used to reconstruct the location, timing and energy of the particles [26].

2.3 INNER CALORIMETER (IC)

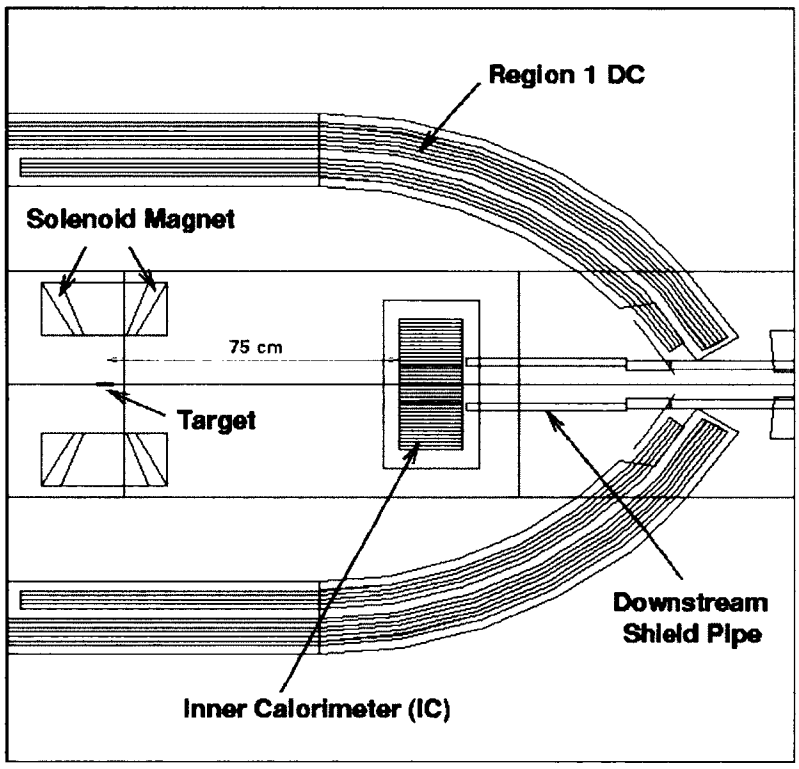

FIG. 27: Diagram showing the location of the Inner Calorimeter within the CLAS detector. Only region 1 of the Drift Chambers of the CLAS detector is shown in the figure.

The CLAS detector has limited acceptance at low polar angle below 18°. It is very important for this analysis to detect very low polar angle photons to reconstruct

low polar angle neutral pions. The lower polar angle neutral pions are of particular importance because they belong primarily to the lowest $P_{h\perp}$ bins. These in turn, contribute significantly to study the $P_{h\perp}$ dependence of the final results, which is very crucial for this analysis. Moreover, the low polar angle neutral pions are important to cover a wider range of the angle between the lepton and hadron plane. Hence an additional detector, called the Inner Calorimeter (IC), was inserted at about 75 cm downstream from the target as shown in Fig. 27 to detect lower polar angle photons. A photograph of the IC is shown in Fig. 28. This addition enabled the detection of photons from 5° in polar angle from the beam line. The IC is shielded against Moller electron by the strong magnetic field of the target solenoid. The Inner Calorimeter is made out of 424 lead-tungsten crystals arranged in an octagonal array. The light radiation in each crystal is read by photo-diodes connected at the end of each crystal. When a photon strikes the detector, it produces an electromagnetic shower that distributes over several crystals. The momenta of the photons are reconstructed by analyzing their electromagnetic showers distributed in the IC. The position of the photon in the x-y plane is the average position of the shower and the energy of the photon is the aggregate of the energies deposited in each crystal.

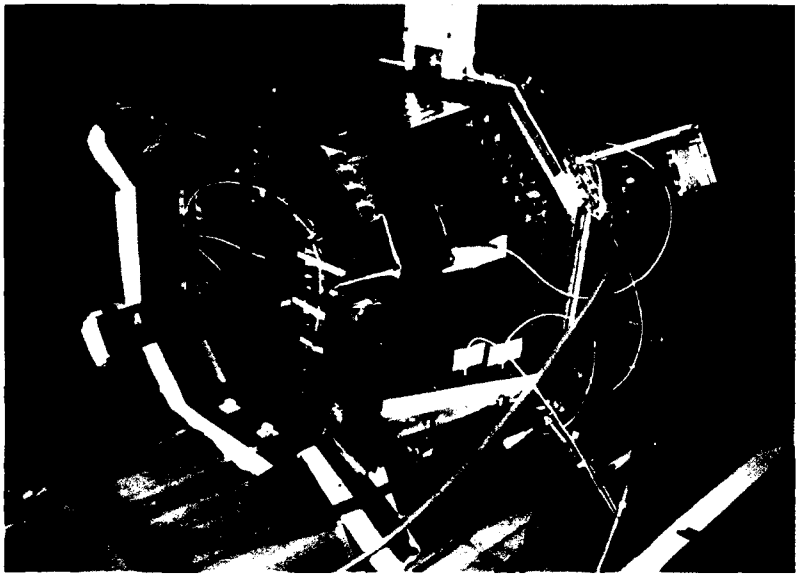

FIG. 28: Photograph of the Inner Calorimeter with its supporting components used in the experiment

2.4 POLARIZED TARGET

The main goal of the EG1-DVCS experiment is to study longitudinally polarized electrons scattering off longitudinally polarized proton and deuteron. Using pure ^{1}H and ^{2}H targets is not feasible due to the difficulty in achieving a large enough sample of polarized protons and deuterons. So instead ^{1}H and ^{2}H in $^{14}NH_3$ and $^{14}ND_3$ molecules were polarized by a method known as dynamic nuclear polarization (DNP) [27]. The polarization of the target was measured by the method of nuclear magnetic resonance (NMR) [27]. Since $^{14}NH_3$ and $^{14}ND_3$ have high radiation resistance, they were chosen over other possible target materials.

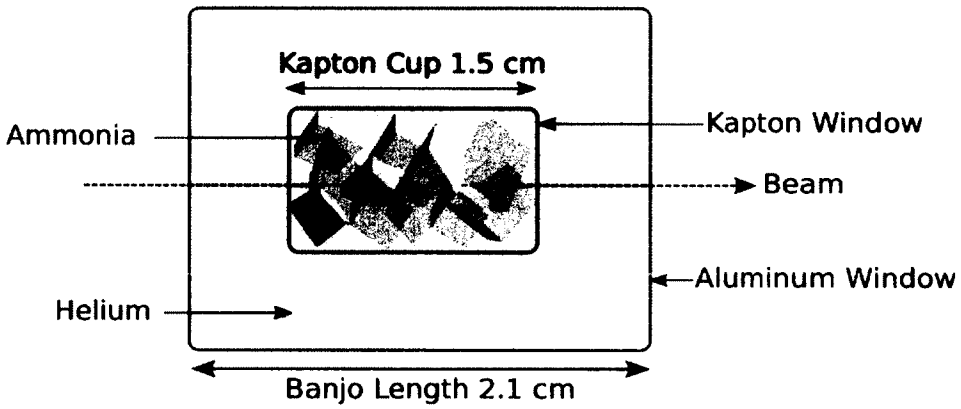

FIG. 29: Target configuration of the EG1-DVCS experiment. The ammonia beads were enclosed in a Kapton cylinder which was immersed in a liquid Helium inside a "banjo".

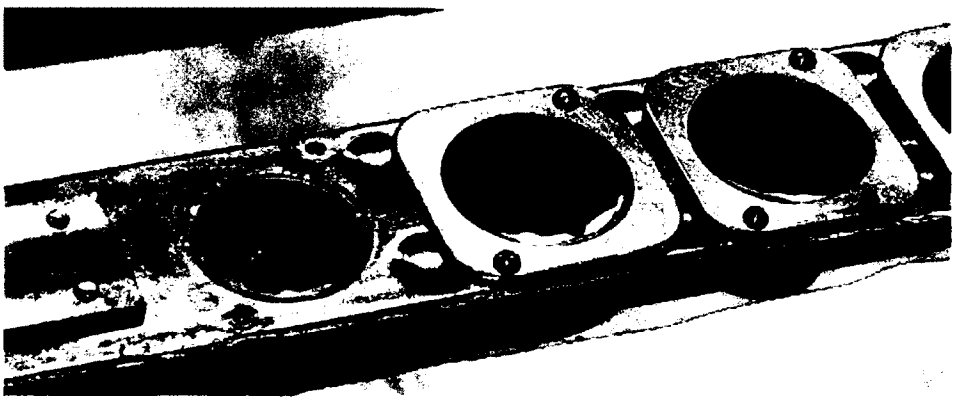

FIG. 30: Photograph of a series of target cups housed in a metal target insert. The cup on the left shows ammonia beads.

A rough sketch of the target configuration is shown in Fig. 29. The ammonia

beads were enclosed in a thin cylinder of Kapton which was immersed in a liquid Helium bath as shown in the photograph of the target insert in Fig. 30. The liquid Helium was pumped on to achieve 1 K temperature which is necessary to maintain the target polarization. The term "banjo" in Fig. 29 refer to a metal vessel made of copper which contains the liquid helium and into which the target stick is immersed. It has beam entrance and exit windows made up of aluminum about 2 cm apart. A superconducting Helmholtz magnet provided a uniform 5 Tesla magnetic field near the target. Numerous subsystems work as a unit to polarize the targets. The main subsystems are: refrigerator, superconducting magnet, microwave system, target insert and NMR system. A schematic diagram of the cutaway view of the polarized target cryostat from the beam-left side is shown in Fig. 31 [28].

A detailed description of DNP is beyond the scope of this thesis. An article by D. G. Crabb and W. Meyer [27] describes in detail the process and the theory of the DNP method to polarize ammonia targets. Basically, in the method of DNP, the higher spin-relaxation time for protons and deuterons than that for electrons is exploited to polarize free nucleons in the $^{14}NH_3$ and $^{14}ND_3$ targets. The target polarizations measured from Nuclear Magnetic Resonance during the run time were around 80% for NH_3 and 30% for ND_3.

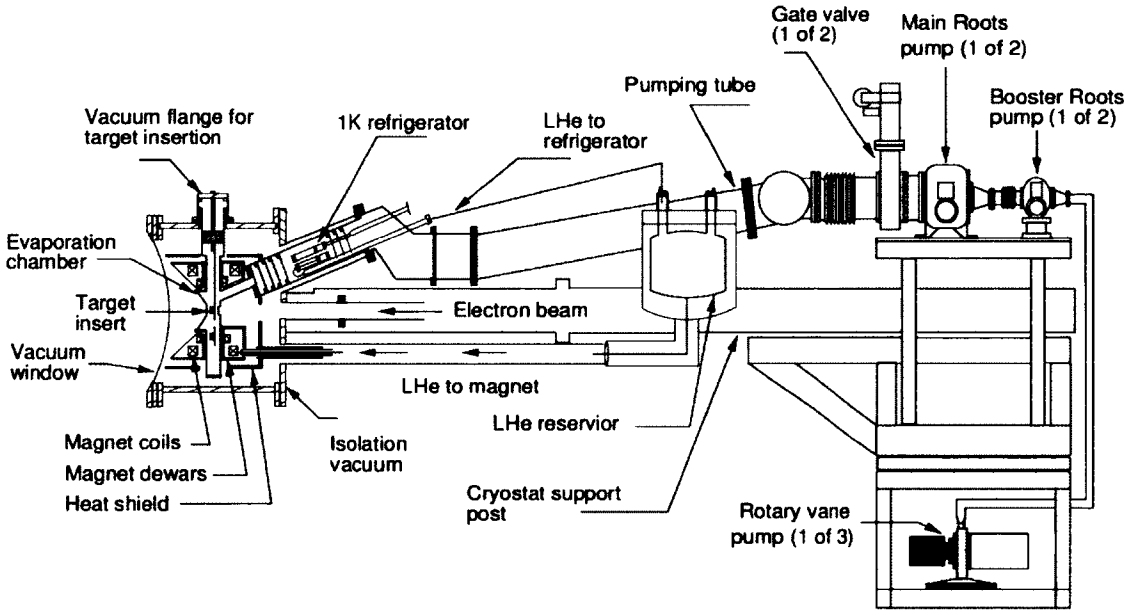

FIG. 31: Cutaway view of the polarized target cryostat from the beam-left side [28].

2.5 DATA PROCESSING

Different components of the CLAS detector generate a huge amount ($\sim$ terabytes) of data during an experiment. Only a fraction of the data are useful. To isolate useful data and convert them to analyzable format, the data goes through various stages of data processing. The first level of data processing starts from implementing a two level trigger system which isolates useful data to a great extent. The first level trigger is activated when there is sufficient energy ($\sim$ 0.5 GeV) deposited in the electromagnetic calorimeters and a signal in the Cherenkov counter. The second level trigger is activated when proper tracks in the drift chambers are found. If both the trigger conditions are satisfied, the signal is digitized.

The readout controllers of different components of the CLAS detector collect data as digital values. The data are then grouped into different events by an event builder process. These events are recorded in the form of Bank Object System (BOS) bank by the event recorder process. The BOS format is the lowest level off-line data format. To convert the raw data in the BOS files to momentum, charge, trajectory and other useful quantities, the data goes through a cooking process. During the cooking process, various calibration constants of the detectors can be adjusted. The cooking process produces ntuple files that are read with the ROOT software package. Due to the large volume of data, the data were skimmed by implementing very loose particle identification cuts for electrons. For electrons it was required that there were signals in DC, CC, SC and EC; moreover it was required that the momentum of the electron was above 0.5 GeV, there were more than one photo-electron in the CC and that a so-called time based track was found for the electron [29].

CHAPTER 3

DATA ANALYSIS I

3.1 DATA CORRECTIONS

Each different part of the EG1-DVCS experiment was divided into different runs, each comprising about 80 files of approximately 2 GB in size. The half-wave plate, target polarization, torus current and the target materials remained unchanged during each run. All raw data were processed with the standard CLAS analysis package. The processing and calibration of the data were done in several iterations. Data fulfilling the basic quality criteria were stored as root files [30][29]. The stored data were analyzed after the following corrections; these corrections were a collective effort of many other collaborators of the EG1-DVCS experiment. All the available corrections for EG1-DVCS data applicable to this analysis were implemented. For this analysis, the pass-1 v3 data set was used for part-A and part-B; for part-C, pass-1 v5 was used.

3.1.1 STANDARD CALIBRATIONS

The data from each component of the CLAS detector underwent standard calibration [30]. The Drift Chamber (DC) alignment was done using a set of straight-through tracks [30][31]. The gas Cherenkov Counter pulse height calibration was done using the single photo-electron peak. The time-of-flight scintillator timing corrections and electromagnetic calorimeter pulse height corrections were done using cosmic rays [30]. Calibrations were done iteratively to ensure the stability of the data over time.

3.1.2 TRACK CORRECTIONS

To minimize depolarization of the target, the beam was rastered over the 1.5 cm diameter of the target. A thorough study to convert the raster magnet ADC readings to the beam position in a plane perpendicular to the beam was done [30][32]. The study also found the nominal target position along the beam axis as a byproduct. The beam position reconstruction from that study was implemented.

The charged particle tracks were extrapolated back to the beam axis for each event depending on the raster position. The direction cosine values of the particles from the Drift Chambers and the x and y positions were fitted to swim the particles through the field map of the target to the Drift Chamber. This method significantly improved the angular resolution [30][33]. The same study also determined that the axis of the solenoid was tilted with respect to the CLAS torus axis. This tilt was taken into account in determining track trajectories.

3.1.3 PHOTON ENERGY CORRECTION IN THE EC

The photon energy in the EC was corrected as given by

$$E_\gamma = E/A + B, \tag{53}$$

where E is the nominal total energy deposited in the EC and A is the sampling fraction of the EC. The values of A and B were found by optimizing the mean and width of the neutral pion invariant mass peak for two photon events with both the photons detected in the EC. The procedure was done separately for each sector and run. The details are given in [30][34].

3.1.4 IC PHOTON TIMING AND ENERGY CORRECTIONS

There were many hot blocks near the beam line and a few random photons throughout the IC. The hot blocks are due to the electromagnetic showers created by the many false low energy photons emitted from other processes. Because of this, it is crucial to put a timing cut on any IC hits to select only in-time photons for a given event. The process to select the optimal timing cut on IC hits is as follows: First of all the alignments of all the blocks with each other were checked for all the runs. It was determined that the timing peaks of the IC hits shifted from zero in four distinct run groups; this was corrected by adding an offset to shift the peak to zero. IC photon timing peaks were narrowed by using the small pulse-height correction as given by [34]

$$t_{Corr} = t_{Uncorr} + 0.16 \times E - 0.15, \tag{54}$$

where E is the energy of the photon in GeV, and t_{Uncorr} and t_{Corr} are the uncorrected and corrected photon times in ns. By looking at signal-to-noise versus timing cut, the best value is 2.0 ns.

A seperate analysis on exclusive neutral pion by P. Bosted [34] showed an offset in the IC photon energy as a function of the distance from the beam line. This offset was corrected by using

$$E_{Corr} = E_{Uncorr} \times \left(1 + 0.04 \times e^{\left(\frac{4-r}{1.5}\right)}\right), \tag{55}$$

where r is the distance of the photon from the beam line along the plane of the IC.

3.1.5 RATE STABILITY CORRECTION

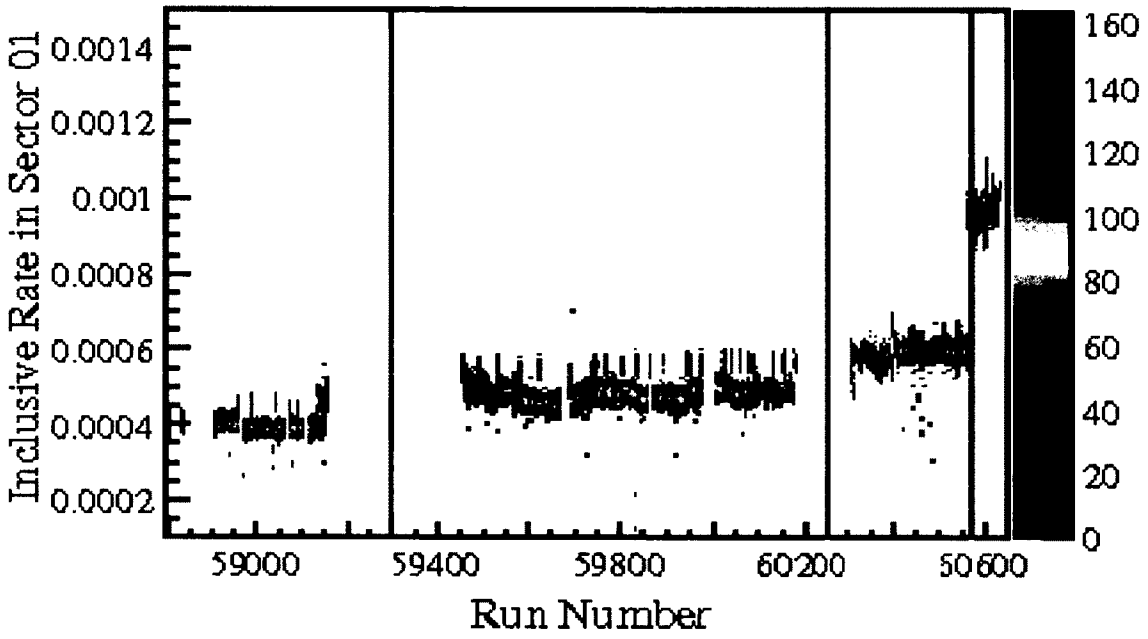

FIG. 32: Inclusive event rates per file in sector 1 for all runs before removing bad files of the EG1-DVCS experiment. Plotted along the x-axis are the different runs and along the y-axis are the event rates. Each point in the histogram correspond to the event rate for a single file. The red line separates part-A and part-B; the blue line separates part-B and part-C; the green line separates the in-bending and the out-bending runs of part-C. For visual clarity the plot has been sliced on top and bottom.

Despite careful on-line monitoring during the experiment, there were a few runs with the beam scraping on the target side walls. Those runs were removed after an off-line check [30][35]. In an off-line study to check the uniformity of beam coverage on the target, raster ADC variables in x and y were used to create occupancy plots for each data file. This procedure helps in the identification of files in which the beam was hitting the target cup walls and other irregularities in beam coverage. Further,

the stability of different event rates were checked separately for all the beam energies, target types, target polarization configurations, target positions, and torus polarity configurations. The rates were measured for each file by dividing the number of events by the integrated beam charge as measured by the Faraday cup as shown in Fig. 32. Files with inclusive event rates outside $\pm 4\sigma$ from the mean of the distribution were removed as shown in Fig. 33.

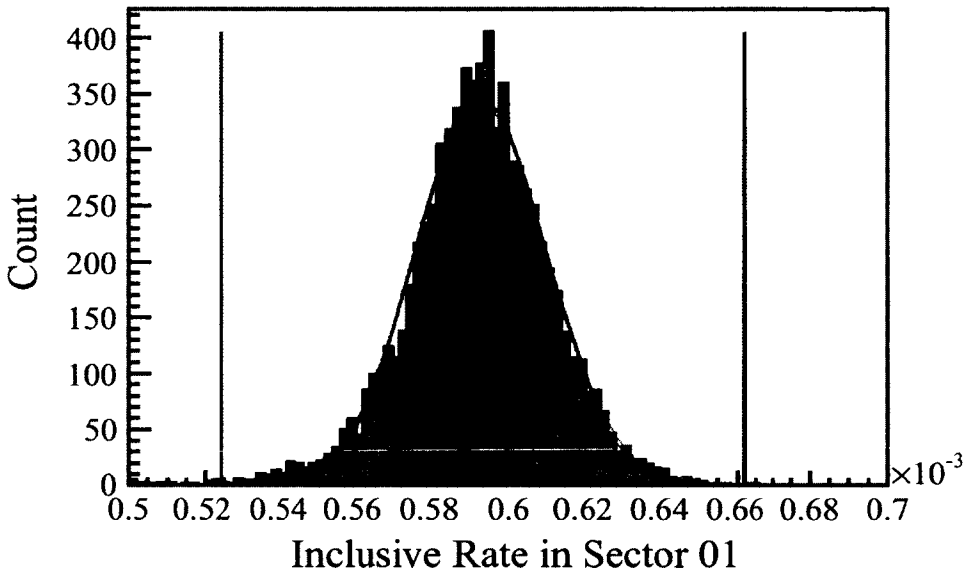

FIG. 33: Event rates per file for inclusive electrons in sector 1. The two green lines show the 4σ width of the distribution on either side of the mean. This distribution is for the ND_3 target of the out-bending runs of part-C.

The checks done above revealed some unexpected lower rates for IC photons for part-C data. It can be seen in the Fig. 34 that around run 60400 the event rate is about 20% lower. Later checks confirmed that this was due to the incomplete timing calibration of the IC. While the IC timing calibration was done, unintentionally the IC events in the lower left quadrature were left out. That issue became apparent at a much later stage of data analysis when the manpower to recalibrate the IC was unavailable. The problem can be seen in Fig. 35. The lower rate of the photons will eventually affect the π^0 rate. Since everything else was fine with these runs and statistics is a major issue, these runs were not discarded, instead, they were analyzed as a different group. The asymmetries from these runs were extracted separately and combined later.

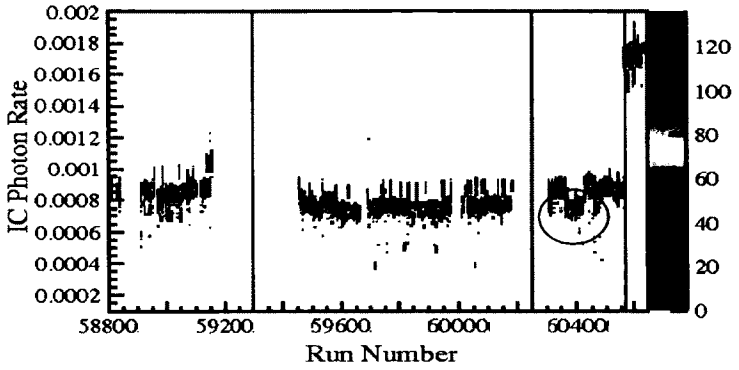

FIG. 34: Same as Fig. 32 except for the IC photon rate. A small dip in the rate around run number 60400 (marked by an ellipse) is due to incomplete calibration of the lower left quadrature of the IC which is shown in Fig. 34.

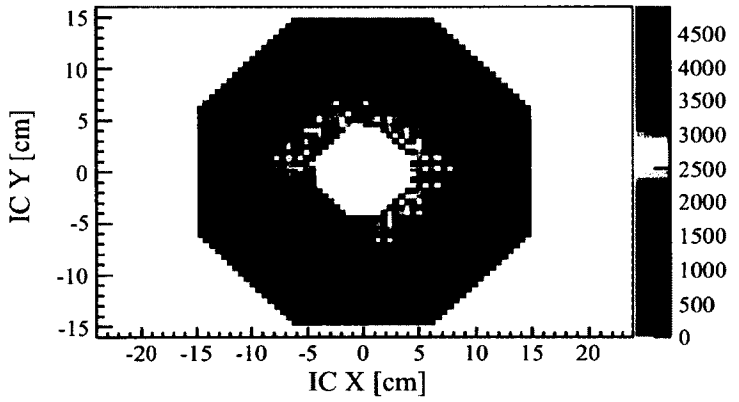

FIG. 35: Distribution of IC photon events in the IC. The event rates are significantly lower on the lower left quadrature due to an incomplete timing calibration.

3.1.6 CORRECTIONS TO THE EXPERIMENTAL DATA BASE

A table of the various experimental configurations was prepared during the experiment run time. Later, a careful check was done on the various experimental configurations that include the target polarization and the target type. The checking methods were: comparing event rates on different targets to discriminate different target materials and comparing the sign of the asymmetries to discriminate between positive and negative target polarizations. Further corrections on the existing table were made to ensure the correctness of the experimental configurations. The

configurations used in this analysis is exactly the same as that used by rest of the EG1-DVCS collaborators including the inclusive analysis [30].

3.2 PARTICLE IDENTIFICATION

Events with an electron and at least one pion in the final state were considered as candidates for SIDIS events. If any event had more than one pion, all the pions in that event were separately paired with the same electron; those separate pairs were considered as separate SIDIS events. The aforementioned selection method was applied also for events that had more than one pion of the same flavor. After the electron and pion pair selection, SIDIS event selection cuts were applied. In this chapter the particle identification cuts for electron and pions are discussed. Since neutral pions were reconstructed from the invariant mass of two photons, the identification cuts for photons are discussed as well. The extraction of the product of beam and target polarization, $P_b P_t$, from the EG1-DVCS data was done from the analysis of elastic events on proton, so the proton selection cuts used in the analysis are also discussed.

All the particle identification cuts mentioned in this section are on top of the nominal particle identification cuts implemented during the pass-1 cooking of the data [29]. All the particle identification cuts of this analysis are practically consistent with the cuts implemented by the other analyses on the EG1-DVCS experiment. In cases where there are differences, the cuts in this analysis are slightly tighter than the cuts implemented for other analyses of the EG1-DVCS experiment. The implementation of the particle identification cuts and selection algorithms were thoroughly cross-checked with a collaborator on this experiment, G. Smith. The cross-check was done by comparing the number of events after each particle selection cut and each step of the neutral pion reconstruction algorithm.

The systematic uncertainty in the final result due to the particle identification cuts were checked by varying the identification cuts by a certain amount depending upon the situation. In all cases, the differences in the final results were insignificant compared to the differences from other major sources of systematic uncertainty. Obviously, those insignificant differences were inherently due to statistical fluctuations and did not systematically depend on the widths of the cuts. Hence, the systematic uncertainties due to particle identification cuts are not included in this analysis; instead the backgrounds were directly assessed from misidentified events.

3.2.1 ELECTRON IDENTIFICATION CUTS

The Cherenkov Counters with a pion threshold of 2.6 GeV and the Electromagnetic Calorimeter with a nominal sampling fraction of 0.3 were the main detectors used for electron selection. The basic cut selection criterion is to differentiate electrons from negative pions. Negatively charged tracks with $y \leq 0.85$ and satisfying the following cuts were considered good electron candidates. The cut on y is to minimize radiative effects and pair-symmetric background.

Electromagnetic Calorimeter Cuts

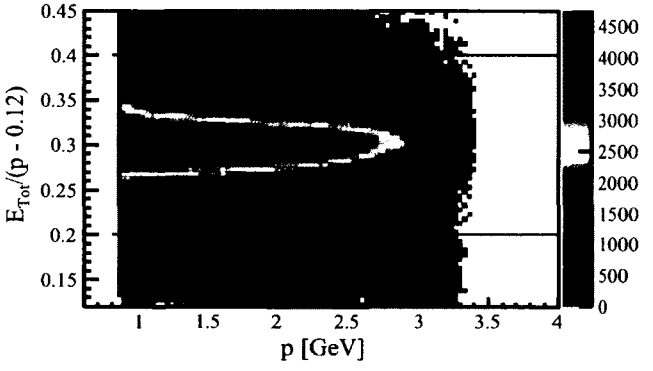

FIG. 36: Distributions of $E_{tot}/(p - 0.12)$ versus p after the application of all other electron identification cuts. For a good electron candidate, $0.2 \leq E_{tot}/(p - 0.12) \leq 0.4$.

Electromagnetic Calorimeters measures the aggregate energy of the electromagnetic showers created by the particle traversing through it. The sampling fraction is the ratio of visible to total shower energy. A cut of $0.2 \leq E_{tot}/(p - 0.12) \leq 0.4$ on the sampling fraction was implemented as shown in Fig. 36. The quantity E_{tot} is the total energy registered in the EC in GeV and p is the momentum of the particle in GeV. Here, $p - 0.12$ GeV is taken instead of p to take into account the energy lost by electrons as they traverse through the other layers of the detector from target to the calorimeter. Charged pion analysis shows that they typically deposit less than 0.06 GeV energy in the inner layer of the calorimeter as shown in Figs. 45 and 46. So a cut, $E_{Inner} \geq 0.06$ GeV, was implemented as shown in Fig. 37. E_{Inner} and E_{Outer} are the energies deposited in the inner and the outer layers of the EC respectively. Ultimate E_{tot} is the analog sum of both E_{Inner} and E_{Outer}. In the analysis, E_{tot} was

taken as the greater of the measured E_{tot} and $E_{Inner} + E_{Outer}$. In events were E_{Inner} was zero, the value of E_{Inner} was fixed by $E_{Inner} = E_{tot} - E_{Outer}$.

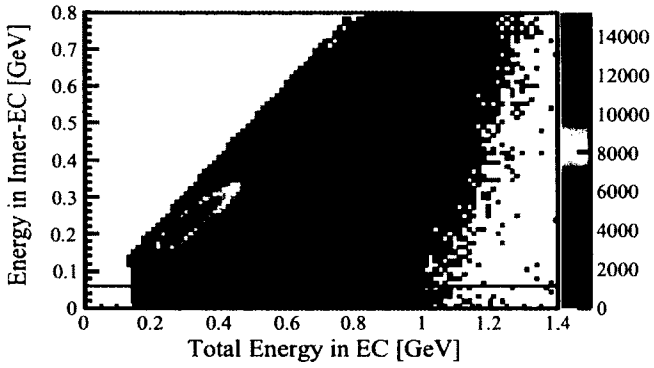

FIG. 37: Distributions of E_{Inner} versus E_{tot} after the application of all other electron identification cuts. For a good electron candidate, $E_{Inner} \geq 0.06$ GeV was required.

Geometric Cuts

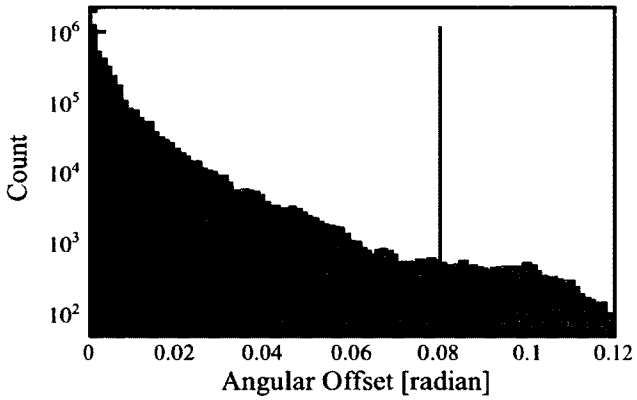

FIG. 38: Distributions of CC_{χ^2}, written as angular offset after the application of all other electron identification cuts. For a good electron candidate, $CC_{\chi^2} \leq 0.08$ was required.

The Cherenkov Counter mirror segment number and the time-of-flight paddle number belonging to a registered hit in a Cherenkov Counter photo-tube should have a one to one correspondence for a good electron candidate. A variable, CC_{χ^2}, was defined such that $CC_{\chi^2} = (1.1M + 0.003M^2 - P)^2/80$, where M is the Cherenkov mirror segment number and P is the SC paddle number associated with a given track [36]. For a good electron candidate, $CC_{\chi^2} \leq 0.08$ was implemented as shown in Fig. 38.

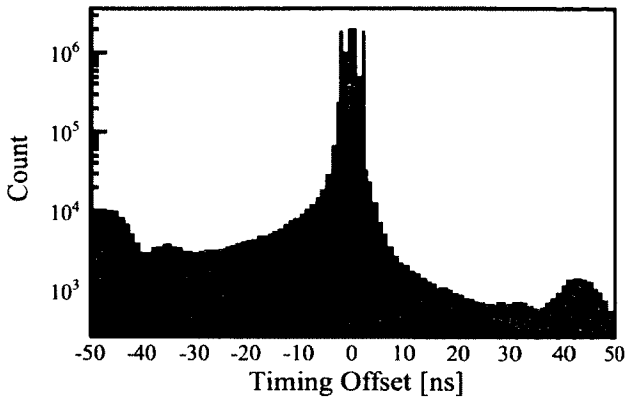

FIG. 39: Timing offset distribution after the application of all other electron identification cuts. For a good electron candidate, timing offset cuts were at 0±2 ns.

The difference between the time recorded for a track in the Cherenkov Counter and the time recorded in the time-of-flight detector corrected by the time of flight between the two detectors is termed timing offset. Tracks outside a timing offset of ±2 ns were rejected for a good electron candidate as shown in Fig. 39.

Vertex Cuts

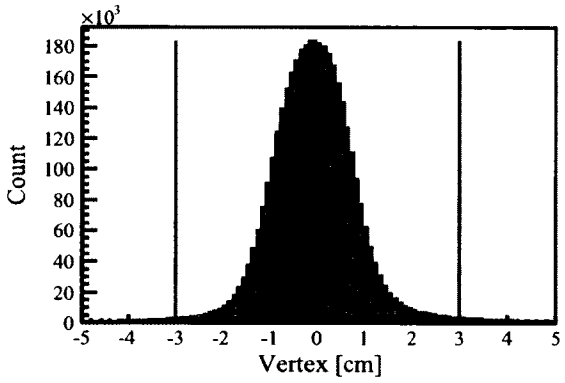

FIG. 40: The distribution of the reconstructed vertex position along the z axis after the application of all other electron identification cuts. For a good electron candidate $-3\,\text{cm} \leq v_z \leq 3\,\text{cm}$ was required.

To isolate events originating from the target materials only, cuts on the vertex position along the z axis, v_z, were implemented. For a good electron candidate $-3\,\text{cm} \leq v_z \leq 3\,\text{cm}$ was required [30] [33].

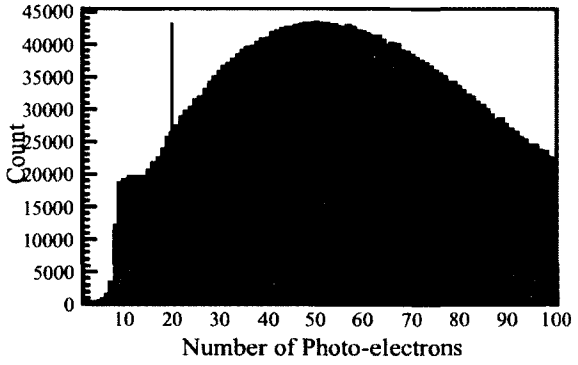

FIG. 41: Distribution of the number of photo-electrons in the CC after the application of all other electron identification cuts. For a good electron candidate, a minimum of 2 photo-electrons were required. In this figure the number of photo-electrons along the x-axis is multiplied by 10.

Cherenkov Counter Cut

Pions below 2.6 GeV normally produce no Cherenkov radiation at all. However, there is a possibility of photo-tube noise or Cherenkov gas scintillation giving 1 or at most 2 photo-electrons. Hence a minimum of 2 photo-electrons were required for a good electron candidate as shown in Fig. 41.

IC Shadow Cuts

The IC detector introduces an obstacle for forward-angle particles that would normally be detected in CLAS at small angles. Though the IC crystals are almost opaque to electrons, a few of the electrons pass through the structure surrounding the crystals with significant energy loss and multiple scatterings. Figs. 42 and 43 show the spatial distribution of the electrons that hit the IC and those that do not hit the IC. The electron tracks that passed through the IC and its supporting structure were removed. The electron tracks passing through the IC were determined by extrapolating their tracks reconstructed from the information from the three layers of the Drift Chamber to the plane along the front face of the IC [37].

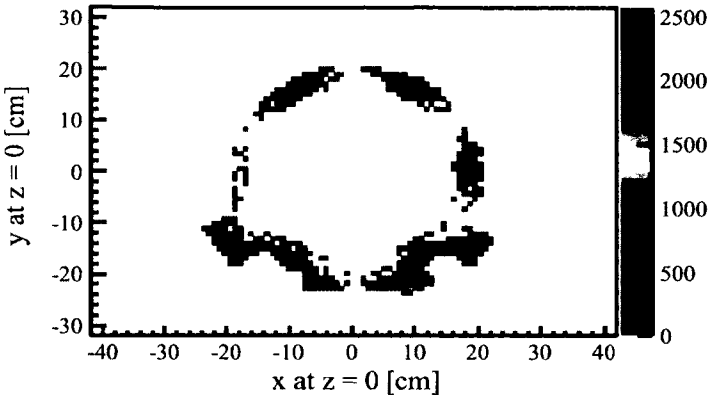

FIG. 42: The distributions of the x and y coordinates of the electron tracks in a plane along the front face of the IC. In this plot, only the electron tracks that hit the IC and its supporting structures are shown; these electrons were removed.

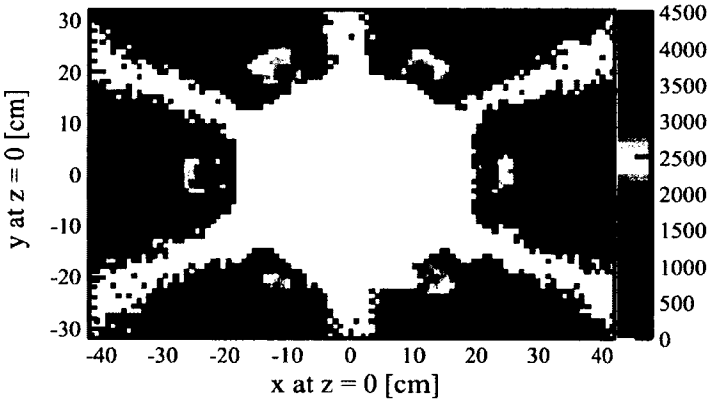

FIG. 43: The distributions of the x and y coordinates of the electron tracks in a plane along the front face of the IC. The electron tracks that do not hit the IC and its supporting structures are shown in the figure; only these electrons were taken into account in the analysis.

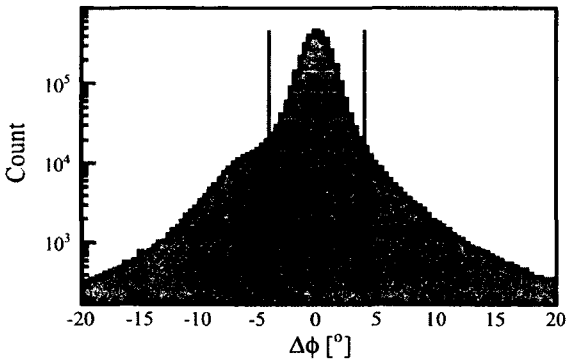

FIG. 44: The distribution of $\Delta\phi_{DC1}$ after the application of all other electron identification cuts. For a good electron candidate, the cuts were $\pm 4°$.

$\Delta\phi_{DC1}$ Cuts

$\Delta\phi_{DC1}$ is defined as the difference between the electron's azimuthal position around the beam axis at the first drift chamber layer and the azimuthal angle derived from the azimuthal component of its momentum at the same location. This difference for a good charged particle track should be close to zero [37]. A range of $\pm 4°$ from zero was set for a good electron candidate as shown in Fig. 44.

3.2.2 CHARGED PION IDENTIFICATION CUTS

The main criterion of the cut selection for charged pions is to isolate them from electrons and positrons as well as kaons and protons. In CLAS, the fact that leptons and charged pions interact with various materials in different ways is exploited to distinguish positrons from positive pions and electrons from negative pions. The interactions of electrons, positrons and charged pions in the Cherenkov Counters (CC) and the Electromagnetic Calorimeters (EC) are useful signals to distinguish a positron from a positive pion and an electron from a negative pion. Moreover, charged pions are separated from other hadrons by looking at the time required for particles of different masses but of the same momentum to reach the CLAS time-of-flight detector. Since at momentum greater than 2.6 GeV the limited time-of-flight resolution cannot distinguish a positive pion from other heavier hadrons, and the Cherenkov Counter cannot distinguish charged pions from electrons and positrons, a maximum momentum of 2.6 GeV was required for a good charged pion candidate. The following cuts are used to select a good charged pion candidate.

Electromagnetic Calorimeter Cut

By comparing the energy deposited by electrons and pions in the inner layer of the EC, a maximum limit of 0.06 GeV was set for charged pions as shown in Figs. 45 and 46. The rationale for this cut can be understood better from the corresponding figure for electrons in Fig. 37.

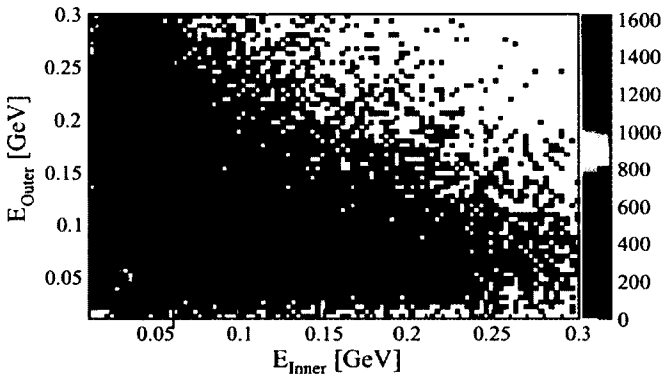

FIG. 45: The distributions of the energy deposited by positive pions in the inner and the outer layer of the electromagnetic calorimeter after applying all other positive pion selection cuts. For positive pions the energy deposited in the inner layer of the EC is required to be less than 0.06 GeV.

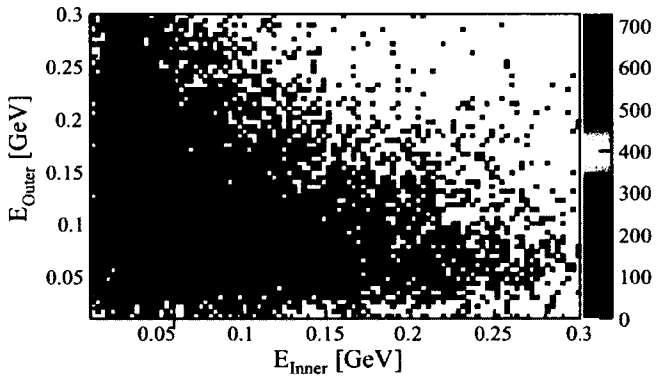

FIG. 46: The distributions of the energy deposited by negative pions in the inner and the outer layer of the electromagnetic calorimeter after applying all other negative pion selection cuts. For negative pions the energy deposited in the inner layer of the EC is required to be less than 0.06 GeV.

Cherenkov Counter Cut

As described for the case of electrons, tracks with less than 2 photo-electrons in the Cherenkov counter were considered as candidates for good charged pions. Figs. 47 and 48 show the number of photo-electrons in the CC for charged pions. The rationale for this cut is clear by comparing the corresponding distribution for electrons as shown in Fig. 41.

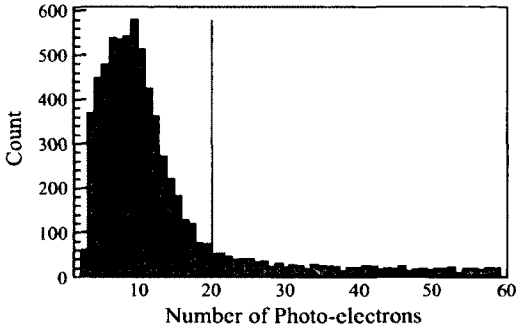

FIG. 47: The distribution of the number of photo-electrons in the Cherenkov counter after applying all other positive pion selection cuts. The number of photo-electrons along the x axis is multiplied by 10. For a good positive pion candidate, the number of photo-electrons is less than 2.

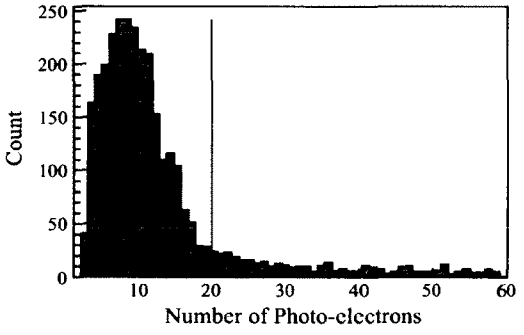

FIG. 48: The distribution of the number of photo-electrons in the Cherenkov counter after applying all other negative pion selection cuts. The number of photo-electrons along the x axis is multiplied by 10. For a good negative pion candidate, the number of photo-electrons is less than 2.

Δt Cuts

Charged pions were isolated from other heavier hadrons of the same momentum by comparing the difference in the time required for particles of different mass to reach the time-of-flight detector from the target. The time of flight can be calculated in two independent ways: first, from the direct measurement of the time variable (t_m) in the time-of-flight detector; second, from the momentum measured by the drift chamber and the mass of the particle (t_c) as well as the path length. Δt is defined as the difference between t_m and t_c. Figs. 49 and 50 show the Δt distributions as a function of momentum for charged pion tracks. t_c and t_m are calculated from

$$t_m = t_{TOF} - t_{Event}, \tag{56}$$

$$t_c = \frac{L_{TOF}\sqrt{m_\pi^2 + p^2}}{pc}, \tag{57}$$

where L_{TOF} is the path length between the target and the interaction point on the time-of-flight counter. A cut on Δt = (-0.5 ns, 0.7 ns) was used to identify a good positive pion candidate as shown in Fig. 49 and Δt = (-0.5 ns, 0.7 ns) was used to identify a good negative pion candidate as shown in Fig. 50. The slight difference between the cuts for positive and negative pions is due to the large number of positive kaons in the positive pion sample which requires a more stringent cut.

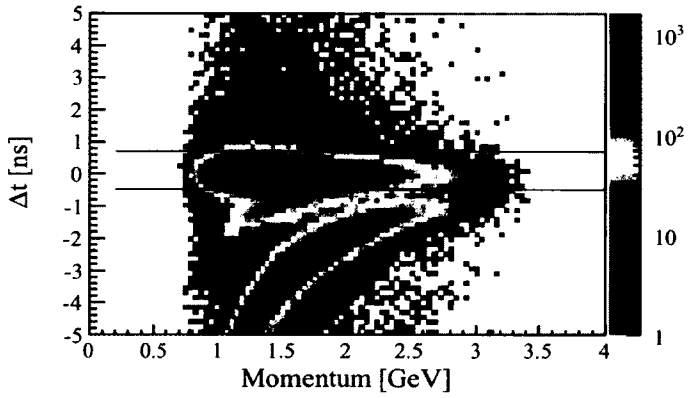

FIG. 49: Δt distribution as a function of momentum after applying all other positive pion selection cuts. For a good positive pion candidate, a cut on Δt = (-0.5 ns, 0.7 ns) was imposed.

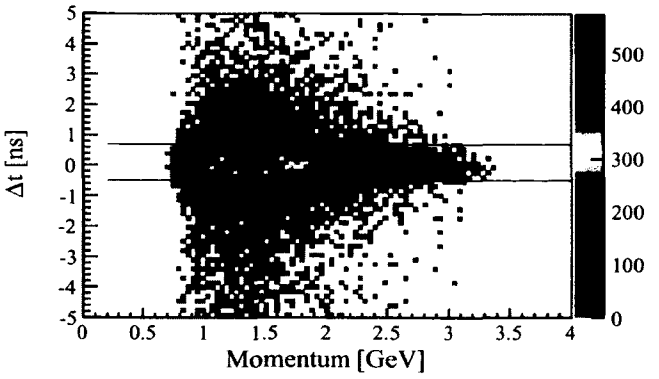

FIG. 50: Δt distribution as a function of momentum after applying all other negative pion selection cuts. For a good negative pion candidate, a cut on Δt = (-0.5 ns, 0.7 ns) was imposed.

Vertex Cuts

Just as in the case of electron selection, to isolate events originating from the target materials only, cuts on the reconstructed z coordinate of the vertex, v_z, were implemented [33]. Cuts of ±3 cm from the nominal position of the target were used. Figs. 51 and 52 show the reconstructed vertex distribution for charged pions.

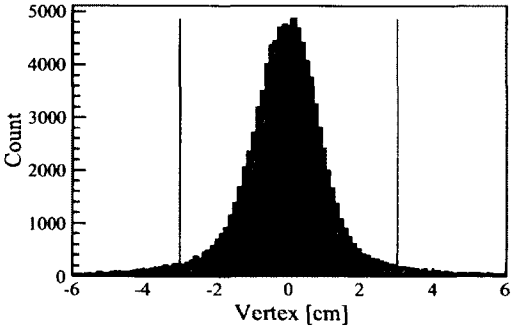

FIG. 51: The distribution of the reconstructed z coordinate of the vertex after applying all other positive pion selection cuts. For a good positive pion candidate, a vertex position v_z = (-3 cm, 3 cm) was imposed.

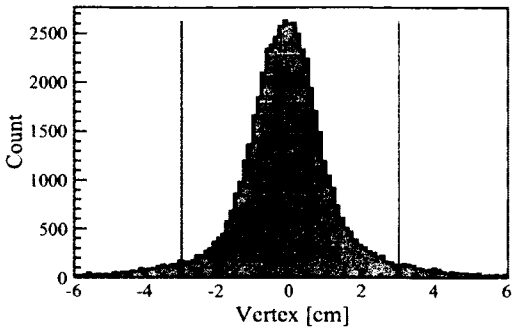

FIG. 52: The distribution of the reconstructed z coordinate of the vertex after applying all other negative pion selection cuts. For a good negative pion candidate, a cut on v_z = (-3 cm, 3 cm) was applied.

$\Delta\phi_{DC1}$ Cuts

Just as in case of electrons, a range of $\pm 4°$ from zero for $\Delta\phi_{DC1}$ was set for a good charged pion candidate as shown in Figs. 53 and 54.

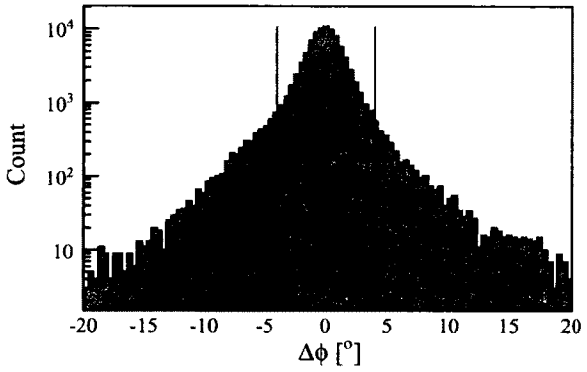

FIG. 53: $\Delta\phi_{DC1}$ distribution after applying all other positive pion selection cuts. The implemented cuts were $\pm 4°$ for a good positive pion candidate.

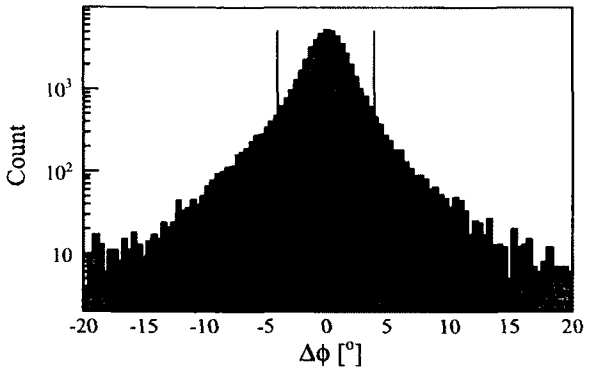

FIG. 54: $\Delta\phi_{DC1}$ distribution after applying all other negative pion selection cuts. The implemented cuts were $\pm 4°$ for a negative charged pion candidate.

IC Shadow Cuts

The IC detector introduces an obstacle for forward-angle particles that would normally be detected in CLAS at small angles. A significant number of charged pions pass through the IC and the other structures associated with it. Since the energy loss and the multiple scattering while traversing through the extra material introduce a significant change in the kinematics of those charged pions, the charged pions that pass through the IC and the structures associated with it were removed. The removal procedure is the same as the one applied in the case of electrons. In Figs. 55 and 56, the distribution of charged pions hitting the IC and passing away from the IC are shown.

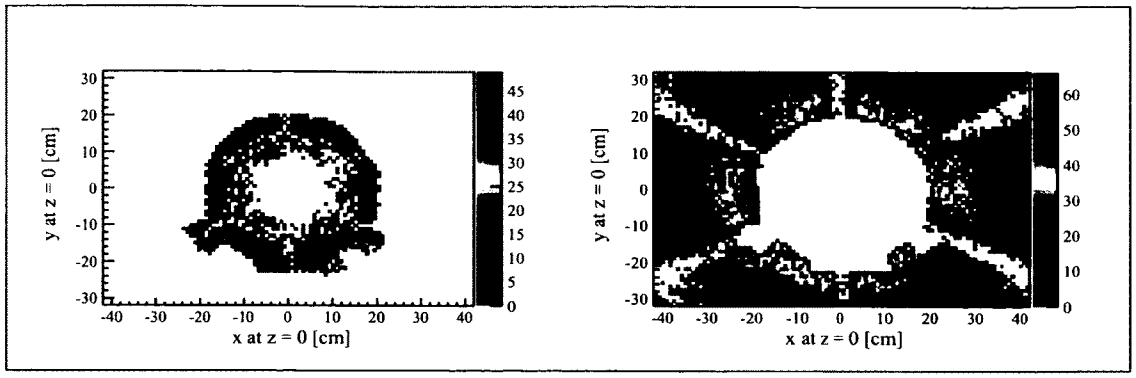

FIG. 55: The left plot shows the positive pions passing through the IC and its supporting structures and the right plot shows the pions passing outside. The positive pions on the left plot are discarded.

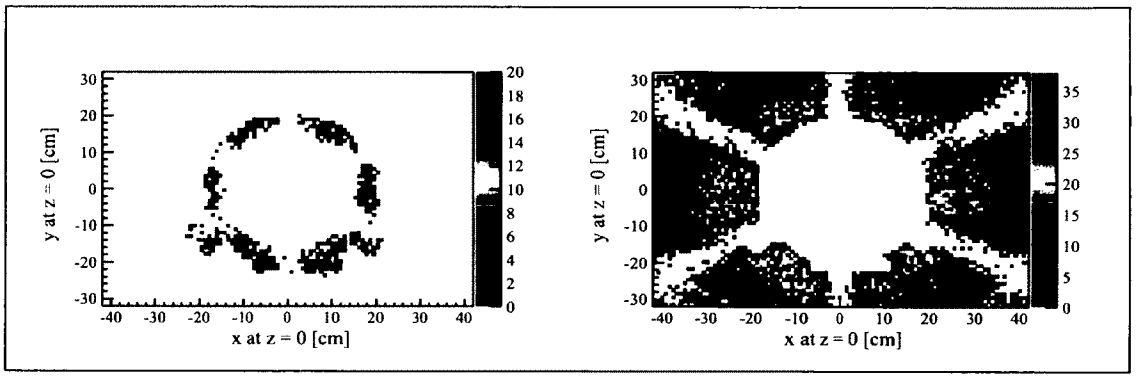

FIG. 56: The left plot shows the negative pions passing through the IC and its supporting structures and the right plot shows the pions passing outside. The negative pions on the left plot are discarded.

3.2.3 EC-PHOTON IDENTIFICATION

Photons in the EC were isolated by measuring the velocity of neutral particles from the length of the track and the time-of-flight. The main criterion of the cut selection is to isolate photons from neutrons. The EC photon energy correction was done as mentioned in Ref. [34], also briefly described in Section 3.1, prior to implementing any selection criteria. The direction cosines for each photon are calculated from the position of the photon in the EC, electron vertex along the z axis and the beam position in the x-y plane.

Photon Energy Threshold

The reconstructed energy threshold for all neutral particles was set at 0.3 GeV [34]. The value of 0.3 GeV was selected based on the fact that the statistical input of the neutral pion signal from two photons are minimal below a threshold of 0.3 GeV. In other words, for photons below 0.3 GeV the combinatorial background is larger than their contribution to strengthening the neutral pion signal.

β cuts

Photons were isolated from neutrons by measuring their velocities from their time-of-flight. The quantity β for the neutral particles is calculated from

$$\beta = \frac{L_{EC}}{c(t_{EC} - t_{Event})} \tag{58}$$

where L_{EC} is the distance between the target and the interaction point on the EC. Cuts at $0.925 \leq \beta \leq 1.0875$ were implemented. The β distribution for neutral particles after applying all other photon selection cuts is shown in Fig. 57.

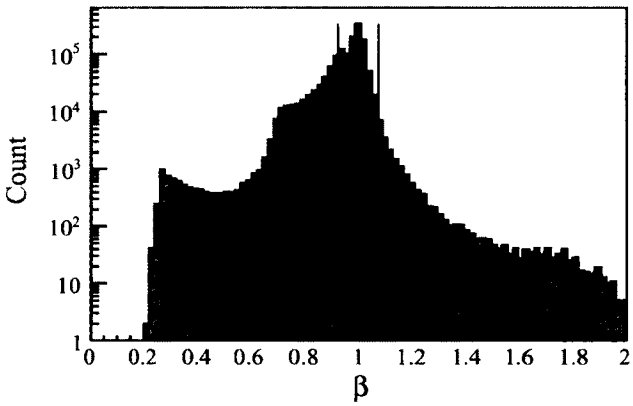

FIG. 57: β distribution for neutral particles after applying all other photon selection cuts. For a good photon candidate, $0.925 \leq \beta \leq 1.0875$ was required.

Bremsstrahlung Photon cuts

A Bremsstrahlung photon tends to go along the direction of the electron before the electron gets deflected in the magnetic field of the DC. The bremsstrahlung photon is removed by implementing a co-linearity cut at the vertex. Fig. 58 shows the

distributions in the difference of direction cosines along the x and y axis, c_x and c_y, between the electron and photon direction, along with the cut of radius 0.06 used to remove those events; it means the events within the circle are removed for a good photon candidate since only photon pairs resulting from pions are important for this analysis.

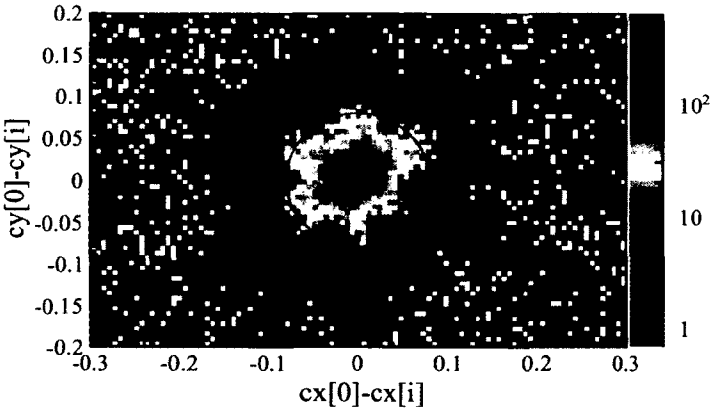

FIG. 58: The distributions of the difference in the direction cosines of the photon and the electron along the x and the y axis after applying all other photon identification cuts. Events within radius 0.06 were removed for a good photon candidate.

Fiducial cuts

Just as for electrons, the photons through the IC and on the edges of the EC were removed. The position of the photon tracks in the x-y plane along the front face of the IC were calculated from the electron vertex along the z axis, raster position in the x-y plane and the position of photon in the EC. Fig. 59 shows the removed and retained photons.

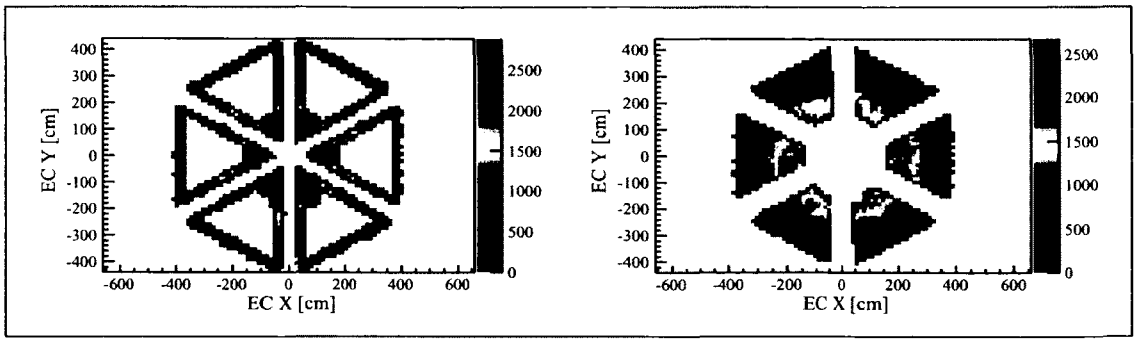

FIG. 59: The distributions of the x and y coordinates of the photons in the EC. The left plot shows the photons in the IC shadow and on the edges of the Electromagnetic Calorimeter; these photons are not candidates for good photons. The right plot shows the good photon candidates with their positions in the x-y plane of the EC.

3.2.4 IC-PHOTON IDENTIFICATION

All signals above 0.10 GeV in the IC were considered as possible photon candidates. No attempt was made to remove signals from other particles, including Møller electrons. The latter were largely suppressed by the polarized target magnetic field. However, to reduce combinatorial background under the invariant mass distributions, the following cuts were applied.

Photon Energy Threshold

The reconstructed energy threshold for all the neutral particles was increased to 0.3 GeV from 0.1 GeV to reduce low energy photon background [34]. The basic criterion of selecting the minimum energy threshold was by minimizing the statistical uncertainty of the neutral pion signal. The statistical uncertainty of a signal with S number of signal events and B number of background events is given by $\sqrt{S+2B}/S$.

Δt cuts

The time difference between the interaction on the IC and the event, corrected by the travel time between the target and the IC, defined as Δt, was required to be within ± 2 ns. Fig. 60 shows the Δt distribution and the implemented cuts for photons.

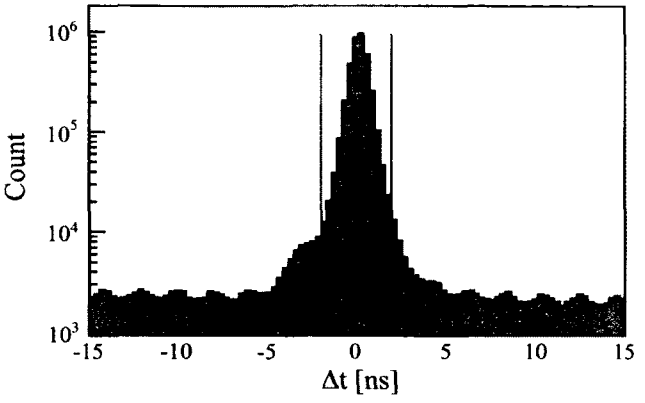

FIG. 60: Δt distribution for IC photons after applying all other photon identification cuts. For a good IC photon candidate, Δt is required to be within ± 2 ns.

Fiducial cuts

The events on the inner and the outer edges of the IC were removed. IC fiducial cuts are octagonal. These fiducial cuts remove the hot blocks near the beam line and the blocks on the outer region where the energy reconstruction is inaccurate. Fig. 61 shows the removed and retained photons.

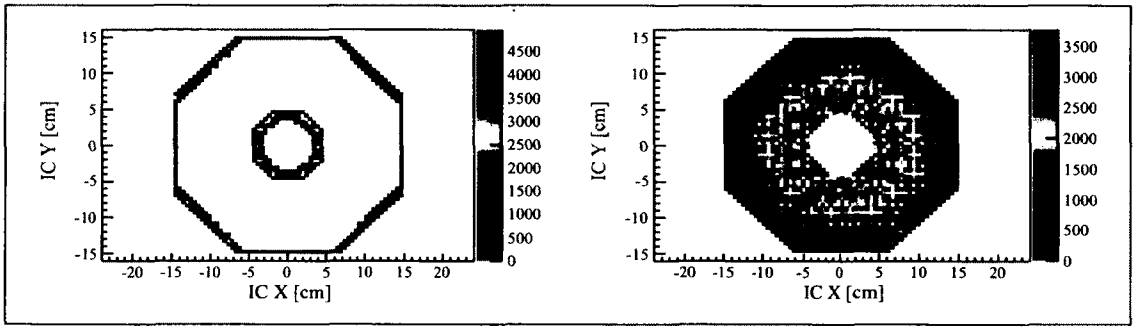

FIG. 61: The position distribution of the photons in the front face of the IC. The left plot shows the removed events; the right plots shows the retained events.

3.2.5 NEUTRAL PION SELECTION

Neutral pions were selected by reconstructing the invariant mass of two photons, $M_{\gamma\gamma}$. All the good photon candidates in an event were paired combinatorially to calculate their invariant mass. The square of the invariant mass of two photons

whose momenta p_1 and p_2 form an angle θ is given by $2p_1p_2(1-\cos\theta)$. Depending upon which part of the detector, EC or IC, the photons were detected in, cuts of different widths were applied to select the neutral pion events. This is mainly due to the difference in angular and energy resolution of the IC and EC. In Figs. 62, 63 and 64 the invariant mass spectra of two photons are shown for the three topologies; the applied cuts are represented by two vertical red lines. The cuts were chosen to minimize the statistical uncertainty of the signal as described in 3.2.4. The resultant momentum vector of the two photons was assigned to the neutral pion candidate. For two photons whose momenta are $\vec{p_1}$ and $\vec{p_2}$, the resultant momentum vector of the neutral pion is $\vec{p_1}+\vec{p_2}$.

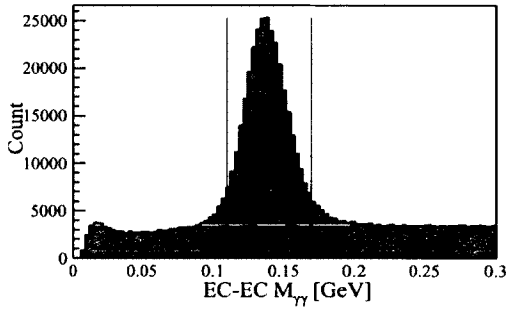

FIG. 62: $M_{\gamma_{EC}-\gamma_{EC}}$. The invariant mass distribution of two photons, both in the EC. The vertical red lines represent the applied cuts, 0.11 GeV $\leq M_{\gamma_{EC}-\gamma_{EC}} \leq$ 0.17 GeV.

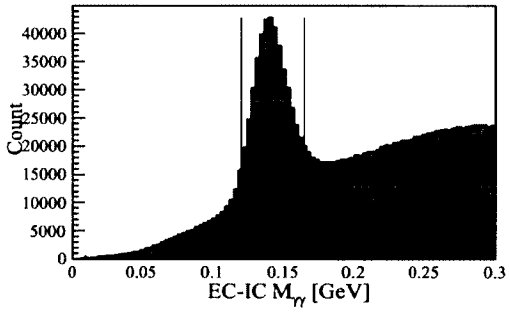

FIG. 63: $M_{\gamma_{EC}-\gamma_{IC}}$. The invariant mass distribution of two photons, one in EC and one in IC. The vertical red lines represent the applied cuts, 0.12 GeV $\leq M_{\gamma_{EC}-\gamma_{IC}} \leq$ 0.165 GeV.

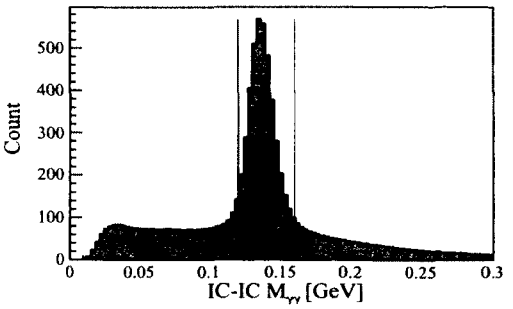

FIG. 64: $M_{\gamma_{IC}-\gamma_{IC}}$. The invariant mass distribution of two photons, both in the IC. The vertical red lines represent the applied cuts, 0.12 GeV $\leq M_{\gamma_{IC}-\gamma_{IC}} \leq$ 0.16 GeV.

3.2.6 PROTON SELECTION

Proton tracks were used in a part of the analysis dedicated to extract the product of the beam and target polarizations. This was done by analyzing the double spin asymmetries of elastic or quasi-elastic events for different bins of Q^2. Since the protons were used only in an exclusive and quasi-exclusive processes, the selection cuts for protons were a bit relaxed. The IC shadow cuts and the $\Delta\phi_{DC1}$ cuts applied for positive pions were applied for protons as well. For separation from other, lighter hadrons, cuts on $\Delta\beta$ = (-0.05, 0.05) were applied as shown in Fig. 65. $\Delta\beta$ is defined as the difference between the β calculated using time-of-flight and β expected from the measured momentum given the proton mass.

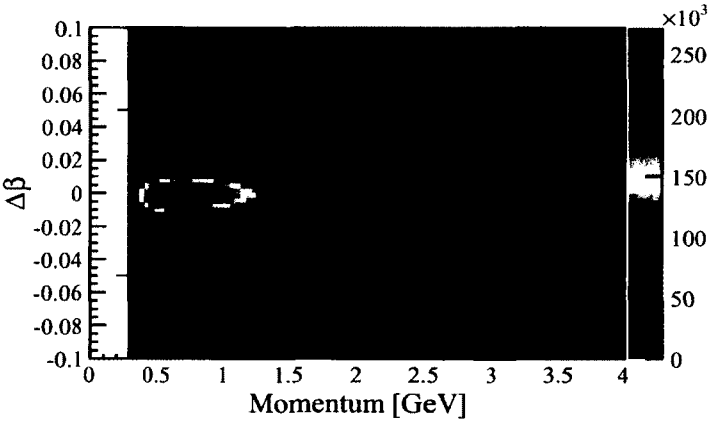

FIG. 65: $\Delta\beta$ and momentum distributions for protons. For a good proton candidate, $\Delta\beta$ was required to be within $\pm$0.05.

3.3 KINEMATIC DISTRIBUTIONS AND EVENT SELECTION

Events with an electron and at least one pion of any flavor in the final state were selected for the main analysis. If any event had more than one pion, all the pions in that event were separately paired with the same electron including pions of the same flavor; those separate pairs were considered as separate SIDIS events. After the electron and pion pair selection, SIDIS event selection cuts were applied. The distributions of kinematic variables shown in this chapter are after applying all SIDIS event selection cuts except on the kinematic variables shown. In all the cases the applied cuts are represented by red lines in the following plots. For convenience, the kinematic distributions are shown for positive pions and neutral pions from all three topologies. The kinematic distributions for positive and negative pions are almost identical. The kinematic distributions for neutral pions are significantly different in the three topologies, especially the ϕ_h distribution.

3.3.1 SIDIS EVENT SELECTION CUTS

The events within the following kinematic regions were identified as SIDIS events.

$$Q^2 > 1 \text{ (GeV)}^2$$
$$0.12 < x_B < 0.48$$
$$0.40 < z < 0.70$$
$$W > 2 \text{ GeV}$$
$$M_x > 1.5 \text{ GeV}$$

The cut on z, $(0.40 < z < 0.70)$, is applied in all cases except for cases where the asymmetries were measured as a function of z. In that case, the dependence of the asymmetries on z is extended down to $0.30 < z < 0.70$. The event selection cuts on the kinematic variable are shown in the following plots.

3.3.2 BIN WIDTHS FOR ANALYSIS

The same bins widths are used for the analysis of all SIDIS reactions. The widths of the kinematic bins are constant for for the entire range of the kinematic variable except for Q^2 which is binned in a logarithmic scale. The table below shows the bin widths for the kinematic variables. In the plots for the kinematic distributions, the

bin boundaries are represented by white lines.

TABLE 3: Bin widths for x_B, z, $P_{h\perp}$ and ϕ_h.

Kinematic Variable	Bin Width
x_B	0.09
z	0.10
$P_{h\perp}$	0.166 GeV
ϕ_h	30^0

TABLE 4: Bin boundaries for Q^2.

Q^2 Bin Number	Lower Boundary
1	1.00 $(GeV)^2$
2	1.25 $(GeV)^2$
3	1.56 $(GeV)^2$
4	1.95 $(GeV)^2$
5	2.44 $(GeV)^2$
6	3.04 $(GeV)^2$

3.3.3 KINEMATIC DISTRIBUTIONS

The Figs. 66, 67, 68 and 69 show the x_B, Q^2, W, M_x, z, $P_{h\perp}$ and ϕ_h distributions for the different SIDIS events on NH_3 targets. The x_B, Q^2, W, M_x and z distributions are very similar for all the pion flavors. However, the $P_{h\perp}$ and ϕ_h distributions are significantly different between charged pions and neutral pion from different topologies. The red lines represent the SIDIS event selection cuts; the white lines represent the bin boundaries.

The kinematic distributions of the different SIDIS events are shown in two dimensional graphs for different combinations of kinematic variables. The main reason for this is to reflect the correlation between the different variables. Moreover, the SIDIS π^0 events are presented for all the three cases on how the π^0 were reconstructed from the two photons. π^0_{EC-EC} means neutral pion reconstructed from two photons both of which were detected in the EC. π^0_{EC-IC} means neutral pion reconstructed from

two photons, one in the EC and the next in the IC. Similarly, π^0_{IC-IC} means neutral pion reconstructed from two photons both of which were detected in the IC.

The kinematic distributions of the three different cases of neutral pions show a huge difference. Comparatively, the kinematic coverage of the neutral pion is very wide and more uniform than the charged pions. In the case of charged pions, the ϕ_h distribution is centered around π radians. This is one of the reason for the larger statistical uncertainty in the asymmetry fit results. It is because the incomplete coverage introduces significant correlation among the simultaneously extracted asymmetry moments.

The kinematic distributions for events on ND_3 targets are very similar, hence they are not shown here. The slight difference is due to the minor differences in the target position and beam energy. One other important difference in the ND_3 target data was that there were some runs with out-bending torus polarity; but this did not introduce a significant difference in the kinematic distributions within the SIDIS event selection cuts. Though the amount of data collected for ND_3 was only somewhat less than that for the NH_3 target (the Faraday cup count for all the NH_3 runs was $\sim 1.8 \times 10^{11}$ and for all the ND_3 was $\sim 4.8 \times 10^{10}$), the significantly lower polarization of the ND_3 target led to much lower statistical significance of the extracted asymmetries, which accounted for by the differences in the analysis. The asymmetries on NH_3 target were determined in two dimensions of x_B, z and $P_{h\perp}$ with the bin widths as mentioned before. However due to the low target polarization and less statistics, the asymmetries on ND_3 were determined in a single dimension without making any changes in the bin widths as mentioned above.

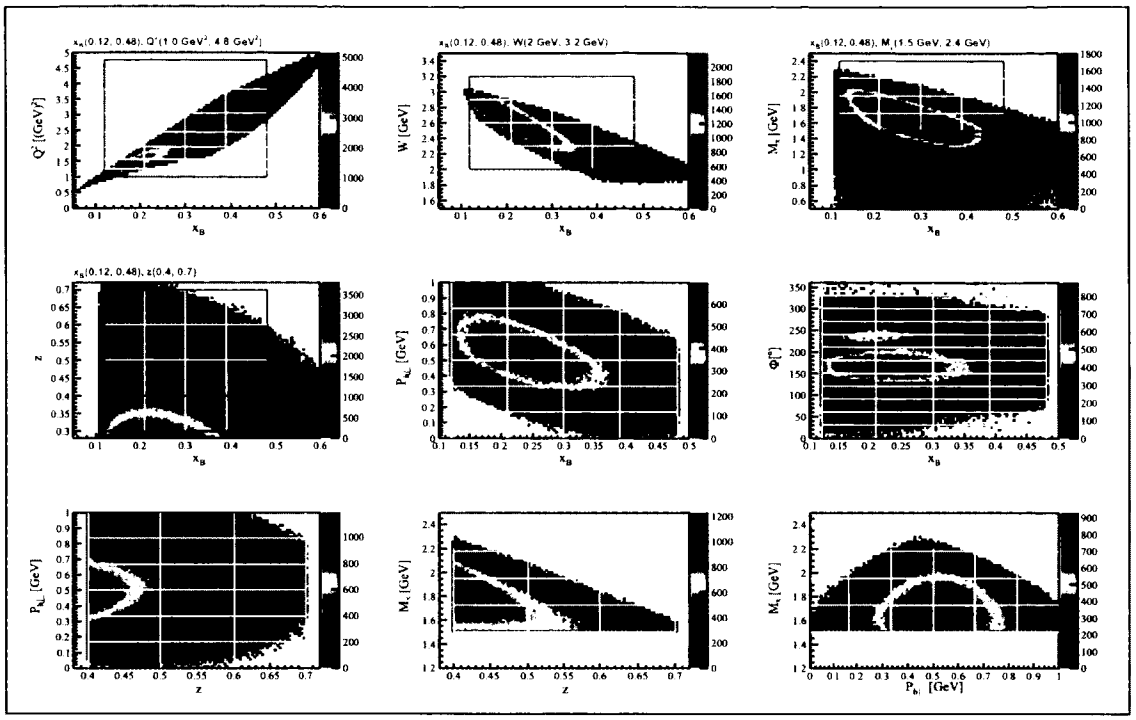

FIG. 66: x_B, Q^2, W, M_x, z, $P_{h\perp}$ and ϕ_h distributions for SIDIS π^+ events.

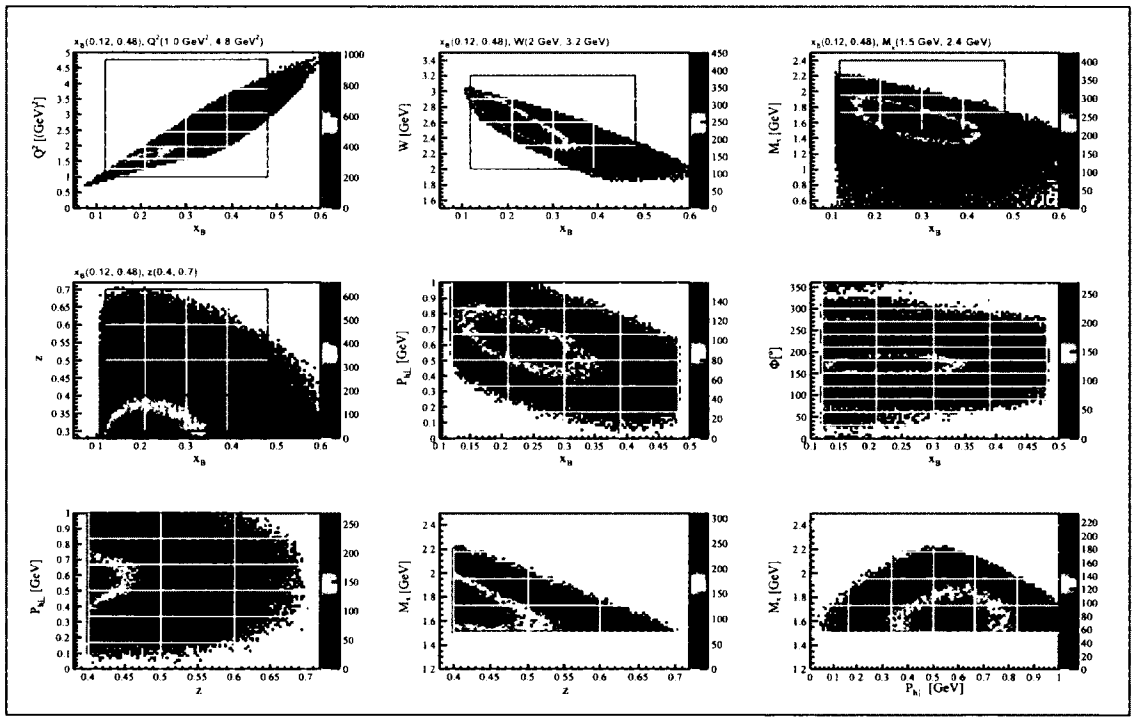

FIG. 67: x_B, Q^2, W, M_x, z, $P_{h\perp}$ and ϕ_h distributions for SIDIS π^0_{EC-EC} events.

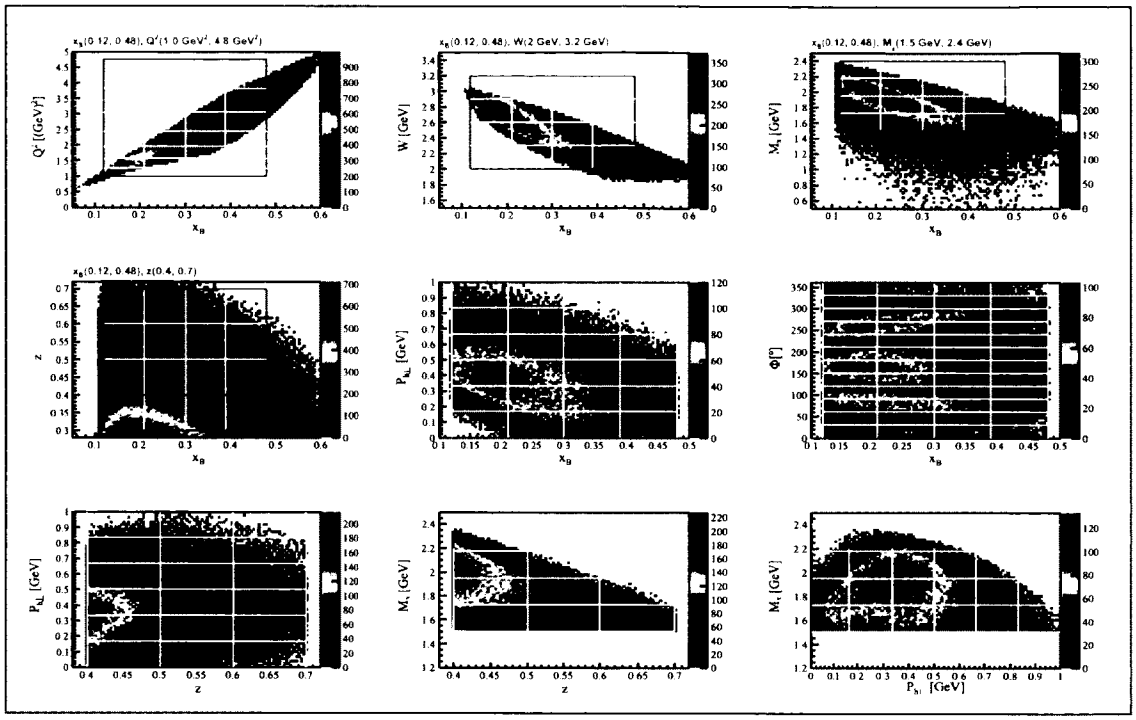

FIG. 68: x_B, Q^2, W, M_x, z, $P_{h\perp}$ and ϕ_h distributions for SIDIS π^0_{EC-IC} events.

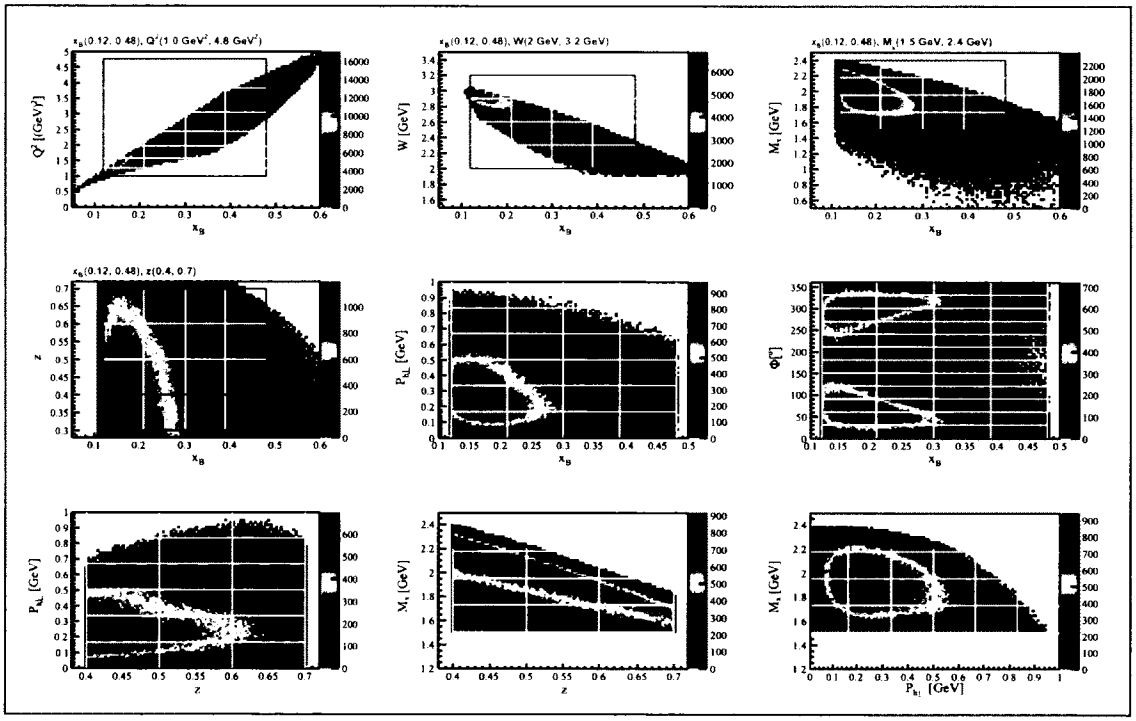

FIG. 69: x_B, Q^2, W, M_x, z, $P_{h\perp}$ and ϕ_h distributions for SIDIS π^0_{IC-IC} events.

3.4 BACKGROUND ESTIMATION

There was a significant number of background events in the $e\pi^+X$ and $e\pi^0X$ channels. On the other hand, the background in the $e\pi^-X$ channel was negligible. The neutral pions were identified by reconstructing the invariant mass of two photons. To increase statistics, all the identified photons in EC and IC were combinatorially paired to reconstruct the invariant mass. This introduces a significant background, termed "combinatorial background". Two different conventional methods, side-band subtraction and fitting with polynomials, were tested to subtract the combinatorial background. Both of these methods are less than optimal, as became apparent in a series of checks. In the first case, with the side-band subtraction method, the effect of varying particle identification cuts on the invariant mass distribution were not uniform in the signal region and in the side-band region. With the second method, fitting a polynomial, the polynomial parameters depend significantly on the range of the fits. So, a third method which is more based on physics than the previous two was implemented. The new method allows us to estimate the systematic uncertainty more reliably.

3.4.1 BACKGROUND UNDER SIDIS π^+ EVENTS

There are four kinds of background within positive pion selection cuts: positrons, positive kaons, protons and accidental coincidences. Here, accidental coincidences refers collectively to positive pions from uncorrelated events and other unidentified events. The positron peak in Δt distribution is not apparent; this indicate that the positron background is insignificant. The fraction of accidental coincidences within the positive pion identification cuts is denoted by NF in this analysis for convenience. Since the fraction of positive kaons, denoted by KF in this analysis for convenience, and protons within the positive pion identification cuts is a function of momentum, it was calculated for various momentum bins. At momenta greater than 2.6 GeV, the fraction is significant and difficult to quantify due to the overlap of the different spectra. Hence an upper limit of 2.6 GeV on the positive pion momentum was implemented to ensure good positive pion selection.

The positive pion contamination fractions were calculated by fitting suitable Δt dependent functions in six different momentum bins. The Δt distributions for proton, positive kaon and positive pion were assumed to be Gaussian; the Δt distribution

for accidental coincidences is assumed to be constant. The fits on Δt distributions in different momentum bins are shown in Fig. 70. It should be noted that the positive pions in this analysis are SIDIS positive pions, i.e. these positive pions belong to events where all the SIDIS event selection cuts are implemented. The positive kaon contamination fractions were calculated by taking the ratio of the area of the positive kaon distribution to the sum of the area of the proton, pion and kaon Δt distributions within the (-0.5 ns, 0.7 ns) cut for positive pions. The kaon contamination within the positive pion cuts were assumed to be a function of momentum only. The fraction of kaons in each SIDIS kinematic bins was then derived from the momentum distribution of the positive pions within that kinematic bin. The fraction of kaons and accidental coincidences in different kinematic bins are shown in Figs. 71, 72 and 73. In the kinematic bins of this analysis the kaon contamination fraction is up to 5.5%, for higher x_B and the highest z bin. So, 5.0% uncertainty is included in the systematic uncertainty due to the uncertainty of the contribution from positive kaons.

The amount of accidental coincidences was taken into account while calculating the asymmetries. The asymmetries were divided by $(1-NF)$, where, NF is the accidental coincidences fraction. This is analogous to dividing the asymmetries with the dilution factor. The background underneath the positive pions could be either unpolarized, in which case our correction is proper, or it could have the same polarization as the real pions so that the asymmetry would be unaffected. So, for estimating the systematic uncertainty in the background underneath positive pions, NF is taken as zero.

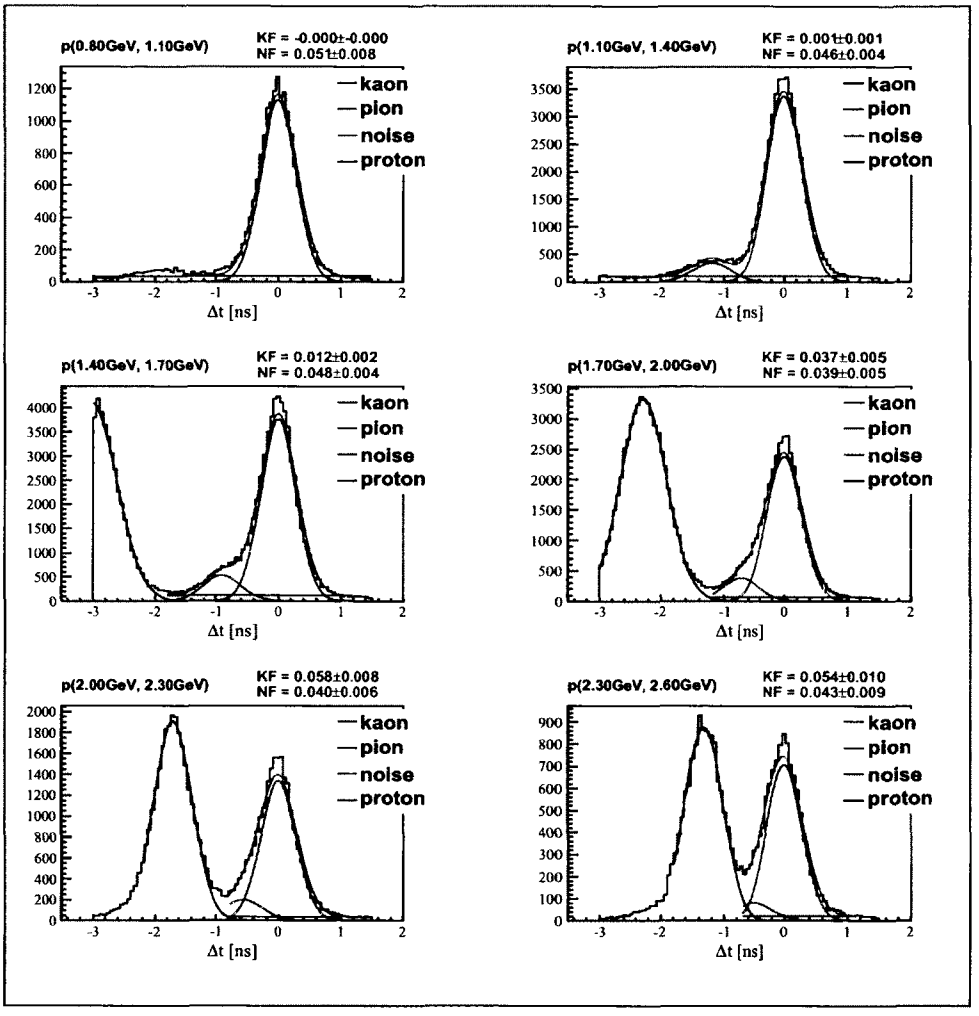

FIG. 70: Δt distribution for SIDIS π^+ in different momentum bins. NF on top of each plot refers to the accidental coincidences fraction. KF refers to fraction of positive kaons. The contributions from different events are represented by differently colored curves.

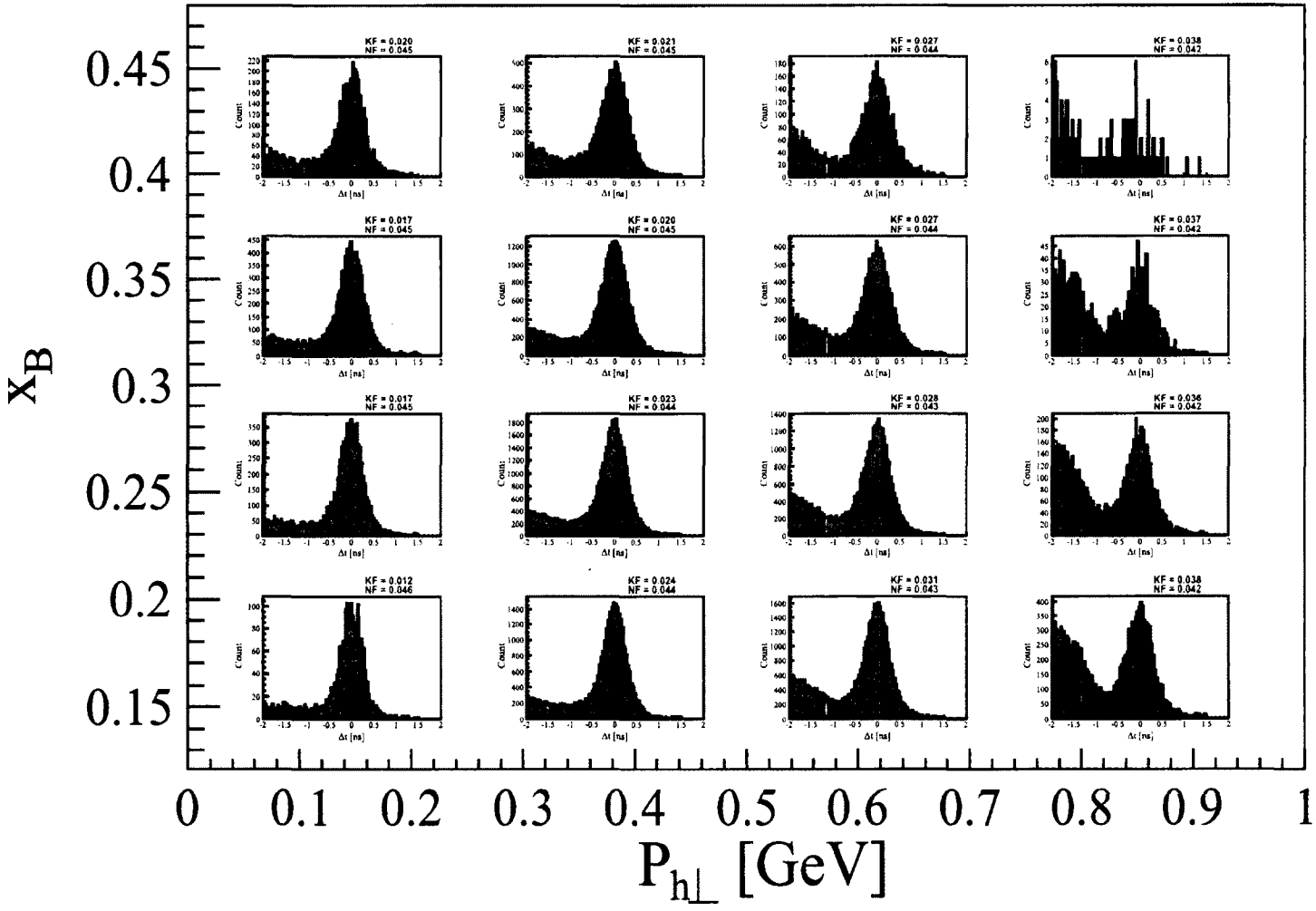

FIG. 71: Δt distribution for π^+ in different x_B, $P_{h\perp}$ bins. NF on top each plot refers to the accidental coincidences fraction. KF refers to fraction of positive kaons

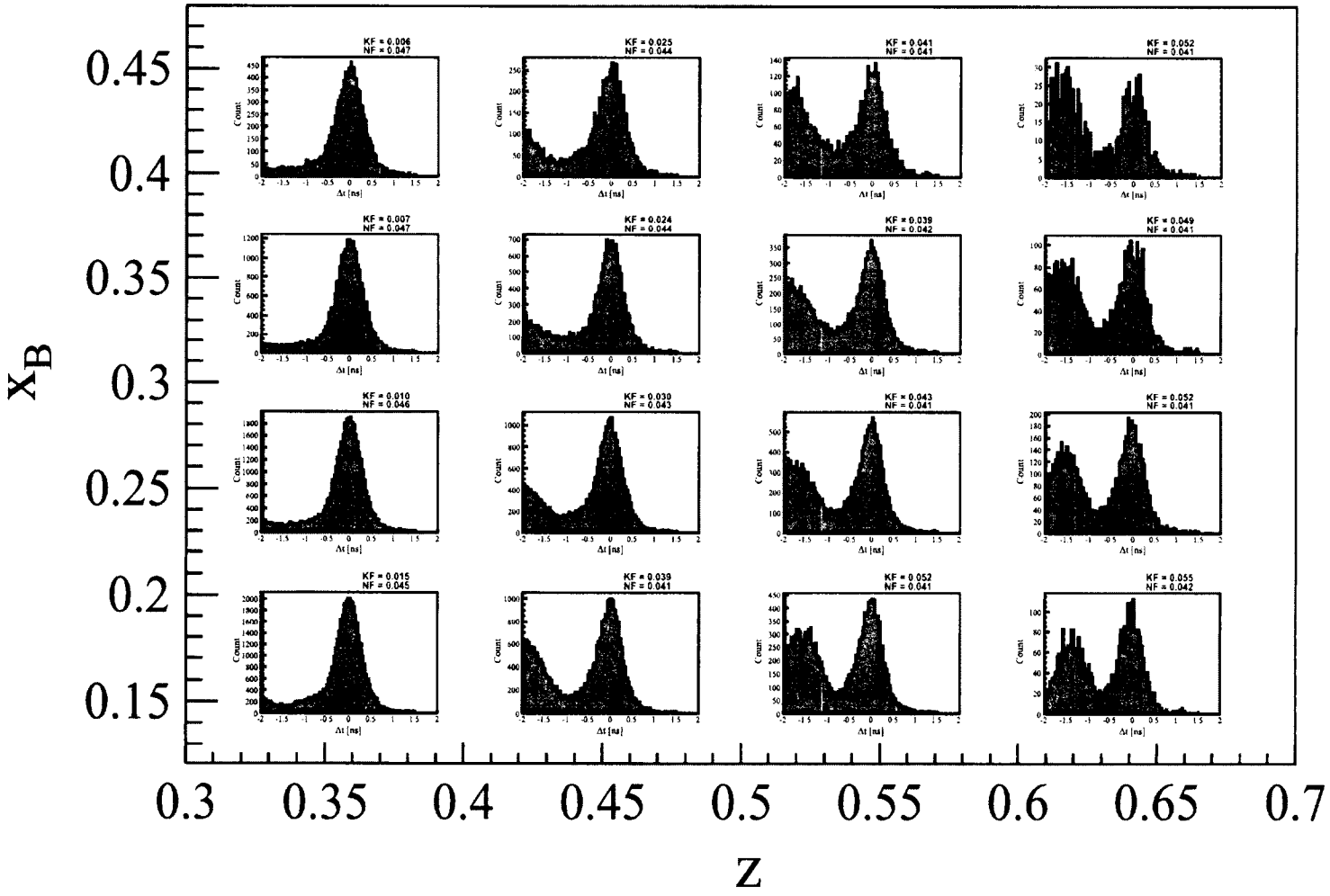

FIG. 72: Δt distribution for π^+ in different x_B, $P_{h\perp}$ bins. NF on top each plot refers to the accidental coincidences fraction. KF refers to fraction of positive kaons.

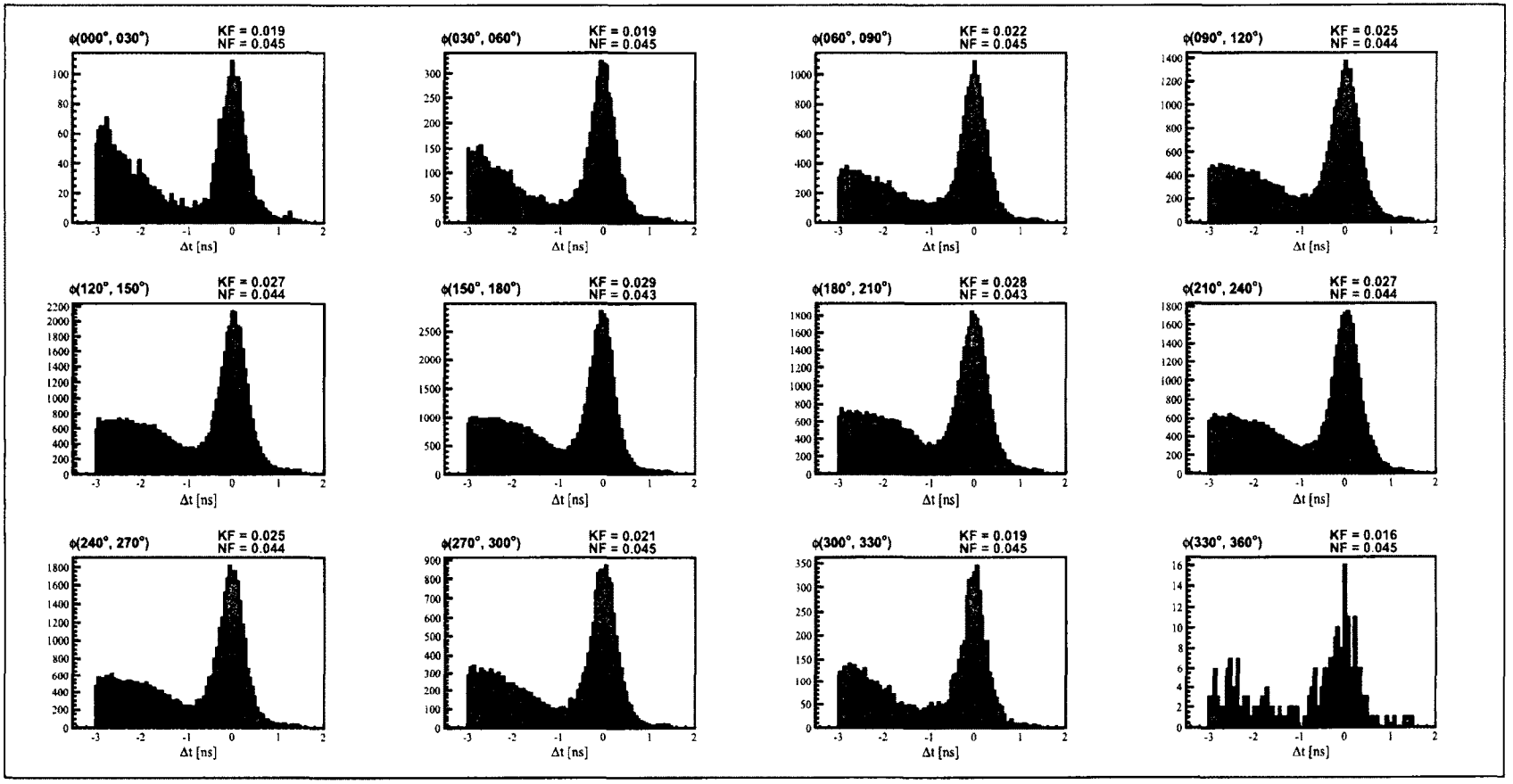

FIG. 73: Δt distribution for π^+ in different ϕ_h bins. NF on top each plot refers to the accidental coincidences fraction. KF refers to fraction of positive kaons.

3.4.2 BACKGROUND UNDER SIDIS π^0 EVENTS

The complicated background under the neutral pion peaks were simulated in different kinematic bins by calculating the invariant mass of two uncorrelated photons. Here, uncorrelated photons means two photons from two different events as shown in Figs. 74, 75 and 76. However, for better background matching, both the uncorrelated photons were chosen from events with the electron in the same sector, x_B and Q^2 bin. The background is then scaled by matching the number of events in the spectrum greater than 3σ above the signal, in the higher mass region of the spectrum. This scale factor is termed here as the normalization constant.

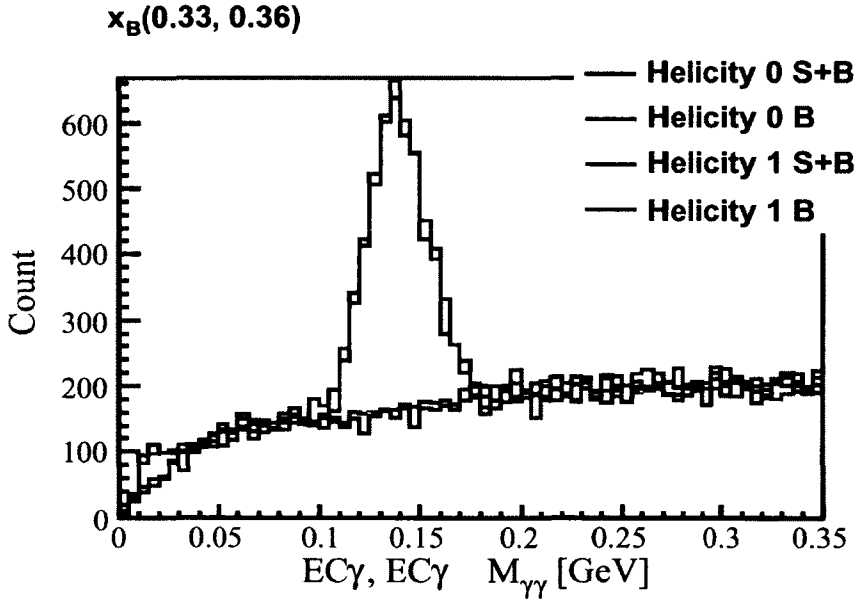

FIG. 74: $M_{\gamma\gamma}$ distribution of two correlated and uncorrelated EC photons.

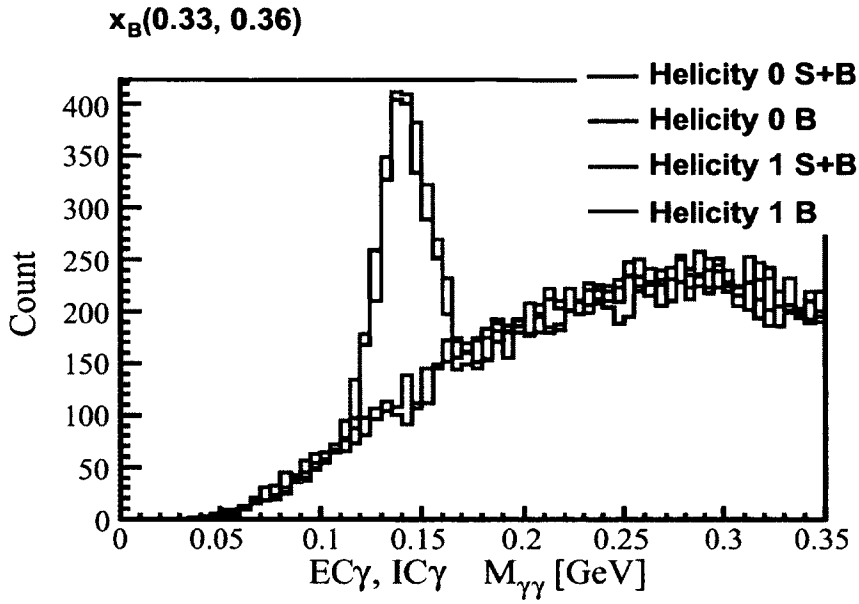

FIG. 75: $M_{\gamma\gamma}$ distribution of correlated and uncorrelated EC-IC photons.

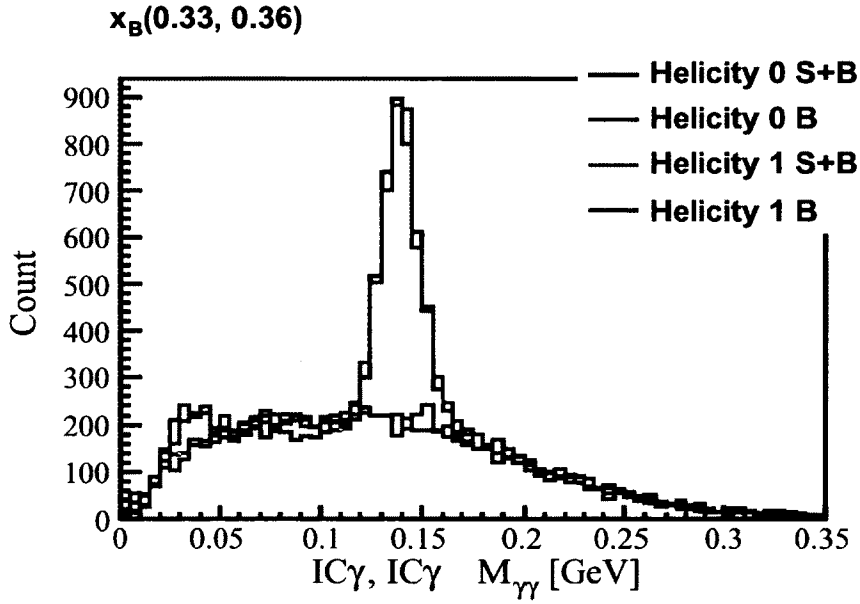

FIG. 76: $M_{\gamma\gamma}$ distribution of two correlated and uncorrelated IC photons.

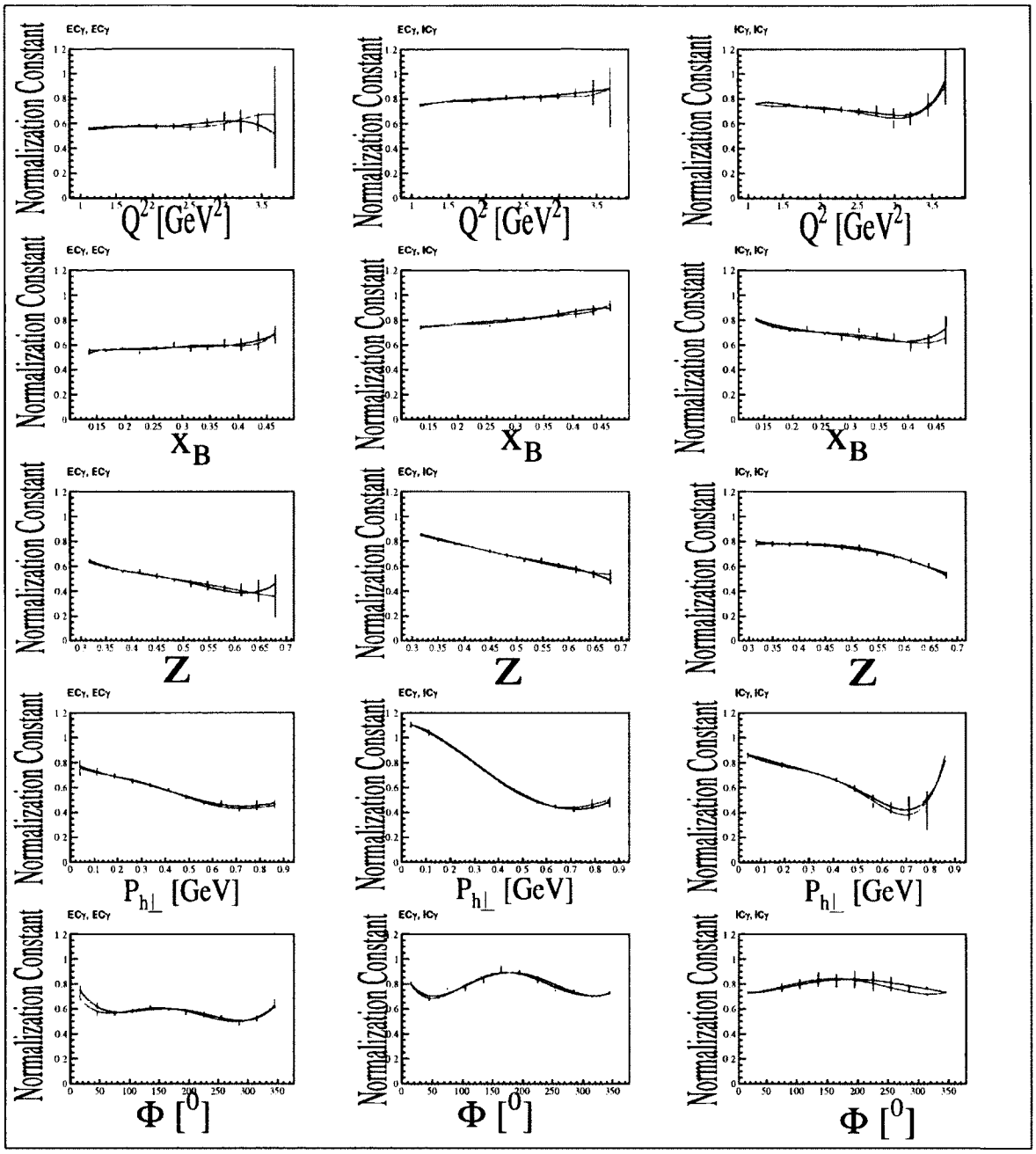

FIG. 77: Normalization constants for the neutral pion background as a function of various kinematic variables. The two colors are for different beam helicity configurations. It is also clear from these plots that $f(P_{h\perp})$ is the leading term in equation [59] because it has the maximum gradient in the entire range. It should be noted that in all these plots the difference between the fits for different helicities show the extent of the systematic uncertainty.

The normalization constants were determined for 12 bins of each SIDIS kinematic variable. The functional form of the dependence of the normalization constants on each kinematic variable was fitted with a fifth degree polynomial as shown in Fig. 77. These individual fits were then combined into an overall normalization constant, N_C.

$$N_C(z, x_B, P_{h\perp}, Q^2, \phi_h) = f(P_{h\perp}) \times \frac{f(x_B)}{< f(x_B) >} \times \frac{f(z)}{< f(z) >} \times \frac{f(Q^2)}{< f(Q^2) >} \times \frac{f(\phi_h)}{< f(\phi_h) >} \tag{59}$$

where, $f(z)$, $f(x_B)$, $f(P_{h\perp})$, $f(Q^2)$, $f(\phi_h)$ are the functional form of the kinematic dependence of the normalization constants. $< f(x_B) >$, $< f(P_{h\perp}) >$, $< f(z) >$, $< f(Q^2) >$ and $< f(\phi_h) >$ are the event weighted averages in the entire range of the respective kinematic range. This process was done separately for each beam helicity, target polarization configurations, target configuration and different part of the EG1-DVCS data. After calculating $N_C(z, x_B, P_{h\perp}, Q^2, \phi_h)$, the background was subtracted from each kinematic bin, separately for each beam helicity, but multiplying the normalization factor N_C by the invariant mass spectrum of the uncorrelated photons and subtracting the result within in the neutral pion invariant mass cuts.

Since the normalization constants were extracted separately for each target polarization and beam helicity configurations, these normalization constants could introduce artificial asymmetries. The difference in the final results by taking two normalization constants (one for the correct beam helicity configuration and the other one for the opposite configuration) were taken as the systematic uncertainty in the background subtraction for neutral pion. The blue and green curves in Figs. 74, 75 and 76 is a good estimation of this systematic uncertainty.

CHAPTER 4

DATA ANALYSIS II

4.1 BEAM, TARGET AND BEAM-TARGET POLARIZATION

The beam and the ammonia targets used during the experiment were polarized. Raw beam asymmetries, target asymmetries and beam-target double spin asymmetries were divided by the beam polarization, target polarization and their product respectively. The beam polarization was periodically measured by a Moller polarimeter during the experiment. Table 5 shows the average values of the beam polarizations obtained from the Moller polarimeter for different parts of the experiment. These values were adopted from Reference [38] which carefully calculated the averages by weighting the values from the polarimeter by the number of events during the interval between two Moller runs. The uncertainty of the beam polarization in Table 5 is included in the systematic uncertainty of the final result.

TABLE 5: Average values of the beam polarizations measured with the Moller polarimeter for different parts of the experiment.

Part of the Experiment	Beam Polarization
Part A	0.87 ± 0.03
Part B	0.84 ± 0.03
Part C	0.78 ± 0.03

Nuclear magnetic resonance (NMR) techniques were used to directly measure the target polarization during the experiment, yielding a value around 0.8 for the proton and 0.32 for the deuteron with large uncertainty. A more precise value, however, can be obtained from elastic scattering asymmetries from which one can extract the product $P_b P_t$. With the known values of beam polarization and $P_b P_t$, the target polarization can be determined. The uncertainty of the target polarization is included in the systematic uncertainty of the final result.

4.1.1 $P_B P_T$ EXTRACTION METHOD

The $P_b P_t$ values for Parts A and B of the EG1-DVCS experiment were calculated separately for negatively and positively polarized target run groups. The method employed here closely resembled that employed by the EG1 experiment [39]. The difference between the values from Reference [40] and this analysis was used to estimate the systematic uncertainty.

$P_b P_t$ is determined from the raw exclusive ep elastic asymmetries at different Q^2 bins using the equation

$$P_b P_t = \frac{A_{raw}}{f_D A_{||}^{th}}, \tag{60}$$

in which A_{raw} is the raw elastic double spin asymmetry, f_D is the elastic dilution factor, and $A_{||}^{th}$ is the theoretical elastic double spin asymmetry which is given by [41]

$$A_{||}^{th} = \frac{2\tau r\left[M/E + r\left(\tau M/E + (1+\tau)\tan^2\theta/2\right)\right]}{1 + r^2\tau/\epsilon}, \tag{61}$$

in which $\tau = Q^2/4M^2$, E is the beam energy, θ is the electron scattering angle, $\epsilon = 1/(1 + 2(1 + \tau\tan^2(\theta/2)))$ and the ratio of proton's electric to magnetic form factor $r = G_M/G_E \approx 2.79$.

Raw, exclusive ep elastic asymmetries were generated for events with invariant mass, $0.80\,\text{GeV} < W < 1.10\,\text{GeV}$, proton transverse momentum, $-0.015\,\text{GeV} < p_\theta < 0.015\,\text{GeV}$, and azimuthal angle between the proton and the electron, $177^\circ < \Phi_{ep} < 183^\circ$. The distributions of the various kinematic variables and the cuts are shown in Fig. 78. Each plot in the figure shows the distribution of a particular variable after implementing the cuts on all the other variables. The missing energy distribution shown in the Fig. 78 has its center at zero; this ensures that the selected events are elastic. Data from ^{12}C were used to simulate the nuclear background. The number of events in the ranges $165^\circ - 173^\circ$ and $187^\circ - 195^\circ$ for Φ_{ep} for both ^{12}C and NH_3 were used to scale the carbon to nitrogen. Fig. 78 shows the elastic events with the scaled nuclear background contribution. The events used for normalization are well outside 3σ of the elastic peak, and therefore the normalization constant is almost constant for small changes in the interval where the events are counted. The elastic dilution factor, f_D, can be calculated from the number of events with ($177^\circ < \Phi_{ep} < 183^\circ$) for ^{12}C and NH_3 targets. The value of f_D shown in Fig. 78 is around 0.9.

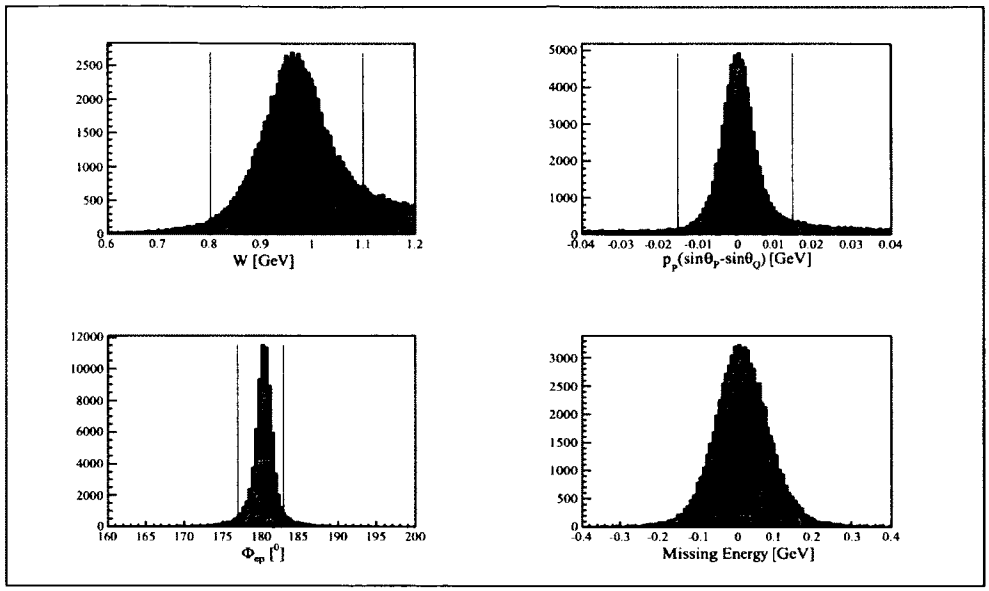

FIG. 78: Kinematic distributions of elastic event candidates. The applied cuts are represented by vertical red lines. For each plot all the other cuts are implemented. In the top right plot, p_P is the momentum of the detected proton, θ_P is the polar angle of the detected proton, θ_Q is the polar angle of the virtual photon; the expression $p_P(\sin\theta_P - \sin\theta_Q)$ gives the polar component of the transverse momentum of the proton which is represented by p_θ in the main text.

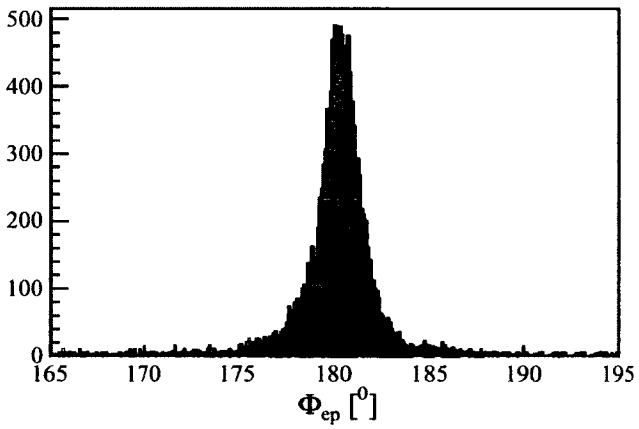

FIG. 79: The azimuthal angle between an electron and a proton, Φ_{ep}, for NH_3 (black) and ^{12}C (red, scaled) after cuts on W and p_θ.

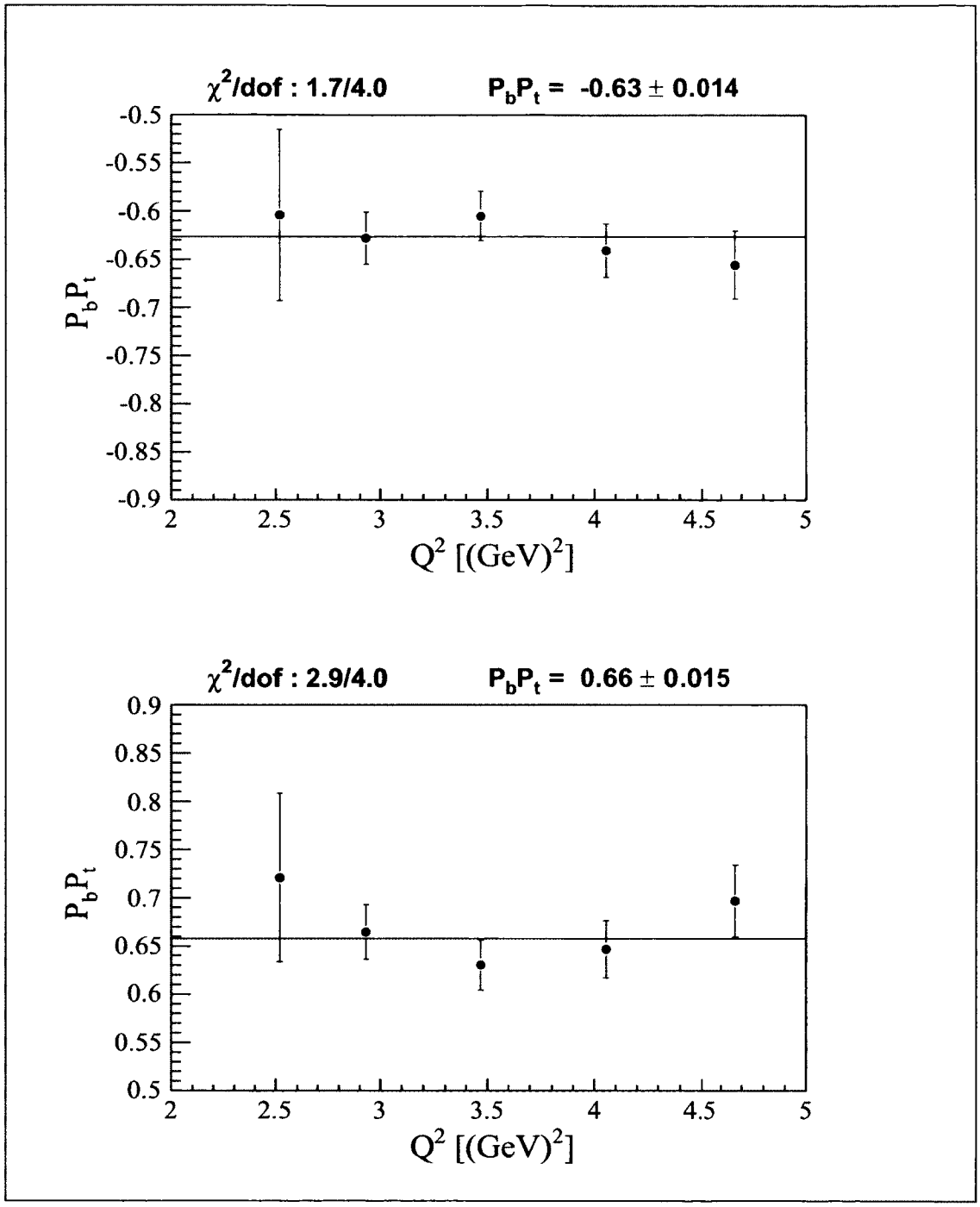

FIG. 80: Final $P_b P_t$ values for positive (upper) and negative (lower) target polarization for part A.

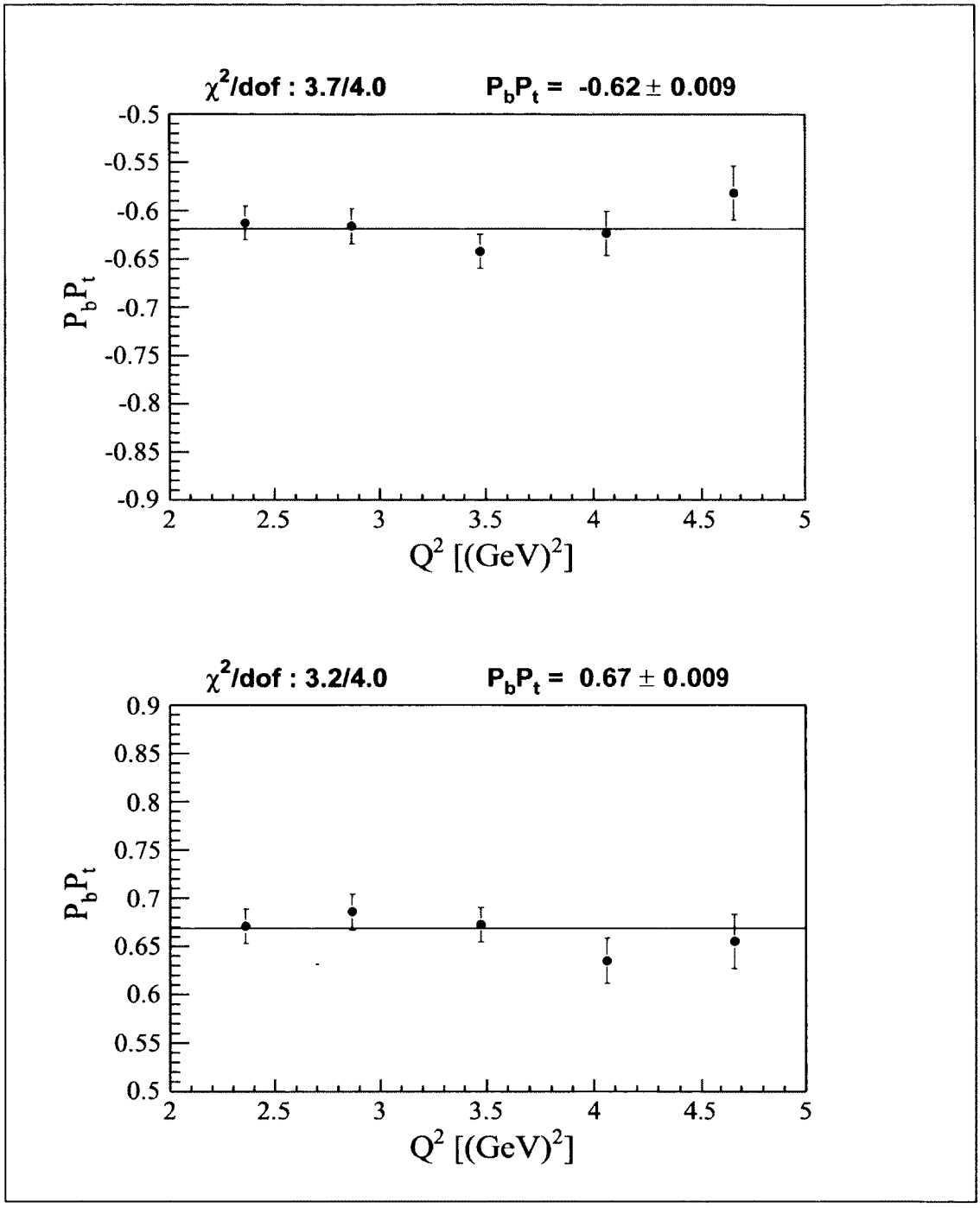

FIG. 81: Same as Fig. 80 except for part B.

4.1.2 $P_B P_T$ RESULTS

The different $P_b P_t$ values as a function of Q^2 are plotted in Figs. 80 and 81 for both target polarizations and for both Parts A and B of the experiment. The horizontal line is the best fit given in blue above the plots. Results for Part A and B of the EG1-DVCS experiment are tabulated in Table 6. The systematic uncertainty in $P_b P_t$ was estimated by taking the difference between the values from this analysis and those obtained by A. Kim for the exclusive pion analysis [40] using a different background subtraction technique.

TABLE 6: $P_b P_t$ results for Parts A and B of the experiment and for different positive and negative polarization. Here Negative and Positive refer to negative and positive target polarizations. The values in the third column are the results from Reference [40].

Part of the Experiment	From This Analysis	From [40]
Part A Negative	-0.63 ± 0.014	-0.63 ± 0.02
Part A Positive	0.66 ± 0.015	0.65 ± 0.02
Part B Negative	-0.62 ± 0.010	-0.63 ± 0.01
Part B Positive	0.67 ± 0.010	0.67 ± 0.01

4.2 TARGET CONTAMINATION

4.2.1 INTRODUCTION

The ND_3 target used for part C of the EG1-DVCS experiment was contaminated with a significant amount of polarized NH_3. This contamination is apparent in the proton transverse momentum, p_θ, distribution in Fig. 82. It is important to determine the contamination fraction as well as the polarization of both proton and deuteron in the mixture. The contamination fraction is defined as the ratio of the elastic events originating from the hydrogen part of the contaminated ND_3 target material to the number of the elastic events originating from the hydrogen in the pure NH_3 target in the same kinematics. In other words, it is the ratio of the effective target length of NH_3 in the contaminated ND_3 target to the length of the pure NH_3 target. This section presents the method employed to extract the target contamination.

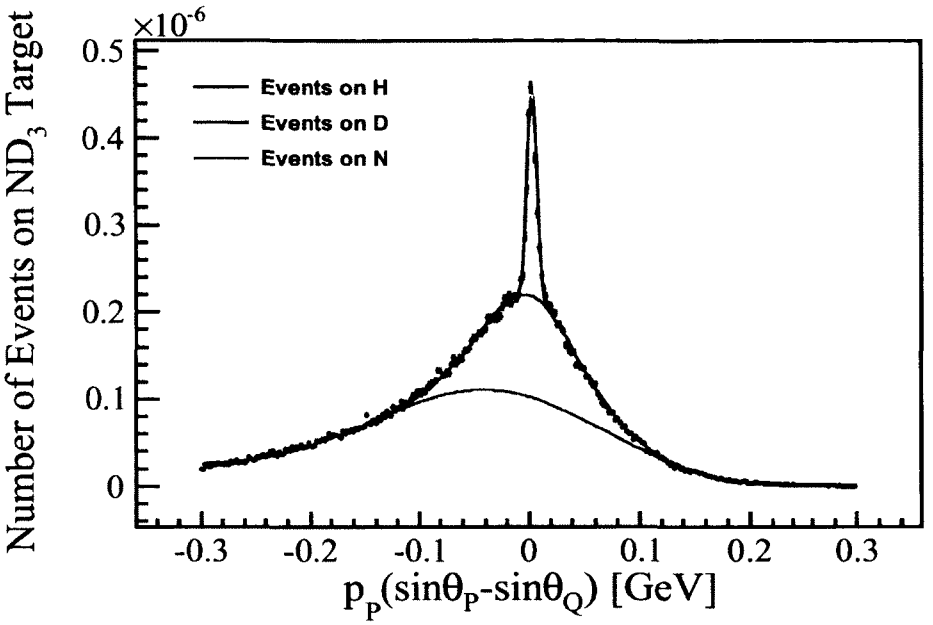

FIG. 82: Radial momentum distribution, p_θ, for elastic and quasi-elastic events. In the plot, p_P is the momentum of the detected proton, θ_P is the polar angle of the detected proton, θ_Q is the polar angle of the virtual photon; the expression $p_P(\sin\theta_P - \sin\theta_Q)$ gives the radial momentum of the proton which is represented by p_θ in the main text. The curves represent the fit to a combination of two pure Gaussians for H and D and a skewed Gaussian for N. The width and centroid of the fit for H were fixed to those for pure NH_3 in Fig. 83, while the shape of the N component was fixed by fitting ^{12}C runs.

4.2.2 CONTAMINATION FRACTION

In CLAS, the best possible resolution to distinguish events from H, D and N was obtained by using the proton's radial momentum (p_θ) as shown in Fig. 82. Elastic events from ^{1}H have narrow width, whereas quasi-elastic events from ^{2}D and ^{14}N are wider due to Fermi motion. The proton's radial momentum, p_θ, is defined as the difference between the radial momentum of the detected and the expected proton for elastic events. This can be written as,

$$p_\theta = p_p(\sin\theta_p - \sin\theta_Q), \tag{62}$$

where p_p is the momentum of the detected proton, θ_p is the polar angle of the detected proton and θ_Q is the polar angle of the virtual photon, given by

$$\theta_Q = \tan^{-1}\left(\frac{1}{\tan\theta_e/2} \times \left(\frac{E_b}{M} + 1\right)\right), \tag{63}$$

for elastic H(e, e'p) events, where θ_e is the polar angle of the detected electron, E_b is the beam energy and M is the proton mass. All these energies and masses are expressed in GeV.

The elastic and quasi-elastic events were selected with $0.8\,\text{GeV} \leq W \leq 1.1\,\text{GeV}$, missing energy $\leq$ 1.20 GeV, and missing longitudinal momentum $\leq$ 0.20 GeV for events with an electron and a proton in the final state. the proton radial momenta distribution were calculated for different torus current, target, target polarization and beam helicity configurations. These distributions were then normalized by their respective integrated beam charges and combined separately for ^{12}C, NH_3 and ND_3 to get the total in each case. Fig. 82 shows the integrated distribution on the ND_3 target for all beam and target polarization configurations. Data on an ^{12}C target shown in the left of Fig. 83 were used to simulate events on ^{14}N. A Gaussian was fitted on the hydrogen part of the pure NH_3 target as shown in Fig. 83 on the right. Two Gaussians were fitted to the contaminated ND_3 distributions. The nuclear contribution was eliminated by subtracting the scaled ^{12}C distribution. The scale factor was obtained by comparing the counts on the sides of the p_θ distribution with $|p_\theta| > 0.15$ GeV. The red curve labeled as "events on N" in Fig. 82 had only one scaling parameter and the rest of the parameters were fixed from the fits shown on the left of Fig. 83. The ratio of the H peak for the contaminated target material in Fig. 82 and the H peak for the pure NH_3 target in Fig. 83 gives the effective packing fraction of the NH_3 present in the contaminated ND_3 target. The statistical uncertainty of the contamination fraction was calculated from the number of counts, calculated from the area underneath the peak, in the numerator and the denominator of the ratio.

4.2.3 $P_B P_T$ FOR THE CONTAMINATED TARGET

$P_b P_t$ was determined as described before in Section 4.1 for each component separately, except now A_{raw} was found either for only proton or only deuteron events in the sample, by integrating the area underneath their peaks, as mentioned in Section

4.2.2. The theoretical value of the quasi-elastic asymmetry on the deuteron is a function of the beam energy and Q^2, and was calculated by S. Kuhn using a model for the deuteron wave function, previously used for an analysis of EG1 data [39]. The method includes the momentum distribution of the nucleons inside the deuteron as well as radiative effects.

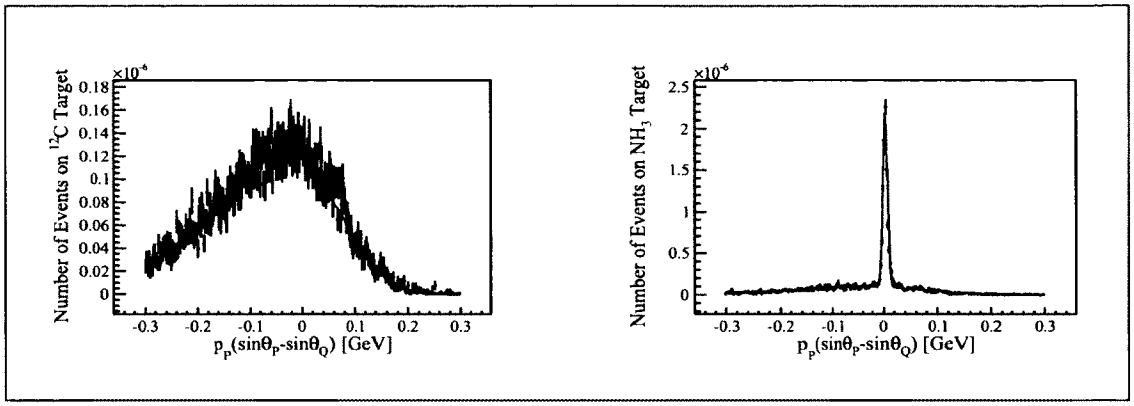

FIG. 83: The transverse momentum distribution for ^{12}C (left) and NH_3 (right). The large width on ^{12}C is due to Fermi motion. A Gaussian is fitted (blue curve) for NH_3 and a skewed Gaussian is fitted (red curve) for ^{12}C.

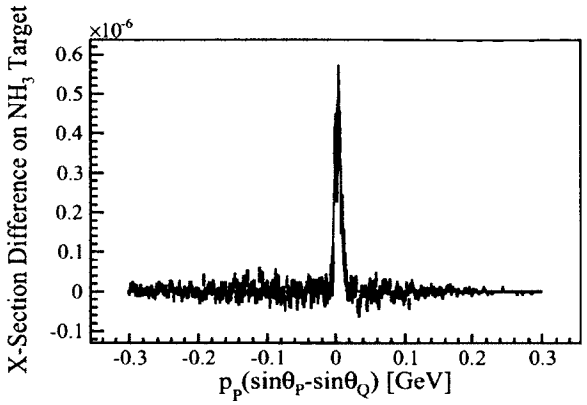

FIG. 84: Beam-target double spin cross-section difference on a pure NH_3 target. The distribution shows the number of events for opposite product of beam and target for pure NH_3 as a function of the proton radial momentum. The blue curve is a fitted Gaussian with its centroid and width fixed from Fig. 83.

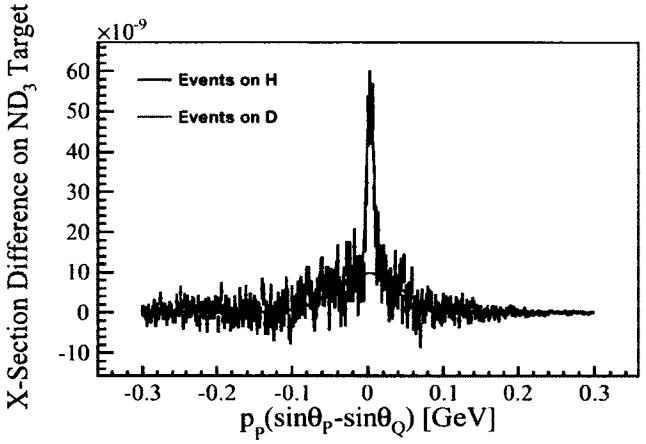

FIG. 85: Beam-target double spin cross-section difference on contaminated ND_3 target. The distribution shows the number of events for opposite product of beam and target for contaminated ND_3 as a function of the proton radial momentum. The large width for events on D is due to Fermi Motion. The blue and green curves are fitted Gaussians; the blue curve is a fitted Gaussian with its centroid and width fixed from Fig. 83. .

4.2.4 CONTAMINATION RESULTS

The results are tabulated in Tables 7 and 8. The effective contamination fraction and polarization of various components of the target changed over time due to the movement of the ammonia beads in the target. For in-bending and out-bending run groups, contamination fraction and target polarization were significantly different. So the analysis was done separately for the two groups, hence, the results are grouped into two tables each for in-bending and out-bending runs of part C. Possible sources of systematic uncertainty were checked, but they were significantly smaller than the statistical uncertainty and were neglected. The possible sources are: elastic and quasi-elastic event selection cuts, width of the bins used in the fits and different models for the fits for the ^{12}C target. The same quantities were measured by P. Bosted for the inclusive analysis using a different method [30]; these are tabulated in the third column of the tables. His method relies entirely on the NMR values to calculate the polarization of the deuteron, but here the NMR values are not taken into account. The difference between the values from the two analyses is the estimated systematic uncertainty.

TABLE 7: Polarizations for the ND_3 target for the in-bending run group from this analysis (column 2) and that of Reference [30] (column 3).

Measured Quantity	From This Analysis	From [30]
Contamination Fraction	0.11 ± 0.0034	0.105 ± 0.01
NH_3 P_bP_t of the Contaminated ND_3 Target	0.50 ± 0.038	0.50 ± 0.04
ND_3 P_bP_t of the Contaminated ND_3 Target	0.23 ± 0.018	0.216 ± 0.010

TABLE 8: Same as Table 7 except for out-bending runs.

Measured Quantity	From This Analysis	From [30]
Contamination Fraction	0.12 ± 0.0040	0.105 ± 0.01
NH_3 P_bP_t of the Contaminated ND_3 Target	0.45 ± 0.052	0.51 ± 0.06
ND_3 P_bP_t of the Contaminated ND_3 Target	0.22 ± 0.035	0.236 ± 0.010

4.3 DILUTION FACTOR

4.3.1 INTRODUCTION

The dilution factor is defined as the number of DIS events from the polarizable nucleons in the target divided by the number from all other nucleons in the target. The dilution factor is dependent on kinematics. In this analysis, it was determined for all three pion channels as a function of Q^2, x_B, z and $P_{h\perp}$. A separate analysis showed that the dilution factor was not strongly dependent on ϕ_h; the result from that analysis is shown in Section 4.3.5.

4.3.2 METHOD

The dilution factor is extracted by fitting a suitable model to the ratio of SIDIS events from reference targets (f_R). There were several runs with a ^{12}C target during the EG1-DVCS experiment for determining the dilution factor. But the statistics on this ^{12}C target from the EG1-DVCS experiment were not sufficient for a direct calculation of the dilution factor dependence on all four kinematic variables. Therefore fits were made to the EG2 data which has very high statistics on ^{12}C, D and Fe targets [42]. Fig. 86 shows the fits to EG2 data. These fits were also tested on the EG1-DVCS data as shown in Figs. 87, 88 and 89. The model takes into account the SIDIS cross-section per nucleon and the attenuation of hadron emission for different target materials. In this section, the method employed is summarized; more details can be found in Ref. [43].

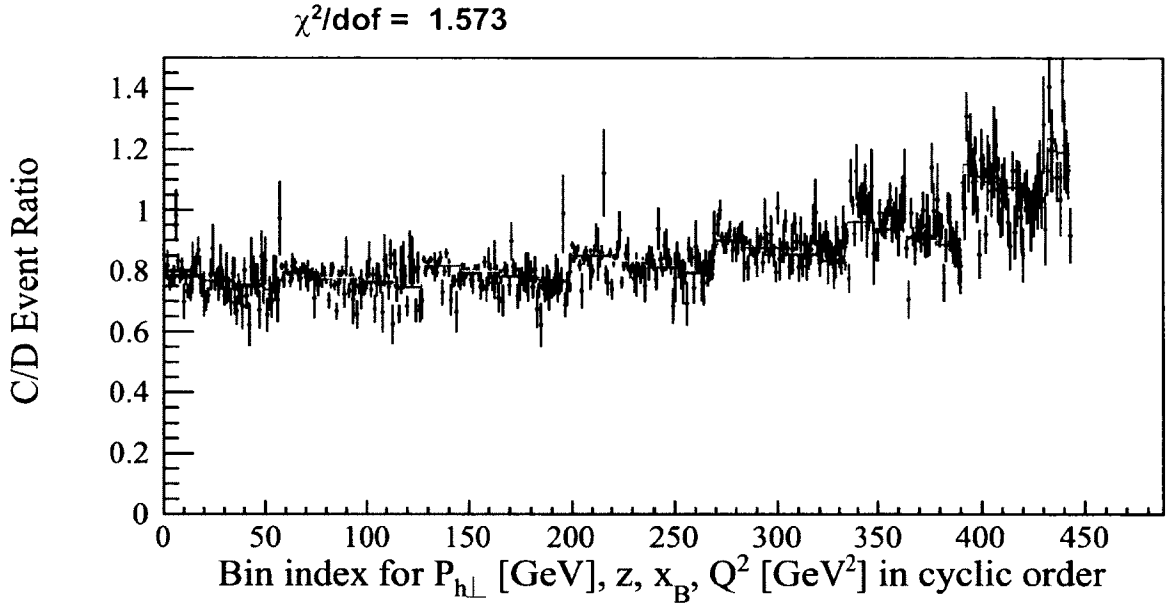

FIG. 86: Fits of the ratio of neutral pion events on ^{12}C and ^{2}H from the EG2 experiment. Plotted along the x-axis are kinematic bins with $P_{h\perp}$ in the outer loop, then z, then x_B and Q^2 in the inner loop. The red line is the best fit; the two orange lines are the $\pm 1\sigma$ uncertainty of the fits. The ordering of the kinematic bin index in this figure is reverse of the following plots.

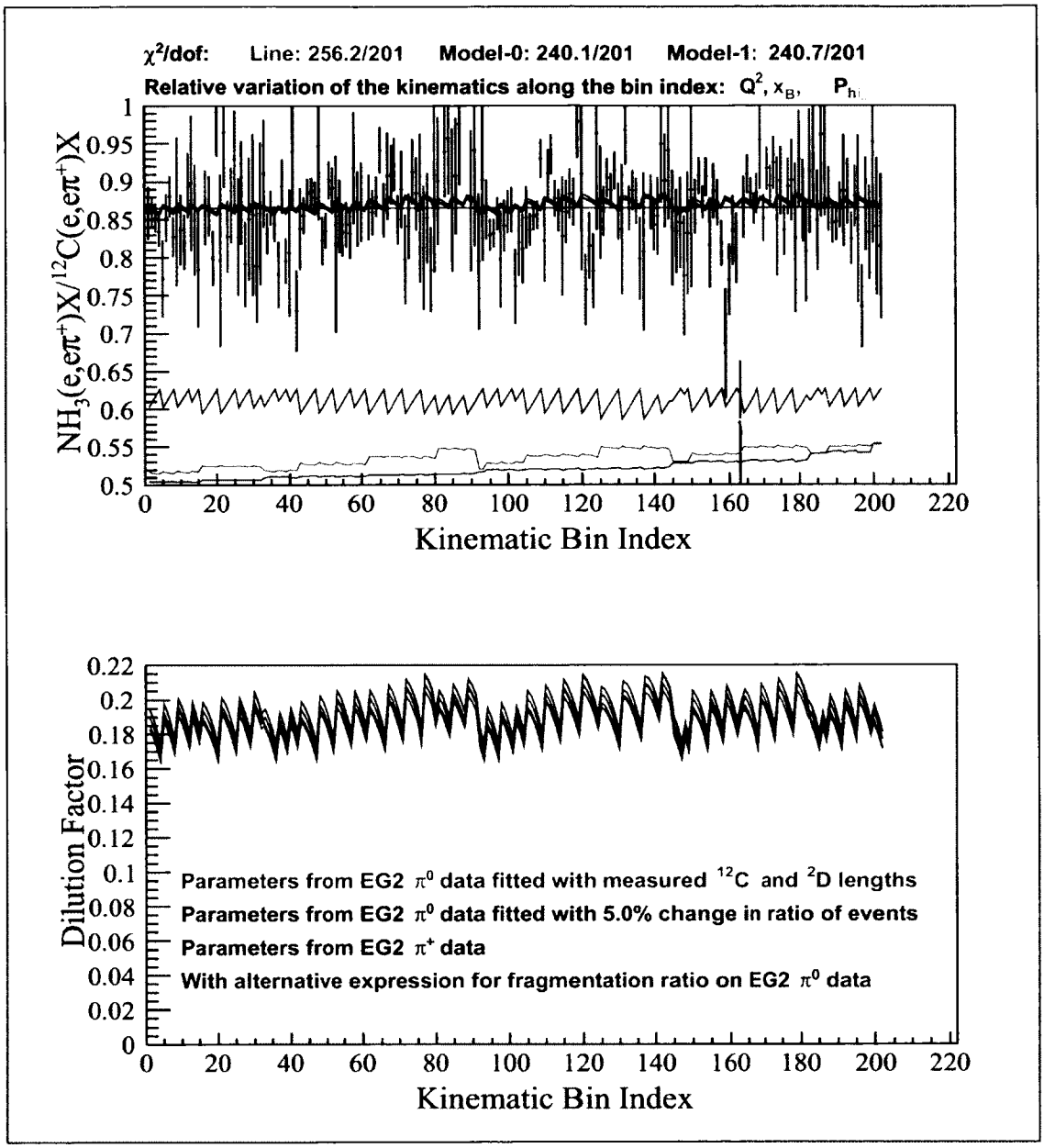

FIG. 87: Ratio of π^+ SIDIS events from NH_3 to ^{12}C and the dilution factor as a function of Q^2, x_B, z and $p_{h_\perp}$. The kinematic bins are indexed as Q^2, x_B, z and $p_{h_\perp}$ from outer to inner loop. This fits were done in the EG1-DVCS data with all the parameters fixed as mentioned in [43].

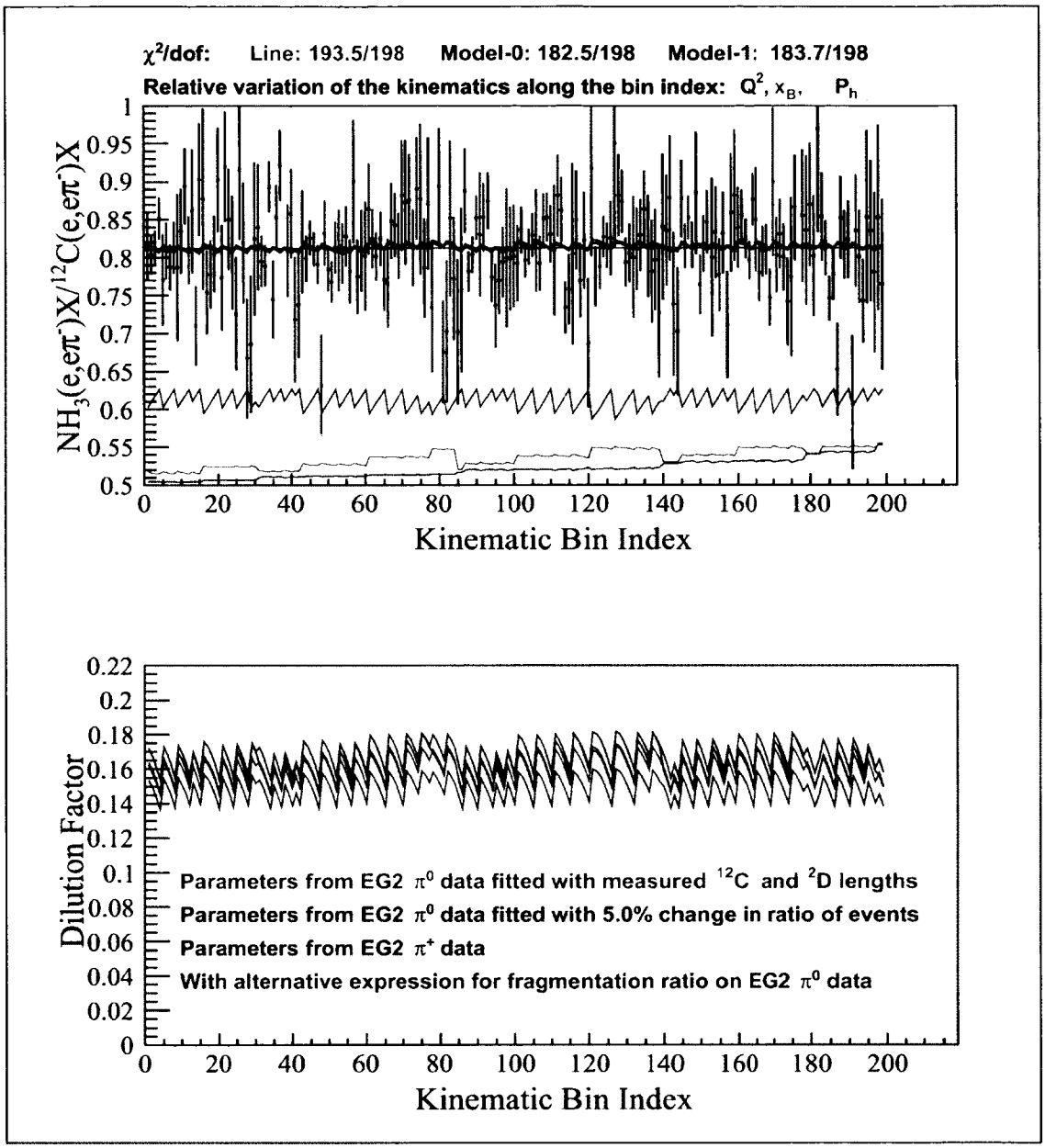

FIG. 88: Ratio of π^- SIDIS events from NH_3 to ^{12}C and the dilution factor as a function of Q^2, x_B, z and $p_{h_\perp}$. The kinematic bins are indexed as Q^2, x_B, z and $p_{h_\perp}$ from outer to inner loop. This fits were done in the EG1-DVCS data with all the parameters fixed as mentioned in [43].

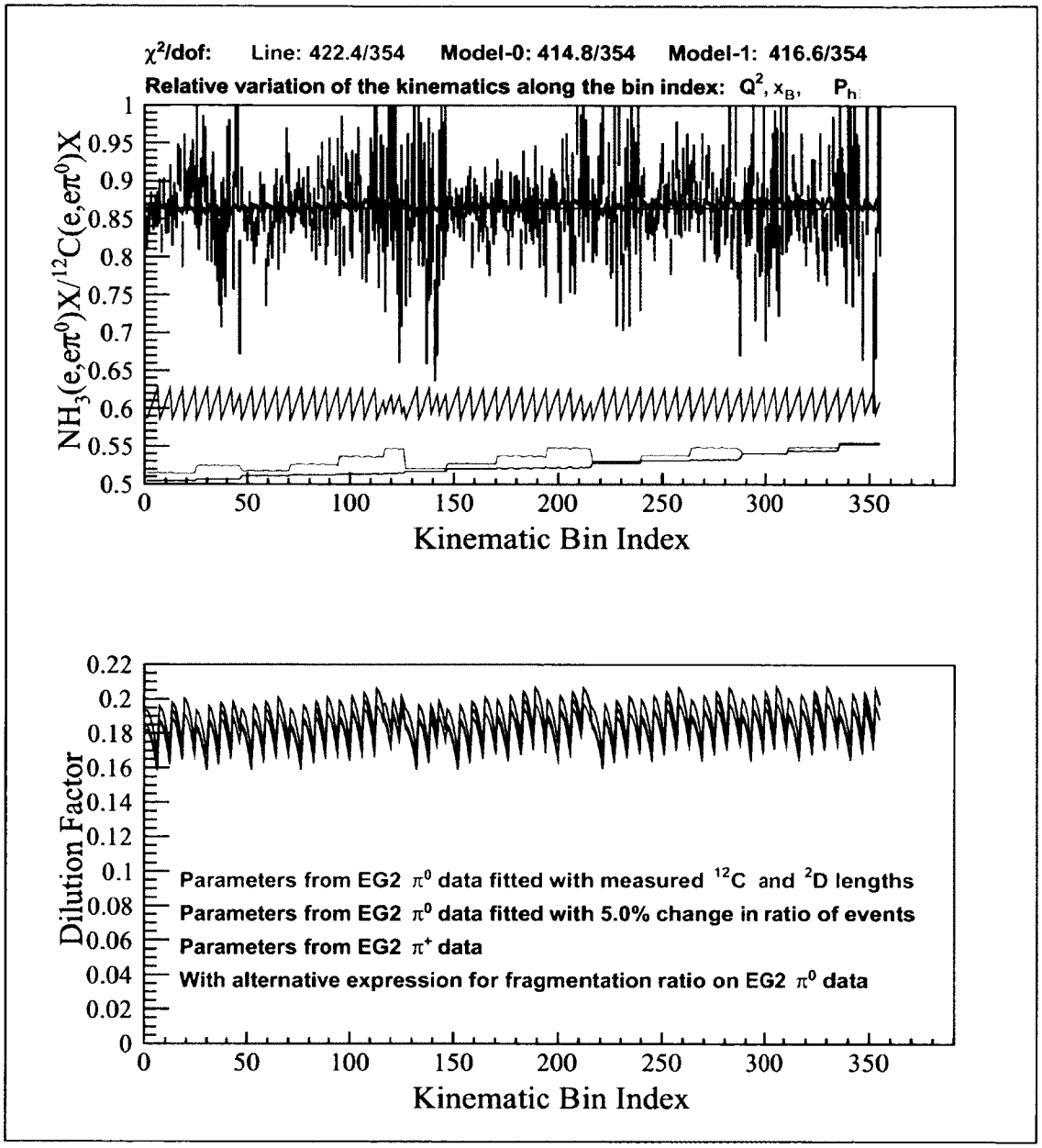

FIG. 89: Ratio of π^0 SIDIS events from NH_3 to ^{12}C and the dilution factor as a function of Q^2, x_B, z and $p_{h_\perp}$. The kinematic bins are indexed as Q^2, x_B, z and $p_{h_\perp}$ from outer to inner loop. This fits were done in the EG1-DVCS data with all the parameters fixed as mentioned in [43].

In terms of the densities, ρ_i, of the target materials, their lengths, l_i, and the SIDIS event cross-sections, σ_i, the ratio of SIDIS events on two targets, f_R, is given by

$$f_R = \frac{\sum_i \rho_i l_i \sigma_i}{\sum_j \rho_j l_j \sigma_j}. \tag{64}$$

The summation runs over all the materials in the beam. The lengths of the target materials were obtained from a dedicated analysis [44]. In the case of the contaminated ND_3 target, the target length for NH_3 was calculated by multiplying the target contamination fraction by the length of the pure NH_3 target; the target length of the ND_3 component was calculated by freely parameterizing its length in the fits for the ratio of SIDIS events for ND_3 to ^{12}C. For NH_3, the parameters from the fit to EG2 data were used without adjusting any parameter to calculate the dilution factor, while for ND_3, a fit to the ND_3 to ^{12}C ratio on the EG1-DVCS data with all parameters from EG2 data fixed except for the ND_3 effective length. σ is the SIDIS event cross-section. Similarly, for a polarizable nucleon of type N, the dilution factor, f_D, in terms of the densities of the target materials, their lengths and the SIDIS event cross-sections, is given by

$$f_D = \frac{\rho_N l_N \sigma_N}{\sum_i \rho_i l_i \sigma_i}. \tag{65}$$

The SIDIS cross-sections on different nucleons for different pion flavors are given by

$$\sigma_p^{\pi^+} \propto 4u + d_s + (4u_s + d) \times r \tag{66}$$

$$\sigma_n^{\pi^+} \propto 4d + u_s + (4d_s + u) \times r \tag{67}$$

$$\sigma_p^{\pi^-} \propto (4u + d_s) \times r + 4u_s + d \tag{68}$$

$$\sigma_n^{\pi^-} \propto (4d + u_s) \times r + 4d_s + u \tag{69}$$

$$\sigma_p^{\pi^0} \propto (4u + d_s) \times [1 + r] + (4u_s + d) \times [1 + r] \tag{70}$$

$$\sigma_n^{\pi^0} \propto (4d + u_s) \times [1 + r] + (4d_s + u) \times [1 + r] \tag{71}$$

where the subscripts and the superscripts on σ respectively represent the nucleon type and the pion flavor. The fragmentation ratio, r, which is the ratio of unfavored over favored fragmentation functions, is a function of z and is given by [45],

$$r = \frac{1}{(1+z)^2}. \tag{72}$$

In the above expressions for various cross-sections, $u_v(Q^2, x_B)$, $u_s(Q^2, x_B)$, $d_v(Q^2, x_B)$ and $d_s(Q^2, x_B)$ are the number densities of the up-valence, up-sea, down-valence and the down-sea quarks. These densities as a function of Q^2 and x_B are obtained from parton distribution functions using [46]. In these equations $u(Q^2, x_B) = u_v(Q^2, x_B) + u_s(Q^2, x_B)$ and $d(Q^2, x_B) = d_v(Q^2, x_B) + d_s(Q^2, x_B)$. Since the ND_3 target used in part-C was contaminated with about 11% of polarized NH_3, the dilution factor for Part C was extracted for both H and D.

To take into account the difference in the cross-section between a free nucleon and a nucleon in the nuclear medium, each cross-section term for nuclear target materials was multiplied by an attenuation factor (at) yielding the final expression

$$f_R = \frac{\sum_i \rho_i l_i \sigma_i a_i}{\sum_j \rho_j l_j \sigma_j a_j}, \tag{73}$$

$$f_D = \frac{\rho_N l_N \sigma_N}{\sum_i \rho_i l_i \sigma_i a_i}. \tag{74}$$

The kinematic dependence of the attenuation was obtained by fitting a four parameter model of f_R to the EG2 data. For a material with atomic mass number A, the attenuation factors were parameterized as

$$a = (1 - \alpha) \times \exp\left[\left(\frac{P_{h\perp}}{p_1 + p_3 \times \frac{z-0.5}{0.4}}\right)^2 \times \log\left(\frac{1}{1-\alpha}\right)\right], \tag{75}$$

where α for a target material with atomic number A is defined as

$$\alpha = p_0 \times [1 + (z - 0.5) \times p_2] \times \frac{1.12 - A^{\frac{1}{3}}}{1.12 - 12^{\frac{1}{3}}}. \tag{76}$$

In the above equations, p_0, p_1, p_2 and p_3 are the free parameters constrained by the deuteron to carbon ratio, f_R, of the π^0 data of the EG2 experiment. In the expression for attenuation, there is no dependence on x_B and Q^2 since it was not observed in the data. It is assumed that the attenuation parameters are the same for the charged pions. Uncertainty from this assumption is estimated by taking the difference between the neutral pion data based fit and parameterizations from fits to alternative data which are discussed in Section 4.3.4.

4.3.3 DILUTION FACTOR GRAPHS

The SIDIS dilution factor as a function of Q^2, x_B, z and $P_{h\perp}$ for the proton is given in the following 5-dimensional graphs in Figs. 90, 91 and 92. The dilution factor for the proton and the deuteron of the contaminated target are presented in Appendix C. The magnitude of the dilution factor is given by the color scale on the right of the plots. Dilution factors are given only for the kinematic region covered by the EG1-DVCS data.

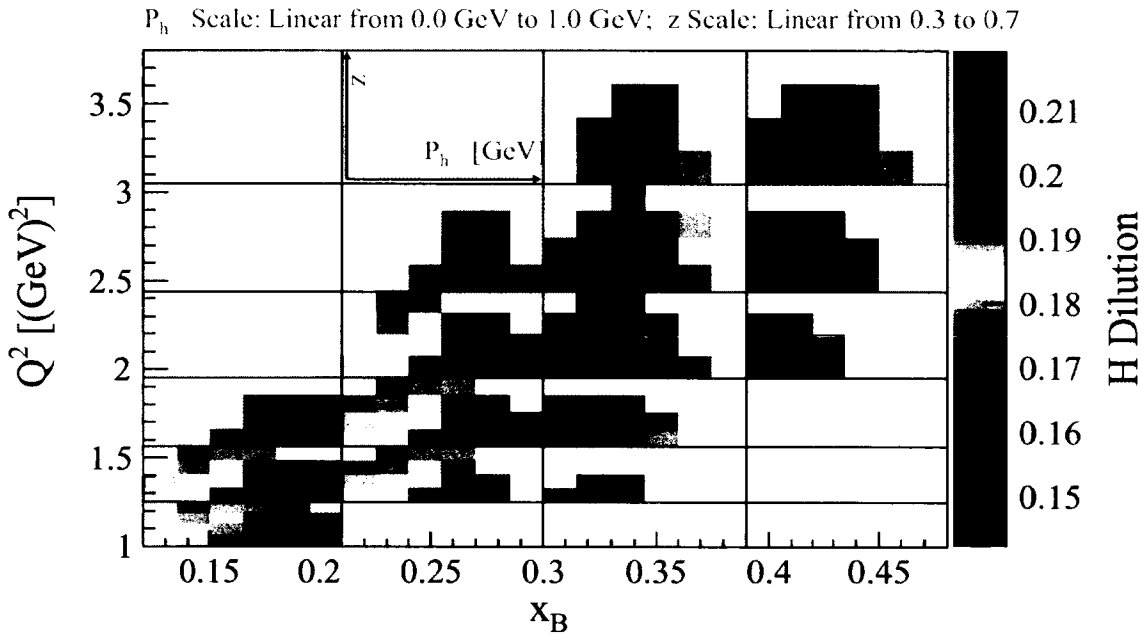

FIG. 90: H dilution factor for SIDIS π^+ events from an NH_3 target as a function of Q^2, x_B, z and $P_{h\perp}$.

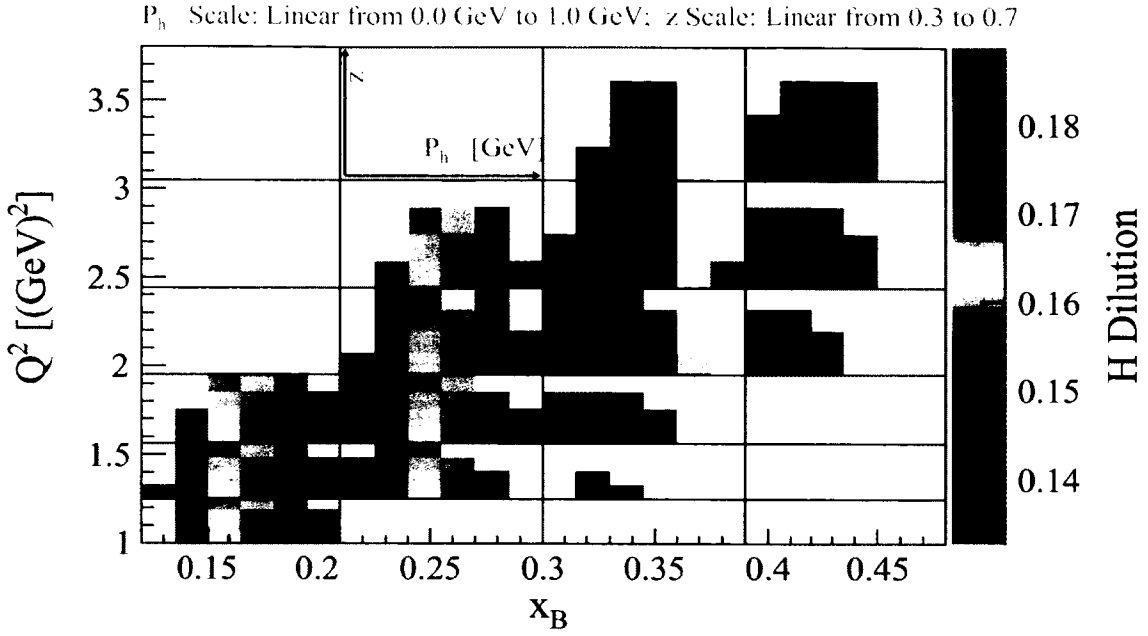

FIG. 91: Same as 90 except for π^-

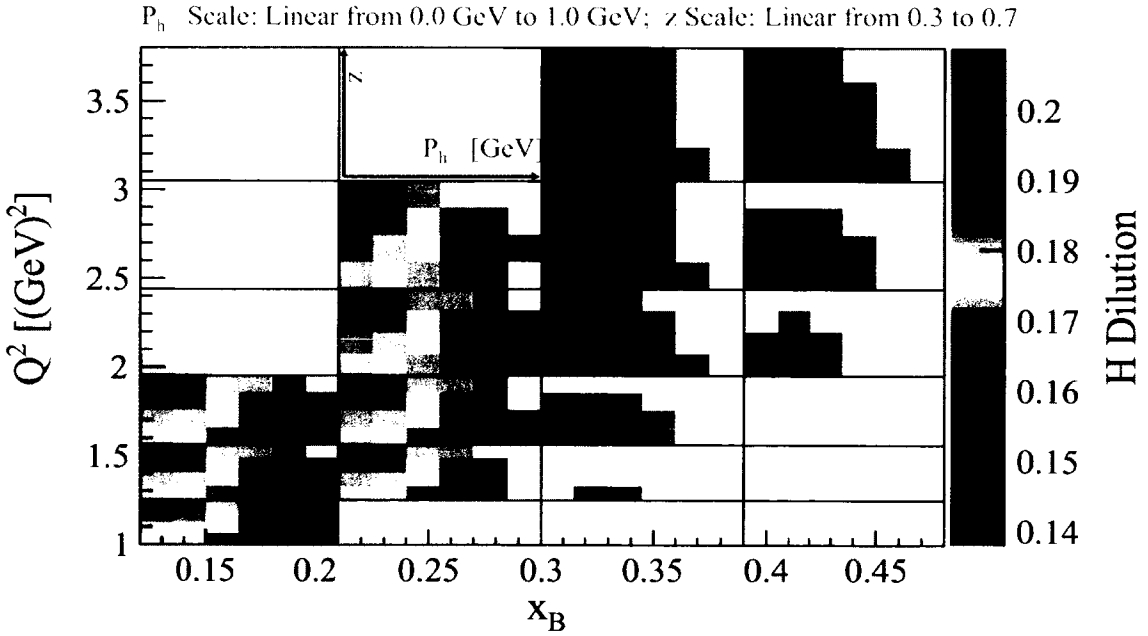

FIG. 92: Same as 90 except for π^0

4.3.4 SYSTEMATIC UNCERTAINTY OF THE DILUTION FACTOR

There are multiple sources of uncertainty for the dilution factor, the most significant of which is the parameterization of the attenuation. To estimate the uncertainty of the dilution factor, the attenuation was parameterized using two different data sets [43]. The first set was the neutral pion data, referred to as EG2 π^0 data [42], on ^{12}C and ^{2}H from the EG2 experiment; the second was the positive pion data, referred to as EG2 π^+ data [47], on ^{56}Fe and ^{2}H in the same experiment. The difference between the dilution factor from the two parameterizations was taken as the uncertainty of the dilution factor. The difference between the two results are shown in Figs. 87, 88 and 89. In addition, EG2 π^0 data was refitted by increasing the event ratio by 5% which is the estimated uncertainty of the analysis; the parameters from the new fit were also used to estimate an additional source of uncertainty in the dilution factor. The expression used for the fragmentation ratio in Equation 72 was changed to $r = 0.5/(1+z)^2$ to estimate the uncertainty in the dilution factor from the knowledge of the fragmentation ratio. This particular expression for the fragmentation ratio, $r = 0.5/(1+z)^2$, was chosen because the χ^2 of the fit increased approximately by one unit with this expression.

Beyond these uncertainties, the uncertainty in the fit of the neutral pion data was negligible as shown in the Fig. 86. In principle, there are a number of other sources of uncertainty associated with the dilution factor, most of which are due to the uncertainties in the quantities associated with the target configurations. Since all the quantities associated with the target materials other than the effective ammonia length were measured very accurately with uncertainty less than 3% and the fact that the areal densities of those materials were only about 5% of ammonia makes the systematic uncertainty in the dilution factor from those quantities negligible compared to uncertainty from the aforementioned sources.

4.3.5 ϕ_H DEPENDENCE OF THE DILUTION FACTOR

The EG2 data set used to extract the attenuation parameters was binned only in Q^2, x_B, z and $P_{h\perp}$. Hence the ϕ_h dependence was tested using the EG1-DVCS data. By introducing a $\cos\phi_h$ term, no significant ϕ_h dependence was observed. Fig. 93 shows the effect of adding an additional $\cos\phi_h$ dependent free parameter to the event ratios. Hence the any uncertainty in the ϕ_h dependence is neglected.

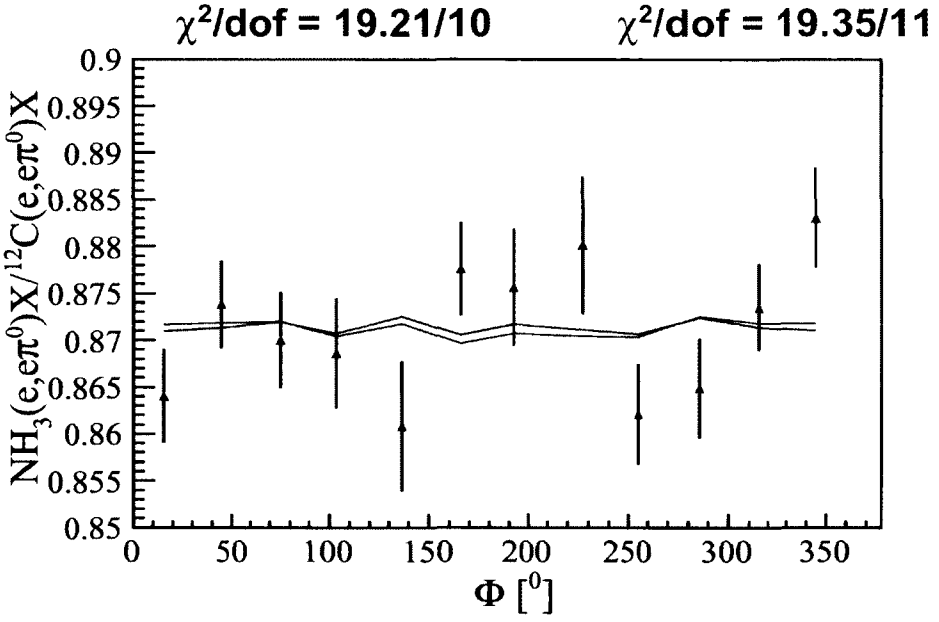

FIG. 93: Ratio of events on NH_3 and C. The purple line is the fit without the ϕ_h dependent free parameter. The green line is with the ϕ_h dependent free parameter.

CHAPTER 5

ASYMMETRIES

An asymmetry is defined as the ratio of the cross-section difference between two polarization states to the total cross-section. The ϕ_h dependence of the asymmetry is termed as azimuthal asymmetry. To extract various azimuthal asymmetry moments, the asymmetries were measured as a function of ϕ_h from 0 to 360° in 12 bins of equal widths. Various functions were fitted on the ϕ_h distributions of the asymmetries to extract the asymmetry moments.

5.1 MEASUREMENT OF ASYMMETRIES

Assuming that the efficiency and the acceptance of the detector remain the same for all beam and target polarization configurations, the absolute differential cross-section is replaced by the number of events normalized to the integrated beam charge in each kinematic bin. In the context of the EG1-DVCS experiment, where the beam and the target were simultaneously polarized, the beam single (A_{LU}), target single (A_{UL}) and beam-target double (A_{LL}) spin asymmetries can be expressed as,

$$A_{LU} = \frac{1}{P_b^{\Updownarrow}} \times \frac{(dn^{\uparrow\Uparrow} - dn^{\downarrow\Uparrow})P_t^{\Downarrow} + (dn^{\uparrow\Downarrow} - dn^{\downarrow\Downarrow})P_t^{\Uparrow}}{(dn^{\uparrow\Uparrow} + dn^{\downarrow\Uparrow})P_t^{\Downarrow} + (dn^{\uparrow\Downarrow} + dn^{\downarrow\Downarrow})P_t^{\Uparrow}}, \tag{77}$$

$$A_{UL} = \frac{1}{f_D} \times \frac{dn^{\uparrow\Uparrow} + dn^{\downarrow\Uparrow} - dn^{\uparrow\Downarrow} - dn^{\downarrow\Downarrow}}{(dn^{\uparrow\Uparrow} + dn^{\downarrow\Uparrow})P_t^{\Downarrow} + (dn^{\uparrow\Downarrow} + dn^{\downarrow\Downarrow})P_t^{\Uparrow}}, \tag{78}$$

$$A_{LL} = \frac{1}{f_D} \times \frac{1}{P_b^{\Updownarrow}} \times \frac{-dn^{\uparrow\Uparrow} + dn^{\downarrow\Uparrow} + dn^{\uparrow\Downarrow} - dn^{\downarrow\Downarrow}}{(dn^{\uparrow\Uparrow} + dn^{\downarrow\Uparrow})P_t^{\Downarrow} + (dn^{\uparrow\Downarrow} + dn^{\downarrow\Downarrow})P_t^{\Uparrow}}, \tag{79}$$

where $\Uparrow$ and $\Downarrow$ represent target polarizations and $\uparrow$ and $\downarrow$ represent beam polarizations. The beam as well as the target polarizations were longitudinal along the beam direction in this experiment. The symbol dn is the number of events in a kinematic bin minus the background divided by the corresponding charge collected in the Faraday cup.

$$dn = \frac{dN - dN_{Bg}}{F_C}. \tag{80}$$

To take into account the beam and target polarizations and the presence of unpolarized nuclei in the target, the asymmetries are divided by the beam polarization, P_b, the target polarization, P_t, and the dilution factor, f_D, wherever applicable [48].

5.2 CORRECTIONS ON THE ASYMMETRIES

The following corrections were applied to the asymmetries. These corrections were applied before fitting the ϕ_h distributions.

5.2.1 RADIATIVE CORRECTIONS

Due to photon radiation in the electromagnetic field of a nucleus, the momenta of incident and scattered electrons can be different from those measured by the detectors. These photons can be emitted either during the passage of beam or scattered electrons through various materials; the correction due to this phenomenon is referred to as the external radiative correction. In addition, the photons can be emitted within the same reaction that leads to the event under study; the correction due to this phenomena is referred to as the internal radiative correction. Corrections were applied to take into account those effects. A dedicated study of SIDIS radiative corrections was done by P. Bosted specially for this analysis [49]. The main points of this study are summarized here. In the analysis the equivalent radiator approximation was used for internal radiative correction whereas for the external radiative correction, the thickness in radiation lengths of the traversed material was used. To evaluate cross-sections and spin asymmetries for exclusive pion production needed as part of the corrections, the MAID model was used. Multi-pion production and asymmetries were modeled by using Kertzer fragmentation functions modified to match the data for $z > 0.7$. The calculations were done with the Monte Carlo integration method. The radiative correction analysis was done only for A_{UL} and A_{LL}.

To apply the radiative corrections in this analysis, the asymmetry moments were extracted after the corrections were made to the five dimensional asymmetry tables. The effects of the radiative corrections on various asymmetry moments are shown in a series of figures in Appendix D. In the case of the proton, it can be seen from the plots that the radiative corrections are negligible at lower $P_{h_\perp}$ and slightly significant at higher $P_{h_\perp}$ for all pion flavors. In the case of the deuteron, the radiative corrections are significantly smaller compared to the statistical uncertainties. The corrections are shown in the two dimensions of $(x_B, P_{h_\perp})$ for SIDIS on the proton

and in a single dimension (of x_B) for SIDIS on the deuteron. The precision of the radiative corrections is affected by the unavailability of enough data on exclusive pion channels in the kinematics of this experiment. The applied radiative corrections from Reference [49] were extracted from the analyses of the presently available data. So, the applied radiative corrections in this analysis have a large relative uncertainty. Hence the systematic uncertainty in the radiative correction is estimated to be 100%. Though this is a very conservative estimation, since the correction is very small, the systematic uncertainty from radiative correction does not dominate the overall systematic uncertainty. The radiative correction itself is less 10% of the typical statistical uncertainties.

5.2.2 CORRECTIONS ON DEUTERON ASYMMETRIES DUE TO TARGET CONTAMINATION

The contribution from the NH_3 part of the contaminated target on the asymmetries measured on the ND_3 target was subtracted using the following simple linear equation.

$$A_{raw} = A^D f_D^D P^D + A^H f_D^H P^H, \tag{81}$$

where A_{raw} is the raw asymmetry on the contaminated target; A^D and A^H are the asymmetries on deuteron and proton; f_D^D and f_D^H are deuteron and proton dilution factors; P^D and P^H are the relevant beam or target polarizations or their products in ND_3 and NH_3 targets respectively. Since the rest of the quantities except A^D can be measured, the above equation can be used to extract A^D. For the systematic uncertainty on the final asymmetries due to the contamination, the uncertainty in the contamination fraction as well as the uncertainties in the polarizations of the different components were taken into account. The details on these uncertainties are listed in Section 4.2.

5.2.3 CORRECTIONS DUE TO NITROGEN POLARIZATION

The contribution from polarized Nitrogen in NH_3 and ND_3 to the asymmetries measured on the proton and the deuteron are evaluated in the inclusive analysis note [30]. The correction for proton asymmetries are negligible, less than 1% and kinematically dependent, whereas for deuteron the correction was a factor of 4% independent of kinematics. The correction for deutron was implemented. For the

deuteron, 10% relative uncertainty in the corrections due to nitrogen polarization is used.

5.3 FITTING FUNCTIONS ON ASYMMETRIES

It follows directly from the SIDIS cross-section in terms of 18 structure functions as found in Chapter 1 that the different asymmetries, $A_{LU}(\phi_h)$, $A_{UL}(\phi_h)$ and $A_{LL}(\phi_h)$, as defined earlier in section 5.1, are of the following forms, respectively.

$$A_{LU} = \frac{A_{LU}^{\sin\phi_h} \sin\phi_h}{1 + A_{UU}^{\cos\phi_h} \cos\phi_h + A_{UU}^{\cos 2\phi_h} \cos 2\phi_h}, \tag{82}$$

$$A_{UL} = A_{\text{Offset}} + \frac{A_{UL}^{\sin\phi_h} \sin\phi_h + A_{UL}^{\sin 2\phi_h} \sin 2\phi_h}{1 + A_{UU}^{\cos\phi_h} \cos\phi_h + A_{UU}^{\cos 2\phi_h} \cos 2\phi_h} \tag{83}$$

and

$$A_{LL} = \frac{A_{LL}^{Const} + A_{LL}^{\cos\phi_h} \cos\phi_h}{1 + A_{UU}^{\cos\phi_h} \cos\phi_h + A_{UU}^{\cos 2\phi_h} \cos 2\phi_h}. \tag{84}$$

In the above equations, the letter A with various superscripts and subscripts are the azimuthal asymmetry moments; they are treated as free parameters during the fits. Since the parameters $A_{UU}^{\cos\phi_h}$ and $A_{UU}^{\cos 2\phi_h}$ are common to all the three asymmetries, they are constrained by all of them. The extra term A_{Offset} is to take into account the difference in detector efficiency between two different target polarization run groups.

5.4 EXTRACTION OF UNPLOARIZED CROSS-SECTION MOMENTS

To correctly extract the various asymmetry moments, the contributions of the two unpolarized structure functions, $A_{UU}^{\cos\phi_h}$ and $A_{UU}^{\cos 2\phi_h}$, on the other asymmetry moments should be properly taken into consideration. At the moment, there is a lack of reliable information about the size of $A_{UU}^{\cos\phi_h}$ and $A_{UU}^{\cos 2\phi_h}$ for this purpose. A dedicated analysis to extract $A_{UU}^{\cos\phi_h}$ and $A_{UU}^{\cos 2\phi_h}$ with different experimental data is underway. Since the data used in this analysis is not optimized for the extraction of $A_{UU}^{\cos\phi_h}$ and $A_{UU}^{\cos 2\phi_h}$, some ad-hoc assumptions have been made about them to aid the analysis; these assumptions are discussed later in this chapter. The main emphasis of this part of the analysis is to ensure that the extracted primary results are not artifacts of the assumptions made about $A_{UU}^{\cos\phi_h}$ and $A_{UU}^{\cos 2\phi_h}$. So the systematic

uncertainties in the final results due to the limited knowledge about $A_{UU}^{\cos\phi_h}$ and $A_{UU}^{\cos 2\phi_h}$ are conservatively evaluated. Several different methods that were tried did not significantly affect the final results; the differences from the different methods were well within the systematic uncertainty evaluated for this part of the analysis.

5.4.1 CHALLENGES IN THE EXTRACTION THE $A_{UU}^{\cos\phi_H}$ AND $A_{UU}^{\cos 2\phi_H}$

Due to limited statistics, limited ϕ_h coverage and a large number of highly correlated free parameters, the extraction of $A_{UU}^{\cos\phi_h}$ and $A_{UU}^{\cos 2\phi_h}$ from simultaneous fits of all three asymmetries was not possible. In the usual process of fitting, χ^2 minimization, by treating all the eight parameters as completely free, the extracted $A_{UU}^{\cos\phi_h}$ fluctuated unexpectedly as a function of kinematic variables, as in the similar analysis in Reference [50]. This is due to the fact that the parameter $A_{UU}^{\cos\phi_h}$ is significantly correlated with all the other parameters; its global correlation coefficient is almost equal to unity. Various fitting methods were tested but they all faced the same challenge. To overcome this challenge, the usual method of data fitting, χ^2 minimization with MINUIT, was slightly modified as described in the next section.

The conventional method is to put rigid boundaries on some of the parameters in the parameter space. Since this technique has multiple defects, an alternative approach was used.

5.4.2 $A_{UU}^{\cos\phi_H}$ AND $A_{UU}^{\cos 2\phi_H}$ EXTRACTION METHOD

Two major changes to the straightforward procedure were implemented to extract these parameters. In the first change, the parameters were extracted as a function of a single kinematic variable x_B, $P_{h\perp}$ and z rather than as a function of two variables as required for the final results. In the second step, a physics-motivated *prior* was imposed to constrain these parameters. These two steps are described in detail in the following sections.

Analysis in Single Dimension

The primary objective of the analysis on the proton was to extract asymmetry moments in two dimensions. However, due to the aforementioned problems, it was not possible to extract all eight parameters by simultaneously fitting the $A_{LU}(\phi_h)$, $A_{UL}(\phi_h)$ and $A_{LL}(\phi_h)$ data. Though the statistics and the ϕ_h coverage for neutral

pions are much better than for charged pions, fitting an eight parameter function was unstable for neutral pions as well as for charged pion. So the analysis was done in a single dimension of x_B, $P_{h\perp}$ and z separately as shown in Figs. 94, 95 and 96 for the example of x_B for positive pions. In the three figures, the terms in the denominators were constrained simultaneously from the fits in A_{LU}, A_{UL} and A_{LL} data. The same procedure was done for other pion flavors as well. The parameters $A_{UU}^{\cos\phi_h}$ and $A_{UU}^{\cos 2\phi_h}$ were extracted as a function of those kinematic variables in an eight free parameter fits as shown in Figs. 97 and 98 for the variable x_B as an example. The complete list of figures illustrating the extractions of $A_{UU}^{\cos\phi_h}$ and $A_{UU}^{\cos 2\phi_h}$ and the comparisons between different fitting methods in multiple dimensions are in Appendix E.

An assumption was made on the kinematic dependence of $A_{UU}^{\cos\phi_h}$ and $A_{UU}^{\cos 2\phi_h}$; they are assumed to be only linearly dependent on any of the three variables considered. So the values of these parameters were fitted with a straight line as a function of any of the three kinematic variables as shown in Figs. 97 and 98. Finally, the dependence of $A_{UU}^{\cos\phi_h}$ and $A_{UU}^{\cos 2\phi_h}$ in multiple dimensions were parameterized as

$$A_{UU}^{\cos\phi_h}(x_B, P_{h\perp}, z) = A_{UU}^{\cos\phi_h}(x_B) \times \frac{A_{UU}^{\cos\phi_h}(P_{h\perp})}{< A_{UU}^{\cos\phi_h}(P_{h\perp}) >} \times \frac{A_{UU}^{\cos\phi_h}(z)}{< A_{UU}^{\cos\phi_h}(z) >} \tag{85}$$

and

$$A_{UU}^{\cos 2\phi_h}(x_B, P_{h\perp}, z) = A_{UU}^{\cos 2\phi_h}(x_B) \times \frac{A_{UU}^{\cos 2\phi_h}(P_{h\perp})}{< A_{UU}^{\cos 2\phi_h}(P_{h\perp}) >} \times \frac{A_{UU}^{\cos 2\phi_h}(z)}{< A_{UU}^{\cos 2\phi_h}(z) >}. \tag{86}$$

Slight Modification of the Fitting Technique

Due to the instability of fitting eight significantly correlated free parameters on a data set of limited statistics and limited ϕ_h coverage, a slight modification was made on the fitting algorithm used in the MINUIT package to stabilize the fits. An additional term,

$$\left(\frac{A_{UU}^{\cos\phi_h}}{0.30}\right)^2 + \left(\frac{A_{UU}^{\cos 2\phi_h}}{0.12}\right)^2,$$

was added in the expression for χ^2 of the fitting algorithm. Adding such terms in the χ^2 is statistically more rational than imposing rigid boundaries for the parameters as commonly practiced. There are two clear benefits of this method. The first one is that the kinematic dependence of the values of $A_{UU}^{\cos\phi_h}$ and $A_{UU}^{\cos 2\phi_h}$ can be measured quite well whereas in the method of rigid-boundaries, the kinematic dependence of the

parameters are distorted if the values of the parameters converge on the boundaries. The second benefit is that any prior knowledge on the values of these parameters can be incorporated more effectively. In the method adopted in this analysis, the prior knowledge was introduced as a smooth parabola in the χ^2 distribution rather than just two rigid boundaries in the conventional method so that there are practically no limits on the values of the parameters.

The different numbers in the above term added to the χ^2 are not randomly chosen; they are judiciously chosen based on numerous trials and errors plus some knowledge about $A_{UU}^{\cos\phi_h}$ and $A_{UU}^{\cos 2\phi_h}$ from other analyses. Though it was asserted earlier that there are no reliable references to $A_{UU}^{\cos\phi_h}$ and $A_{UU}^{\cos 2\phi_h}$, there are two analyses which have measured them. One of the analyses [51] measured $A_{UU}^{\cos\phi_h}$ and $A_{UU}^{\cos 2\phi_h}$ only for positive pion but in a slightly different kinematics. $A_{UU}^{\cos\phi_h}$ in the analysis [51] is larger than -0.06 and is almost constant as a function of $P_{h\perp}$; $A_{UU}^{\cos 2\phi_h}$ is consistent with 0. The other analysis [52] measured $A_{UU}^{\cos\phi_h}$ for neutral pions in a very similar kinematics as compared to this analysis. According to that analysis $A_{UU}^{\cos\phi_h}$ is around -0.1 ± 0.15; the dependence on the kinematics was not measured in that analysis.

The addition to χ^2 imposes the prior assumption that the value of $A_{UU}^{\cos\phi_h}$ and $A_{UU}^{\cos 2\phi_h}$ is around 0. Just as in any good Bayesian statistics, these prior knowledge were not imposed very strictly; they were imposed with the highest possible degree of flexibility by choosing large values in the denominators. The numbers in the denominators closely resemble the uncertainties of the imposed constraints. The other reason for choosing large values in the denominators was not to over constrain the fits. In this way the kinematic dependence of $A_{UU}^{\cos\phi_h}$ and $A_{UU}^{\cos 2\phi_h}$ remains largely undistorted.

The systematic effect on the other parameters due to the enforcement of subtle subjectivities in the form of additional constraints and an assumption on the kinematic dependence was treated with due caution in this analysis as explained in the following section. The worst consequence of these modifications was in the significantly higher overall systematic uncertainty for $A_{LL}^{\cos\phi_h}$; but for other parameters the contribution to the overall systematic uncertainty was less pronounced. Since $A_{LL}^{\cos\phi_h}$ and $A_{UU}^{\cos\phi_h}$ are highly correlated, any little amount of uncertainty in $A_{UU}^{\cos\phi_h}$ propagates directly to the uncertainty of $A_{LL}^{\cos\phi_h}$. This is the reason why $A_{LL}^{\cos\phi_h}$, compared to other asymmetry moments, has large overall systematic uncertainty.

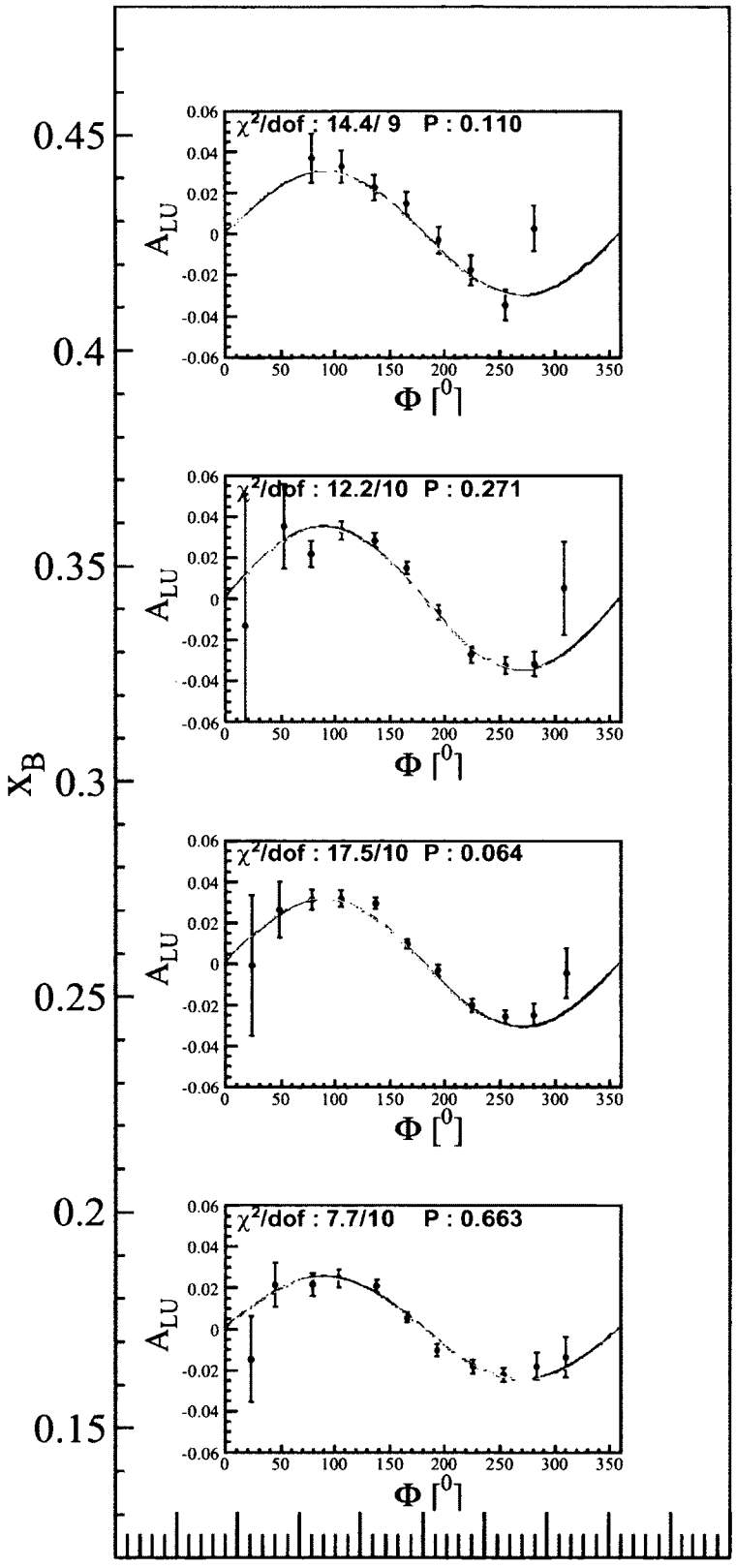

FIG. 94: $A_{LU}(x_B)$ fits for π^+. Cyan: without any term in the denominator. Golden: simultaneous fits with both terms in the denominators.

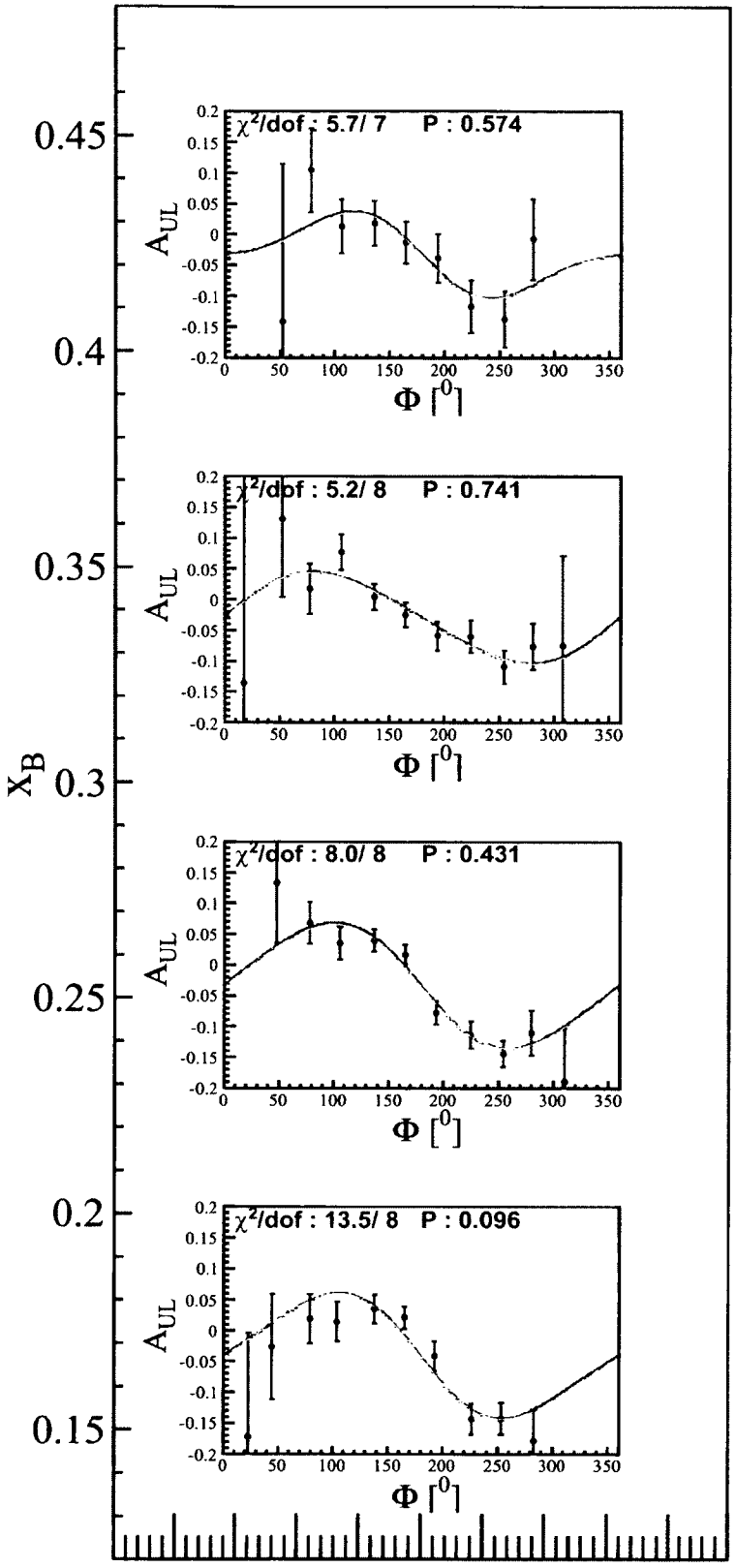

FIG. 95: $A_{UL}(x_B)$ fits for π^+. Cyan: without any term in the denominator. Golden: simultaneous fits with both terms in the denominators.

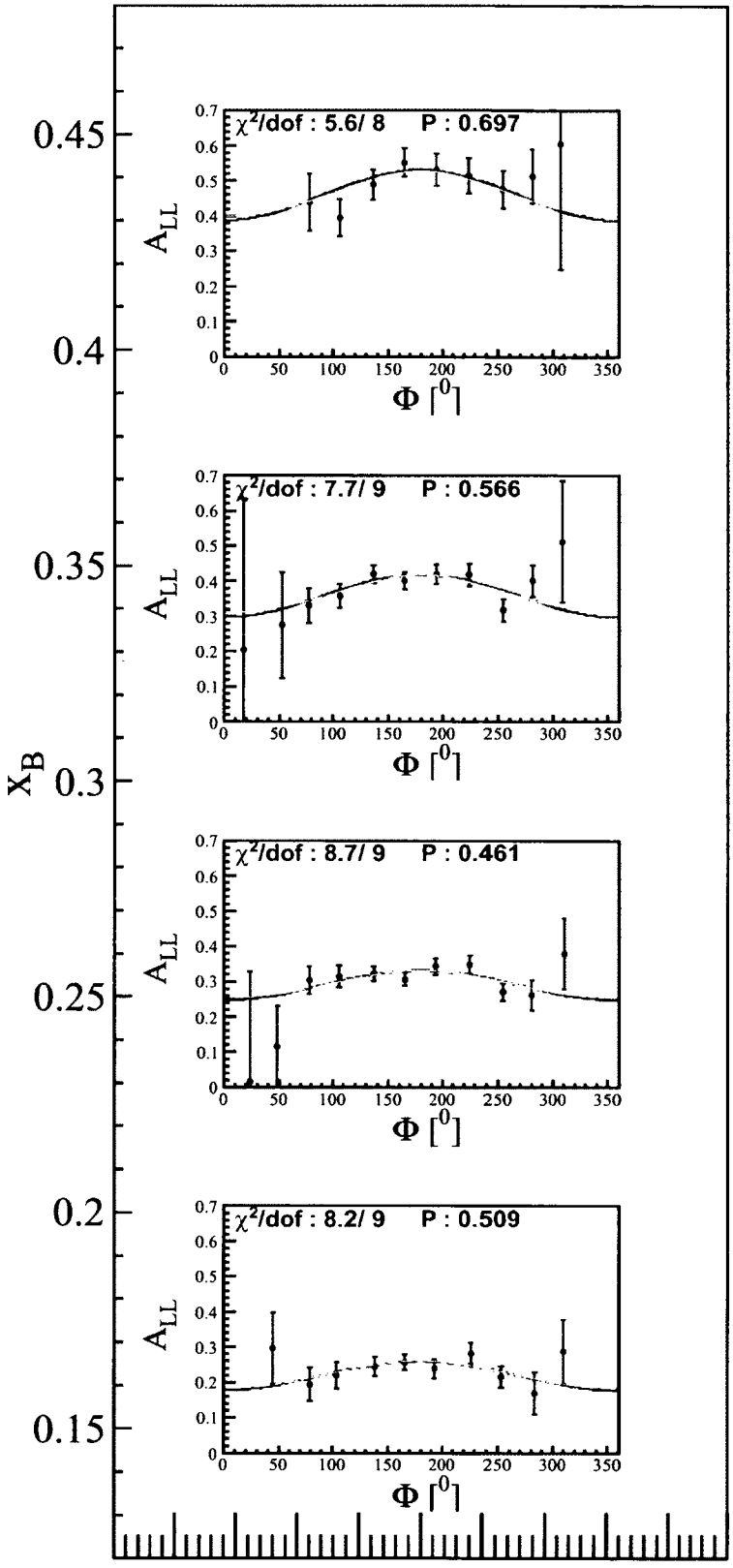

FIG. 96: $A_{LL}(x_B)$ fits for π^+. Cyan: without any term in the denominator. Golden: simultaneous fits with both terms in the denominators.

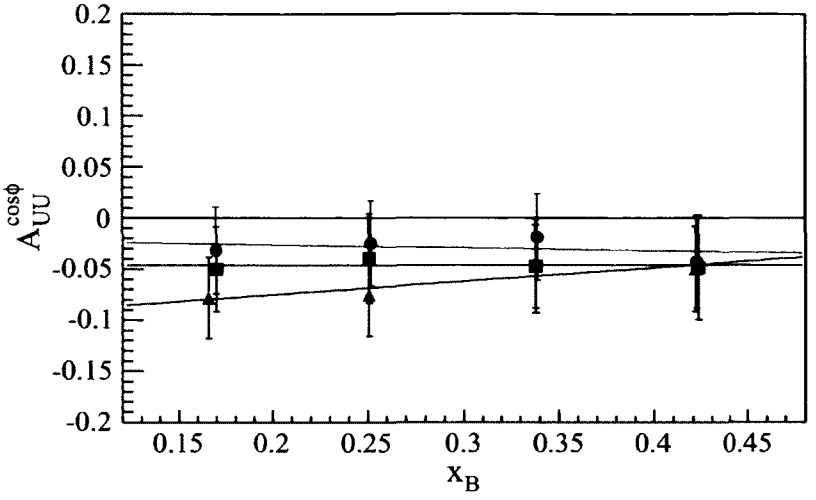

FIG. 97: $A_{UU}^{\cos\phi_h}(x_B)$ from the global fits. A linear function is fitted to the results. Red: π^+, blue: π^- and green: π^0

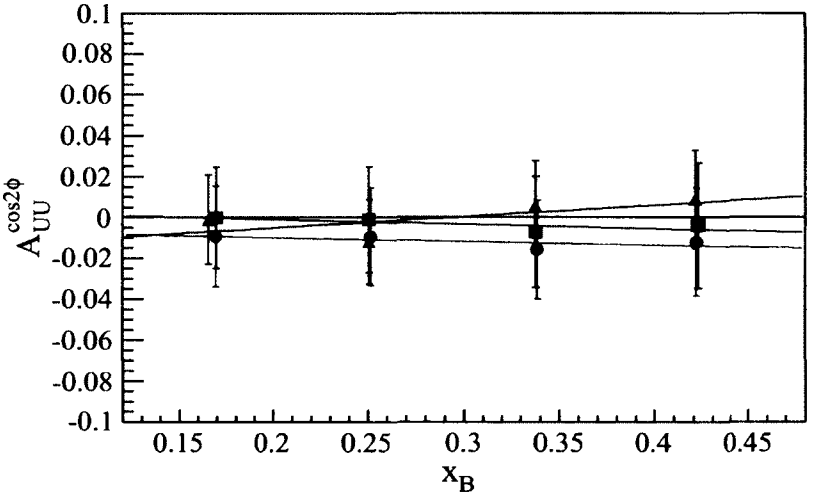

FIG. 98: $A_{UU}^{\cos 2\phi_h}(x_B)$ from global fits. A linear function is fitted to the results. Red: π^+, blue: π^- and green: π^0

5.4.3 SYSTEMATIC UNCERTAINTIES ON $A_{UU}^{\cos\phi_H}$ AND $A_{UU}^{\cos 2\phi_H}$

As stated above, the main purpose of the inclusion of $A_{UU}^{\cos\phi_h}$ and $A_{UU}^{\cos 2\phi_h}$ in the fit was to estimate their effect on other asymmetry moments. All the polarized asymmetry moments were extracted by two methods, first, by treating $A_{UU}^{\cos\phi_h}$ and $A_{UU}^{\cos 2\phi_h}$ as described above, second, by equating both of them to zero. The difference from the two methods is the estimated systematic uncertainty. Though this is a highly conservative estimate, its contribution to the final systematic uncertainty is not very significant except for $A_{LL}^{\cos\phi_h}$. The resultant systematic uncertainties from this method of estimation are shown in a series of figures in Appendix E.

5.4.4 $A_{UU}^{\cos\phi_H}$ AND $A_{UU}^{\cos 2\phi_H}$ FOR SIDIS ON THE DEUTERON

Since the statistics on the deuteron is more limited, the extraction of $A_{UU}^{\cos\phi_h}$ and $A_{UU}^{\cos 2\phi_h}$ as described above on deuteron data was not possible. The same values of $A_{UU}^{\cos\phi_h}$ and $A_{UU}^{\cos 2\phi_h}$ from the proton data were used for the extraction of asymmetry moments from the deuteron data. The systematic uncertainty for the deuteron was evaluated in the exact way as for the proton in this case.

5.5 ϕ_H DISTRIBUTION PLOTS

Some of the typical ϕ_h distributions of the asymmetries are presented in the following pages. Figs. 99, 100 and 101 show the beam single, target single and beam-target double spin asymmetry fits on the proton in (x_B, $P_{h\perp}$) bins for neutral pions; Figs. 102, 103 and 104 show the beam single, target single and beam-target double spin asymmetry fits on the deuteron in x_B bins for neutral pion. A complete list of plots in other dimensions and for other flavors on the proton and the deuteron are in Appendix E.

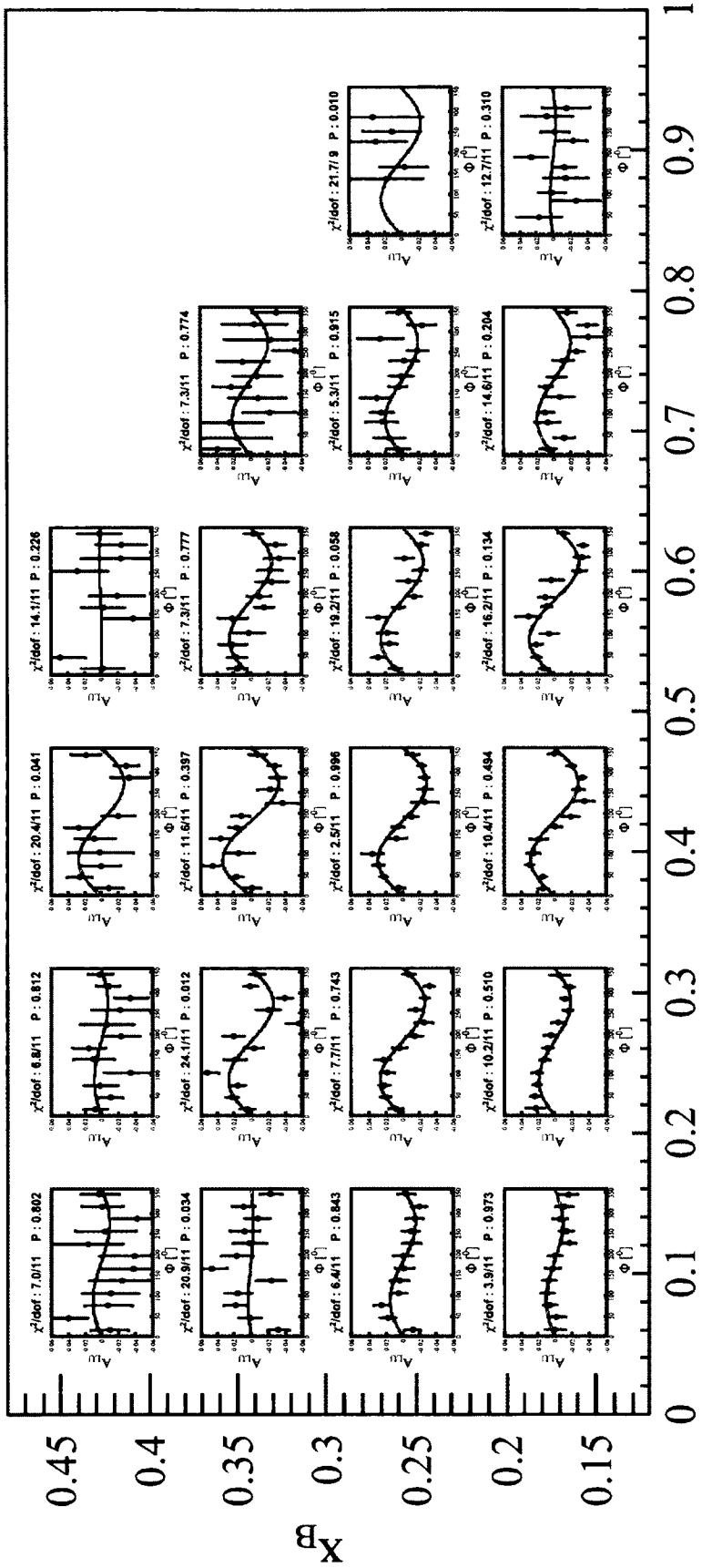

FIG. 99: $A_{LU}(x_B, P_{h\perp}, \phi_h)$ on the proton for π^0

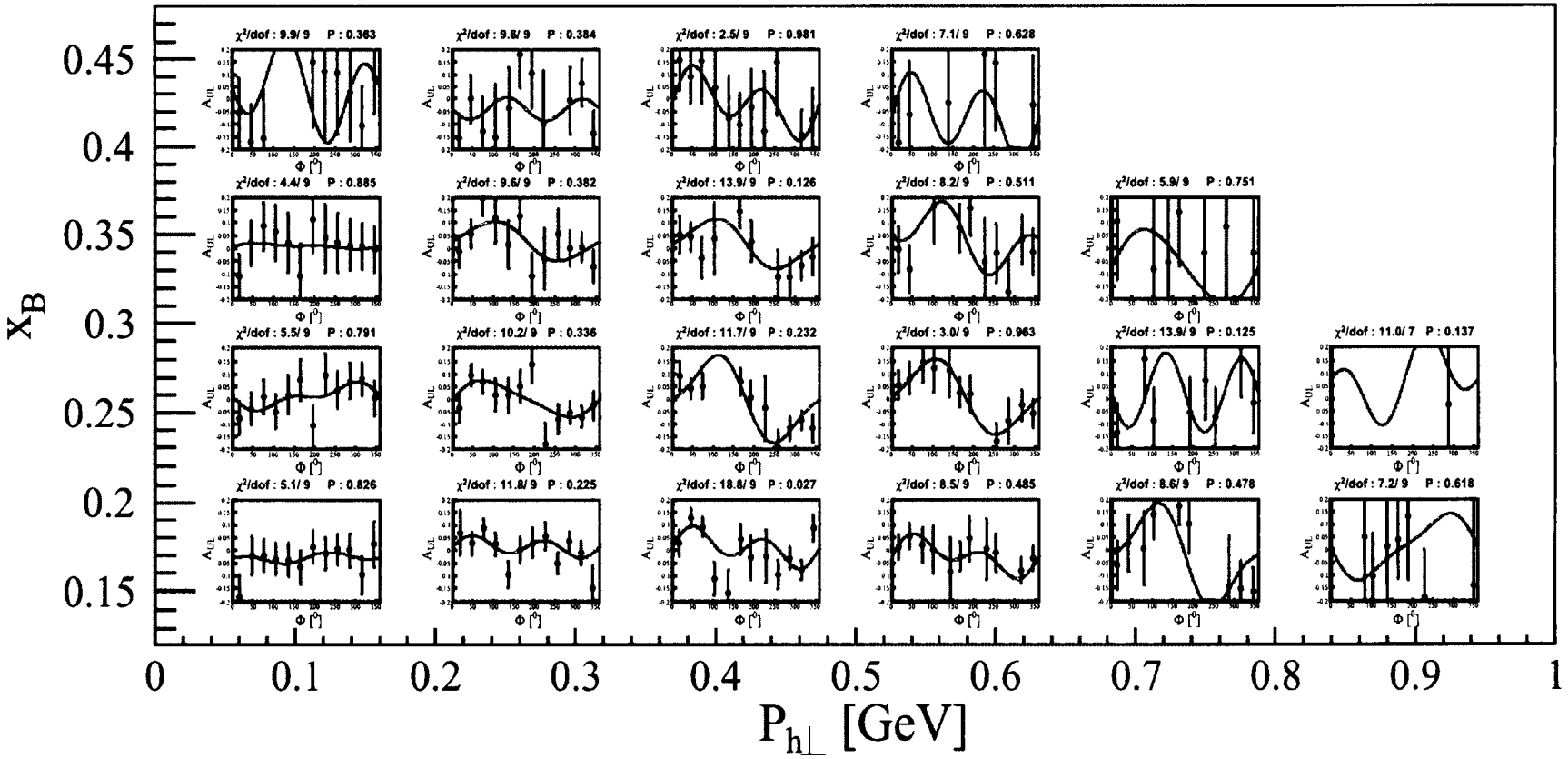

FIG. 100: $A_{UL}(x_B, P_{h\perp}, \phi_h)$ on the proton for π^0

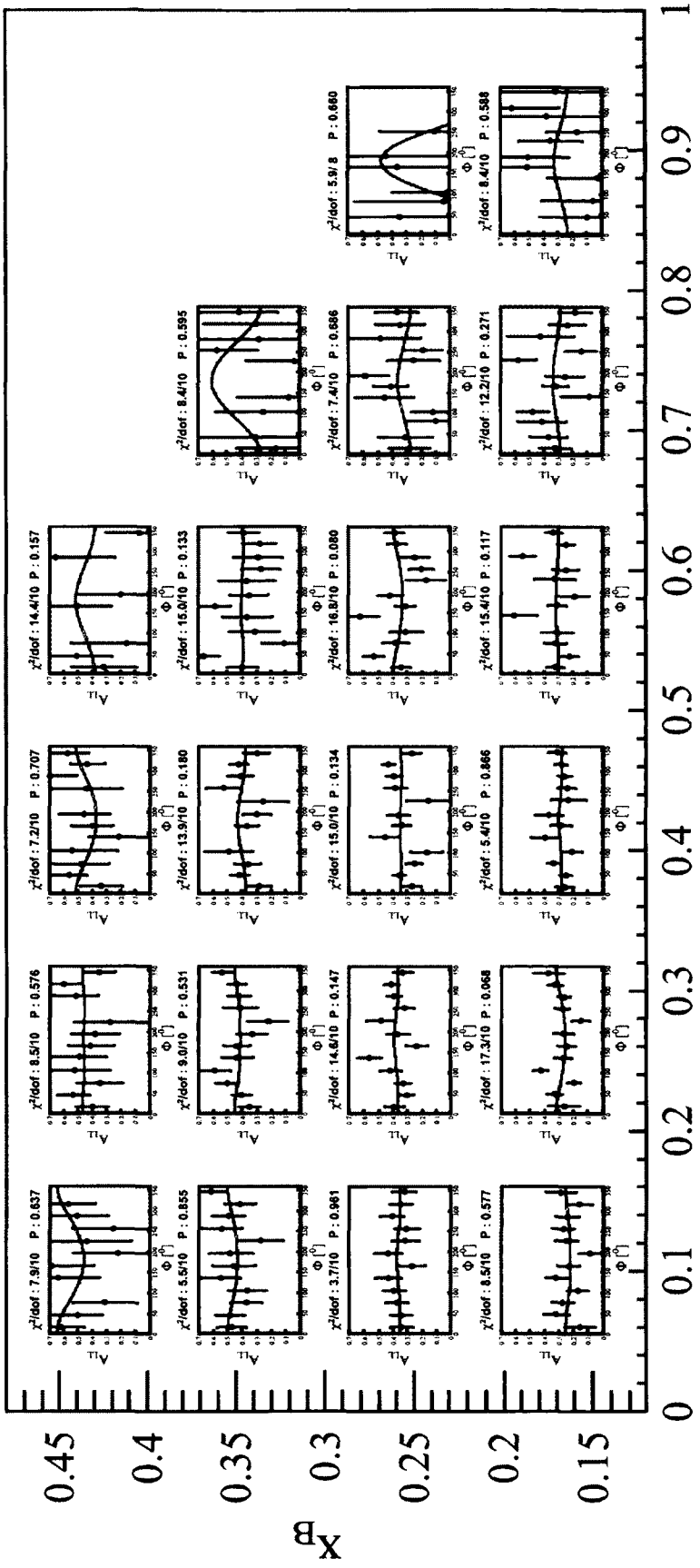

FIG. 101: $A_{LL}(x_B, P_{h\perp}, \phi_h)$ on the proton for π^0

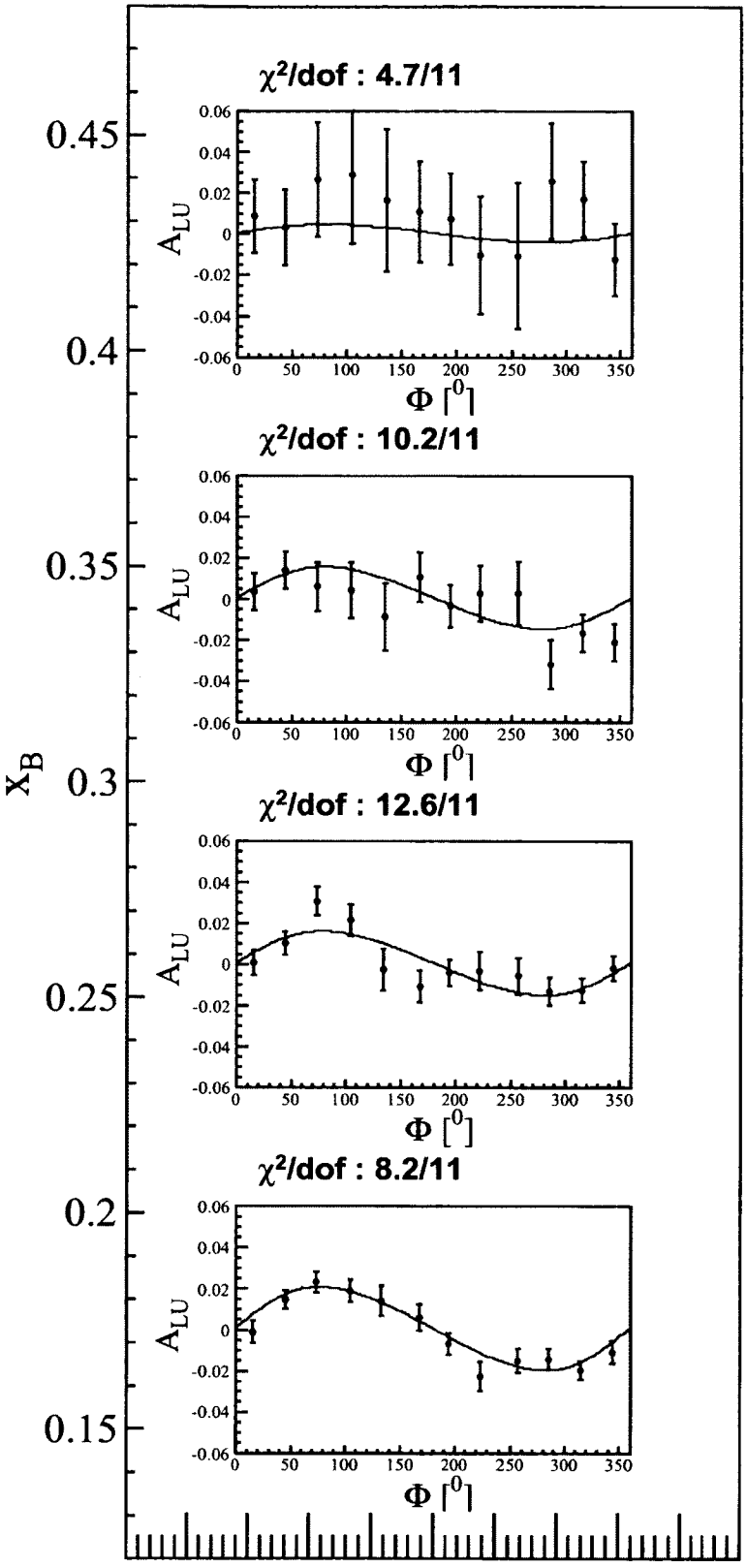

FIG. 102: $A_{LU}(x_B, \phi_h)$ on the deuteron for π^0

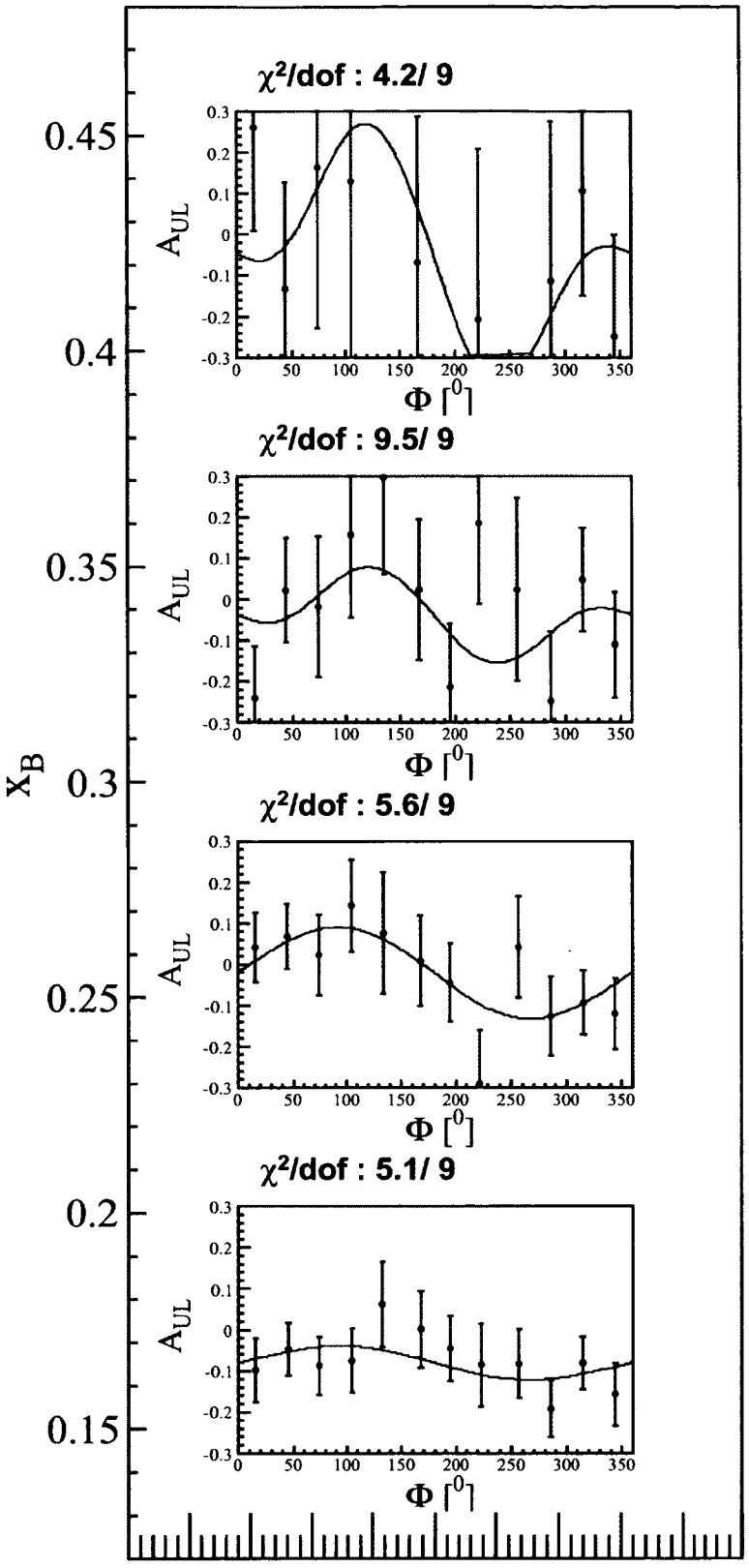

FIG. 103: $A_{UL}(x_B, \phi_h)$ on the deuteron for π^0

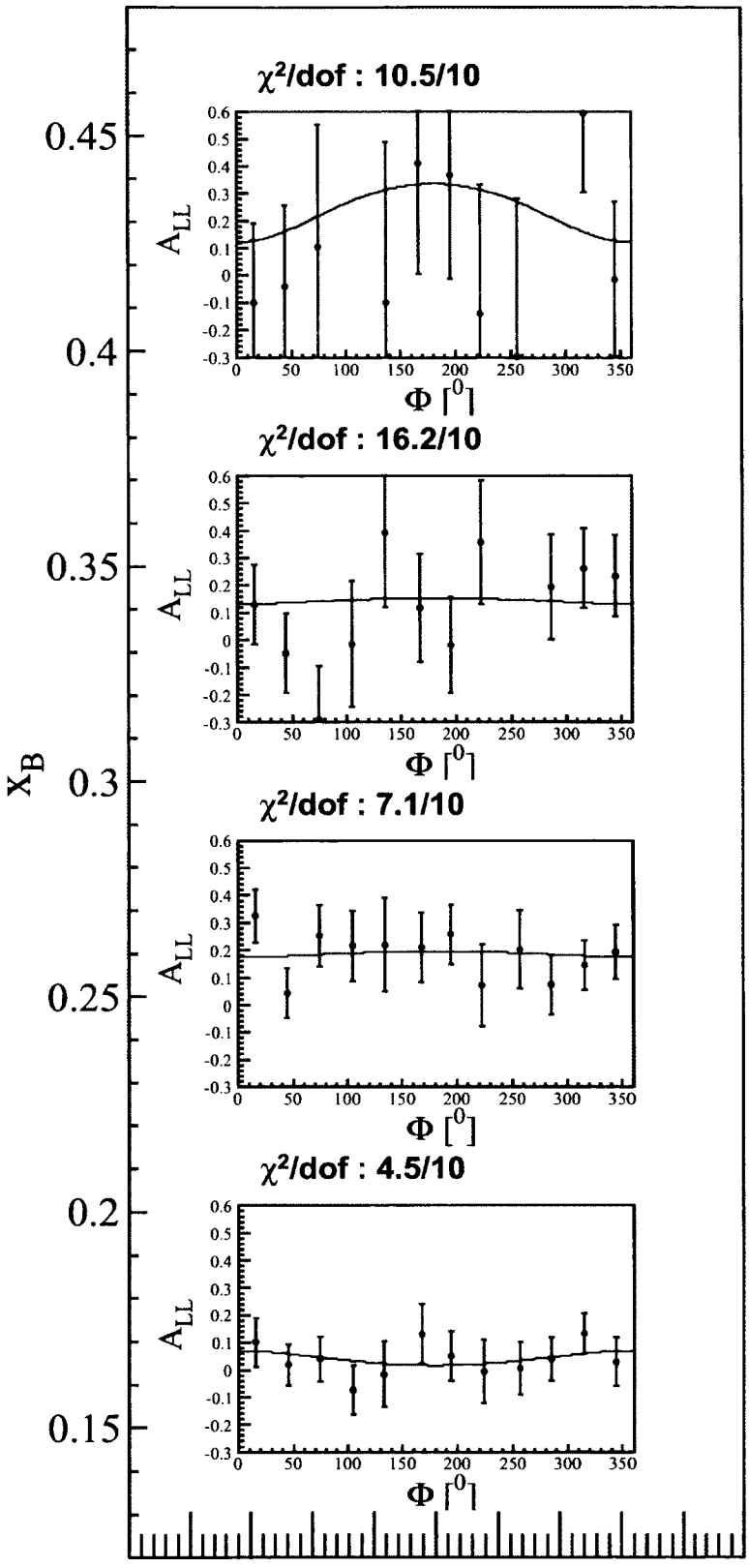

FIG. 104: $A_{LL}(x_B, \phi_h)$ on the deuteron for π^0

5.6 COMPARISONS BETWEEN GENERATED AND RECONSTRUCTED ASYMMETRIES

For the present analysis charged pions passing through the inner calorimeter (IC) were discarded because their kinematics would be significantly altered. Their removal resulted in a narrower ϕ_h coverage centered around π. On the other hand, for neutral pions, the inclusion of the IC enhanced the ϕ_h coverage. Limited coverage in ϕ_h can have detrimental consequences for the extraction of the true asymmetry moments. Though the asymmetry moments are orthogonal in principle, in the limited ϕ_h region they cease to be so. This deviation from the orthogonality introduces a correlation between the azimuthal asymmetry moments during their extraction from the fits. Comparisons were made between Monte Carlo generated and reconstructed single and double spin azimuthal asymmetries to check if the limited ϕ_h coverage has significant effect on the extraction of the asymmetry moments from the data. Moreover, the comparison between the generated and the reconstructed asymmetries can reveal other hidden problems in the analysis procedure.

For this purpose, a multi-hadron SIDIS event generator was used which generates events uniformly in ϕ_h. Depending upon the kind of asymmetry under study, suitable helicity values were attributed as a function of ϕ_h in the generated events. The generated events were run through GSIM, a simulated CLAS detector, and the results were stored as root files. The simulated data were compared to the experimental ones to ensure that they describe the physics realistically. The distributions of various kinematic variables were very similar in both the experimental and the simulated data. Most importantly, the gaps in the ϕ_h distributions in various $P_{h\perp}$ and x_B bins for charged pions closely resemble the experimental data as shown in Fig. 105. To compare the generated and the reconstructed asymmetries, generated SIDIS events with only a single pion of the type of flavor under study were selected. Azimuthal asymmetries with reasonable moments (from 5% to 20%) were generated and compared with the reconstructed asymmetry moments. In Figs. 106 and 107, 10% $\sin\phi_h$ and 0% $\sin 2\phi_h$ moments were generated for single spin asymmetries and 20% Const and 0% $\cos\phi_h$ moments were generated for double spin asymmetries. In the figures, the generated asymmetries are shown by golden curves; the reconstructed data points and the fits to them are shown by cyan curves and symbols. The generated and the reconstructed parameters are shown as text of corresponding colors. The reconstructed asymmetry moments are within the statistical expectations. The

four plots in all cases correspond to four bins in $P_{h\perp}$ or x_B. The same comparison was repeated numerous times to check if there is a systematic difference between the generated and the reconstructed asymmetry moments - the check did not show any significant difference; the differences were within the statistical uncertainties. From this study it can be concluded that none of the asymmetry moments extracted from the EG1-DVCS data are artifacts of the CLAS detector acceptance (with the IC) for detecton of SIDIS events.

The complete list of figures showing comparisons of simulation versus data and generated versus reconstructed single and double spin asymmetries for all the pion flavors are presented in Appendix F.

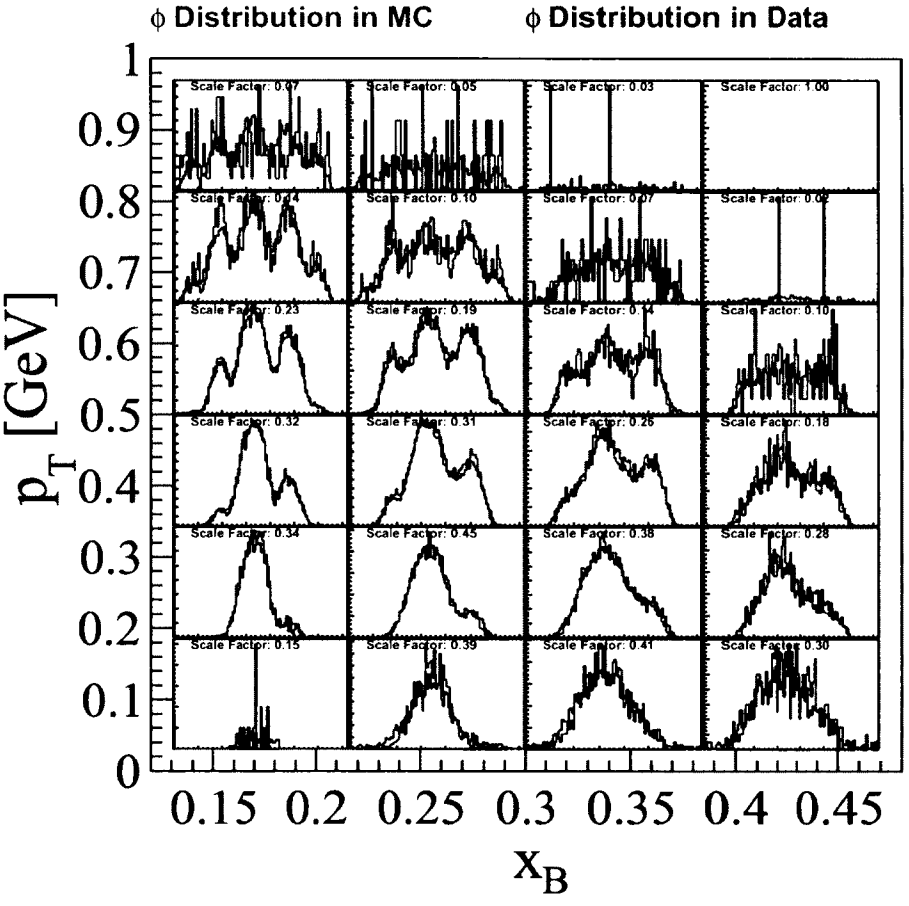

FIG. 105: Comparison between simulation and data for the azimuthal distribution of π^+

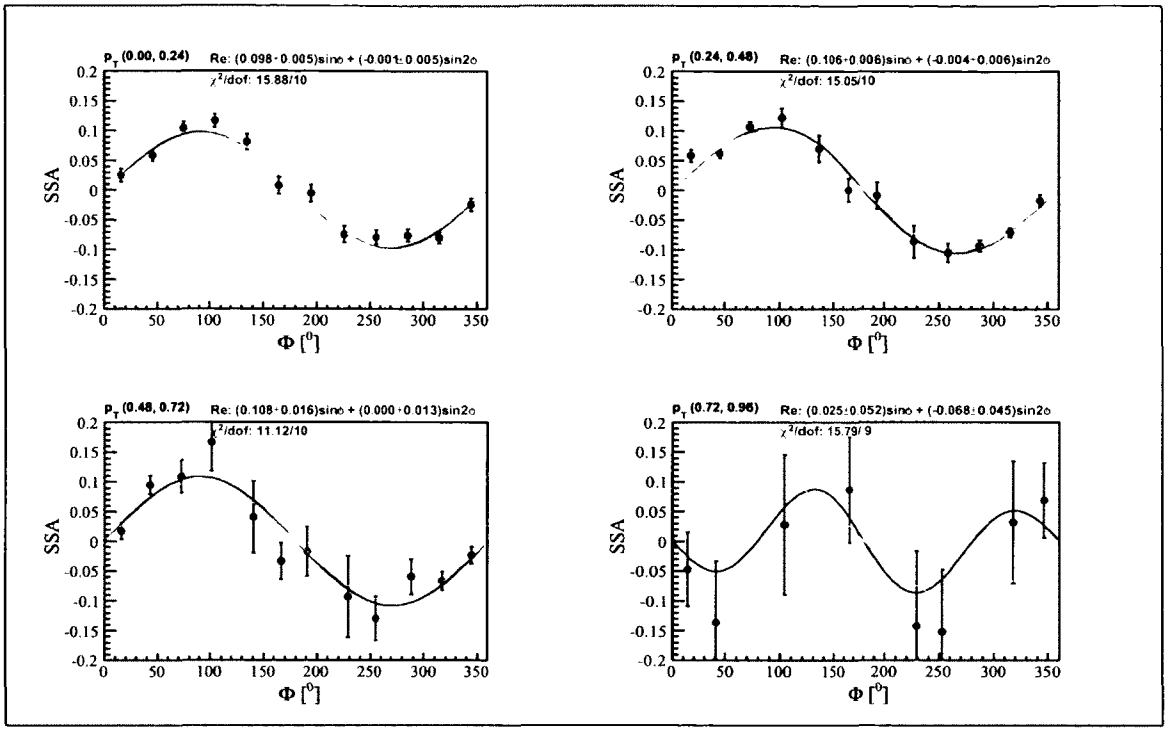

FIG. 106: Comparison of generated and reconstructed single spin asymmetries as a function of $P_{h\perp}$ for neutral pion.

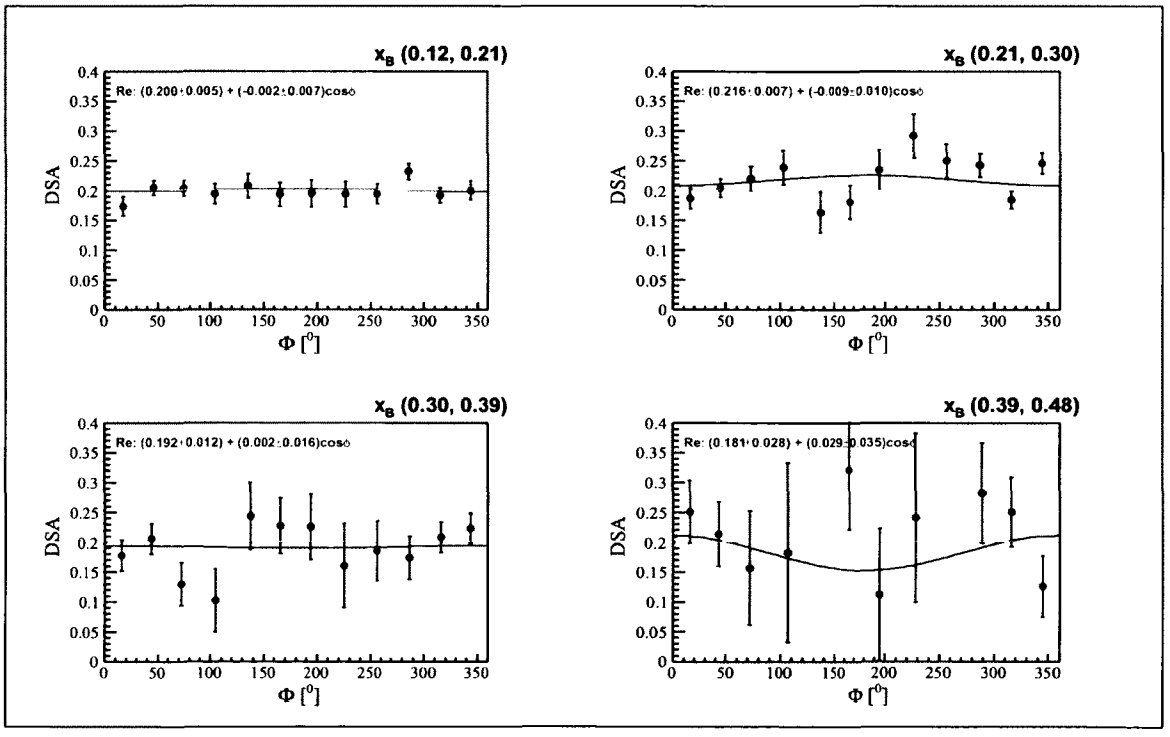

FIG. 107: Comparison of generated and reconstructed double spin asymmetries as a function of $P_{h\perp}$ for neutral pion.

CHAPTER 6

RESULTS

In this chapter the asymmetry moments extracted according to the procedures described in the previous chapter are plotted together for different pion flavors. Results for proton and deuteron are plotted separately. Since the kinematic distributions for the neutral pion were slightly different from that of charged pions, some bins have results only for neutral pions. In this section, only the plots representing the results are presented; the detailed numerical tables are in Appendix B. These tables have separate columns for statistical and systematic uncertainties.

In all plots of this chapter, the different pion flavors are identified by different colors: red, blue and green respectively for positive, negative and neutral pion. The asymmetry moments for the proton are plotted in two dimensional bins of (x_B, $P_{h\perp}$), (z, $P_{h\perp}$) and (x_B, z). The asymmetry moments for the deuteron are plotted in single dimensional bins: x_B, z and $P_{h\perp}$. Figures from 118 to 112 are for the proton. Figures from 113 to 117 are for the deuteron. In each of the figures for the proton, the four plots correspond to four bins in different kinematics whose values are written at the top of each plot.

The statistical errors are shown by inner horizontal risers and the point-to-point systematic uncertainties are indicated by the outer vertical bars. The systematic uncertainty for each point was calculated by adding the differences in the final results from all the possible sources of systematic uncertainties in quadrature and taking their square root. For convenience, the differences in the final results due to the uncertainties in the various sources are presented in Appendix G. The uncertainties described in the following are the main contributors to the overall systematic uncertainties in the final results. In some cases the uncertainties are statistical whereas in most of the cases, they are estimated based on reasonable variation of parameters or methods. The details about the sources of systematic uncertainties are discussed in the corresponding previous sections. In this chapter, the sources of uncertainties are briefly summarized. All these sources except the polarizations of various components of the contaminated target are assumed to be uncorrelated.

Beam, Target and Beam-Target Polarizations

The details on these uncertainties are in Sections 4.1 and 4.2; they have both statistical as well as systematic components. Their uncertainties are around 4%. They affect all the three types of asymmetries. In case of the contaminated target, the polarizations of NH_3 and ND_3 were anti-correlated; this was handled by taking the difference in the final result by the suitable combinations of polarizations of the target components, i.e. when the polarization of one of the component is increased by 1σ, the polarization of the other component is decreased by 1σ.

Dilution Factor

Details can be found in Section 4.3. This uncertainty affects A_{UL} and A_{LL} only. Four sources were considered to estimate the overall uncertainty in the dilution factor: two different parameterizations of the attenuation factors from two different data sets, the statistical as well as the systematic uncertainties in the data used to extract the attenuation factors, 3% uncertainty in the packing fraction of NH_3 and an alternative form of the fragmentation ratio. The uncertainty in the dilution factor depends on kinematics. The detailed plots showing the systematic uncertainties in the final results due to theis uncertainty are in Appendix G.

Background Subtraction

Deetails can be found in Section 3.4. The background subtraction affects all three asymmetries. For the neutral pion, alternative fit parameters were used. For charged pions, the background was set to zero. It is assumed that the positive kaon contamination in positive pions affects the asymmetries by 4%; this is also included in the overall systematic uncertainty for positive pions.

Radiative Corrections

Details can be found in Section 5.2.1. It is estimated that the existing radiative correction has 100% uncertainty. Since radiative corrections were applied only for A_{UL} and A_{LL} this uncertainty affects A_{UL} and A_{LL} only.

Unpolarized Cross-Section Terms

The details are in Section 5.4. The unpolarized cross-section terms in the denominators were set to zero as an estimation of the uncertainty, affecting all three asymmetries.

Target Contamination Fraction

Details can be found in Section 4.2. The statistical uncertainty of the target contamination was used. This affects only the A_{UL} and A_{LL} asymmetries on the deuteron.

Nitrogen polarization

Details can be found in Section 5.2.3. The contribution from the nitrogen polarization to the asymmetries on the deuteron were calculated with a precision of 25% [30]. This affects only the A_{UL} and A_{LL} asymmetries on the deuteron.

6.1 $A_{LU}^{\sin\phi_H}(X_B, P_{H\perp})$ ON THE NH_3

The $A_{LU}^{\sin\phi_h}$ moment of the beam single spin asymmetry as a function of x_B and $P_{h\perp}$ on the NH_3 is shown in Fig. 118. Since the SIDIS events originating from different nucleons cannot be isolated in this experiment, single-beam spin asymmetry in this analysis is measured on NH_3. For positive and neutral pion the asymmetry is positive whereas for negative pion it is inconclusive. A clear $P_{h\perp}$ dependence is seen for neutral pion.

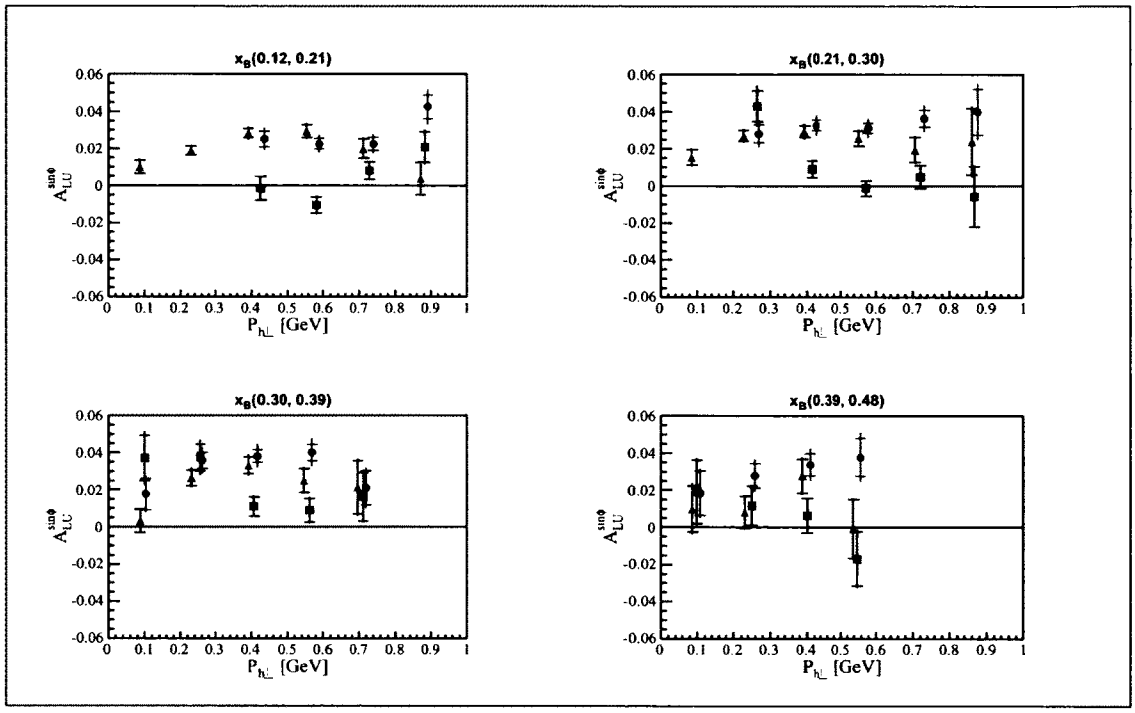

FIG. 108: $A_{LU}^{\sin\phi_h}(x_B, P_{h\perp})$ on the NH_3, red: π^+, blue: π^-, green: π^0.

6.2 $A_{UL}^{\sin\phi_H}(X_B, P_{H\perp})$ ON THE PROTON

The $A_{UL}^{\sin\phi_h}$ moment of the target single spin asymmetry as a function of x_B and $P_{h\perp}$ on the proton is shown in Fig. 119. The asymmetry appears positive for positive and neutral pion; negative for negative pion. This asymmetry is due to a higher twist effect.

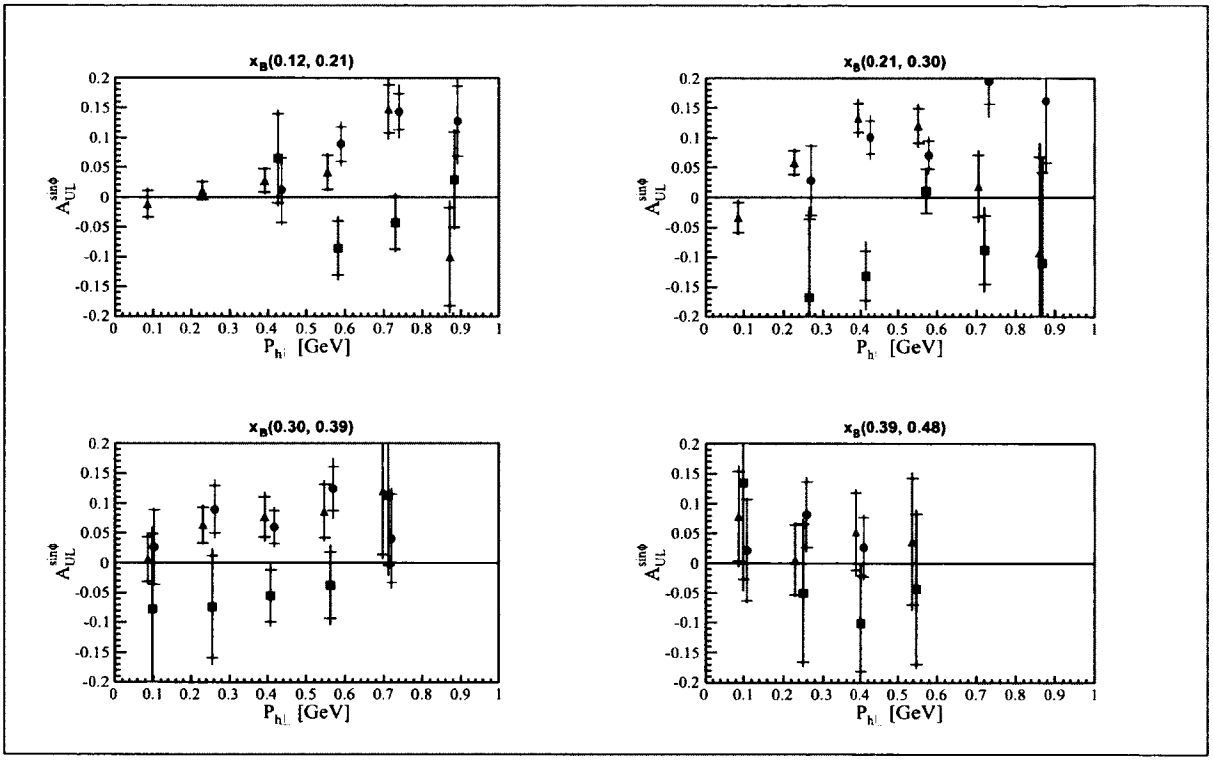

FIG. 109: $A_{UL}^{\sin\phi_h}(x_B, P_{h\perp})$ on the proton, red: π^+, blue: π^-, green: π^0.

6.3 $A_{UL}^{\sin 2\phi_H}(X_B, P_{H\perp})$ ON THE PROTON

The $A_{UL}^{\sin 2\phi_h}$ moment of the target single spin asymmetry as a function of x_B and $P_{h\perp}$ on the proton is shown in Fig. 110. The asymmetry is a leading twist effect and is sensitive to the TMD $h_{1L}^{\perp}$. It appears consistent with zero for all the pions at higher x_B; at lower x_B bins, the asymmetry is about -4% for positive pion and about $+4\%$ for neutral pion.

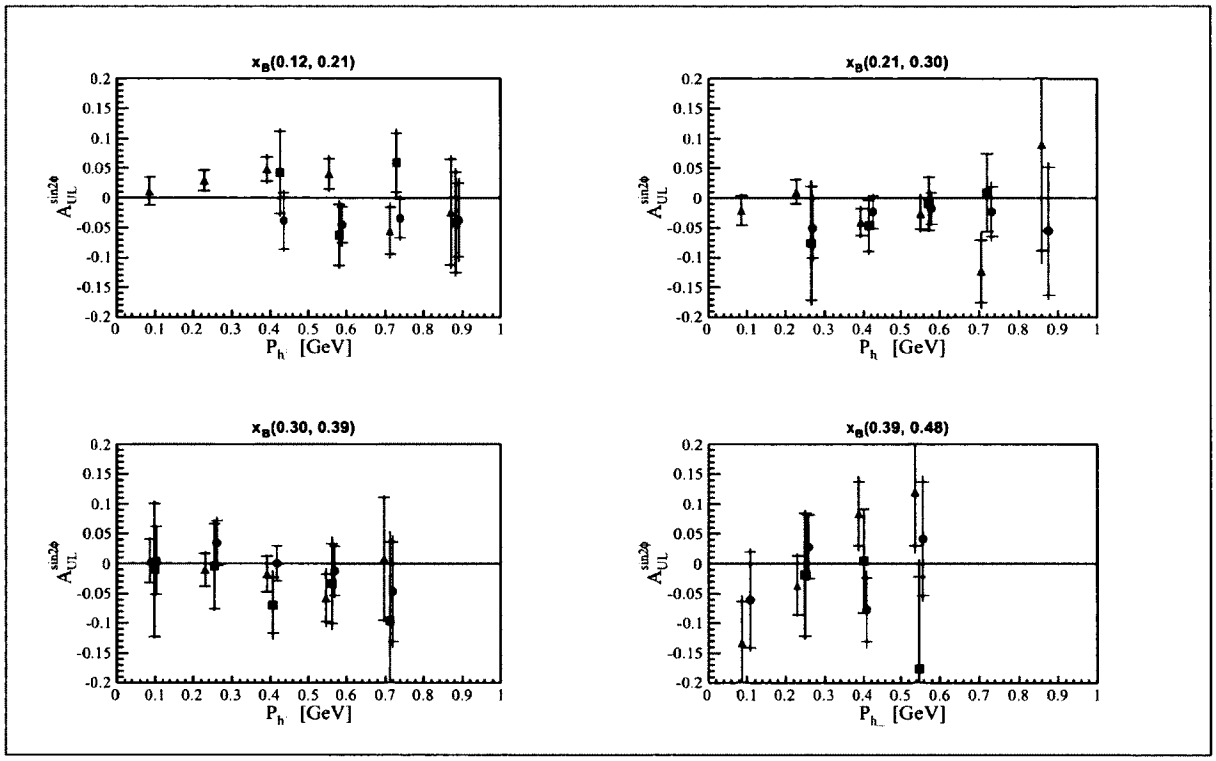

FIG. 110: $A_{UL}^{\sin 2\phi_h}(x_B, P_{h\perp})$ on the proton, red: π^+, blue: π^-, green: π^0.

6.4 $A_{LL}^{\mathrm{CONST}}(X_B, P_{H\perp})$ ON THE PROTON

The A_{LL}^{Const} moment of the beam-target double spin asymmetry as a function of x_B and $P_{h\perp}$ on the proton is shown in Fig. 111. This asymmetry is related with g_1/F_1 but this asymmetry is not corrected with the depolarization factor. The $P_{h\perp}$ dependence of the asymmetry is not apparent.

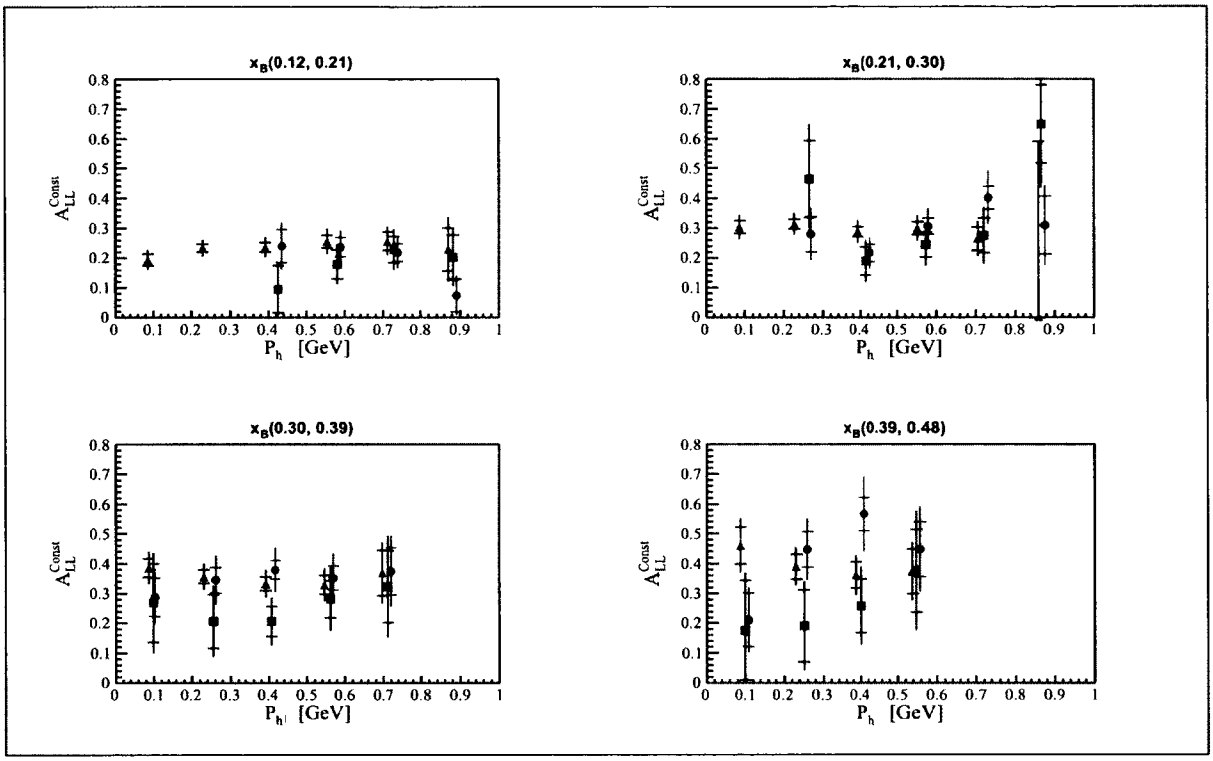

FIG. 111: $A_{LL}^{\mathrm{Const}}(x_B, P_{h\perp})$ on the proton, red: π^+, blue: π^-, green: π^0.

6.5 $A_{LL}^{\cos\phi}(X_B, P_{H\perp})$ ON THE PROTON

The $A_{LL}^{\cos\phi}$ moment of the beam-target double spin asymmetry as a function of x_B and $P_{h\perp}$ on the proton is shown in Fig. 112. This asymmetry is purely due to higher twist effect. It is consistent with zero.

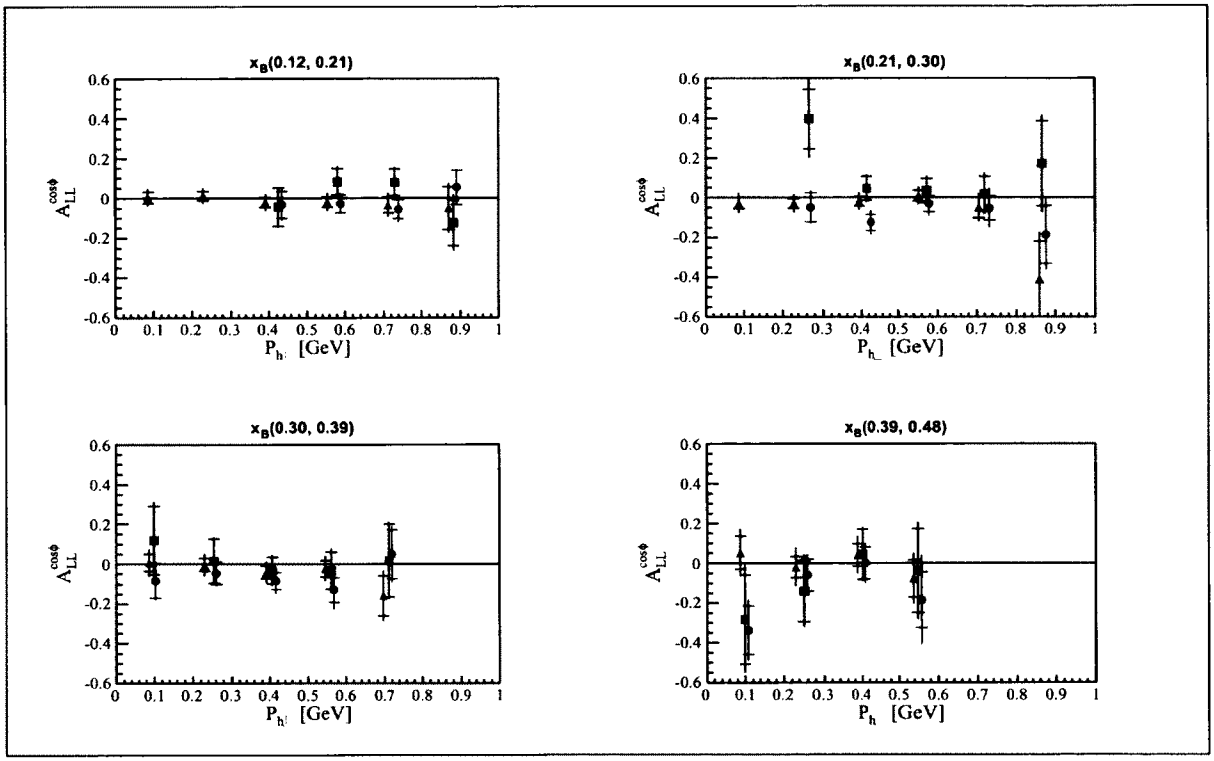

FIG. 112: $A_{LL}^{\cos\phi_h}(x_B, P_{h\perp})$ on the proton, red: π^+, blue: π^-, green: π^0.

6.6 $A_{LU}^{\sin\phi_H}(X_B)$ ON THE ND_3

The $A_{LU}^{\sin\phi_h}$ moment of the beam single spin asymmetry as a function of x_B on the ND_3 is shown in Fig. 113. The asymmetry is positive for positive and neutral pions and consistent with zero for negative pion.

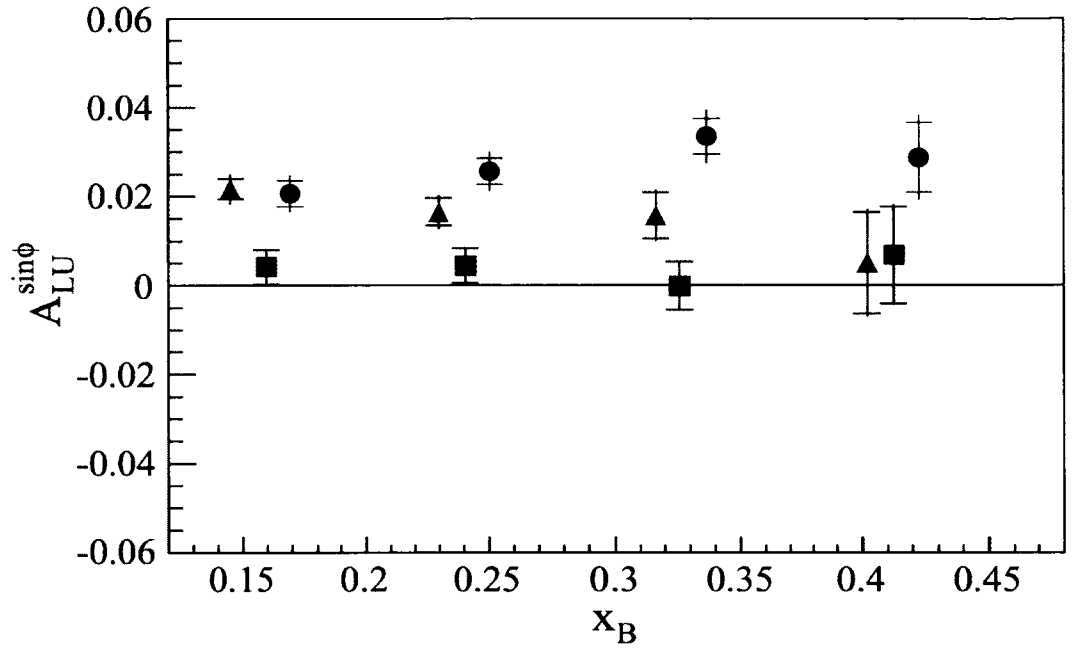

FIG. 113: $A_{LU}^{\sin\phi_h}(x_B)$ on the ND_3, red: π^+, blue: π^-, green: π^0.

6.7 $A_{UL}^{\sin\phi_H}(X_B)$ ON THE DEUTERON

The $A_{UL}^{\sin\phi_h}$ moment of the target single spin asymmetry as a function of x_B on the deuteron is shown in Fig. 114. This asymmetry is purely due to higher twist effect. It is consistent with zero.

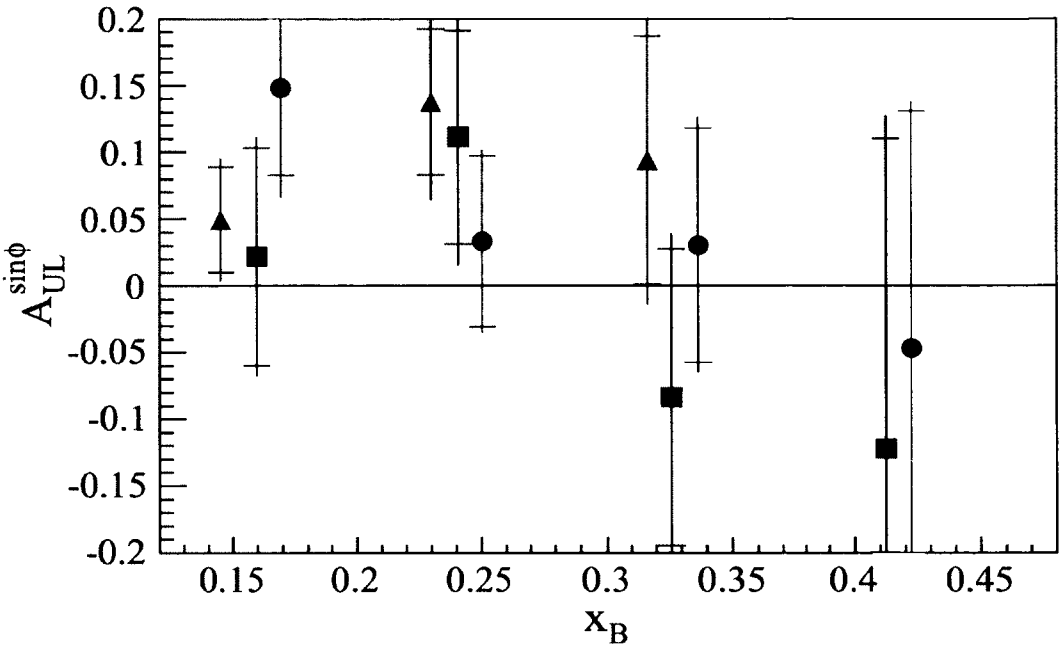

FIG. 114: $A_{UL}^{\sin\phi_h}(x_B)$ on the deuteron, red: π^+, blue: π^-, green: π^0.

6.8 $A_{UL}^{\sin 2\phi_H}(X_B)$ ON THE DEUTERON

The $A_{UL}^{\sin 2\phi_h}$ moment of the target single spin asymmetry as a function of x_B on the deuteron is shown in Fig. 115. This asymmetry is due to leading twist effect and is sensitive to $h_{1L}^{\perp}$. It is consistent with zero for all the pions.

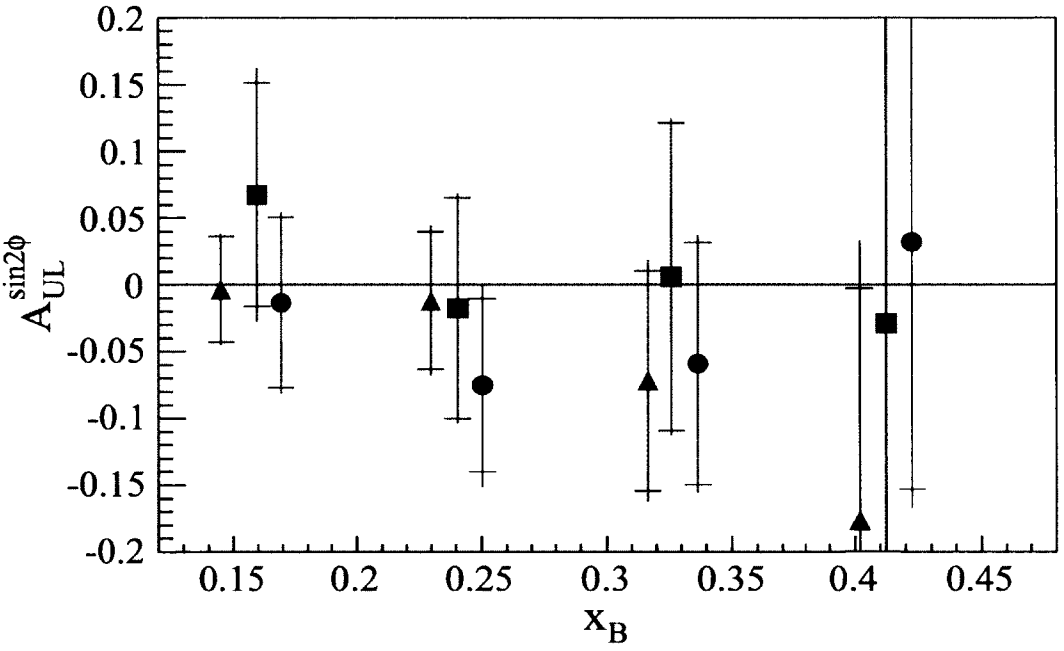

FIG. 115: $A_{UL}^{\sin 2\phi_h}(x_B)$ on the deuteron, red: π^+, blue: π^-, green: π^0.

6.9 $A_{LL}^{\mathrm{CONST}}(X_B)$ ON THE DEUTERON

The A_{LL}^{Const} moment of the beam-target double spin asymmetry as a function of x_B on the deuteron is shown in Fig. 116. This asymmetry is related to g_1/F_1. It is positive for positive and neutral pions and consistent with zero for negative pion.

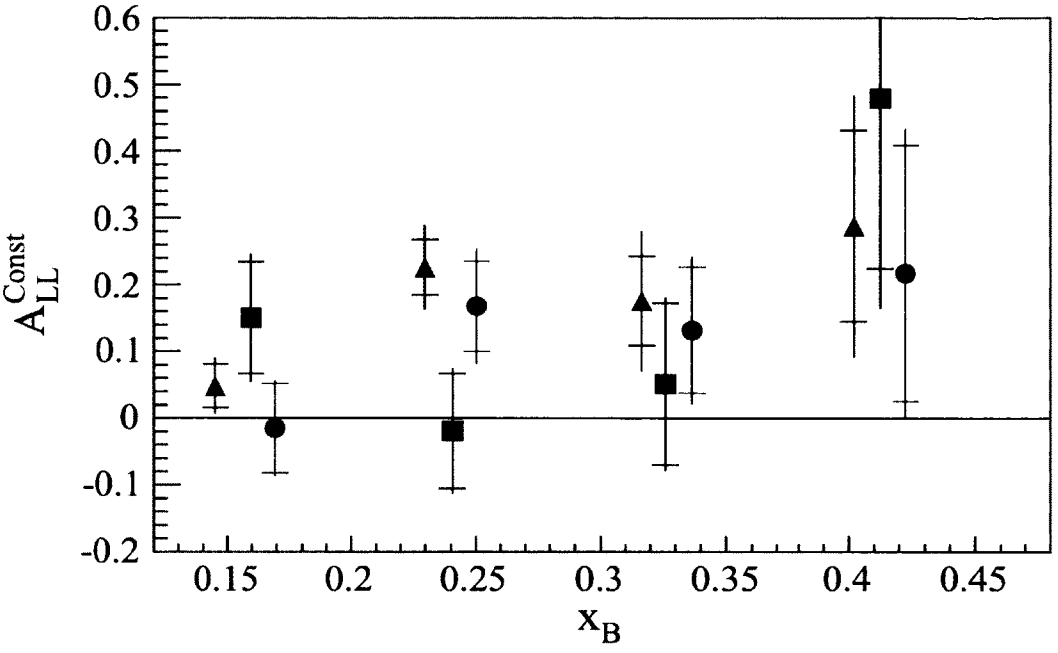

FIG. 116: $A_{LL}^{\mathrm{Const}}(x_B)$ on the deuteron, red: π^+, blue: π^-, green: π^0.

6.10 $A_{LL}^{\cos\phi}(X_B)$ ON THE DEUTERON

The $A_{LL}^{\cos\phi}$ moment of the beam-target double spin asymmetry as a function of x_B on the deuteron is shown in Fig. 117. This asymmetry is due to higher twist effect; it is consistent with zero.

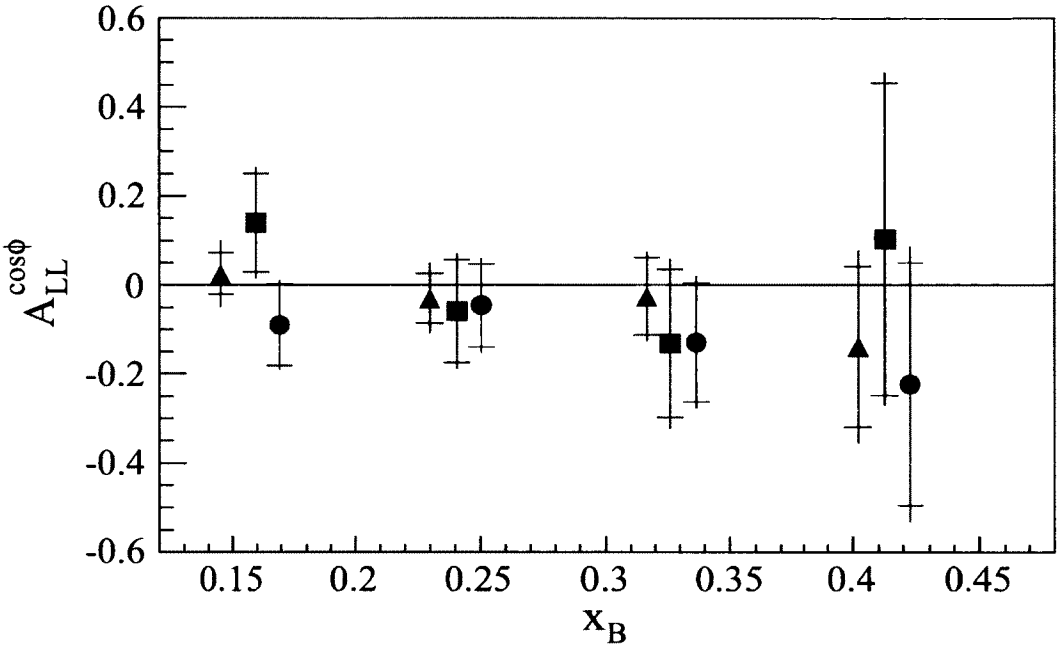

FIG. 117: $A_{LL}^{\cos\phi_h}(x_B)$ on the deuteron, red: π^+, blue: π^-, green: π^0.

CHAPTER 7

COMPARISONS WITH PREDICTIONS AND OTHER RESULTS

Some of the results from this analysis were compared with some theoretical and phenomenological predictions as well as with some previously published similar results.

7.1 COMPARISON WITH OTHER EXPERIMENTAL RESULTS

M. Aghasyan et al. [52] published SIDIS single beam spin azimuthal asymmetries for neutral pions on the proton. These results were from CLAS data and the kinematics of the experiment were similar to this analysis. Since this analysis measured the single beam spin azimuthal asymmetries for neutral pions on an NH_3 target, comparisons between the two results can reveal nuclear effects. The four plots in Figure 118 show the comparisons between the two results in four x_B bins as a function of $P_{h\perp}$. The similarities between the two results indicate that the nuclear effect on neutral pion single beam spin asymmetries is not significant, moreover, it shows that the contribution from the neutron is also not significant.

7.2 COMPARISON WITH PREDICTIONS

Zhun Lu *et al.* have published predictions for the SIDIS single target spin asymmetries for all three pion flavors [53]. The predictions are based on a di-quark spectator model including the scalar and the axial-vector diquark components in a semi-inclusive neutral pion electro-production contributed by the twist-3 distribution function $g^{\perp}$ [54]. The same methods were earlier employed to predict single beam spin asymmetries . The comparisons between the predictions and the results from this analysis are shown in Figure 119. The predicted values are the $A_{UL}^{\sin\phi_h}$ moments as a function of x_B for all pion flavors, which are distinguished by different colors. The comparisons show that the predictions for neutral pions agree very well with the data; the predictions for positive pions agrees reasonably well with the data

except for the lower x_B bins. However, the predictions for negative pions do not agree at all; even the signs of the asymmetries are opposite.

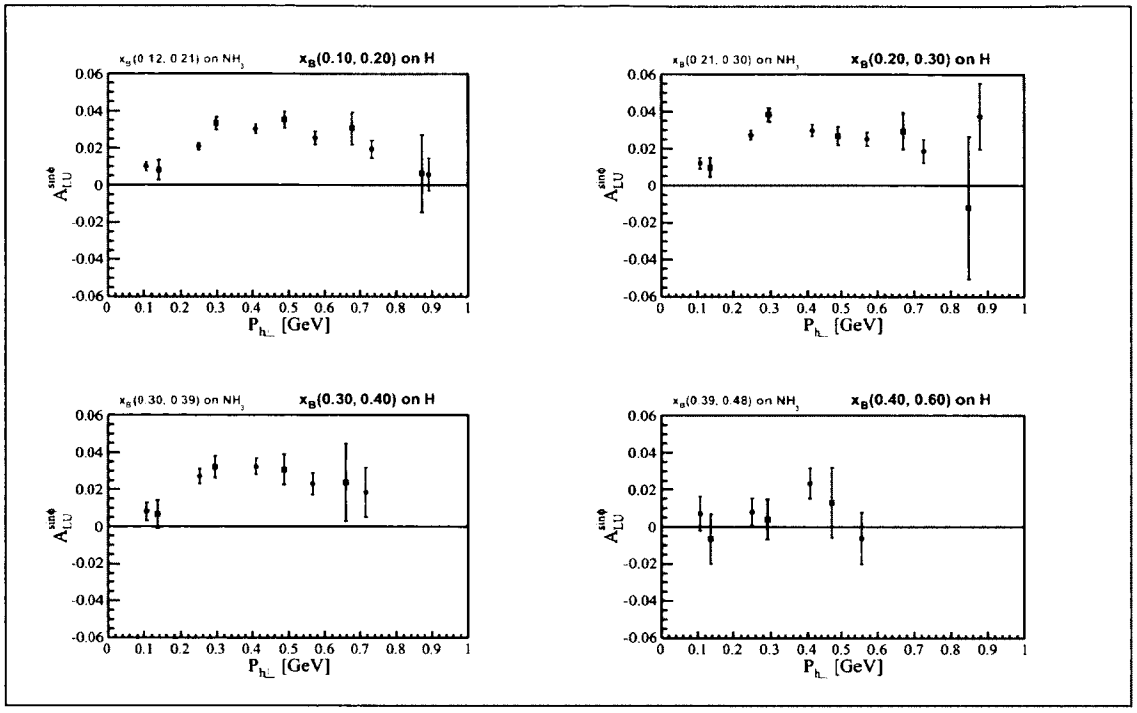

FIG. 118: Comparison with M. Aghasyan's $A_{LU}^{\sin\phi_h}$ results for neutral pion [52]. The blue points are the values from Aghasyan's analysis. Red points are the values from this analysis for neutral pions.

M. Anselmino *et al.* calculated A_{LL} within the CLAS kinematics, based on a leading order QCD parton model with unintegrated quark distributions and fragmentation functions [17]. Comparisons between the predictions and the measurements from this analysis are shown in Figure 120. The different curves in the figure correspond to different values of μ_2^2. The symbol μ_2 correspond to the the width of the parton transverse momentum distribution which is assumed to be Gaussian. The assumptions are: $f_1 \sim e^{-p_T^2/\mu_1^2}$ and $g_1 \sim e^{-p_T^2/\mu_2^2}$, $\mu_1^2 = 0.25$ is kept fixed and different values of A_{LL}^{Const} for different values of μ_2^2 are calculated. These predictions were evaluated with the exact kinematics of each data point by B. Parsamyan. It can be seen from the following plots that $\mu_2 = 0.25$ agrees better with the data compared to the other values in the case of neutral pions.

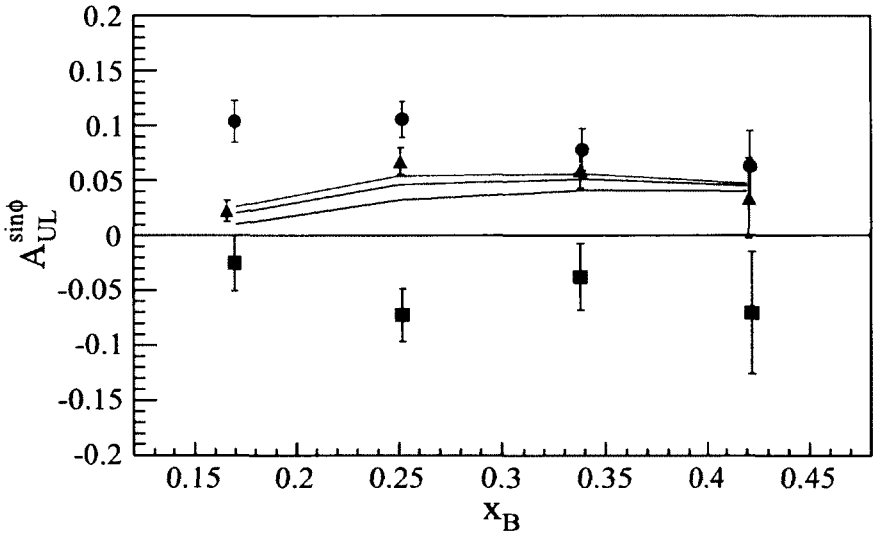

FIG. 119: $A_{UL}^{\sin\phi_h}$ comparisons with the predictions from Reference [53]. The lines are the predictions from di-quark spectator model including the scalar and the axial-vector diquark components by Zhun Lu et al. [53]. As usual, red, blue and green are for positive, negative and neutral pions respectively.

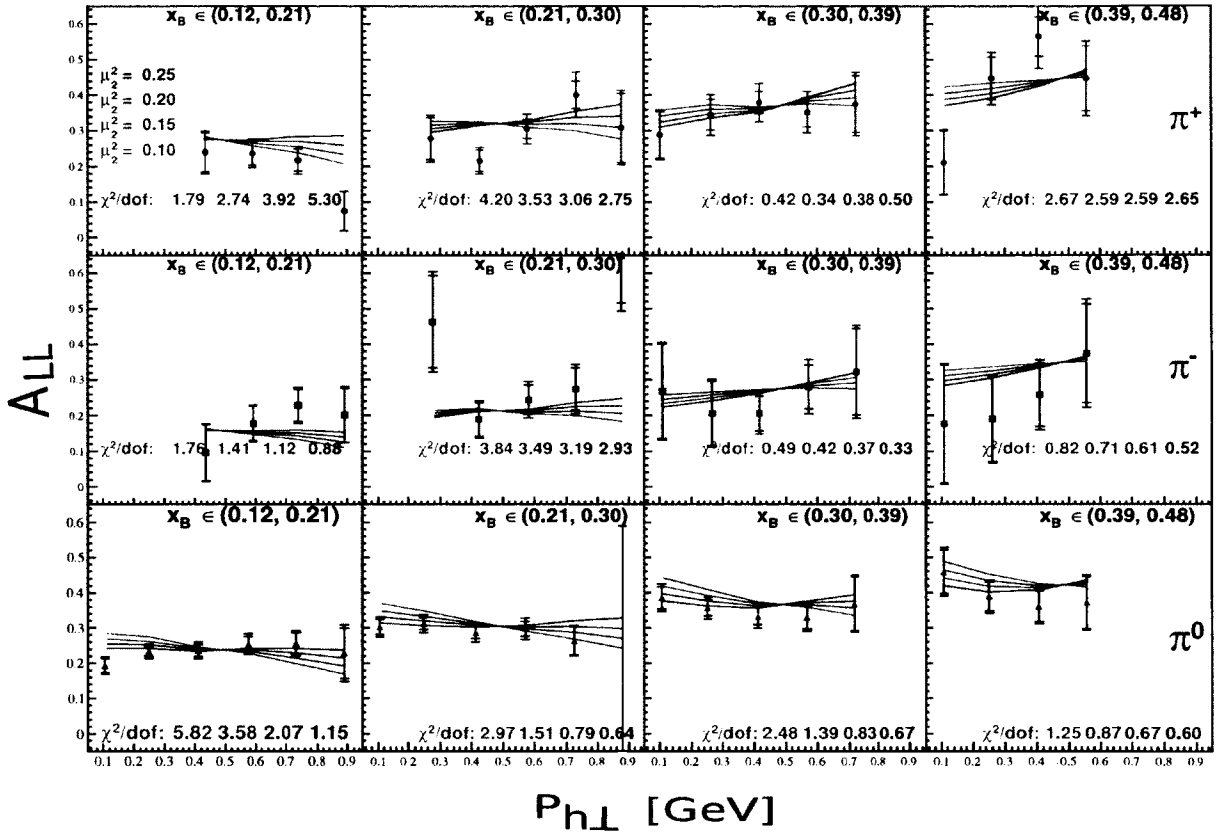

FIG. 120: Comparison between prediction and measurement of A_{LL}. The predictions are shown by cyan curves for various values of the width of the parton transverse momentum distribution.

CHAPTER 8

CONCLUSION

Five azimuthal asymmetry moments $A_{LU}^{\sin\phi_h}$, $A_{UL}^{\sin\phi_h}$, $A_{UL}^{\sin 2\phi_h}$, A_{LL}^{Const} and $A_{LL}^{\cos\phi_h}$ were extracted on two different targets, proton and deuteron, in all three pion channels with unprecedented high statistics. In the case of the proton, the asymmetry moments were extracted in two dimensions. Due to limited statistics, the asymmetry moments on the deuteron were extracted in three different single dimensions.

The primary motivation of this analysis was to extract the moments for single target and double spin asymmetries. The single beam spin asymmetry moments were a byproduct of this analysis. These have been measured earlier with a comparable precision only on a proton target [50] [52]. Within the statistical precision of the different results, there are only slight differences between the values from the proton and from NH_3 and ND_3 targets, which suggests that nuclear effects are not very significant. The results for $A_{LU}^{\sin\phi_h}$ from this analysis can be useful in the extraction of beam single spin asymmetries on nuclei.

The predictions for the SIDIS single target spin asymmetries for all three pions by Zhun Lu et al. [53] based on di-quark spectator model including the scalar and the axial-vector di-quark components, agree well with the data for neutral pions. There is a significant difference at lower x_B for positive pions while negative pions do not agree at all. The predictions from M. Anselmino *et al.* for A_{LL} on the proton, based on the leading order QCD parton model with unintegrated quark distribution and fragmentation functions, are within the overall measurement ucertainty. The phenomenological calculations of beam-target double spin asymmetry moments, A_{LL}^{Const} and $A_{LL}^{\cos\phi_h}$, based on different models is underway. The comparison will be done once the predictions become available. This analysis shows significantly positive A_{LL}^{Const} for the neutral pion and the positive pion channels on the deuteron. The $A_{LL}^{\cos\phi_h}$ moments are consistent with zero in both targets and in all pion channels.

All results have been tabulated for further analysis with averages of all the relevant kinematic variables as well as the dilution factor. Since some of the tables are too big to fit into this thesis, they are made available in the directory http://wwwold.jlab.org/Hall-B/secure/eg1-dvcs/skoirala/Tables/. It is hoped that

with the significant precision of the results from this analysis, global data fits to extract TMDs will be highly constrained.

BIBLIOGRAPHY

[1] M. Anselmino, A. Efremov and E. Leader, Phys. Reports **261**, 124 (1995).

[2] A. Bacchetta, Proceedings of the International School of Physics, Enrico Fermi, Course CLXXX, 107 (2011).

[3] R.L. Jaffe and A. Manohar, Nucl. Phys. B **337**, 509 (1990).

[4] D. Florian, R. Sassot, M. Stratmann and W. Vogelsang, Phys. Rev. Lett. **113**, 5 (2014)

[5] G. Smith, *Measurements of Spin Asymmetries for Deeply Virtual Compton Scattering off the Proton using the Extended Maximum Likelihood Method* (Ph.D. Thesis, University of Glasgow, 2013).

[6] B. Pasquini, C. Lorce and M. Vanderhaeghen, JHEP, (2011).

[7] A. W. Thomas and W. Weise, *The Structure of the Nucleon*, (Wiley-VCH, 2001).

[8] R. Hofstadter and R. McAllister, Phys. Rev. **98**, 217 (1955).

[9] R. Hofstadter, Rev. Mod. Phys. **28**, 214 (1956).

[10] J. Beringer et al. Phys. Rev. D **86**, 10001 (2012).

[11] A. Bacchetta, U. D'Alesio, M. Diehl and C. Miller, Phys. Rev. D **70**, 117504 (2004).

[12] A. Bacchetta, M. Diehl, K. Goeke, A. Metz and P. Mulders, JHEP, **0702**, 093 (2007).

[13] J. C. Collins, Nucl. Phys. **B396**, 161 (1993).

[14] H. Avakian et al. Phys.Rev.Lett. **105**, 262002 (2010).

[15] A.V. Efremov, K. Goeke and P. Schweitzer, Phys.Rev. **D73**, 094025 (2006).

[16] M. Gluck and E. Reya and M. Stratmann and W. Vogelsang, Phys.Rev. **D53**, 4775 (1996).

[17] M. Anselmino and A. Efremov and A. Kotzinian and B. Parsamyan, Phys.Rev. **D74**, 074015 (2006).

[18] M. Alekseev et al. Phys.Lett. B, **680**, 217 (2009).

[19] Airapetian et al. Phys. Rev. D, **71**, 012003 (2005).

[20] A.V. Efremov, K. Goeke and P. Schweitzer, Phys.Rev. **D67**, 114014 (2003).

[21] A.V. Efremov, K. Goeke and P. Schweitzer, Phys. Lett. B, **522**, 37 (2001).

[22] A.V. Efremov and K. Goeke and P. Schweitzer, Phys.Lett. **B522**, 37 (2001).

[23] J. Zhu and B. Q. Ma, Phys.Lett. **B696**, 246 (2011).

[24] C.W. Leemann, D.R. Douglas and G.A. Krafft, Ann. Rev. Nucl. Part. Sci. **51**, 413 (2001).

[25] E.S. Smith et al. Nucl. Inst. and Meth. **432**, 265 (1999).

[26] M. Amarian et al. Nucl. Inst. and Meth. **460**, 239 (2001).

[27] D. G. Crabb and W. Meyer, Ann. Rev. Nucl. Part. Sci. **47**, 67 (1997).

[28] C.D Keith et al. **501**, 327 (2003).

[29] S. Jawalkar and P. Bosted, *Ntuple 22*, CLAS Technical Note, Jefferson Lab url: https://clasweb.jlab.org/rungroups/eg1-dvcs/wiki/index.php/TechnicalNotes (2010).

[30] P. Bosted, N. Kvaltine and Y. Prok, *Inclusive Polarized Structure Functions from the Eg1-Dvcs Experiment*, CLAS Analysis Note, Jefferson Lab, (2014).

[31] B. Zhao, *Drift Chamber Alignment*, CLAS Technical Note, Jefferson Lab url: https://clasweb.jlab.org/rungroups/eg1-dvcs/wiki/index.php/TechnicalNotes (2010).

[32] P. Bosted and A. Kim, *Beam Position (x,y) and Target Center (z) from Raster ADCs*, CLAS Technical Note, Jefferson Lab url: https://clasweb.jlab.org/rungroups/eg1-dvcs/wiki/index.php/TechnicalNotes (2010).

[33] P. Bosted, *Tracking from Drift Chambers to Target Solenoid*, CLAS Technical Note, Jefferson Lab url: https://clasweb.jlab.org/rungroups/eg1-dvcs/wiki/index.php/TechnicalNotes (2010).

[34] P. Bosted, *Photon Energy Corrections*, CLAS Technical Note, Jefferson Lab url: https://clasweb.jlab.org/rungroups/eg1-dvcs/wiki/index.php/TechnicalNotes (2011)

[35] Y. Prok, *Checking for beam scraping on target edges using raster ADCs*, CLAS Technical Note, Jefferson Lab url: https://clasweb.jlab.org/rungroups/eg1-dvcs/wiki/index.php/TechnicalNotes (2010)

[36] P. Bosted, *New way of doing Cherenkov mirror matching*, CLAS Technical Note, Jefferson Lab url: https://clasweb.jlab.org/rungroups/eg1-dvcs/wiki/index.php/TechnicalNotes (2010).

[37] P. Bosted, *Fiducial Cuts based on IC Shielding*, CLAS Technical Note, Jefferson Lab url: https://clasweb.jlab.org/rungroups/eg1-dvcs/wiki/index.php/TechnicalNotes (2011).

[38] E. Seder, *PbPt analysis on Parts A and B*, CLAS Technical Note, Jefferson Lab url: https://clasweb.jlab.org/rungroups/eg1-dvcs/wiki/index.php/TechnicalNotes (2011).

[39] N. Guler,*Spin Structure of the Deuteron*, CLAS Technical Note, Jefferson Lab url: https://clasweb.jlab.org/rungroups/eg1-dvcs/wiki/index.php/TechnicalNotes (2009).

[40] A. Kim,*Single and Double Spin Asymmetries for Deeply Virtual Exclusive Pizero Production on Longitudinally Polarized Proton Target with CLAS* (2014).

[41] T.W Donnelly and A.S Raskin, Annals of Phys. **169**, 247 (1986).

[42] T. Mineeva, *Hadronization Studies via neutral pion Electroproduction off D, C, Fe, and Pb*, (Ph.D. Thesis, University of Connecticutt, 2013)

[43] P. Bosted, *Dilution Factor for SIDIS*, CLAS Technical Note, Jefferson Lab url: https://clasweb.jlab.org/rungroups/eg1-dvcs/wiki/index.php/TechnicalNotes (2010).

[44] S. Jawalkar and P. Bosted, *Determination of the Banjo and Ammonia Lengths from Event Rates*, CLAS Technical Note, Jefferson Lab url: https://clasweb.jlab.org/rungroups/eg1-dvcs/wiki/index.php/TechnicalNotes (2010).

[45] H. Mkrtchyan and P.E. Bosted, Phys. Lett. B **665**, 20 (2008).

[46] R.G. Roberts, W.J. Stirling, A.D. Martin and R.S. Thorneuman, *MRST 2004-QED Parton Distributions*, url = "http://wwwold.jlab.org/Hall-B/secure/eg1-dvcs/skoirala/PdfV0/PdfV0.f (2012).

[47] H. Hakobyan, *Observation of Quark Propagation Pattern in Nuclear Medium* (Ph.D. Thesis, Yerevan State University, 2008).

[48] S. Kuhn, *How to calculate single target- and double-spin asymmetries in SIDIS*, CLAS Technical Note, Jefferson Lab url: https://clasweb.jlab.org/rungroups/eg1-dvcs/wiki/index.php/TechnicalNotes (2011).

[49] P. Bosted, *SIDIS Radiative Corrections*, CLAS Technical Note, Jefferson Lab url: https://clasweb.jlab.org/rungroups/eg1-dvcs/wiki/index.php/TechnicalNotes (2012).

[50] W. Gohn, *Probing the Proton's Quark Dynamics in Semi-inclusive Pion Electroproduction*, (Ph.D. Thesis, University of Connecticut, 2012).

[51] M. Osipenko et al. Phys. Rev. D. **80**, (2009).

[52] M. Aghasyan et al. Phys.Lett. **B704**, 397 (2011).

[53] W. Mao and Z. Lu, *Private Communication*, (2014).

[54] W. Mao and Z. Lu", Phys.Rev. **D87**, 014012 (2013).

APPENDIX A

RESULTS

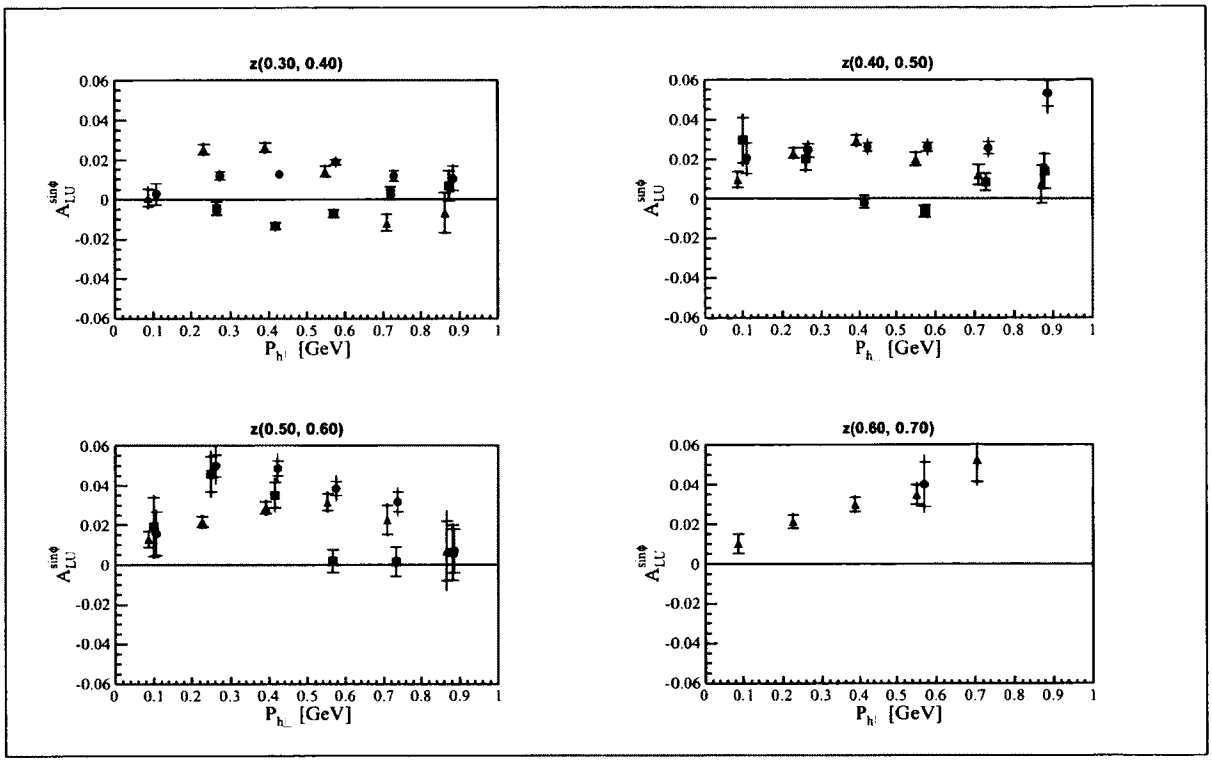

FIG. 121: $A_{LU}^{\sin\phi_h}(z, P_{h\perp})$ on the proton, red: π^+, blue: π^-, green: π^0

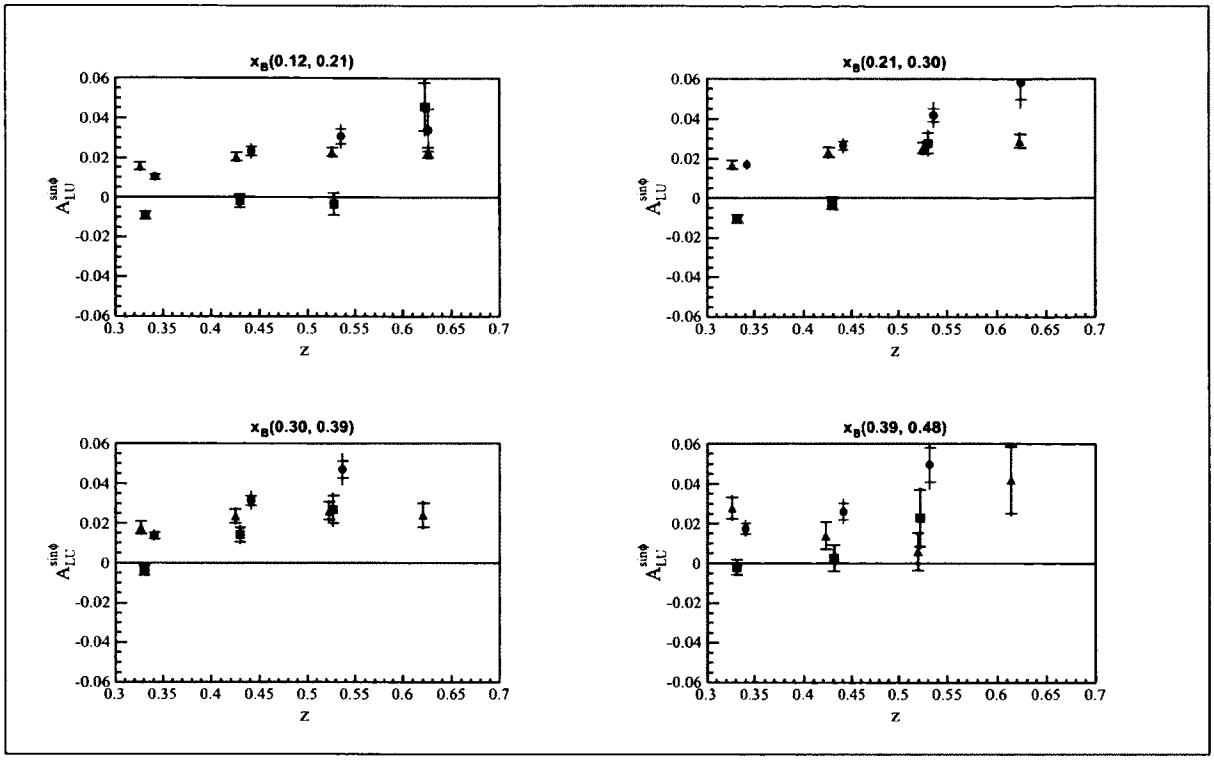

FIG. 122: $A_{LU}^{\sin\phi_h}(x_B, z)$ on the proton, red: π^+, blue: π^-, green: π^0

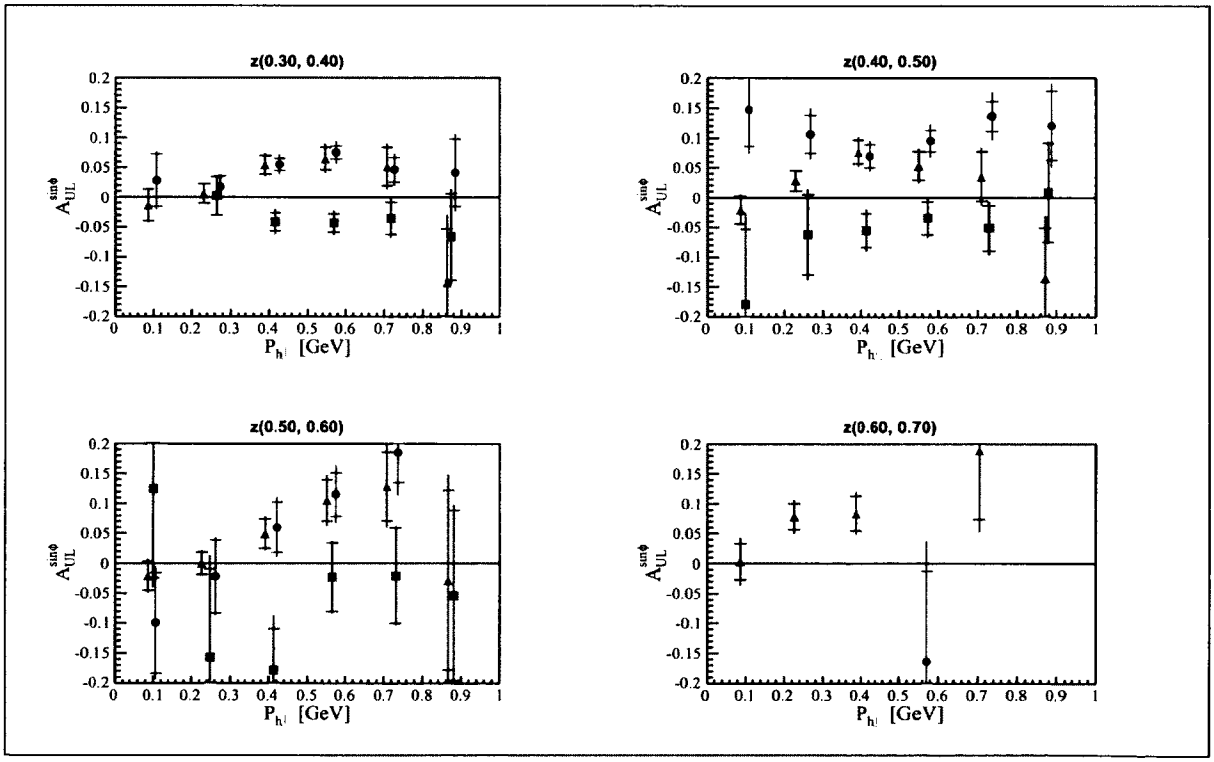

FIG. 123: $A_{UL}^{\sin\phi_h}(z, P_{h\perp})$ on the proton, red: π^+, blue: π^-, green: π^0

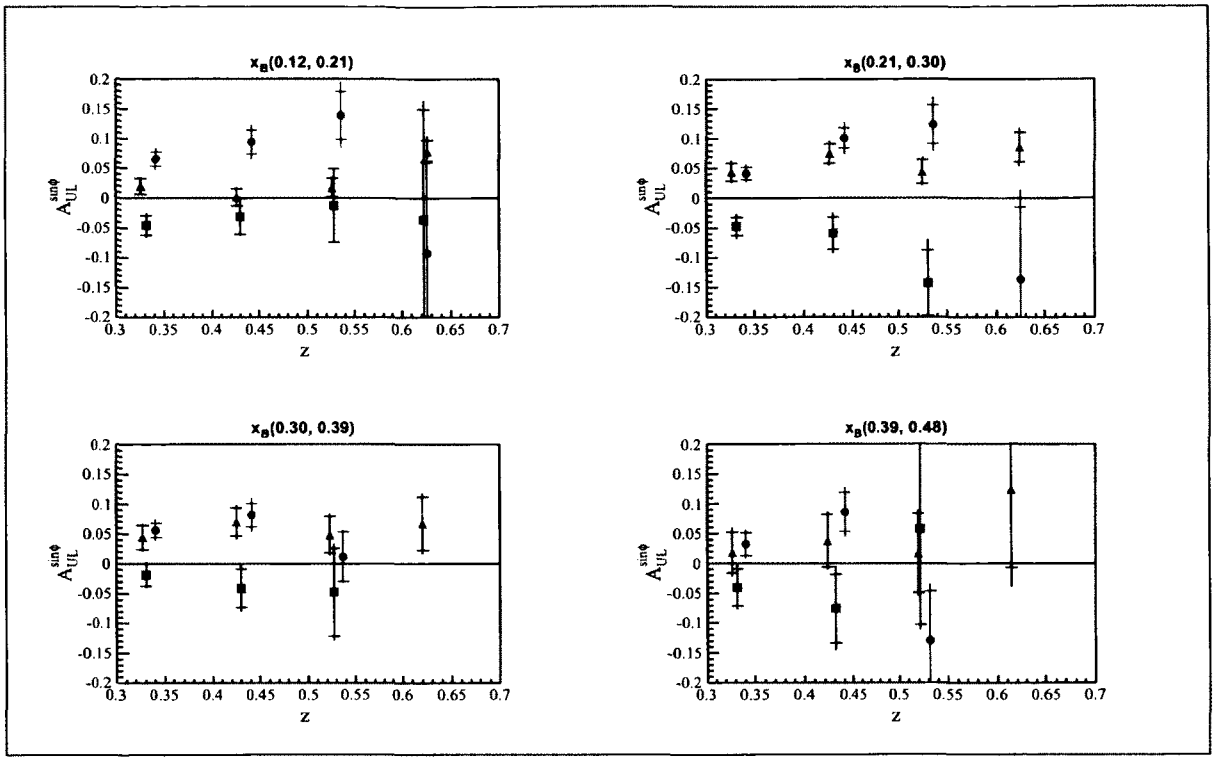

FIG. 124: $A_{UL}^{\sin\phi_h}(x_B, z)$ on the proton, red: π^+, blue: π^-, green: π^0

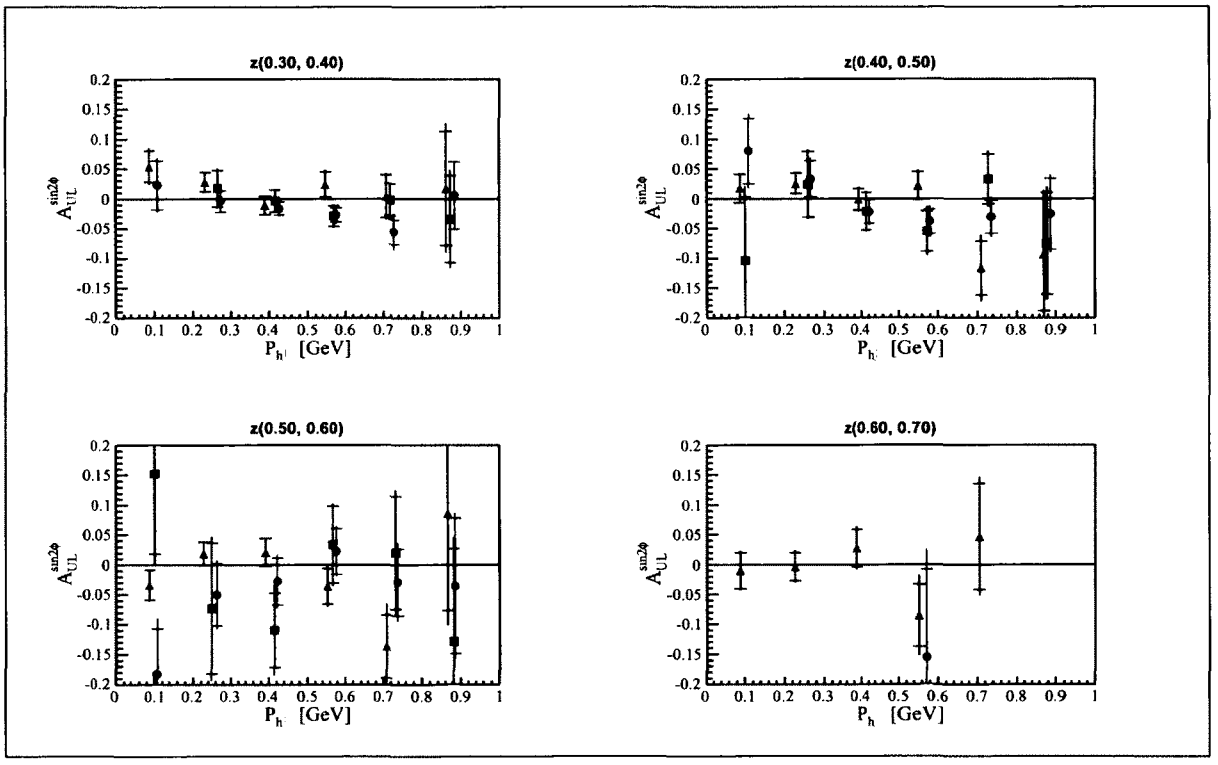

FIG. 125: $A_{UL}^{\sin 2\phi_h}(z, P_{h\perp})$ on the proton, red: π^+, blue: π^-, green: π^0

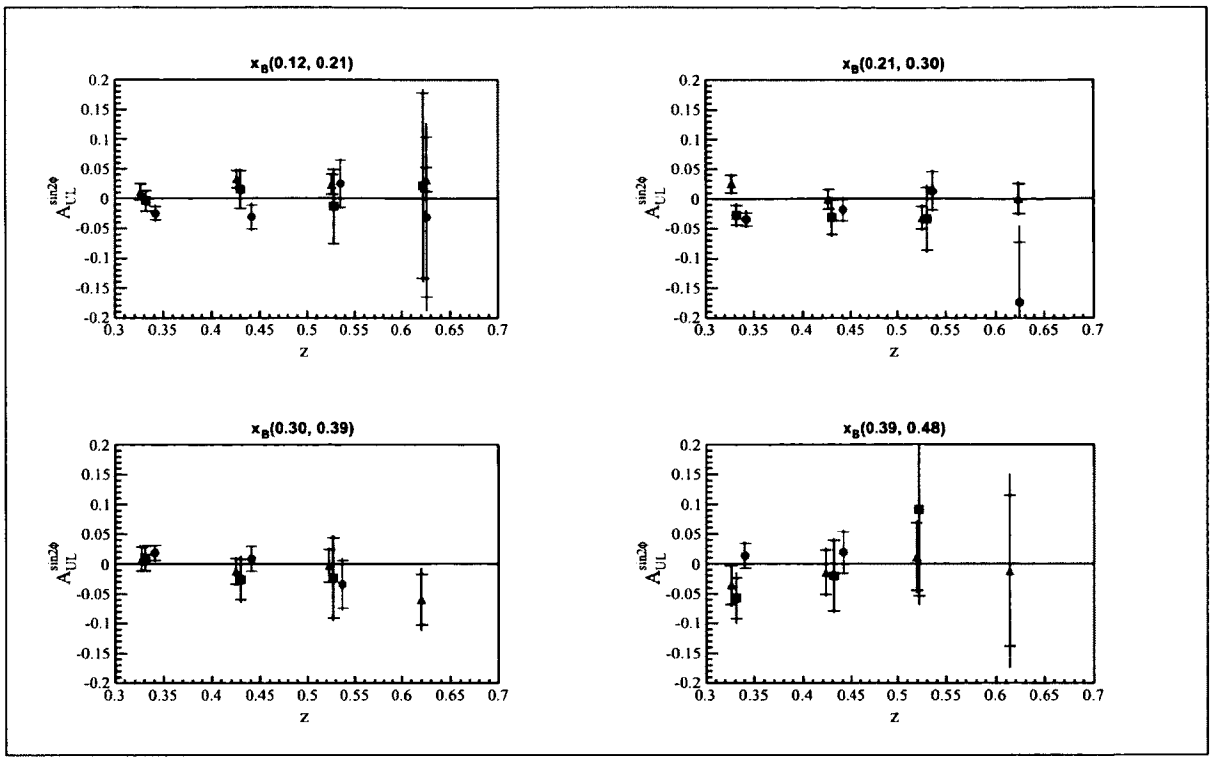

FIG. 126: $A_{UL}^{\sin 2\phi_h}(x_B, z)$ on the proton, red: π^+, blue: π^-, green: π^0

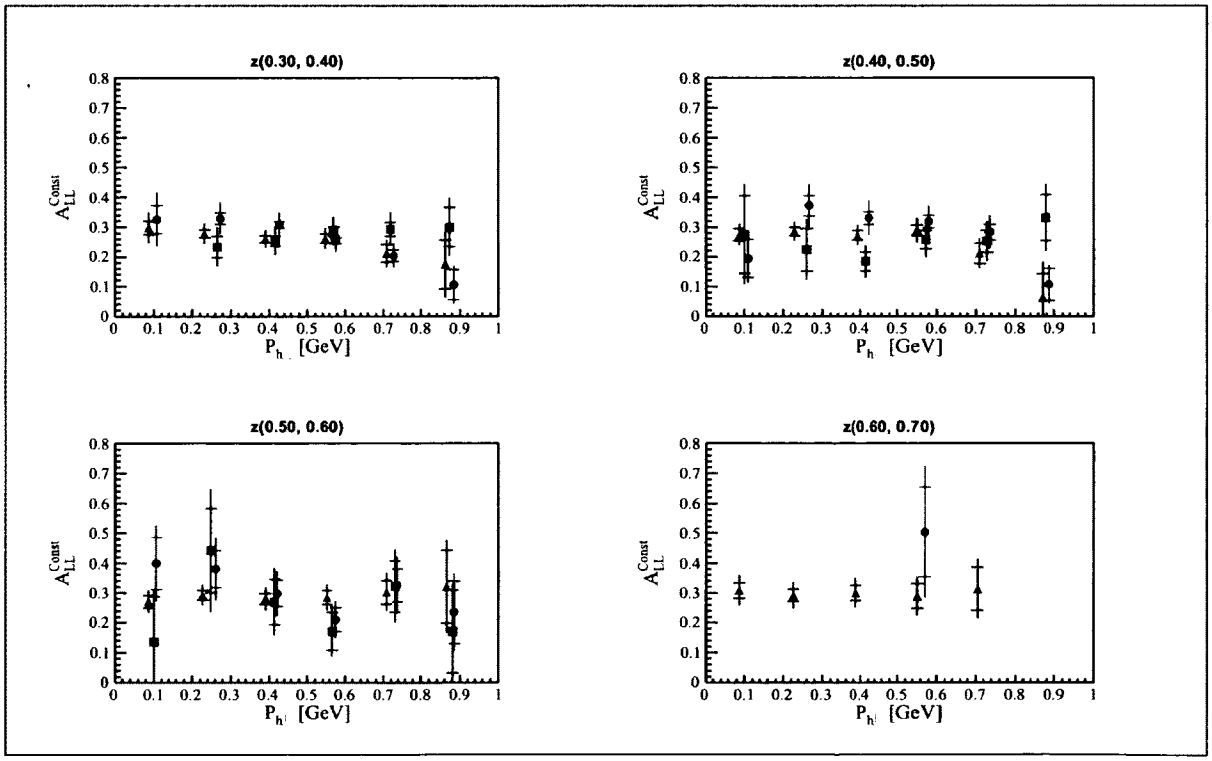

FIG. 127: $A_{LL}^{\text{Const}}(z, P_{h\perp})$ on the proton, red: π^+, blue: π^-, green: π^0

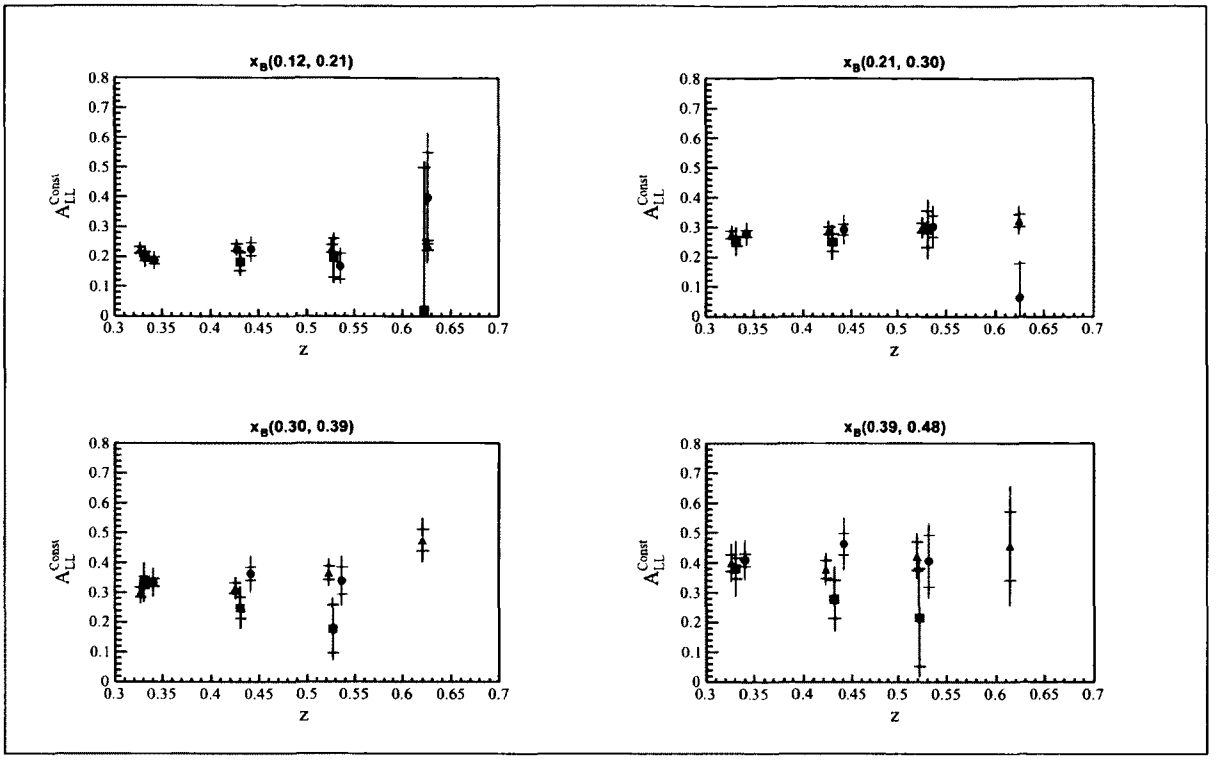

FIG. 128: $A_{LL}^{\text{Const}}(x_B, z)$ on the proton, red: π^+, blue: π^-, green: π^0

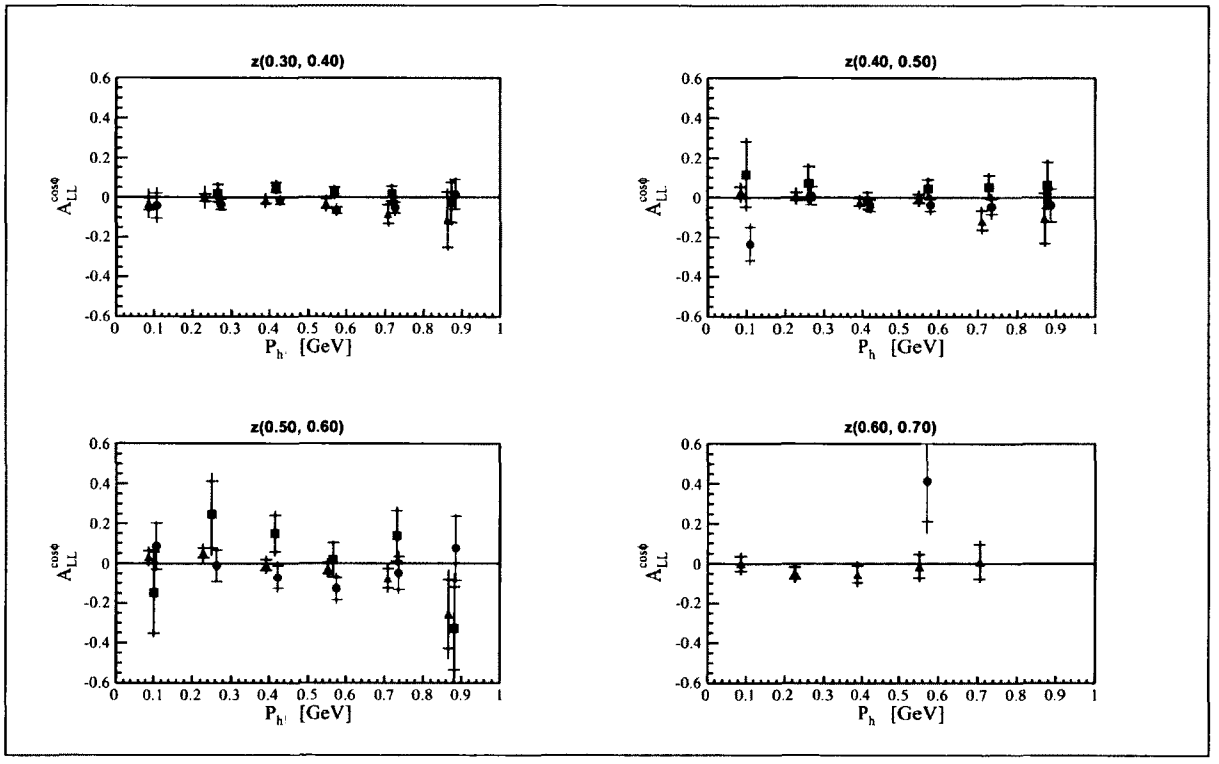

FIG. 129: $A_{LL}^{\cos\phi_h}(z, P_{h\perp})$ on the proton, red: π^+, blue: π^-, green: π^0

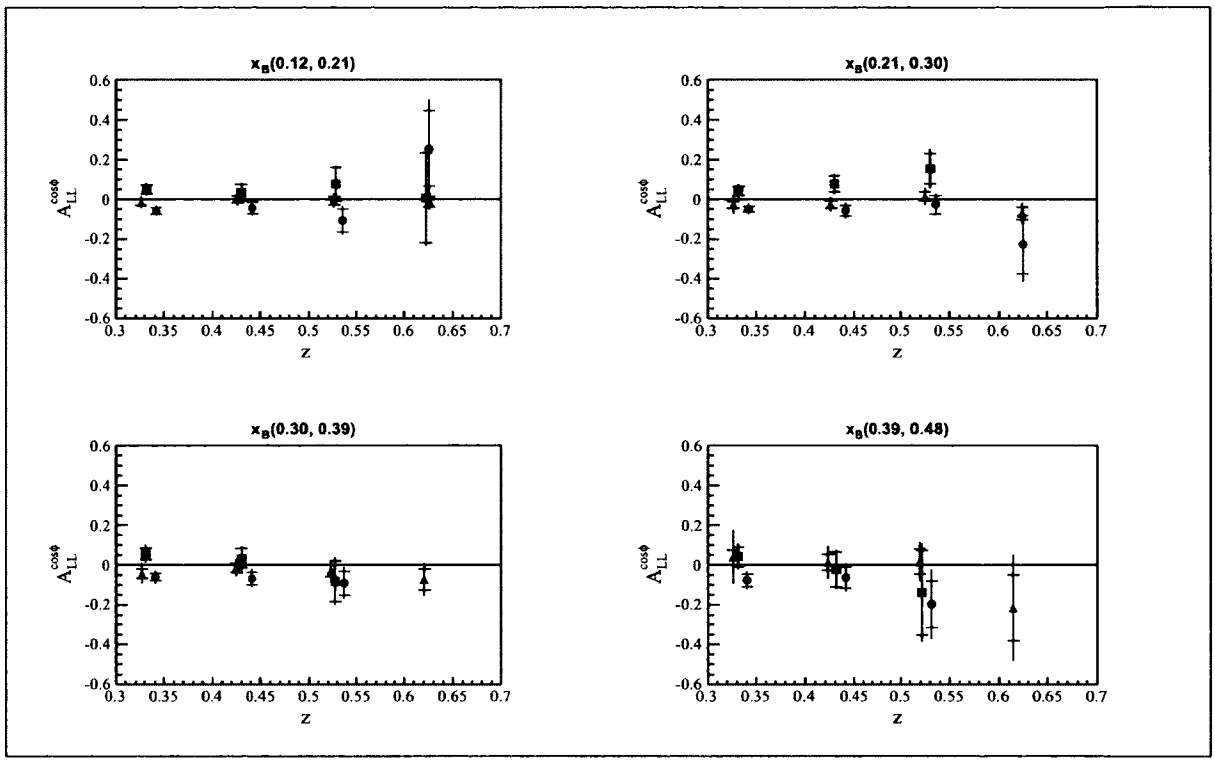

FIG. 130: $A_{LL}^{\cos\phi_h}(x_B, z)$ on the proton, red: π^+, blue: π^-, green: π^0

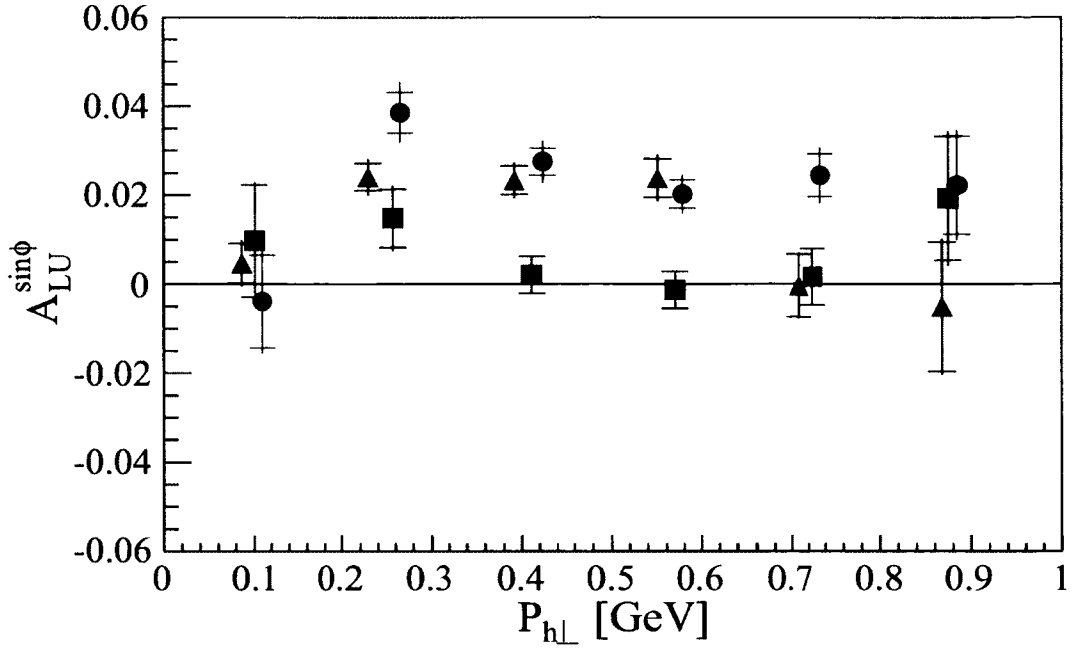

FIG. 131: $A_{LU}^{\sin\phi_h}(P_{h\perp})$ on the deuteron, red: π^+, blue: π^-, green: π^0

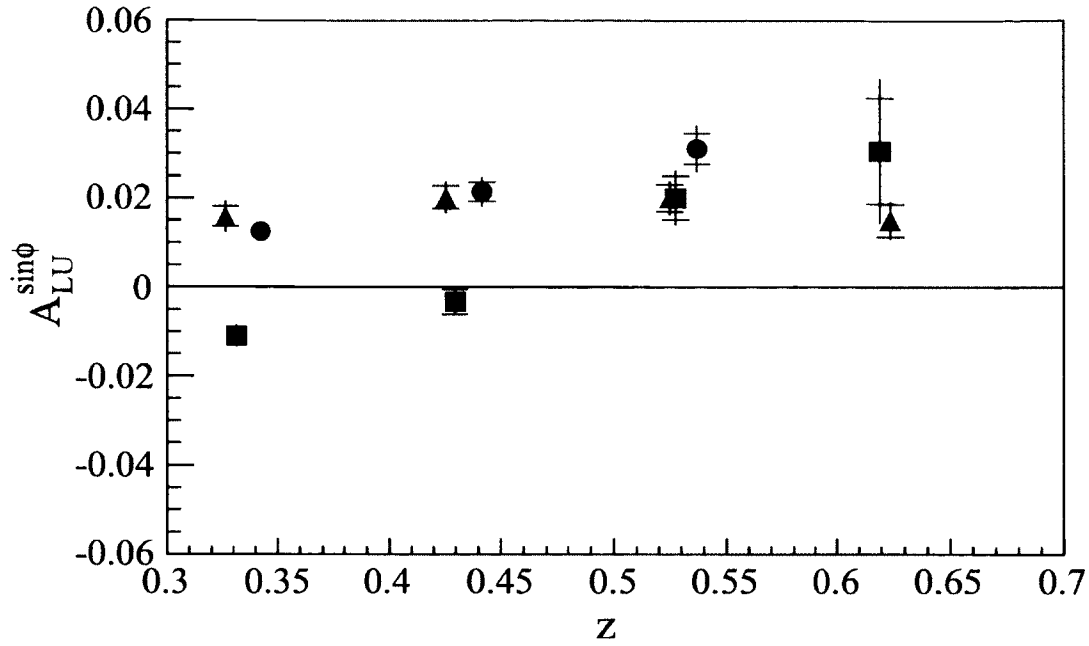

FIG. 132: $A_{LU}^{\sin\phi_h}(z)$ on the deuteron, red: π^+, blue: π^-, green: π^0

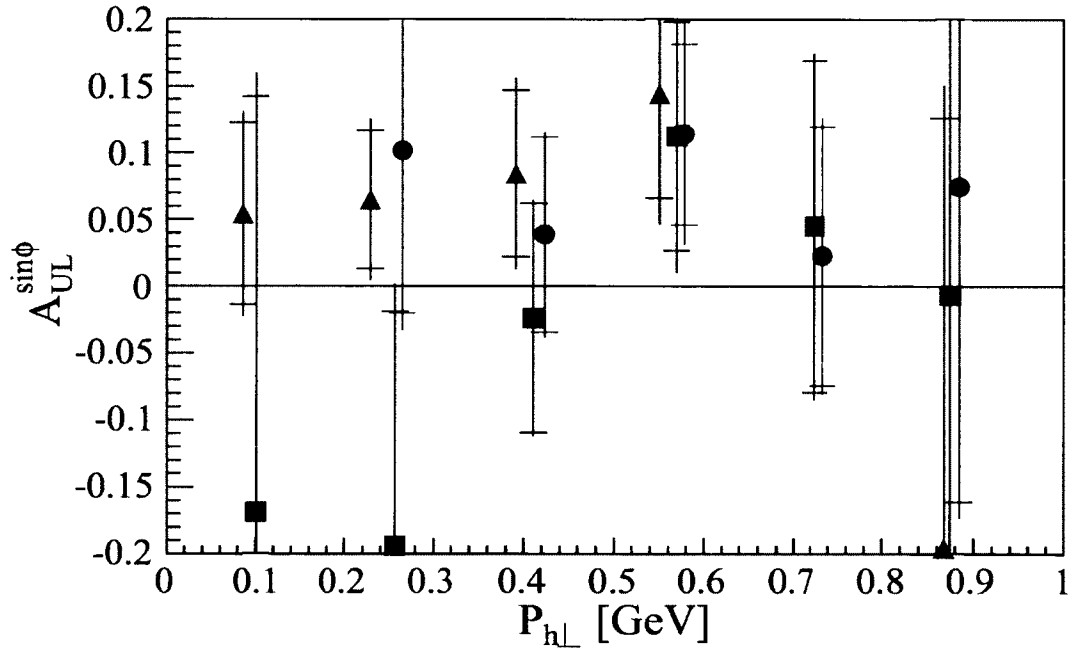

FIG. 133: $A_{UL}^{\sin\phi_h}(P_{h\perp})$ on the deuteron, red: π^+, blue: π^-, green: π^0

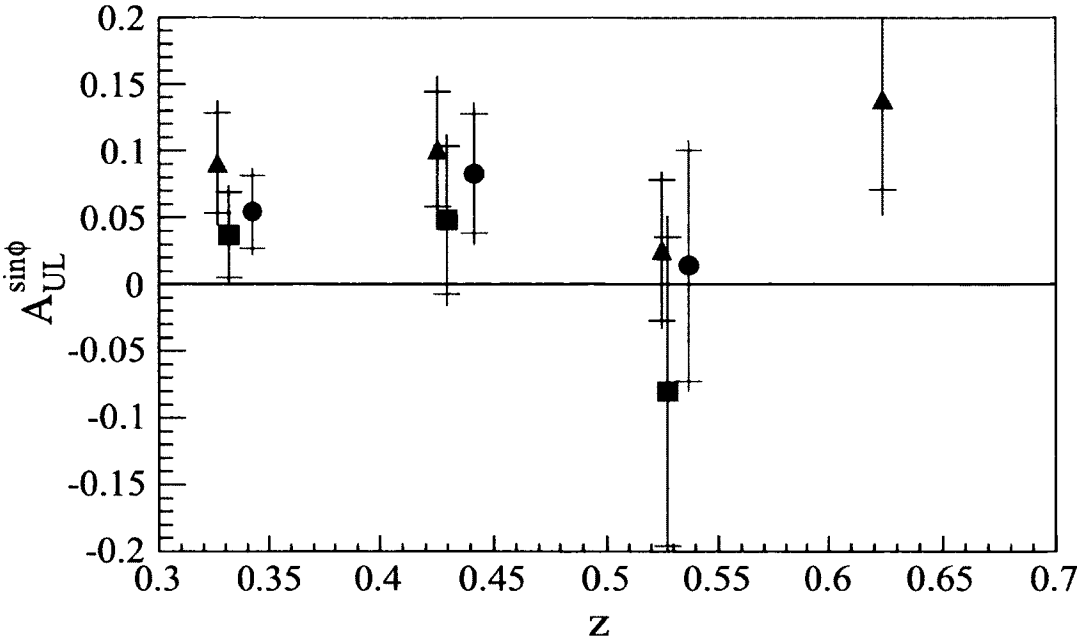

FIG. 134: $A_{UL}^{\sin\phi_h}(z)$ on the deuteron, red: π^+, blue: π^-, green: π^0

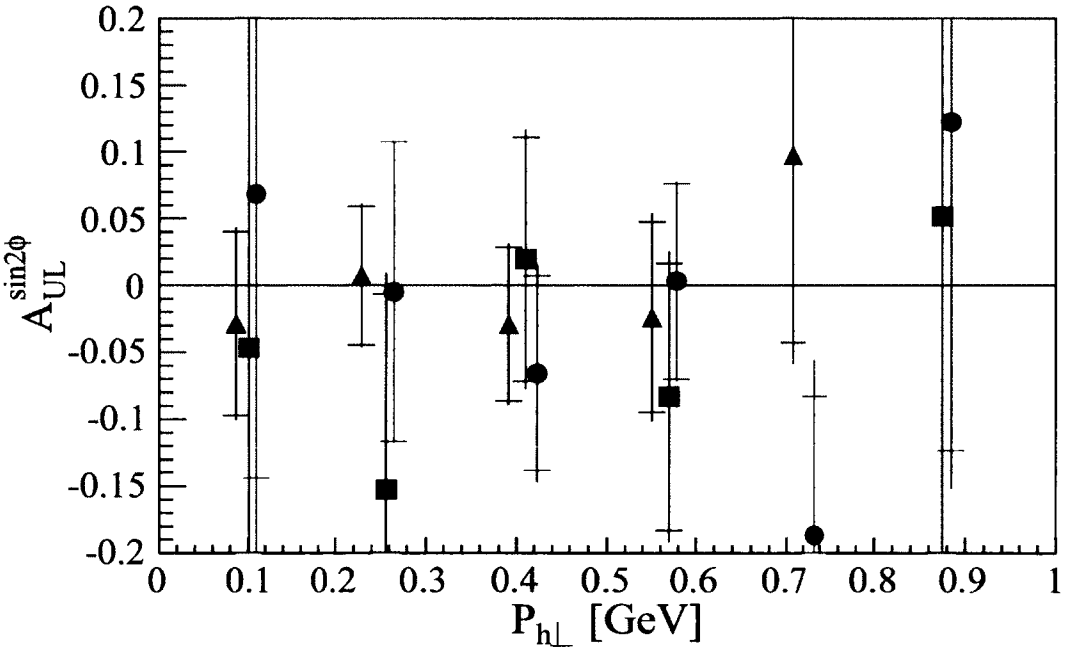

FIG. 135: $A_{UL}^{\sin 2\phi_h}(P_{h\perp})$ on the deuteron, red: π^+, blue: π^-, green: π^0

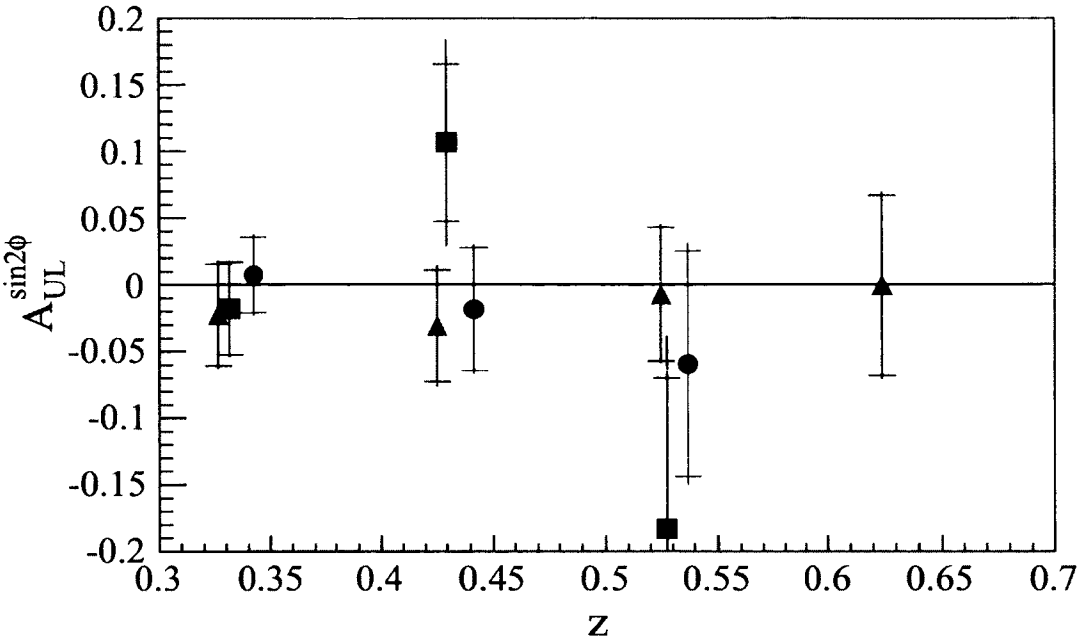

FIG. 136: $A_{UL}^{\sin 2\phi_h}(z)$ on the deuteron, red: π^+, blue: π^-, green: π^0

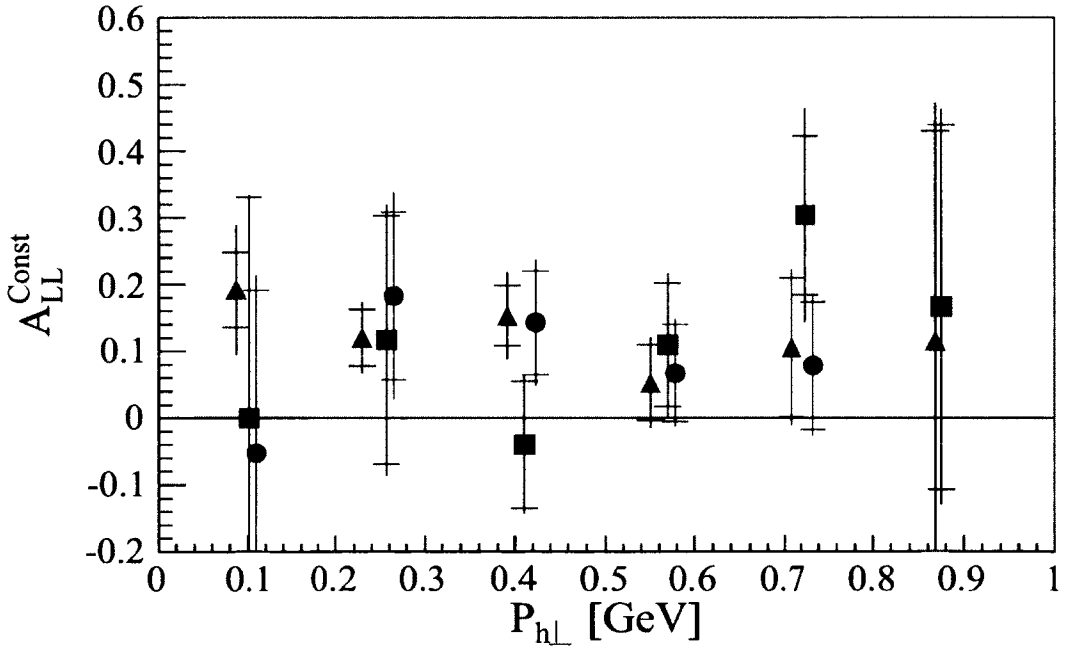

FIG. 137: $A_{LL}^{\text{Const}}(P_{h\perp})$ on the deuteron, red: π^+, blue: π^-, green: π^0

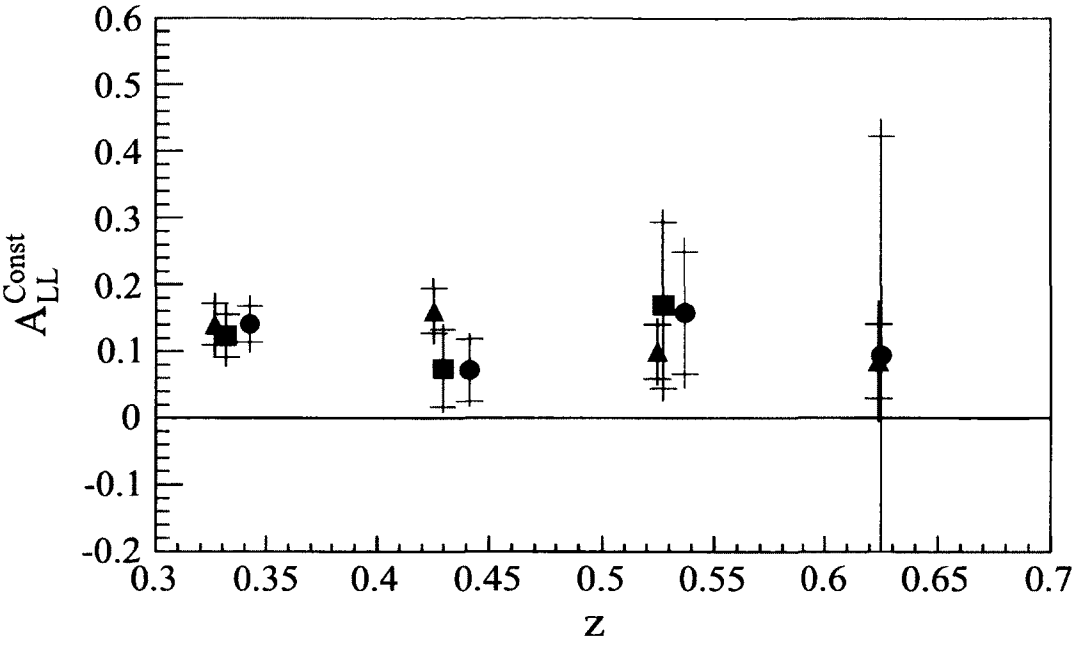

FIG. 138: $A_{LL}^{\text{Const}}(z)$ on the deuteron, red: π^+, blue: π^-, green: π^0

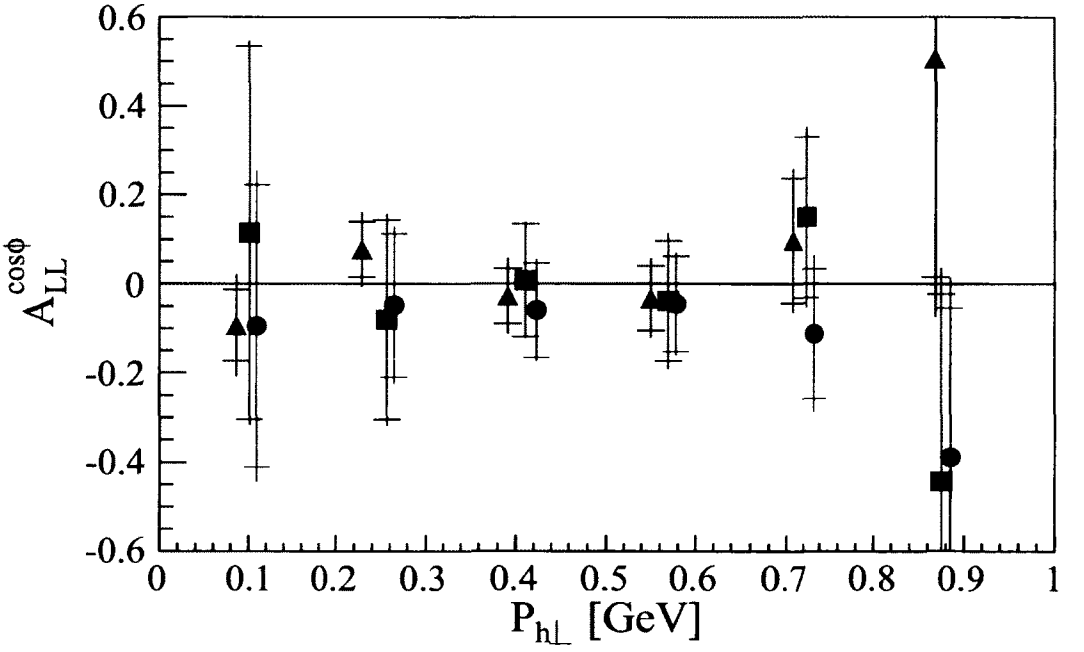

FIG. 139: $A_{LL}^{\cos\phi_h}(P_{h\perp})$ on the deuteron, red: π^+, blue: π^-, green: π^0

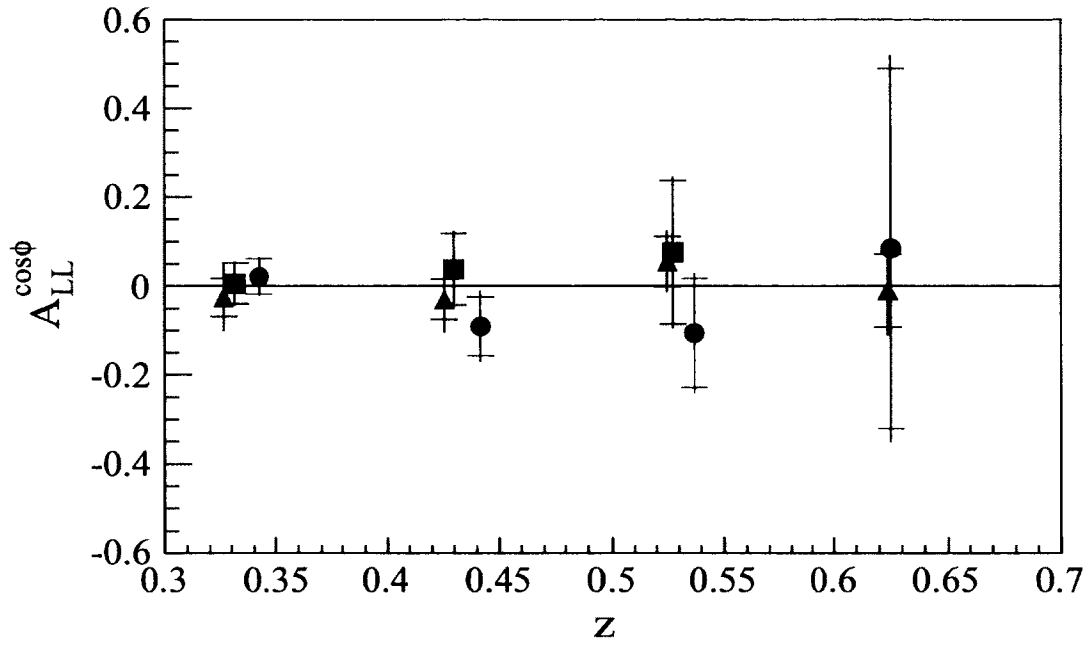

FIG. 140: $A_{LL}^{\cos\phi_h}(z)$ on the deuteron, red: π^+, blue: π^-, green: π^0

APPENDIX B

TABULATED RESULTS

TABLE 9: $A_{LU}^{\sin\phi_h}(x_B, P_{h\perp})$ on the proton for π^+

x_B	$\overline{x_B}$	$P_{h\perp}$	$\overline{P_{h\perp}}$	$\overline{Q^2}$	$\overline{z}$	$\overline{M_x}$	$\overline{y}$	$\overline{\epsilon}$	$\overline{D'}$	$\overline{f_D}$	$A_{LU}^{\sin\phi_h}$	$\sigma_{A_{LU}^{\sin\phi_h}}^{Stat}$	$\sigma_{A_{LU}^{\sin\phi_h}}^{Syst}$			
0	0.18	2	0.43	1.33	0.47	1.91	0.67	0.56	0.75	0.1787	0.0255	0.0042	0.0019	0.0000	0.0000	0.0000
0	0.17	3	0.59	1.34	0.47	1.86	0.70	0.51	0.79	0.1692	0.0229	0.0030	0.0017	0.0000	0.0000	0.0000
0	0.17	4	0.74	1.36	0.47	1.78	0.73	0.46	0.82	0.1578	0.0226	0.0035	0.0016	0.0000	0.0000	0.0000
0	0.16	5	0.89	1.37	0.47	1.67	0.77	0.41	0.85	0.1446	0.0426	0.0064	0.0029	0.0000	0.0000	0.0000
1	0.26	1	0.27	1.67	0.48	1.75	0.57	0.68	0.67	0.2001	0.0287	0.0050	0.0022	0.0000	0.0000	0.0000
1	0.26	2	0.43	1.74	0.47	1.74	0.61	0.63	0.71	0.1927	0.0331	0.0030	0.0024	0.0000	0.0000	0.0000
1	0.25	3	0.58	1.82	0.47	1.70	0.65	0.57	0.75	0.1830	0.0314	0.0029	0.0022	0.0000	0.0000	0.0000
1	0.25	4	0.73	1.95	0.46	1.66	0.71	0.48	0.82	0.1706	0.0365	0.0045	0.0025	0.0000	0.0000	0.0000
1	0.24	5	0.88	2.10	0.46	1.59	0.78	0.37	0.89	0.1571	0.0396	0.0123	0.0027	0.0000	0.0000	0.0000
2	0.35	0	0.10	1.96	0.49	1.64	0.51	0.75	0.62	0.2159	0.0178	0.0087	0.0013	0.0000	0.0000	0.0000
2	0.34	1	0.26	2.12	0.48	1.66	0.56	0.69	0.67	0.2117	0.0366	0.0044	0.0028	0.0000	0.0000	0.0000
2	0.34	2	0.42	2.22	0.46	1.64	0.59	0.65	0.71	0.2039	0.0386	0.0034	0.0028	0.0000	0.0000	0.0000
2	0.34	3	0.57	2.47	0.46	1.63	0.66	0.55	0.79	0.1940	0.0403	0.0044	0.0028	0.0000	0.0000	0.0000
2	0.33	4	0.72	2.76	0.45	1.60	0.75	0.41	0.88	0.1815	0.0213	0.0093	0.0015	0.0000	0.0000	0.0000
3	0.42	0	0.11	2.60	0.47	1.61	0.55	0.69	0.69	0.2248	0.0184	0.0122	0.0013	0.0000	0.0000	0.0000
3	0.42	1	0.26	2.77	0.47	1.61	0.58	0.64	0.73	0.2206	0.0283	0.0066	0.0021	0.0000	0.0000	0.0000
3	0.42	2	0.41	2.98	0.46	1.60	0.63	0.57	0.79	0.2133	0.0340	0.0061	0.0024	0.0000	0.0000	0.0000
3	0.42	3	0.56	3.27	0.45	1.58	0.71	0.47	0.86	0.2034	0.0383	0.0103	0.0029	0.0000	0.0000	0.0000

TABLE 10: $A_{LU}^{\sin\phi_h}(x_B, P_{h\perp})$ on the proton for π^-

x_B	$\overline{x_B}$	$P_{h\perp}$	$\overline{P_{h\perp}}$	$\overline{Q^2}$	$\overline{z}$	$\overline{M_x}$	$\overline{y}$	$\overline{\epsilon}$	$\overline{D'}$	$\overline{f_D}$	$A_{LU}^{\sin\phi_h}$	$\sigma^{Stat}_{A_{LU}^{\sin\phi_h}}$	$\sigma^{Syst}_{A_{LU}^{\sin\phi_h}}$			
0	0.18	2	0.44	1.33	0.47	1.91	0.67	0.56	0.75	0.1623	-0.0017	0.0066	0.0003	0.0000	0.0000	0.0000
0	0.17	3	0.59	1.34	0.47	1.87	0.71	0.51	0.79	0.1534	-0.0110	0.0044	0.0007	0.0000	0.0000	0.0000
0	0.17	4	0.74	1.36	0.48	1.77	0.74	0.46	0.82	0.1432	0.0079	0.0049	0.0005	0.0000	0.0000	0.0000
0	0.16	5	0.89	1.38	0.48	1.67	0.77	0.40	0.86	0.1308	0.0210	0.0083	0.0013	0.0000	0.0000	0.0000
1	0.26	1	0.28	1.66	0.48	1.75	0.57	0.69	0.66	0.1757	0.0439	0.0085	0.0033	0.0000	0.0000	0.0000
1	0.26	2	0.42	1.76	0.48	1.75	0.62	0.62	0.72	0.1698	0.0089	0.0045	0.0006	0.0000	0.0000	0.0000
1	0.25	3	0.58	1.82	0.47	1.70	0.65	0.57	0.75	0.1606	-0.0016	0.0042	0.0002	0.0000	0.0000	0.0000
1	0.25	4	0.73	1.96	0.47	1.65	0.72	0.48	0.82	0.1501	0.0044	0.0064	0.0005	0.0000	0.0000	0.0000
1	0.24	5	0.88	2.10	0.46	1.59	0.79	0.37	0.89	0.1380	-0.0063	0.0165	0.0007	0.0000	0.0000	0.0000
2	0.35	0	0.11	1.98	0.49	1.63	0.51	0.74	0.63	0.1866	0.0378	0.0125	0.0023	0.0000	0.0000	0.0000
2	0.34	1	0.26	2.10	0.47	1.66	0.55	0.69	0.67	0.1831	0.0382	0.0074	0.0025	0.0000	0.0000	0.0000
2	0.34	2	0.42	2.28	0.47	1.66	0.60	0.62	0.73	0.1770	0.0110	0.0053	0.0007	0.0000	0.0000	0.0000
2	0.34	3	0.57	2.47	0.46	1.62	0.66	0.55	0.79	0.1679	0.0091	0.0064	0.0006	0.0000	0.0000	0.0000
2	0.33	4	0.72	2.76	0.45	1.60	0.75	0.41	0.88	0.1569	0.0163	0.0133	0.0009	0.0000	0.0000	0.0000
3	0.42	0	0.11	2.61	0.48	1.61	0.55	0.69	0.69	0.1920	0.0194	0.0175	0.0015	0.0000	0.0000	0.0000
3	0.42	1	0.26	2.74	0.46	1.61	0.58	0.65	0.73	0.1886	0.0117	0.0109	0.0007	0.0000	0.0000	0.0000
3	0.42	2	0.41	2.96	0.45	1.60	0.63	0.58	0.78	0.1825	0.0061	0.0095	0.0004	0.0000	0.0000	0.0000
3	0.42	3	0.56	3.26	0.45	1.58	0.70	0.47	0.86	0.1739	-0.0176	0.0150	0.0010	0.0000	0.0000	0.0000

TABLE 11: $A_{LU}^{\sin\phi_h}(x_B, P_{h\perp})$ on the proton for π^0

x_B	$\overline{x_B}$	$P_{h\perp}$	$\overline{P_{h\perp}}$	$\overline{Q^2}$	$\overline{z}$	$\overline{M_x}$	$\overline{y}$	$\overline{\epsilon}$	$\overline{D'}$	$\overline{f_D}$	$A_{LU}^{\sin\phi_h}$	$\sigma^{Stat}_{A_{LU}^{\sin\phi_h}}$	$\sigma^{Syst}_{A_{LU}^{\sin\phi_h}}$			
0	0.17	0	0.11	1.39	0.53	2.01	0.75	0.44	0.83	0.1846	0.0099	0.0036	0.0005	0.0000	0.0000	0.0000
0	0.17	1	0.25	1.38	0.53	2.00	0.75	0.43	0.84	0.1814	0.0188	0.0023	0.0006	0.0000	0.0000	0.0000
0	0.16	2	0.41	1.38	0.52	1.95	0.76	0.42	0.84	0.1749	0.0281	0.0024	0.0011	0.0000	0.0000	0.0000
0	0.17	3	0.57	1.38	0.52	1.85	0.75	0.44	0.83	0.1657	0.0292	0.0034	0.0008	0.0000	0.0000	0.0000
0	0.17	4	0.73	1.39	0.52	1.74	0.75	0.43	0.84	0.1543	0.0199	0.0052	0.0004	0.0000	0.0000	0.0000
0	0.16	5	0.89	1.39	0.49	1.65	0.78	0.39	0.87	0.1399	0.0037	0.0089	0.0005	0.0000	0.0000	0.0000
1	0.25	0	0.11	1.99	0.53	1.89	0.72	0.47	0.82	0.1964	0.0153	0.0041	0.0004	0.0000	0.0000	0.0000
1	0.25	1	0.25	1.96	0.53	1.85	0.70	0.49	0.81	0.1931	0.0268	0.0029	0.0009	0.0000	0.0000	0.0000
1	0.25	2	0.41	1.92	0.51	1.80	0.69	0.51	0.79	0.1856	0.0289	0.0030	0.0011	0.0000	0.0000	0.0000
1	0.25	3	0.57	1.94	0.50	1.72	0.70	0.50	0.80	0.1759	0.0255	0.0040	0.0007	0.0000	0.0000	0.0000
1	0.25	4	0.73	2.02	0.50	1.65	0.74	0.44	0.85	0.1644	0.0194	0.0068	0.0004	0.0000	0.0000	0.0000
1	0.24	5	0.88	2.10	0.46	1.59	0.79	0.37	0.89	0.1493	0.0240	0.0180	0.0013	0.0000	0.0000	0.0000
2	0.34	0	0.11	2.62	0.53	1.78	0.70	0.48	0.83	0.2064	0.0029	0.0062	0.0002	0.0000	0.0000	0.0000
2	0.34	1	0.25	2.52	0.52	1.73	0.67	0.53	0.80	0.2026	0.0260	0.0043	0.0012	0.0000	0.0000	0.0000
2	0.34	2	0.41	2.47	0.49	1.68	0.66	0.55	0.79	0.1949	0.0327	0.0045	0.0014	0.0000	0.0000	0.0000
2	0.34	3	0.57	2.61	0.48	1.64	0.70	0.49	0.83	0.1850	0.0249	0.0064	0.0005	0.0000	0.0000	0.0000
2	0.33	4	0.72	2.80	0.48	1.59	0.76	0.39	0.89	0.1732	0.0215	0.0145	0.0009	0.0000	0.0000	0.0000
3	0.42	0	0.11	3.17	0.51	1.69	0.68	0.50	0.83	0.2138	0.0098	0.0124	0.0014	0.0000	0.0000	0.0000
3	0.42	1	0.25	3.06	0.50	1.65	0.65	0.54	0.81	0.2097	0.0077	0.0085	0.0007	0.0000	0.0000	0.0000
3	0.42	2	0.41	3.09	0.47	1.61	0.66	0.54	0.81	0.2020	0.0271	0.0091	0.0011	0.0000	0.0000	0.0000
3	0.42	3	0.56	3.30	0.46	1.59	0.71	0.46	0.87	0.1921	-0.0005	0.0159	0.0012	0.0000	0.0000	0.0000

TABLE 12: $A_{UL}^{\sin\phi_h}(x_B, P_{h\perp})$ and $A_{UL}^{\sin 2\phi_h}(x_B, P_{h\perp})$ on the proton for π^+

x_B	$\overline{x_B}$	$P_{h\perp}$	$\overline{P_{h\perp}}$	$\overline{Q^2}$	$\overline{z}$	$\overline{M_x}$	$\overline{y}$	$\overline{\epsilon}$	$\overline{D'}$	$\overline{f_D}$	$A_{UL}^{\sin\phi_h}$	$\sigma^{Stat}_{A_{UL}^{\sin\phi_h}}$	$\sigma^{Syst}_{A_{UL}^{\sin\phi_h}}$	$A_{UL}^{\sin 2\phi_h}$	$\sigma^{Stat}_{A_{UL}^{\sin 2\phi_h}}$	$\sigma^{Syst}_{A_{UL}^{\sin 2\phi_h}}$
0	0.18	2	0.43	1.33	0.47	1.91	0.67	0.56	0.75	0.1787	0.0124	0.0546	0.0052	-0.0396	0.0482	0.0056
0	0.17	3	0.59	1.34	0.47	1.86	0.70	0.51	0.79	0.1692	0.0900	0.0292	0.0087	-0.0475	0.0306	0.0074
0	0.17	4	0.74	1.36	0.47	1.78	0.73	0.46	0.82	0.1578	0.1454	0.0300	0.0148	-0.0365	0.0325	0.0075
0	0.16	5	0.89	1.37	0.47	1.67	0.77	0.41	0.85	0.1446	0.1284	0.0585	0.0138	-0.0424	0.0615	0.0123
1	0.26	1	0.27	1.67	0.48	1.75	0.57	0.68	0.67	0.2001	0.0281	0.0590	0.0031	-0.0534	0.0513	0.0072
1	0.26	2	0.43	1.74	0.47	1.74	0.61	0.63	0.71	0.1927	0.1016	0.0276	0.0097	-0.0259	0.0278	0.0060
1	0.25	3	0.58	1.82	0.47	1.70	0.65	0.57	0.75	0.1830	0.0716	0.0240	0.0074	-0.0189	0.0268	0.0038
1	0.25	4	0.73	1.95	0.46	1.66	0.71	0.48	0.82	0.1706	0.1957	0.0377	0.0210	-0.0275	0.0417	0.0120
1	0.24	5	0.88	2.10	0.46	1.59	0.78	0.37	0.89	0.1571	0.1648	0.1034	0.0172	-0.0551	0.1076	0.0080
2	0.35	0	0.10	1.96	0.49	1.64	0.51	0.75	0.62	0.2159	0.0262	0.0623	0.0028	0.0053	0.0575	0.0007
2	0.34	1	0.26	2.12	0.48	1.66	0.56	0.69	0.67	0.2117	0.0895	0.0399	0.0097	0.0336	0.0385	0.0073
2	0.34	2	0.42	2.22	0.46	1.64	0.59	0.65	0.71	0.2039	0.0597	0.0280	0.0064	-0.0014	0.0298	0.0037
2	0.34	3	0.57	2.47	0.46	1.63	0.66	0.55	0.79	0.1940	0.1244	0.0367	0.0136	-0.0161	0.0415	0.0089
2	0.33	4	0.72	2.76	0.45	1.60	0.75	0.41	0.88	0.1815	0.0423	0.0744	0.0094	-0.0471	0.0841	0.0101
3	0.42	0	0.11	2.60	0.47	1.61	0.55	0.69	0.69	0.2248	0.0227	0.0851	0.0041	-0.0622	0.0813	0.0061
3	0.42	1	0.26	2.77	0.47	1.61	0.58	0.64	0.73	0.2206	0.0809	0.0549	0.0089	0.0264	0.0548	0.0051
3	0.42	2	0.41	2.98	0.46	1.60	0.63	0.57	0.79	0.2133	0.0271	0.0501	0.0049	-0.0798	0.0542	0.0132
3	0.42	3	0.56	3.27	0.45	1.58	0.71	0.47	0.86	0.2034	0.2297	0.0827	0.0227	0.0375	0.0968	0.0144

TABLE 13: $A_{UL}^{\sin\phi_h}(x_B, P_{h\perp})$ and $A_{UL}^{\sin 2\phi_h}(x_B, P_{h\perp})$ on the proton for π^-

x_B	$\overline{x_B}$	$P_{h\perp}$	$\overline{P_{h\perp}}$	$\overline{Q^2}$	$\overline{z}$	$\overline{M_x}$	$\overline{y}$	$\overline{\epsilon}$	$\overline{D'}$	$\overline{f_D}$	$A_{UL}^{\sin\phi_h}$	$\sigma^{Stat}_{A_{UL}^{\sin\phi_h}}$	$\sigma^{Syst}_{A_{UL}^{\sin\phi_h}}$	$A_{UL}^{\sin 2\phi_h}$	$\sigma^{Stat}_{A_{UL}^{\sin 2\phi_h}}$	$\sigma^{Syst}_{A_{UL}^{\sin 2\phi_h}}$
0	0.18	2	0.44	1.33	0.47	1.91	0.67	0.56	0.75	0.1623	0.0665	0.0763	0.0069	0.0437	0.0708	0.0048
0	0.17	3	0.59	1.34	0.47	1.87	0.71	0.51	0.79	0.1534	-0.0870	0.0456	0.0088	-0.0630	0.0519	0.0066
0	0.17	4	0.74	1.36	0.48	1.77	0.74	0.46	0.82	0.1432	-0.0446	0.0444	0.0056	0.0608	0.0491	0.0078
0	0.16	5	0.89	1.38	0.48	1.67	0.77	0.40	0.86	0.1308	0.0301	0.0804	0.0043	-0.0414	0.0841	0.0067
1	0.26	1	0.28	1.66	0.48	1.75	0.57	0.69	0.66	0.1757	-0.1713	0.1345	0.0203	-0.0771	0.0974	0.0095
1	0.26	2	0.42	1.76	0.48	1.75	0.62	0.62	0.72	0.1698	-0.1341	0.0420	0.0165	-0.0469	0.0434	0.0072
1	0.25	3	0.58	1.82	0.47	1.70	0.65	0.57	0.75	0.1606	0.0101	0.0373	0.0016	-0.0108	0.0450	0.0040
1	0.25	4	0.73	1.96	0.47	1.65	0.72	0.48	0.82	0.1501	-0.0900	0.0577	0.0142	0.0092	0.0651	0.0027
1	0.24	5	0.88	2.10	0.46	1.59	0.79	0.37	0.89	0.1380	-0.1068	0.1526	0.0260	-0.3018	0.1579	0.0458
2	0.35	0	0.11	1.98	0.49	1.63	0.51	0.74	0.63	0.1866	-0.0803	0.1282	0.0122	-0.0110	0.1139	0.0052
2	0.34	1	0.26	2.10	0.47	1.66	0.55	0.69	0.67	0.1831	-0.0754	0.0869	0.0128	-0.0041	0.0724	0.0082
2	0.34	2	0.42	2.28	0.47	1.66	0.60	0.62	0.73	0.1770	-0.0563	0.0439	0.0083	-0.0712	0.0481	0.0108
2	0.34	3	0.57	2.47	0.46	1.62	0.66	0.55	0.79	0.1679	-0.0381	0.0560	0.0108	-0.0336	0.0679	0.0085
2	0.33	4	0.72	2.76	0.45	1.60	0.75	0.41	0.88	0.1569	0.1162	0.1176	0.0188	-0.0975	0.1334	0.0172
3	0.42	0	0.11	2.61	0.48	1.61	0.55	0.69	0.69	0.1920	0.1337	0.1637	0.0207	0.2040	0.1527	0.0310
3	0.42	1	0.26	2.74	0.46	1.61	0.58	0.65	0.73	0.1886	-0.0538	0.1180	0.0107	-0.0210	0.1052	0.0084
3	0.42	2	0.41	2.96	0.45	1.60	0.63	0.58	0.78	0.1825	-0.1037	0.0808	0.0188	0.0047	0.0880	0.0030
3	0.42	3	0.56	3.26	0.45	1.58	0.70	0.47	0.86	0.1739	-0.0430	0.1271	0.0088	-0.1792	0.1574	0.0300

TABLE 14: $A_{UL}^{\sin\phi_h}(x_B, P_{h\perp})$ and $A_{UL}^{\sin 2\phi_h}(x_B, P_{h\perp})$ on the proton for π^0

x_B	$\overline{x_B}$	$P_{h\perp}$	$\overline{P_{h\perp}}$	$\overline{Q^2}$	$\overline{z}$	$\overline{M_x}$	$\overline{y}$	$\overline{\epsilon}$	$\overline{D'}$	$\overline{f_D}$	$A_{UL}^{\sin\phi_h}$	$\sigma^{Stat}_{A_{UL}^{\sin\phi_h}}$	$\sigma^{Syst}_{A_{UL}^{\sin\phi_h}}$	$A_{UL}^{\sin 2\phi_h}$	$\sigma^{Stat}_{A_{UL}^{\sin 2\phi_h}}$	$\sigma^{Syst}_{A_{UL}^{\sin 2\phi_h}}$
0	0.17	0	0.11	1.39	0.53	2.01	0.75	0.44	0.83	0.1846	-0.0123	0.0226	0.0043	0.0107	0.0236	0.0013
0	0.17	1	0.25	1.38	0.53	2.00	0.75	0.43	0.84	0.1814	0.0097	0.0152	0.0027	0.0285	0.0172	0.0024
0	0.16	2	0.41	1.38	0.52	1.95	0.76	0.42	0.84	0.1749	0.0270	0.0199	0.0031	0.0463	0.0201	0.0049
0	0.17	3	0.57	1.38	0.52	1.85	0.75	0.44	0.83	0.1657	0.0413	0.0289	0.0029	0.0384	0.0256	0.0058
0	0.17	4	0.73	1.39	0.52	1.74	0.75	0.43	0.84	0.1543	0.1496	0.0404	0.0114	-0.0561	0.0392	0.0076
0	0.16	5	0.89	1.39	0.49	1.65	0.78	0.39	0.87	0.1399	-0.1003	0.0821	0.0123	-0.0224	0.0885	0.0087
1	0.25	0	0.11	1.99	0.53	1.89	0.72	0.47	0.82	0.1964	-0.0341	0.0251	0.0043	-0.0208	0.0249	0.0023
1	0.25	1	0.25	1.96	0.53	1.85	0.70	0.49	0.81	0.1931	0.0582	0.0201	0.0035	0.0090	0.0200	0.0028
1	0.25	2	0.41	1.92	0.51	1.80	0.69	0.51	0.79	0.1856	0.1334	0.0244	0.0077	-0.0417	0.0226	0.0045
1	0.25	3	0.57	1.94	0.50	1.72	0.70	0.50	0.80	0.1759	0.1207	0.0292	0.0074	-0.0278	0.0265	0.0062
1	0.25	4	0.73	2.02	0.50	1.65	0.74	0.44	0.85	0.1644	0.0204	0.0521	0.0095	-0.1231	0.0518	0.0110
1	0.24	5	0.88	2.10	0.46	1.59	0.79	0.37	0.89	0.1493	-0.0911	0.1601	0.0235	0.0945	0.1784	0.0273
2	0.34	0	0.11	2.62	0.53	1.78	0.70	0.48	0.83	0.2064	0.0055	0.0376	0.0050	0.0032	0.0364	0.0028
2	0.34	1	0.25	2.52	0.52	1.73	0.67	0.53	0.80	0.2026	0.0633	0.0302	0.0037	-0.0118	0.0276	0.0030
2	0.34	2	0.41	2.47	0.49	1.68	0.66	0.55	0.79	0.1949	0.0768	0.0339	0.0080	-0.0188	0.0297	0.0025
2	0.34	3	0.57	2.61	0.48	1.64	0.70	0.49	0.83	0.1850	0.0870	0.0449	0.0068	-0.0593	0.0398	0.0093
2	0.33	4	0.72	2.80	0.48	1.59	0.76	0.39	0.89	0.1732	0.1206	0.1062	0.0079	0.0059	0.1022	0.0045
3	0.42	0	0.11	3.17	0.51	1.69	0.68	0.50	0.83	0.2138	0.0796	0.0761	0.0100	-0.1331	0.0701	0.0089
3	0.42	1	0.25	3.06	0.50	1.65	0.65	0.54	0.81	0.2097	0.0056	0.0591	0.0044	-0.0364	0.0495	0.0035
3	0.42	2	0.41	3.09	0.47	1.61	0.66	0.54	0.81	0.2020	0.0512	0.0654	0.0070	0.0816	0.0536	0.0095
3	0.42	3	0.56	3.30	0.46	1.59	0.71	0.46	0.87	0.1921	0.0331	0.1069	0.0102	0.1165	0.0904	0.0147

TABLE 15: $A_{LL}^{\text{Const}}(x_B, P_{h\perp})$ and $A_{LL}^{\cos\phi_h}(x_B, P_{h\perp})$ on the proton for π^+

x_B	$\overline{x_B}$	$P_{h\perp}$	$\overline{P_{h\perp}}$	$\overline{Q^2}$	$\overline{z}$	$\overline{M_x}$	$\overline{y}$	$\overline{\epsilon}$	$\overline{D'}$	$\overline{f_D}$	A_{LL}^{Const}	$\sigma^{Stat}_{A_{LL}^{\text{Const}}}$	$\sigma^{Syst}_{A_{LL}^{\text{Const}}}$	$A_{LL}^{\cos\phi_h}$	$\sigma^{Stat}_{A_{LL}^{\cos\phi_h}}$	$\sigma^{Syst}_{A_{LL}^{\cos\phi_h}}$
0	0.18	2	0.43	1.33	0.47	1.91	0.67	0.56	0.75	0.1787	0.2417	0.0559	0.0251	-0.0415	0.0697	0.0363
0	0.17	3	0.59	1.34	0.47	1.86	0.70	0.51	0.79	0.1692	0.2378	0.0321	0.0231	-0.0363	0.0454	0.0287
0	0.17	4	0.74	1.36	0.47	1.78	0.73	0.46	0.82	0.1578	0.2195	0.0303	0.0220	-0.0636	0.0469	0.0287
0	0.16	5	0.89	1.37	0.47	1.67	0.77	0.41	0.85	0.1446	0.0742	0.0546	0.0113	0.0536	0.0854	0.0072
1	0.26	1	0.27	1.67	0.48	1.75	0.57	0.68	0.67	0.2001	0.2803	0.0602	0.0303	-0.0610	0.0745	0.0430
1	0.26	2	0.43	1.74	0.47	1.74	0.61	0.63	0.71	0.1927	0.2170	0.0302	0.0228	-0.1389	0.0411	0.0417
1	0.25	3	0.58	1.82	0.47	1.70	0.65	0.57	0.75	0.1830	0.3072	0.0265	0.0312	-0.0461	0.0397	0.0400
1	0.25	4	0.73	1.95	0.46	1.66	0.71	0.48	0.82	0.1706	0.4023	0.0384	0.0484	-0.0732	0.0599	0.0576
1	0.24	5	0.88	2.10	0.46	1.59	0.78	0.37	0.89	0.1571	0.3104	0.0963	0.0356	-0.2065	0.1455	0.0478
2	0.35	0	0.10	1.96	0.49	1.64	0.51	0.75	0.62	0.2159	0.2893	0.0647	0.0262	-0.0985	0.0871	0.0389
2	0.34	1	0.26	2.12	0.48	1.66	0.56	0.69	0.67	0.2117	0.3468	0.0435	0.0391	-0.0609	0.0580	0.0463
2	0.34	2	0.42	2.22	0.46	1.64	0.59	0.65	0.71	0.2039	0.3824	0.0312	0.0434	-0.1009	0.0444	0.0504
2	0.34	3	0.57	2.47	0.46	1.63	0.66	0.55	0.79	0.1940	0.3544	0.0408	0.0402	-0.1476	0.0620	0.0584
2	0.33	4	0.72	2.76	0.45	1.60	0.75	0.41	0.88	0.1815	0.3778	0.0787	0.0386	0.0395	0.1239	0.0297
3	0.42	0	0.11	2.60	0.47	1.61	0.55	0.69	0.69	0.2248	0.2159	0.0893	0.0226	-0.3515	0.1226	0.0495
3	0.42	1	0.26	2.77	0.47	1.61	0.58	0.64	0.73	0.2206	0.4498	0.0599	0.0442	-0.0777	0.0825	0.0598
3	0.42	2	0.41	2.98	0.46	1.60	0.63	0.57	0.79	0.2133	0.5688	0.0555	0.0700	-0.0194	0.0817	0.0638
3	0.42	3	0.56	3.27	0.45	1.58	0.71	0.47	0.86	0.2034	0.4526	0.0922	0.0514	-0.2026	0.1423	0.1015

x_B	$\overline{x_B}$	$P_{h\perp}$	$\overline{P_{h\perp}}$	$\overline{Q^2}$	$\overline{z}$	$\overline{M_x}$	$\overline{y}$	$\overline{\epsilon}$	$\overline{D'}$	$\overline{f_D}$	A_{LL}^{Const}	$\sigma^{Stat}_{A_{LL}^{\text{Const}}}$	$\sigma^{Syst}_{A_{LL}^{\text{Const}}}$	$A_{LL}^{\cos\phi_h}$	$\sigma^{Stat}_{A_{LL}^{\cos\phi_h}}$	$\sigma^{Syst}_{A_{LL}^{\cos\phi_h}}$
0	0.18	2	0.44	1.33	0.47	1.91	0.67	0.56	0.75	0.1623	0.0971	0.0816	0.0114	-0.0473	0.0978	0.0175
0	0.17	3	0.59	1.34	0.47	1.87	0.71	0.51	0.79	0.1534	0.1790	0.0491	0.0183	0.0804	0.0673	0.0192
0	0.17	4	0.74	1.36	0.48	1.77	0.74	0.46	0.82	0.1432	0.2272	0.0447	0.0226	0.0731	0.0663	0.0205
0	0.16	5	0.89	1.38	0.48	1.67	0.77	0.40	0.86	0.1308	0.2053	0.0753	0.0220	-0.1313	0.1136	0.0296
1	0.26	1	0.28	1.66	0.48	1.75	0.57	0.69	0.66	0.1757	0.4735	0.1321	0.0572	0.4032	0.1522	0.0495
1	0.26	2	0.42	1.76	0.48	1.75	0.62	0.62	0.72	0.1698	0.1909	0.0475	0.0240	0.0426	0.0613	0.0194
1	0.25	3	0.58	1.82	0.47	1.70	0.65	0.57	0.75	0.1606	0.2453	0.0415	0.0311	0.0290	0.0607	0.0290
1	0.25	4	0.73	1.96	0.47	1.65	0.72	0.48	0.82	0.1501	0.2746	0.0585	0.0360	0.0074	0.0882	0.0297
1	0.24	5	0.88	2.10	0.46	1.59	0.79	0.37	0.89	0.1380	0.6453	0.1310	0.0808	0.1431	0.2127	0.0611
2	0.35	0	0.11	1.98	0.49	1.63	0.51	0.74	0.63	0.1866	0.2708	0.1343	0.0387	0.1166	0.1753	0.0317
2	0.34	1	0.26	2.10	0.47	1.66	0.55	0.69	0.67	0.1831	0.2086	0.0915	0.0305	0.0106	0.1128	0.0252
2	0.34	2	0.42	2.28	0.47	1.66	0.60	0.62	0.73	0.1770	0.2088	0.0499	0.0303	-0.0376	0.0684	0.0235
2	0.34	3	0.57	2.47	0.46	1.62	0.66	0.55	0.79	0.1679	0.2839	0.0628	0.0422	-0.0404	0.0938	0.0322
2	0.33	4	0.72	2.76	0.45	1.60	0.75	0.41	0.88	0.1569	0.3267	0.1213	0.0495	0.0108	0.1842	0.0238
3	0.42	0	0.11	2.61	0.48	1.61	0.55	0.69	0.69	0.1920	0.1788	0.1688	0.0294	-0.2935	0.2288	0.0622
3	0.42	1	0.26	2.74	0.46	1.61	0.58	0.65	0.73	0.1886	0.1934	0.1223	0.0306	-0.1477	0.1575	0.0401
3	0.42	2	0.41	2.96	0.45	1.60	0.63	0.58	0.78	0.1825	0.2602	0.0904	0.0422	0.0390	0.1282	0.0264
3	0.42	3	0.56	3.26	0.45	1.58	0.70	0.47	0.86	0.1739	0.3821	0.1408	0.0631	-0.0440	0.2149	0.0421

TABLE 16: $A_{LL}^{\text{Const}}(x_B, P_{h\perp})$ and $A_{LL}^{\cos\phi_h}(x_B, P_{h\perp})$ on the proton for π^-

TABLE 17: $A_{LL}^{\text{Const}}(x_B, P_{h\perp})$ and $A_{LL}^{\cos\phi_h}(x_B, P_{h\perp})$ on the proton for π^0

x_B	$\overline{x_B}$	$P_{h\perp}$	$\overline{P_{h\perp}}$	$\overline{Q^2}$	$\overline{z}$	$\overline{M_x}$	$\overline{y}$	$\overline{\epsilon}$	$\overline{D'}$	$\overline{f_D}$	A_{LL}^{Const}	$\sigma^{Stat}_{A_{LL}^{\text{Const}}}$	$\sigma^{Syst}_{A_{LL}^{\text{Const}}}$	$A_{LL}^{\cos\phi_h}$	$\sigma^{Stat}_{A_{LL}^{\cos\phi_h}}$	$\sigma^{Syst}_{A_{LL}^{\cos\phi_h}}$
0	0.17	0	0.11	1.39	0.53	2.01	0.75	0.44	0.83	0.1846	0.1925	0.0197	0.0114	-0.0027	0.0293	0.0202
0	0.17	1	0.25	1.38	0.53	2.00	0.75	0.43	0.84	0.1814	0.2335	0.0141	0.0124	0.0070	0.0236	0.0219
0	0.16	2	0.41	1.38	0.52	1.95	0.76	0.42	0.84	0.1749	0.2359	0.0168	0.0161	-0.0297	0.0251	0.0214
0	0.17	3	0.57	1.38	0.52	1.85	0.75	0.44	0.83	0.1657	0.2534	0.0206	0.0205	-0.0266	0.0263	0.0260
0	0.17	4	0.73	1.39	0.52	1.74	0.75	0.43	0.84	0.1543	0.2549	0.0304	0.0162	-0.0418	0.0395	0.0267
0	0.16	5	0.89	1.39	0.49	1.65	0.78	0.39	0.87	0.1399	0.2301	0.0718	0.0353	-0.0524	0.1053	0.0228
1	0.25	0	0.11	1.99	0.53	1.89	0.72	0.47	0.82	0.1964	0.3016	0.0211	0.0157	-0.0371	0.0297	0.0289
1	0.25	1	0.25	1.96	0.53	1.85	0.70	0.49	0.81	0.1931	0.3123	0.0168	0.0172	-0.0390	0.0248	0.0294
1	0.25	2	0.41	1.92	0.51	1.80	0.69	0.51	0.79	0.1856	0.2864	0.0174	0.0190	-0.0282	0.0242	0.0273
1	0.25	3	0.57	1.94	0.50	1.72	0.70	0.50	0.80	0.1759	0.2959	0.0211	0.0195	-0.0015	0.0269	0.0269
1	0.25	4	0.73	2.02	0.50	1.65	0.74	0.44	0.85	0.1644	0.2630	0.0394	0.0151	-0.0582	0.0515	0.0231
1	0.24	5	0.88	2.10	0.46	1.59	0.79	0.37	0.89	0.1493	0.0000	0.6182	0.0000	-0.4179	0.1918	0.0471
2	0.34	0	0.11	2.62	0.53	1.78	0.70	0.48	0.83	0.2064	0.3844	0.0314	0.0191	-0.0063	0.0432	0.0348
2	0.34	1	0.25	2.52	0.52	1.73	0.67	0.53	0.80	0.2026	0.3548	0.0230	0.0182	-0.0165	0.0310	0.0342
2	0.34	2	0.41	2.47	0.49	1.68	0.66	0.55	0.79	0.1949	0.3316	0.0234	0.0211	-0.0526	0.0311	0.0333
2	0.34	3	0.57	2.61	0.48	1.64	0.70	0.49	0.83	0.1850	0.3278	0.0325	0.0194	-0.0335	0.0412	0.0287
2	0.33	4	0.72	2.80	0.48	1.59	0.76	0.39	0.89	0.1732	0.3694	0.0765	0.0218	-0.1702	0.0976	0.0346
3	0.42	0	0.11	3.17	0.51	1.69	0.68	0.50	0.83	0.2138	0.4570	0.0623	0.0258	0.0370	0.0827	0.0444
3	0.42	1	0.25	3.06	0.50	1.65	0.65	0.54	0.81	0.2097	0.3872	0.0411	0.0199	-0.0332	0.0521	0.0522
3	0.42	2	0.41	3.09	0.47	1.61	0.66	0.54	0.81	0.2020	0.3578	0.0440	0.0206	0.0299	0.0565	0.0454
3	0.42	3	0.56	3.30	0.46	1.59	0.71	0.46	0.87	0.1921	0.3699	0.0747	0.0220	-0.0897	0.0933	0.0443

TABLE 18: $A_{LU}^{\sin\phi_h}(x_B)$ on the deuteron for π^+

x_B	$\overline{x_B}$	$\overline{Q^2}$	$\overline{P_{h\perp}}$	$\overline{z}$	$\overline{M_x}$	$\overline{y}$	$\overline{\epsilon}$	$\overline{D'}$	$\overline{f_D}$	$A_{LU}^{\sin\phi_h}$	$\sigma^{Stat}_{A_{LU}^{\sin\phi_h}}$	$\sigma^{Syst}_{A_{LU}^{\sin\phi_h}}$
0	0.17	1.28	0.62	0.47	1.79	0.71	0.50	0.79	0.2029	0.0206	0.0029	0.0013
1	0.25	1.72	0.52	0.47	1.68	0.64	0.58	0.74	0.2099	0.0256	0.0029	0.0016
2	0.34	2.20	0.41	0.46	1.63	0.61	0.62	0.73	0.2173	0.0334	0.0040	0.0021
3	0.42	2.88	0.34	0.46	1.60	0.63	0.58	0.79	0.2212	0.0287	0.0078	0.0018

TABLE 19: $A_{LU}^{\sin\phi_h}(x_B)$ on the deuteron for π^-

x_B	$\overline{x_B}$	$\overline{Q^2}$	$\overline{P_{h\perp}}$	$\overline{z}$	$\overline{M_x}$	$\overline{y}$	$\overline{\epsilon}$	$\overline{D'}$	$\overline{f_D}$	$A_{LU}^{\sin\phi_h}$	$\sigma^{Stat}_{A_{LU}^{\sin\phi_h}}$	$\sigma^{Syst}_{A_{LU}^{\sin\phi_h}}$
0	0.17	1.28	0.63	0.47	1.78	0.70	0.51	0.79	0.2024	0.0041	0.0039	0.0002
1	0.25	1.70	0.50	0.47	1.69	0.63	0.60	0.73	0.2122	0.0044	0.0039	0.0003
2	0.34	2.18	0.40	0.46	1.62	0.60	0.63	0.72	0.2180	-0.0002	0.0055	0.0000
3	0.42	2.84	0.33	0.46	1.60	0.62	0.59	0.78	0.2220	0.0067	0.0109	0.0004

TABLE 20: $A_{LU}^{\sin\phi_h}(x_B)$ on the deuteron for π^0

x_B	$\overline{x_B}$	$\overline{Q^2}$	$\overline{P_{h\perp}}$	$\overline{z}$	$\overline{M_x}$	$\overline{y}$	$\overline{\epsilon}$	$\overline{D'}$	$\overline{f_D}$	$A_{LU}^{\sin\phi_h}$	$\sigma^{Stat}_{A_{LU}^{\sin\phi_h}}$	$\sigma^{Syst}_{A_{LU}^{\sin\phi_h}}$
0	0.17	1.31	0.39	0.52	1.89	0.74	0.45	0.83	0.2199	0.0216	0.0023	0.0010
1	0.25	1.84	0.38	0.51	1.76	0.68	0.52	0.79	0.2204	0.0165	0.0031	0.0007
2	0.34	2.41	0.35	0.50	1.68	0.66	0.54	0.79	0.2215	0.0157	0.0052	0.0006
3	0.42	3.03	0.33	0.48	1.62	0.67	0.52	0.82	0.2224	0.0049	0.0114	0.0006

TABLE 21: $A_{UL}^{\sin\phi_h}(x_B)$ and $A_{UL}^{\sin 2\phi_h}(x_B)$ on the deuteron for π^+

x_B	$\overline{x_B}$	$\overline{Q^2}$	$\overline{P_{h\perp}}$	$\overline{z}$	$\overline{M_x}$	$\overline{y}$	$\overline{\epsilon}$	$\overline{D'}$	$\overline{f_D}$	$A_{UL}^{\sin\phi_h}$	$\sigma^{Stat}_{A_{UL}^{\sin\phi_h}}$	$\sigma^{Syst}_{A_{UL}^{\sin\phi_h}}$	$A_{UL}^{\sin 2\phi_h}$	$\sigma^{Stat}_{A_{UL}^{\sin 2\phi_h}}$	$\sigma^{Syst}_{A_{UL}^{\sin 2\phi_h}}$
0	0.17	1.28	0.62	0.47	1.79	0.71	0.50	0.79	0.2029	0.1483	0.0654	0.0168	-0.0134	0.0639	0.0043
1	0.25	1.72	0.52	0.47	1.68	0.64	0.58	0.74	0.2099	0.0331	0.0641	0.0046	-0.0754	0.0647	0.0117
2	0.34	2.20	0.41	0.46	1.63	0.61	0.62	0.73	0.2173	0.0304	0.0878	0.0083	-0.0593	0.0909	0.0057
3	0.42	2.88	0.34	0.46	1.60	0.63	0.58	0.79	0.2212	-0.0470	0.1777	0.0071	0.0317	0.1853	0.0136

TABLE 22: $A_{UL}^{\sin\phi_h}(x_B)$ and $A_{UL}^{\sin 2\phi_h}(x_B)$ on the deuteron for π^-

x_B	$\overline{x_B}$	$\overline{Q^2}$	$\overline{P_{h\perp}}$	$\overline{z}$	$\overline{M_x}$	$\overline{y}$	$\overline{\epsilon}$	$\overline{D'}$	$\overline{f_D}$	$A_{UL}^{\sin\phi_h}$	$\sigma^{Stat}_{A_{UL}^{\sin\phi_h}}$	$\sigma^{Syst}_{A_{UL}^{\sin\phi_h}}$	$A_{UL}^{\sin 2\phi_h}$	$\sigma^{Stat}_{A_{UL}^{\sin 2\phi_h}}$	$\sigma^{Syst}_{A_{UL}^{\sin 2\phi_h}}$
0	0.17	1.28	0.63	0.47	1.78	0.70	0.51	0.79	0.2024	0.0216	0.0818	0.0080	0.0672	0.0837	0.0113
1	0.25	1.70	0.50	0.47	1.69	0.63	0.60	0.73	0.2122	0.1111	0.0801	0.0160	-0.0179	0.0827	0.0033
2	0.34	2.18	0.40	0.46	1.62	0.60	0.63	0.72	0.2180	-0.0838	0.1110	0.0118	0.0056	0.1154	0.0034
3	0.42	2.84	0.33	0.46	1.60	0.62	0.59	0.78	0.2220	-0.1225	0.2326	0.0170	-0.0293	0.2396	0.0312

TABLE 23: $A_{UL}^{\sin\phi_h}(x_B)$ and $A_{UL}^{\sin 2\phi_h}(x_B)$ on the deuteron for π^0

x_B	$\overline{x_B}$	$\overline{Q^2}$	$\overline{P_{h\perp}}$	$\overline{z}$	$\overline{M_x}$	$\overline{y}$	$\overline{\epsilon}$	$\overline{D'}$	$\overline{f_D}$	$A_{UL}^{\sin\phi_h}$	$\sigma^{Stat}_{A_{UL}^{\sin\phi_h}}$	$\sigma^{Syst}_{A_{UL}^{\sin\phi_h}}$	$A_{UL}^{\sin 2\phi_h}$	$\sigma^{Stat}_{A_{UL}^{\sin 2\phi_h}}$	$\sigma^{Syst}_{A_{UL}^{\sin 2\phi_h}}$
0	0.17	1.31	0.39	0.52	1.89	0.74	0.45	0.83	0.2199	0.0494	0.0394	0.0064	-0.0036	0.0397	0.0019
1	0.25	1.84	0.38	0.51	1.76	0.68	0.52	0.79	0.2204	0.1376	0.0548	0.0190	-0.0120	0.0516	0.0048
2	0.34	2.41	0.35	0.50	1.68	0.66	0.54	0.79	0.2215	0.0939	0.0929	0.0150	-0.0722	0.0826	0.0079
3	0.42	3.03	0.33	0.48	1.62	0.67	0.52	0.82	0.2224	0.2847	0.2069	0.0418	-0.1767	0.1737	0.0357

TABLE 24: $A_{LL}^{\text{Const}}(x_B)$ and $A_{LL}^{\cos\phi_h}(x_B)$ on the deuteron for π^+

x_B	$\overline{x_B}$	$\overline{Q^2}$	$\overline{P_{h\perp}}$	$\overline{z}$	$\overline{M_x}$	$\overline{y}$	$\overline{\epsilon}$	$\overline{D'}$	$\overline{f_D}$	A_{LL}^{Const}	$\sigma^{Stat}_{A_{LL}^{\text{Const}}}$	$\sigma^{Syst}_{A_{LL}^{\text{Const}}}$	$A_{LL}^{\cos\phi_h}$	$\sigma^{Stat}_{A_{LL}^{\cos\phi_h}}$	$\sigma^{Syst}_{A_{LL}^{\cos\phi_h}}$
0	0.17	1.28	0.62	0.47	1.79	0.71	0.50	0.79	0.2029	-0.0153	0.0670	0.0051	-0.0899	0.0910	0.0109
1	0.25	1.72	0.52	0.47	1.68	0.64	0.58	0.74	0.2099	0.1677	0.0678	0.0190	-0.0457	0.0934	0.0141
2	0.34	2.20	0.41	0.46	1.63	0.61	0.62	0.73	0.2173	0.1316	0.0946	0.0168	-0.1292	0.1336	0.0157
3	0.42	2.88	0.34	0.46	1.60	0.63	0.58	0.79	0.2212	0.2171	0.1915	0.0257	-0.2230	0.2730	0.0381

TABLE 25: $A_{LL}^{\text{Const}}(x_B)$ and $A_{LL}^{\cos\phi_h}(x_B)$ on the deuteron for π^-

x_B	$\overline{x_B}$	$\overline{Q^2}$	$\overline{P_{h\perp}}$	$\overline{z}$	$\overline{M_x}$	$\overline{y}$	$\overline{\epsilon}$	$\overline{D'}$	$\overline{f_D}$	A_{LL}^{Const}	$\sigma^{Stat}_{A_{LL}^{\text{Const}}}$	$\sigma^{Syst}_{A_{LL}^{\text{Const}}}$	$A_{LL}^{\cos\phi_h}$	$\sigma^{Stat}_{A_{LL}^{\cos\phi_h}}$	$\sigma^{Syst}_{A_{LL}^{\cos\phi_h}}$
0	0.17	1.28	0.63	0.47	1.78	0.70	0.51	0.79	0.2024	0.1501	0.0837	0.0125	0.1386	0.1107	0.0145
1	0.25	1.70	0.50	0.47	1.69	0.63	0.60	0.73	0.2122	-0.0198	0.0861	0.0080	-0.0596	0.1155	0.0145
2	0.34	2.18	0.40	0.46	1.62	0.60	0.63	0.72	0.2180	0.0506	0.1213	0.0090	-0.1321	0.1662	0.0254
3	0.42	2.84	0.33	0.46	1.60	0.62	0.59	0.78	0.2220	0.4791	0.2551	0.0604	0.1026	0.3511	0.0233

TABLE 26: $A_{LL}^{\text{Const}}(x_B)$ and $A_{LL}^{\cos\phi_h}(x_B)$ on the deuteron for π^0

x_B	$\overline{x_B}$	$\overline{Q^2}$	$\overline{P_{h\perp}}$	$\overline{z}$	$\overline{M_x}$	$\overline{y}$	$\overline{\epsilon}$	$\overline{D'}$	$\overline{f_D}$	A_{LL}^{Const}	$\sigma^{Stat}_{A_{LL}^{\text{Const}}}$	$\sigma^{Syst}_{A_{LL}^{\text{Const}}}$	$A_{LL}^{\cos\phi_h}$	$\sigma^{Stat}_{A_{LL}^{\cos\phi_h}}$	$\sigma^{Syst}_{A_{LL}^{\cos\phi_h}}$
0	0.17	1.31	0.39	0.52	1.89	0.74	0.45	0.83	0.2199	0.0480	0.0322	0.0101	0.0247	0.0464	0.0282
1	0.25	1.84	0.38	0.51	1.76	0.68	0.52	0.79	0.2204	0.2258	0.0415	0.0220	-0.0299	0.0560	0.0233
2	0.34	2.41	0.35	0.50	1.68	0.66	0.54	0.79	0.2215	0.1755	0.0672	0.0386	-0.0259	0.0875	0.0131
3	0.42	3.03	0.33	0.48	1.62	0.67	0.52	0.82	0.2224	0.2876	0.1432	0.0539	-0.1394	0.1808	0.0373

APPENDIX C

DILUTION FACTOR

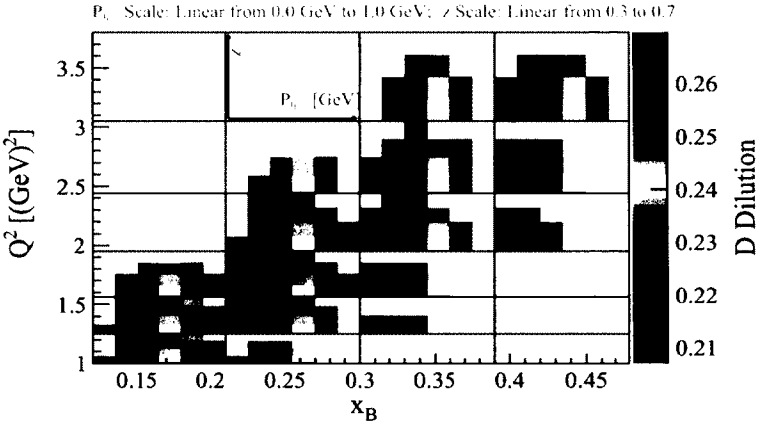

FIG. 141: D dilution factor for SIDIS π^+ events from the ND_3 target as a function of Q^2, x_B, z and $P_{h\perp}$.

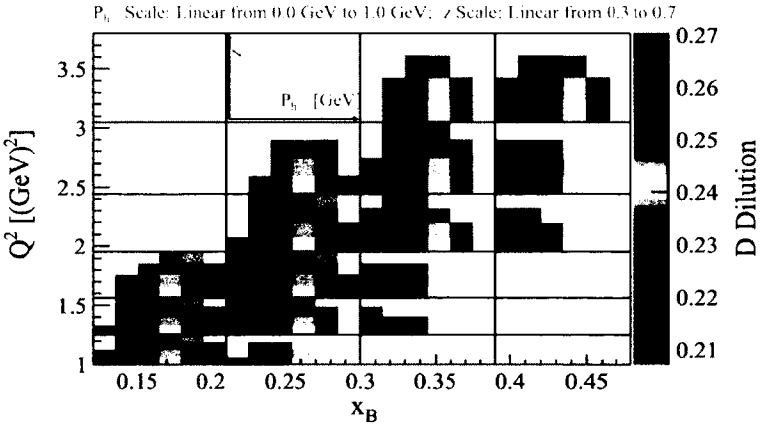

FIG. 142: Same as 141 except for π^-

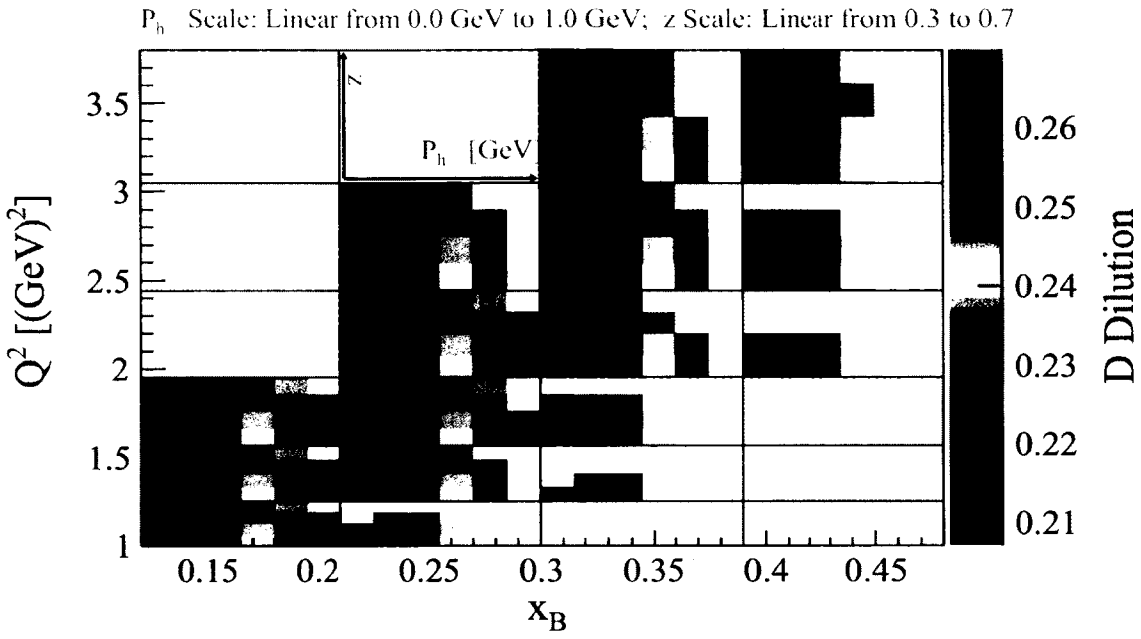

FIG. 143: Same as 141 except for π^0

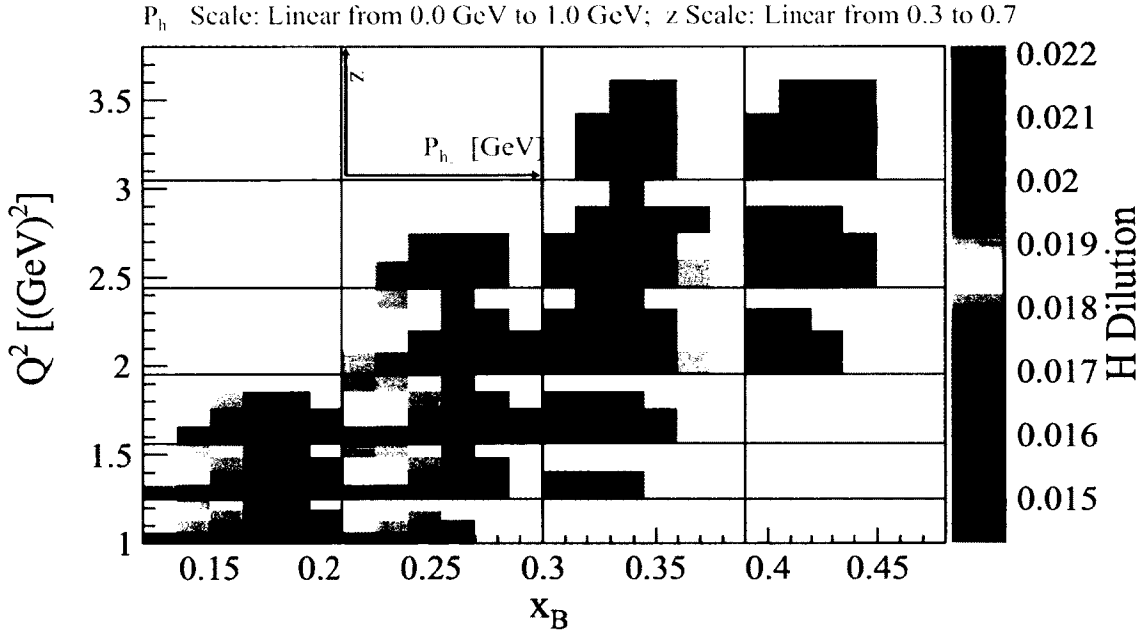

FIG. 144: H dilution factor for SIDIS π^+ events from the ND_3 target as a function of Q^2, x_B, z and $P_{h\perp}$.

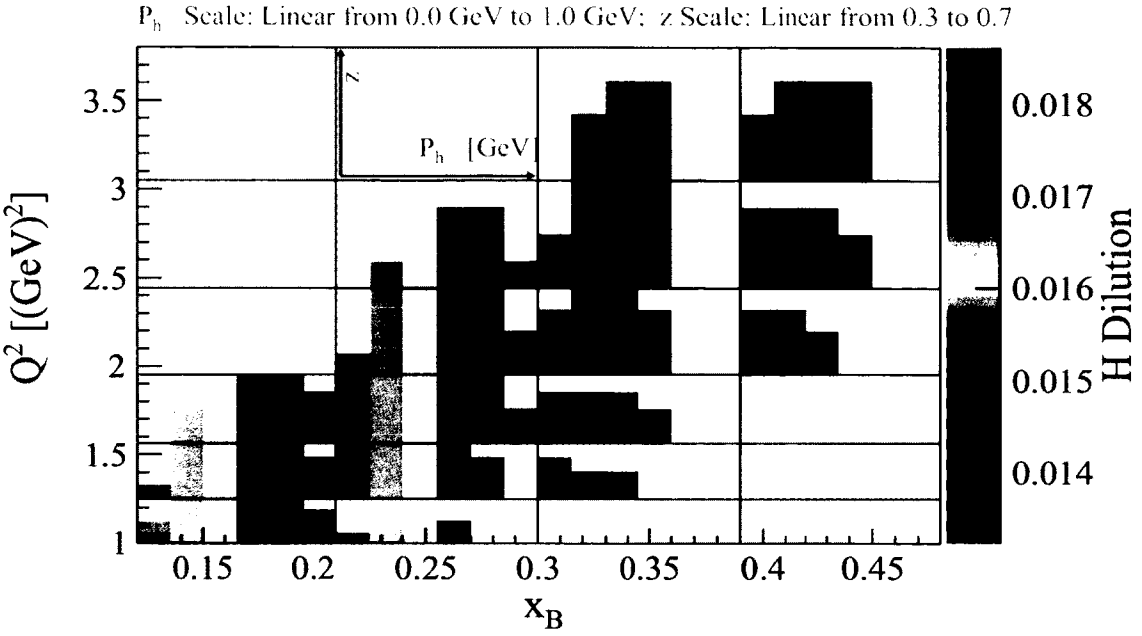

FIG. 145: Same as 144 except for π^-

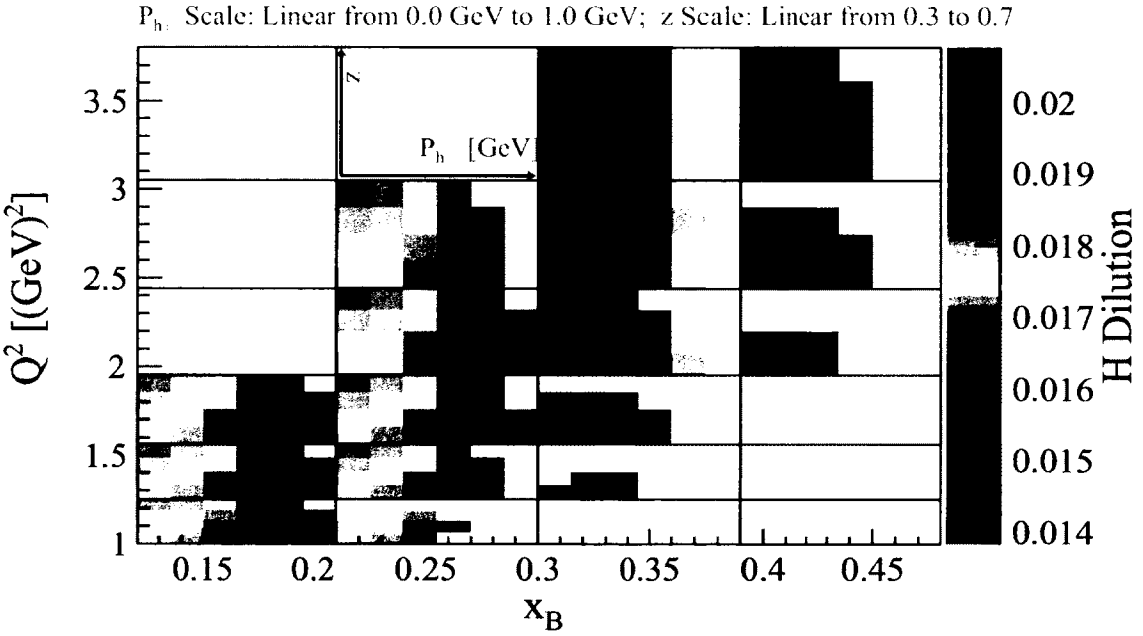

FIG. 146: Same as 144 except for π^0

APPENDIX D

RADIATIVE CORRECTIONS

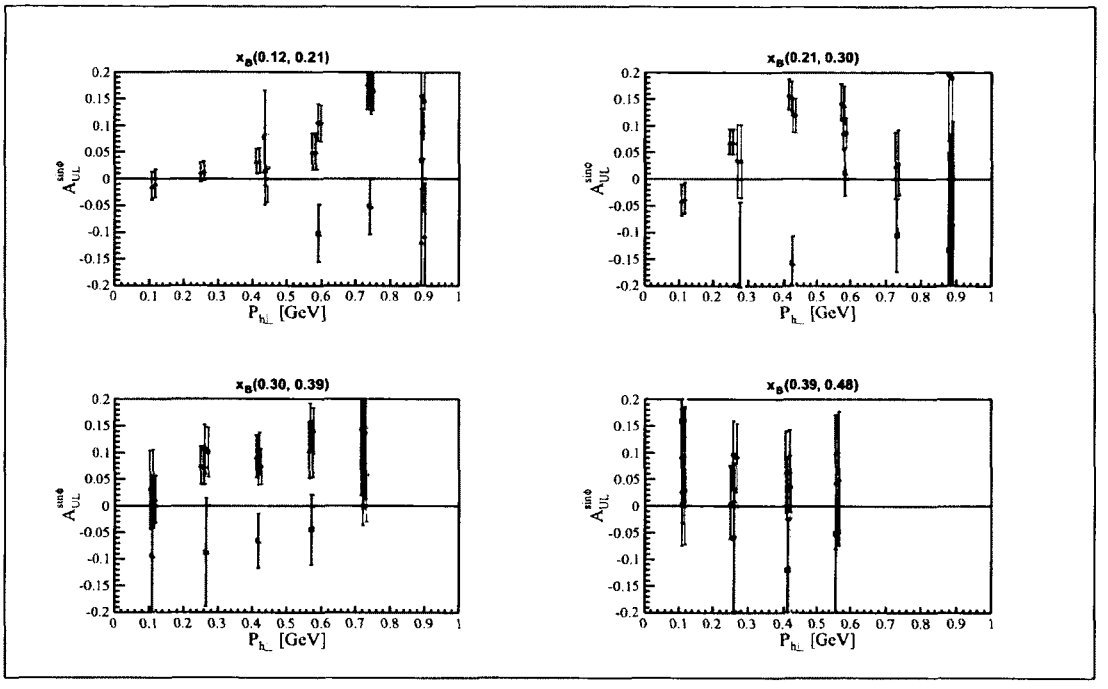

FIG. 147: Radiative correction for $A_{UL}^{\sin\phi_h}(x_B, p_{h_\perp})$ on the proton. Red, blue and green respectively for π^+, π^- and π^0 before correction; pink, gold and light green respectively for π^+, π^- and π^0 after radiative correction.

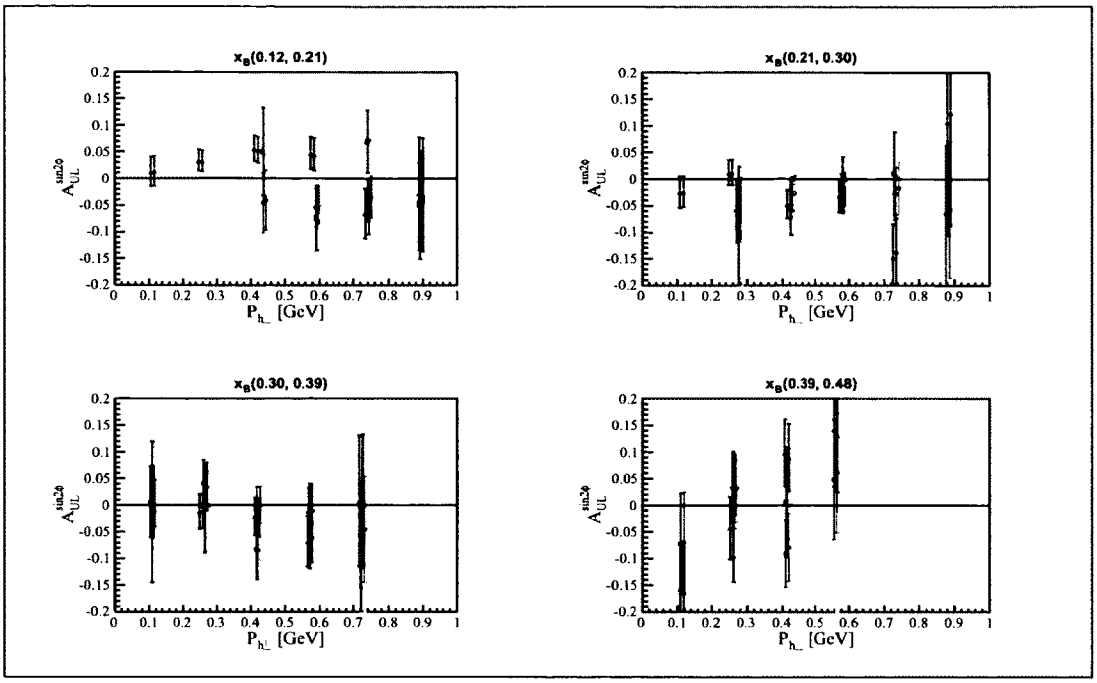

FIG. 148: Radiative correction for $A_{UL}^{\sin 2\phi_h}(x_B, p_{h_\perp})$ on the proton. Red, blue and green respectively for π^+, π^- and π^0 before correction; pink, gold and light green respectively for π^+, π^- and π^0 after radiative correction.

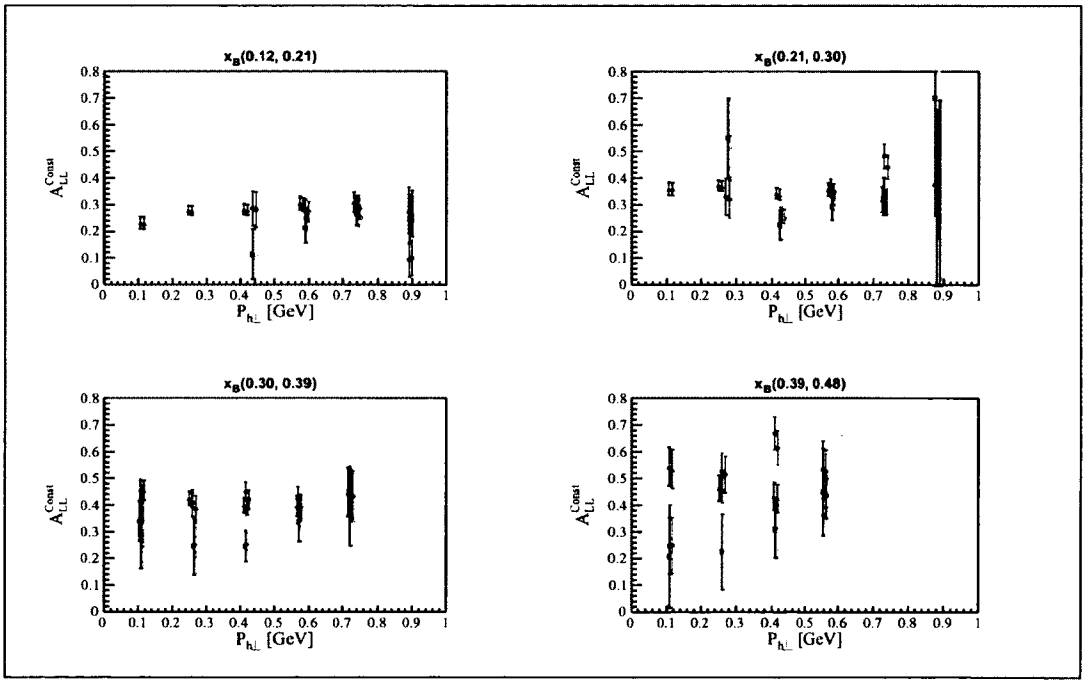

FIG. 149: Radiative correction for $A_{LL}^{\text{Const}}(x_B, p_{h_\perp})$ on the proton. Red, blue and green respectively for π^+, π^- and π^0 before correction; pink, gold and light green respectively for π^+, π^- and π^0 after radiative correction.

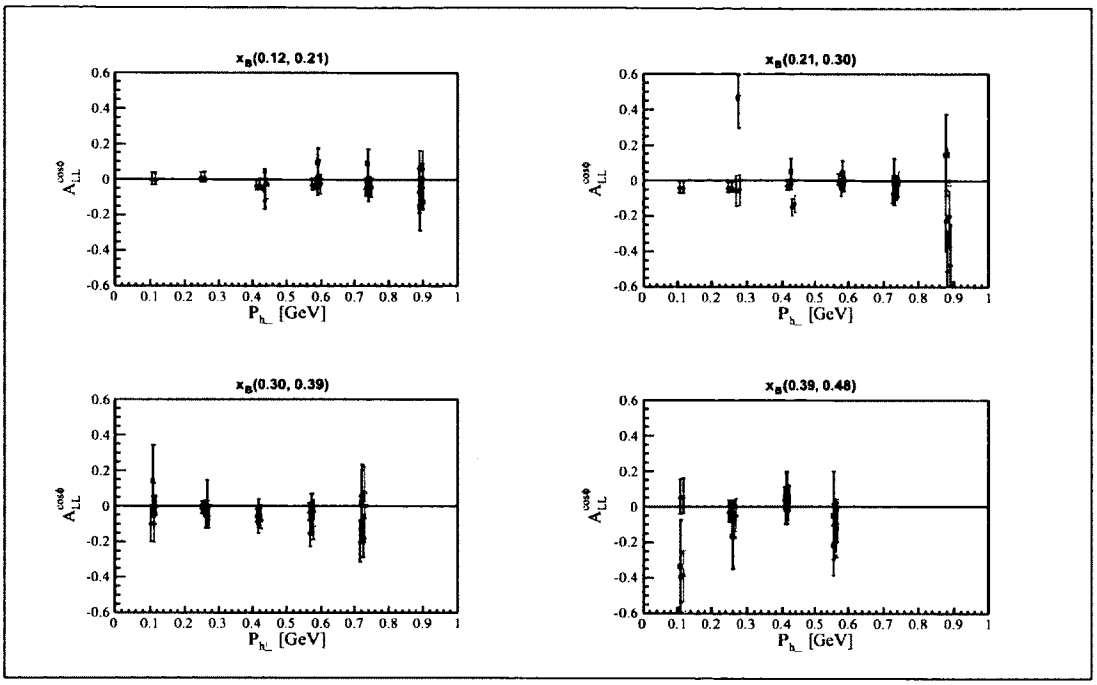

FIG. 150: Radiative correction for $A_{LL}^{\cos\phi_h}(x_B, p_{h_\perp})$ on the proton. Red, blue and green respectively for π^+, π^- and π^0 before correction; pink, gold and light green respectively for π^+, π^- and π^0 after radiative correction.

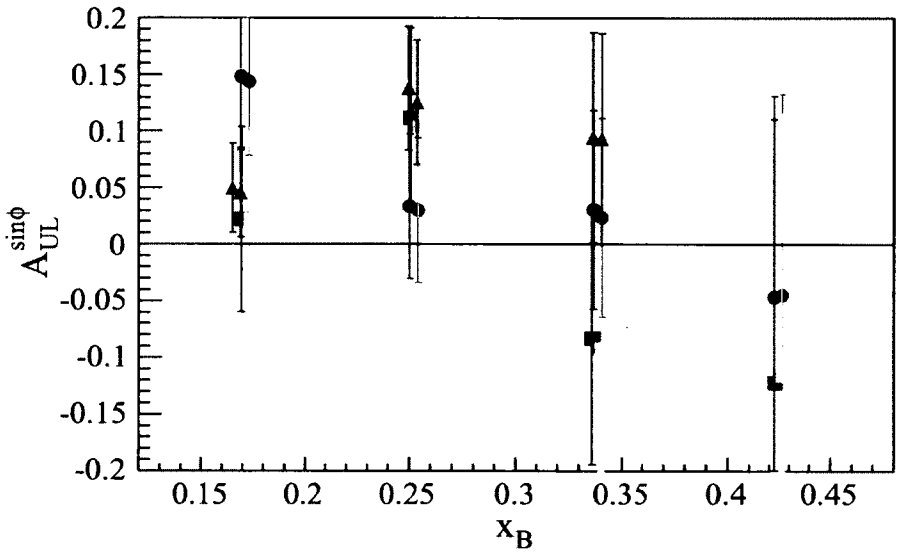

FIG. 151: Radiative correction for $A_{UL}^{\sin\phi_h}(x_B)$ on the deuteron. Red, blue and green respectively for π^+, π^- and π^0 before correction; pink, gold and light green respectively for π^+, π^- and π^0 after radiative correction.

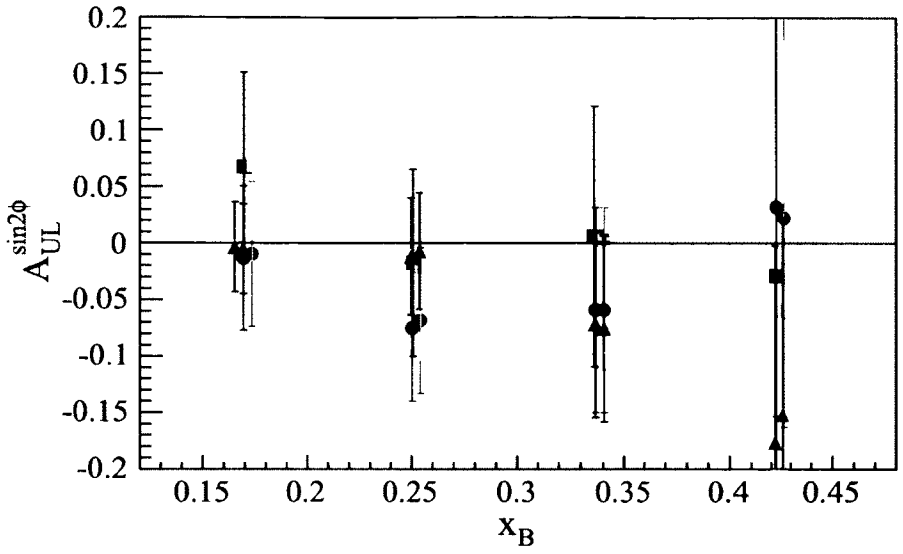

FIG. 152: Radiative correction for $A_{UL}^{\sin 2\phi_h}(x_B)$ on the deuteron. Red, blue and green respectively for π^+, π^- and π^0 before correction; pink, gold and light green respectively for π^+, π^- and π^0 after radiative correction.

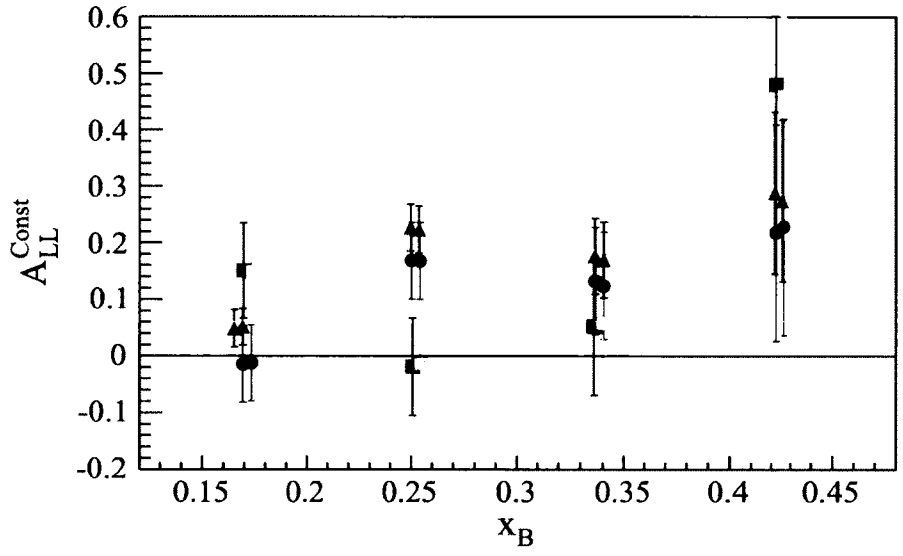

FIG. 153: Radiative correction for $A_{LL}^{\text{Const}}(x_B)$ on the deuteron. Red, blue and green respectively for π^+, π^- and π^0 before correction; pink, gold and light green respectively for π^+, π^- and π^0 after radiative correction.

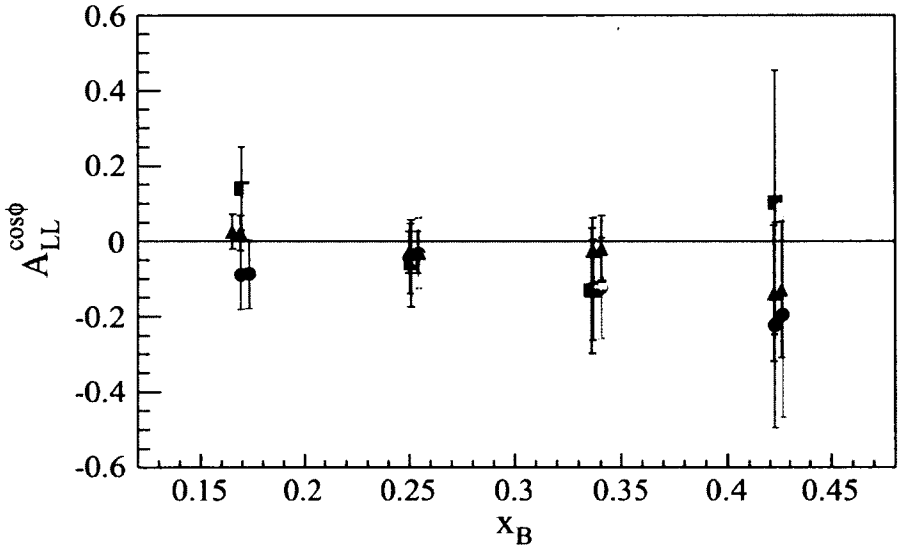

FIG. 154: Radiative correction for $A_{LL}^{\cos\phi_h}(x_B)$ on the deuteron. Red, blue and green respectively for π^+, π^- and π^0 before correction; pink, gold and light green respectively for π^+, π^- and π^0 after radiative correction.

APPENDIX E

FITS ON ASYMMETRIES

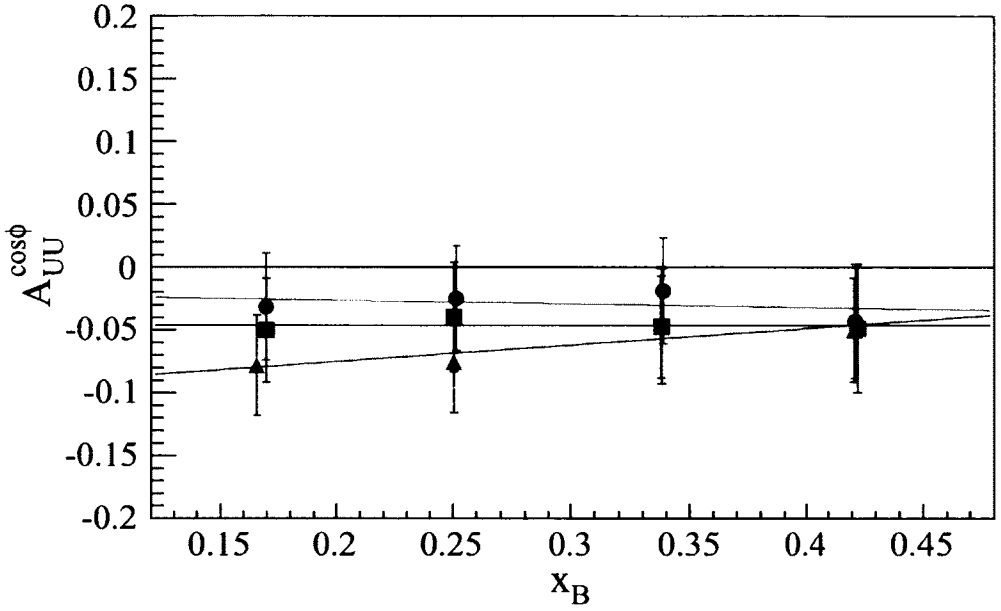

FIG. 155: $A_{UU}^{\cos\phi_h}(x_B)$ from simultaneous fits, together with a linear fit of the x_B dependence. Red: π^+, blue: π^- and green: π^0

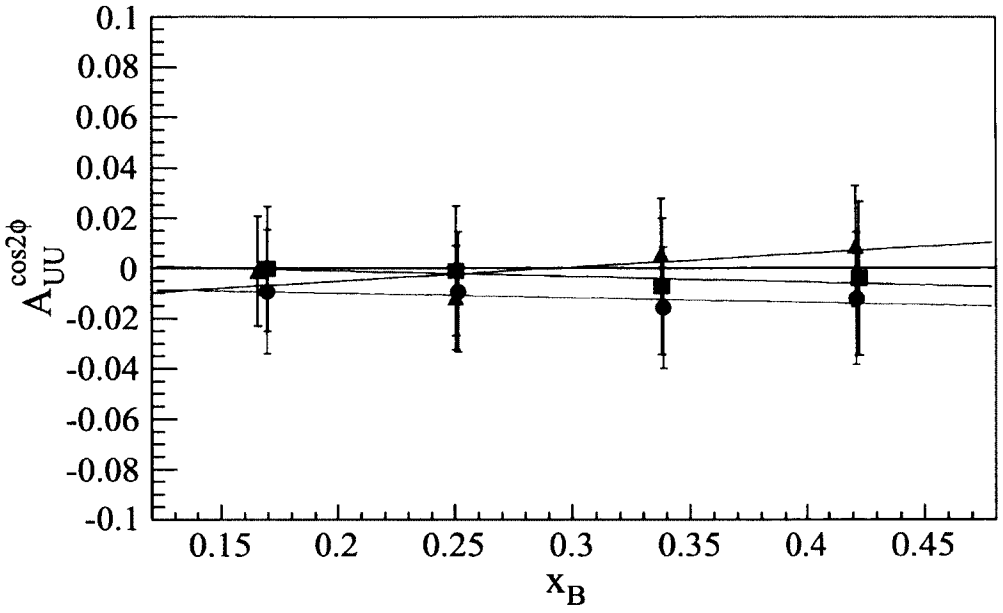

FIG. 156: $A_{UU}^{\cos 2\phi_h}(x_B)$ from simultaneous fits, together with a linear fit of the x_B dependence. Red: π^+, blue: π^- and green: π^0

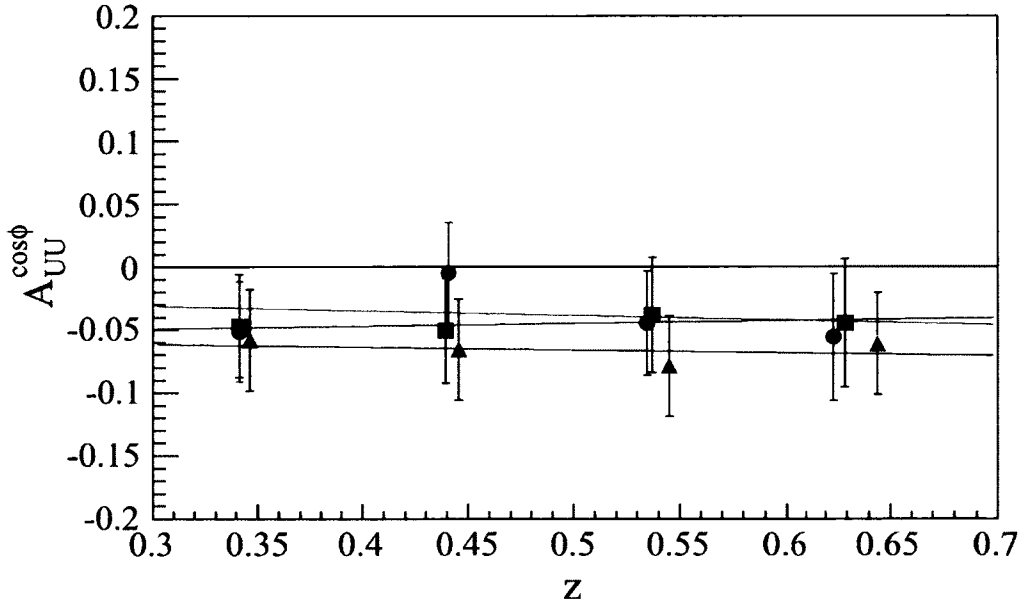

FIG. 157: $A_{UU}^{\cos\phi_h}(z)$ from simultaneous fits, together with a linear fit of the z dependence. Red: π^+, blue: π^- and green: π^0

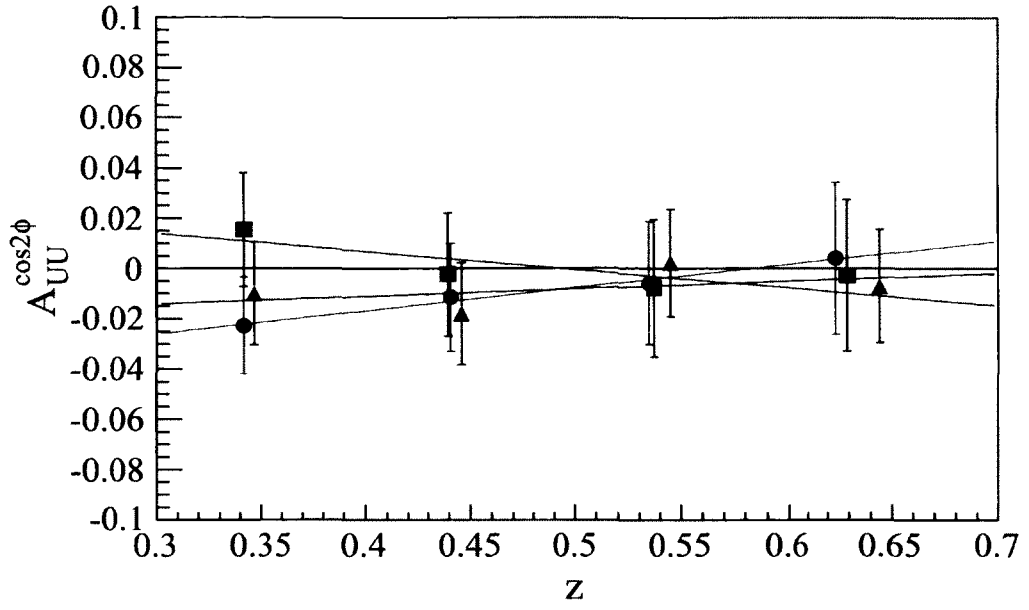

FIG. 158: $A_{UU}^{\cos 2\phi_h}(z)$ from simultaneous fits, together with a linear fit of the z dependence. Red: π^+, blue: π^- and green: π^0

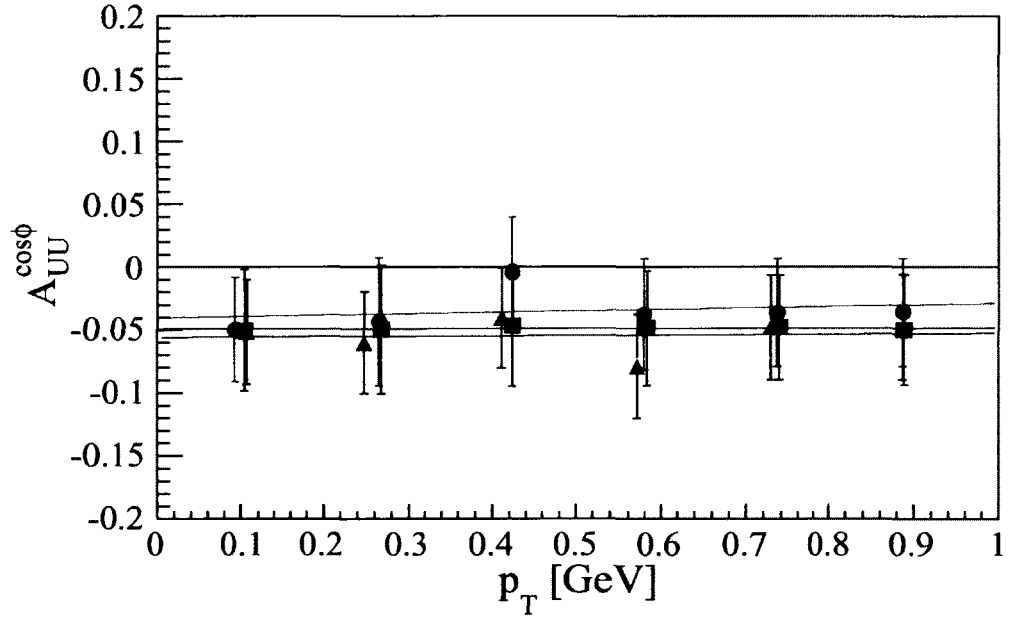

FIG. 159: $A_{UU}^{\cos\phi_h}(P_{h\perp})$ from simultaneous fits, together with a linear fit of the $P_{h\perp}$ dependence. Red: π^+, blue: π^- and green: π^0

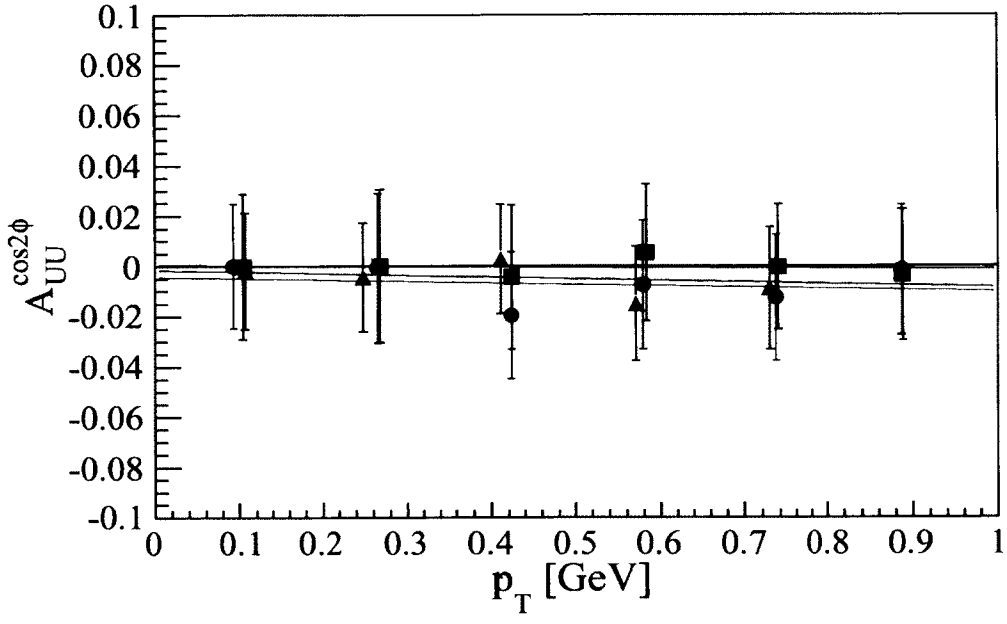

FIG. 160: $A_{UU}^{\cos 2\phi_h}(P_{h_\perp})$ from simultaneous fits, together with a linear fit of the $P_{h_\perp}$ dependence. Red: π^+, blue: π^- and green: π^0

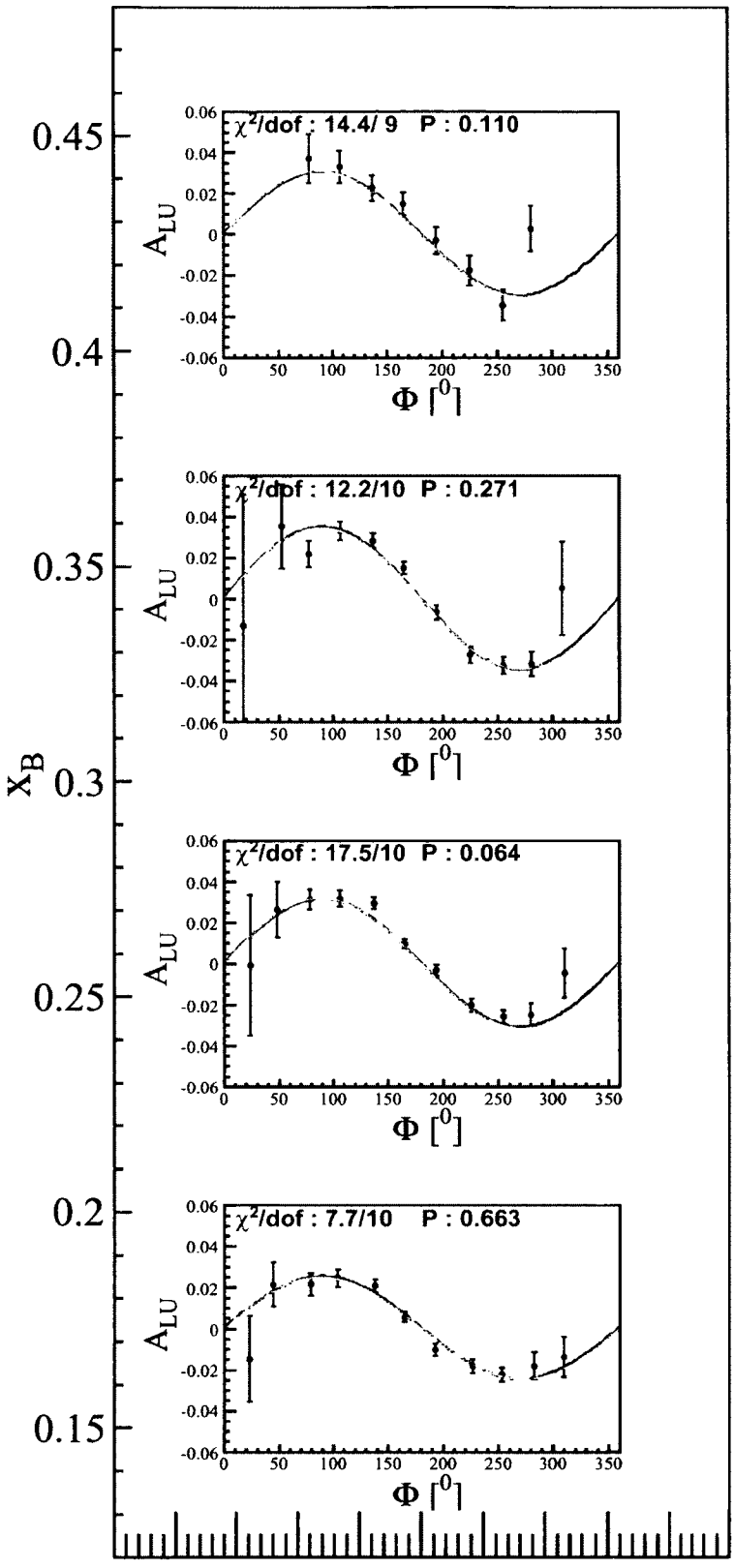

FIG. 161: $A_{LU}(x_B)$ fits for π^+. Cyan: without any extra term in the denominator. Golden: simultaneous fits with both extra terms in the denominators.

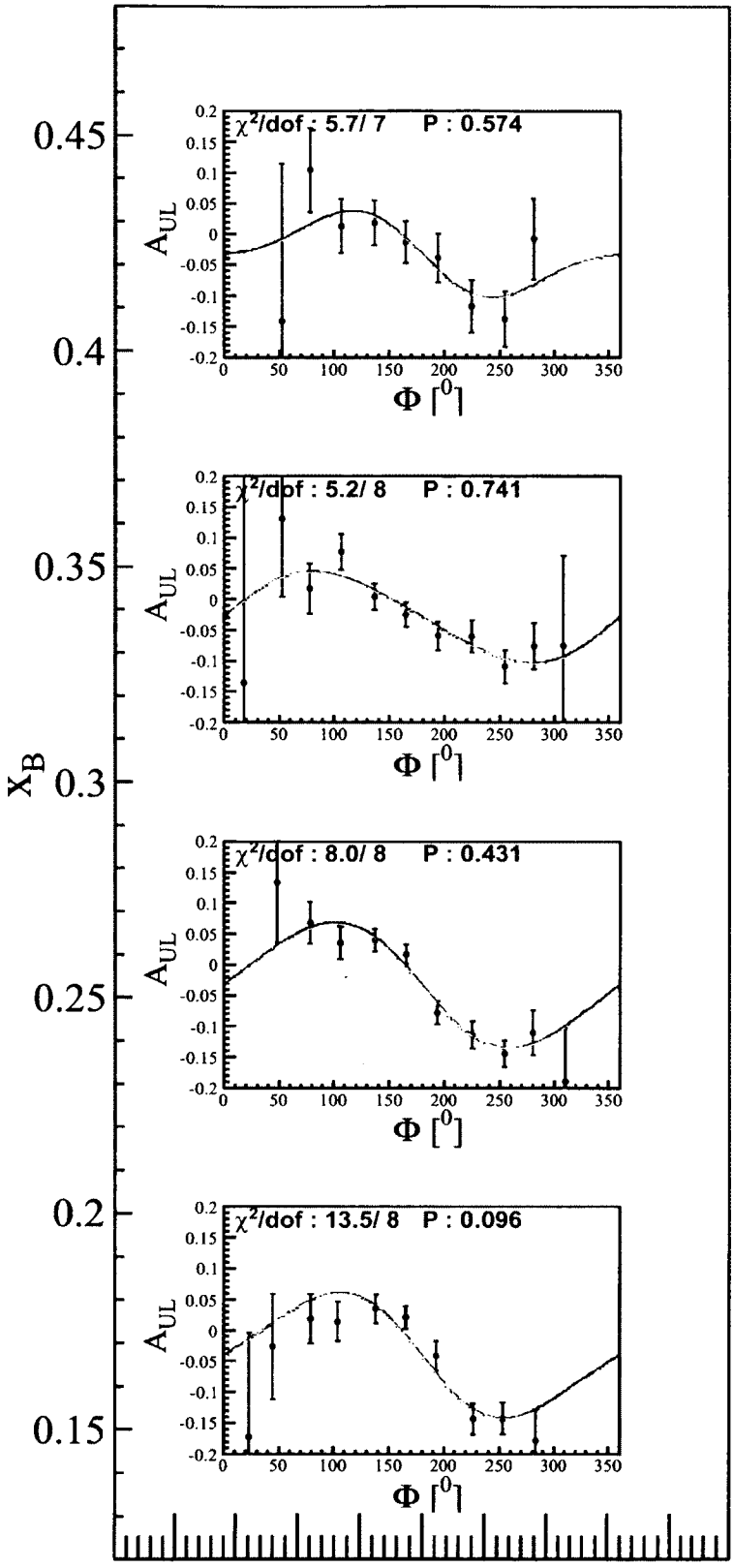

FIG. 162: $A_{UL}(x_B)$ fits for π^+. Cyan: without any extra term in the denominator. Golden: simultaneous fits with both extra terms in the denominators.

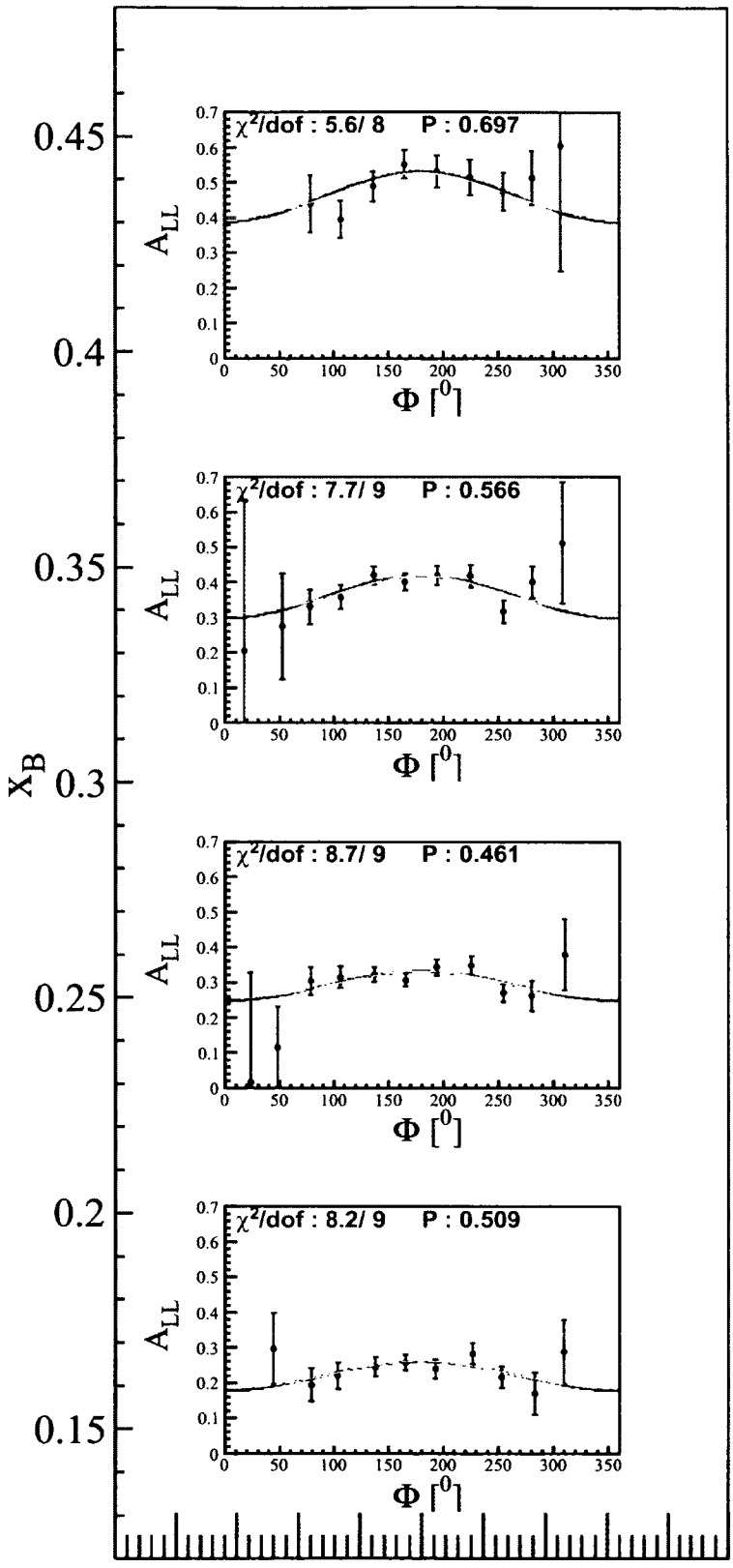

FIG. 163: $A_{LL}(x_B)$ fits for π^+. Cyan: without any extra term in the denominator. Golden: simultaneous fits with both extra terms in the denominators.

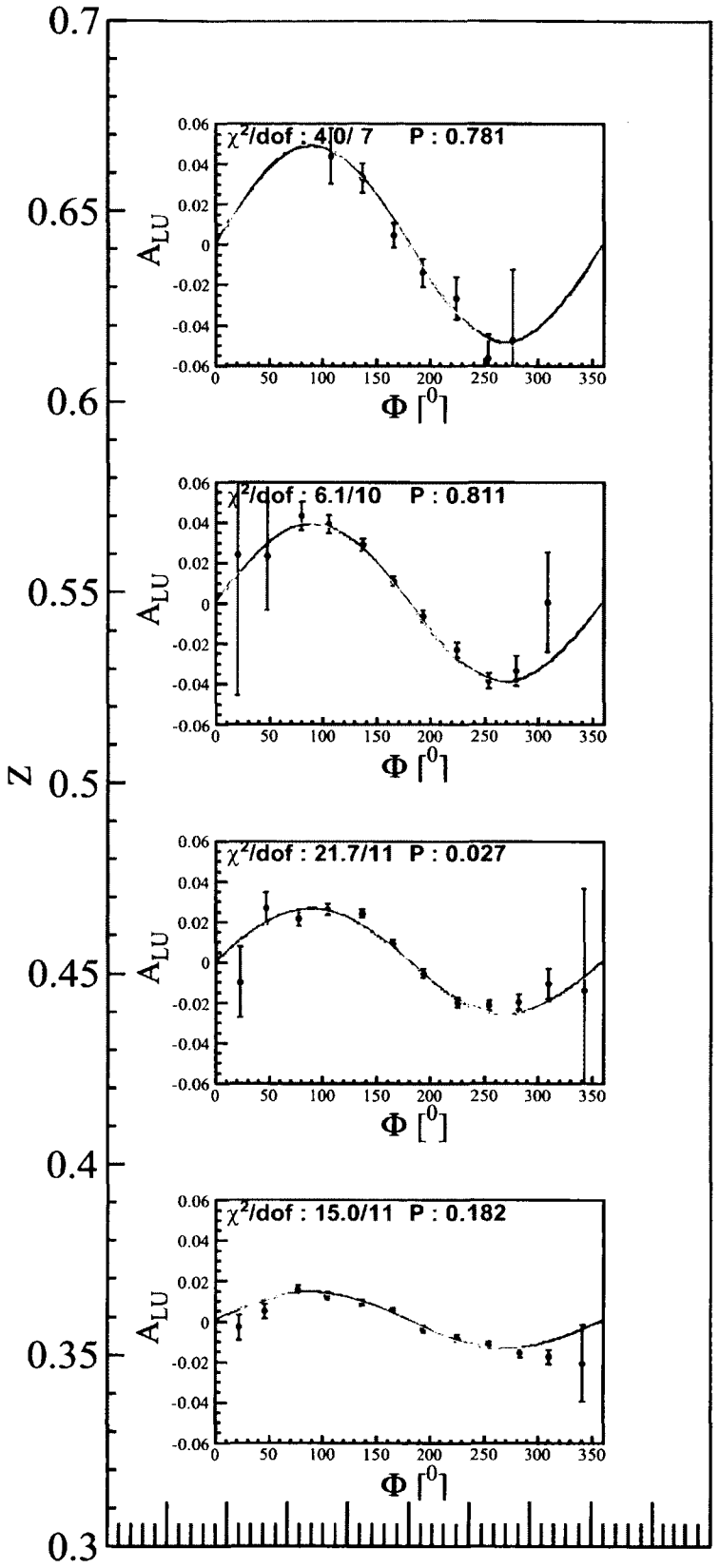

FIG. 164: $A_{LU}(z)$ fits for π^+. Cyan: without any extra term in the denominator. Golden: simultaneous fits with both extra terms in the denominators.

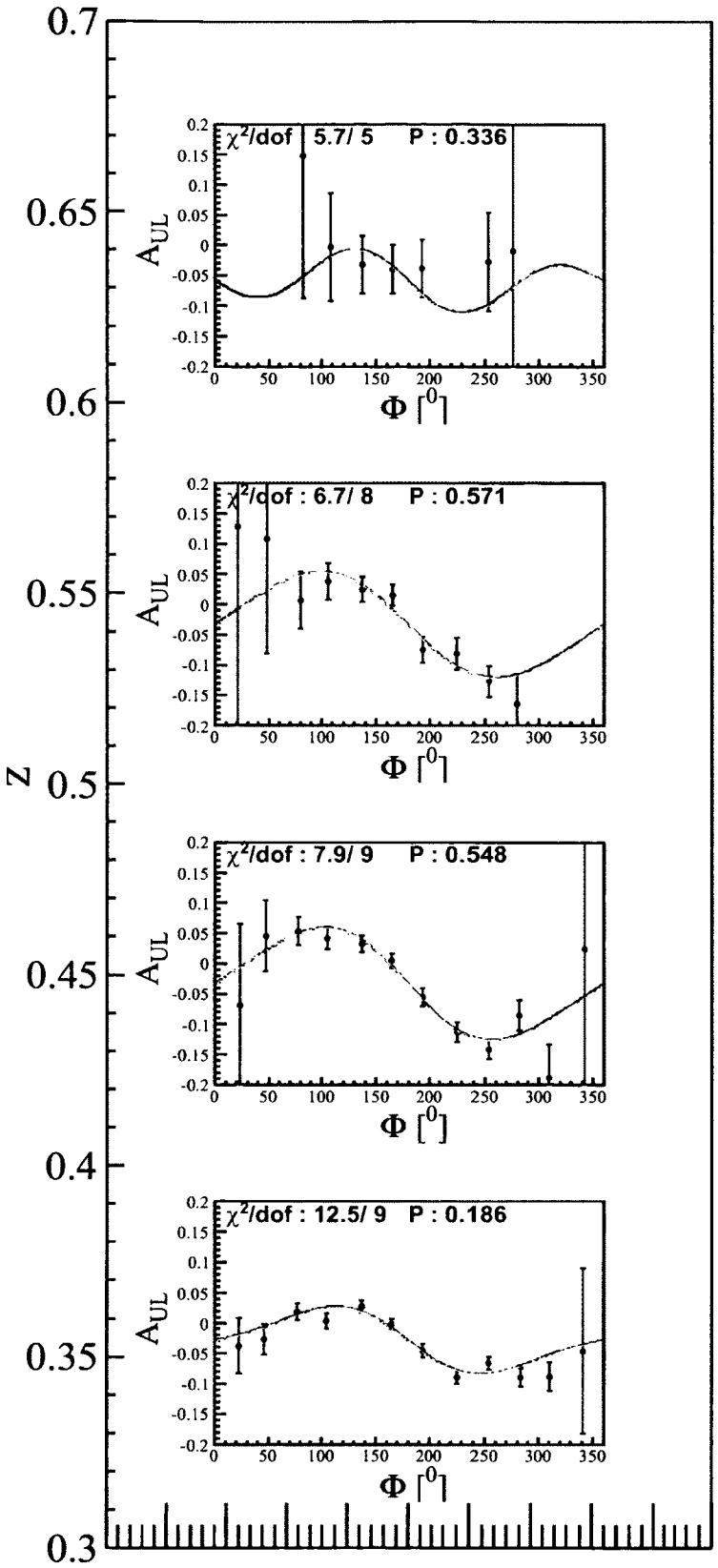

FIG. 165: $A_{UL}(z)$ fits for π^+. Cyan: without any extra term in the denominator. Golden: simultaneous fits with both extra terms in the denominators.

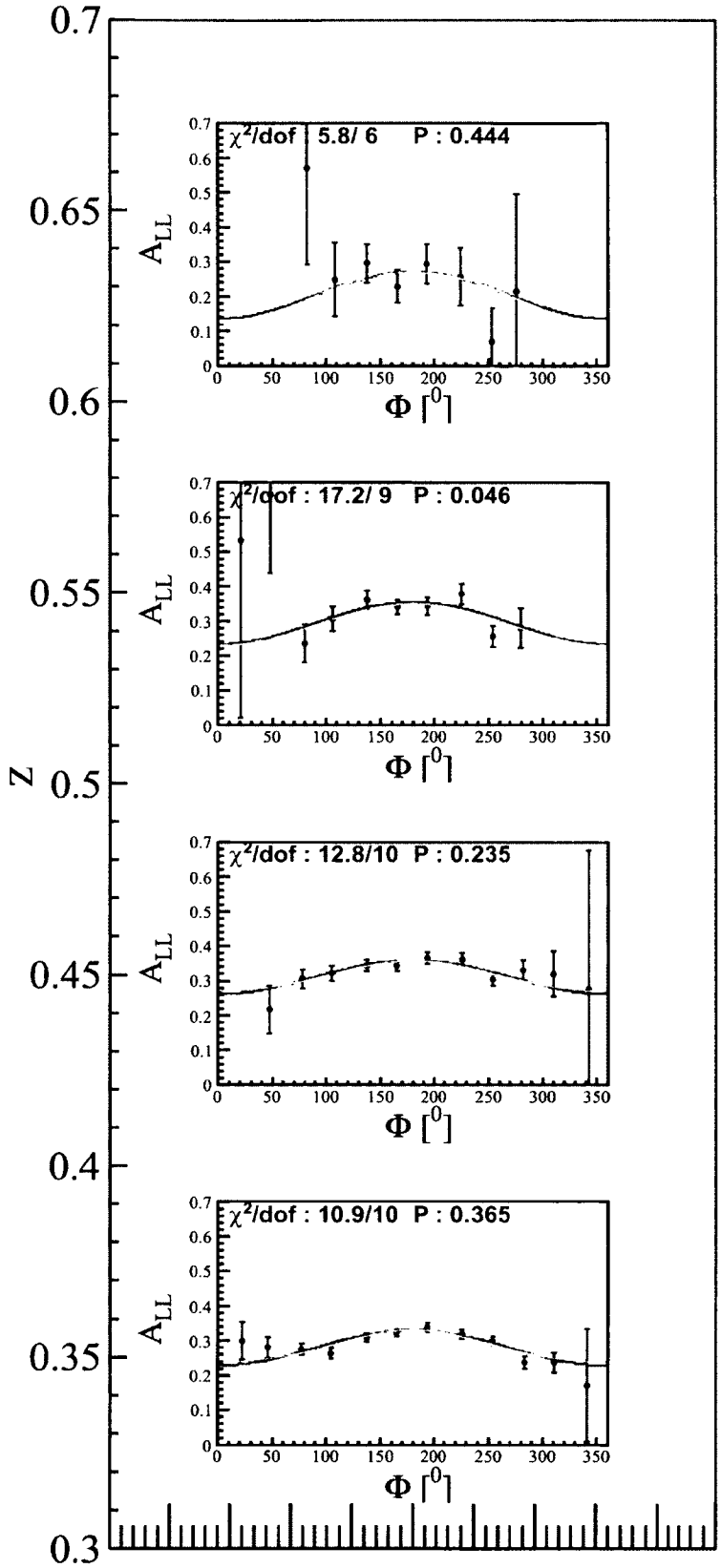

FIG. 166: $A_{LL}(z)$ fits for π^+. Cyan: without any extra term in the denominator. Golden: simultaneous fits with both extra terms in the denominators.

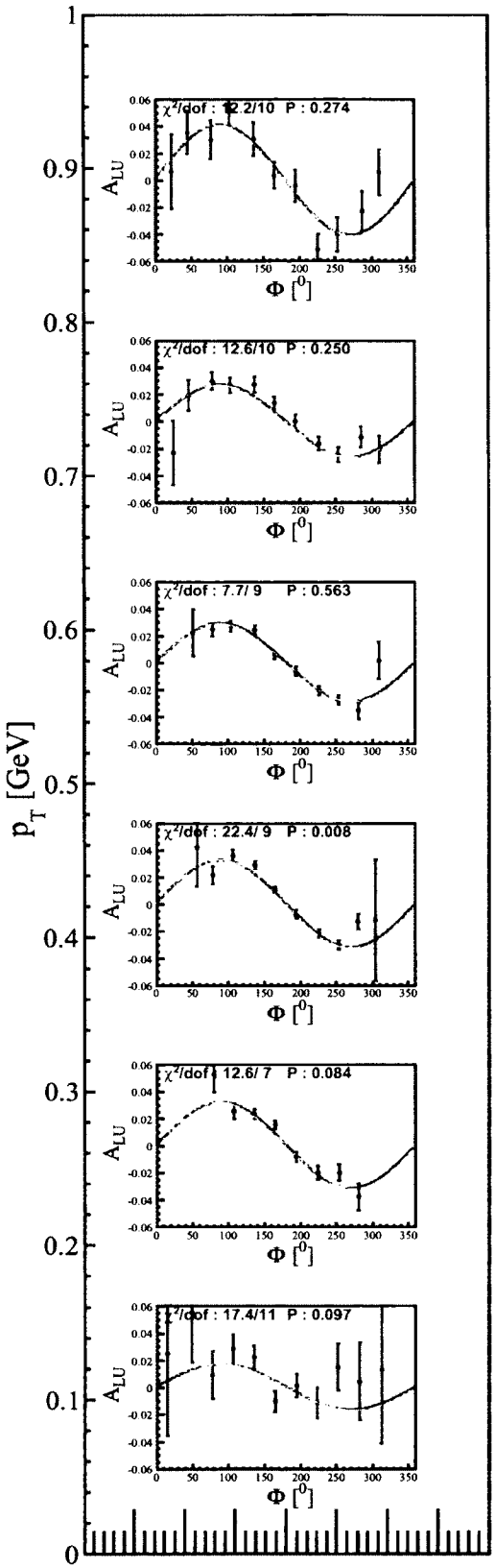

FIG. 167: $A_{LU}(P_{h_\perp})$ fits for π^+. Cyan: without any extra term in the denominator. Golden: simultaneous fits with both extra terms in the denominators.

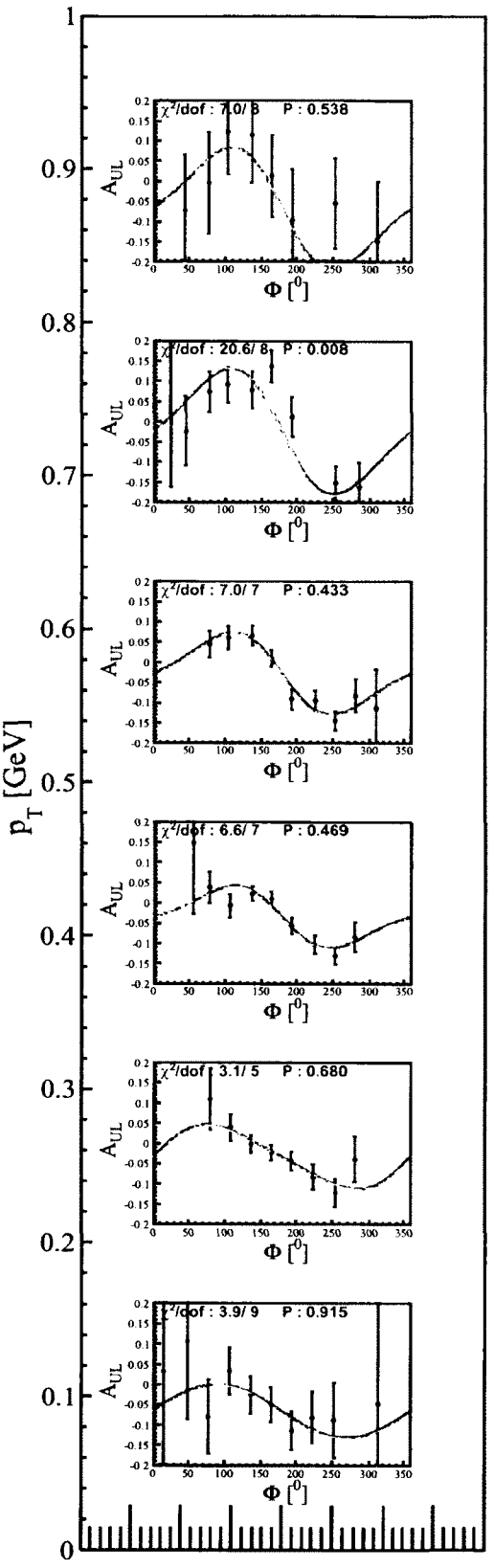

FIG. 168: $A_{UL}(P_{h_\perp})$ fits for π^+. Cyan: without any extra term in the denominator. Golden: simultaneous fits with both extra terms in the denominators.

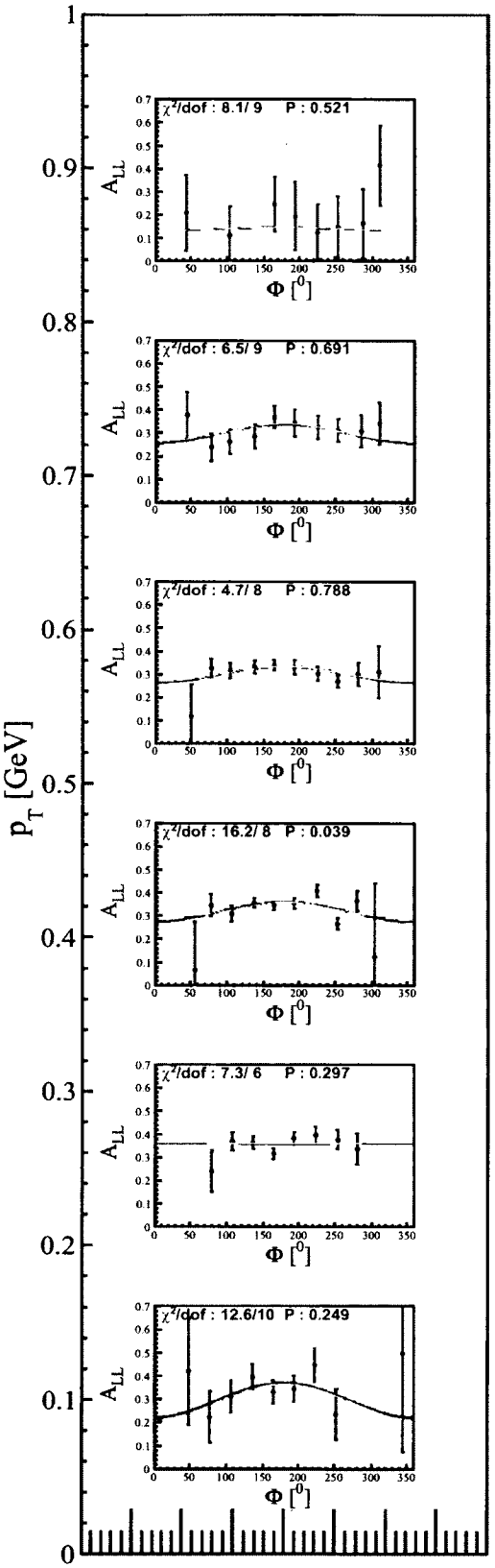

FIG. 169: $A_{LL}(P_{h_\perp})$ fits for π^+. Cyan: without any extra term in the denominator. Golden: simultaneous fits with both extra terms in the denominators.

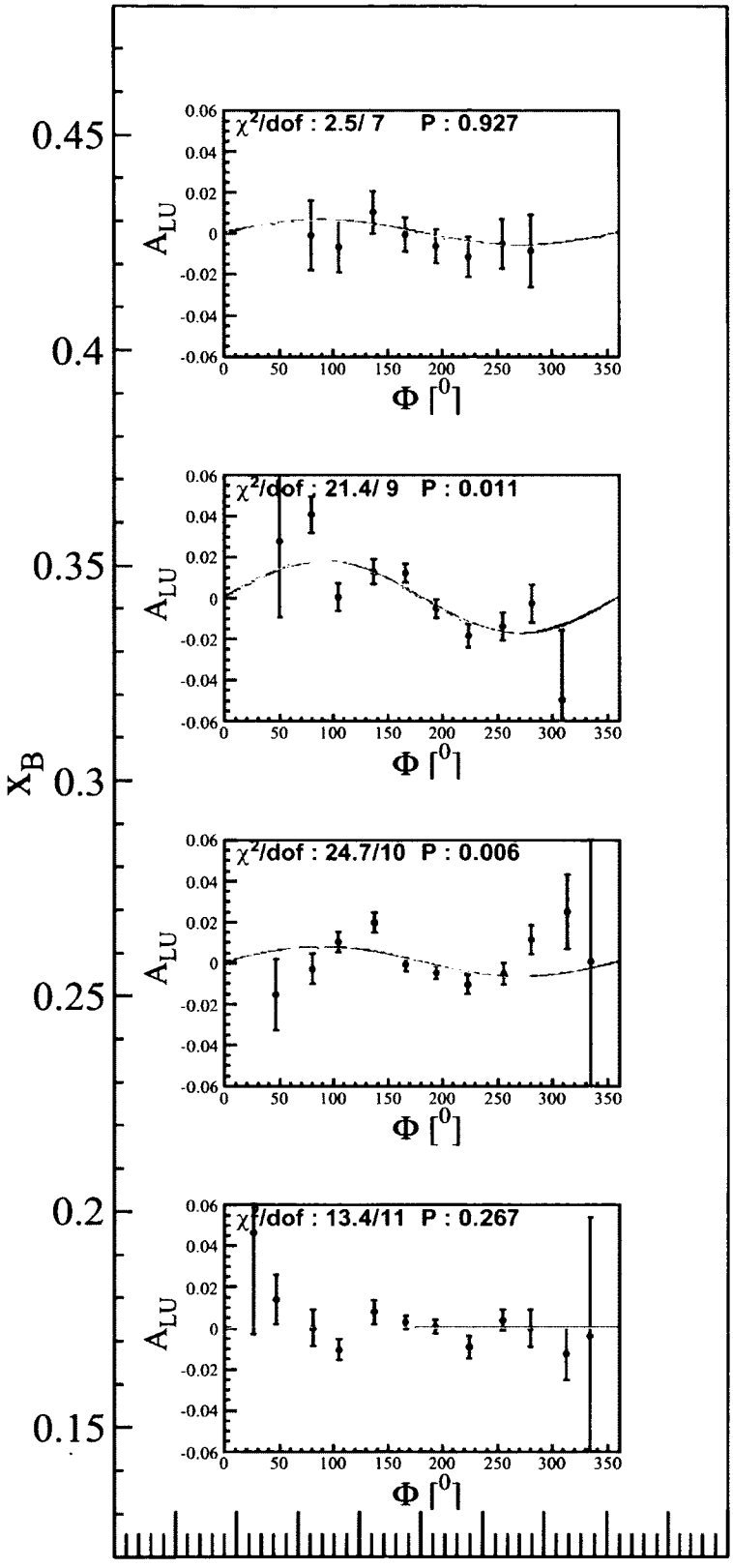

FIG. 170: $A_{LU}(x_B)$ fits for π^-. Cyan: without any extra term in the denominator. Golden: simultaneous fits with both extra terms in the denominators.

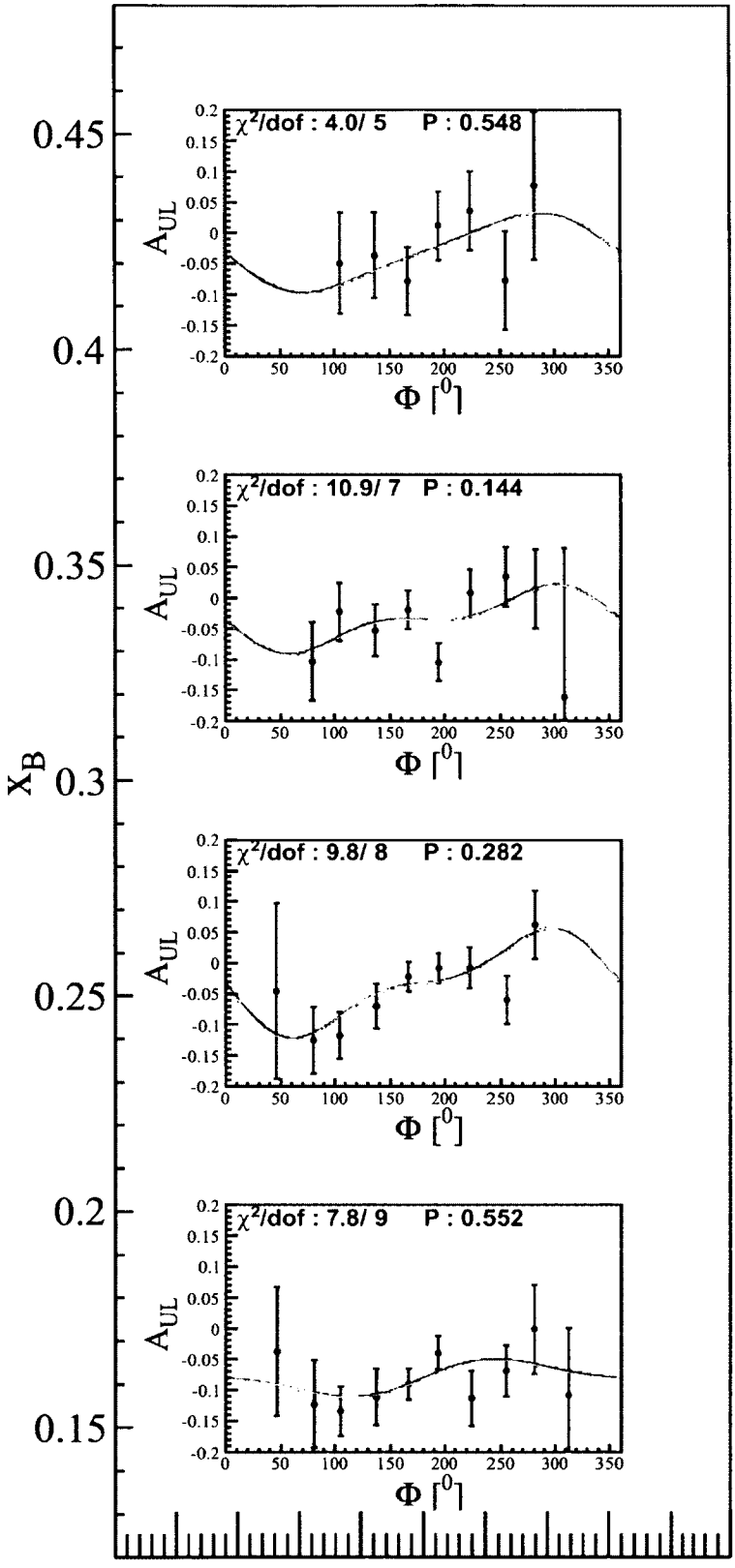

FIG. 171: $A_{UL}(x_B)$ fits for π^-. Cyan: without any extra term in the denominator. Golden: simultaneous fits with both extra terms in the denominators.

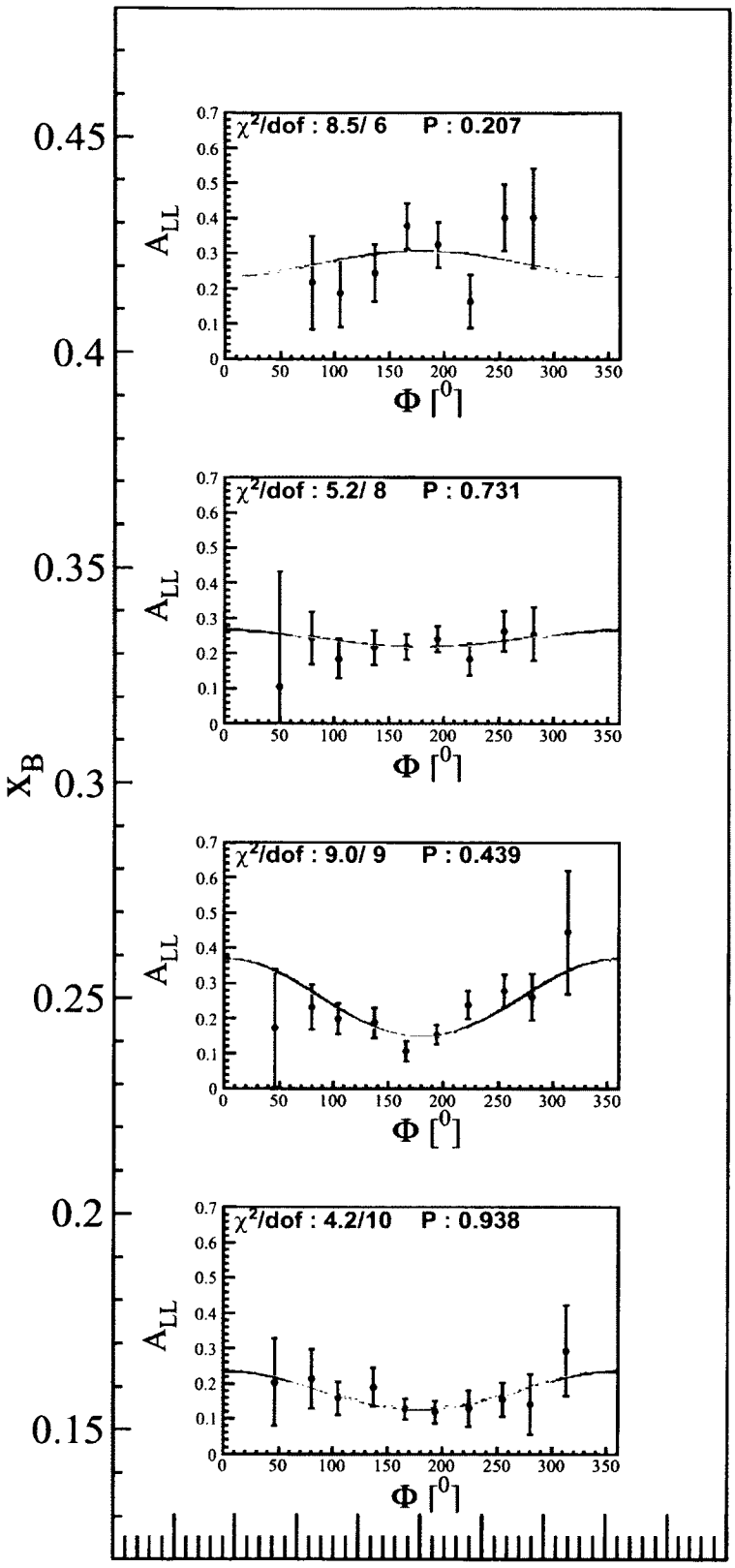

FIG. 172: $A_{LL}(x_B)$ fits for π^-. Cyan: without any extra term in the denominator. Golden: simultaneous fits with both extra terms in the denominators.

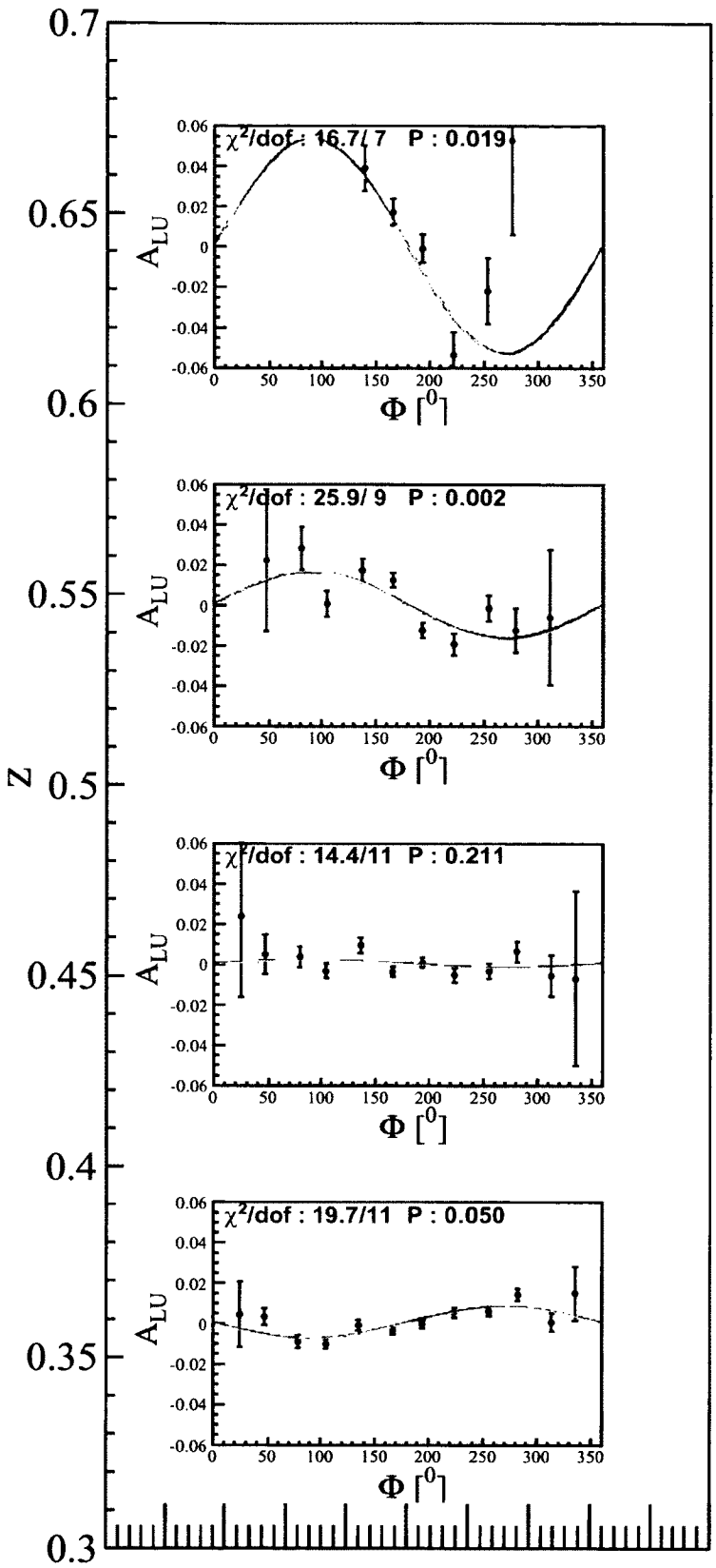

FIG. 173: $A_{LU}(z)$ fits for π^-. Cyan: without any extra term in the denominator. Golden: simultaneous fits with both extra terms in the denominators.

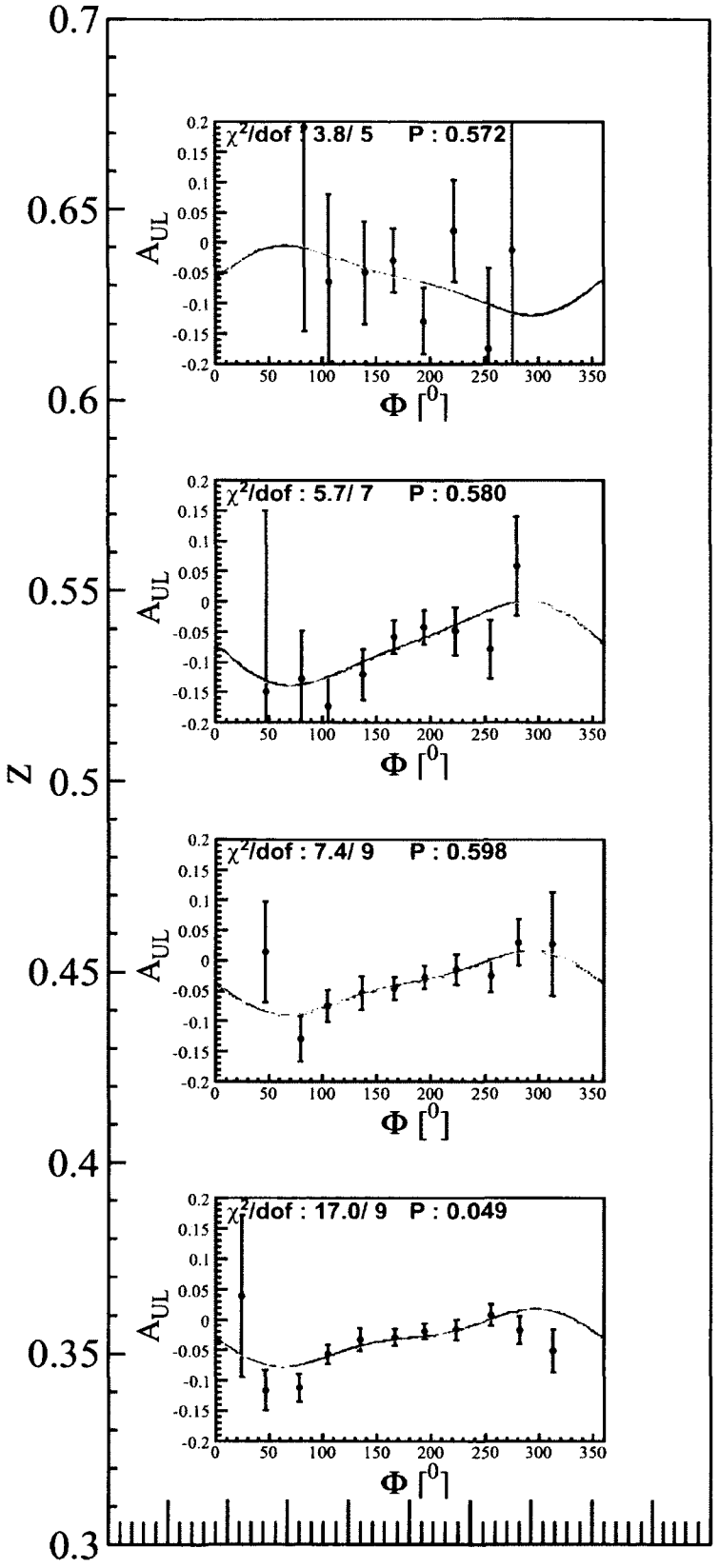

FIG. 174: $A_{UL}(z)$ fits for π^-. Cyan: without any extra term in the denominator. Golden: simultaneous fits with both extra terms in the denominators.

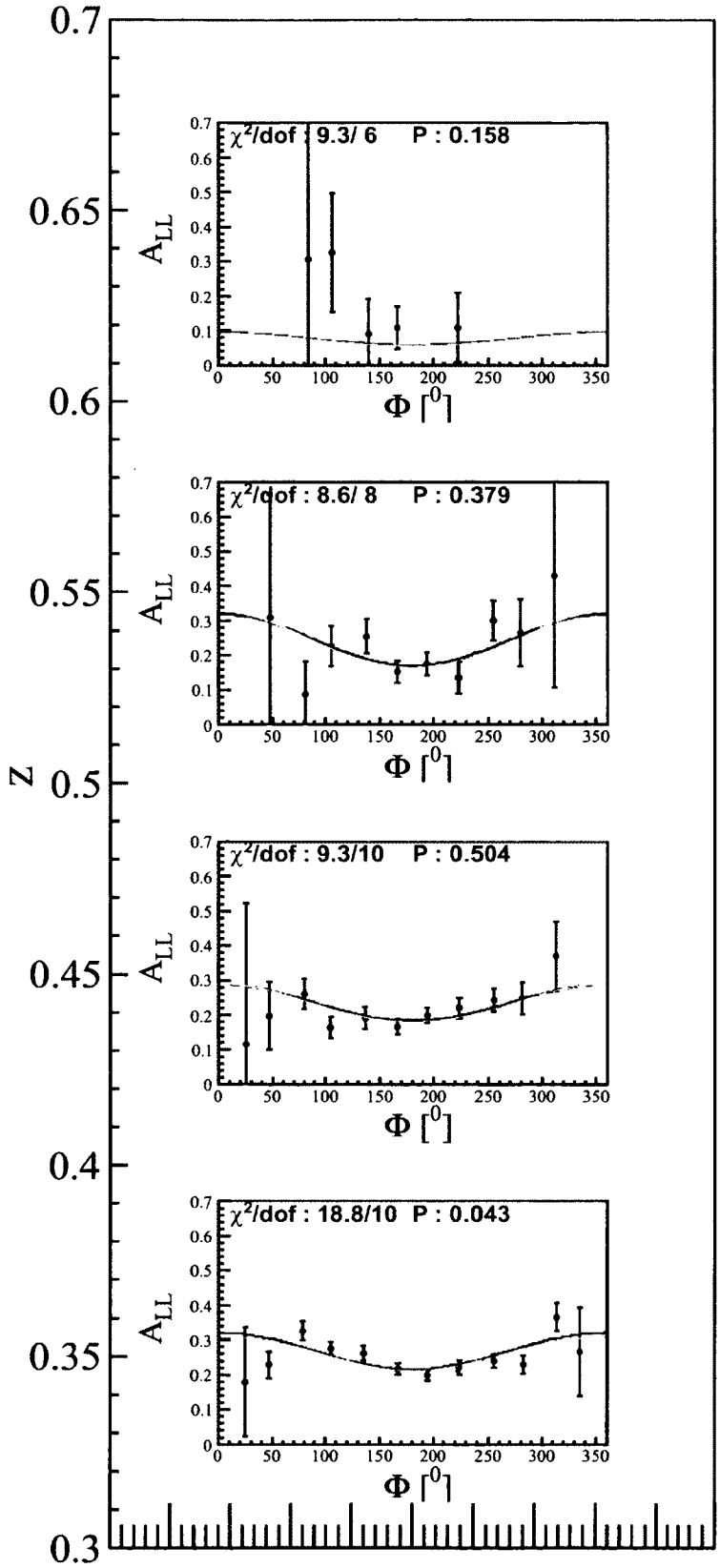

FIG. 175: $A_{LL}(z)$ fits for π^-. Cyan: without any extra term in the denominator. Golden: simultaneous fits with both extra terms in the denominators.

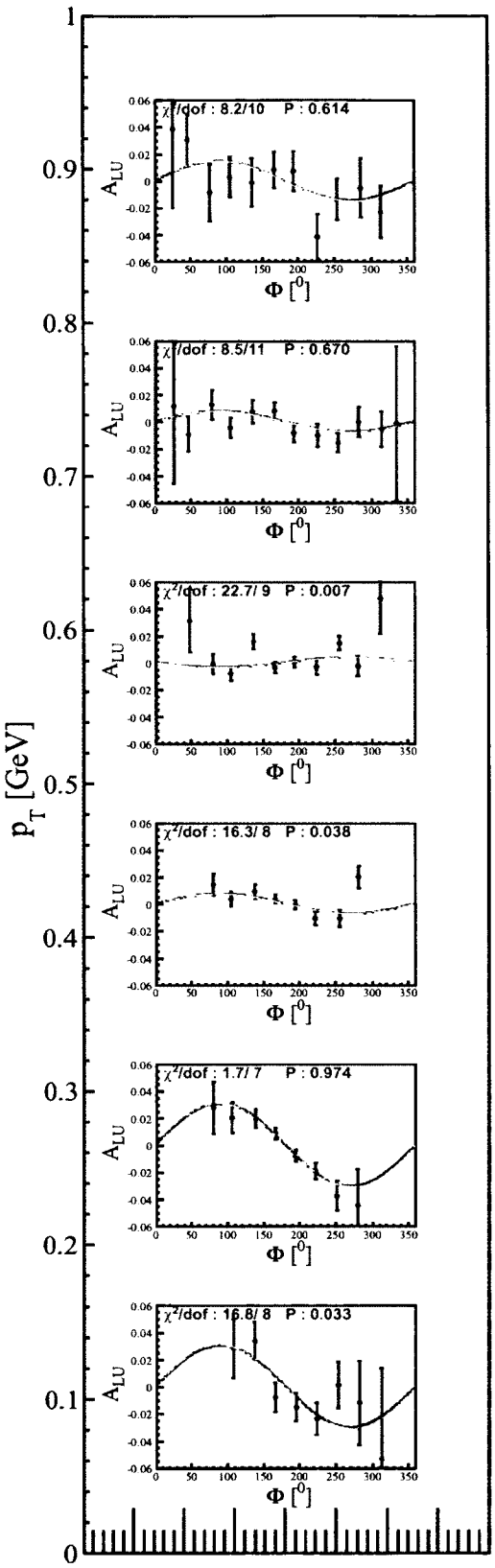

FIG. 176: $A_{LU}(P_{h_\perp})$ fits for π^-. Cyan: without any extra term in the denominator. Golden: simultaneous fits with both extra terms in the denominators.

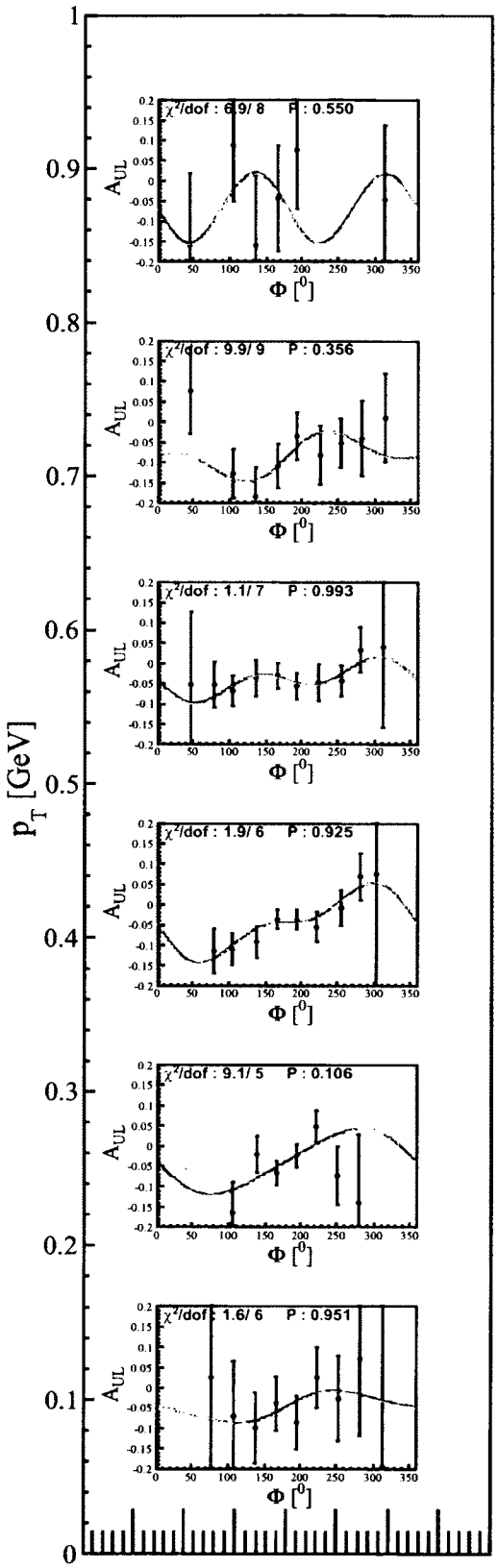

FIG. 177: $A_{UL}(P_{h_\perp})$ fits for π^-. Cyan: without any extra term in the denominator. Golden: simultaneous fits with both extra terms in the denominators.

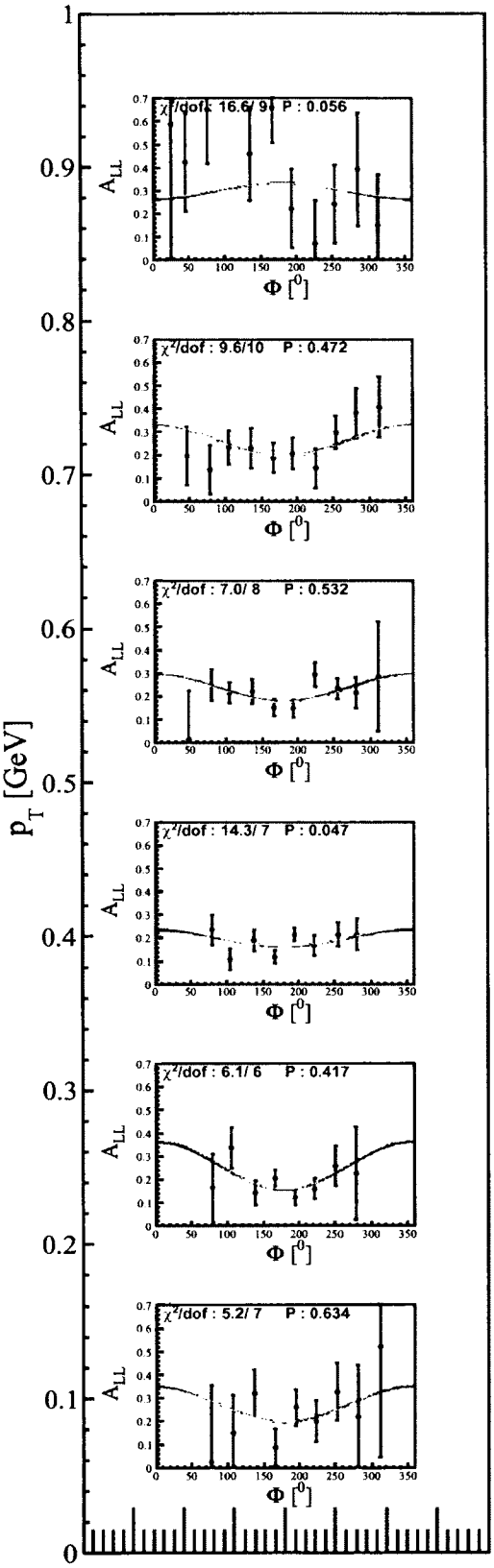

FIG. 178: $A_{LL}(P_{h_\perp})$ fits for π^-. Cyan: without any extra term in the denominator. Golden: simultaneous fits with both extra terms in the denominators.

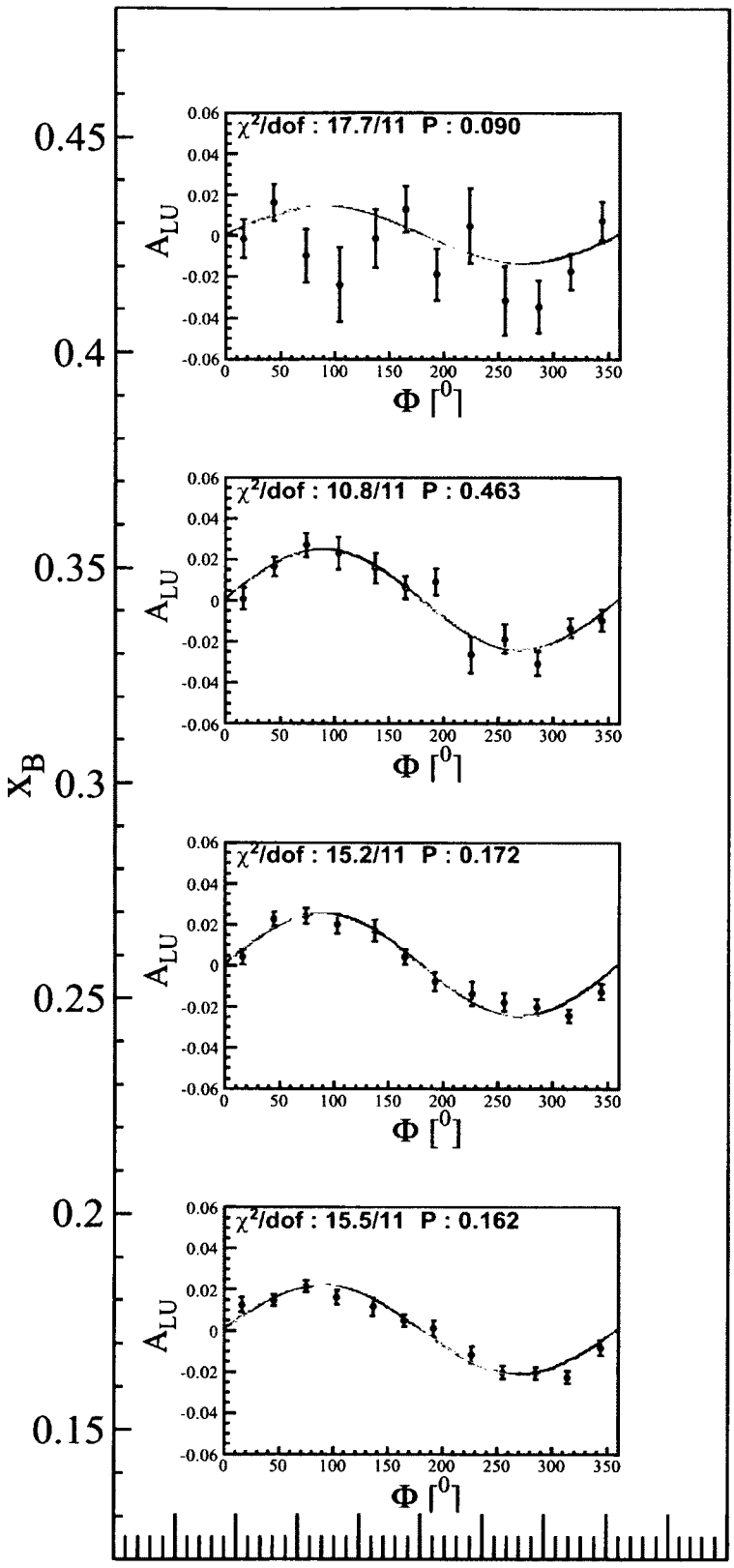

FIG. 179: $A_{LU}(x_B)$ fits for π^0. Cyan: without any extra term in the denominator. Golden: simultaneous fits with both extra terms in the denominators.

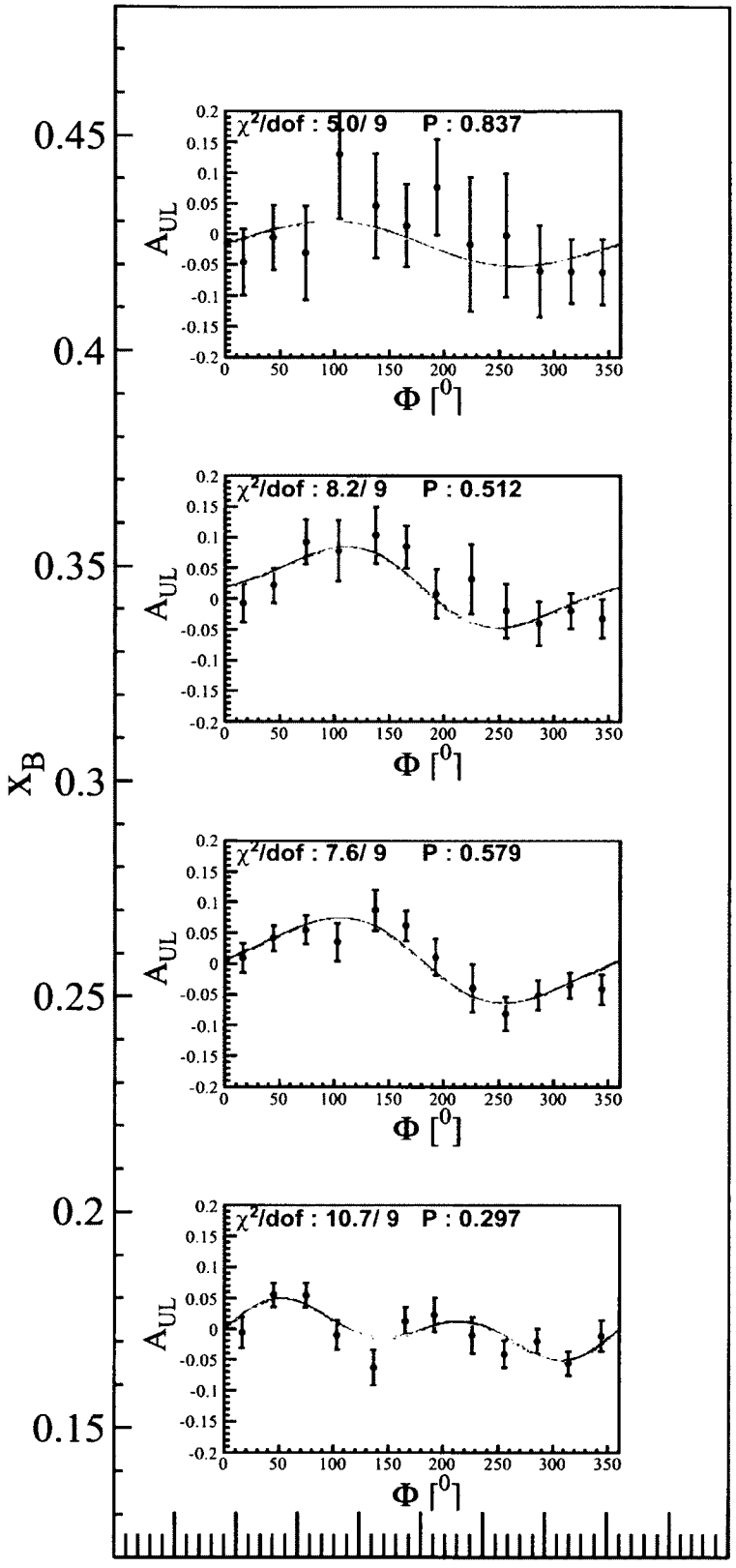

FIG. 180: $A_{UL}(x_B)$ fits for π^0. Cyan: without any extra term in the denominator. Golden: simultaneous fits with both extra terms in the denominators.

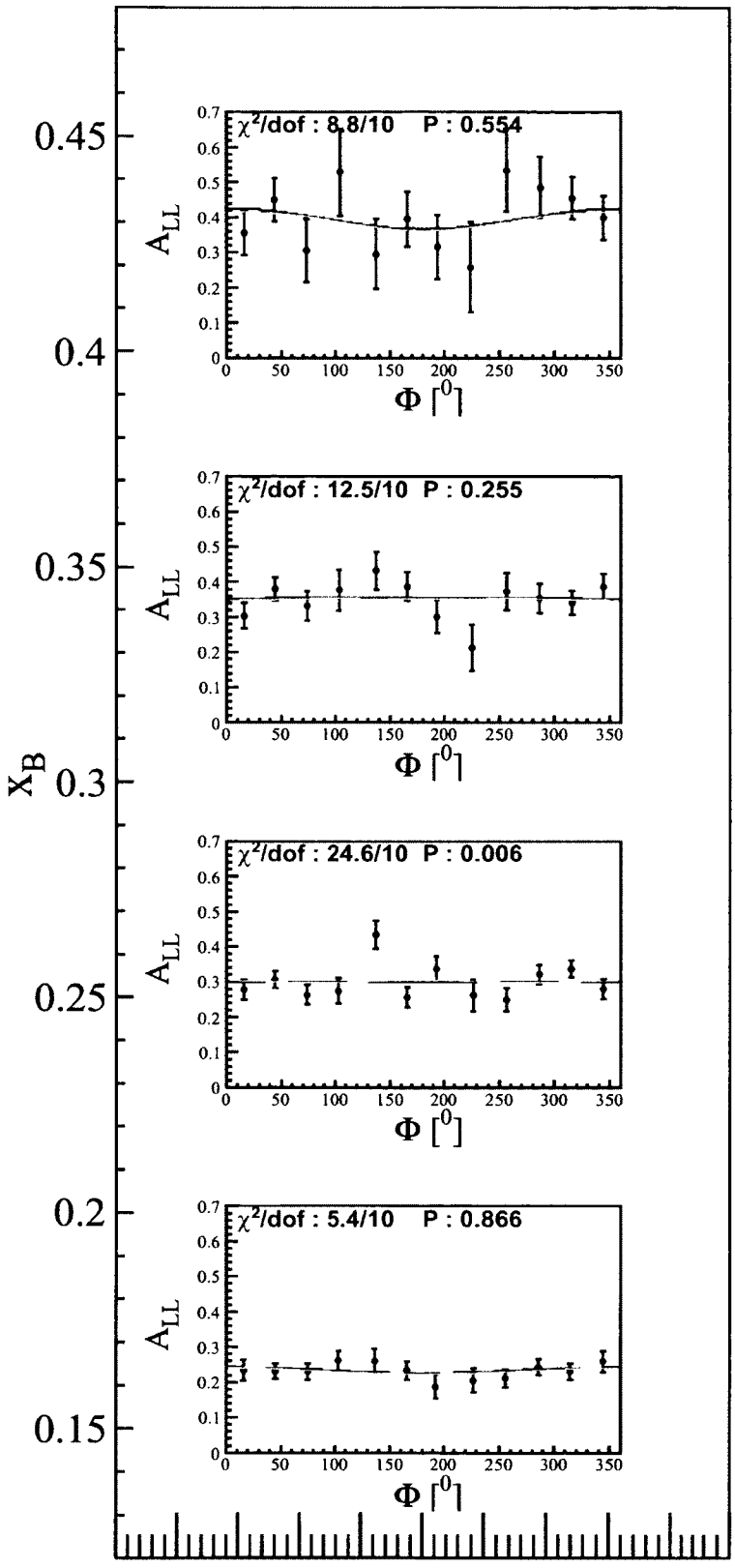

FIG. 181: $A_{LL}(x_B)$ fits for π^0. Cyan: without any extra term in the denominator. Golden: simultaneous fits with both extra terms in the denominators.

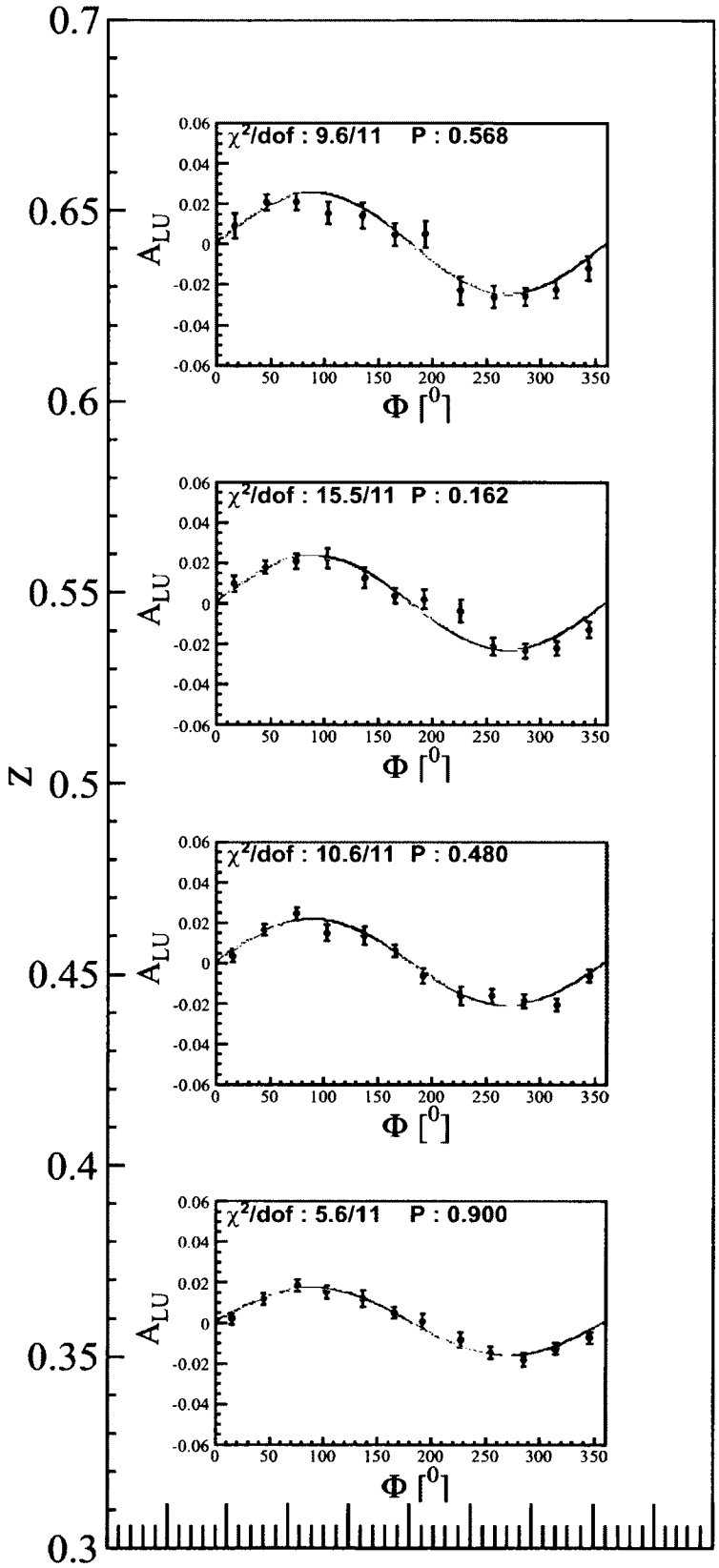

FIG. 182: $A_{LU}(z)$ fits for π^0. Cyan: without any extra term in the denominator. Golden: simultaneous fits with both extra terms in the denominators.

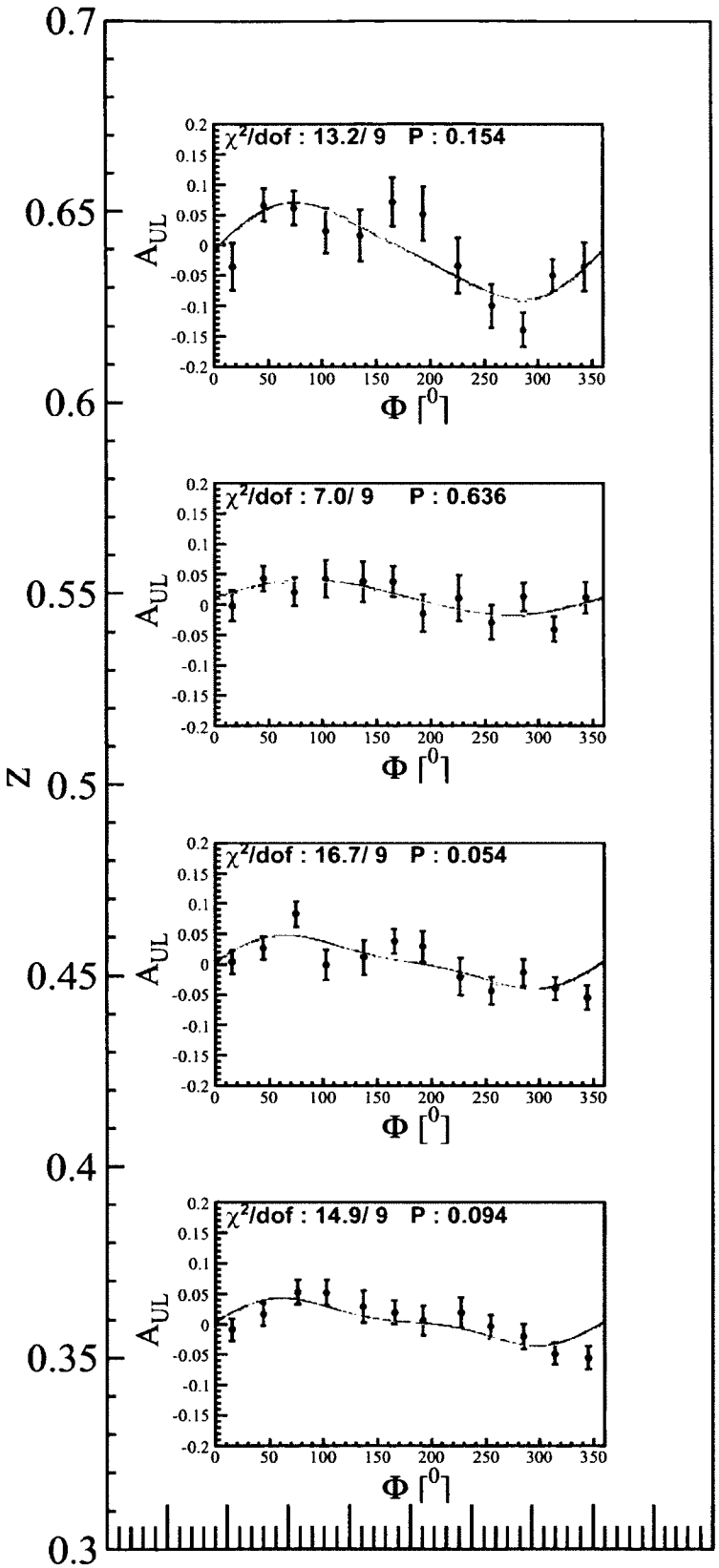

FIG. 183: $A_{UL}(z)$ fits for π^0. Cyan: without any extra term in the denominator. Golden: simultaneous fits with both extra terms in the denominators.

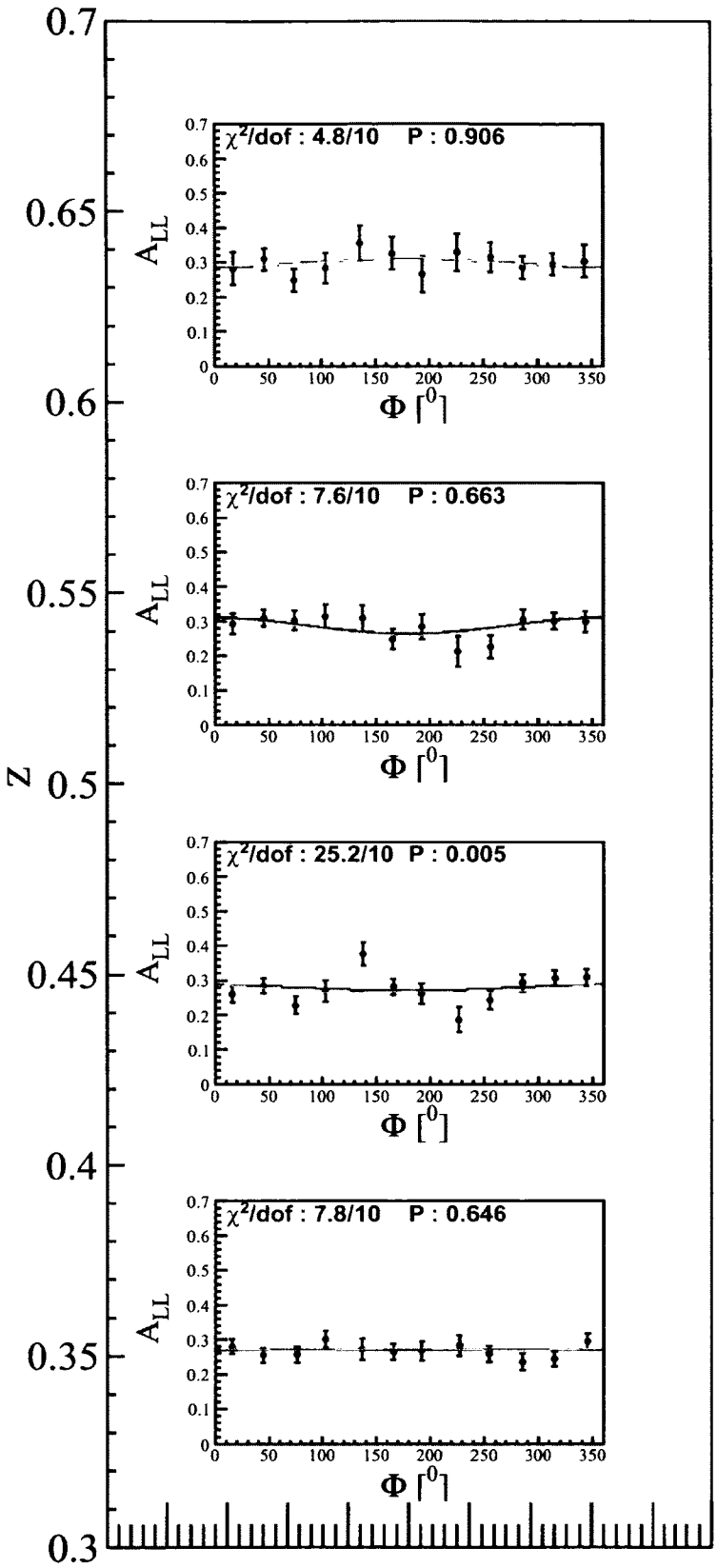

FIG. 184: $A_{LL}(z)$ fits for π^0. Cyan: without any extra term in the denominator. Golden: simultaneous fits with both extra terms in the denominators.

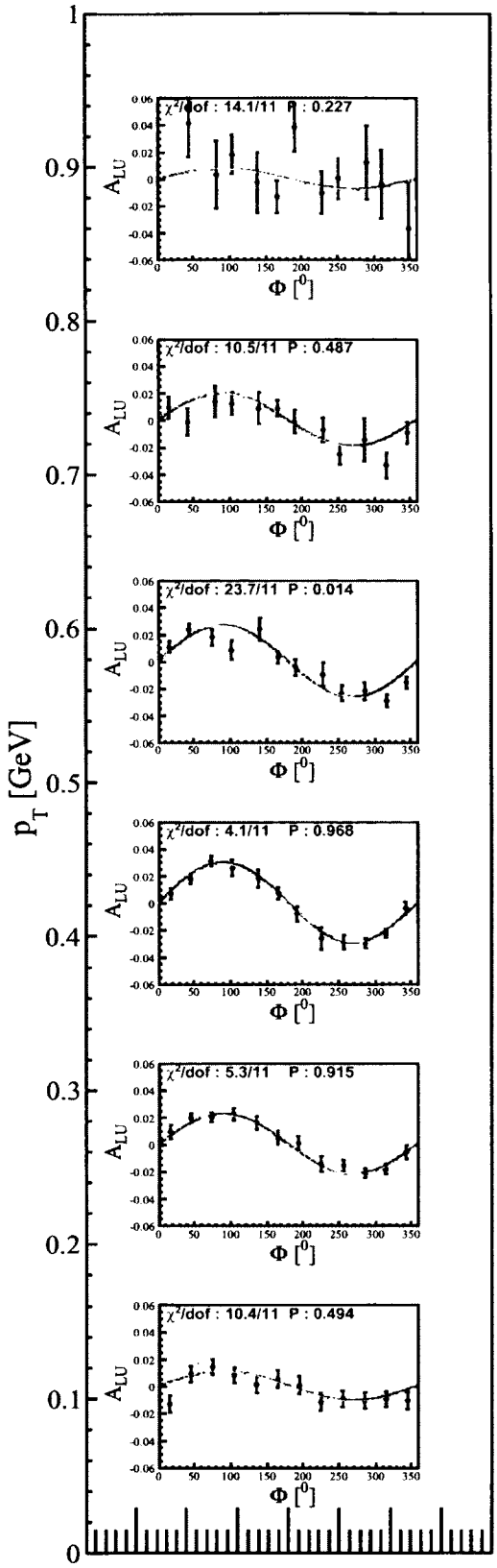

FIG. 185: $A_{LU}(P_{h_\perp})$ fits for π^0. Cyan: without any extra term in the denominator. Golden: simultaneous fits with both extra terms in the denominators.

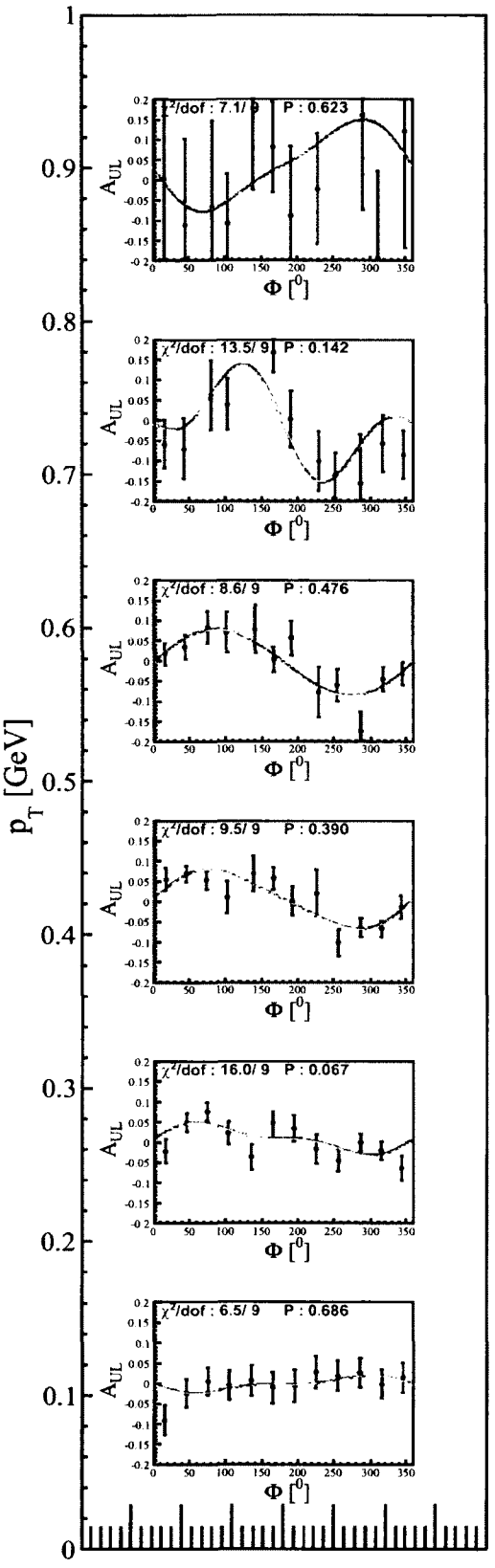

FIG. 186: $A_{UL}(P_{h_\perp})$ fits for π^0. Cyan: without any extra term in the denominator. Golden: simultaneous fits with both extra terms in the denominators.

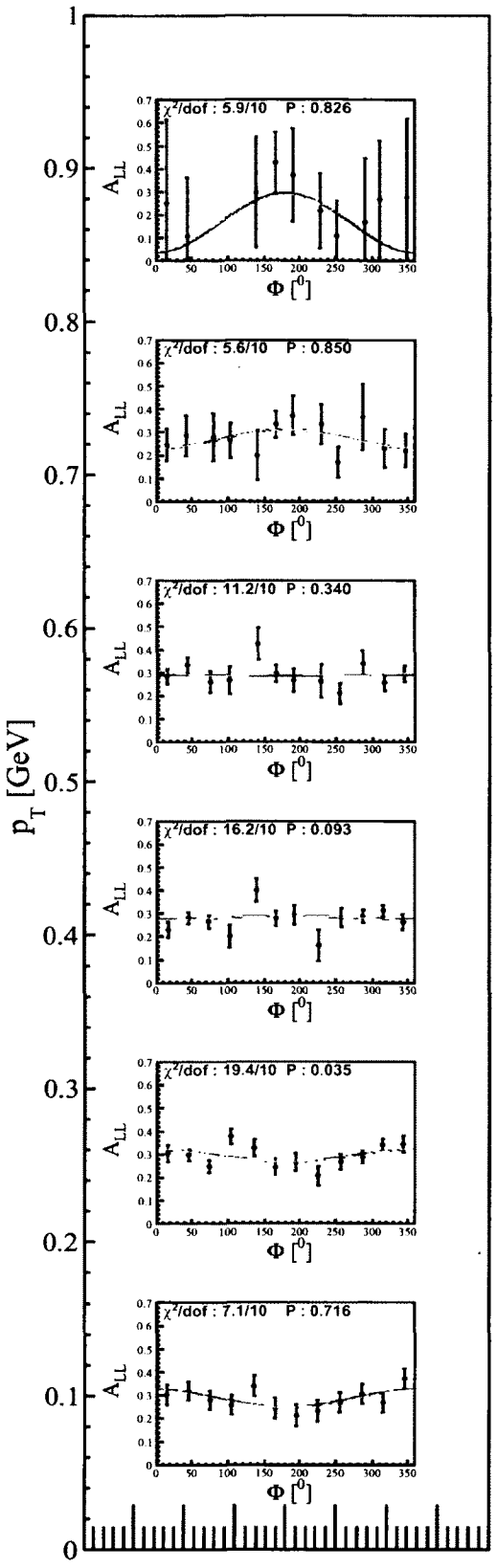

FIG. 187: $A_{LL}(P_{h_\perp})$ fits for π^0. Cyan: without any extra term in the denominator. Golden: simultaneous fits with both extra terms in the denominators.

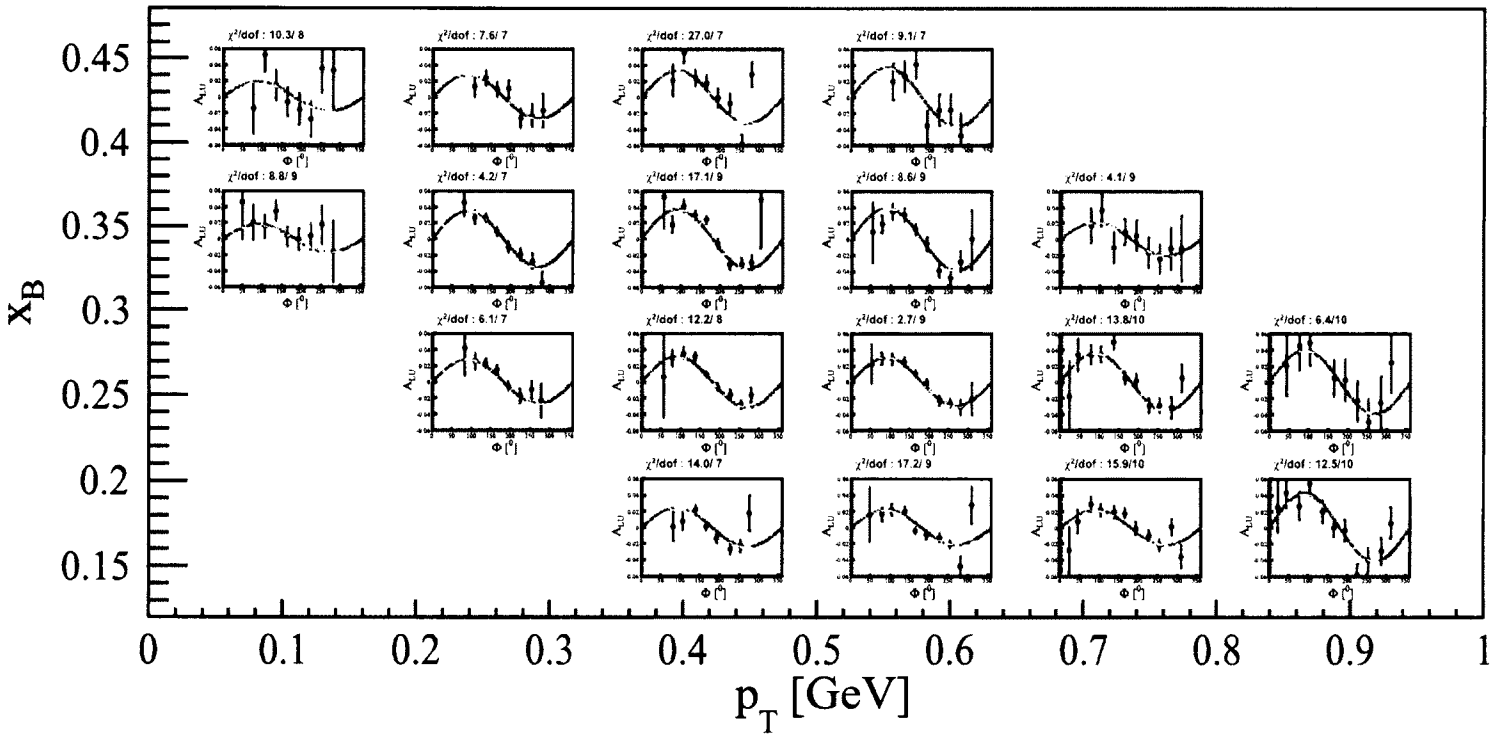

FIG. 188: $A_{LU}(x_B, P_{h_\perp})$ fits for π^+. Cyan: without any extra term in the denominator. Golden: simultaneous fits with both extra terms in the denominators.

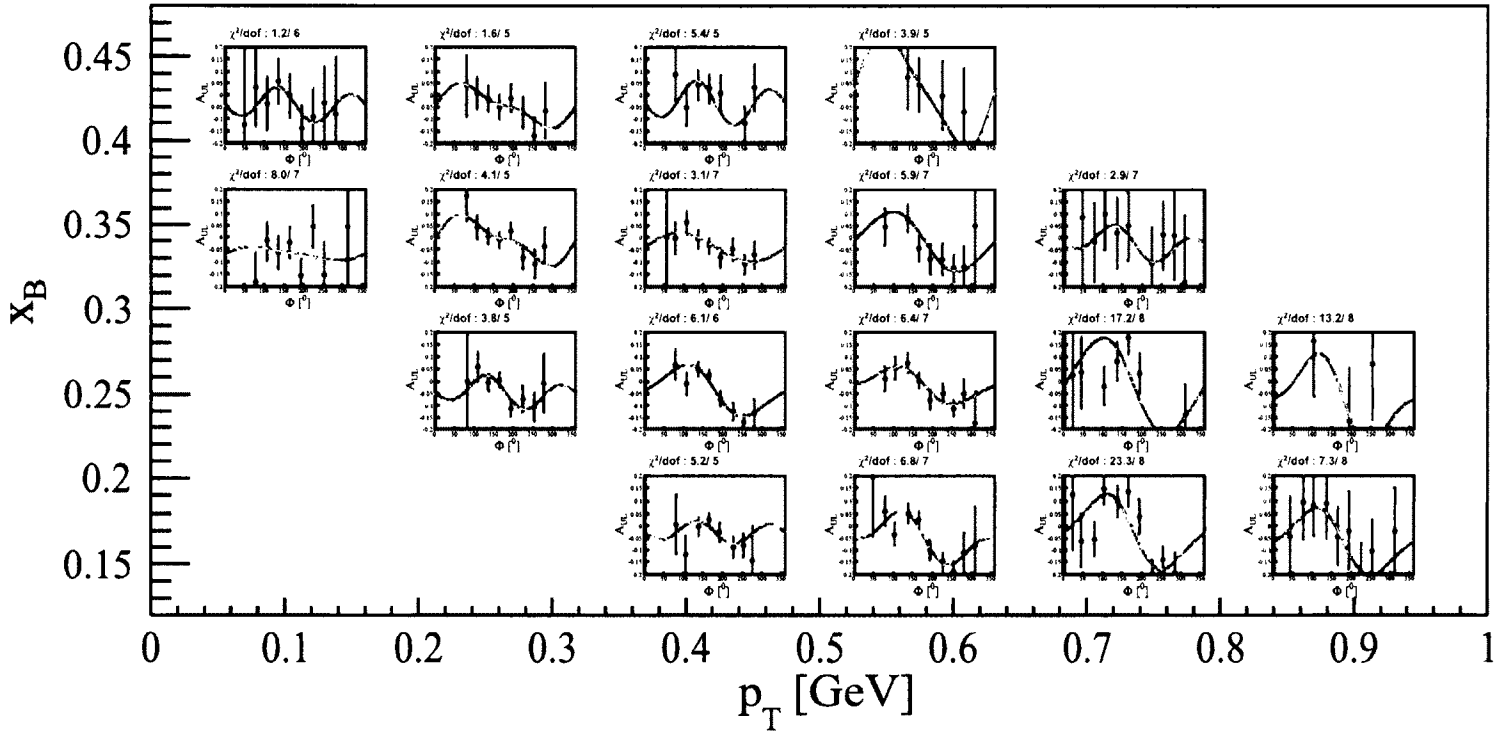

FIG. 189: $A_{UL}(x_B, P_{h_\perp})$ fits for π^+. Cyan: without any extra term in the denominator. Golden: simultaneous fits with both extra terms in the denominators.

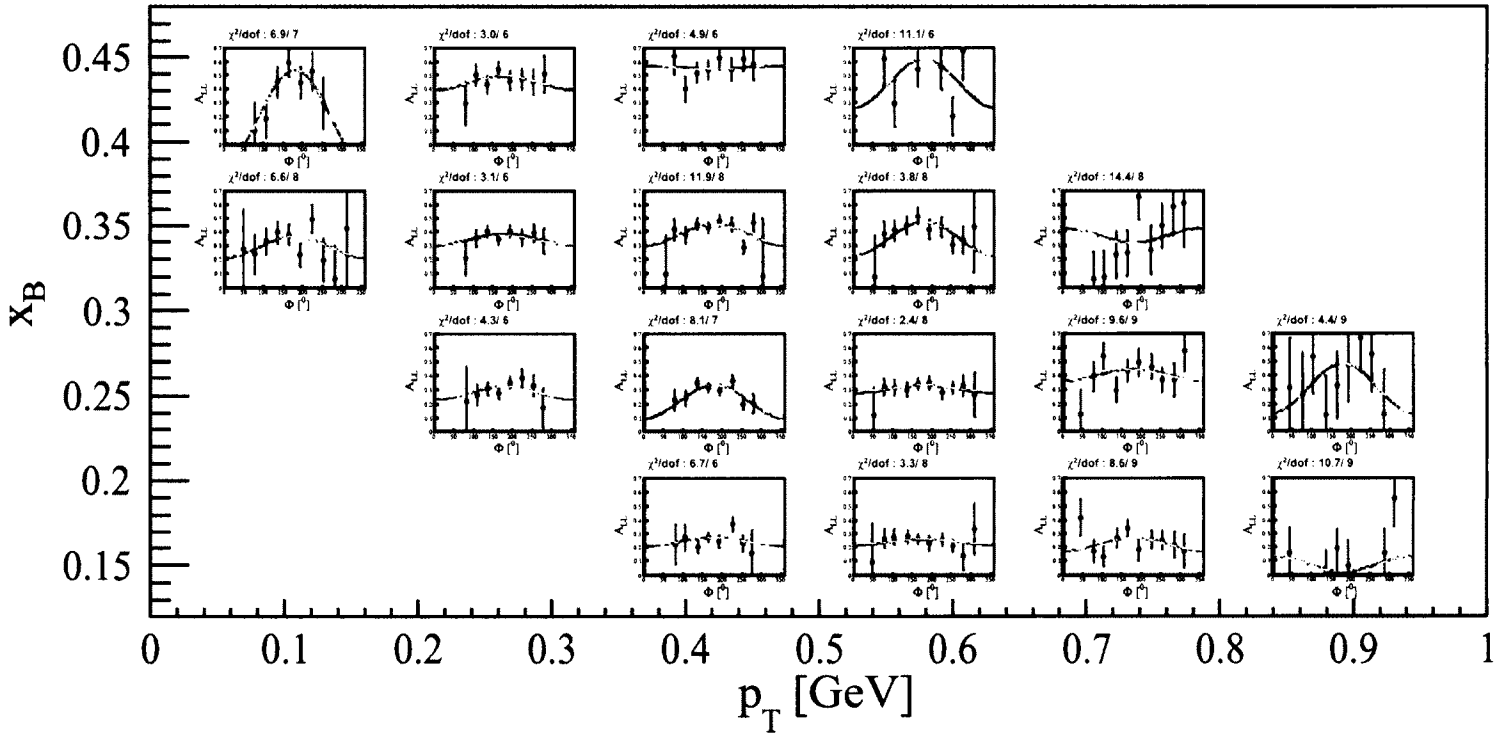

FIG. 190: $A_{LL}(x_B, P_{h_\perp})$ fits for π^+. Cyan: without any extra term in the denominator. Golden: simultaneous fits with both extra terms in the denominators.

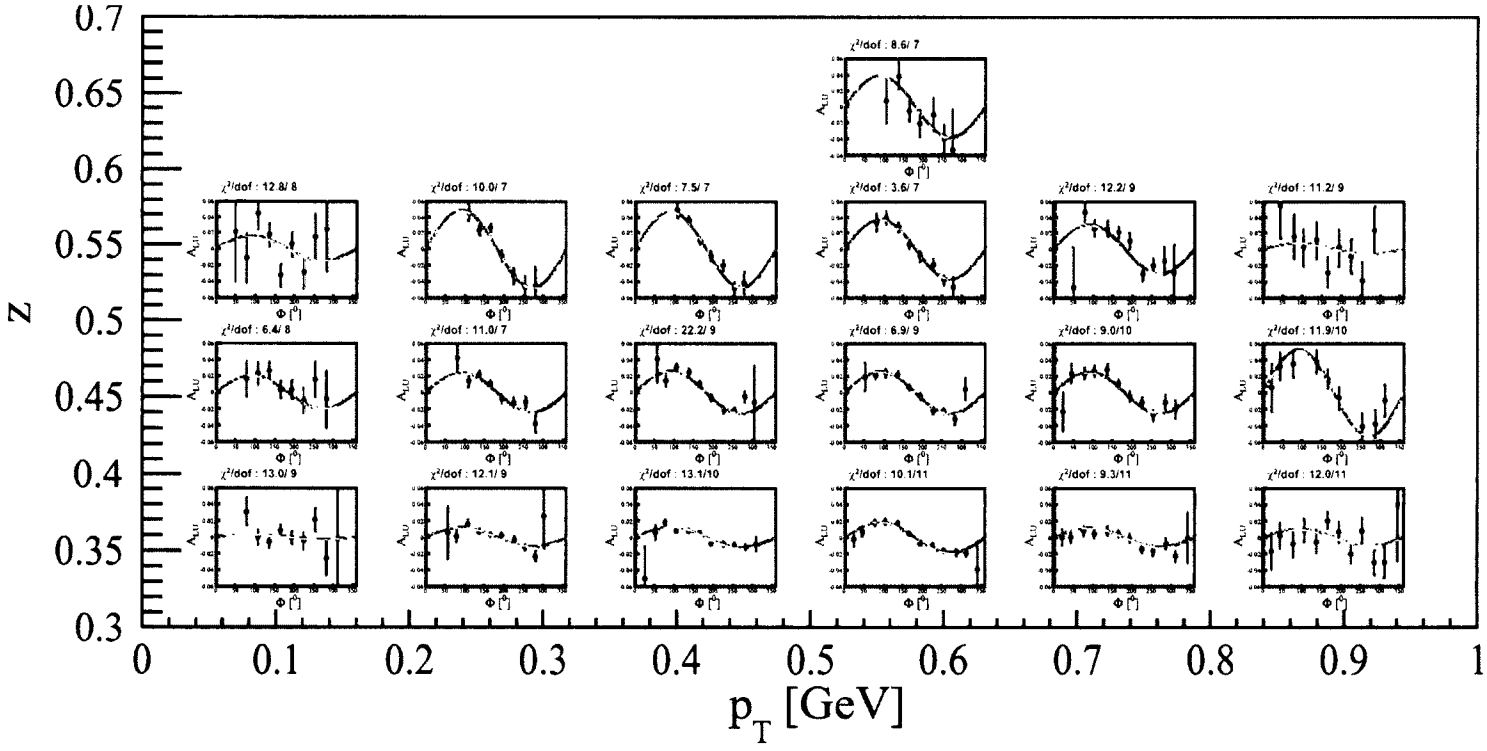

FIG. 191: $A_{LU}(z, P_{h_\perp})$ fits for π^+. Cyan: without any extra term in the denominator. Golden: simultaneous fits with both extra terms in the denominators.

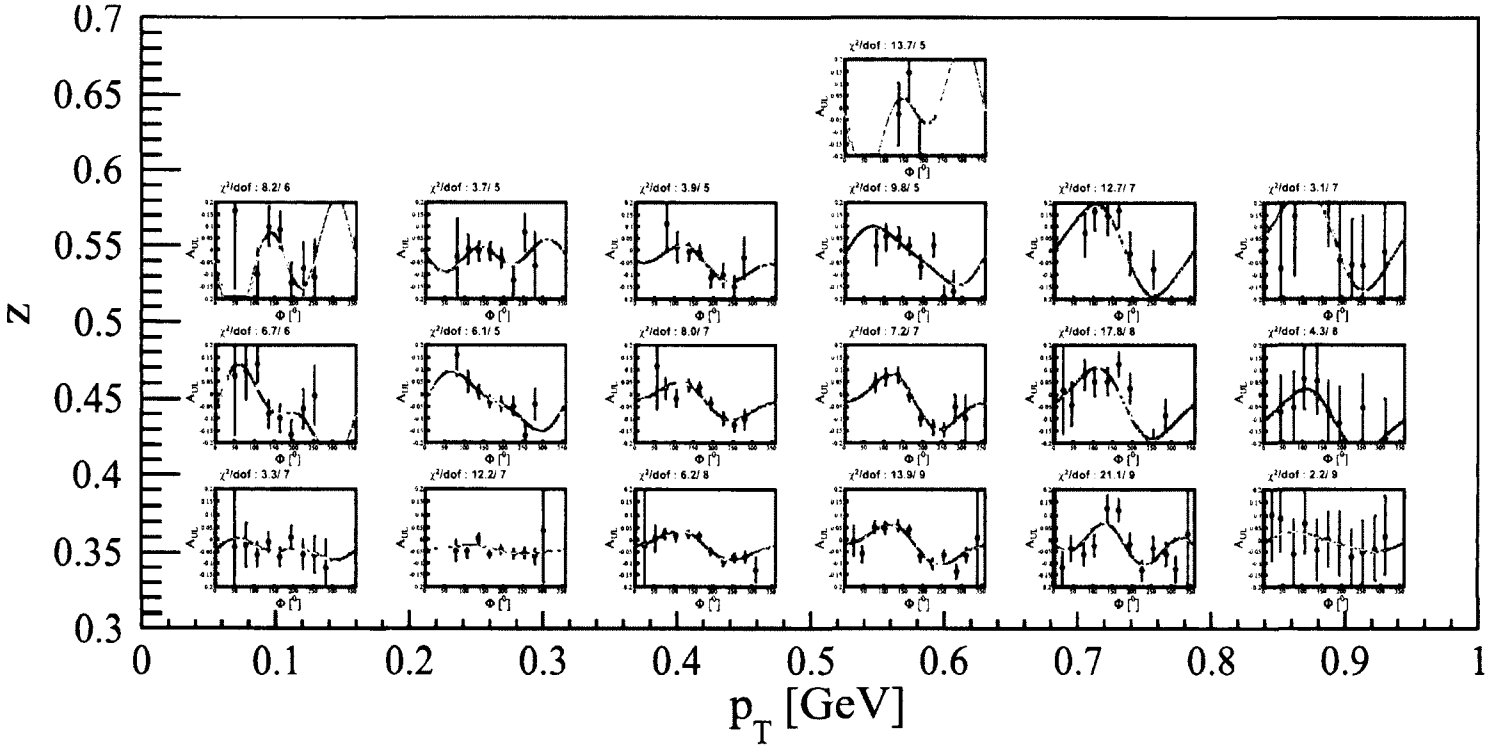

FIG. 192: $A_{UL}(z, P_{h_\perp})$ fits for π^+. Cyan: without any extra term in the denominator. Golden: simultaneous fits with both extra terms in the denominators.

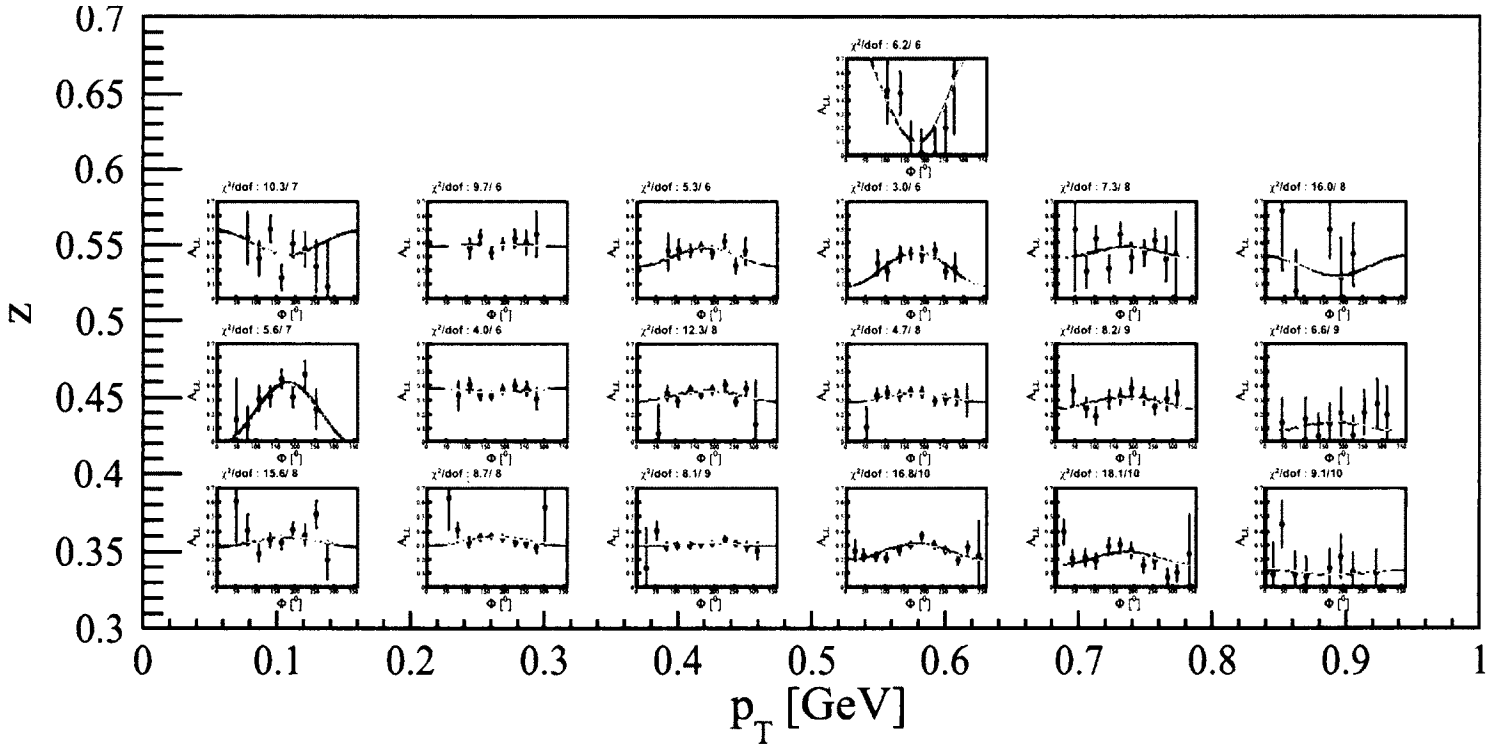

FIG. 193: $A_{LL}(z, P_{h_\perp})$ fits for π^+. Cyan: without any extra term in the denominator. Golden: simultaneous fits with both extra terms in the denominators.

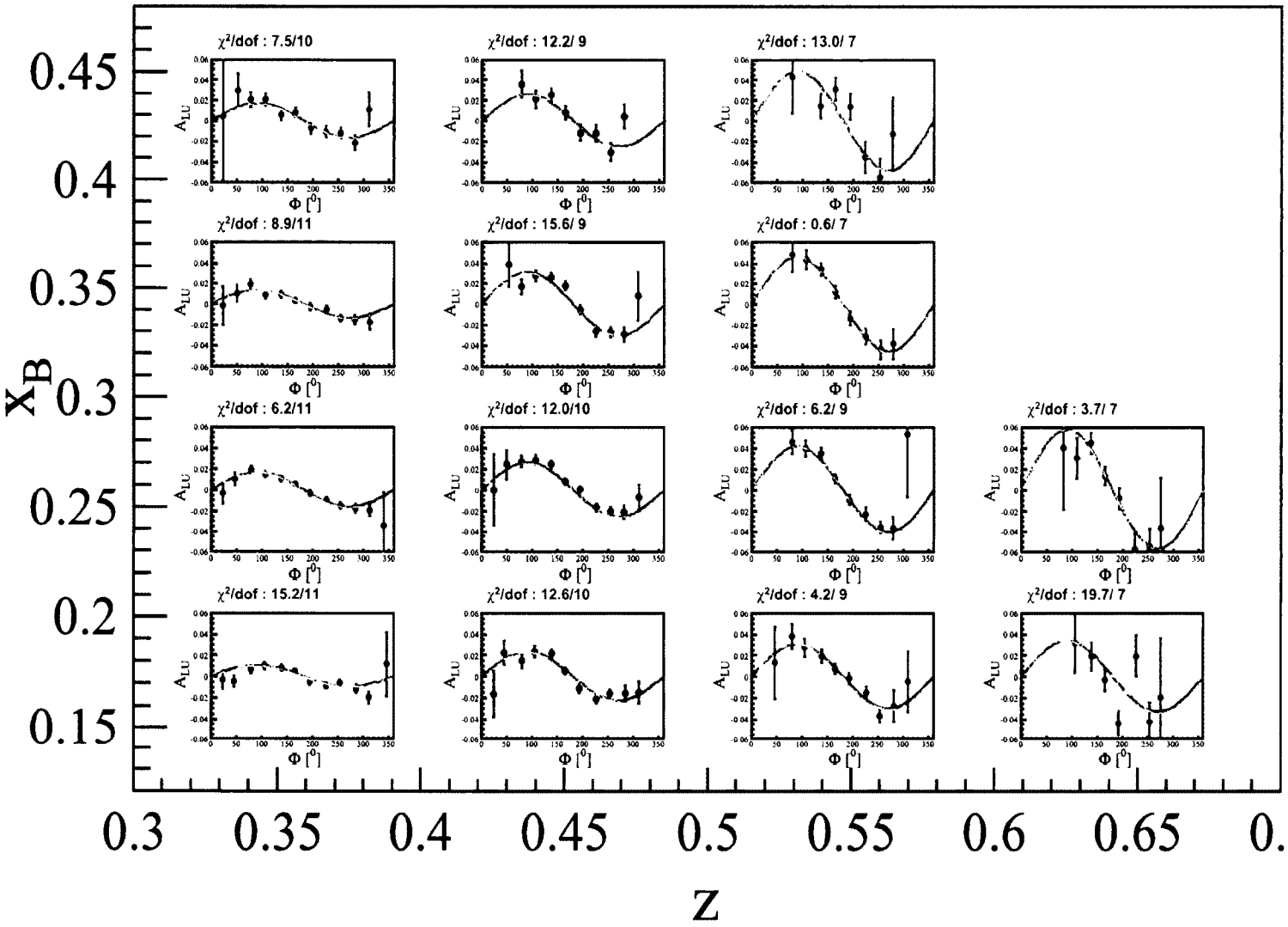

FIG. 194: $A_{LU}(x_B, z)$ fits for π^+. Cyan: without any extra term in the denominator. Golden: simultaneous fits with both extra terms in the denominators.

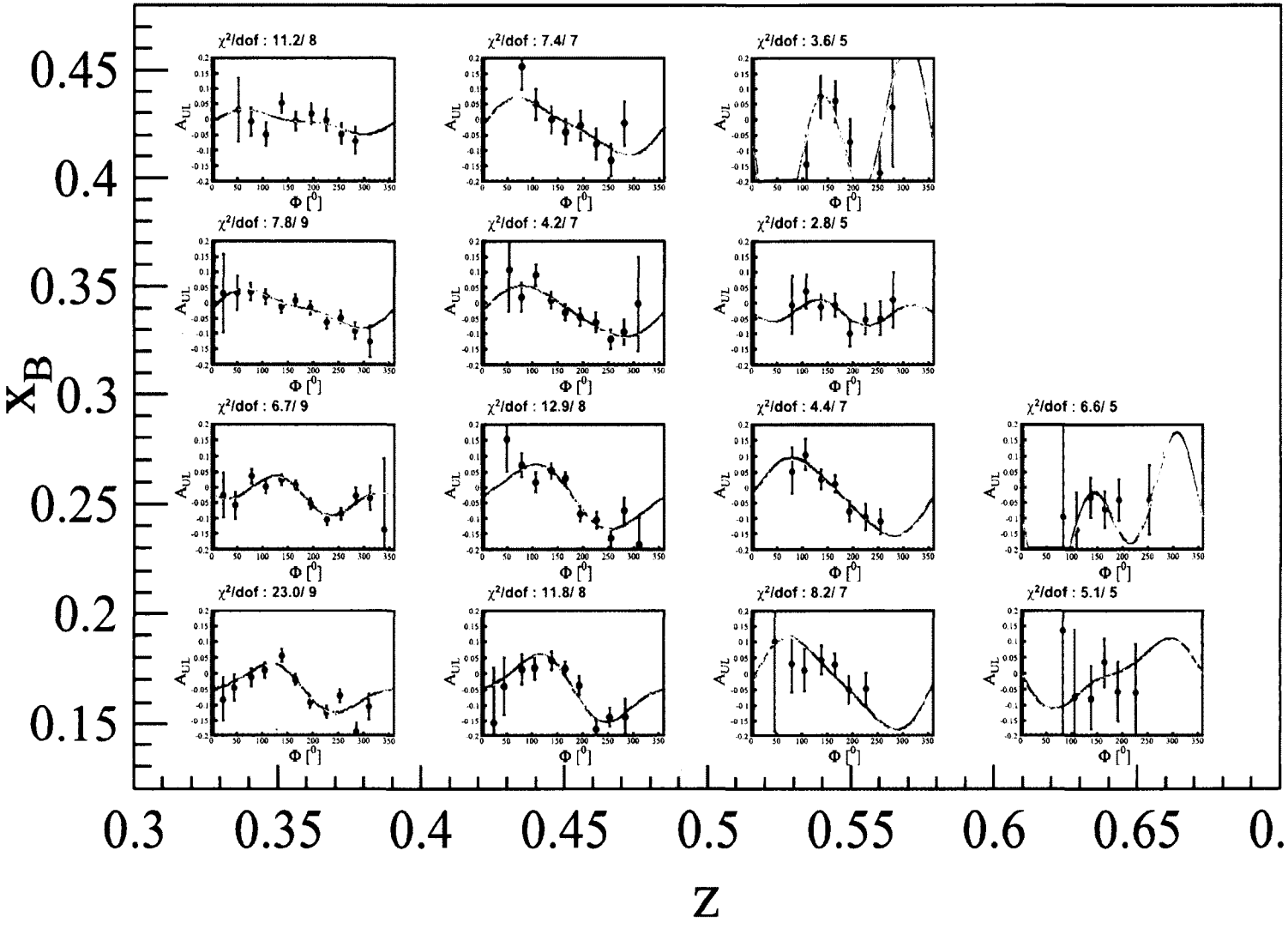

FIG. 195: $A_{UL}(x_B, z)$ fits for π^+. Cyan: without any extra term in the denominator. Golden: simultaneous fits with both extra terms in the denominators.

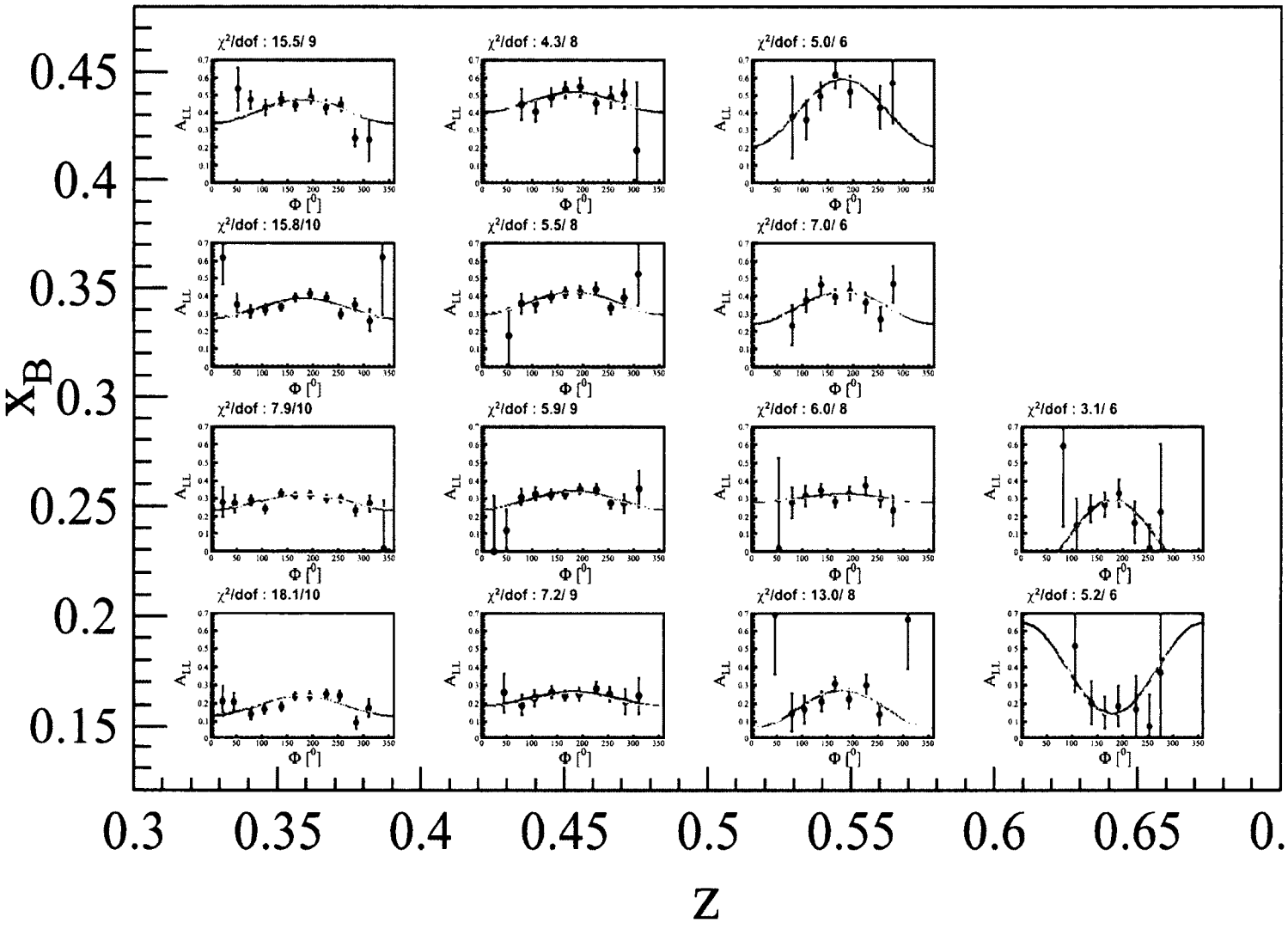

FIG. 196: $A_{LL}(x_B, z)$ fits for π^+. Cyan: without any extra term in the denominator. Golden: simultaneous fits with both extra terms in the denominators.

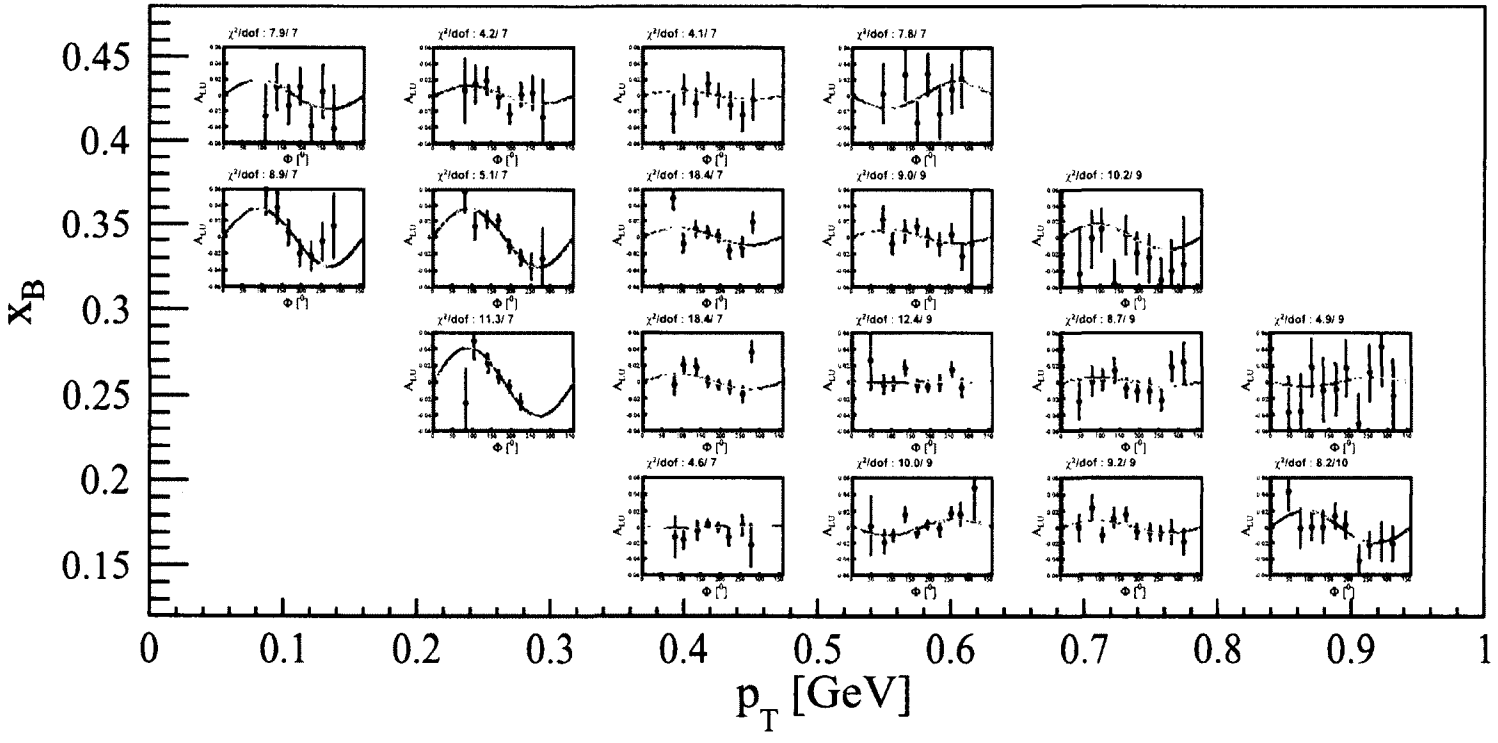

FIG. 197: $A_{LU}(x_B, P_{h_\perp})$ fits for π^-. Cyan: without any extra term in the denominator. Golden: simultaneous fits with both extra terms in the denominators.

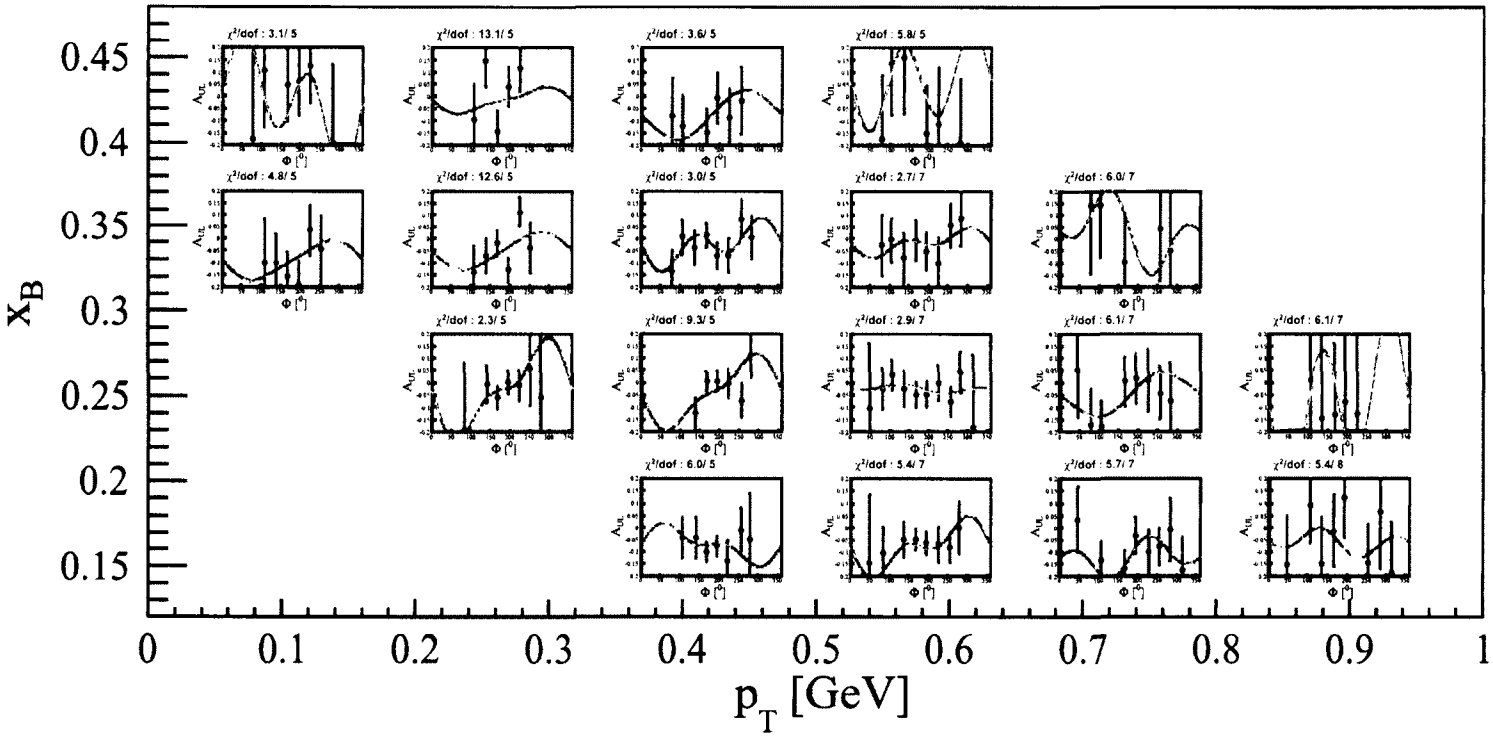

FIG. 198: $A_{UL}(x_B, P_{h\perp})$ fits for π^-. Cyan: without any extra term in the denominator. Golden: simultaneous fits with both extra terms in the denominators.

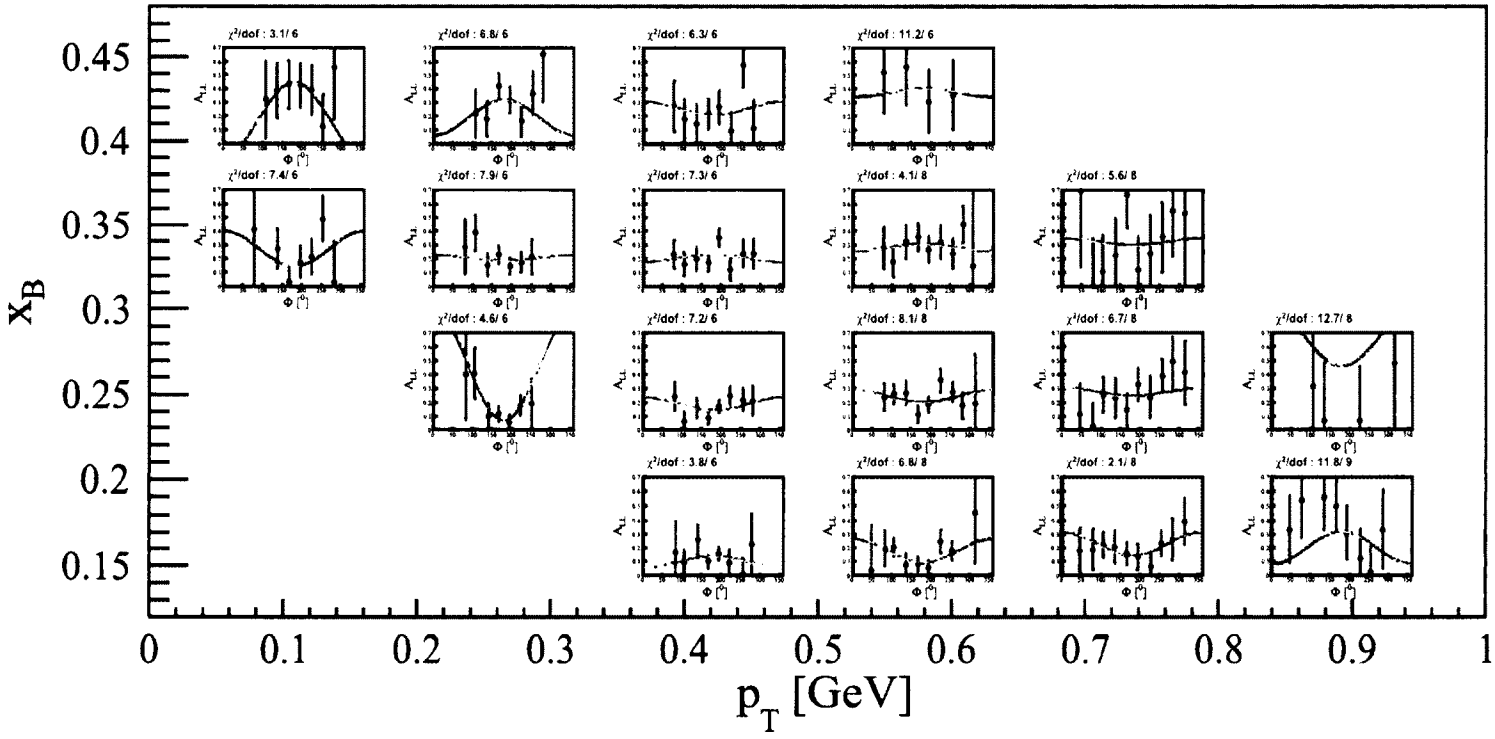

FIG. 199: $A_{LL}(x_B, P_{h_\perp})$ fits for π^-. Cyan: without any extra term in the denominator. Golden: simultaneous fits with both extra terms in the denominators.

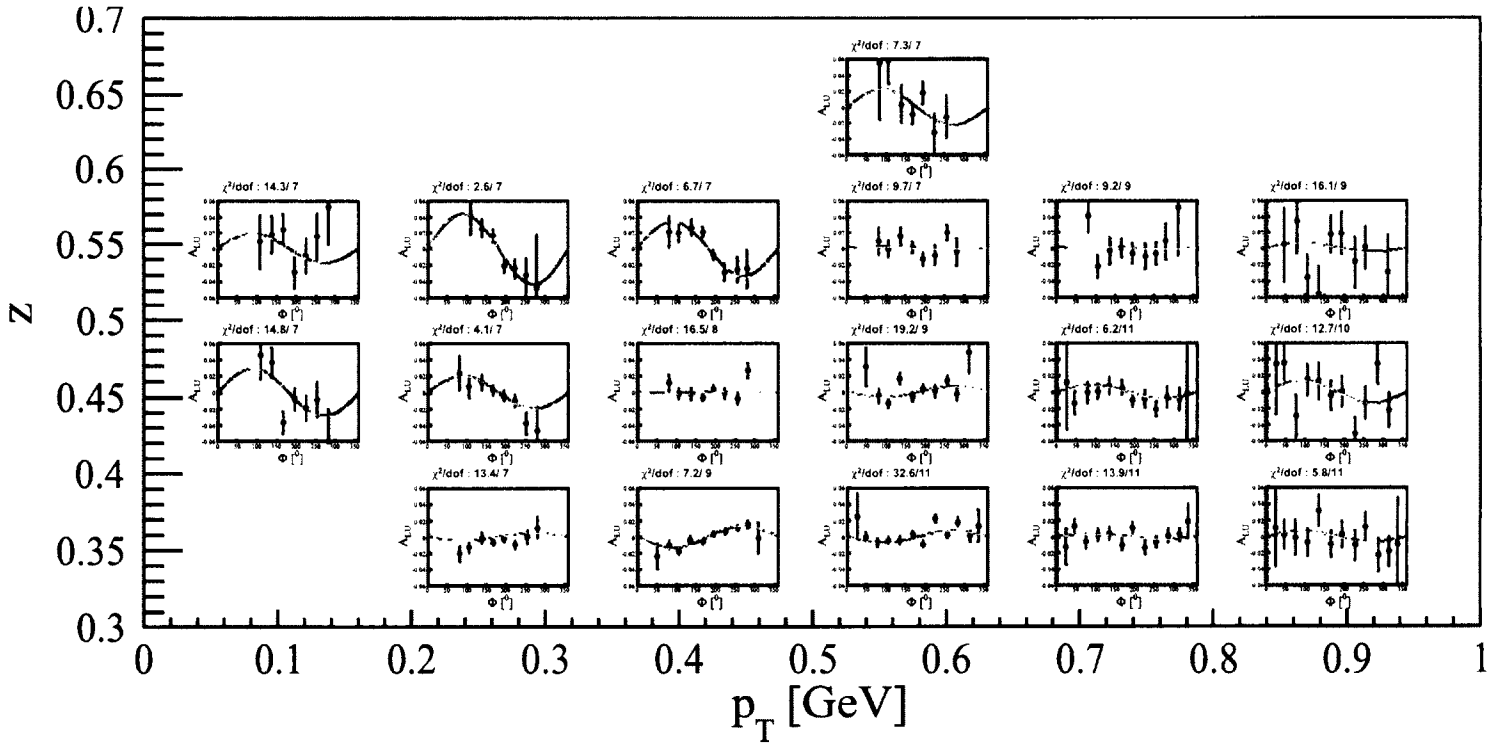

FIG. 200: $A_{LU}(z, P_{h\perp})$ fits for π^-. Cyan: without any extra term in the denominator. Golden: simultaneous fits with both extra terms in the denominators.

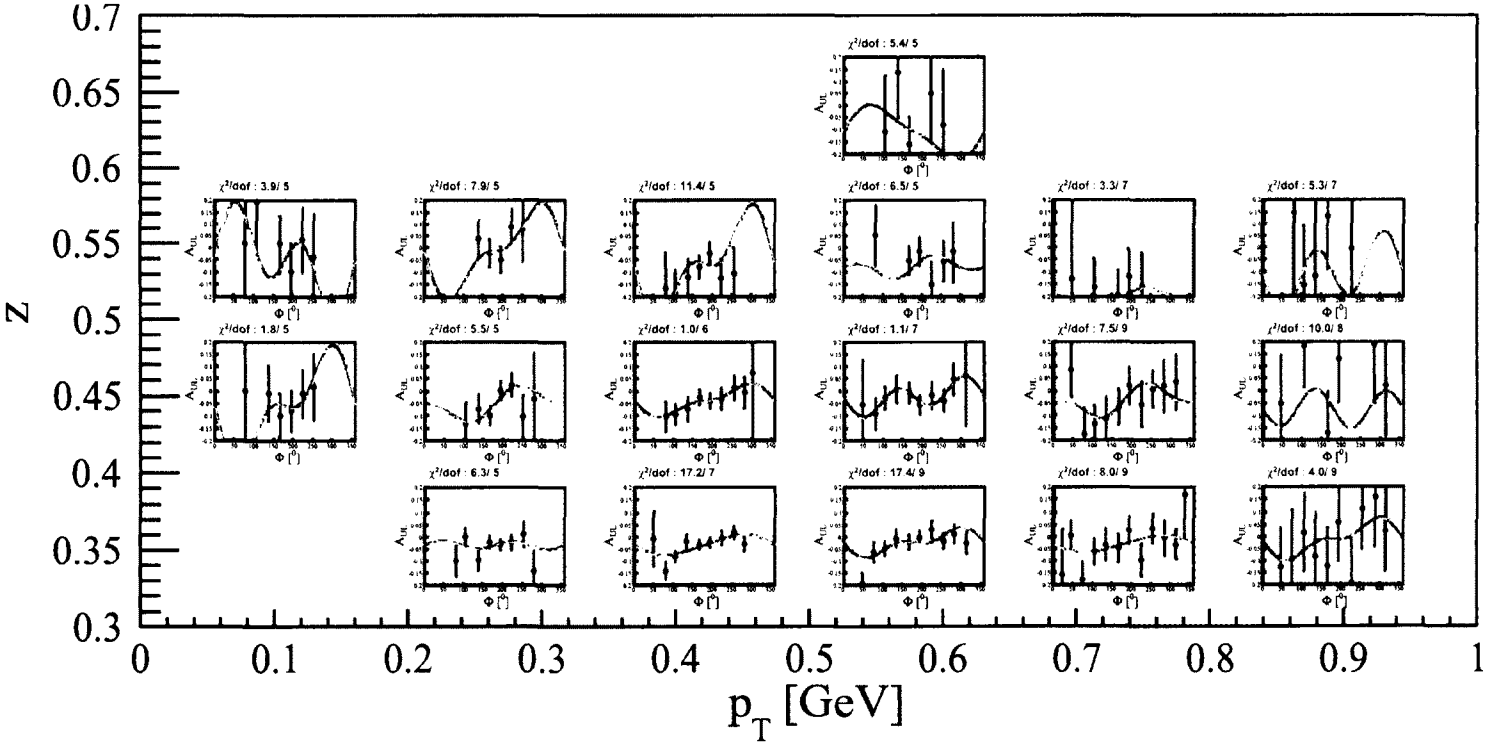

FIG. 201: $A_{UL}(z, P_{h_\perp})$ fits for π^-. Cyan: without any extra term in the denominator. Golden: simultaneous fits with both extra terms in the denominators.

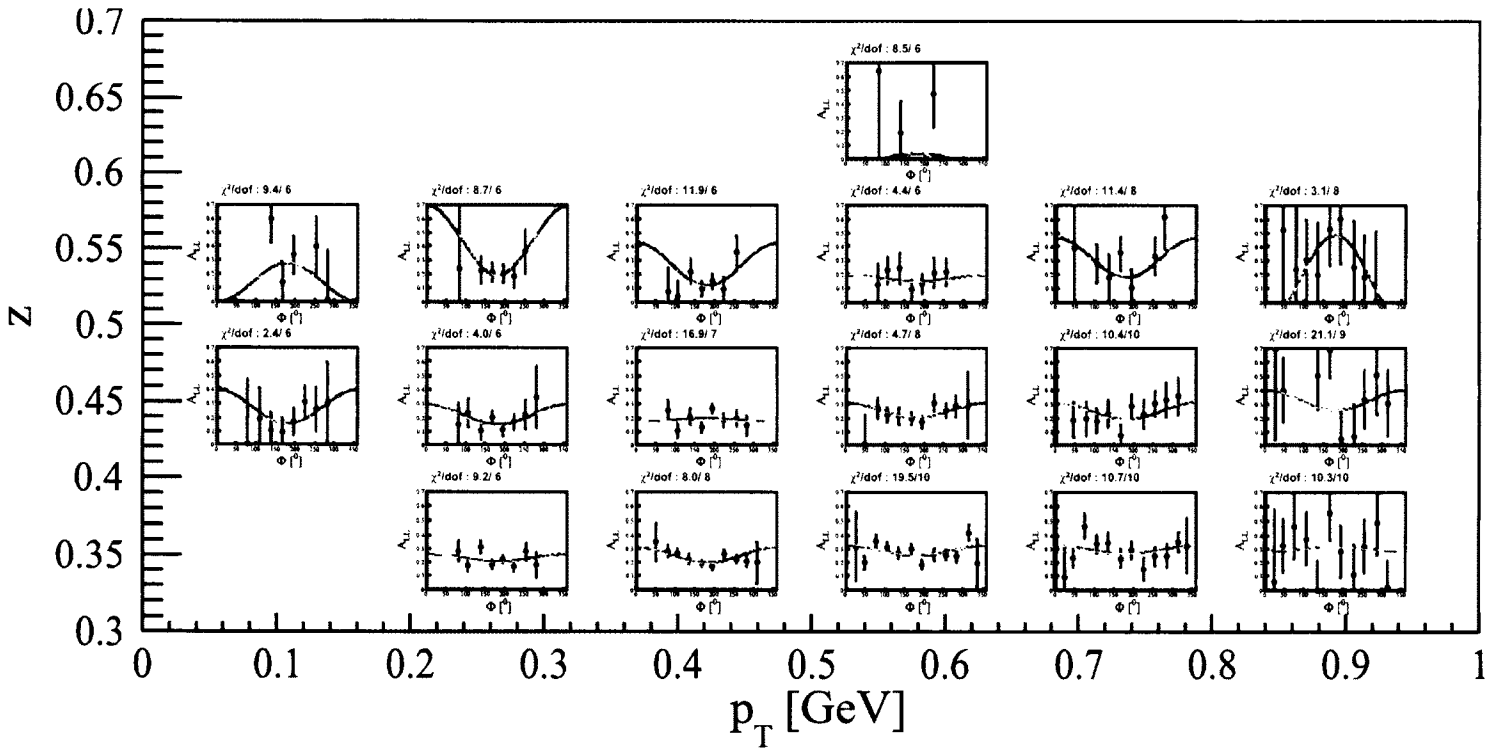

FIG. 202: $A_{LL}(z, P_{h_\perp})$ fits for π^-. Cyan: without any extra term in the denominator. Golden: simultaneous fits with both extra terms in the denominators.

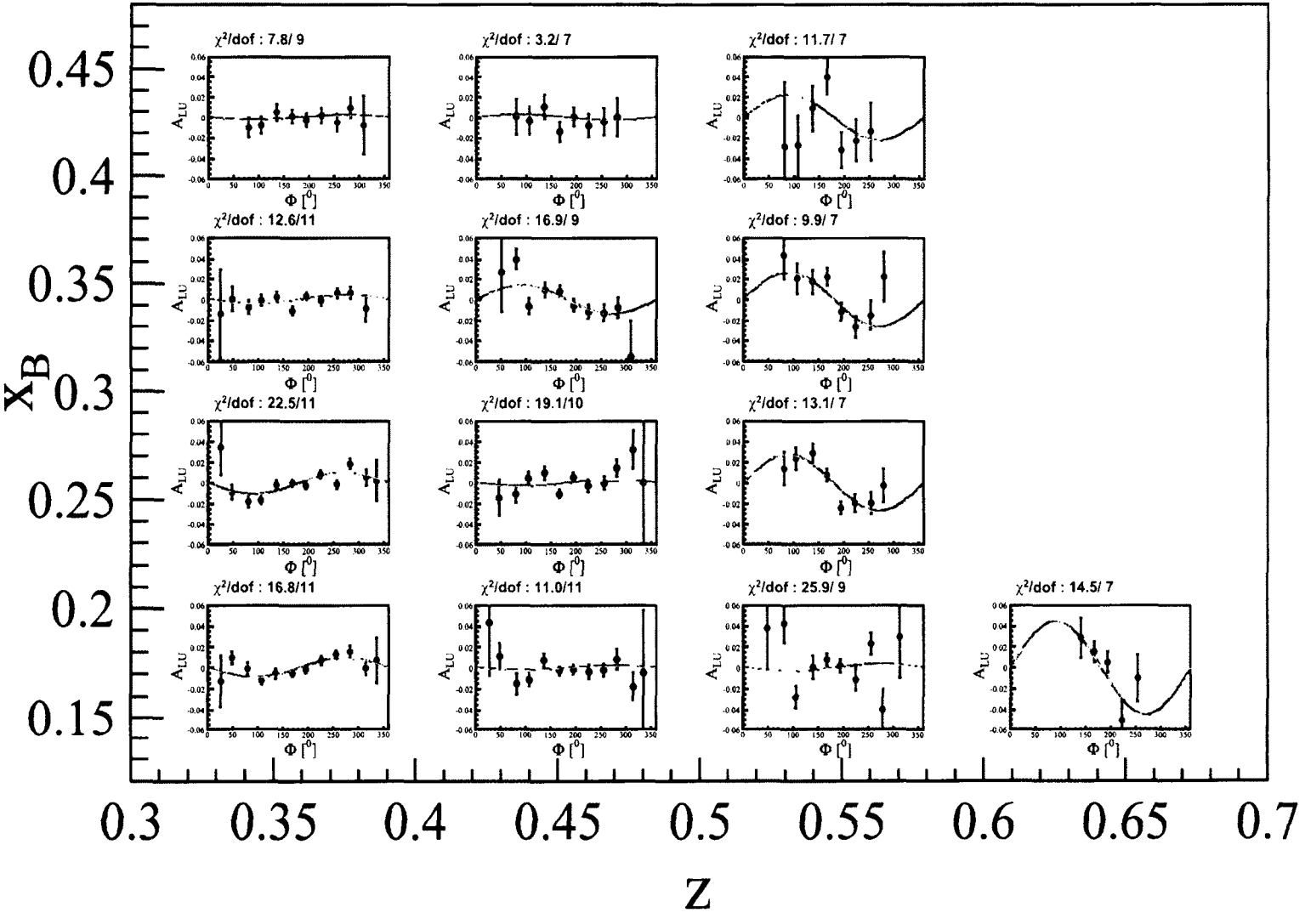

FIG. 203: $A_{LU}(x_B, z)$ fits for π^-. Cyan: without any extra term in the denominator. Golden: simultaneous fits with both extra terms in the denominators.

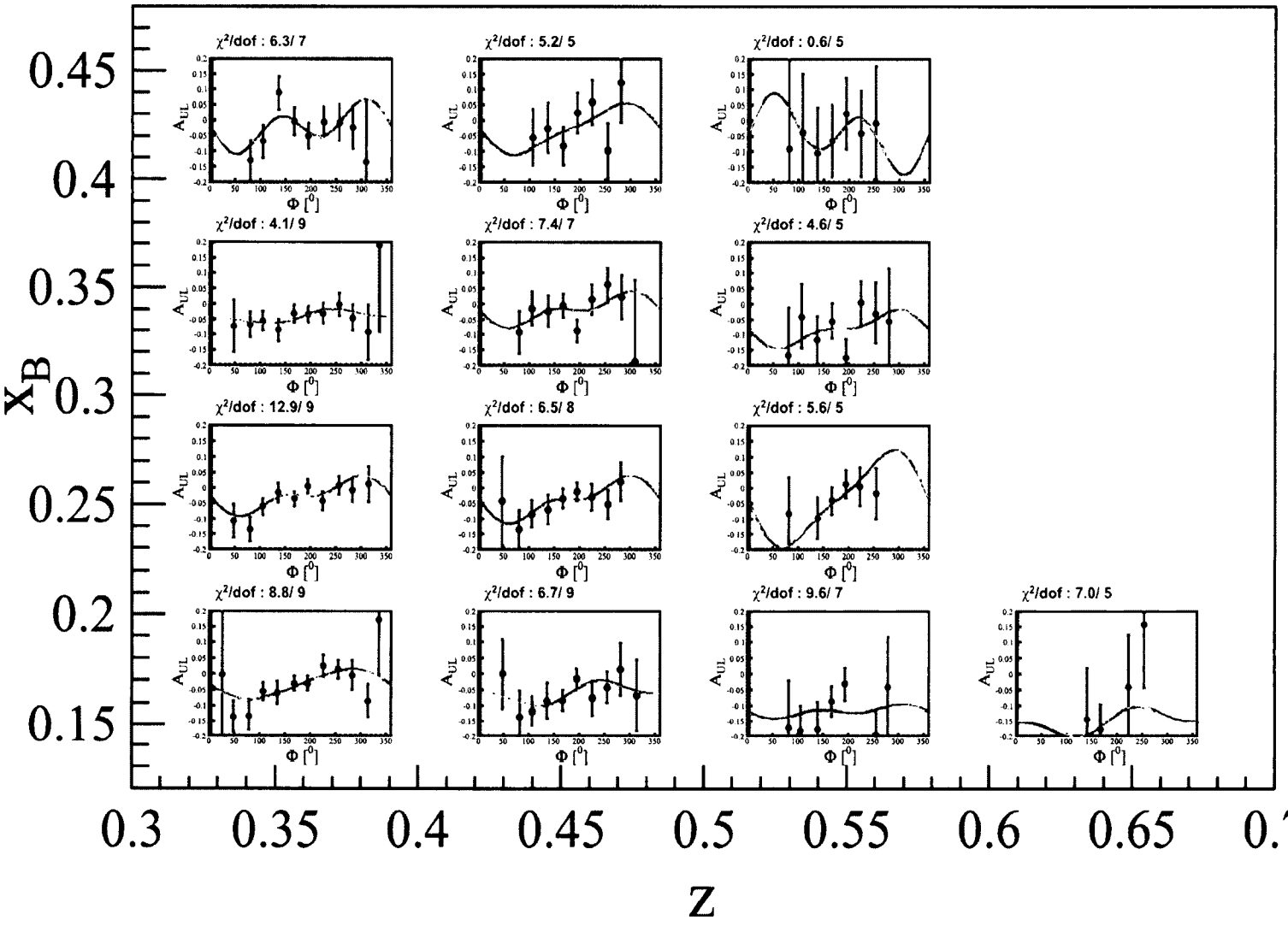

FIG. 204: $A_{UL}(x_B, z)$ fits for π^-. Cyan: without any extra term in the denominator. Golden: simultaneous fits with both extra terms in the denominators.

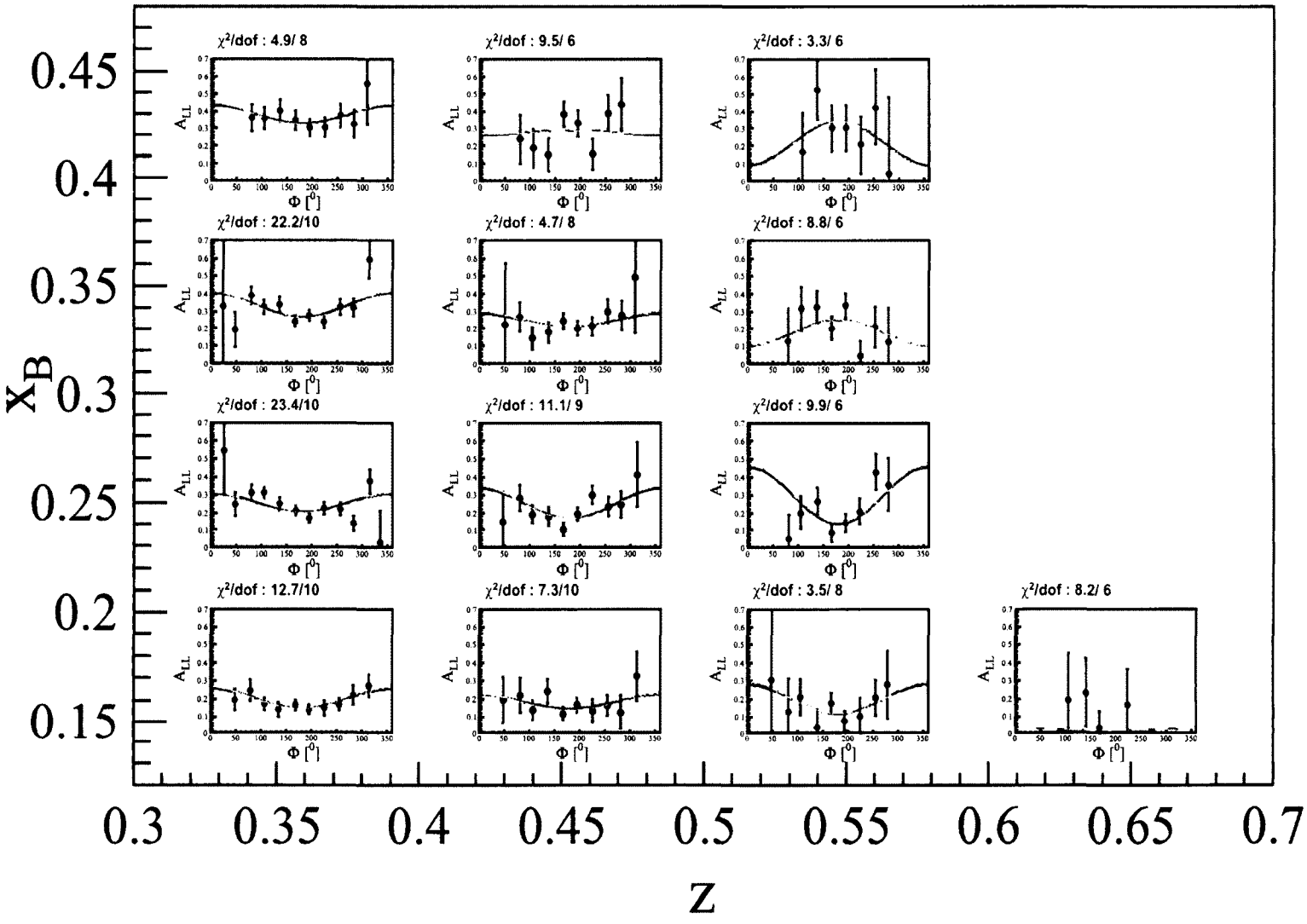

FIG. 205: $A_{LL}(x_B, z)$ fits for π^-. Cyan: without any extra term in the denominator. Golden: simultaneous fits with both extra terms in the denominators.

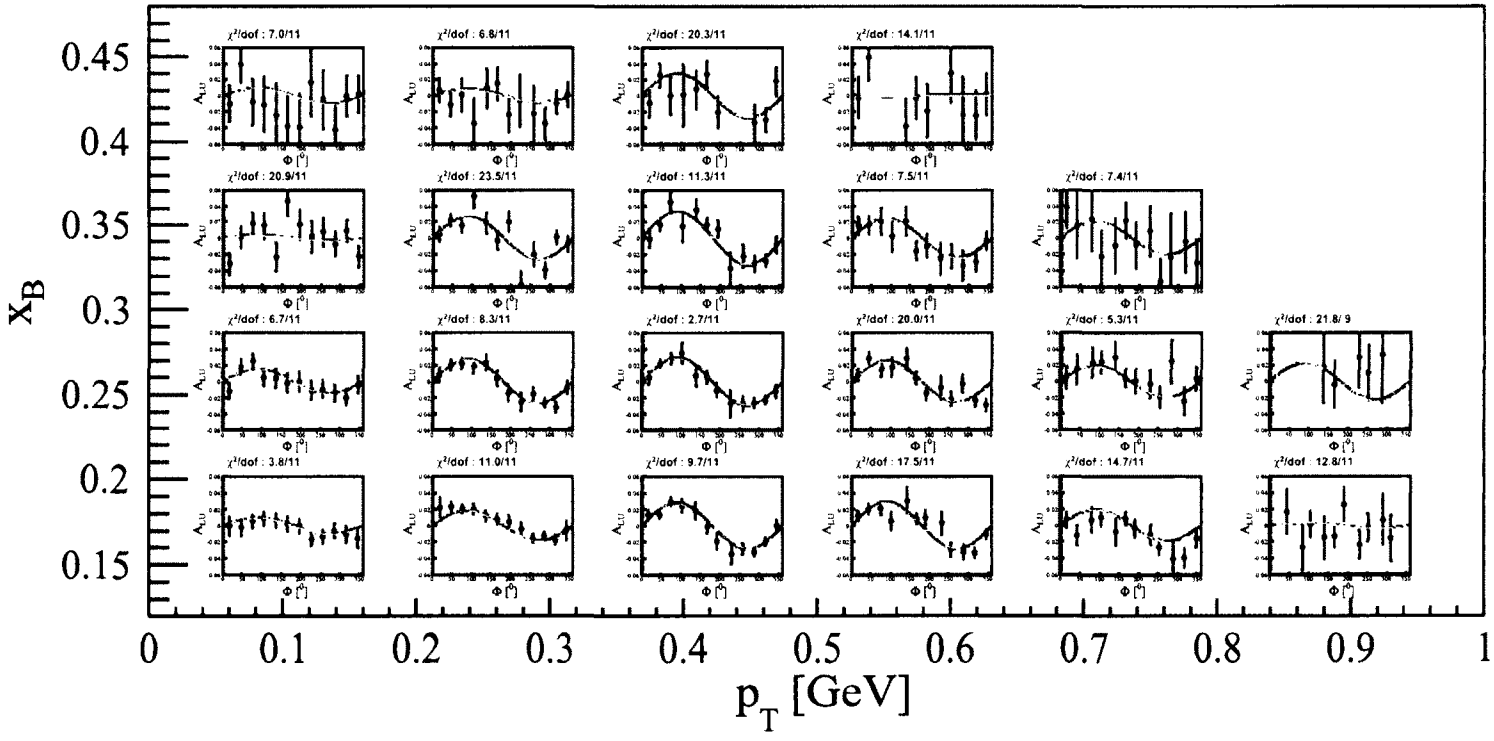

FIG. 206: $A_{LU}(x_B, P_{h_\perp})$ fits for π^0. Cyan: without any extra term in the denominator. Golden: simultaneous fits with both extra terms in the denominators.

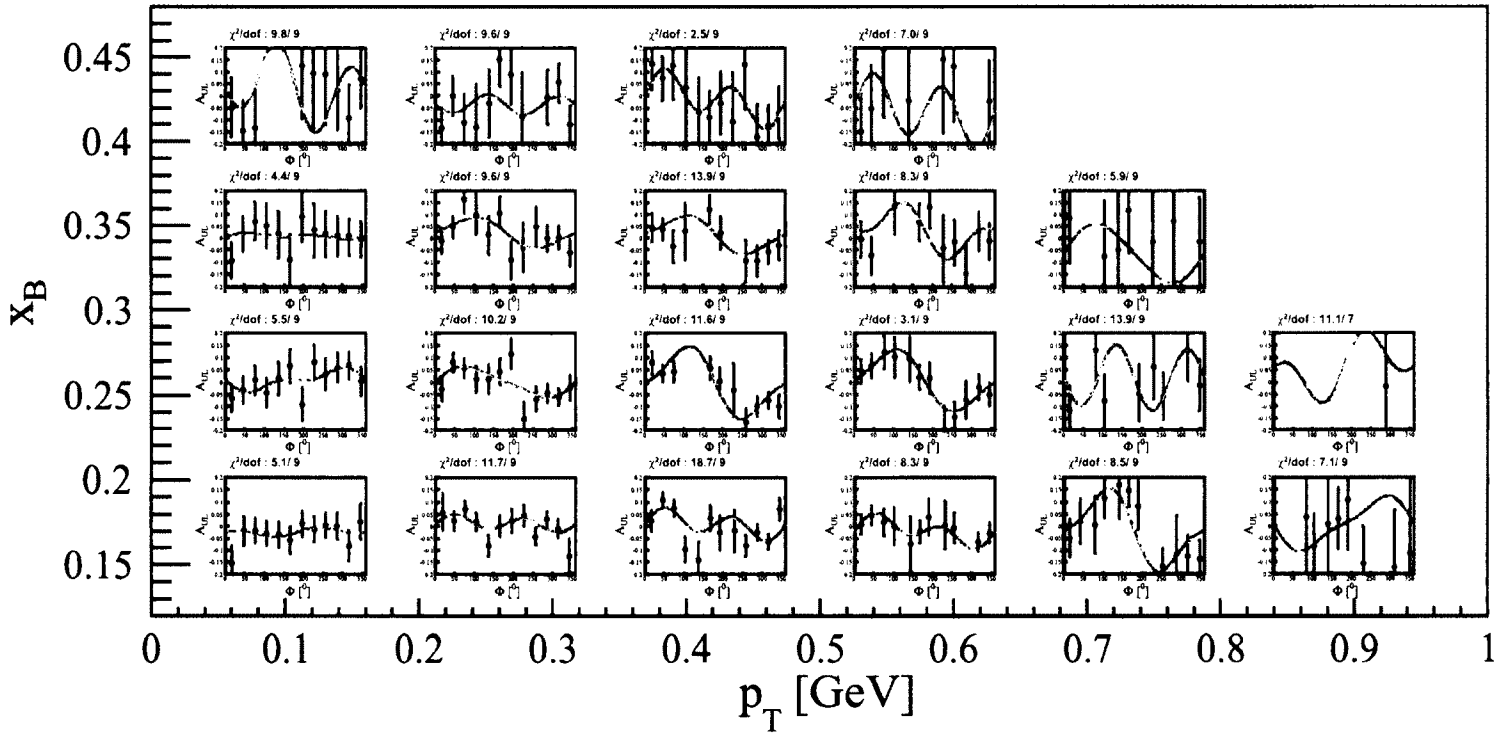

FIG. 207: $A_{UL}(x_B, P_{h_\perp})$ fits for π^0. Cyan: without any extra term in the denominator. Golden: simultaneous fits with both extra terms in the denominators.

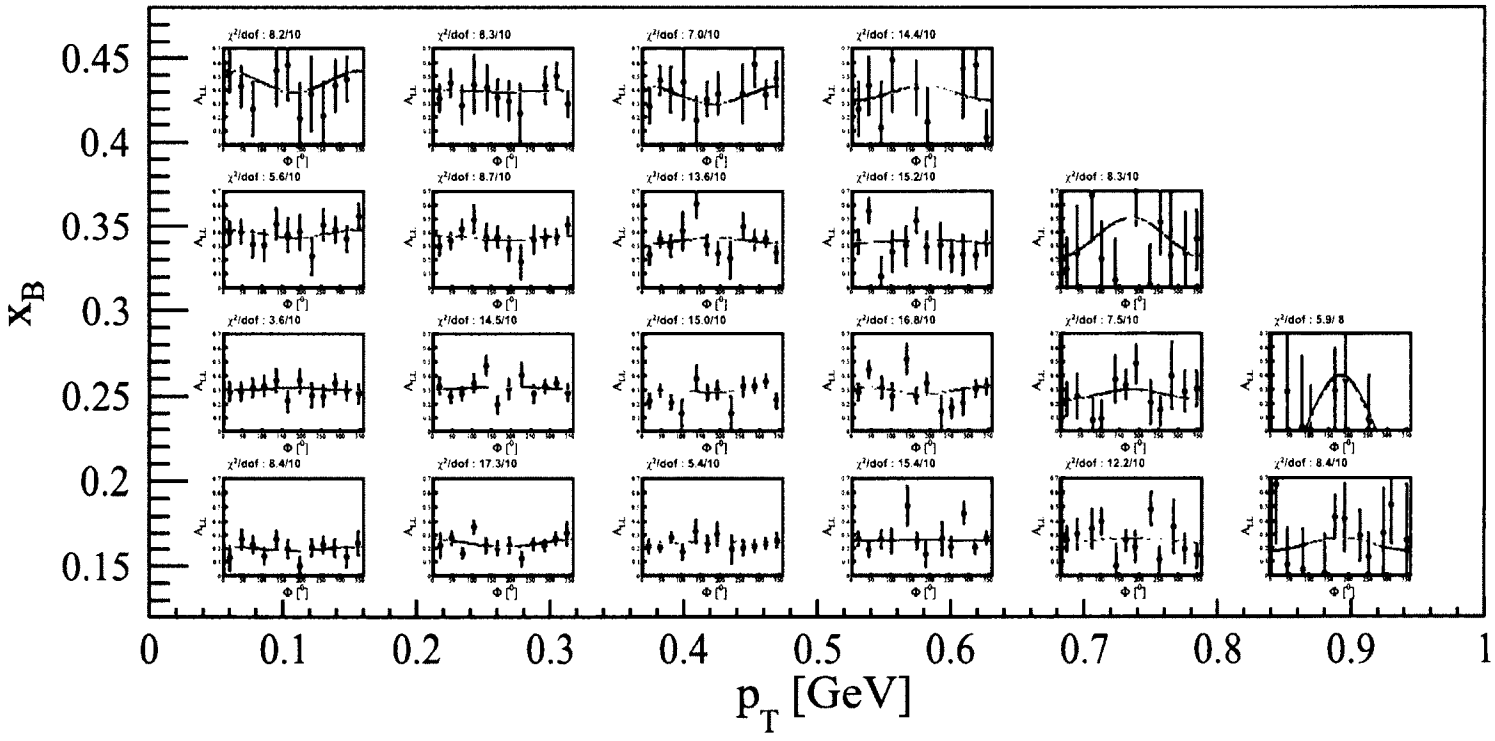

FIG. 208: $A_{LL}(x_B, P_{h_\perp})$ fits for π^0. Cyan: without any extra term in the denominator. Golden: simultaneous fits with both extra terms in the denominators.

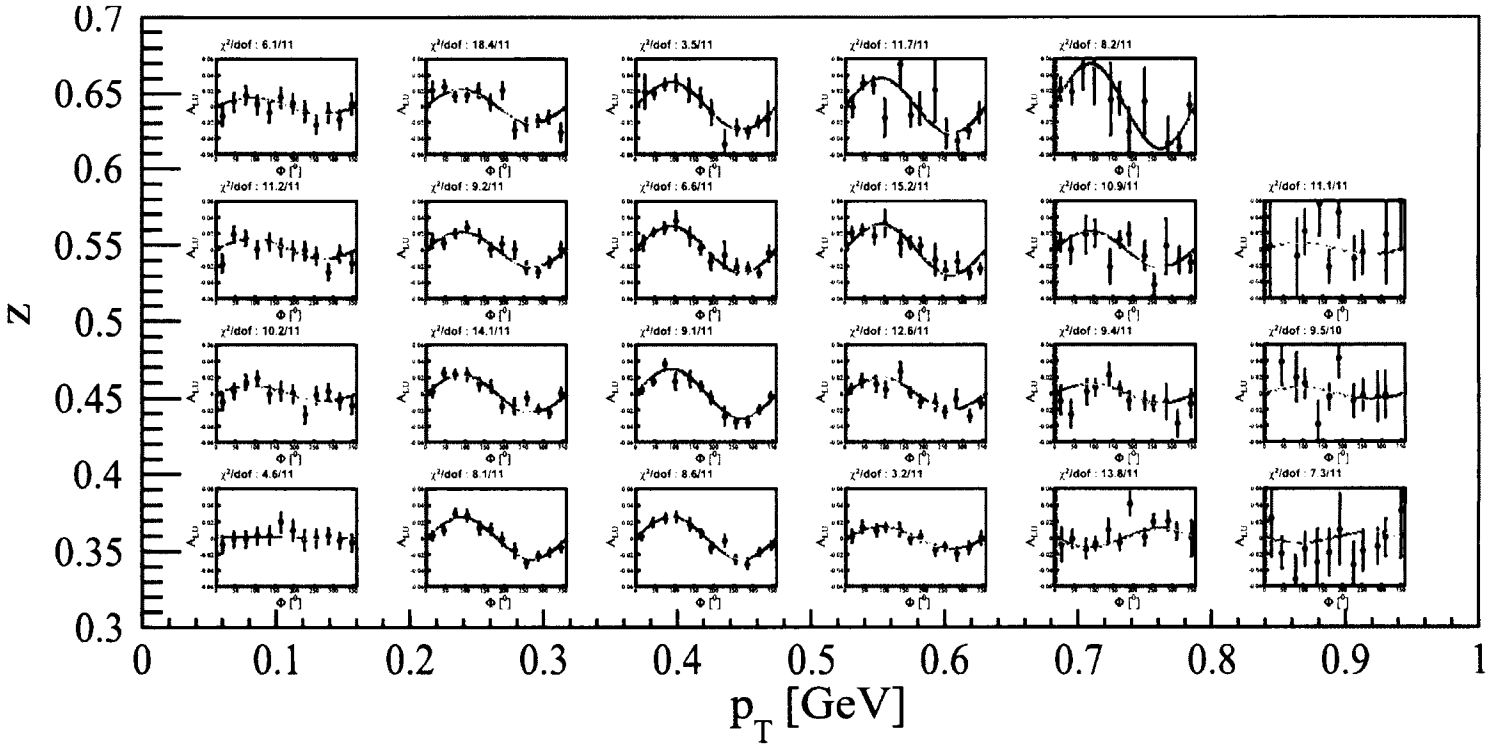

FIG. 209: $A_{LU}(z, P_{h\perp})$ fits for π^0. Cyan: without any extra term in the denominator. Golden: simultaneous fits with both extra terms in the denominators.

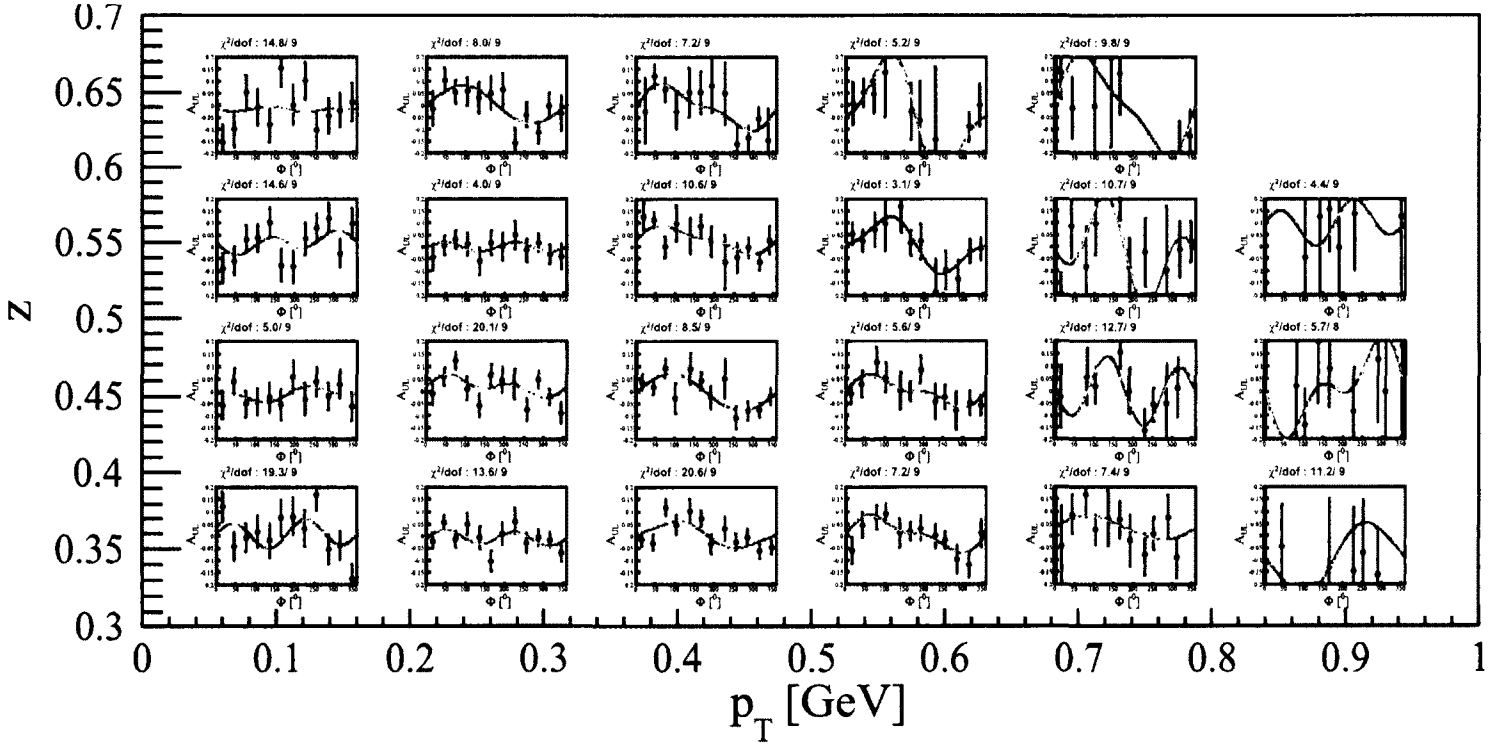

FIG. 210: $A_{UL}(z, P_{h_\perp})$ fits for π^0. Cyan: without any extra term in the denominator. Golden: simultaneous fits with both extra terms in the denominators.

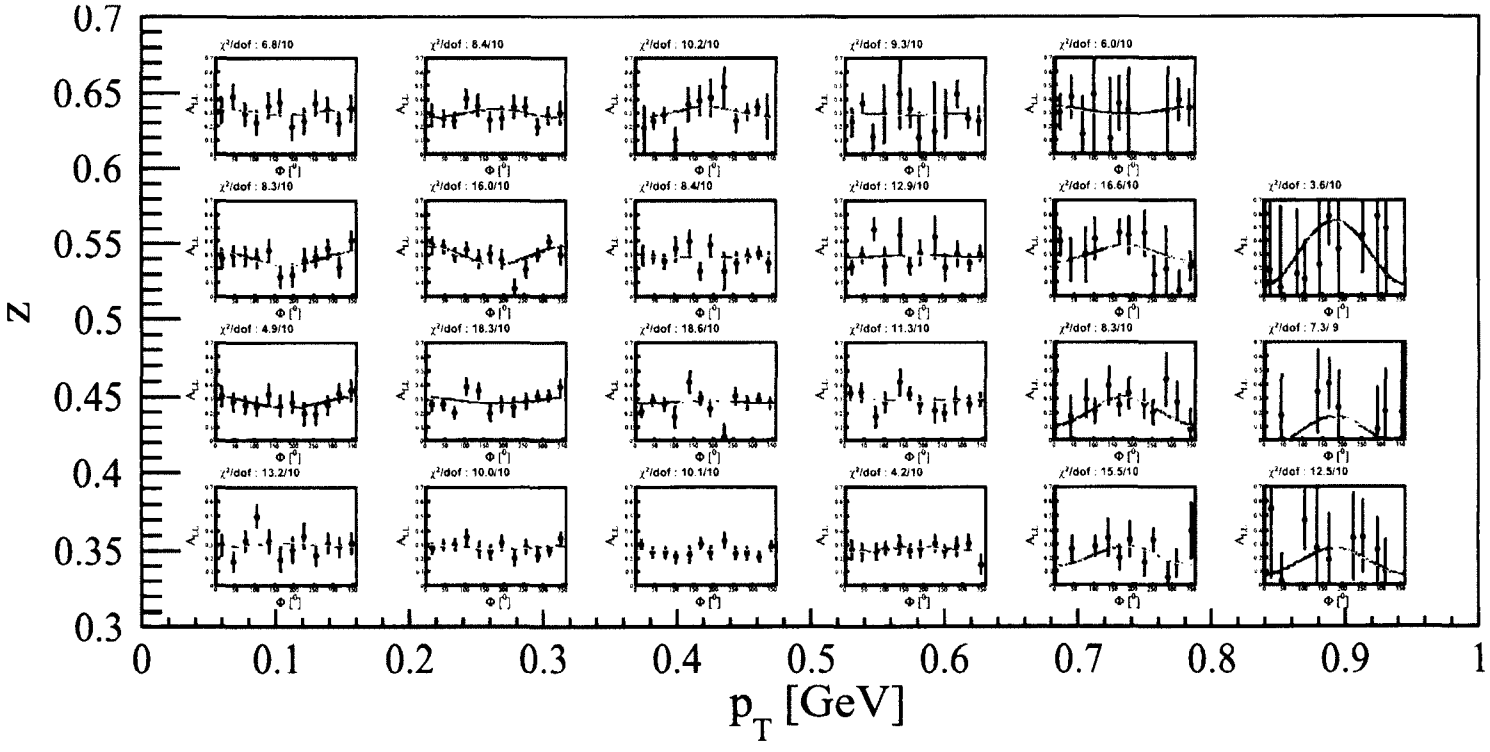

FIG. 211: $A_{LL}(z, P_{h_\perp})$ fits for π^0. Cyan: without any extra term in the denominator. Golden: simultaneous fits with both extra terms in the denominators.

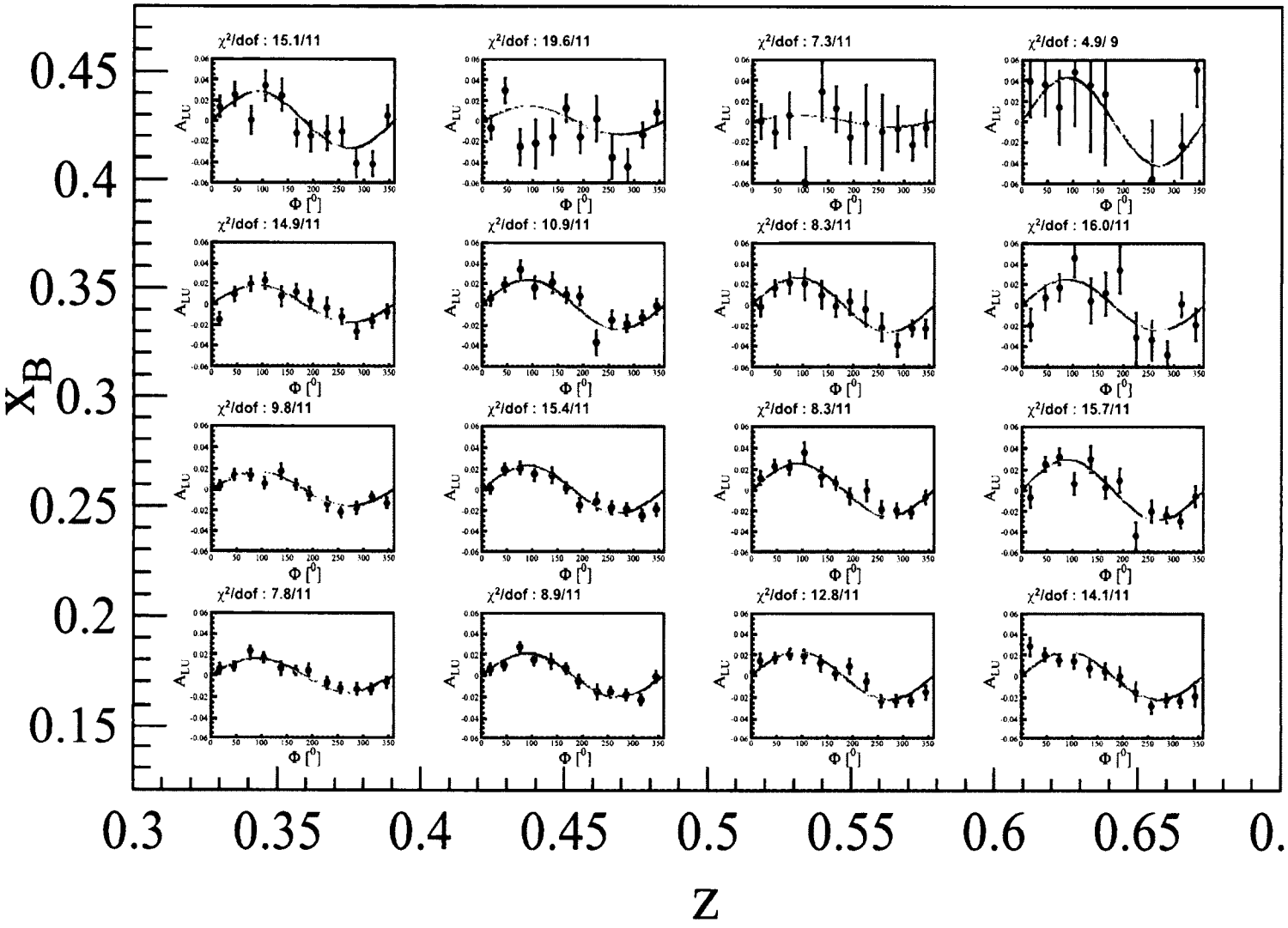

FIG. 212: $A_{LU}(x_B, z)$ fits for π^0. Cyan: without any extra term in the denominator. Golden: simultaneous fits with both extra terms in the denominators.

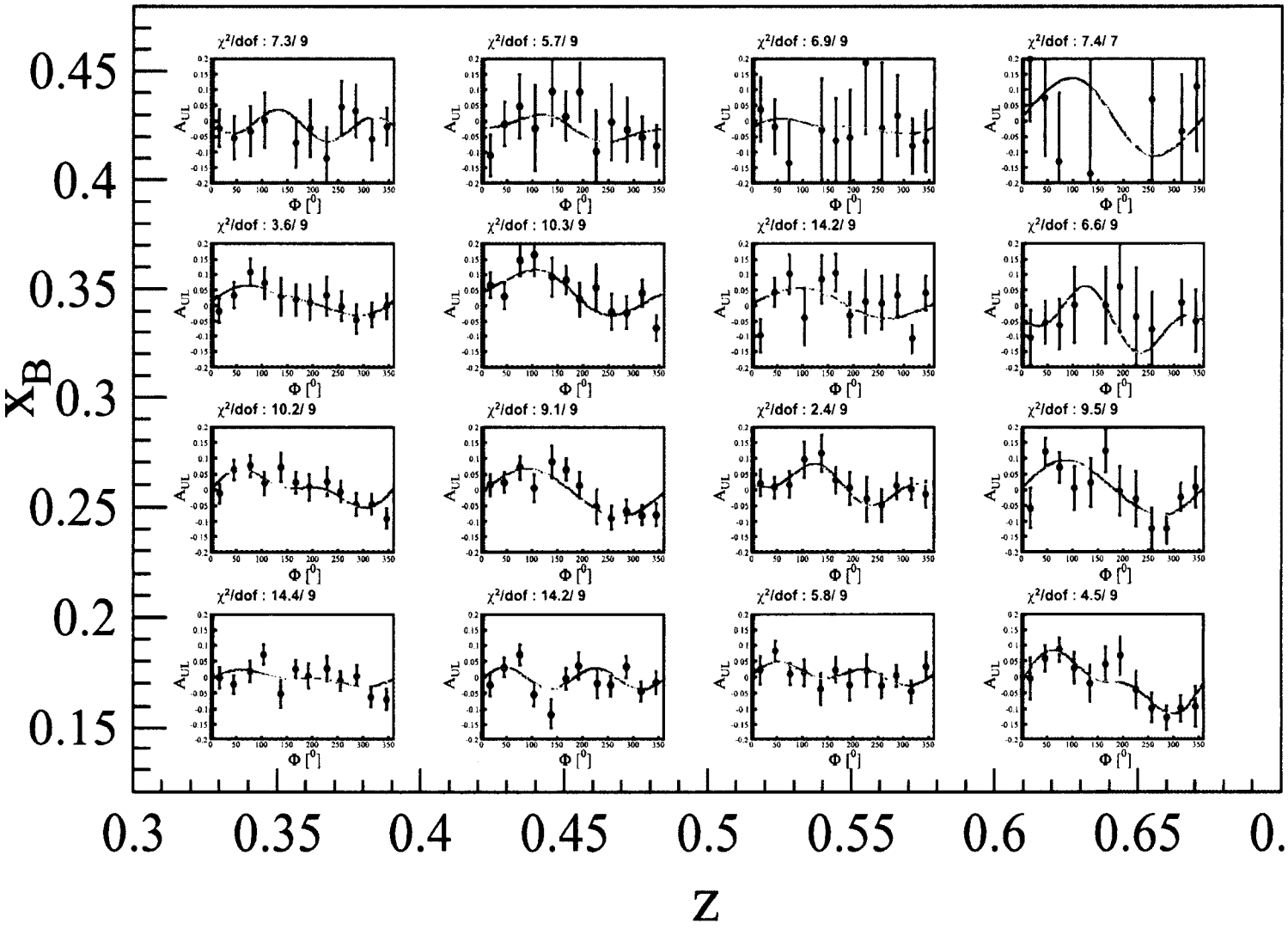

FIG. 213: $A_{UL}(x_B, z)$ fits for π^0. Cyan: without any extra term in the denominator. Golden: simultaneous fits with both extra terms in the denominators.

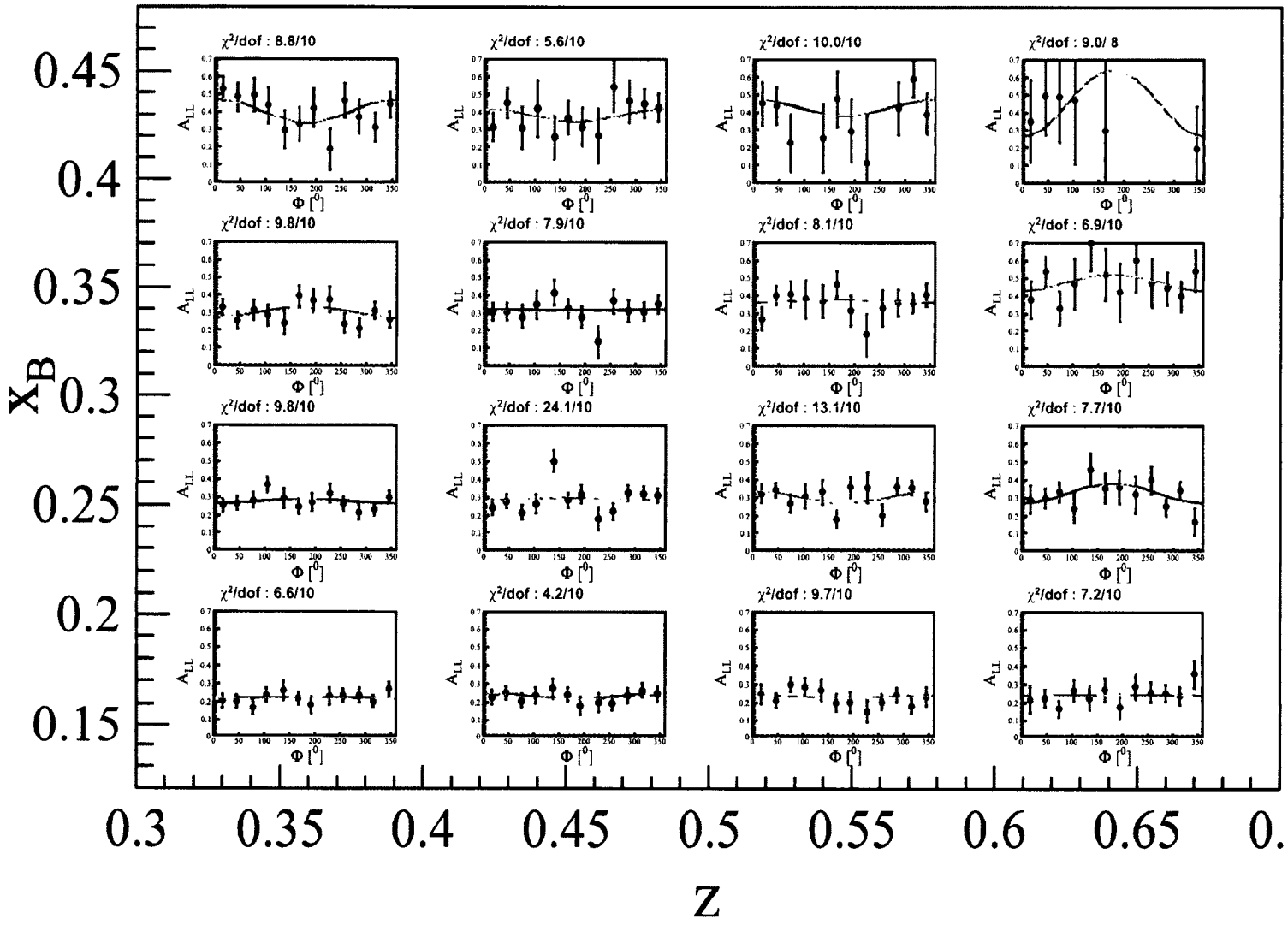

FIG. 214: $A_{LL}(x_B, z)$ fits for π^0. Cyan: without any extra term in the denominator. Golden: simultaneous fits with both extra terms in the denominators.

APPENDIX F

COMPARISON BETWEEN DATA AND SIMULATION

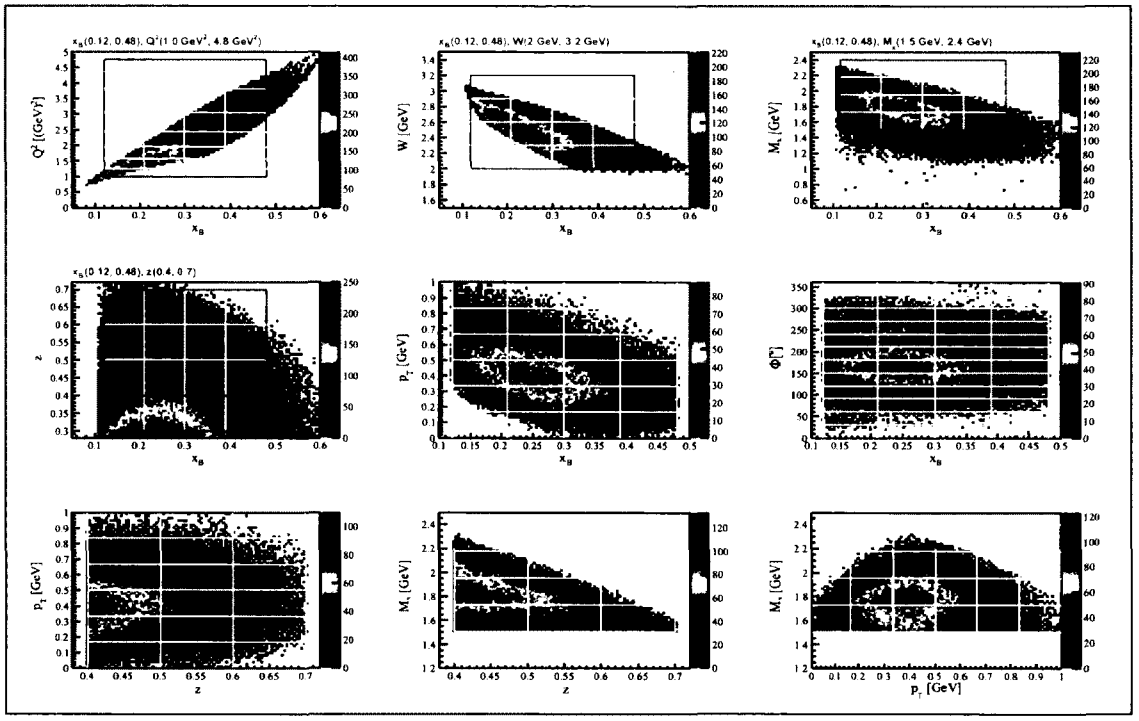

FIG. 215: x_B, Q^2, W, M_x, z, $P_{h\perp}$ and ϕ_h distributions for simulated SIDIS π^+ events.

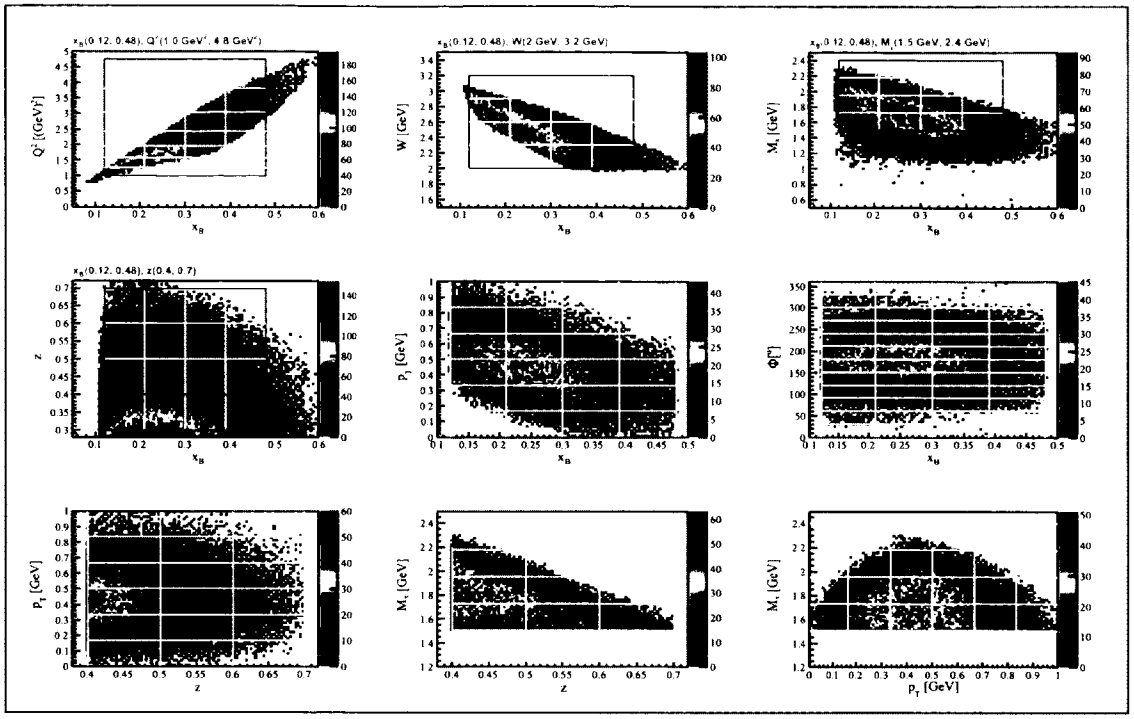

FIG. 216: x_B, Q^2, W, M_x, z, $P_{h\perp}$ and ϕ_h distributions for simulated SIDIS π^- events.

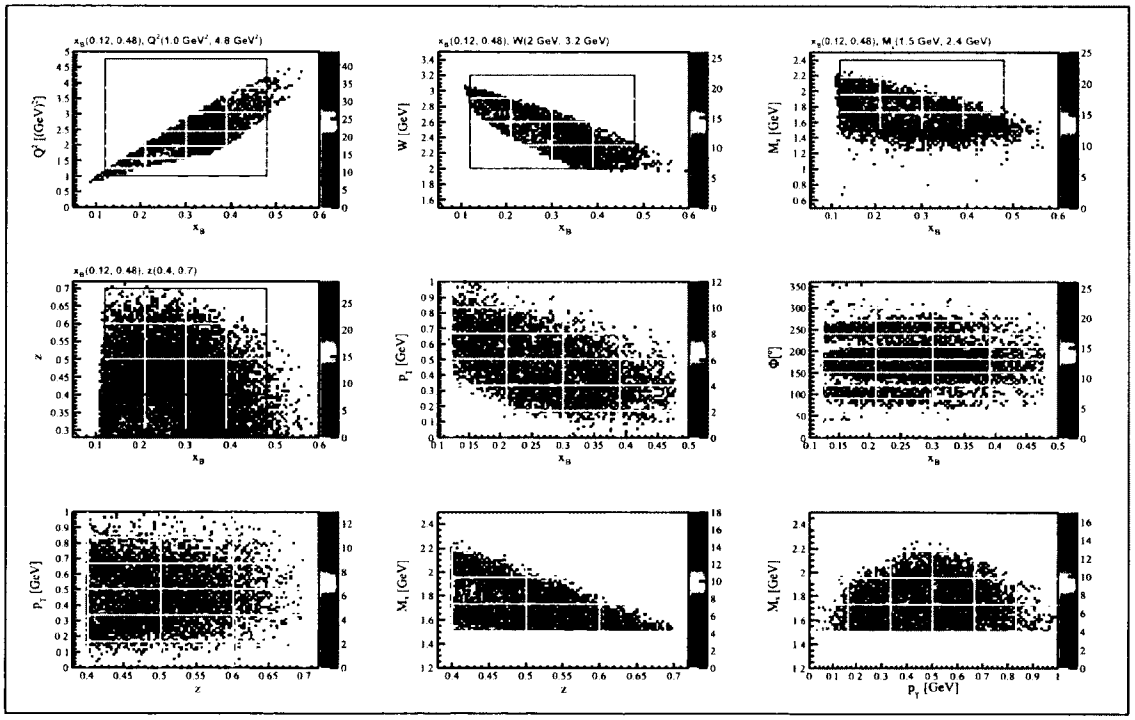

FIG. 217: x_B, Q^2, W, M_x, z, $P_{h\perp}$ and ϕ_h distributions for simulated SIDIS π^0 events with both the photons detected in the EC.

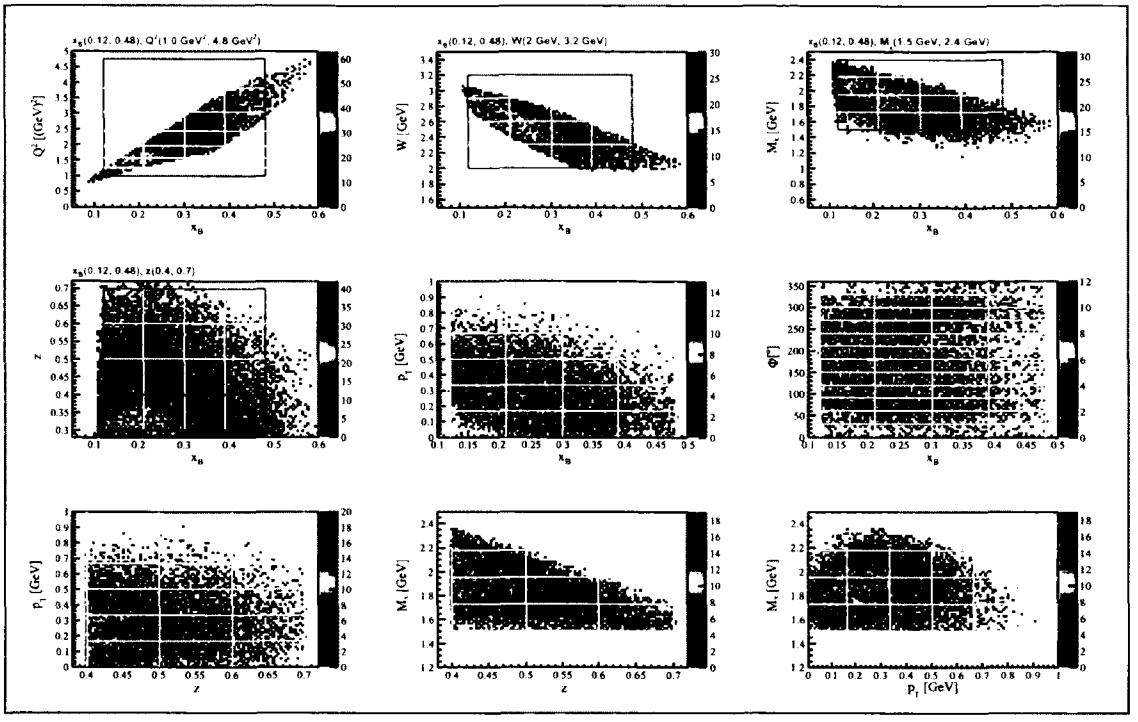

FIG. 218: x_B, Q^2, W, M_x, z, $P_{h\perp}$ and ϕ_h distributions for simulated SIDIS π^0 events with one photon detected in the EC and the other detected in the IC.

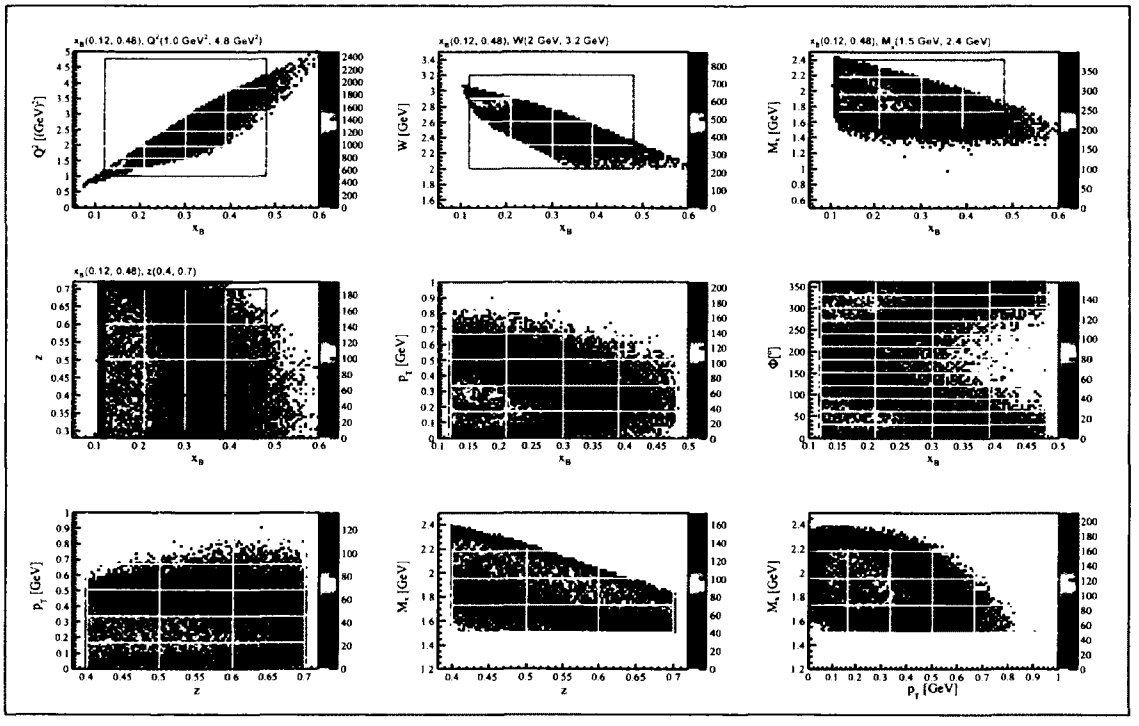

FIG. 219: x_B, Q^2, W, M_x, z, $P_{h\perp}$ and ϕ_h distributions for simulated SIDIS π^0 events with both the photons detected in the IC.

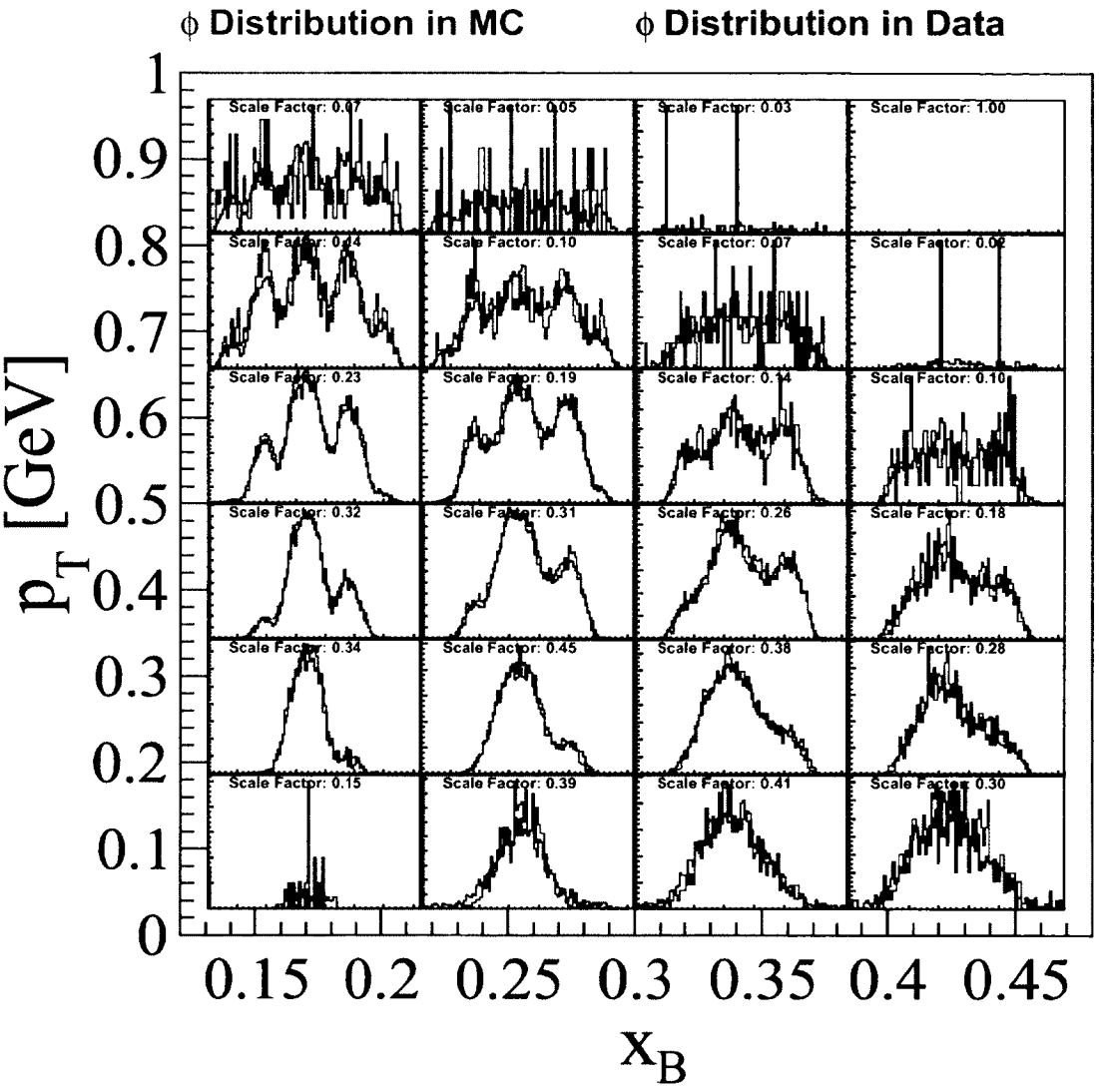

FIG. 220: Comparison between simulation and data for the azimuthal distribution of π^+

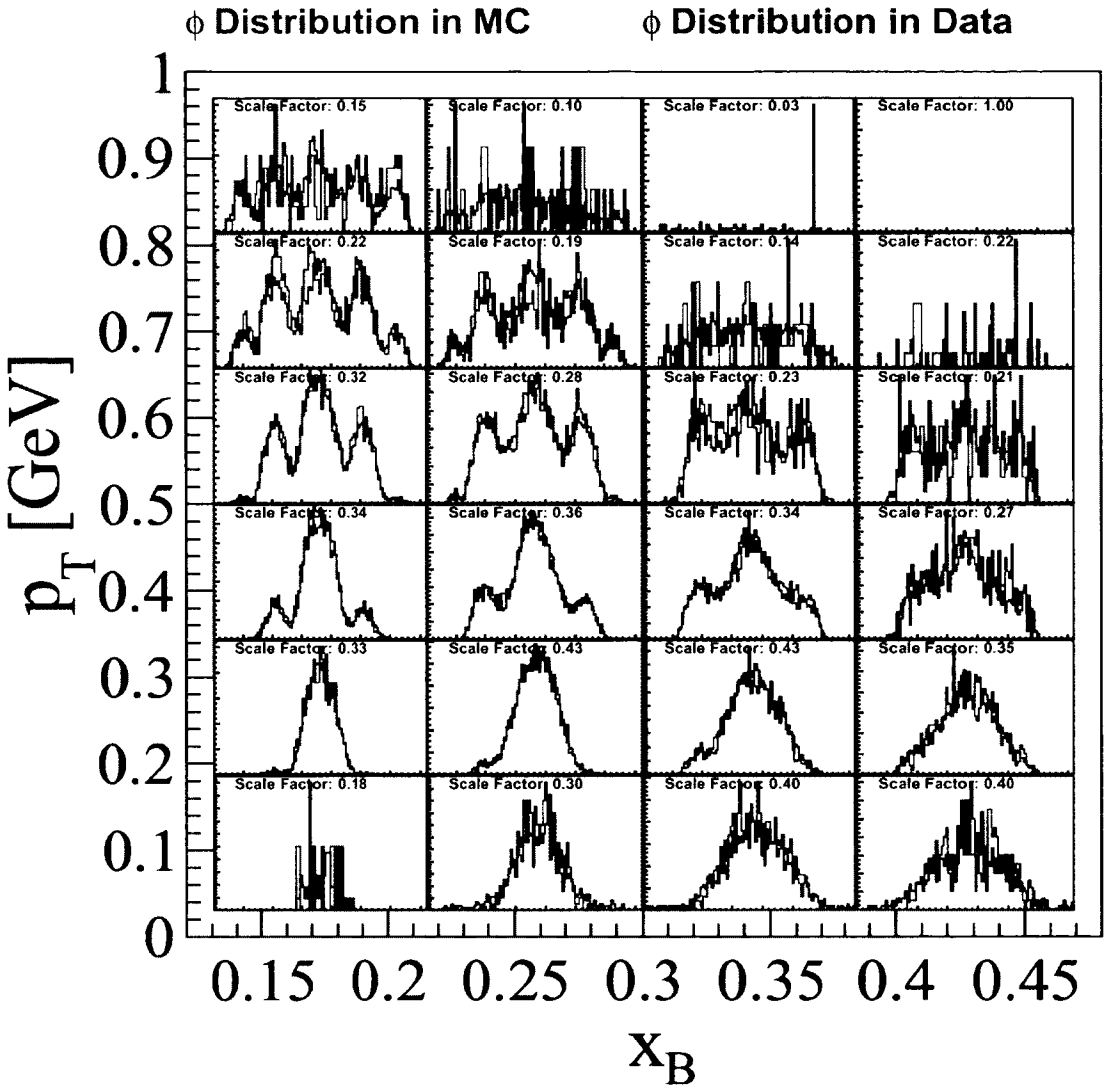

FIG. 221: Comparison between simulation and data for the azimuthal distribution of π^-

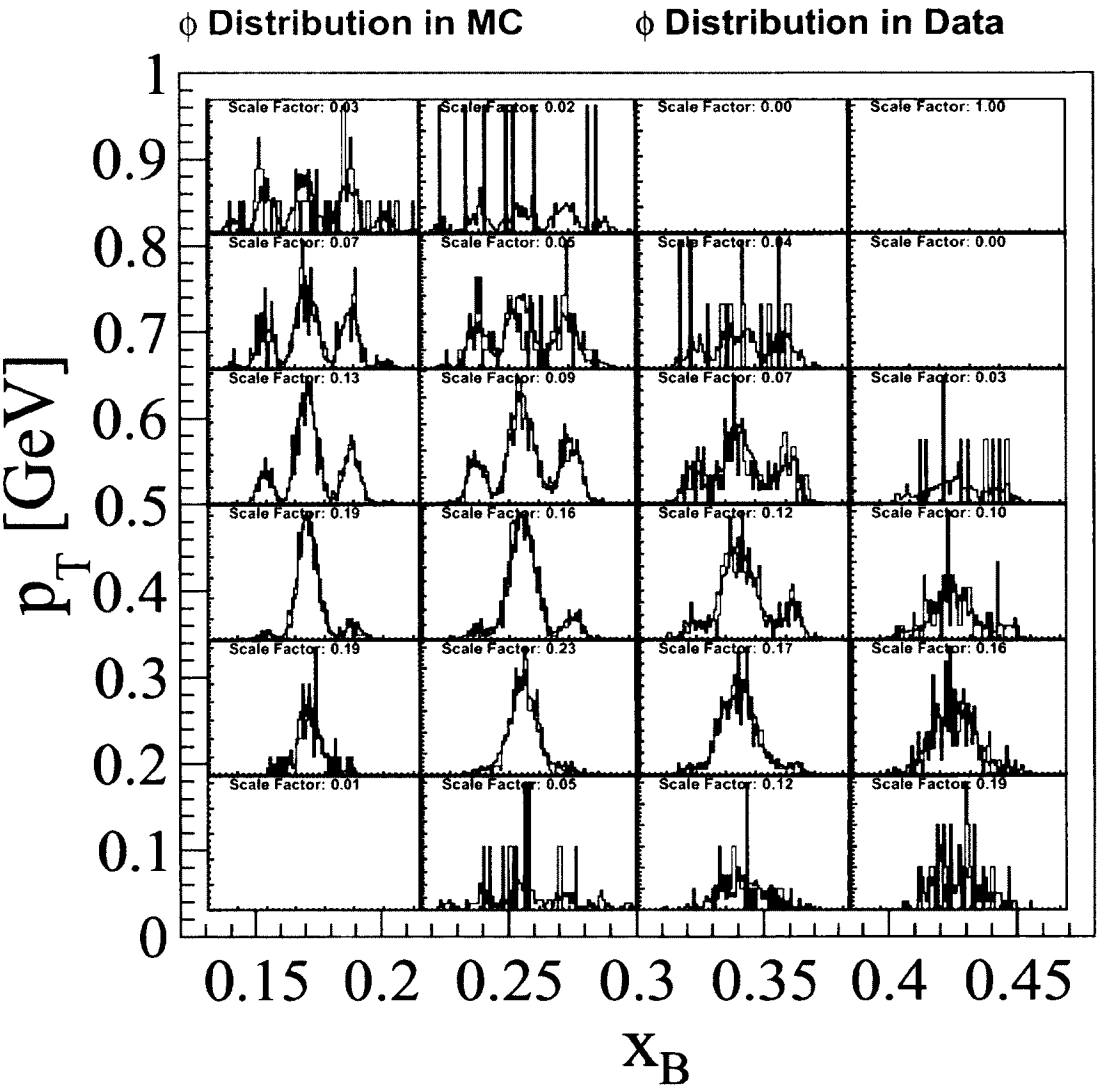

FIG. 222: Comparison between simulation and data for the azimuthal distribution of π^0 with both the photons detected in the EC.

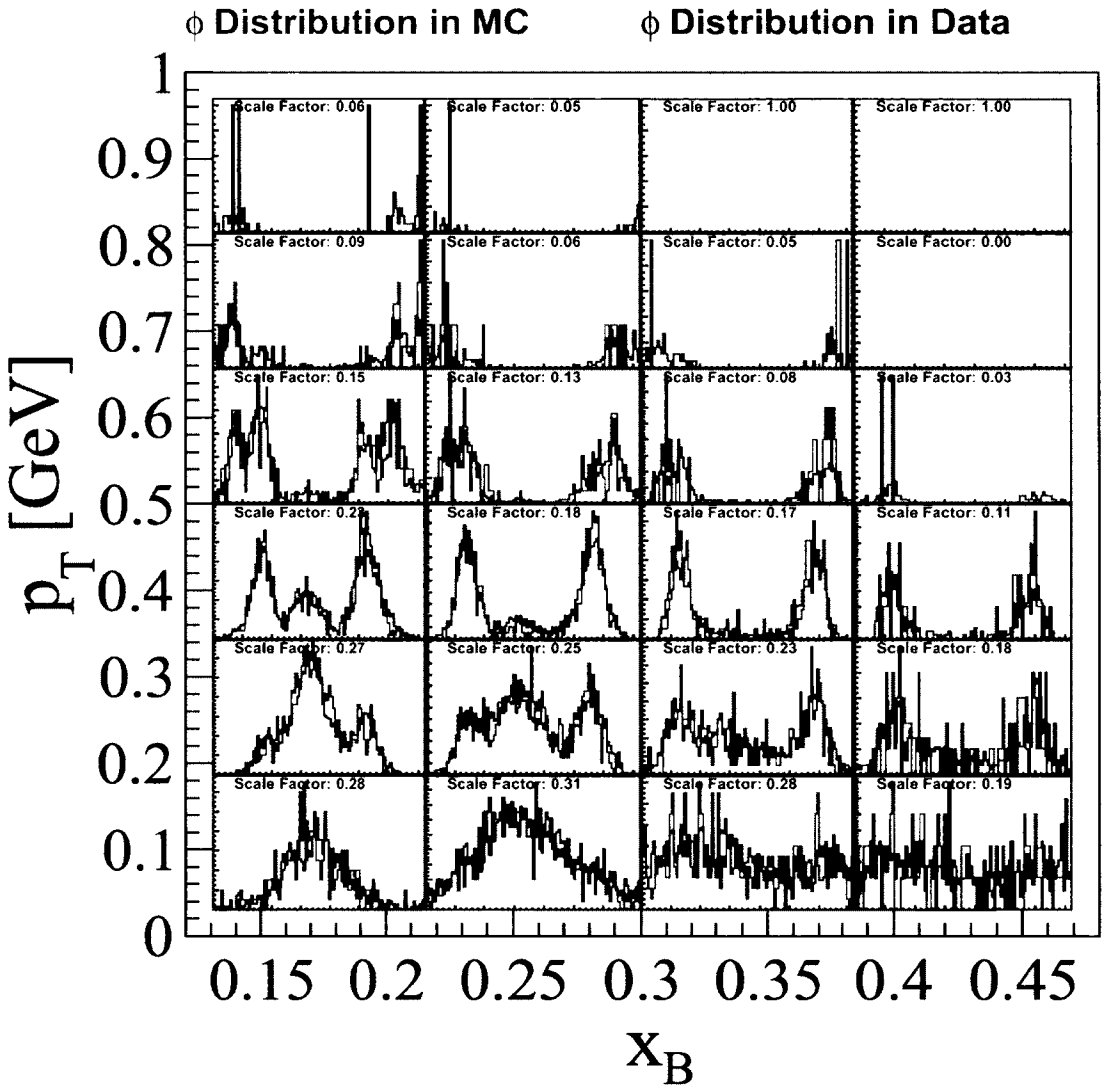

FIG. 223: Comparison between simulation and data for the azimuthal distribution of π^0 with one photon detected in the EC and the other detected in the IC.

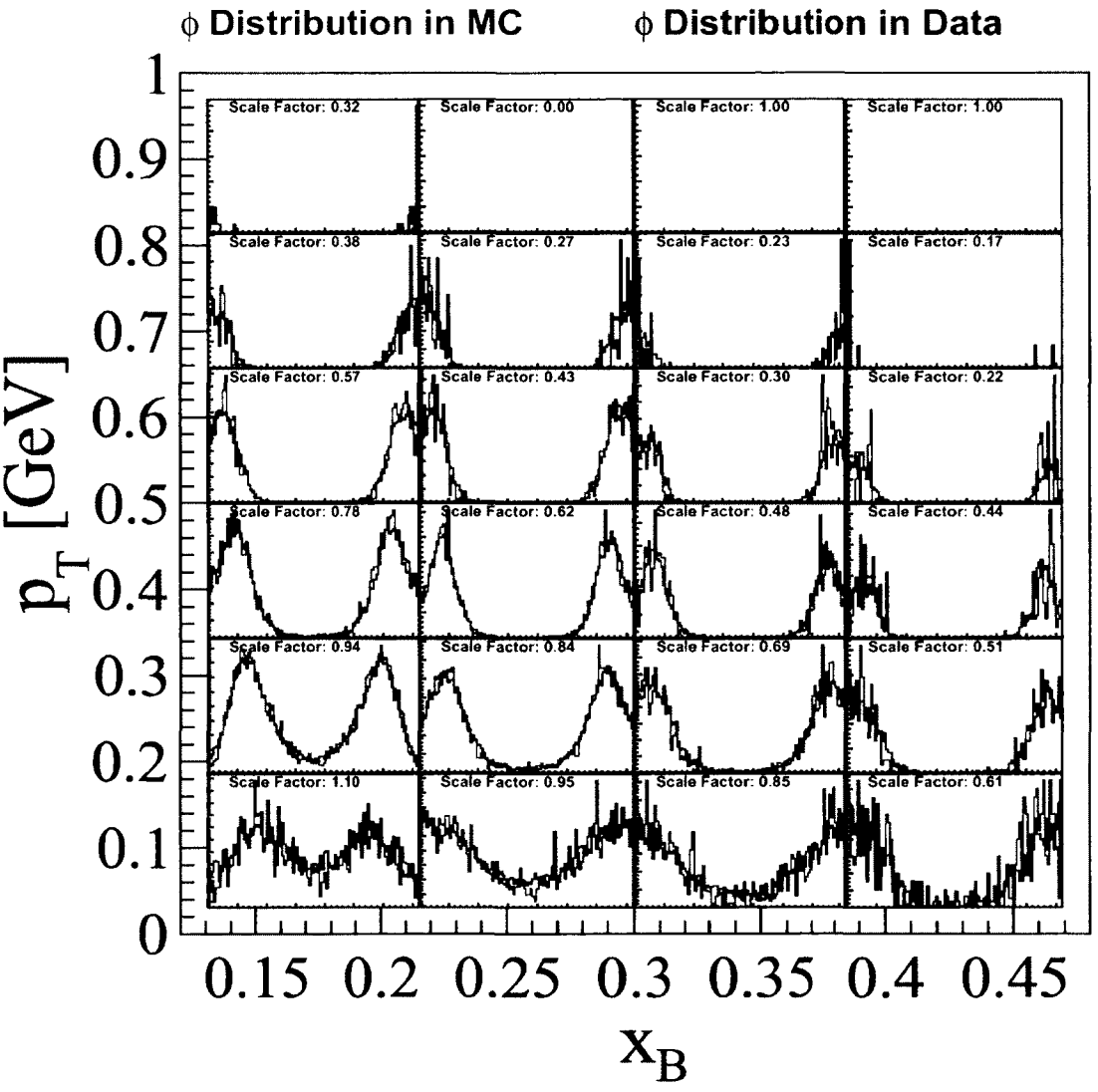

FIG. 224: Comparison between simulation and data for the azimuthal distribution of π^0 with both the photons detected in the IC.

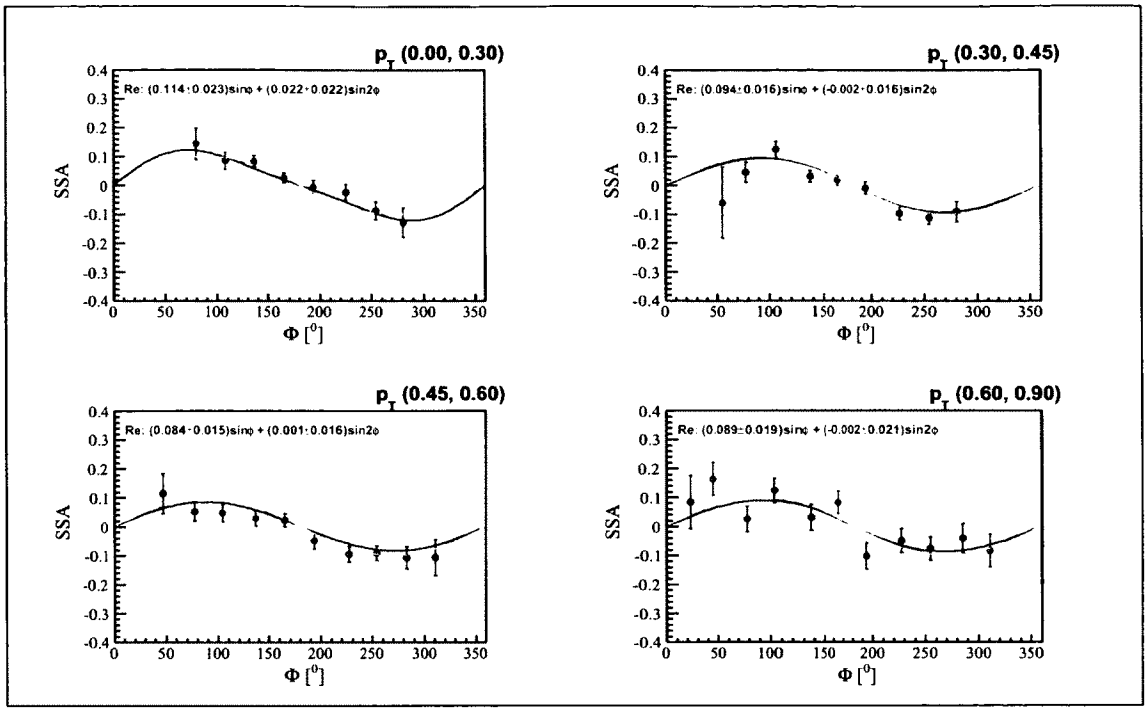

FIG. 225: Comparison of generated and reconstructed single spin asymmetries as a function of $P_{h\perp}$ for positive pions

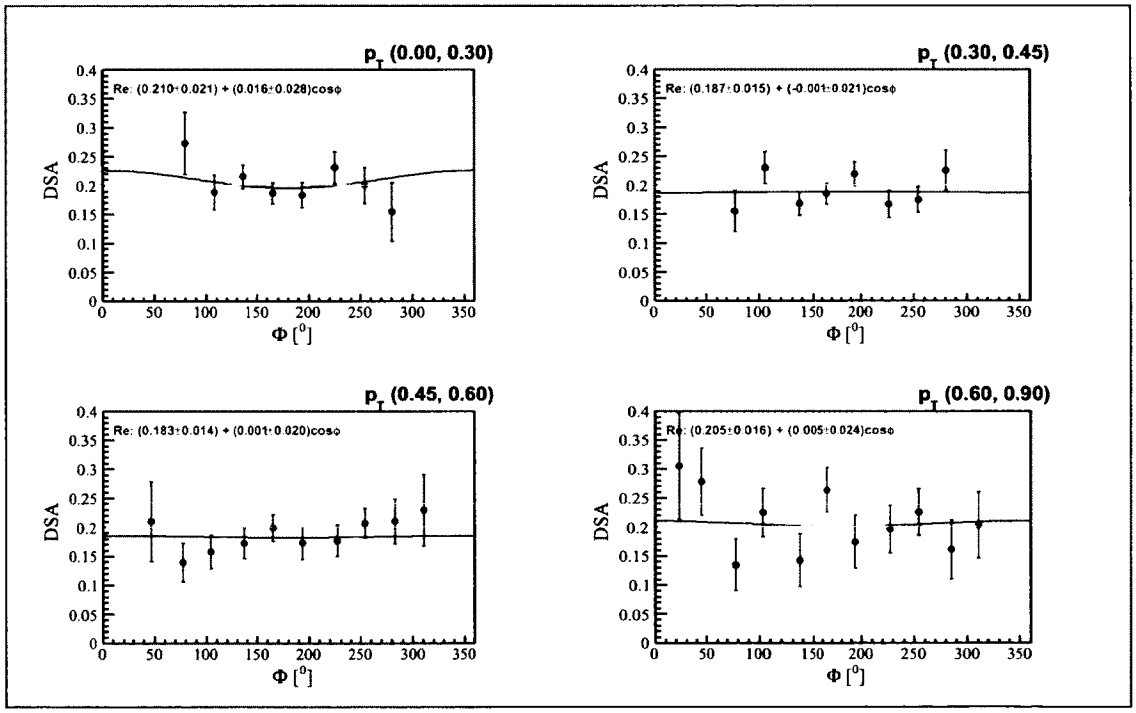

FIG. 226: Comparison of generated and reconstructed double spin asymmetries as a function of $P_{h\perp}$ for positive pions

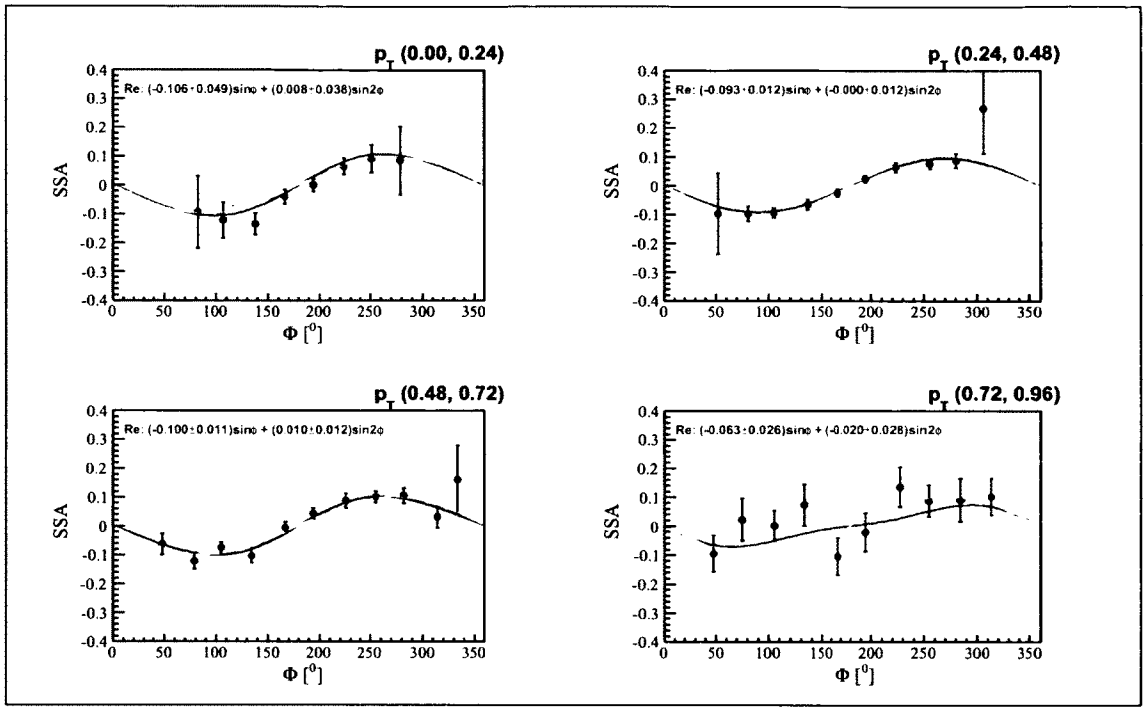

FIG. 227: Comparison of generated and reconstructed single spin asymmetries as a function of $P_{h\perp}$ for negative pions

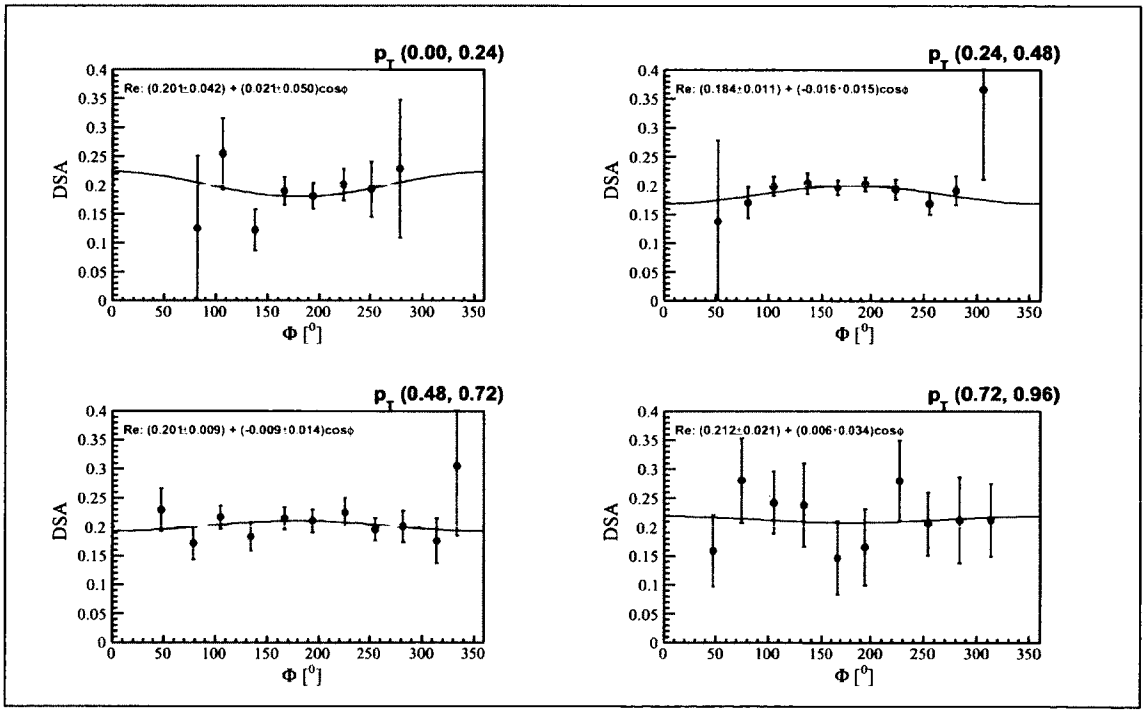

FIG. 228: Comparison of generated and reconstructed double spin asymmetries as a function of $P_{h\perp}$ for negative pions

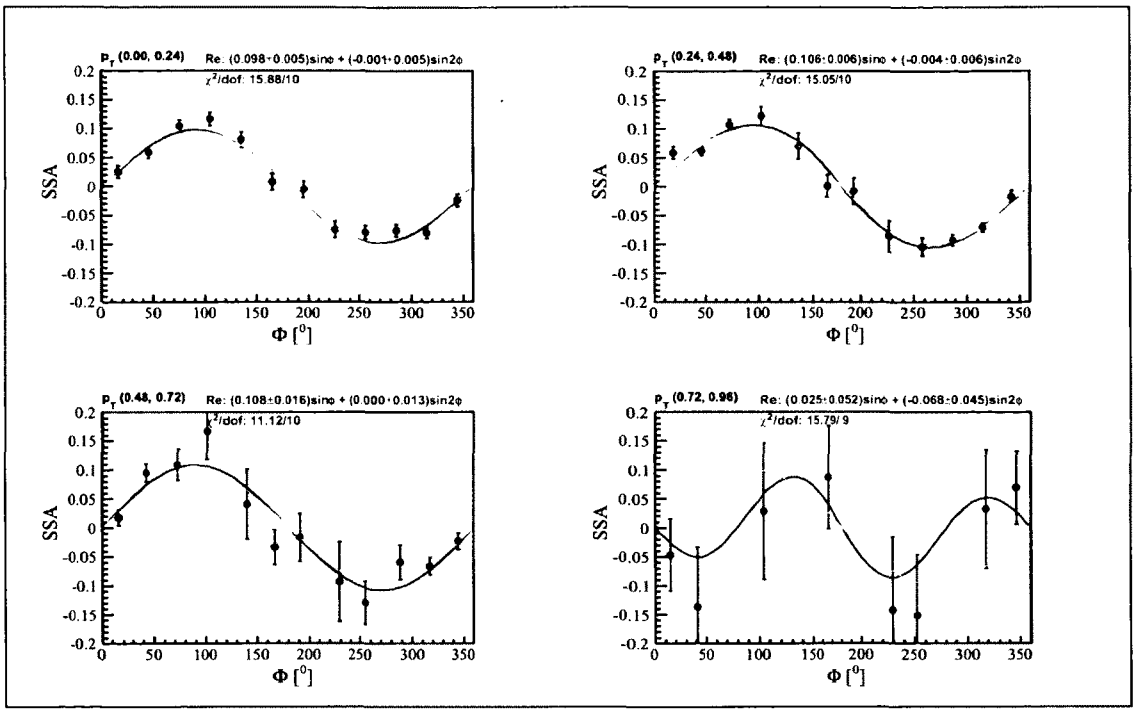

FIG. 229: Comparison of generated and reconstructed single spin asymmetries as a function of $P_{h\perp}$ for neutral pions

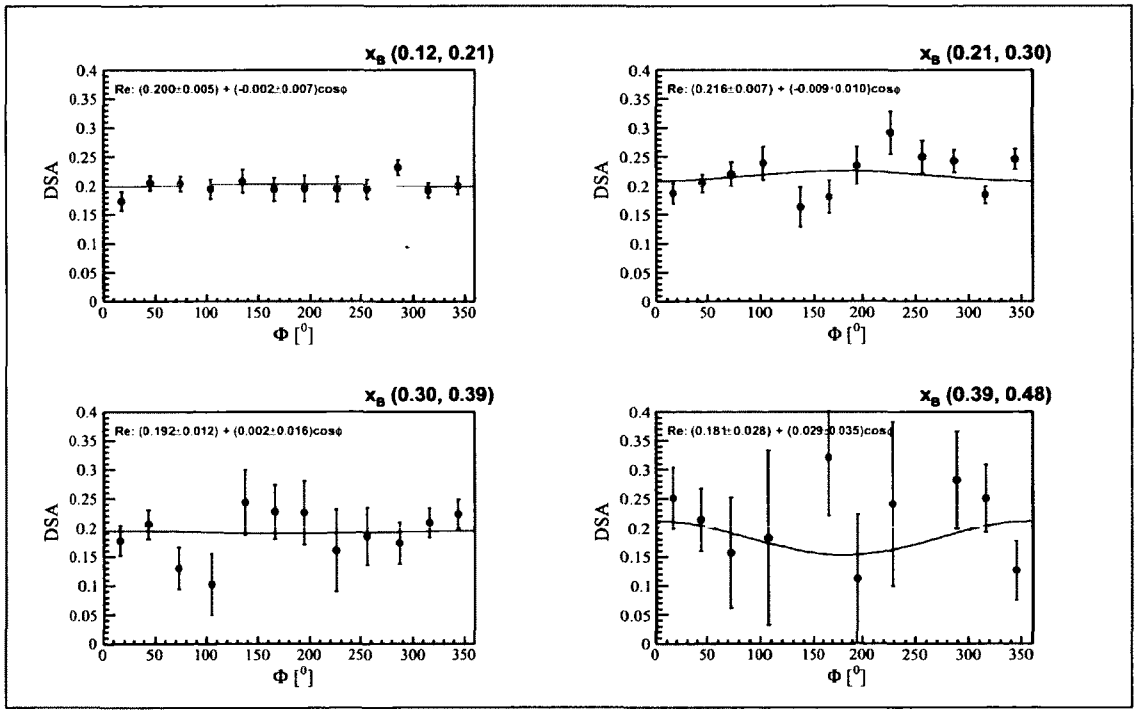

FIG. 230: Comparison of generated and reconstructed double spin asymmetries as a function of $P_{h\perp}$ for neutral pions

APPENDIX G

SYSTEMATIC UNCERTAINTIES

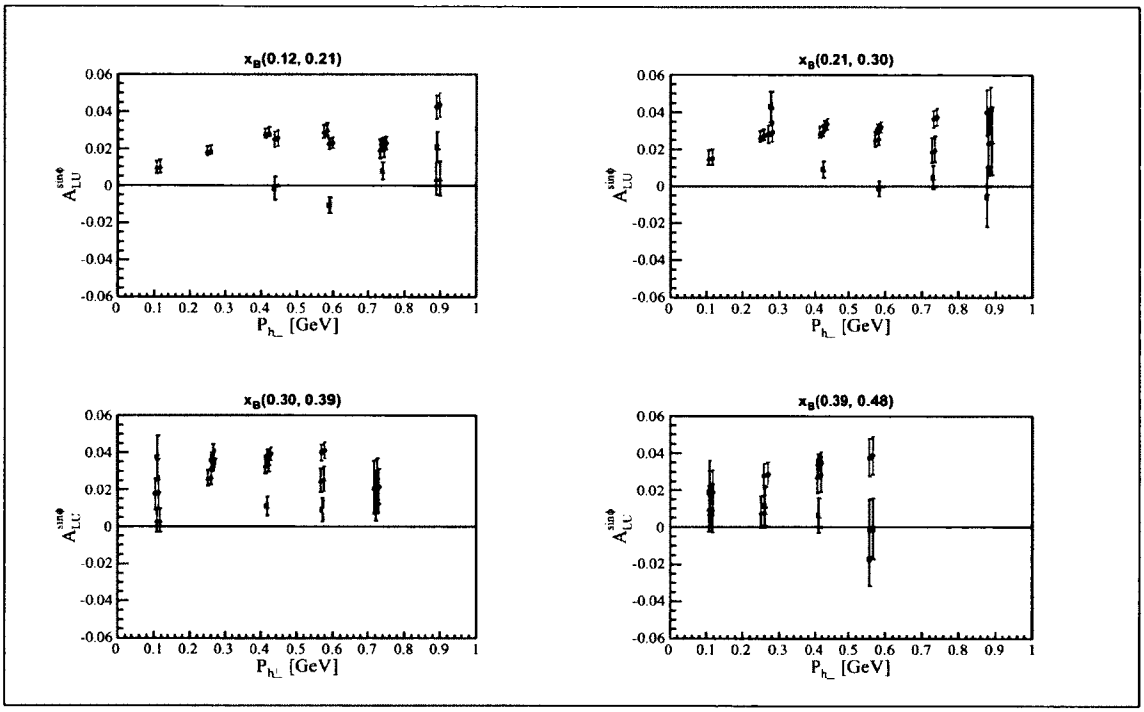

FIG. 231: Systematic uncertainty due to the uncertainty in beam and target polarizations for $A_{LU}^{\sin\phi_h}(x_B, P_{h_\perp})$ on the proton; circles: π^+, squares:π^- triangles:π^0

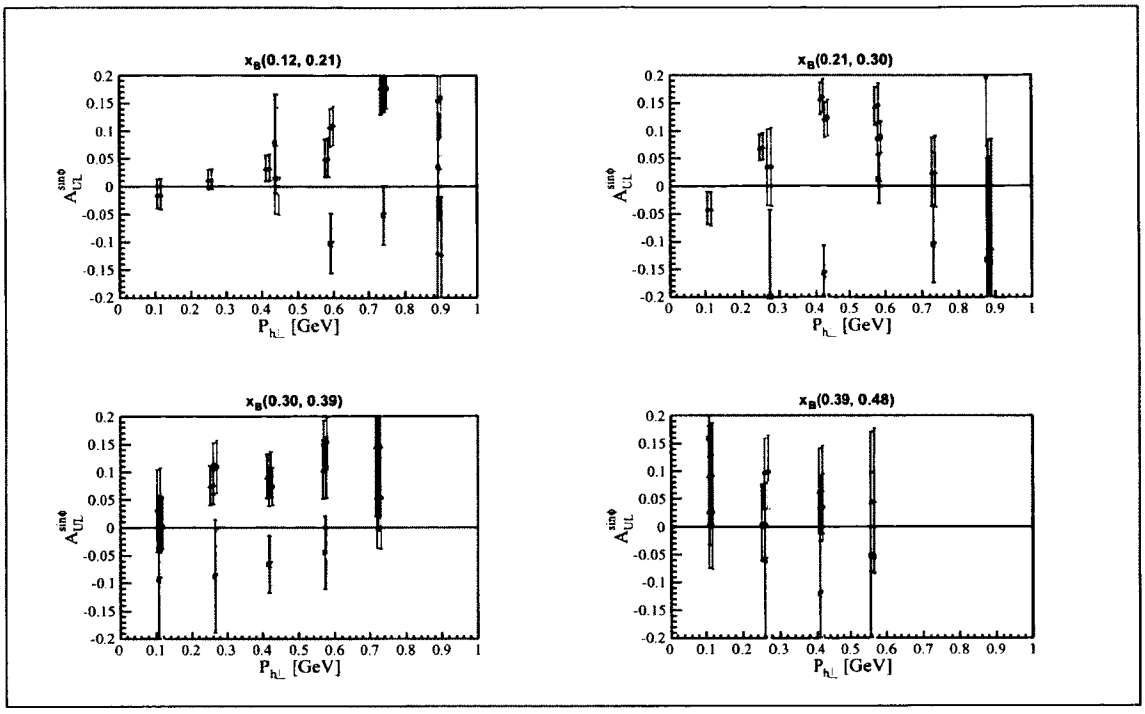

FIG. 232: Systematic uncertainty due to the uncertainty in beam and target polarizations for $A_{UL}^{\sin\phi_h}(x_B, P_{h\perp})$ on the proton; circles: π^+, squares:π^- triangles:π^0

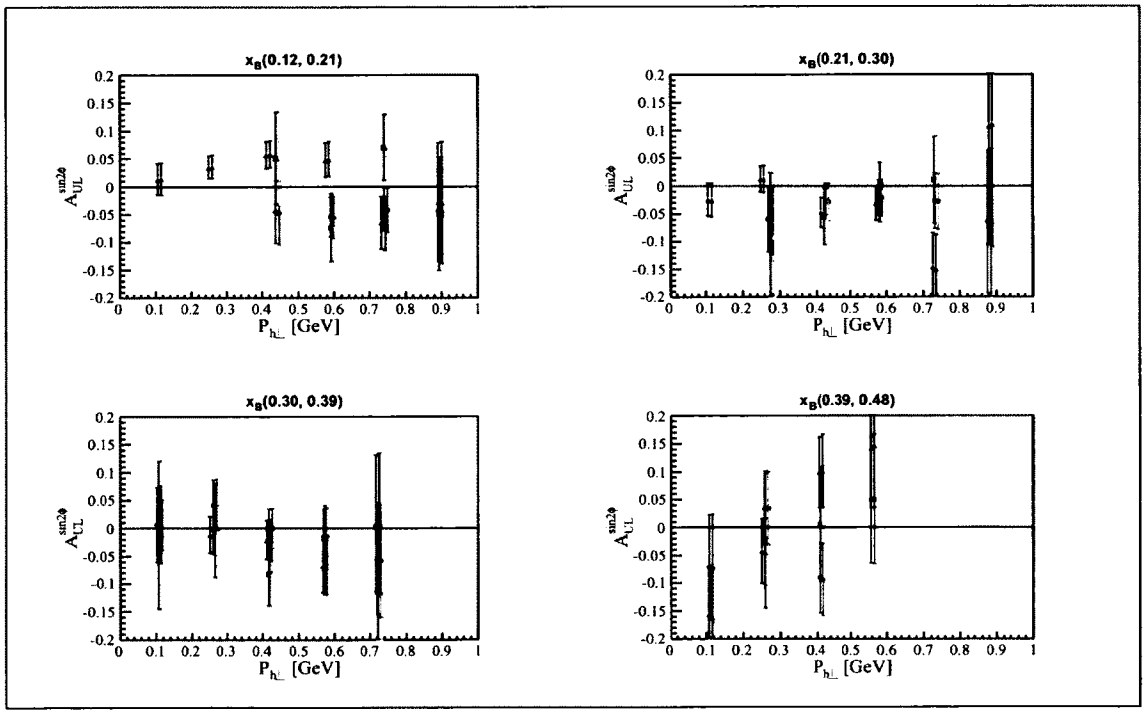

FIG. 233: Systematic uncertainty due to the uncertainty in beam and target polarizations for $A_{UL}^{\sin 2\phi_h}(x_B, P_{h\perp})$ on the proton; circles: π^+, squares:π^- triangles:π^0

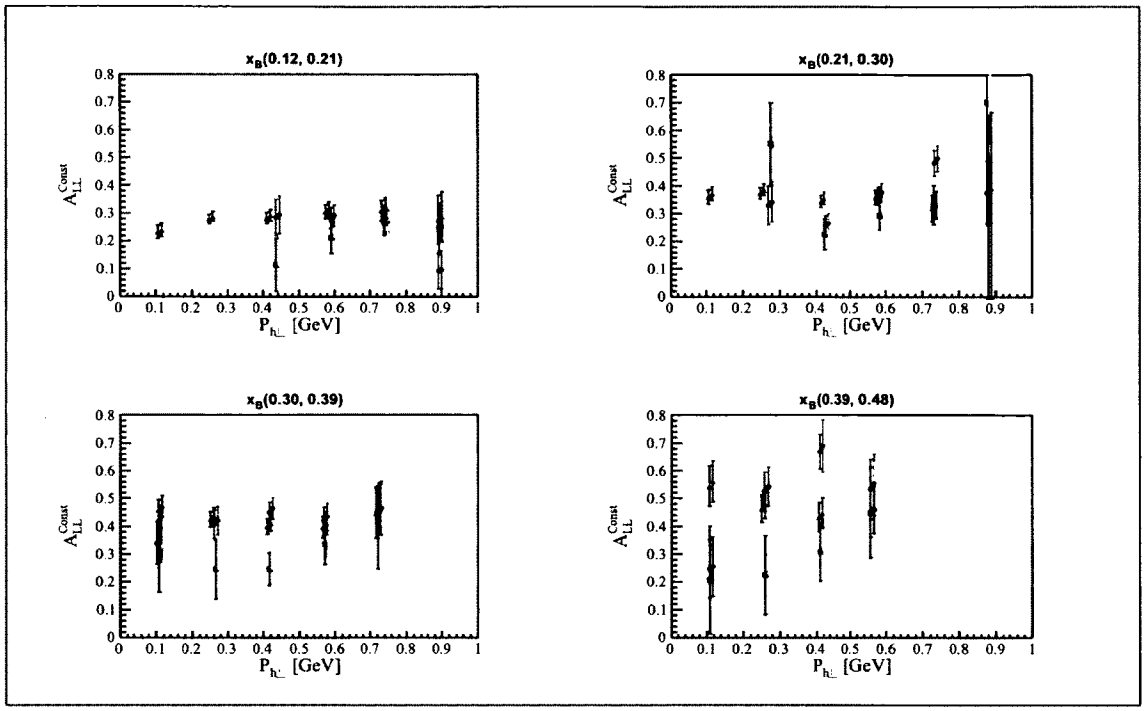

FIG. 234: Systematic uncertainty due to the uncertainty in beam and target polarizations for $A_{LL}^{\text{Const}}(x_B, P_{h_\perp})$ on the proton; circles: π^+, squares:π^- triangles:π^0

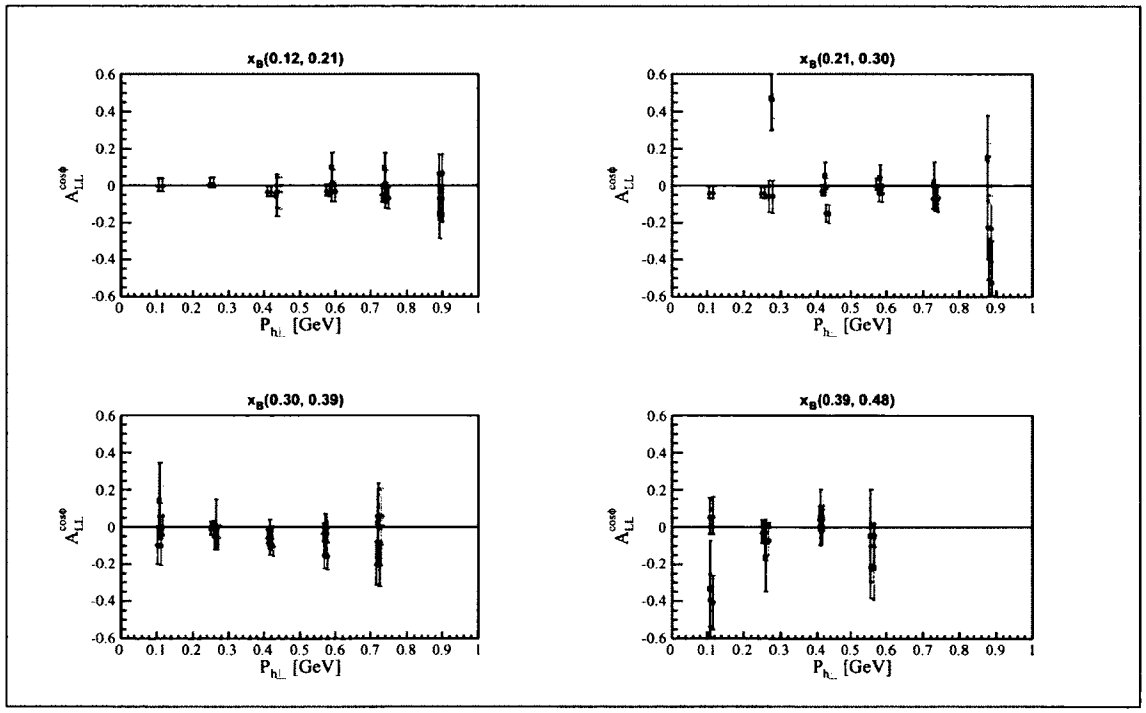

FIG. 235: Systematic uncertainty due to the uncertainty in beam and target polarizations for $A_{LL}^{\cos\phi_h}(x_B, P_{h_\perp})$ on the proton; circles: π^+, squares:π^- triangles:π^0

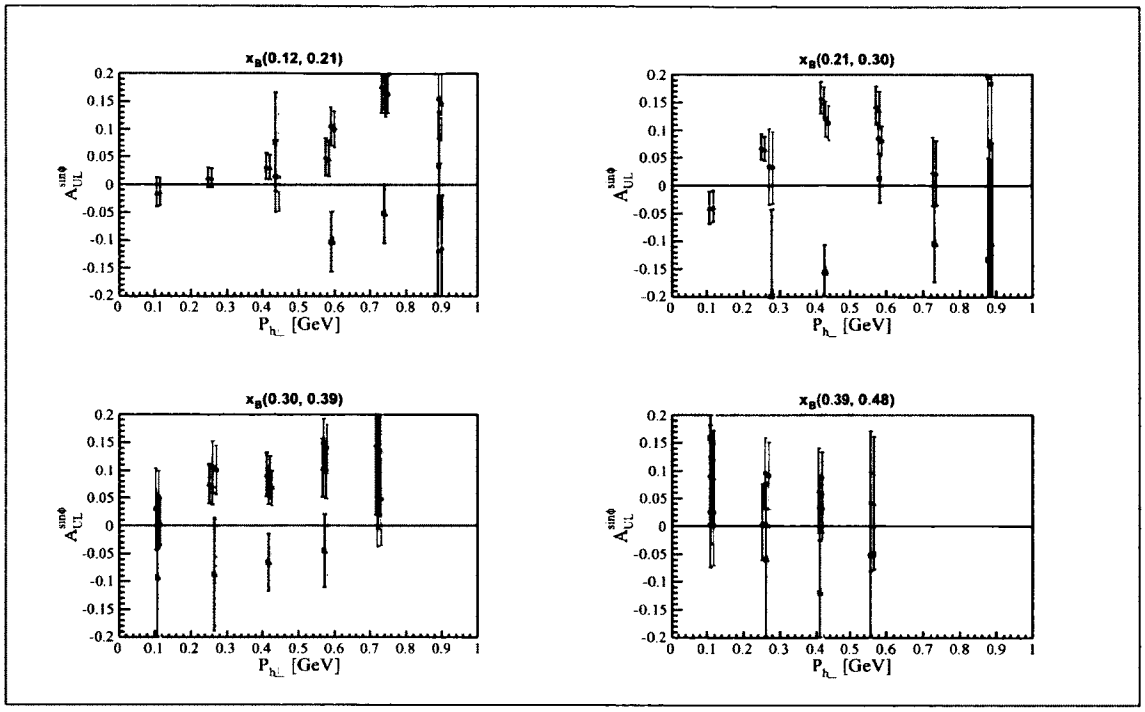

FIG. 236: Systematic uncertainty due to the uncertainty in dilution factor, assuming 5% normalizationuncertainty in EG2 π^0 data, for $A_{UL}^{\sin\phi_h}(x_B, P_{h\perp})$ on the proton; circles: π^+, squares:π^- triangles:π^0

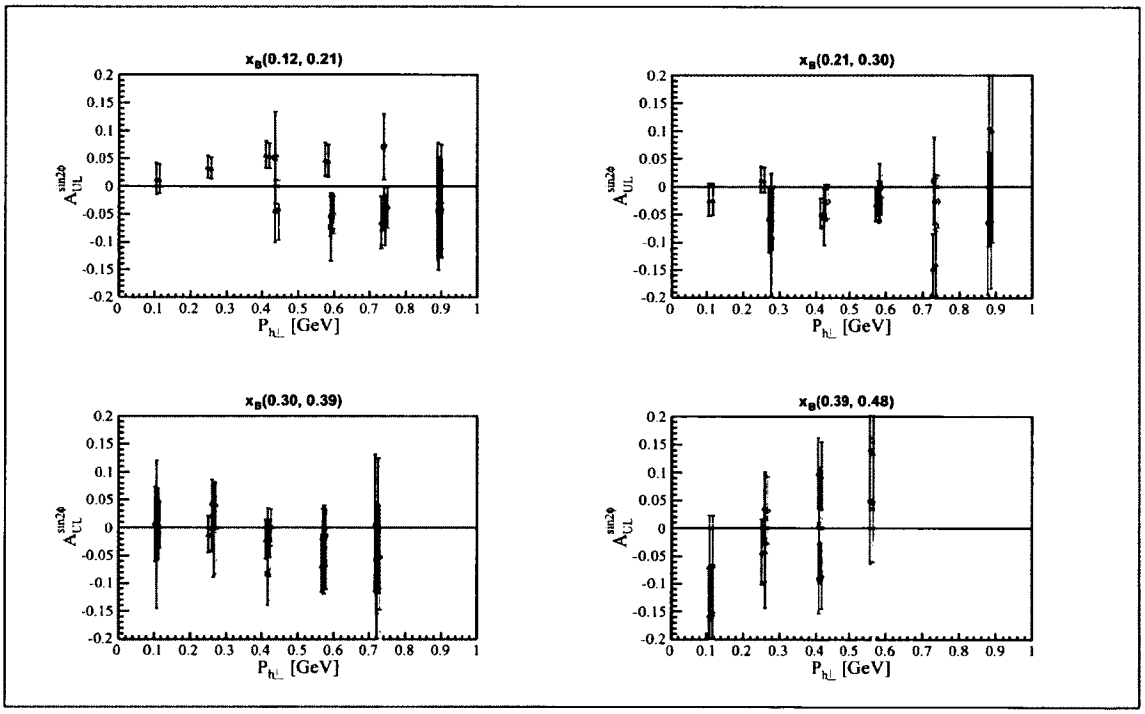

FIG. 237: Systematic uncertainty due to the uncertainty in dilution factor, assuming 5% normalizationuncertainty in EG2 π^0 data, for $A_{UL}^{\sin 2\phi_h}(x_B, P_{h\perp})$ on the proton; circles: π^+, squares:π^- triangles:π^0

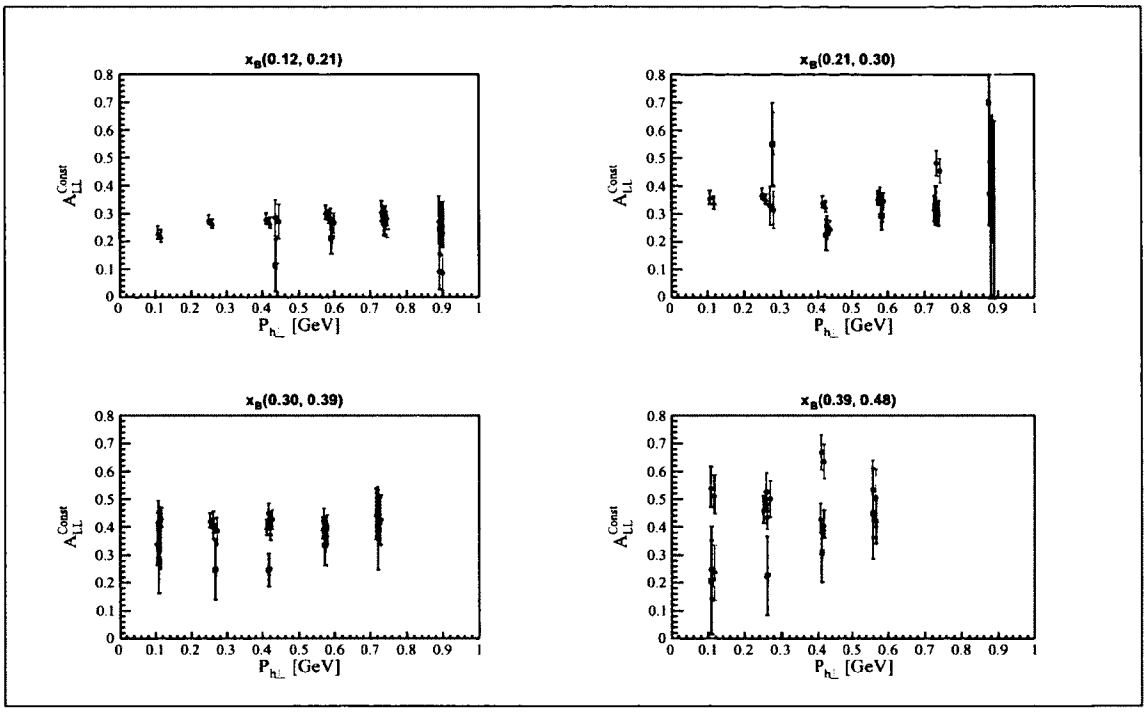

FIG. 238: Systematic uncertainty due to the uncertainty in dilution factor, assuming 5% normalizationuncertainty in EG2 π^0 data, for $A_{LL}^{\text{Const}}(x_B, P_{h_\perp})$ on the proton; circles: π^+, squares:π^- triangles:π^0

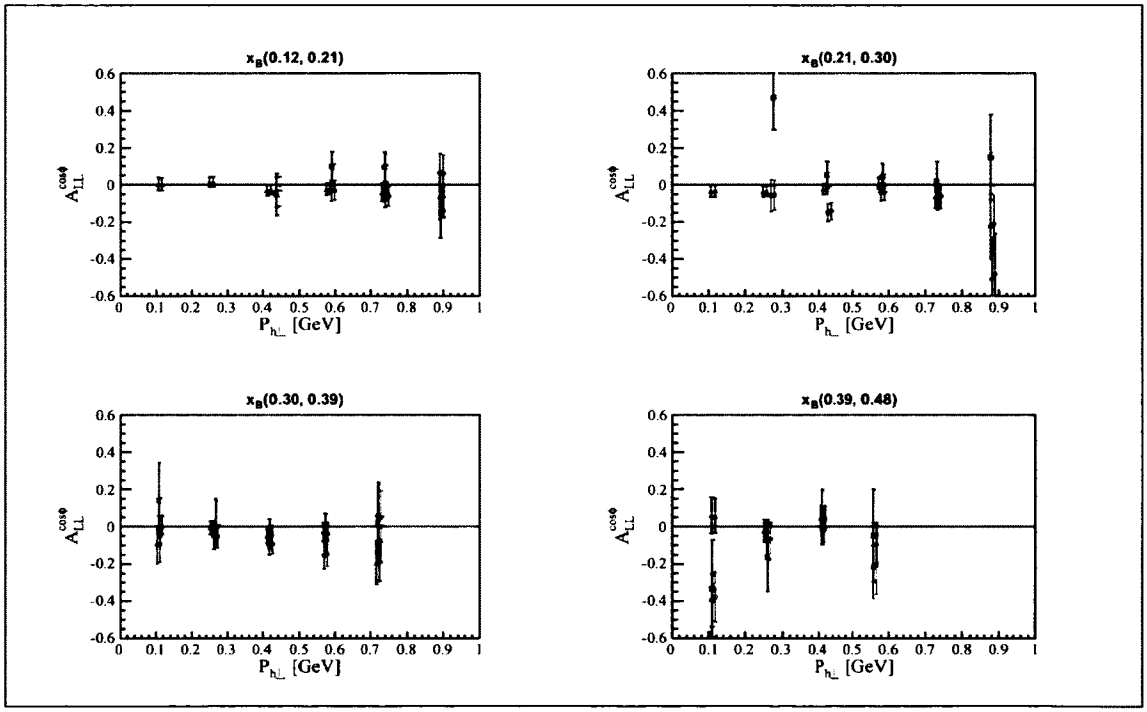

FIG. 239: Systematic uncertainty due to the uncertainty in dilution factor, assuming 5% normalizationuncertainty in EG2 π^0 data, for $A_{LL}^{\cos\phi_h}(x_B, P_{h_\perp})$ on the proton; circles: π^+, squares:π^- triangles:π^0

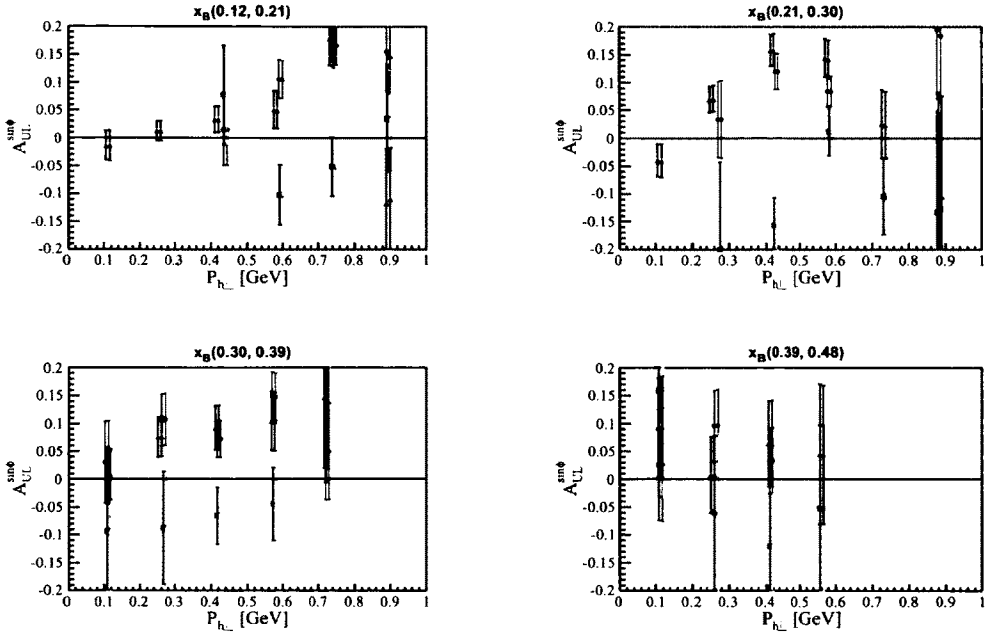

FIG. 240: Systematic uncertainty due to the uncertainty in the dilution factor, extracted with EG2 π^+ data, for $A_{UL}^{\sin\phi_h}(x_B)$ on the proton; circles: π^+, squares: π^- and triangles: π^0

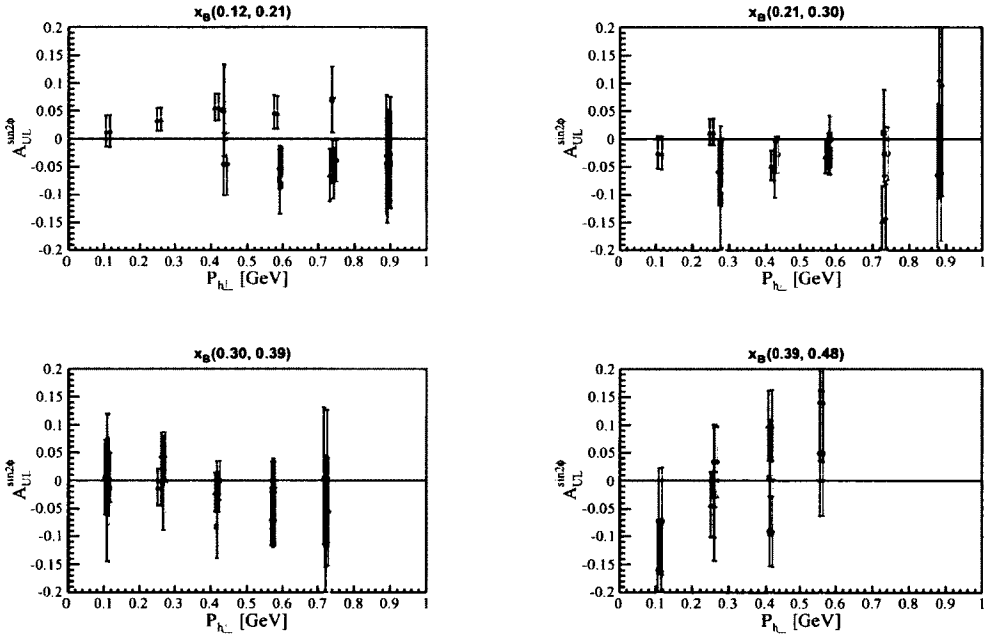

FIG. 241: Systematic uncertainty due to the uncertainty in the dilution factor, extracted with EG2 π^+ data, for $A_{UL}^{\sin 2\phi_h}(x_B)$ on the proton; circles: π^+, squares: π^- and triangles: π^0

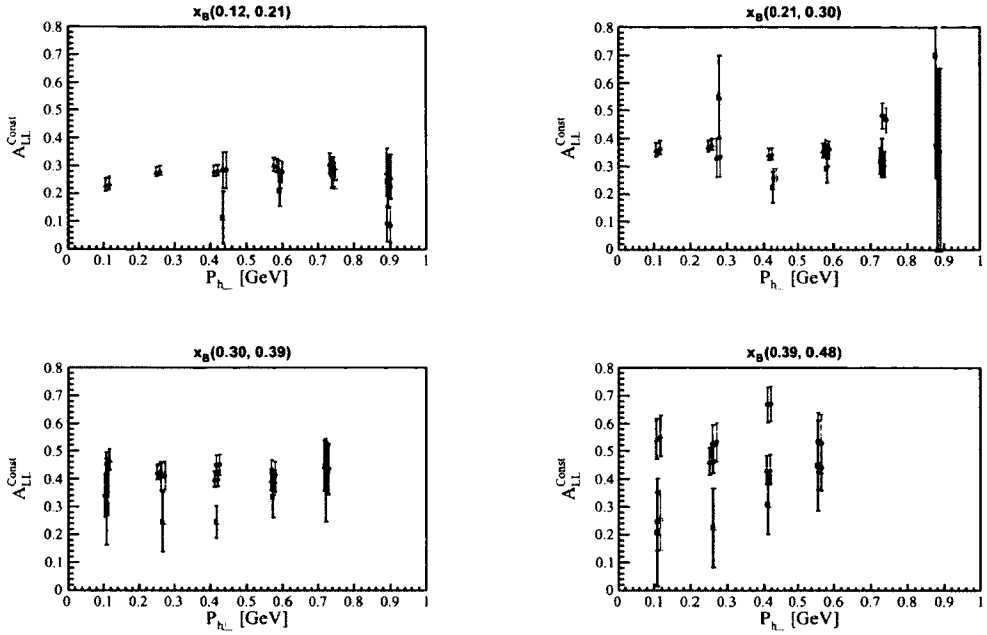

FIG. 242: Systematic uncertainty due to the uncertainty in the dilution factor, extracted with EG2 π^+ data, for $A_{LL}^{\text{Const}}(x_B)$ on the proton; circles: π^+, squares: π^- and triangles: π^0

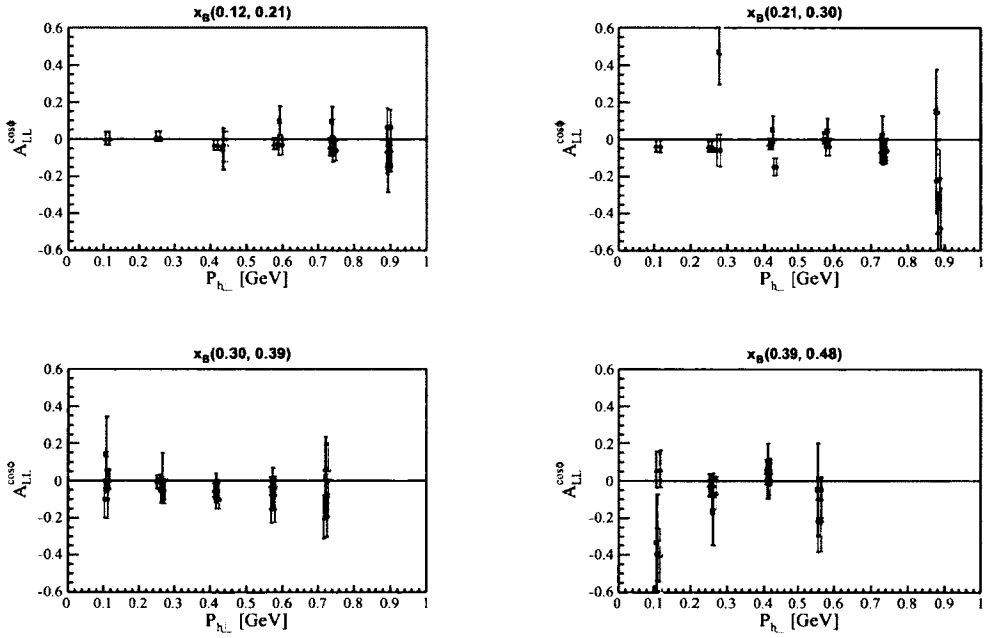

FIG. 243: Systematic uncertainty due to the uncertainty in the dilution factor, extracted with EG2 π^+ data, for $A_{LL}^{\cos\phi_h}(x_B)$ on the proton; circles: π^+, squares: π^- and triangles: π^0

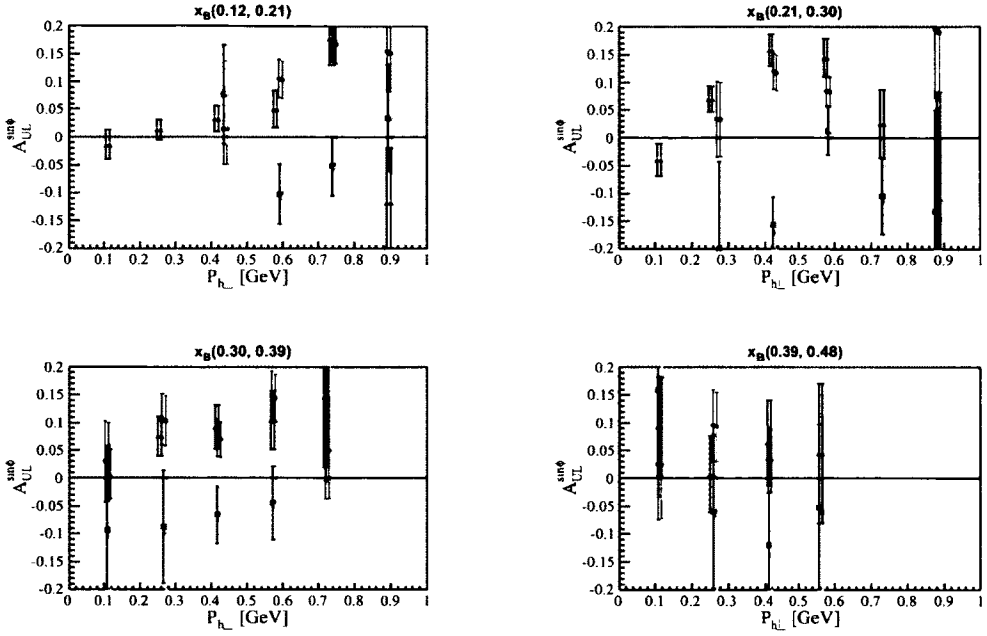

FIG. 244: Systematic uncertainty due to the uncertainty in the dilution factor, extracted with an alternative expression for the fragmentation ratio, for $A_{UL}^{\sin\phi_h}(x_B)$ on the proton; circles: π^+, squares: π^- and triangles: π^0

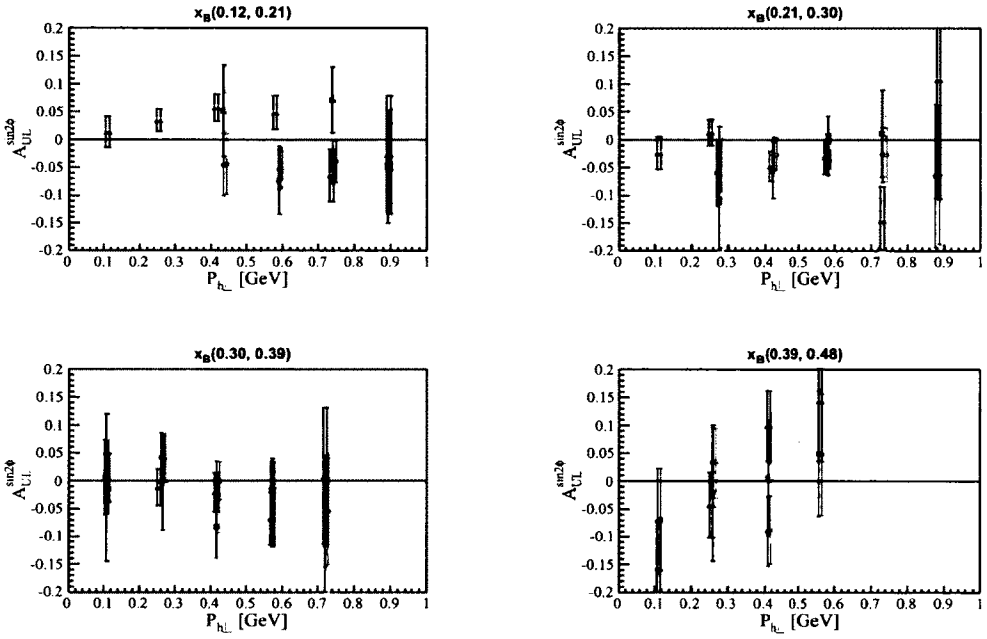

FIG. 245: Systematic uncertainty due to the uncertainty in the dilution factor, extracted with an alternative expression for the fragmentation ratio, for $A_{UL}^{\sin2\phi_h}(x_B)$ on the proton; circles: π^+, squares: π^- and triangles: π^0

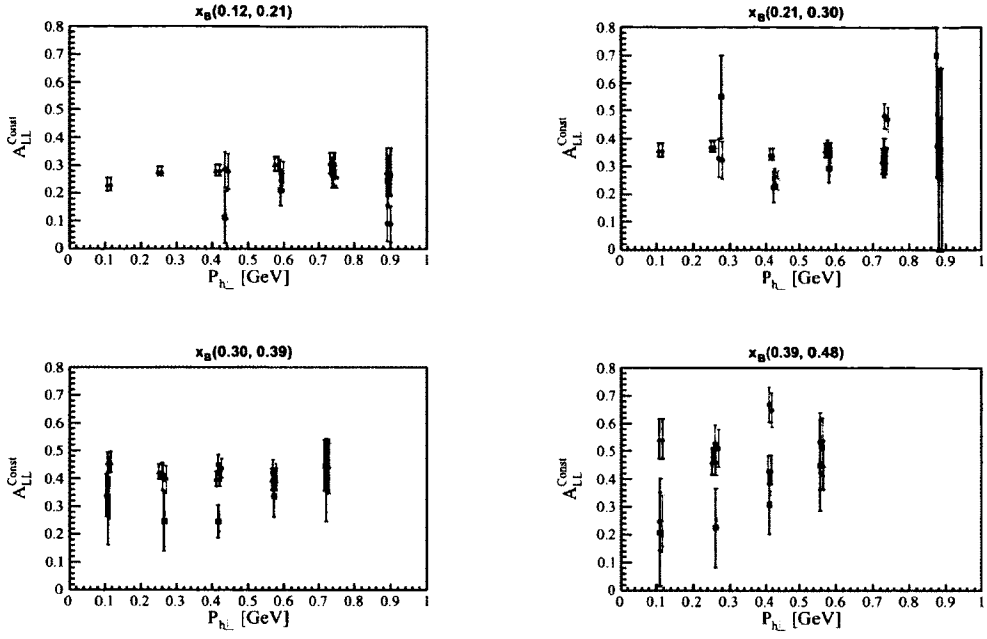

FIG. 246: Systematic uncertainty due to the uncertainty in the dilution factor, extracted with an alternative expression for the fragmentation ratio, for $A_{LL}^{\mathrm{Const}}(x_B)$ on the proton; circles: π^+, squares: π^- and triangles: π^0

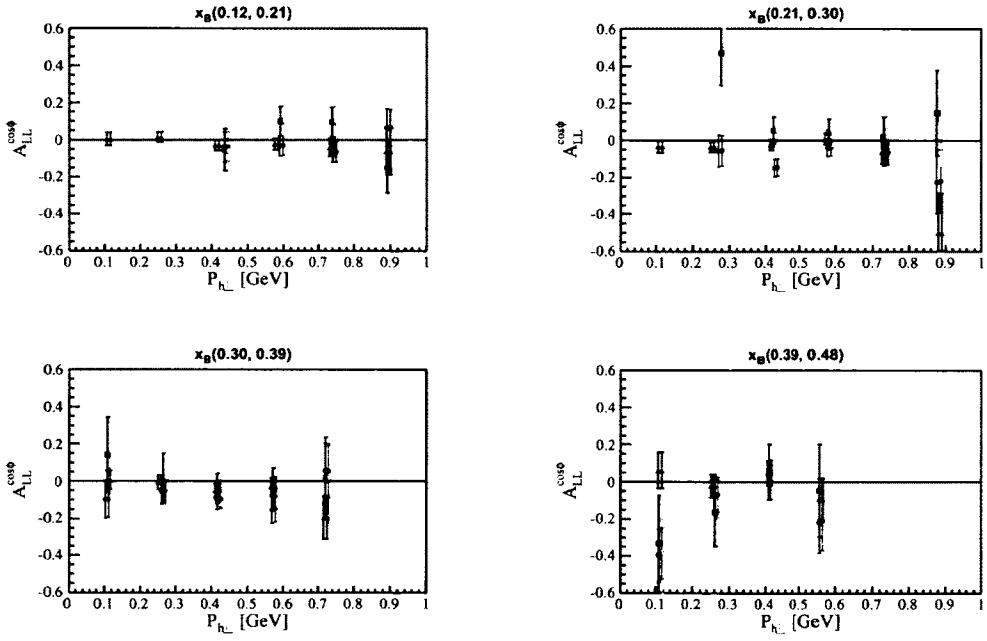

FIG. 247: Systematic uncertainty due to the uncertainty in the dilution factor, extracted with an alternative expression for the fragmentation ratio, for $A_{LL}^{\cos\phi_h}(x_B)$ on the proton; circles: π^+, squares: π^- and triangles: π^0

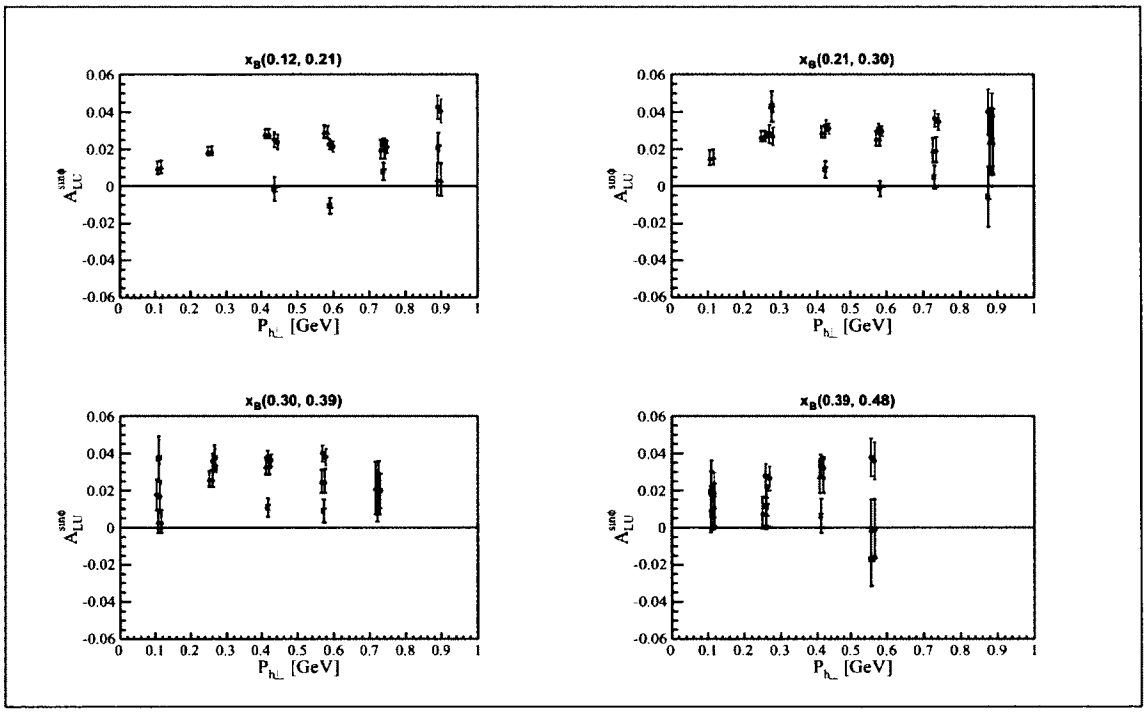

FIG. 248: Systematic uncertainty due to the uncertainty in background subtraction for $A_{LU}^{\sin\phi_h}(x_B, P_{h_\perp})$ on the proton; circles: π^+, squares:π^- triangles:π^0

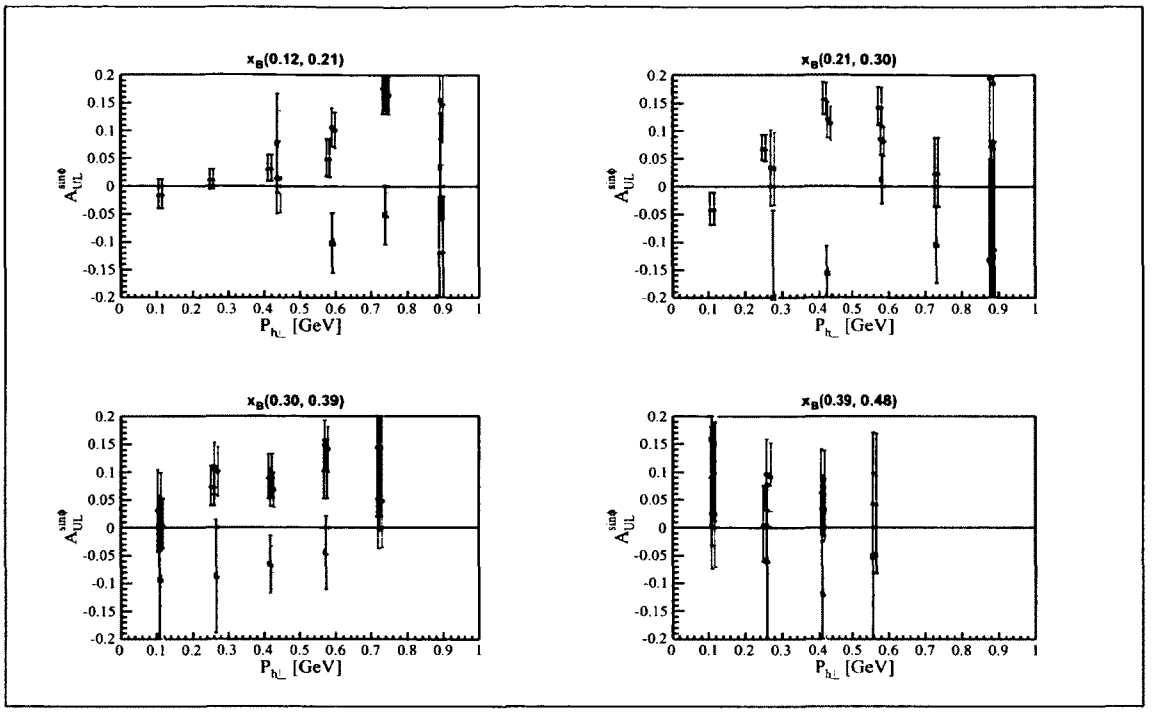

FIG. 249: Systematic uncertainty due to the uncertainty in background subtraction for $A_{UL}^{\sin\phi_h}(x_B, P_{h_\perp})$ on the proton; circles: π^+, squares:π^- triangles:π^0

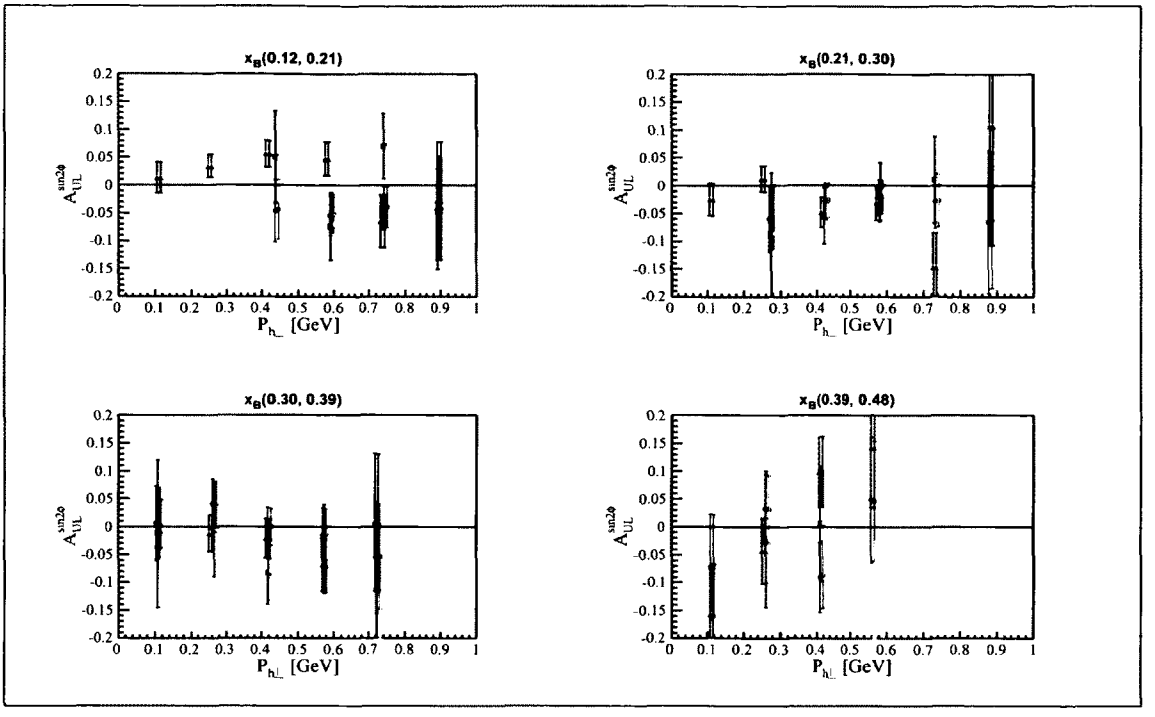

FIG. 250: Systematic uncertainty due to the uncertainty in background subtraction for $A_{UL}^{\sin 2\phi_h}(x_B, P_{h\perp})$ on the proton; circles: π^+, squares:π^- triangles:π^0

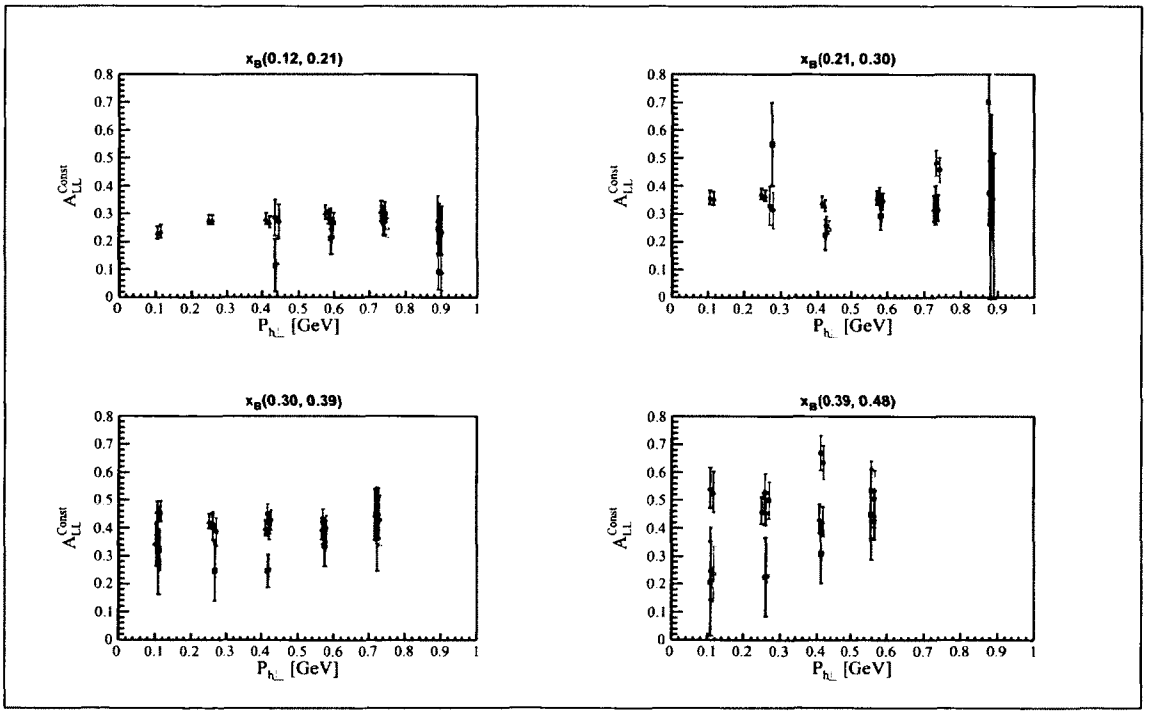

FIG. 251: Systematic uncertainty due to the uncertainty in background subtraction for $A_{LL}^{\text{Const}}(x_B, P_{h\perp})$ on the proton; circles: π^+, squares:π^- triangles:π^0

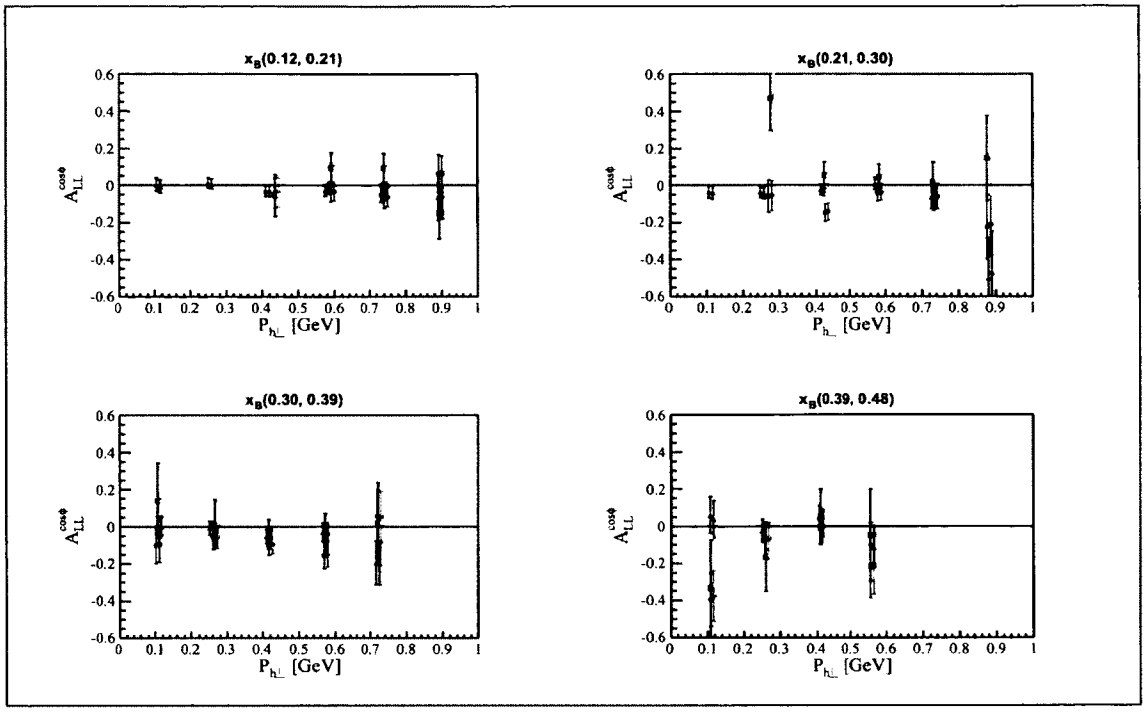

FIG. 252: Systematic uncertainty due to the uncertainty in background subtraction for $A_{LL}^{\cos\phi_h}(x_B, P_{h_\perp})$ on the proton; circles: π^+, squares:π^- triangles:π^0

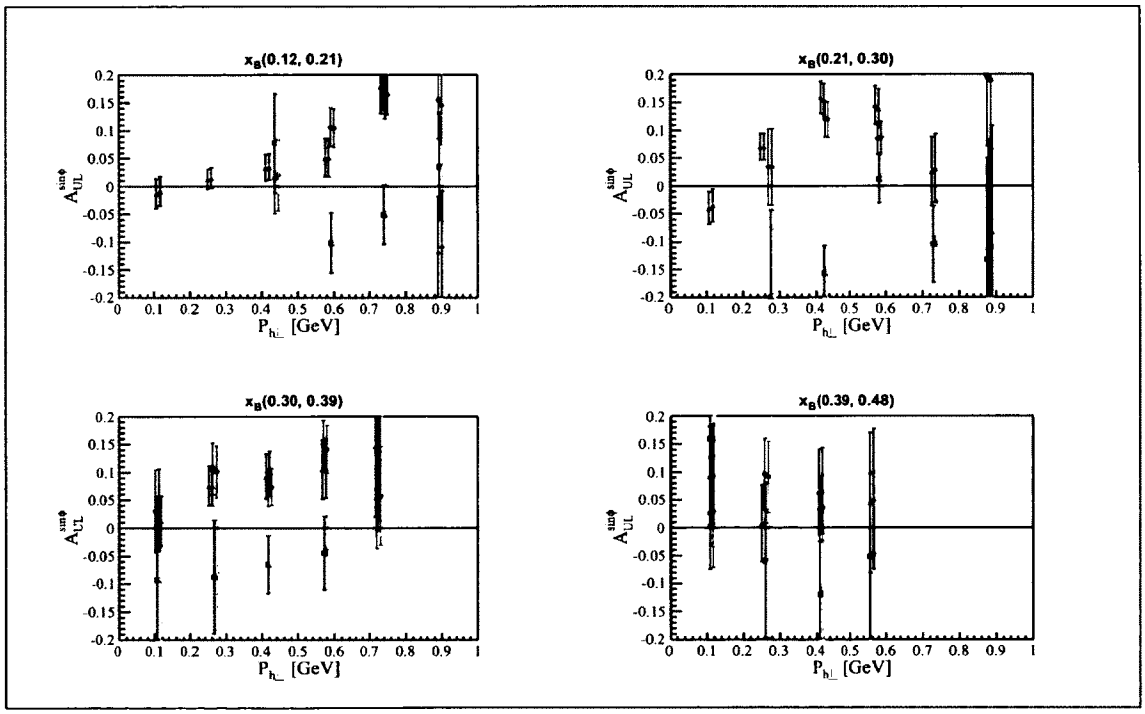

FIG. 253: Systematic uncertainty due to the uncertainty in the radiative corrections for $A_{UL}^{\sin\phi_h}(x_B, P_{h_\perp})$ on the proton; circles: π^+, squares:π^- triangles:π^0

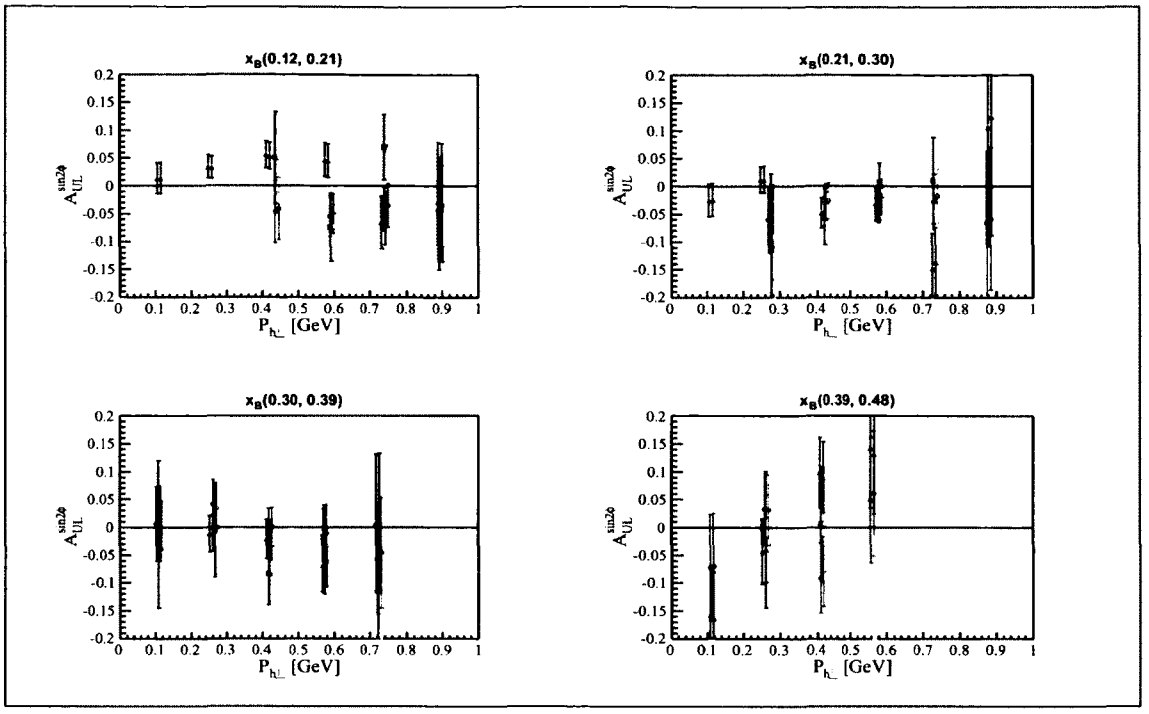

FIG. 254: Systematic uncertainty due to the uncertainty in the radiative corrections for $A_{UL}^{\sin 2\phi_h}(x_B, P_{h_\perp})$ on the proton; circles: π^+, squares:π^- triangles:π^0

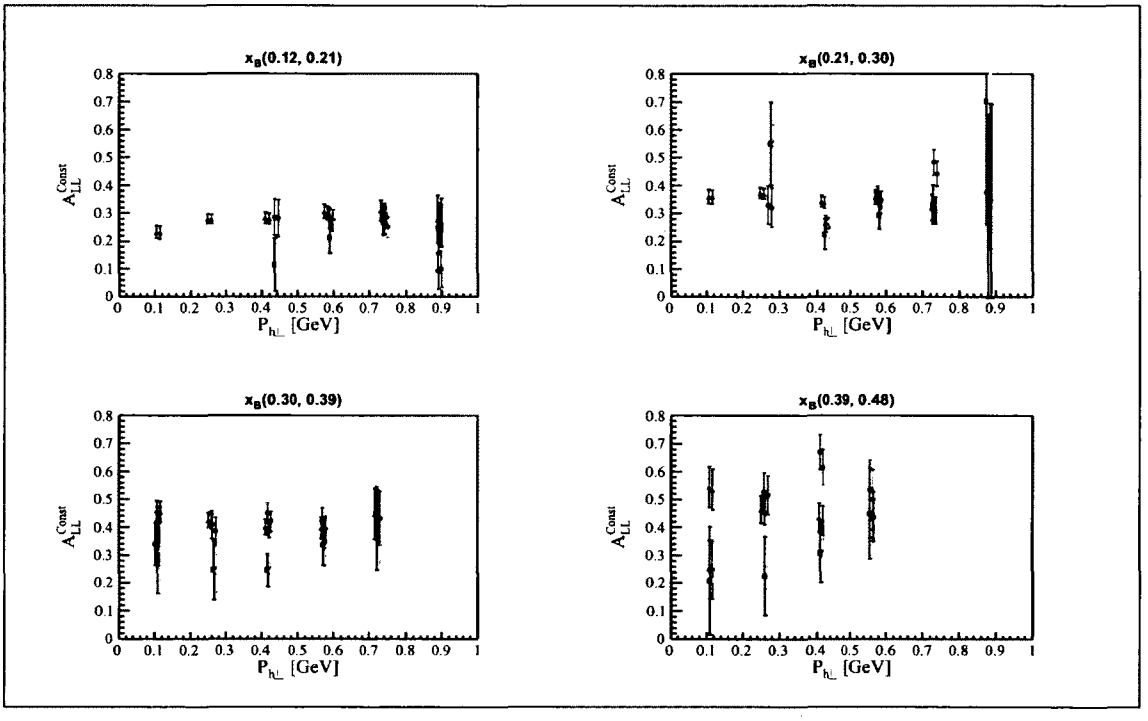

FIG. 255: Systematic uncertainty due to the uncertainty in the radiative corrections for $A_{LL}^{\text{Const}}(x_B, P_{h_\perp})$ on the proton; circles: π^+, squares:π^- triangles:π^0

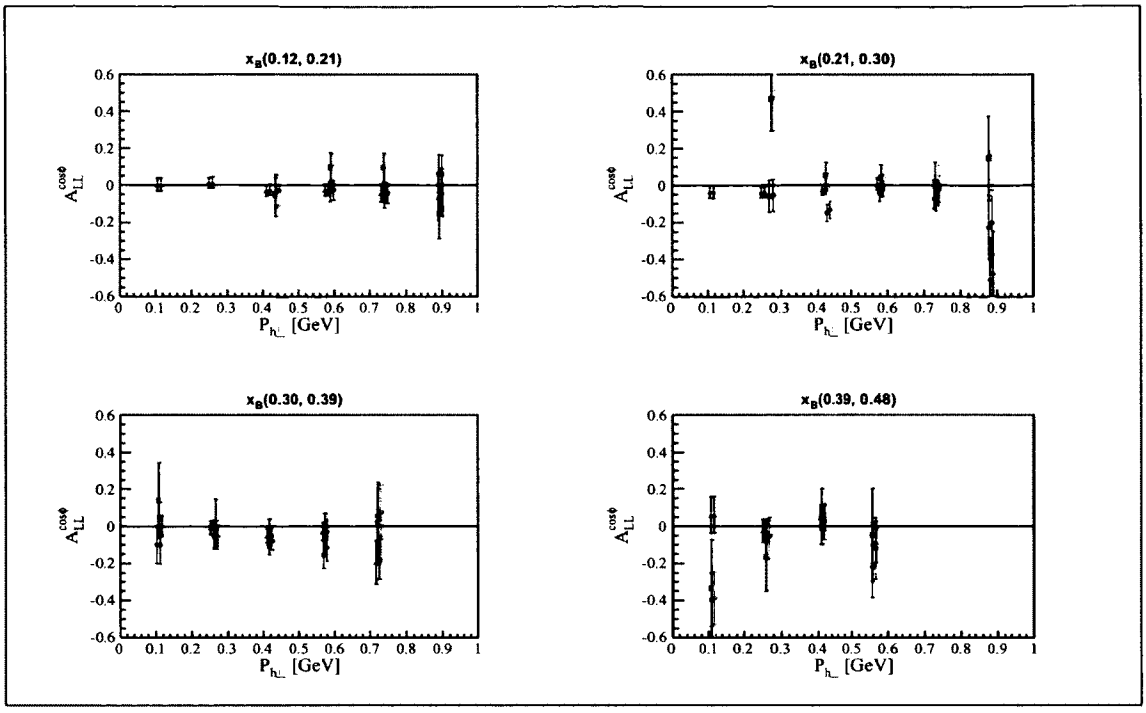

FIG. 256: Systematic uncertainty due to the uncertainty in the radiative corrections for $A_{LL}^{\cos\phi_h}(x_B, P_{h_\perp})$ on the proton; circles: π^+, squares:π^- triangles:π^0

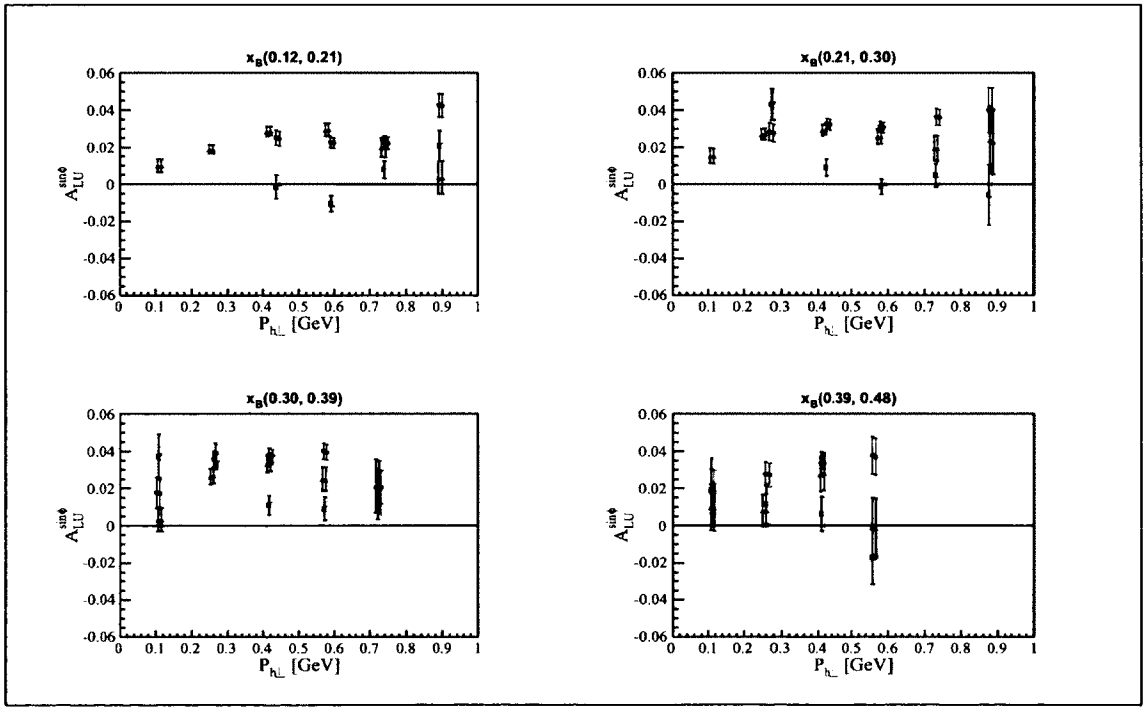

FIG. 257: Systematic uncertainty due to the uncertainty in the cosine terms of the unpolarized cross-section for $A_{LU}^{\sin\phi_h}(x_B, P_{h_\perp})$ on the proton; circles: π^+, squares:π^- triangles:π^0

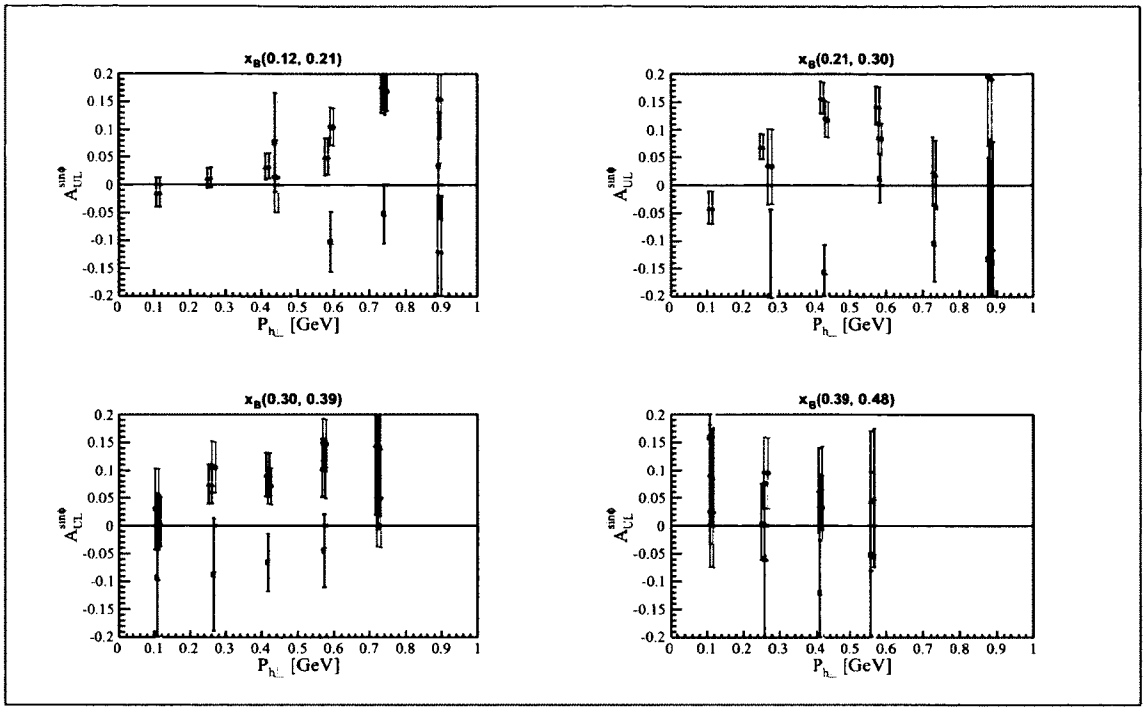

FIG. 258: Systematic uncertainty due to the uncertainty in the cosine terms of the unpolarized cross-section for $A_{UL}^{\sin\phi_h}(x_B, P_{h_\perp})$ on the proton; circles: π^+, squares:π^- triangles:π^0

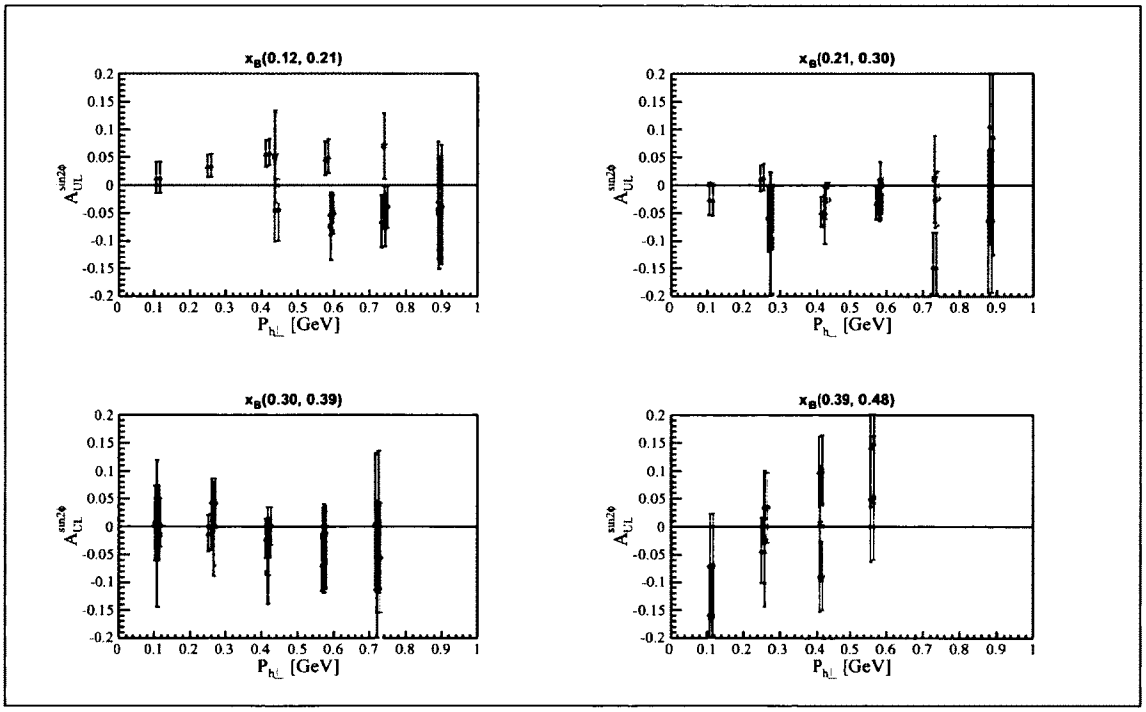

FIG. 259: Systematic uncertainty due to the uncertainty in the cosine terms of the unpolarized cross-section for $A_{UL}^{\sin 2\phi_h}(x_B, P_{h_\perp})$ on the proton; circles: π^+, squares:π^- triangles:π^0

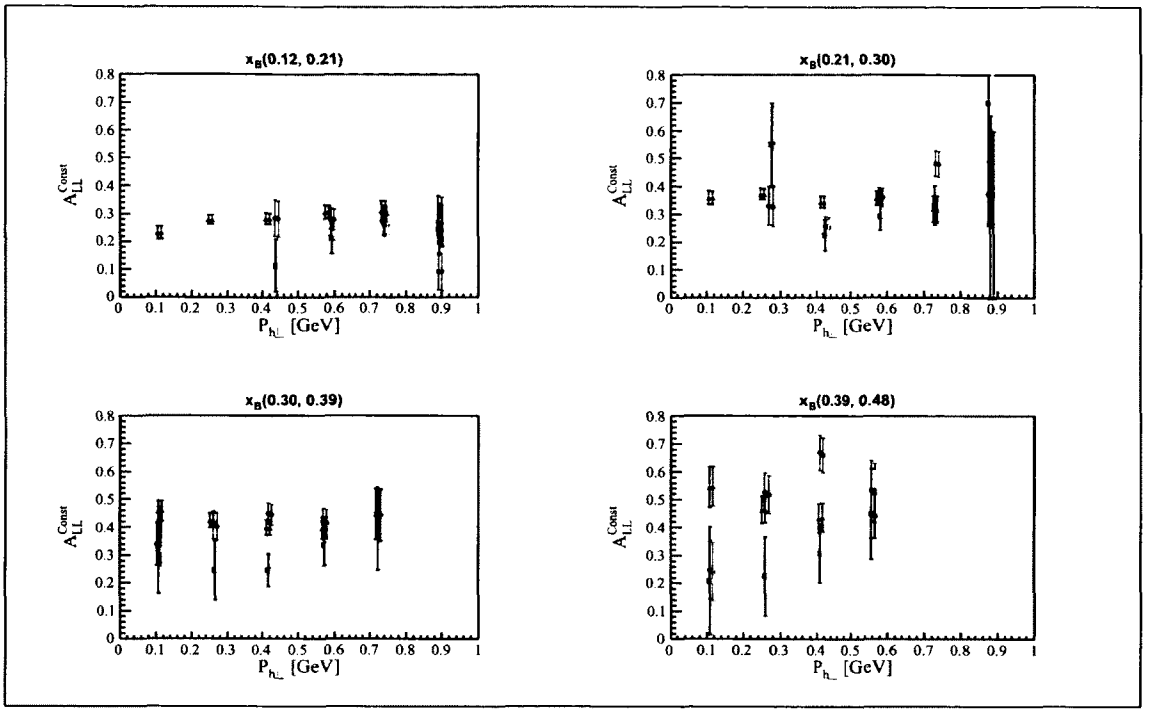

FIG. 260: Systematic uncertainty due to the uncertainty in the cosine terms of the unpolarized cross-section for $A_{LL}^{\text{Const}}(x_B, P_{h_\perp})$ on the proton; circles: π^+, squares:π^- triangles:π^0

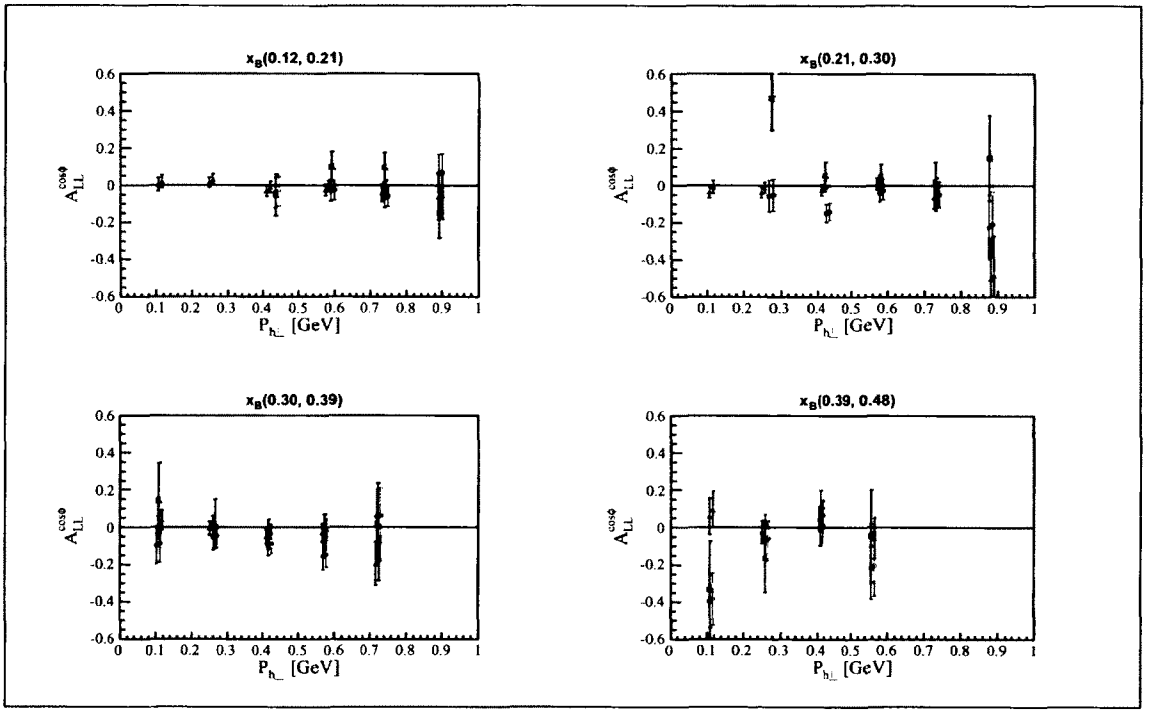

FIG. 261: Systematic uncertainty due to the uncertainty in the cosine terms of the unpolarized cross-section for $A_{LL}^{\cos\phi_h}(x_B, P_{h_\perp})$ on the proton; circles: π^+, squares:π^- triangles:π^0

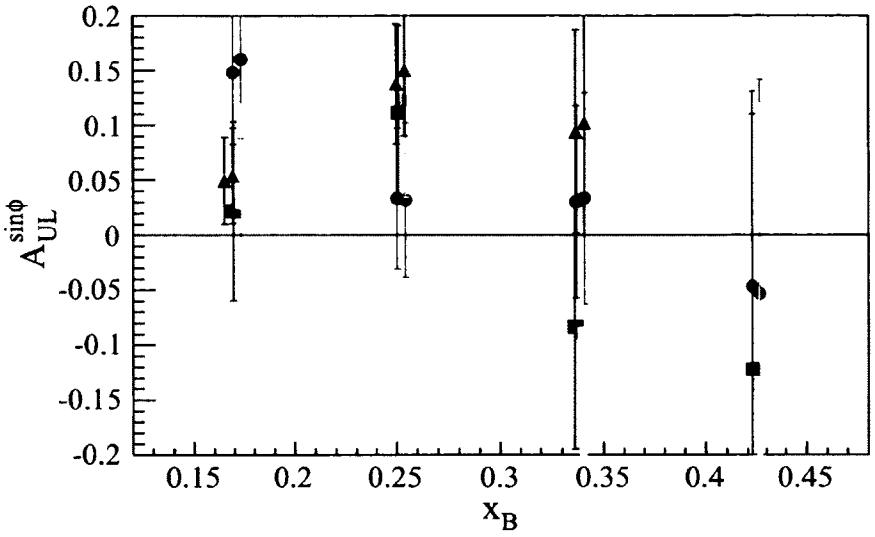

FIG. 262: Systematic uncertainty due to the uncertainty in beam and target polarizations for $A_{UL}^{\sin\phi_h}(x_B)$ on the deuteron; circles: π^+, squares: π^- and triangles: π^0

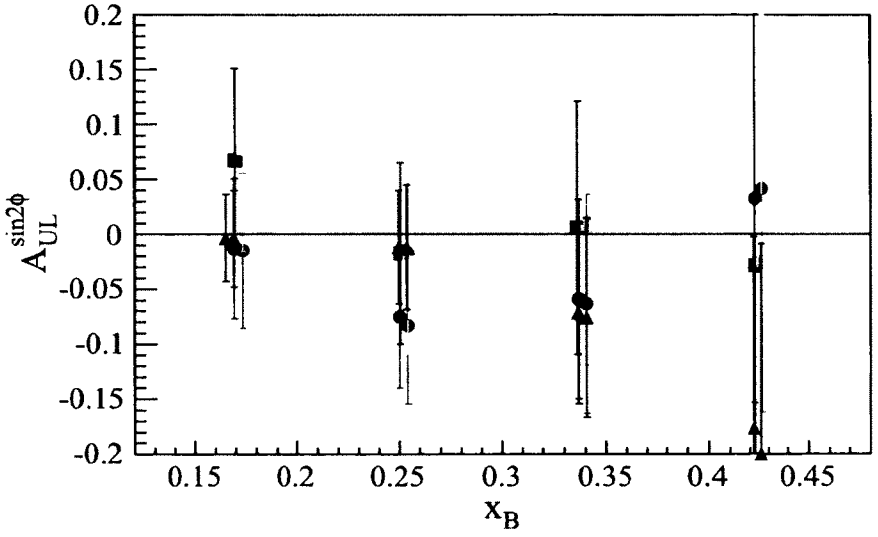

FIG. 263: Systematic uncertainty due to the uncertainty in beam and target polarizations for$A_{UL}^{\sin 2\phi_h}(x_B)$ on the deuteron; circles: π^+, squares: π^- and triangles: π^0

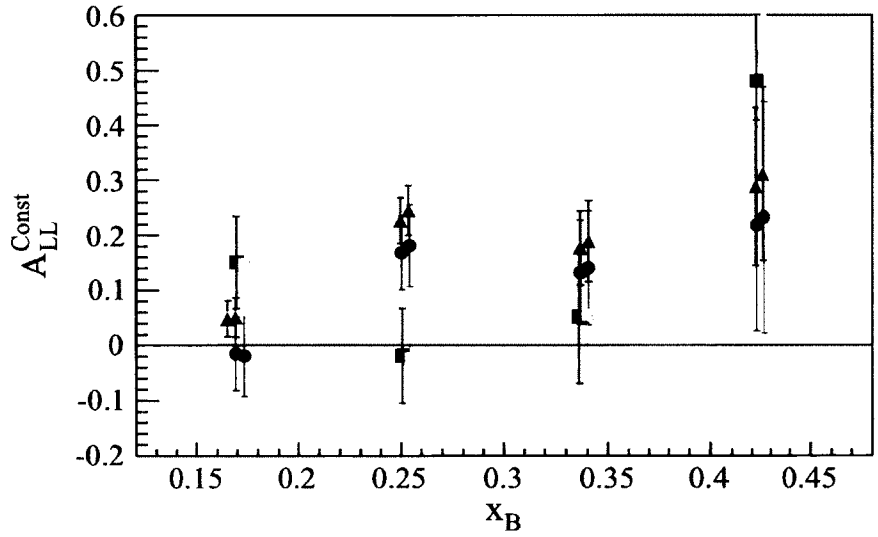

FIG. 264: Systematic uncertainty due to the uncertainty in beam and target polarizations for$A_{LL}^{\text{Const}}(x_B)$ on the deuteron; circles: π^+, squares: π^- and triangles: π^0

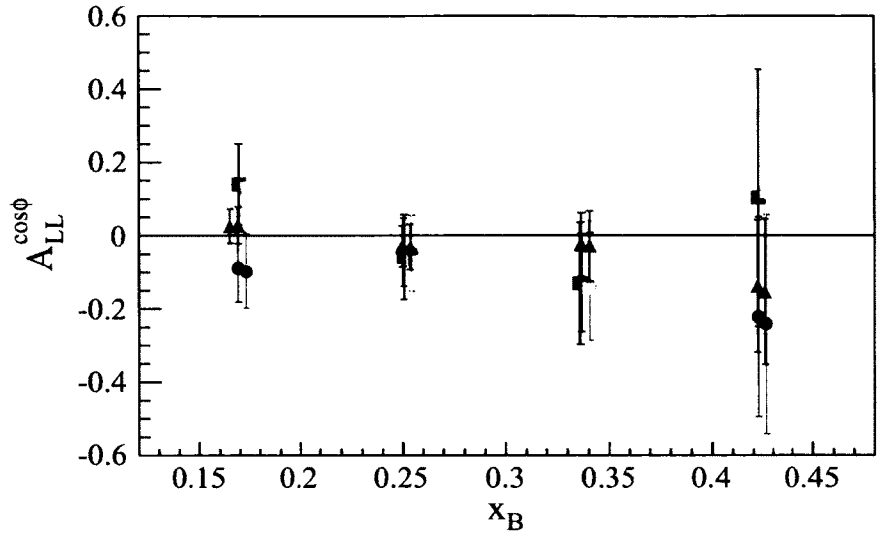

FIG. 265: Systematic uncertainty due to the uncertainty in beam and target polarizations for$A_{LL}^{\cos\phi_h}(x_B)$ on the deuteron; circles: π^+, squares: π^- and triangles: π^0

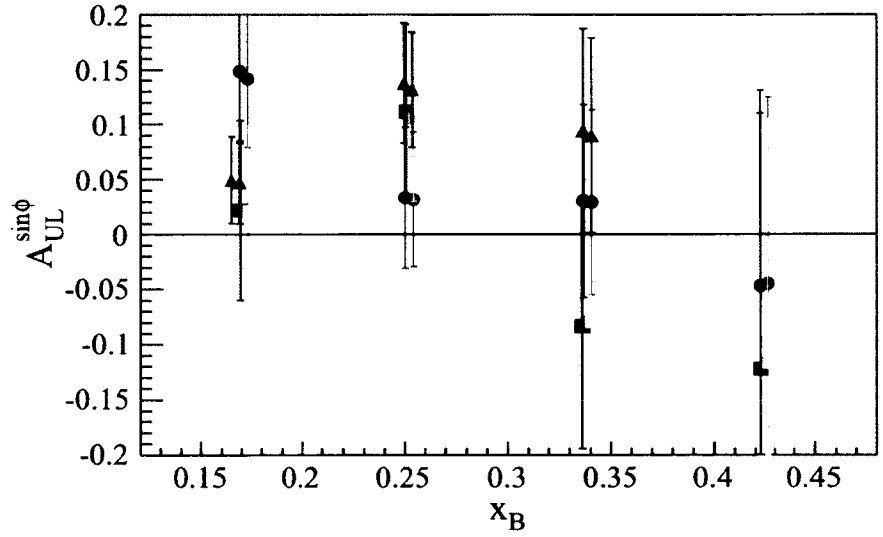

FIG. 266: Systematic uncertainty due to the uncertainty in the dilution factor, assuming 5% normalization uncertainty in EG2 π^0 data, for $A_{UL}^{\sin\phi_h}(x_B)$ on the deuteron; circles: π^+, squares: π^- and triangles: π^0

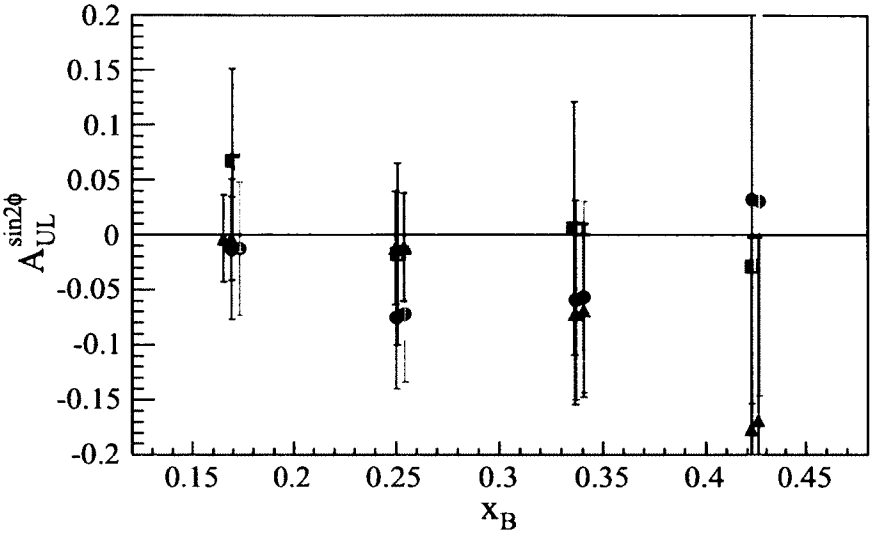

FIG. 267: Systematic uncertainty due to the uncertainty in the dilution factor, assuming 5% normalization uncertainty in EG2 π^0 data, for $A_{UL}^{\sin 2\phi_h}(x_B)$ on the deuteron; circles: π^+, squares: π^- and triangles: π^0

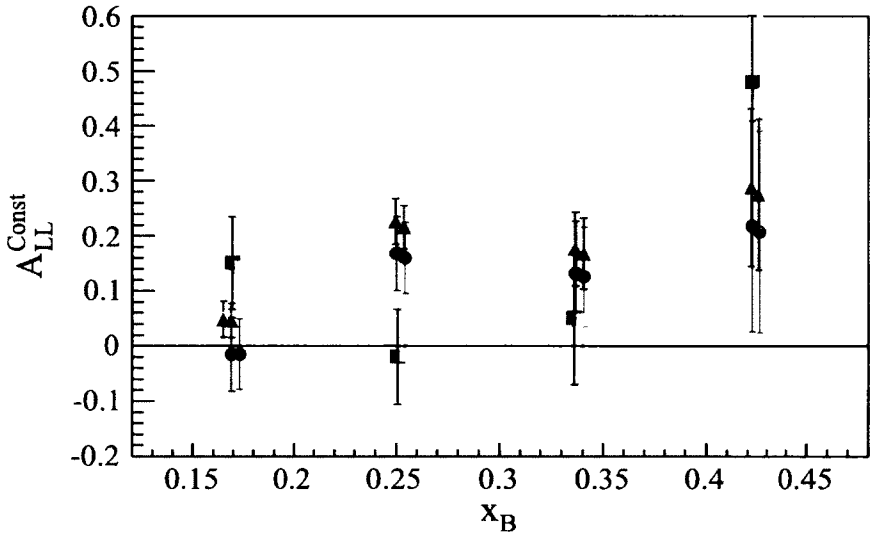

FIG. 268: Systematic uncertainty due to the uncertainty in the dilution factor, assuming 5% normalization uncertainty in EG2 π^0 data, for $A_{LL}^{\text{Const}}(x_B)$ on the deuteron; circles: π^+, squares: π^- and triangles: π^0

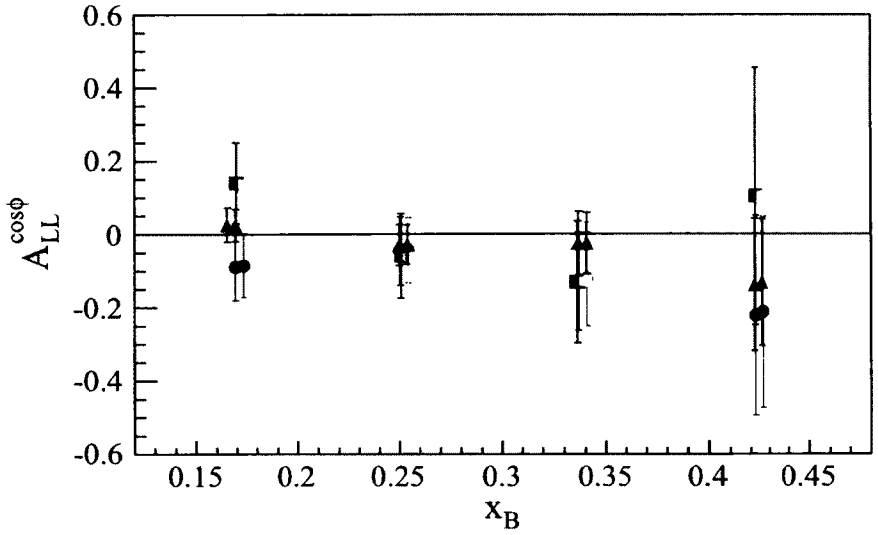

FIG. 269: Systematic uncertainty due to the uncertainty in the dilution factor, assuming 5% normalization uncertainty in EG2 π^0 data, for $A_{LL}^{\cos\phi_h}(x_B)$ on the deuteron; circles: π^+, squares: π^- and triangles: π^0

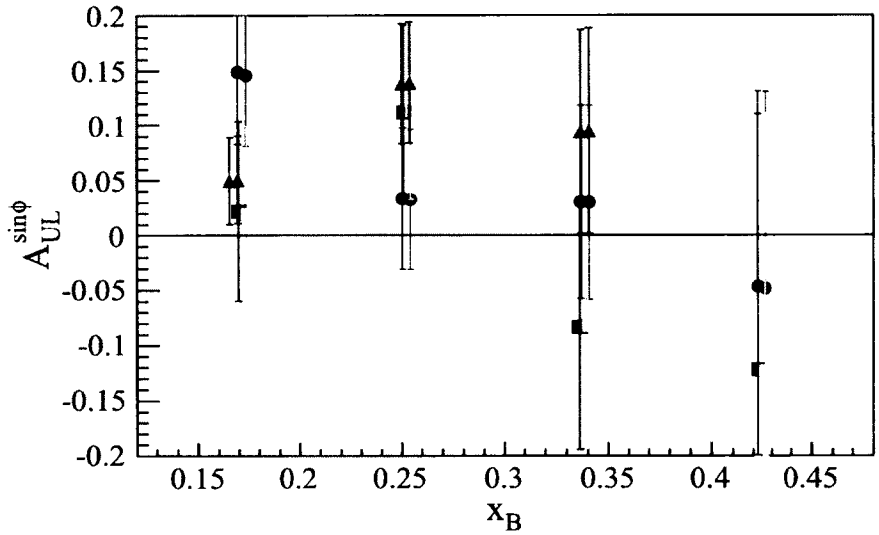

FIG. 270: Systematic uncertainty due to the uncertainty in the dilution factor, extracted with EG2 π^+data, for $A_{UL}^{\sin\phi_h}(x_B)$ on the deuteron; circles: π^+, squares: π^- and triangles: π^0

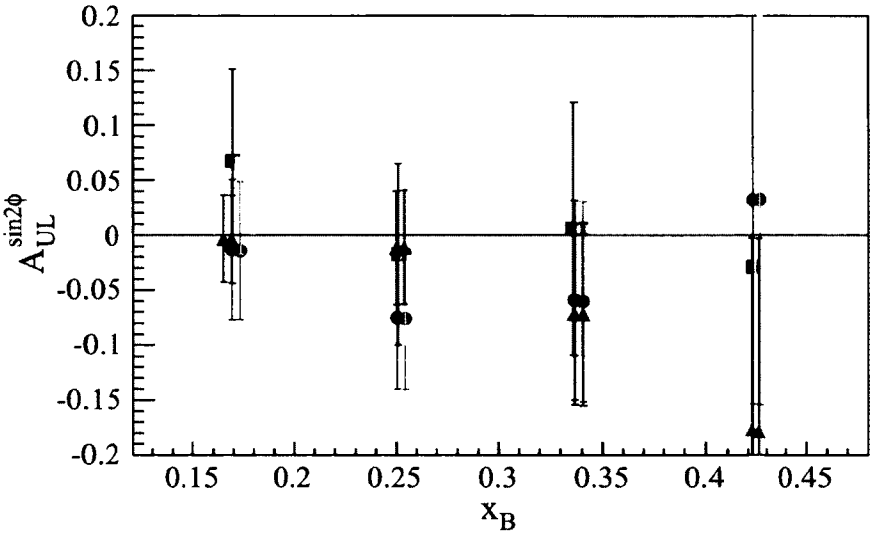

FIG. 271: Systematic uncertainty due to the uncertainty in the dilution factor, extracted with EG2 π^+data, for $A_{UL}^{\sin 2\phi_h}(x_B)$ on the deuteron; circles: π^+, squares: π^- and triangles: π^0

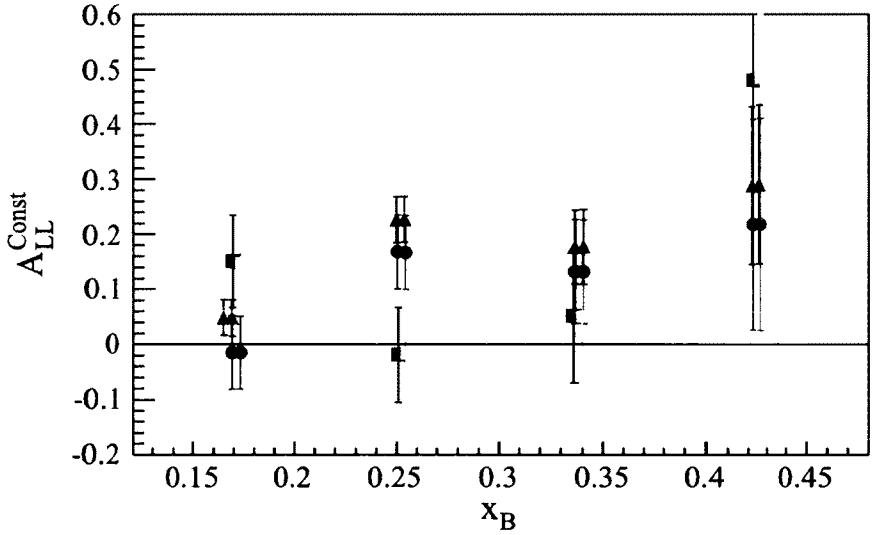

FIG. 272: Systematic uncertainty due to the uncertainty in the dilution factor, extracted with EG2 π^+data, for $A_{LL}^{\text{Const}}(x_B)$ on the deuteron; circles: π^+, squares: π^- and triangles: π^0

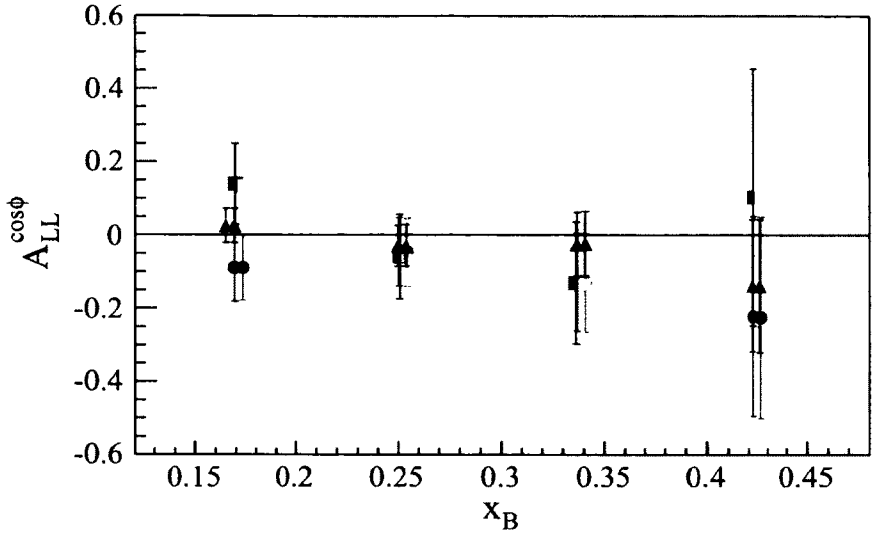

FIG. 273: Systematic uncertainty due to the uncertainty in the dilution factor, extracted with EG2 π^+data, for $A_{LL}^{\cos\phi_h}(x_B)$ on the deuteron; circles: π^+, squares: π^- and triangles: π^0

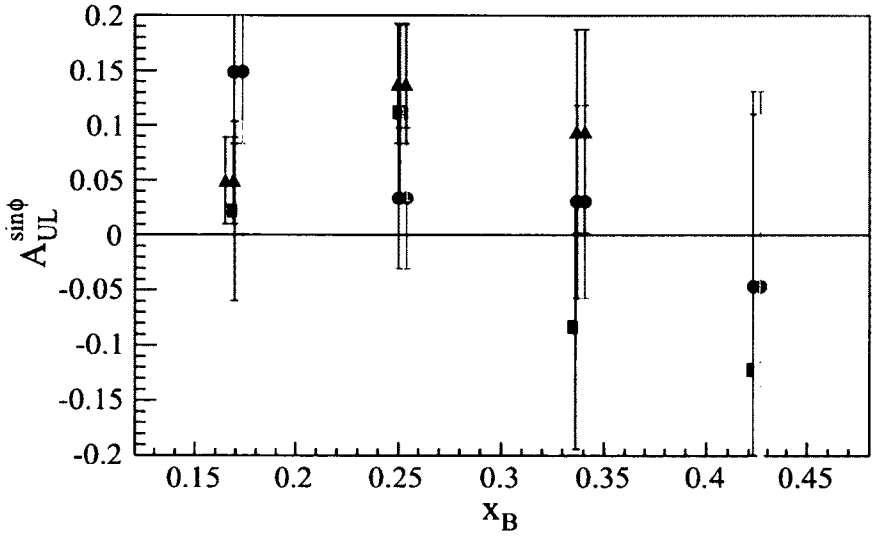

FIG. 274: Systematic uncertainty due to the uncertainty in the dilution factor, extracted with an alternative expression for the fragmentation ratio, for $A_{UL}^{\sin\phi_h}(x_B)$ on the deuteron; circles: π^+, squares: π^- and triangles: π^0

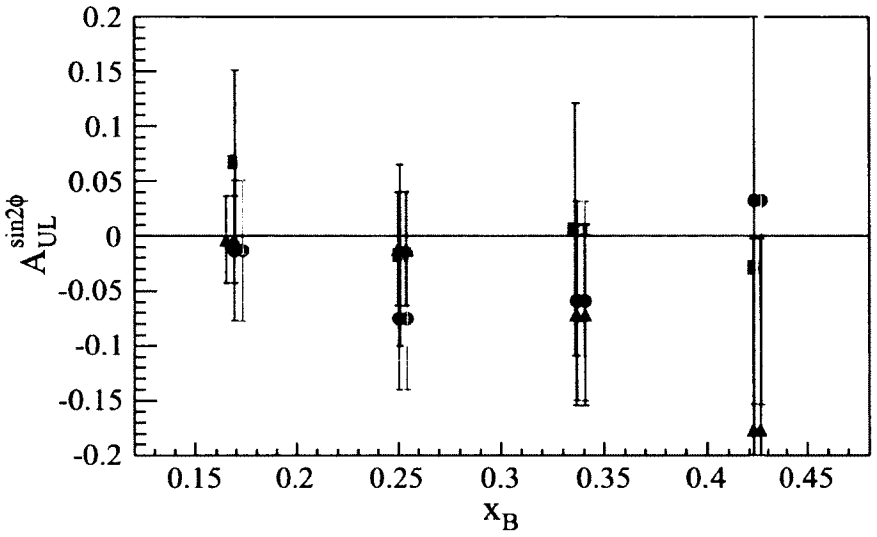

FIG. 275: Systematic uncertainty due to the uncertainty in the dilution factor, extracted with an alternative expression for the fragmentation ratio, for $A_{UL}^{\sin 2\phi_h}(x_B)$ on the deuteron; circles: π^+, squares: π^- and triangles: π^0

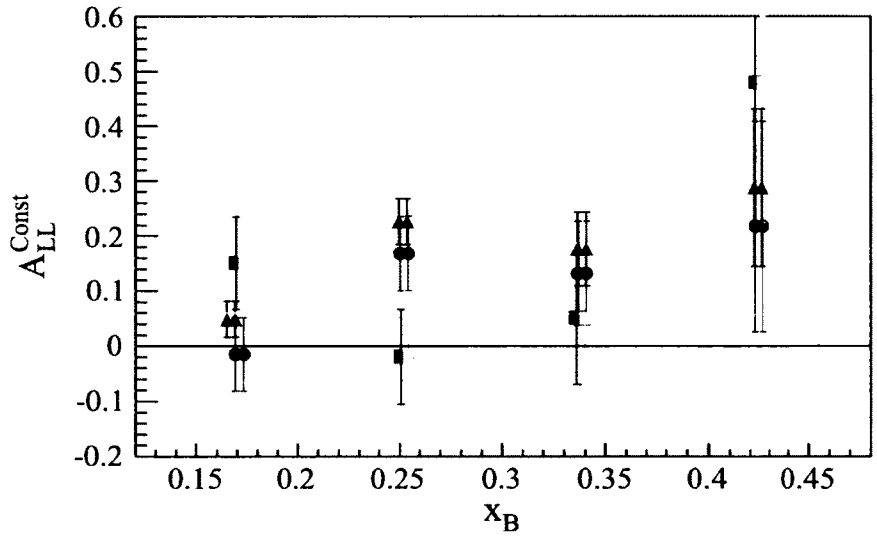

FIG. 276: Systematic uncertainty due to the uncertainty in the dilution factor, extracted with an alternative expression for the fragmentation ratio, for $A_{LL}^{\text{Const}}(x_B)$ on the deuteron; circles: π^+, squares: π^- and triangles: π^0

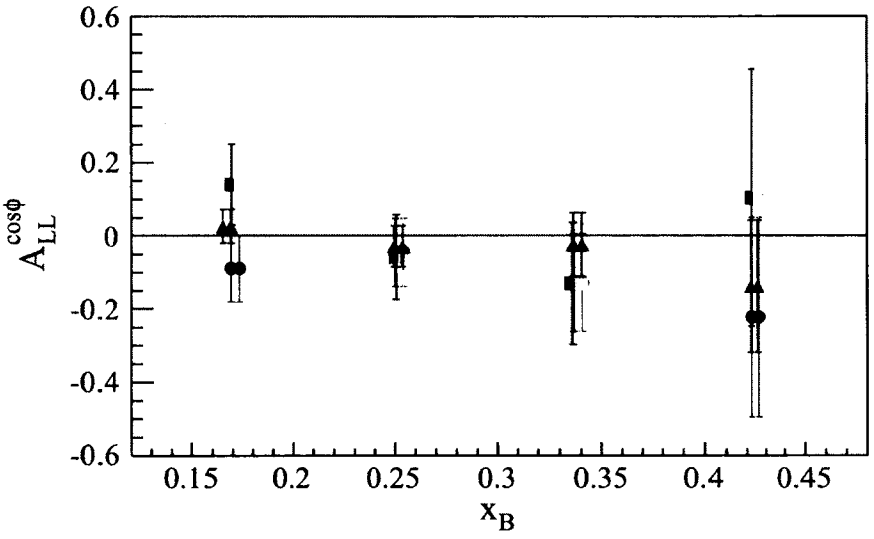

FIG. 277: Systematic uncertainty due to the uncertainty in the dilution factor, extracted with an alternative expression for the fragmentation ratio, for $A_{LL}^{\cos\phi_h}(x_B)$ on the deuteron; circles: π^+, squares: π^- and triangles: π^0

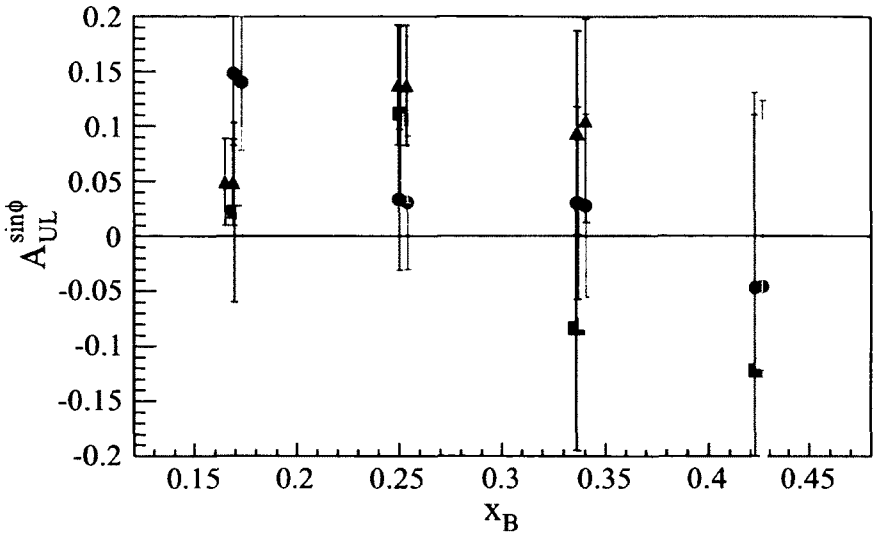

FIG. 278: Systematic uncertainty due to the uncertainty in the background subtraction for $A_{UL}^{\sin\phi_h}(x_B)$ on the deuteron; circles: π^+, squares: π^- and triangles: π^0

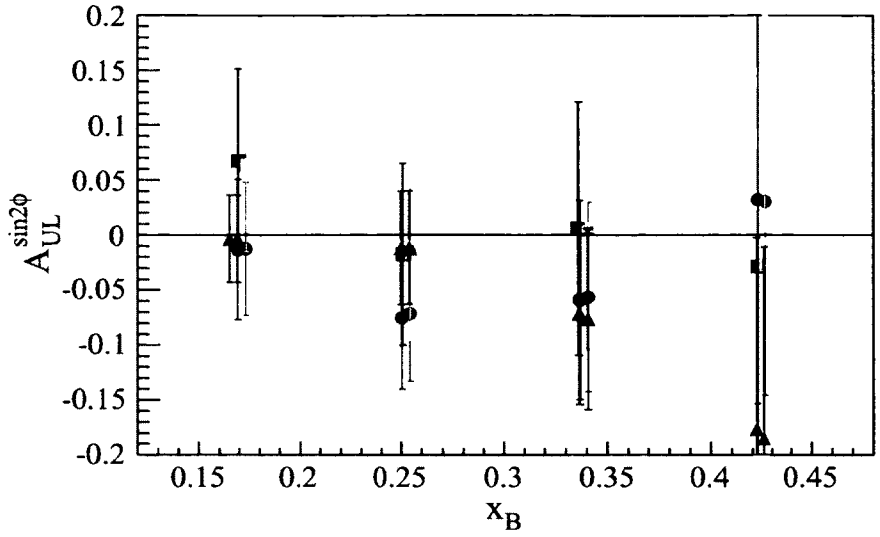

FIG. 279: Systematic uncertainty due to the uncertainty in the background subtraction for $A_{UL}^{\sin 2\phi_h}(x_B)$ on the deuteron; circles: π^+, squares: π^- and triangles: π^0

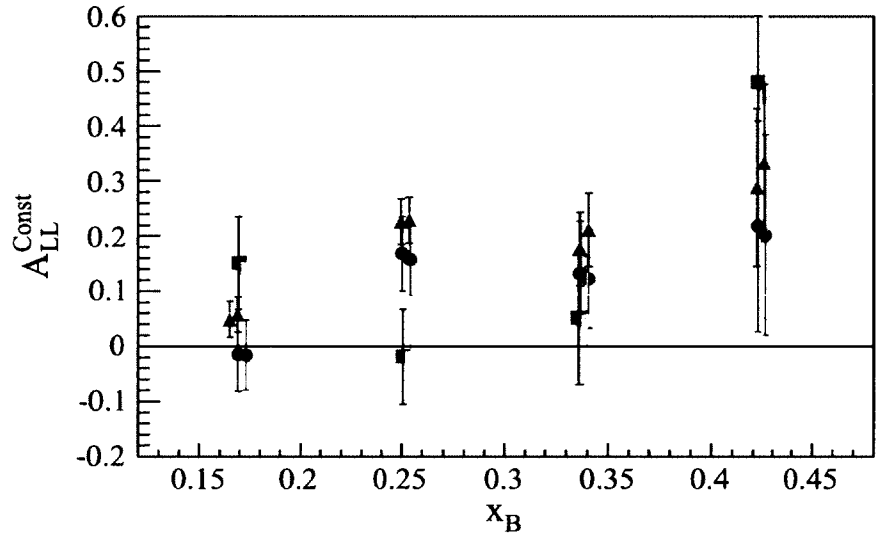

FIG. 280: Systematic uncertainty due to the uncertainty in the background subtraction for $A_{LL}^{\text{Const}}(x_B)$ on the deuteron; circles: π^+, squares: π^- and triangles: π^0

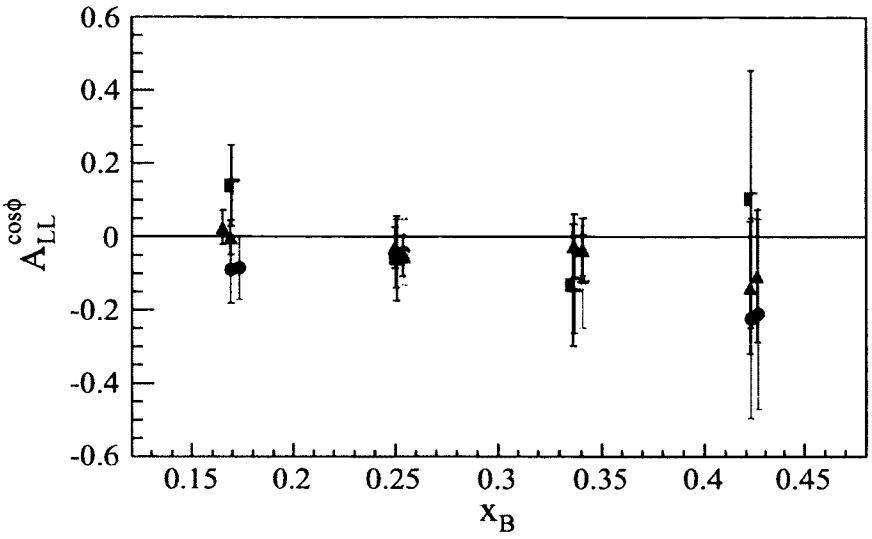

FIG. 281: Systematic uncertainty due to the uncertainty in the background subtraction for $A_{LL}^{\cos\phi_h}(x_B)$ on the deuteron; circles: π^+, squares: π^- and triangles: π^0

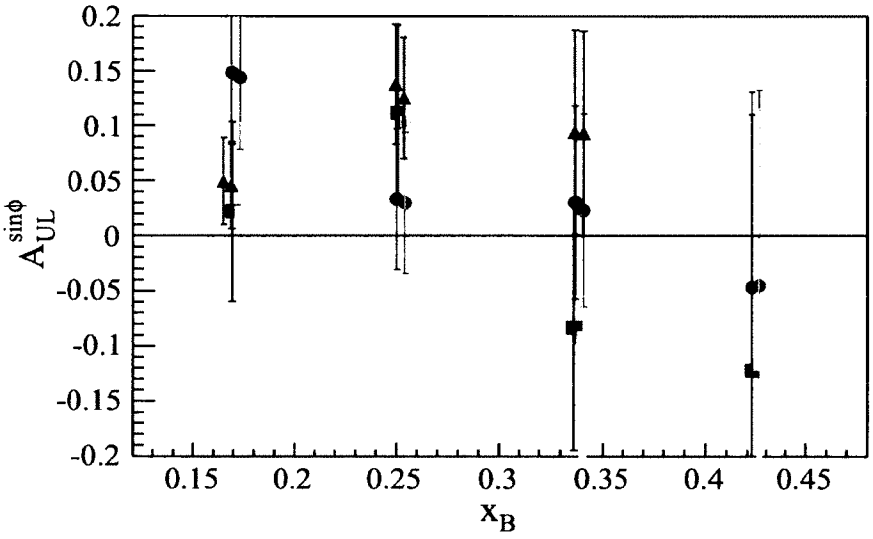

FIG. 282: Systematic uncertainty due to the uncertainty in the radiative correction for $A_{UL}^{\sin\phi_h}(x_B)$ on the deuteron; circles: π^+, squares: π^- and triangles: π^0

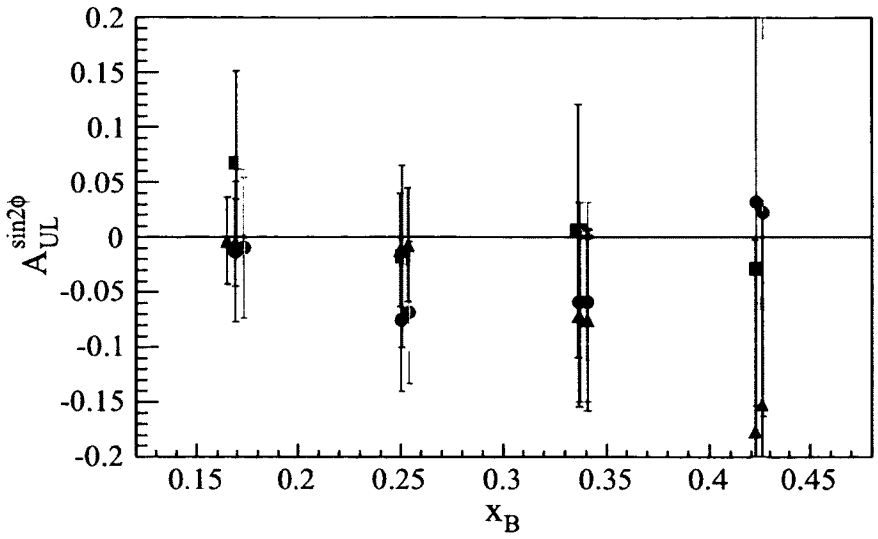

FIG. 283: Systematic uncertainty due to the uncertainty in the radiative correction for $A_{UL}^{\sin 2\phi_h}(x_B)$ on the deuteron; circles: π^+, squares: π^- and triangles: π^0

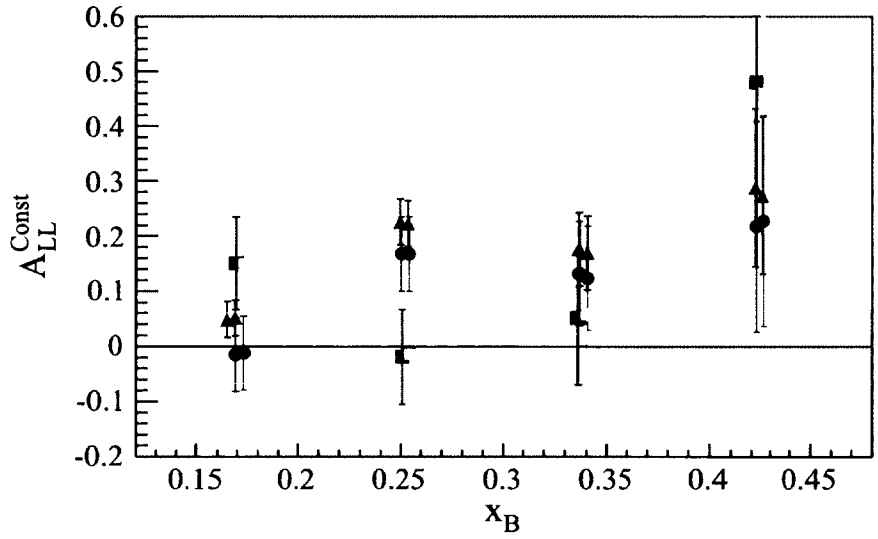

FIG. 284: Systematic uncertainty due to the uncertainty in the radiative correction for $A_{LL}^{\text{Const}}(x_B)$ on the deuteron; circles: π^+, squares: π^- and triangles: π^0

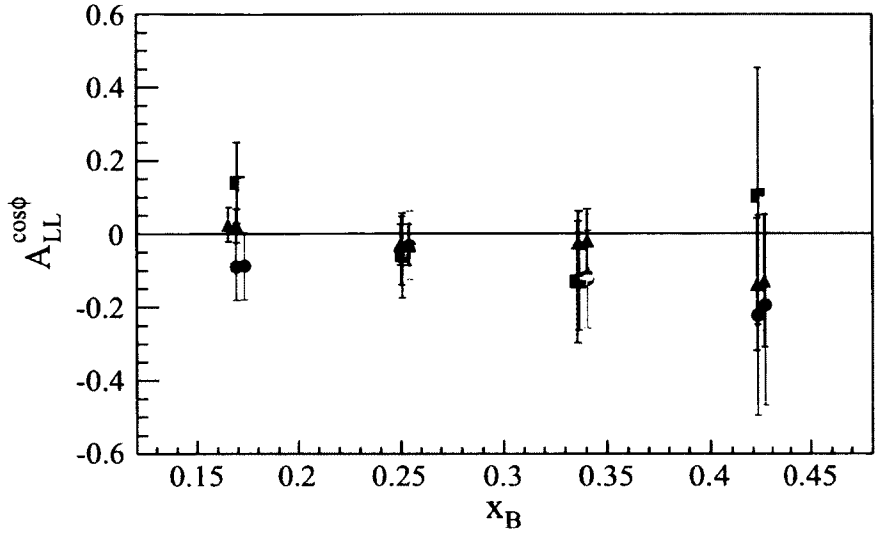

FIG. 285: Systematic uncertainty due to the uncertainty in the radiative correction for $A_{LL}^{\cos\phi_h}(x_B)$ on the deuteron; circles: π^+, squares: π^- and triangles: π^0

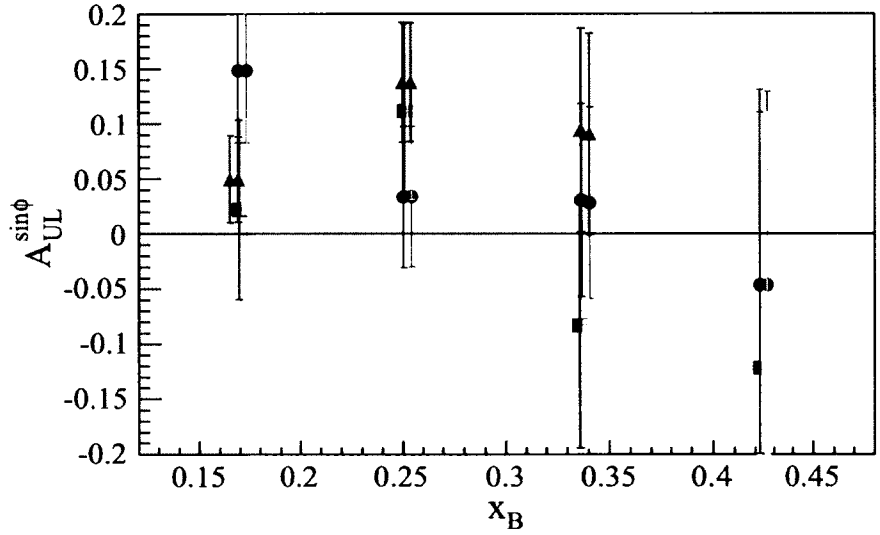

FIG. 286: Systematic uncertainty due to the uncertainty in the cosine terms of the unpolarized cross-section for $A_{UL}^{\sin\phi_h}(x_B)$ on the deuteron; circles: π^+, squares: π^- and triangles: π^0

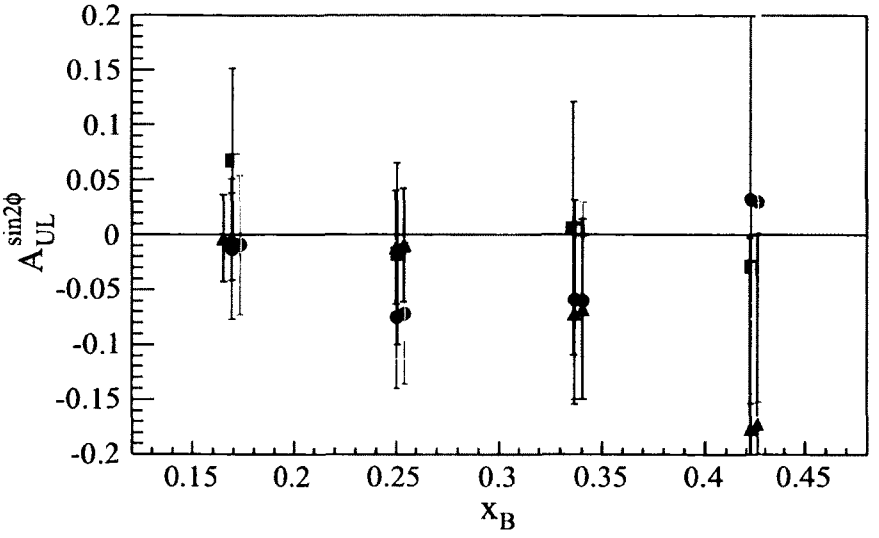

FIG. 287: Systematic uncertainty due to the uncertainty in the cosine terms of the unpolarized cross-section $A_{UL}^{\sin 2\phi_h}(x_B)$ on the deuteron; circles: π^+, squares: π^- and triangles: π^0

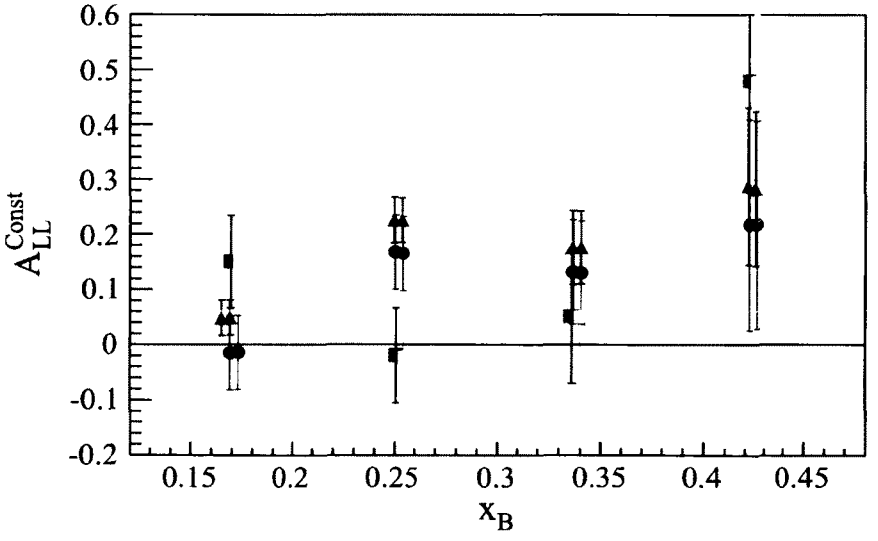

FIG. 288: Systematic uncertainty due to the uncertainty in the cosine terms of the unpolarized cross-section $A_{LL}^{\text{Const}}(x_B)$ on the deuteron; circles: π^+, squares: π^- and triangles: π^0

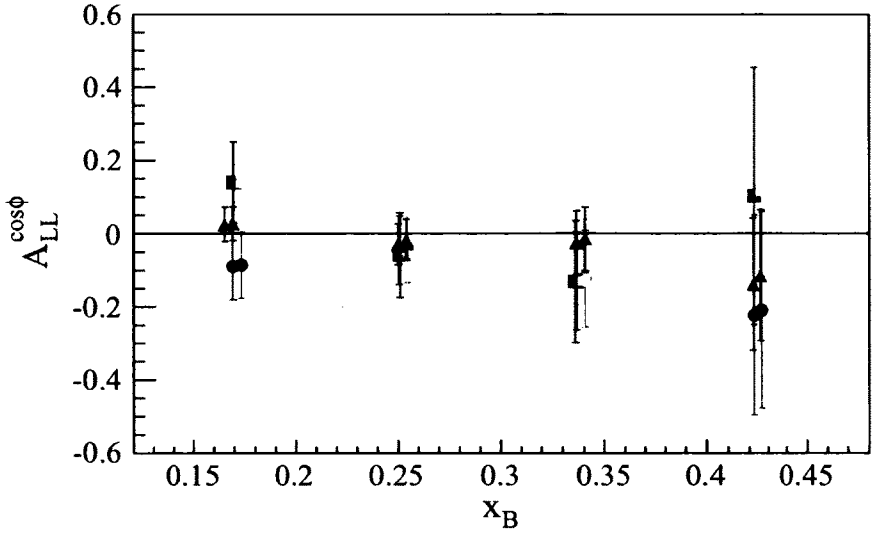

FIG. 289: Systematic uncertainty due to the uncertainty in the cosine terms of the unpolarized cross-section $A_{LL}^{\cos\phi_h}(x_B)$ on the deuteron; circles: π^+, squares: π^- and triangles: π^0

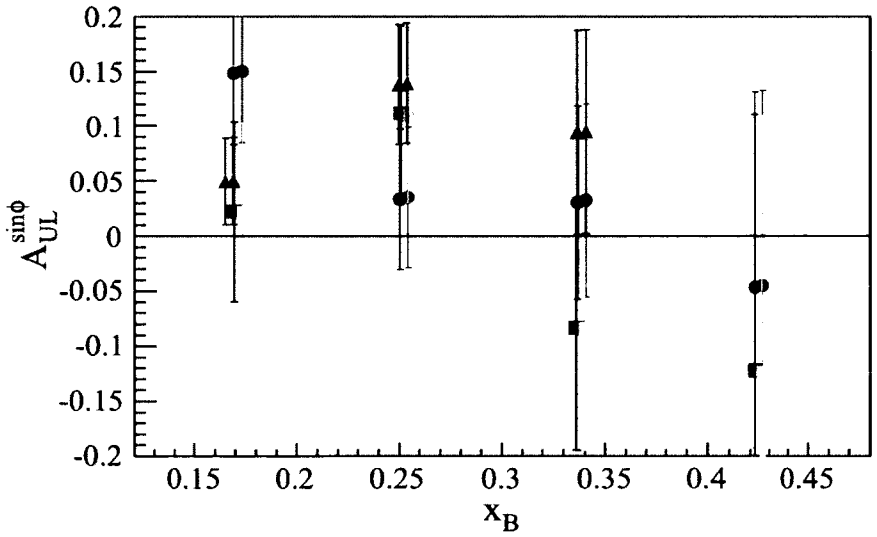

FIG. 290: Systematic uncertainty due to the uncertainty in the target contamination fraction for $A_{UL}^{\sin\phi_h}(x_B)$ on the deuteron; circles: π^+, squares: π^- and triangles: π^0

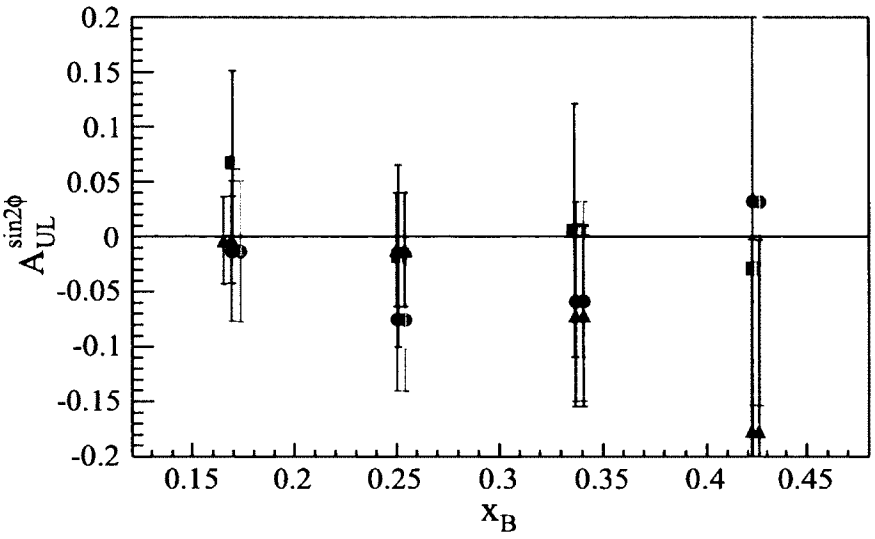

FIG. 291: Systematic uncertainty due to the uncertainty in the target contamination fraction for $A_{UL}^{\sin 2\phi_h}(x_B)$ on the deuteron; circles: π^+, squares: π^- and triangles: π^0

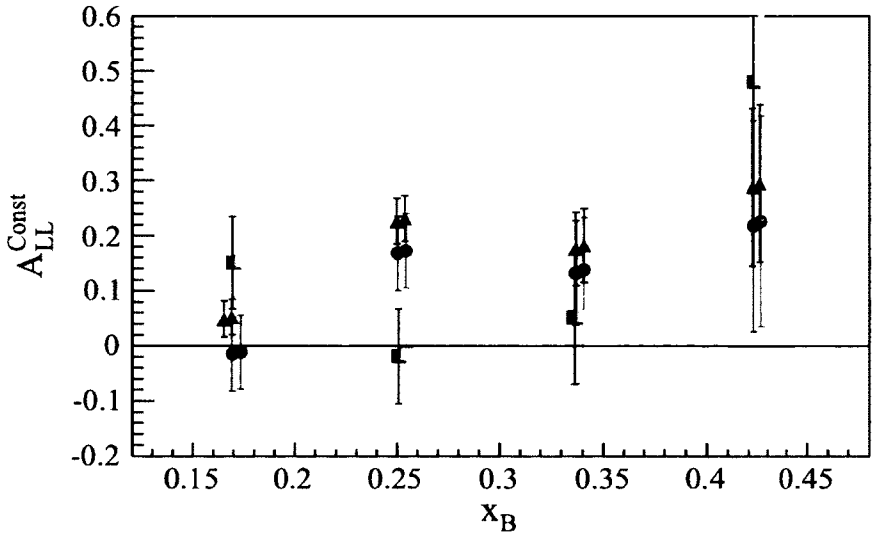

FIG. 292: Systematic uncertainty due to the uncertainty in the target contamination fraction for $A_{LL}^{\text{Const}}(x_B)$ on the deuteron; circles: π^+, squares: π^- and triangles: π^0

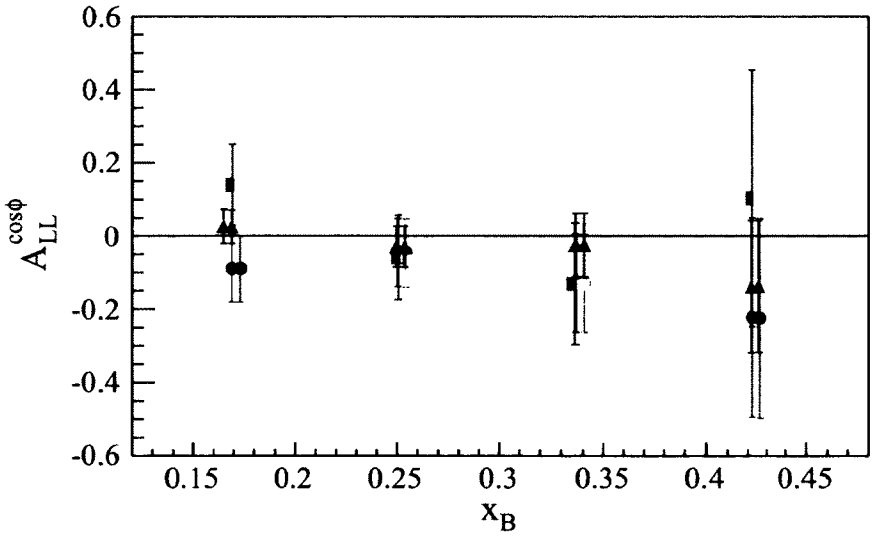

FIG. 293: Systematic uncertainty due to the uncertainty in the target contamination fraction for $A_{LL}^{\cos\phi_h}(x_B)$ on the deuteron; circles: π^+, squares: π^- and triangles: π^0

VITA

Suman Bandhu Koirala
Department of Physics
Old Dominion University
Norfolk, VA 23529

EDUCATION

- M.S. Physics, Old Dominion University, Norfolk, Virginia, USA, 2010
- M.Sc. Physics, Tribhuvan University, Kathmandu, Nepal, 2000
- B.Sc. Physical Science, Trichandra College, Kathmandu Nepal, 1998

PROFESSIONAL EXPERIENCE

- 2010 - Present: Research Assistant, Nuclear Physics Group, Old Dominion University, Norfolk VA
- 2008 - 2010: Teaching Assistant, Department of Physics, Old Dominion University, Norfolk VA
- 2006 - 2008: High School Physics Teacher, Lincoln High School, Kathmandu, Nepal
- 2003 - 2006: Part-time Physics Lecturer, Kathmandu University School of Science, Kavre, Nepal
- 2001 - 2006: High School Physics Teacher, Kathmandu University High School, Kavre, Nepal